

# 2015 Sensor Signal Processing for Defence (SSPD)

Edinburgh, UK  
9 – 10 September 2015



[SSPD 2015 Welcome](#)   [Poster Sessions](#)   [Keynote](#)   [Conference Committee](#)  
[Schedule](#)   [Speakers](#)   [TOC](#)   [Proceedings](#)



**IEEE Catalog Number:** CFP15SPD-ART (Xplore)  
**ISBN:** 978-1-4799-7444-3 (Xplore)

**IEEE Catalog Number:** CFP15SPD-USB (USB)  
**ISBN:** 978-1-4799-7443-6 (USB)

# 2015 Sensor Signal Processing for Defence (SSPD)

**Copyright © 2015 by the Institute of Electrical and Electronic Engineers, Inc.  
All rights reserved.**

## *Copyright and Reprint Permissions*

Abstracting is permitted with credit to the source. Libraries are permitted to photocopy beyond the limit of U.S. copyright law for private use of patrons those articles in this volume that carry a code at the bottom of the first page, provided the per-copy fee indicated in the code is paid through Copyright Clearance Center, 222 Rosewood Drive, Danvers, MA 01923.

For other copying, reprint or republication permission, write to IEEE Copyrights Manager, IEEE Service Center, 445 Hoes Lane, Piscataway, NJ 08854. All rights reserved.

IEEE Catalog Number: CFP15SPD-ART  
ISBN 15: 978-1-4799-7444-3

IEEE Catalog Number: CFP15SPD-USB  
ISBN 15: 978-1-4799-7443-6

## **Printed copies of this publication are available from:**

Curran Associates, Inc  
57 Morehouse Lane  
Red Hook, NY 12571 USA  
Phone: (845) 758-0400  
Fax: (845) 758-2633  
E-mail: [curran@proceedings.com](mailto:curran@proceedings.com)

Produced by IEEE eXpress Conference Publishing

For information on producing a conference proceedings and receiving an estimate, contact [conferencepublishing@ieee.org](mailto:conferencepublishing@ieee.org)  
<http://www.ieee.org/conferencepublishing>

# SSPD Conference 2015 - Welcome

---

Dear Colleagues,

We warmly welcome you to the 5<sup>th</sup> Sensor Signal Processing for Defence Conference (SSPD 2015). Held this year in Edinburgh at the prestigious Royal College of Physicians in Edinburgh's New Town on the **9th and 10th September 2015**, this event provides a chance to present and listen to the latest scientific findings in signal processing for defence.

We are privileged to have our two keynote speakers, Dr Branko Ristic from the Defence Science and Technology Organisation (DSTO) and Prof Penelope Endersby from the Defence Science and Technology Laboratory (Dstl). It is also with great pleasure we welcome our industrial and military speakers and all the researchers of scientific papers presenting their novel research through oral presentations and poster sessions. We look forward to some interesting debate and discussion during the day and also into the evening with our SSPD Dinner held at the Royal College of Physicians.

We hope you enjoy our conference.

Mike Davies  
Jonathon Chambers  
Paul Thomas

**Chairs, SSPD 2015**

---

Technical sponsorship is provided by the IEEE Signal Processing Society and the IEEE Aerospace and Electronic Systems Society. Proceedings will be submitted to the Xplore Digital Library. The conference is organised by the University Defence Research Collaboration (UDRC) in Signal Processing, sponsored by the Defence Science and Technology Laboratory (Dstl) and the Engineering and Physical Sciences Research Council (EPSRC).



# SSPD2015 Wednesday 9<sup>th</sup> September

---

8:45 **Registration and Refreshments**

9:15 **Welcome and opening** Mike Davies, University of Edinburgh

9:25 Plenary Keynote: **Signal Processing for CBR Defence**, Branko Ristic, DSTO

---

## Session 1: Target Tracking – Mike Davies, University of Edinburgh

---

10:25 1.1 **Sensor Management with Regional Statistics for the PHD Filter**, Marian Andrecki<sup>1</sup>, Emmanuel D. Delande<sup>1</sup>, Jeremie Houssineau<sup>1</sup> and Daniel E. Clark<sup>1</sup>, <sup>1</sup>Heriot-Watt University.

10:50 **Refreshments and Poster Session**

12:05 1.2 **Joint Navigation and Synchronization using SOOP in GPS-denied environments: Algorithm and Empirical Study**, Mei Leng<sup>1</sup>, François Quitin<sup>1</sup>, Chi Cheng<sup>1</sup>, Wee Peng Tay<sup>1</sup>, Sirajudeen Gulam Razul<sup>1</sup> and Chong Meng Samson See<sup>1</sup>, <sup>1</sup>Nanyang Technological University.

12:30 1.3 **Variational Bayesian PHD filter with Deep Learning Network Updating for Multiple Human Tracking**, Pengming Feng<sup>1</sup>, Wenwu Wang<sup>2</sup>, Syed Mohsen Naqvi<sup>3</sup>, Jonathon A. Chambers<sup>1</sup>, <sup>1</sup>Newcastle University, <sup>2</sup>University of Surrey, <sup>3</sup>Loughborough University.

12:55 **Lunch**

14:00 Plenary Keynote: **How Signal Processing Underpins Military Information Superiority**, Penelope Endersby, Dstl

---

## Session 2: Target Detection – Chair – Jonathon Chambers, Newcastle University

---

15:00 2.1 **GPU-Accelerated Gaussian Processes for Object Detection**, Calum Blair<sup>1</sup>, John Thompson<sup>1</sup> and Neil Robertson<sup>2</sup>, <sup>1</sup>University of Edinburgh, <sup>2</sup>Heriot-Watt University.

15:25 2.2 **Micro-Doppler based Recognition of Ballistic Targets using 2-D Gabor Filters**, Adriano Persico<sup>1</sup>, Carmine Clemente<sup>1</sup>, Christos V. Ilioudis<sup>1</sup>, Domenico Gaglione<sup>1</sup>, Jianlin Cao<sup>1</sup> and John J Soraghan<sup>1</sup>, <sup>1</sup>University of Strathclyde.

15:50 2.3 **Maximum Likelihood Signal Parameter Estimation via Track Before Detect**, Murat Uney<sup>1</sup>, Bernard Mulgrew<sup>1</sup> and Daniel E Clark<sup>2</sup>, <sup>1</sup>University of Edinburgh, <sup>2</sup>Heriot Watt University.

16:15 **Refreshments**

**16:30 3.1 Direction of Arrival Estimation Using a Cluster of Beams in a Cone-Shaped Digital Array Radar**, Micaela Contu<sup>1</sup>, Marta Bucciarelli<sup>1</sup>, Pierfrancesco Lombardo<sup>1</sup>, <sup>1</sup>University of Rome "La Sapienza".

**16:55 3.2 Low-Complexity Robust Adaptive Beamforming Algorithms Exploiting Shrinkage for Mismatch Estimation**, Hang Ruan<sup>1</sup>, Rodrigo C. de Lamare<sup>1,2</sup>, <sup>1</sup>University of York, <sup>2</sup>Pontifical Catholic University of Rio de Janeiro.

**17:20** Close and End of Day 1

**19:30 Wine Reception and Meal (Library and Great Hall, Royal College of Physicians)**

# SSPD2015 Thursday 10<sup>th</sup> September

---

8:30 **Registration and Refreshments**

---

**Session 4: Signal Processing Challenges – Military User Perspective - Chair, Paul Thomas, Dstl**

---

9:00 **MOD Speakers and Panel Discussion**

---

**Session 5: Underwater Acoustics – Chair – Yvan Petillot, Heriot-Watt University**

---

10:05 **5.1 Normalised Multi-Stage Clustering Equaliser for Underwater Acoustic Channels**, Rangeet Mitra<sup>1</sup> and Vimal Bhatia<sup>1</sup>, <sup>1</sup>Indian Institute of Technology Indore.

10:30 **5.2 Wideband CDMA waveforms for large MIMO sonar systems**, Yvan Petillot<sup>1</sup> and Yan Pailhas<sup>1</sup>, <sup>1</sup>Heriot-Watt University.

10:55 **Refreshments and Poster Session**

---

**Session 6: MIMO – Chair – Yvan Petillot, Heriot-Watt University**

---

12:10 **6.1 Performance Analysis of Polynomial Matrix SVD-based Broadband MIMO Systems**, Andre Sandmann<sup>1</sup>, Andreas Ahrens<sup>1</sup> and Steffen Lochmann<sup>1</sup>, <sup>1</sup>Hochschule Wismar.

12:35 **6.2 Low Complexity Parameter Estimation for Off-the-Grid Targets**, Seifallah Jardak<sup>1</sup>, <sup>1</sup>Sajid Ahmed and <sup>1</sup>Mohamed-Slim Alouini, <sup>1</sup>King Abdullah University of Science and Technology.

13:00 **Lunch**

---

**Session 7: Signal Processing Challenges – Industrial Perspective – Chair, Paul Thomas, Dstl**

---

14:00 **Industrial Speakers and Panel Discussion** Roke

Manor Research, ATLAS Elektronik UK, Mathworks

15:00 Refreshments

---

**Session 8: Synthetic Aperture Radar – Chair – John Soraghan, University of Strathclyde**

---

15:20 **8.1 Sparsity Based Ground Moving Target Imaging via Multi-Channel SAR**, Di Wu<sup>1</sup>, Mehrdad Yaghoobi<sup>1</sup> and Mike Davies<sup>1</sup>, <sup>1</sup>University of Edinburgh.

**15:40 8.2 A Location Scale Based CFAR Detection Framework for FOPEN SAR Images**, Marco Liguori<sup>1</sup>, Alessio Izzo<sup>1</sup> Carmine Clemente<sup>2</sup>, Carmela Galdi<sup>1</sup>, Maurizio Di Bisceglie<sup>1</sup> and John J Soraghan<sup>2</sup>,  
<sup>1</sup>University of Sannio, <sup>2</sup>University of Strathclyde.

16:10 Closing Remarks and End of Conference

# Poster Session - 9<sup>th</sup> September and 10<sup>th</sup> September

---

- P01 Velocity Estimation of moving ships using C-band SLC SAR data**, Andrea Radius<sup>1</sup>, Paulo Marques<sup>2</sup>, <sup>1</sup>Metasensing, Italy, <sup>2</sup>ISEL-IT Lisboa.
- P02 On the Target Detection in OFDM Passive Radar Using MUSIC and Compressive Sensing**, Watcharapong Ketpan<sup>1</sup>, Seksan Phonsri<sup>1</sup>, Rongrong Qian<sup>1</sup> and Mathini Sellathurai<sup>1</sup>, <sup>1</sup>Heriot-Watt University.
- P03 Radar Imaging With Quantized Measurements Based on Compressed Sensing**, Xiao Dong<sup>1</sup> and Yunhua Zhang<sup>1</sup>, <sup>1</sup>Chinese Academy of Sciences.
- P04 Traffic Scheduling Algorithm for Wireless Mesh Networks based Defense Networks Incorporating Centralized Scheduling Architecture**, Sidharth Shukla<sup>1</sup> and Vimal Bhatia<sup>1</sup>, <sup>1</sup>Indian Institute of Technology Indore.
- P05 Outage Analysis of OFDM based AF Cooperative Systems in Selection Combining Receiver over Nakagami-m fading Channels with Nonlinear Power Amplifier**, Nagendra Kumar<sup>1</sup> and Vimal Bhatia<sup>1</sup>, <sup>1</sup>Indian Institute of Technology Indore, India.
- P06 A Novel Self Localization Approach for Sensors**, Serap Karagol<sup>1</sup>, Dogan Yildiz<sup>1</sup>, Okan Ozgonenel<sup>1</sup>, Marwan Bikdash<sup>2</sup> and Satish Tadiparthi<sup>3</sup>, <sup>1</sup>Ondokuz Mayıs University, <sup>2</sup>North Carolina Agricultural and Technical State University, <sup>3</sup>Prolifics New York.
- P07 Quadrature Filters for Underwater Passive Bearings-Only Target Tracking**, Rahul Radhakrishnan<sup>1</sup>, Abhinoy Kumar Singh<sup>1</sup>, Shovan Bhaumik<sup>1</sup> and Nutan Tomar<sup>1</sup>, <sup>1</sup>Institute of Technology Patna.
- P08 Fusion of Radar and Secondary Sensor Data Using Kinematic Models of Multiple Simultaneous Targets**, Brian Karlsen<sup>1</sup>, Esben Nielsen<sup>1</sup> and Morten Pedersen<sup>1</sup>, <sup>1</sup>Terma A/S Denmark.
- P09 Improved High-Degree Cubature Kalman Filter**, Abhinoy Kumar Singh<sup>1</sup> and Shovan Bhaumik<sup>1</sup>, <sup>1</sup>Indian Institute of Technology Patna.
- P10 Shortening of Paraunitary Matrices Obtained by Polynomial Eigenvalue Decomposition Algorithms**, Jamie Corr<sup>1</sup>, Keith Thompson<sup>1</sup>, Stephan Weiss<sup>1</sup>, Ian Proudler<sup>2</sup> and John G McWhirter<sup>3</sup>, <sup>1</sup>University of Strathclyde, <sup>2</sup>Loughborough University, <sup>3</sup>Cardiff University.

**P11 Observing the Dynamics of Waterborne Pathogens for Assessing the Level of Contamination**, Isabella McKenna<sup>1</sup>, Francesco Tonolini<sup>1</sup>, Rachael Tobin<sup>1</sup>, Jeremie Houssineau<sup>1</sup>, Helen Bridle<sup>1</sup>, Craig McDougall<sup>2</sup>, Isabel Schlangen<sup>1</sup>, John S. McGrath<sup>1</sup> and Melanie Jimenez<sup>1</sup>, Daniel E. Clark<sup>1</sup>, <sup>1</sup>Heriot Watt, <sup>2</sup>University of Dundee.

**P12 Distributed Implementation for Person Re-identification**, Saurav Sthapit<sup>1</sup> and John Thompson<sup>1</sup>, James R Hopgood<sup>1</sup> and Neil Robertson<sup>2</sup>, <sup>1</sup>University of Edinburgh, <sup>2</sup>Heriot-Watt University.

**P13 Extraction of Pulse Repetition Interval Based on Incomplete, Noisy TOA Measurements by the Moving Passive Receiver**, Liu Yang<sup>1</sup>, Fucheng Guo<sup>1</sup>, Zhang Min<sup>1</sup> and Wenli Jiang<sup>1</sup>, <sup>1</sup>National University of Defense Technology China.

**P14 Removing Speckle Noise by Analysis Dictionary Learning**, Jing Dong<sup>1</sup>, Wenwu Wang<sup>1</sup> and Jonathon Chambers<sup>2</sup>, <sup>1</sup>University of Surrey, <sup>2</sup>Newcastle University.

**P15 Link-by-Link Coded Physical Layer Network Coding on Impulsive Noise Channels**, Yuanyi Zhao<sup>1</sup>, Martin Johnston<sup>1</sup>, Charalampos C. Tsimenidis<sup>1</sup> and Li Chen<sup>2</sup>, <sup>1</sup>Newcastle University, <sup>2</sup>Sun Yat-sen University.

**P16 A New Asymmetric Correlation Kernel for GNSS Multipath Mitigation**, Steven Miller<sup>1</sup>, Xue Zhang<sup>1</sup> and Andreas Spanias<sup>1</sup>, <sup>1</sup>Arizona State University.

**P17 Fractional Cosine Transform (FrCT)-Turbo based OFDM for Underwater Acoustic Communication**, Yixin Chen<sup>1</sup>, Carmine Clemente<sup>1</sup>, John J Soraghan<sup>1</sup> and Stephan Weiss<sup>1</sup>, <sup>1</sup>University of Strathclyde.

**P18 Practical Identification of Specific Emitters used in the Automatic Identification System**, Takashi Iwamoto<sup>1</sup>, <sup>1</sup>Mitsubishi Electric Corporation.

# Keynote Speakers

---

## Dr Branko Ristic

### Signal Processing for CBR Defence Abstract

CBR defence comprises collective measures against a chemical (C), biological (B) or radiological (R) attack. This talk will focus on statistical signal processing and data fusion algorithms for CBR defence. In particular, it will cover: autonomous search techniques for localisation of sources of (deliberate or accidental) release of CB agents in unknown structured environment; the search for sources of gamma radiation; parametric RMS gamma-ray image reconstruction; source term estimation in turbulent flow using binary sensors; forecasting of epidemic outbreaks; evolutionary dynamics with forecasting the event of extinction.

### Biography



Branko Ristic received all degrees in electrical engineering: Ph.D. from Queensland University of Technology (QUT) in 1995, M.Sc. from Belgrade University in 1991, and B. Eng. from The University of Novi Sad in 1984. He held various research/engineering positions until he joined in 1996 the Defence Science and Technology Organisation (DSTO), where he stayed until present. His role in DSTO has been to carry out research, develop new capabilities and provide technical advice related to signal processing and sensor fusion. Dr Ristic co-authored two books (Beyond the Kalman filter: Particle filters for tracking applications, Artech House, 2004 and Particle filters for Random Set Models, Springer, 2013), and publisher over 70 journal articles. He presented several invited talks, numerous short courses and tutorials. He was the Chair of the 4th Australian Data Fusion Symposium in 2007. Since 2013 he an Associate Editor of IEEE Trans. Signal Processing. He won several awards for his papers (Information Fusion conference in 2005, 2010; DICTA conference in 2005, 2009; IET RSN Premium Award in 2014).

# Prof Penelope Endersby

## How Signal Processing Underpins Military Information Superiority Abstract

The Military has a number of critical challenges for information superiority, resulting from global changes such as the transforming character of warfare and conflict, the rapid onset of the “information age” and the ever-present downward pressure on spending. Military information superiority, i.e. the ability to out-sense, out-process and out-think our adversaries, is a critical competitive advantage but one that is becoming increasingly difficult to maintain. Trends such as novel information age threats, ubiquity of information and changes to the operating environment create astonishing challenges for the Military. However, at a fundamental level the technical problem remains the same: extraction of useful, timely information from ‘signals’, in their widest form.

This presentation discusses the nature of military signal processing and how it has, in the past, and can, in the future, support military information superiority. Prof. Endersby discusses global trends and the impact they will have on military requirements for signal processing, and how opportunities exist if we exploit the convergence of military and civilian signal processing developments.

## Biography



Penny studied Natural Sciences at Cambridge University and joined DRA (a Dstl predecessor) as a scientist in 1993 after two years doing materials science research with British Gas. She spent ten years researching novel armours for fighting vehicles, becoming the national expert on electric armours and working closely with peers in the US. She then led groups of physicists including Dstl’s capabilities on Materials Science, Acoustics, Power Sources, CBRN hazard prediction and impact physics, before becoming head of Physical Sciences Department in 2009. In 2012 after a short secondment leading Dstl’s Safety and Estates function she became Head of Information Management Department with responsibility for 270 staff engaged on information superiority (cyber and C4ISTAR) research and human sciences. Penny holds a Royal Academy of Engineering visiting Professorship at the University of Southampton and is a fellow and former member of the governing council of the Institute of Physics. She became division head of the expanded Cyber and Information Systems Division in April 2015, with 400 staff and a £120M annual programme of research both in house and in industry and academia.

# SSPD Conference Committee

---

## **General Chairs**

Mike Davies – University of Edinburgh

Jonathon Chambers – Loughborough University

Paul Thomas – Dstl

## **Publicity and Local Arrangements Chair**

Janet Forbes – University of Edinburgh

## **Technical Programme Committee**

Professor Yvan Petillot, Heriot-Watt University

Professor John Soraghan, University of Strathclyde

Professor Bernard Mulgrew, University of Edinburgh

Professor John Thompson, University of Edinburgh

Dr. Neil Robertson, Heriot-Watt University

Dr. James Hopgood, University of Edinburgh

Dr. Daniel Clark - Heriot-Watt University

Professor Andrew Wallace - Heriot-Watt University

Dr. Mathini Sellathurai - Heriot-Watt University

Professor David Parish - Loughborough University

Professor Sangarapillai Lambothoran- Loughborough University

Professor Ian Proudler - Loughborough University

Professor Wen-Hua Chen - Loughborough University

Dr. Wenwu Wang - University of Surrey

Professor Josef Kittler - University of Surrey

Dr. Philip Jackson - University of Surrey

Dr. Stephan Weiss - University of Strathclyde

Dr. Carmine Clemente - University of Strathclyde

Professor John McWhirter - Cardiff University

Professor Stephen McLaughlin - Heriot-Watt University

Professor Ayre Nehorai - Washington University

Professor Danilo Mandic - Imperial College London

Professor Maria S. Greco - University of Pisa  
Dr. Keith Brown - Heriot-Watt University  
Dr. Rodrigo C. de Lamare - University of York  
Professor Andreas Spanias - Arizona State University  
Professor Randy Moses - Ohio State University  
Dr. Vaughan Clarkson - University of Queensland  
Dr. Mahesh K. Banavar - Clarkson University  
Dr. Brian Sadler - Army Research Laboratory  
Professor Chris Baker - Ohio State University  
Professor William Moran - University of Melbourne  
Professor Douglas Cochran - Arizona State University  
Xue Zhang - Arizona State University  
Alan Wisler - Arizona State University  
Neil Cade - Selex ES  
Andy Stove - Thales UK  
Neil Gordon - DSTO  
Dave Nethercott - Dstl  
Jordi Barr - Dstl  
Brian Barber - Dstl  
Gary Heald - Dstl  
Steve Moore - Dstl



## Table of Contents

<b>Sensor Management with Regional Statistics for the PHD Filter</b> .....	1
<i>Marian Andrecki, Emmanuel D. Delande, Jeremie Houssineau, and Daniel E. Clark</i>	
<b>Joint Navigation and Synchronization Using SOOP in GPS-denied Environments: Algorithm and Empirical Study</b> .....	6
<i>Mei Leng, Sirajudeen Gulam Razul, Chong Meng Samson See, Francois Quitin, Chi Cheng, and Wee Peng Tay</i>	
<b>Variational Bayesian PHD Filter with Deep Learning Network Updating for Multiple Human Tracking</b> .....	11
<i>Pengming Feng, Wenwu Wang, Syed Mohsen Naqvi, and Jonathon A. Chambers</i>	
<b>GPU-Accelerated Gaussian Processes for Object Detection</b> .....	16
<i>Calum Blair, John Thompson, and Neil M. Robertson</i>	
<b>Micro-Doppler Based Recognition of Ballistic Targets Using 2D Gabor Filters</b> .....	21
<i>Adriano Rosario Persico, Carmine Clemente, Christos V. Ilioudis, Domenico Gaglione, Jianlin Cao, and John Soraghan</i>	
<b>Maximum Likelihood Signal Parameter Estimation via Track Before Detect</b> .....	26
<i>Murat Uney, Bernard Mulgrew, and Daniel Clark</i>	
<b>Direction of Arrival Estimation Using a Cluster of Beams in a Cone-shaped Digital Array Radar</b> .....	31
<i>Micaela Contu, Marta Bucciarelli, Pierfrancesco Lombardo, Francesco Madia, Rossella Stallone, and Marco Massardo</i>	
<b>Low Complexity Parameter Estimation for Off-the-Grid Targets</b> .....	36
<i>Seifallah Jardak, Sajid Ahmed, and Mohamed-Slim Alouini</i>	
<b>Normalised Multi-stage Clustering Equaliser for Underwater Acoustic Channels</b> .....	41
<i>Rangeet Mitra and Vimal Bhatia</i>	
<b>Wideband CDMA Waveforms for Large MIMO Sonar Systems</b> .....	46
<i>Yan Pailhas and Yvan Petillot</i>	
<b>Performance Analysis of Polynomial Matrix SVD-based Broadband MIMO Systems</b> .....	50
<i>Andre Sandmann, Andreas Ahrens, and Steffen Lochmann</i>	
<b>Low-Complexity Robust Adaptive Beamforming Algorithms Exploiting Shrinkage for Mismatch Estimation</b> .....	55
<i>Hang Ruan and Rodrigo C. de Lamare</i>	

<b>Sparsity Based Ground Moving Target Imaging via Multi-Channel SAR</b> .....	60
<i>Di Wu, Mehrdad Yaghoobi, and Mike Davies</i>	
<b>A Location Scale Based CFAR Detection Framework for FOPEN SAR Images</b> .....	65
<i>Marco Liguori, Alessio Izzo, Carmine Clemente, Carmela Galdi, Maurizio Di Bisceglie, and John J. Soraghan</i>	
<b>Velocity Estimation of Moving Ships Using C-band SLC SAR Data</b> .....	70
<i>Andrea Radius and Paulo Marques</i>	
<b>On the Target Detection in OFDM Passive Radar Using MUSIC and Compressive Sensing</b> .....	74
<i>Watcharapong Ketpan, Seksan Phonsri, Rongrong Qian, and Mathini Sellathurai</i>	
<b>Radar Imaging With Quantized Measurements Based on Compressed Sensing</b> .....	79
<i>Xiao Dong and Yunhua Zhang</i>	
<b>Traffic Scheduling Algorithm for Wireless Mesh Networks Based Defense Networks Incorporating Centralized Scheduling Architecture</b> .....	84
<i>Sidharth Shukla and Vimal Bhatia</i>	
<b>Outage Analysis of OFDM based AF Cooperative Systems in Selection Combining Receiver over Nakagami-<math>m</math> fading channels with Nonlinear Power Amplifier</b> .....	89
<i>Nagendra Kumar and Vimal Bhatia</i>	
<b>A Novel Self Localization Approach for Sensors</b> .....	94
<i>Dogan Yildiz, Serap Karagol, Okan Ozgonenel, Satish Tadiparthi, and Marwan Bikdash</i>	
<b>Quadrature Filters for Underwater Passive Bearings-Only Target Tracking</b> .....	99
<i>Rahul Radhakrishnan, Abhinoy Kumar Singh, Shovan Bhaumik, and Nutan Kumar Tomar</i>	
<b>Fusion of Radar and Secondary Sensor Data Using Kinematic Models of Multiple Simultaneous Targets</b> .....	104
<i>Brian L. Karlsten, Esben Nielsen, and Morten T. Pedersen</i>	
<b>Improved High-degree Cubature Kalman Filter</b> .....	109
<i>Abhinoy Kumar Singh and Shovan Bhaumik</i>	
<b>Shortening of Paraunitary Matrices Obtained by Polynomial Eigenvalue Decomposition Algorithms</b> .....	113
<i>Jamie Corr, Keith Thompson, Stephan Weiss, Ian K. Proudler, and John G. McWhirter</i>	

<b>Observing the Dynamics of Waterborne Pathogens for Assessing the Level of Contamination</b> .....	118
<i>Isabella McKenna, Francesco Tonolini, Rachael Tobin, Jeremie Houssineau, Helen Bridle, Craig McDougall, Isabel Schlangen, John S. McGrath, Melanie Jimenez, and Daniel E. Clark</i>	
<b>Distributed Implementation for Person Re-identification</b> .....	123
<i>Saurav Sthapit, John Thompson, James R. Hopgood, and Neil M. Robertson</i>	
<b>Extraction of Pulse Repetition Interval Based on Incomplete, Noisy TOA Measurements by the Moving Passive Receiver</b> .....	128
<i>Yang Liu, Fucheng Guo, Min Zhang, and Wenli Jiang</i>	
<b>Removing Speckle Noise by Analysis Dictionary Learning</b> .....	132
<i>Jing Dong, Wenwu Wang, and Jonathon Chambers</i>	
<b>Link-by-Link Coded Physical Layer Network Coding on Impulsive Noise Channels</b> .....	137
<i>Yuanyi Zhao, Martin Johnston, Charalampos Tsimenidis, and Li Chen</i>	
<b>A New Asymmetric Correlation Kernel for GNSS Multipath Mitigation</b> .....	142
<i>Steven Miller, Xue Zhang, and Andreas Spanias</i>	
<b>Fractional Cosine Transform (FRCT)-Turbo Based OFDM for Underwater Acoustic Communication</b> .....	147
<i>Yixin Chen, John. J. Soraghan, Carmine Clamente, and Stephan Weiss</i>	
<b>Practical Identification of Specific Emitters Used in the Automatic Identification System</b> .....	152
<i>Takashi Iwamoto</i>	



# Sensor management with regional statistics for the PHD filter

Marian Andrecki, Emmanuel D. Delande, Jérémie Houssineau, and Daniel E. Clark  
School of Engineering & Physical Sciences, Heriot-Watt University, Edinburgh, UK

**Abstract**—This paper investigates a sensor management scheme that aims at minimising the regional variance in the number of objects present in regions of interest whilst performing multi-target filtering with the Probability Hypothesis Density (PHD) filter. The experiments are conducted in a simulated environment with groups of targets moving through a scene in order to inspect the behaviour of the manager. The results demonstrate that computing the variance in the number of objects in different regions provides a viable means of increasing situational awareness where complete coverage is not possible. A discussion follows, highlighting the limitations of the PHD filter and discussing the applicability of the proposed method to alternative available approaches in multi-object filtering.

## I. INTRODUCTION

Exploring sensor management problems becomes a topic of increasing interest as the controllability of modern sensor systems advances. In the context of Bayesian estimation for target detection/tracking, the information acquired by the operator on the object of interests - the targets - is provided by one or several sensors observing the surveillance scene. If the operator has some degree of freedom in the dynamical control of these sensors (e.g. orientation of camera, selection of radar scanning modes), its efficiency can be improved by solving a sensor management problem through finding a suitable sensor policy, i.e., a principled decision-making procedure that will dynamically select a sensor control based on the acquired information in order to achieve some surveillance objective.

Approaches to the sensor management problem are extremely varied, and their applicability depend on the nature of the information propagated by the tracking algorithm (see [1] for a recent account on the topic). The regional statistics provide first- and second-order information on the target activity in any region of the surveillance space, i.e., the expected number of targets lying within the said region and associated uncertainty [2], [3]. Because they produce a principled and meaningful quantification of the estimated target activity in any desired region of the surveillance space, the regional statistics provide grounds for a simple sensor policy aiming at focusing the surveillance activity on regions of critical interest to the operator – say, the surroundings of a facility.

Naturally available to any multi-object filter maintaining a probabilistic representation of the population of targets, the regional statistics for filtering solutions stemming from the

Finite Set Statistics (FISST) framework [4] are derived in [2], [5], [6] for the PHD filter [7] and the Cardinalized Probability Hypothesis Density (CPHD) filter [8], and discussed in [3] for the multi-Bernoulli filter [4]. Applicability to traditional track-based filters such as the Multiple Hypothesis Tracking (MHT) and Joint Probabilistic Density Association (JPDA) approaches [9] is less straightforward and will be briefly discussed in this paper.

This paper aims at illustrating the concept of regional statistics as a basis for a sensor policy in the context of the PHD filter, the simplest solution derived from the FISST framework [4]. Section II provides a brief description of the PHD filter with regional statistics (a detailed construction can be found in [2]). Section III describes the surveillance activity on which the sensor policy exploiting regional statistics will be illustrated, and simulation results are presented in Section IV. Section V analyses the limited applicability of the PHD filter in this context and discusses leads for further development.

## II. PHD FILTERING WITH REGIONAL STATISTICS

### A. Multi-object filtering and regional statistics

The FISST [8] is a filtering framework in which the acquired information about the multi-target state, i.e., the states of all the targets currently living in the surveillance scene, is represented by a random object  $\Phi$  called a Random Finite Set (RFS). A realization  $\varphi = \{x_1, \dots, x_n\}$  of  $\Phi$  is a set of individual target states  $x_i$  in a (single-)target state space  $\mathbf{X} \subset \mathbb{R}^d$ , which is a  $d$ -dimensional space describing the targets' physical characteristics of interest to the operator (position, velocity, etc.). As with any random object, a RFS is described by its probability distribution  $P_\Phi$ , defined on the process state space  $\mathcal{X}$ , i.e., the space of all the finite sets of points in  $\mathbf{X}$ .

The multitarget Bayes filter [4] integrates the Bayesian paradigm within the FISST framework and provides filtering equations for the propagation of the multi-target probability distribution  $P_\Phi$ , but it is intractable in the general case. Practical filters rely on assumptions on the multi-target RFS  $\Phi$  leading to more tractable equations propagating *reduced information* on  $\Phi$ . As with any random variables, statistical moments can be defined on any RFS  $\Phi$  to produce a reduced, yet meaningful description out of the full probability distribution  $P_\Phi$ . The *first-order moment measure*<sup>1</sup>  $\mu_\Phi$  plays a central

<sup>1</sup>In this paper we follow the approach in [2] and describe RFSs with probability measures handled with standard integrals, rather than with multi-object densities handled with set integrals [8], for the measure-theoretic formulation is required for the expression of the regional statistics.

M. Andrecki, E. D. Delande, J. Houssineau, and D. E. Clark are with the School of Engineering & Physical Sciences, Heriot-Watt University, Edinburgh, UK (e-mails: ma804@hw.ac.uk, E.D.Delande@hw.ac.uk, J.Houssineau@hw.ac.uk and D.E.Clark@hw.ac.uk).

role in the construction of RFS-based filters and is propagated by both PHD [7] and CPHD [8] filters. The *centred second moment* or *variance*  $\text{var}_\Phi$  was introduced more recently in the context of the PHD and CPHD [2], [5], [6], and the multi-Bernoulli [3] filters.

Given some RFS  $\Phi$  and some arbitrary<sup>2</sup> region  $B \subseteq \mathbf{X}$ , the regional statistics  $\mu_\Phi(B)$ ,  $\text{var}_\Phi(B)$  are defined in [2] and can be interpreted as follows:

- $\mu_\Phi(B)$  is the expected number of targets within  $B$ ,
- $\text{var}_\Phi(B)$  quantifies the spread, around its expected value, of the estimated number of targets within  $B$ .

### B. The PHD filter with regional statistics

For any time step  $k$ , we denote by  $\Phi_{k|k-1}$  (respectively (resp.)  $\Phi_k$ ) the predicted (resp. posterior) RFS representing the current multi-target configuration, given the measurements collected up to time step  $k-1$  (and  $k$ ). The first-order moment measure of the predicted (and posterior) RFS is denoted by  $\mu_{k|k-1}$  (resp.  $\mu_k$ ). Further denoting by  $\mu_{b,k}$  (and  $\mu_{fa,k}$ ) the first-order moment measure (resp. density) of the newborn target RFS  $\Phi_{b,k}$  (and false alarm RFS  $\Psi_{fa,k}$ ), the filtering equations of the PHD filter are given by [7]

$$\mu_{k|k-1}(dy) = \int p_{s,k}(x) f_{s,k}(dy|x) \mu_{k-1}(dx) + \mu_{b,k}(dy), \quad (1)$$

$$\mu_k(dy) = C_k(y|Z_k) \mu_{k|k-1}(dy), \quad (2)$$

with

$$C_k(y|Z_k) = g_k(\phi|y) + \sum_{z \in Z_k} \frac{g_k(z|y)}{\mu_{fa,k}(z) + \int g_k(z|x) \mu_{k|k-1}(dx)}, \quad (3)$$

where  $g_k$  is the extended sensor likelihood function given by

$$\begin{cases} g_k(\phi|\cdot) &= 1 - p_{d,k}(\cdot), \\ g_k(z|\cdot) &= p_{d,k}(\cdot) \ell_k(z|\cdot), \end{cases} \quad (4)$$

and where

- $p_{s,k}$  is the target probability of survival,
- $f_{s,k}$  is the Markov transition kernel,
- $p_{d,k}$  is the sensor probability of detection,
- $\ell_k$  is the sensor likelihood function,
- $Z_k$  is the set of collected observations.

The posterior regional statistics  $\mu_k(B)$ ,  $\text{var}_k(B)$  are given by [2]

$$\mu_k(B) = \mu_\phi(B) + \sum_{z \in Z_k} \frac{\mu_z(B)}{\mu_{fa,k}(z) + \mu_z(\mathbf{X})}, \quad (5)$$

$$\begin{aligned} \text{var}_k(B) &= \mu_\phi(B) \\ &+ \sum_{z \in Z_k} \frac{\mu_z(B)}{\mu_{fa,k}(z) + \mu_z(\mathbf{X})} \left( 1 - \frac{\mu_z(B)}{\mu_{fa,k}(z) + \mu_z(\mathbf{X})} \right), \end{aligned} \quad (6)$$

where, for any region  $B \subseteq \mathbf{X}$ ,

$$\begin{cases} \mu_\phi(B) &= \int_B g_k(\phi|x) \mu_{k|k-1}(dx), \\ \mu_z(B) &= \int_B g_k(z|x) \mu_{k|k-1}(dx). \end{cases} \quad (7)$$

<sup>2</sup>Provided that it is measurable, see [2] for more details.

An analysis of the posterior regional statistics for the PHD filter is given in [5].

From now on, the newborn target RFS  $\Phi_{b,k}$  (resp. the false alarm RFS  $\Psi_{fa,k}$ ) is assumed Poisson [4] with rate  $\lambda_{b,k}$  (resp.  $\lambda_{fa,k}$ ). Also, time subscripts will be omitted when there is no ambiguity.

## III. SENSOR MANAGEMENT PROBLEM

### A. Surveillance activity

The surveillance scene is 2D region of the physical space, in which targets of interest are expected to enter the scene from the west (left edge), and leave through the east. Little is known by the operator about the population of incoming targets. The general surveillance objective is to estimate as accurately as possible the size of the population within specific regions of the scene at every time step. The sensor coverage is very limited (see Section III-B), and the surveillance is primarily focussed on three regions of the scene (dotted rectangles in Figure 1). Note that the identification and classification of individual targets are out of scope in this context, for the sole purpose of this surveillance activity is to provide a first estimate of the amount of incoming target activity. This situation could correspond to the first task in a border surveillance activity, where target identification, classification and accurate state estimation would be carried on by another sensor system further east.

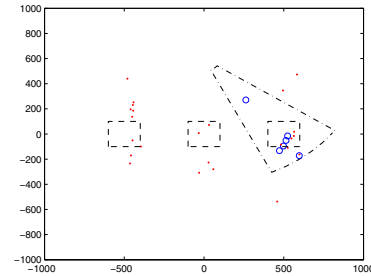


Fig. 1: Example of scenario. The focus regions are denoted by dotted rectangles, and the current field of view is denoted by a dotted triangle. The targets are red dots, and the current detections are blue circles.

From now on,  $B_1$  (resp.  $B_2$ ,  $B_3$ ) will denote the westernmost (resp. centred, easternmost) focus region within the surveillance area.

### B. Sensor

The only available sensor is a radar providing range and bearing, positioned north of the scene. The sensor can be oriented towards one, and only one, of the three focus regions at any time. Note that the sensor's field of view (dotted triangle in Figure 1) is not limited to the focus region the sensor is oriented at, but the three possible field of views do not overlap. Note that the observation process is usually noisy, for *a*) the targets lying within the field of view may be miss-detected, and *b*) the sensor may produce spurious measurements (false alarms), and *c*) Gaussian noise is added to the bearing and range measurements.

### C. Sensor control policy

The regional statistics computed in the three focus regions provide a natural tool to quantify the quality of the estimation, for the variance gives the uncertainty in the level of target activity *as maintained by the filter*. The straightforward policy that we explore in this paper is therefore to focus the sensor, at each time step, on the region whose variance is the *highest*.

It is important to note from the PHD filtering equations (1), (2) that the posterior variance (6) of the multi-target process is *not* propagated across time, but merely extracted at each time step (this limitation of the PHD filter is discussed in Section V).

The proposed sensor control policy is given, at any time  $k$ , as follows:

- 1) Compute posterior variances  $\text{var}_{k-1}(B_i)$ ,  $1 \leq i \leq 3$ ;
- 2) Focus sensor towards region  $\arg \max \text{var}_{k-1}(B_i)$ .

## IV. SIMULATION RESULTS

### A. Implementation

The simulated targets appear in the scene in groups, whose size is Poisson with mean 15. Newborn targets appear along the western edge of the scene, move eastward and leave the scene from its eastern edge.

In order to illustrate the value of a sensor control policy, a scarcity in sensing resources was necessary so that the options of *exploitation* – keeping the sensor focussed on the same region to refine the estimation of the target population currently looked at – and *exploration* – orienting the sensor to another region to learn about a different population – were competitive. To this end, the sensor is modelled with poor measurement accuracy (12 m on range,  $2.86^\circ$  on bearing), and either low probability of detection and low false alarm rate ( $p_d = 0.6$ ,  $\lambda_{fa} = 1$ ), or higher probability of detection and but higher false alarm rate as well ( $p_d = 0.8$ ,  $\lambda_{fa} = 10$ ).

A target’s state is described by its position and velocity coordinates in the surveillance scene. The PHD filter is implemented with Gaussian mixtures [10], and the regional statistics are computed in the three focus regions using (5), (6). The target behaviour is modelled with a near constant velocity model, with a slight noise to account for the model mismatches, and initial velocity towards the east.

A critical component of the filter parametrisation is the target birth model. Recall that little is known by the operator regarding the population of incoming targets. Introducing an overestimated number of potential targets in the scene through the birth model proved an incentive for the sensor to explore regularly the foremost region  $B_1$  in order to prevent incoming waves from being missed by the operator. The influence of the intensity of the birth RFS in Eq. (1) on the performance of the filter is further discussed in Section IV-C; the default value for the birth rate, used in the experiment in Section IV-B, is  $\lambda_b = 1$  (e.g. on average, one target is expected to enter the scene at each time step).

### B. Comparison of naive/variance-based control policies

This scenario aims at illustrating the behaviour of the variance-based sensor control policy proposed in Section III-C

compared to a “naive” sensor control policy sequentially scanning the three focus regions. A single wave of targets goes through the surveillance scene, unknown to the operator. In this situation, the naive controller is expected to waste sensing resources on void regions, while the variance-based controller should focus either on the region where the wave of targets is (exploitation), or focus on the first region to look for potential incoming targets (exploration).

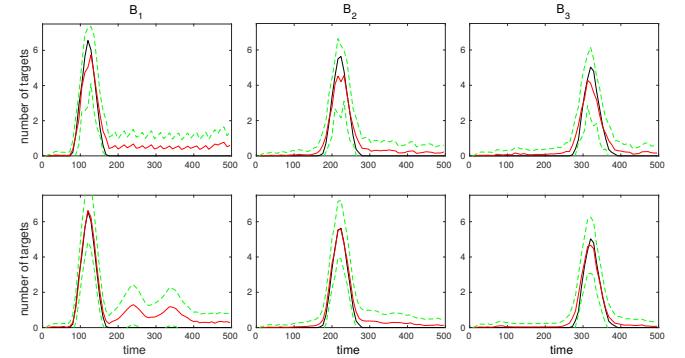


Fig. 2: Estimated target activity for naive (top) and variance-based (bottom) controllers ( $p_d = 0.6$ ,  $\lambda_{fa} = 1$ ). True target number is in black, mean target number is in red, +/- standard deviation is in green.

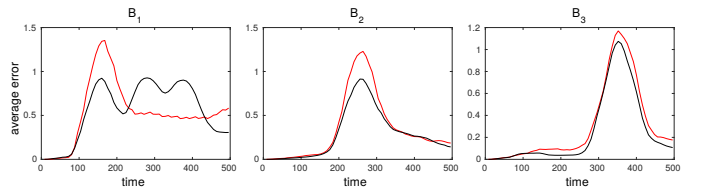


Fig. 3: Absolute error in target number ( $p_d = 0.6$ ,  $\lambda_{fa} = 1$ ). Naive controller is in red, variance-based controller is in black.

Figures 2 and 3 depict the results of the scenario with low probability of detection and low false alarm rate, averaged over 30 Monte Carlo runs. Overall, the variance-based controller performs better than the naive controller, for in the former case the sensor will tend to focus longer on a region while it is crossed by the wave of targets. Note that the target number is overestimated in the foremost region  $B_1$ , regardless of the chosen controller, once the wave of true targets has passed (from time step 180 onwards). Recall from Section IV-A that the intensity of the birth model must be significant enough to introduce “uncertainty” in the composition of the incoming population and provide an incentive to check the foremost region regularly enough for the detection of potential incoming targets. It creates a bias in the estimated target number in that particular region, especially for the variance-based controller during the later stages of the scenario where the sensor spreads its attention on the three regions. This point is further discussed in Section V. While the bias is clear in the foremost region  $B_1$ , it seems to disappear in the following two regions, for the false alarm rate is low enough to prevent a gross overestimation

of the populations once the initial bias is corrected through successive observations.

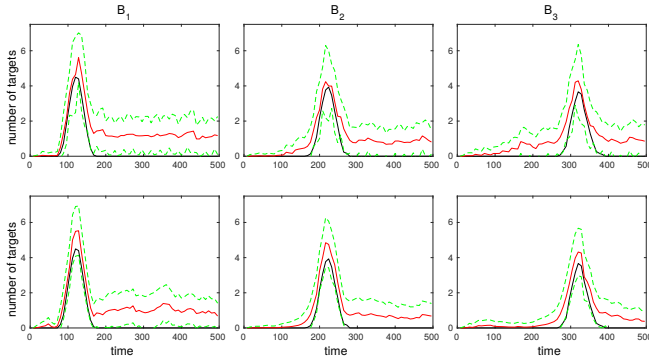


Fig. 4: Estimated target activity for naive (top) and variance-based (bottom) controllers ( $p_d = 0.8$ ,  $\lambda_{fa} = 10$ ). True target number is in black, mean target number is in red, +/- standard deviation is in green.

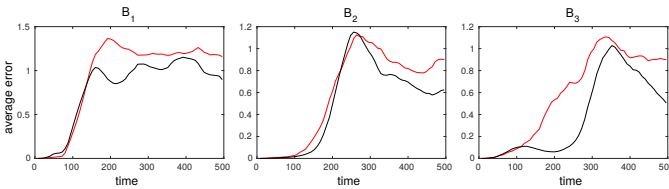


Fig. 5: Absolute error in target number ( $p_d = 0.8$ ,  $\lambda_{fa} = 10$ ). Naive controller is in red, variance-based controller is in black.

Figures 4 and 5 depict the results of the scenario with higher probability of detection and higher false alarm rate, averaged over 20 Monte Carlo runs. Regardless of the controller, the higher false alarm rate seems to induce an overestimation of the target activity that is not fully corrected by the filter. The variance-based controller still performs slightly better than the naive controller, especially in regions  $B_2$  and  $B_3$  when they are void of true targets. The variance-based controller is likely to focus on a region while the uncertainty in the target number is high enough, and in the process discards previous target evidence as false alarms if not backed by new measurements. On the other hand, a constant swiping between the different regions may not allow the filter to acquire enough evidence in a region to discriminate between false alarms and true targets.

### C. Effect of the intensity of the birth model

This scenario aims at illustrating the dependence of the variance-based controller to the intensity of the birth model. Several groups of targets are spawned throughout the scenario, with a random time interval between two successive waves (the number and frequency of waves varied with the different Monte Carlo runs). The variance-based controller is tested with three different intensities for the birth model:  $\lambda_b = 0.05, 1, 20$ . In all three cases, the probability of detection is set to  $p_d = 0.8$  and the false alarm rate to  $\lambda_{fa} = 1$ .

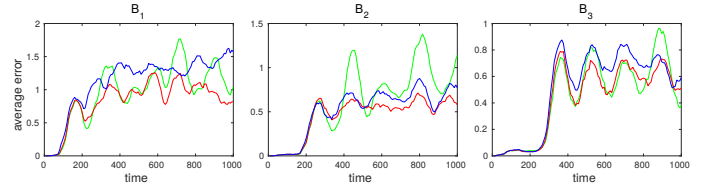


Fig. 6: Absolute error in target number ( $p_d = 0.8$ ,  $\lambda_{fa} = 1$ ).  $\lambda_b = 0.05$  is in green,  $\lambda_b = 1$  is in red,  $\lambda_b = 20$  is in blue.

Figure 6 depicts the results of the scenario, averaged over 20 Monte Carlo runs. Note that the three controllers perform similarly in the estimation of the first wave of targets hitting the foremost region  $B_1$ : at this point, the first wave receives full attention of the controllers as there are no other populations to focus on. Once the first wave of targets leave region  $B_1$ , the behaviour of the three controllers present noticeable differences.

The controller with low intensity birth model (green in Figure 6) has little incentive to explore the foremost region  $B_1$ . It tends to focus on region  $B_1$  until hit by the first wave of targets, and then follows the first wave as it progresses eastward through regions  $B_2$  and  $B_3$ . In overall it performs better than the other controllers in the estimation of the first wave, but tends to miss some of the subsequent incoming waves, resulting in large spikes in the estimation error. The errors are less significant in the easternmost region  $B_3$ , suggesting that by the time the subsequent waves have reach  $B_3$  they have usually been detected. In overall this controller seems to performs the worst as it is prone to miss incoming waves.

The controller with high intensity birth model (blue in Figure 6) has strong incentive to check regularly on the foremost region  $B_1$ , since a large number of incoming targets are expected. All the target waves are detected when they hit the foremost region, and are subsequently tracked in the following regions; however, the controller spends little time focussing on a given wave a target as the exploration of the foremost region  $B_1$  requires significant attention.

Overall, the controller with medium intensity birth model (red in Figure 6) seems to perform best, as it is more likely to balance the need for exploration and tracking of confirmed target waves properly.

## V. CONCLUSION AND FURTHER DEVELOPMENT

This paper proposes a novel sensor control policy for RFS-based filters based on the recently developed regional statistics. We exploit the concept of regional variance in the target number [2], which provides a principled quantification of the uncertainty in the estimation of the target activity in any desired region of the surveillance scene. It is implemented for the PHD filter [7] illustrated on a scenario simulating a border surveillance activity. The posterior regional statistics have a remarkably simple expression in the context of the PHD filter, and they can be implemented without incurring a significant computational cost. The inherent simplicity of the underlying filter, however, limits the applicability of the regional statistics for sensor management in complex scenarios.

The discussions in Section IV showed the critical importance of the birth model in this sensor management scenario. Because the sensor coverage is very limited and the targets are not detected upon entering the scene, the birth model must be designed in order to balance the need for exploitation of previously confirmed targets and exploration of the surveillance scene for the detection of new individuals. The structure of the PHD filter is such that the birth model is only described by its intensity  $\mu_b$ , and therefore no second-order information is available for a more refined modelling of the incoming targets. A birth model with a large enough intensity seems necessary to provide incentive for the controller to check the activity in the foremost region  $B_1$  regularly enough, but it induces an undesirable bias leading to an overestimation of the target activity in this region. An interesting lead to follow would be to model the newborn targets with a RFS with a regional variance *larger* than its regional mean, such as an over-dispersed Poisson point process [11], and derive an appropriate RFS-based filter able to capture its features. An obvious limitation of the PHD filtering framework, in the context of sensor management for the estimation of regional target activity, is that the uncertainty on the filtered estimate is not propagated across time – recall that the regional variance is *extracted* from the posterior probability distribution, yet *not* propagated to the next time step. Since the regional statistics can be produced through a principled procedure for any multi-target filter providing a probabilistic representation of the population of targets [2], a natural follow-up to this paper would be to design a similar controller for more recent filtering solutions propagating higher-order information. Promising candidates would be the Hypothesised and Independent Stochastic Populations (HISP) filter [12], whose computational complexity is similar to the PHD filter, or the more involved Distinguishable and Independent Stochastic Populations (DISP) filter [13] for more challenging scenarios.

On a broader perspective, alternative statistical tools to the regional statistics should be explored for the design of more generic control policies. Indeed, the applicability and relevance of the regional statistics for more traditional track-based approaches such as the MHT or JPDA approaches [9] remain unclear, for they do not maintain a probabilistic description of the whole population of targets. The recent information-theoretic and track-based control policy [14], although designed for the filtering solutions stemming from the

novel estimation framework for stochastic populations [15], should be easily adaptable to the traditional track-based filters and could provide grounds for a generic sensor management solution.

#### ACKNOWLEDGEMENTS

This work was supported by the Engineering and Physical Sciences Research Council (EPSRC) Platform Grant (EP/J015180/1), the MOD University Defence Research Centre on Signal Processing (UDRC) Phase 2 (EP/K014227/1). Jeremie Houssineau is supported by Dstl task ED TIN 2-3.

#### REFERENCES

- [1] A. O. Hero III, “Sensor Management: Past, Present, and Future,” *IEEE Sensor Journals*, vol. 11, no. 12, pp. 3064–3075, Dec. 2011.
- [2] E. Delande, M. Uney, J. Houssineau, and D. E. Clark, “Regional Variance for Multi-Object Filtering,” *IEEE Transactions on Signal Processing*, vol. 62, no. 13, pp. 3415 – 3428, 2014.
- [3] E. Delande, J. Houssineau, and D. E. Clark, “Regional variance in target number: analysis and application for multi-Bernoulli point processes,” in *Data Fusion & Target Tracking Conference (DF&TT 2014): Algorithms & Applications, 10th IET*, Apr. 2014.
- [4] R. P. S. Mahler, *Statistical Multisource-Multitarget Information Fusion*. Artech House, 2007.
- [5] E. Delande, J. Houssineau, and D. E. Clark, “PHD filtering with localised target number variance,” in *Signal Processing, Sensor Fusion, and Target Recognition XXII, Proceedings of SPIE*, Apr. 2013, p. 87450E.
- [6] —, “Localised variance in target number for the Cardinalized Hypothesis Density Filter,” in *Information Fusion, Proceedings of the 16th International Conference on*, Jul. 2013.
- [7] R. P. S. Mahler, “Multitarget Bayes Filtering via First-Order Multitarget Moments,” *Aerospace and Electronic Systems, IEEE Transactions on*, vol. 39, no. 4, pp. 1152–1178, Oct. 2003.
- [8] —, “PHD Filters of Higher Order in Target Number,” *Aerospace and Electronic Systems, IEEE Transactions on*, vol. 43, no. 4, pp. 1523–1543, Oct. 2007.
- [9] W. D. Blair and Y. Bar-Shalom, Eds., *Multitarget-Multisensor Tracking: Applications and Advances (Volume III)*. Artech House, 2000.
- [10] B.-N. Vo and W.-K. Ma, “The Gaussian Mixture Probability Hypothesis Density Filter,” *Signal Processing, IEEE Transactions on*, vol. 54, no. 11, pp. 4091–4104, Nov. 2006.
- [11] D. J. Daley and D. Vere-Jones, *An Introduction to the Theory of Point Processes*, 2nd ed. Springer, 2003, vol. 1.
- [12] J. Houssineau and D. E. Clark, “Hypothesised filter for independent stochastic populations,” 2014, arXiv:1404.7408.
- [13] E. Delande, J. Houssineau, and D. E. Clark, “A filter for distinguishable and independent populations,” arXiv:1501.04671.
- [14] —, “Performance metric in closed-loop sensor management for stochastic populations,” in *Sensor Signal Processing for Defence (SSPD)*, 2014.
- [15] J. Houssineau, “Representation and estimation of stochastic populations,” Ph.D. dissertation, Heriot Watt University, 2015.

# Joint Navigation and Synchronization using SOOP in GPS-denied environments: Algorithm and Empirical Study

Mei Leng, Sirajudeen Gulam Razul,  
and Chong Meng Samson See  
TL@NTU  
Singapore

Email: {lengmei, samsonsee, ESirajudeen}@ntu.edu.sg

François Quitin, Chi Cheng, and Wee Peng Tay  
School of Electrical and Electronic Engineering  
Nanyang Technological University  
Singapore

Email: {fquitin, chengchi, wptay}@ntu.edu.sg

**Abstract**—We consider the problem of tracking a receiver using signals of opportunity (SOOP) from beacons and a reference anchor with known positions and velocities, and where all devices have asynchronous local clocks or oscillators. Based on an extended Kalman filter, we propose a sequential estimator to jointly track the receiver location, velocity, and its clock parameters using time-difference-of-arrival and frequency-difference-of-arrival measurements obtained from the SOOP samples collected by the receiver and reference anchor. Field experiments are carried out using a software defined radio testbed, and Iridium satellites as the SOOP beacons. Experiment demonstrate that our measurement model has a good fit, and our proposed estimator can successfully track both the receiver location, velocity, and the relative clock offset and skew with respect to the reference anchor with good accuracy.

**Index Terms**—navigation, synchronization, signal-of-opportunity, EKF, USRP

## I. INTRODUCTION

Signals-of-opportunity (SOOP) refer to public signals transmitted from an established signal infrastructure for non-navigation purposes. These signals conform to well-established standards and can be easily detected in most urban areas with relatively high signal-to-noise ratio (SNR). We call their transmitters *beacons*. Depending on their signal characteristics and transmitter properties, various SOOP signals have found useful applications as alternatives to the use of Global Navigation Satellite Systems (GNSS) for navigation services [1]. As most GNSS are medium earth orbit systems, their SNRs are lower than typical SOOP, and navigation services based on GNSS are usually only available when there is a clear sky view. Moreover, since GNSS techniques have become more mature, it is likely that GNSS may be jammed or disabled by adversaries during war time. Therefore, navigation using SOOP has gained increasing interest recently [2], [3].

Since SOOP have not been designed for navigation purposes, and SOOP beacons act as uncooperative broadcast anchors, it may be difficult to have a priori knowledge of the signal structure and certain characteristics like transmit power and transmit time. Therefore, typical localization metrics that can be extracted from SOOP are limited to received signal strength, angle-of-arrival, time-difference-of-arrival (TDOA)

and frequency-difference-of-arrival (FDOA) of the same signal between two receivers. Compared with the first two metrics, which have poor measurement accuracies in cluttered environments [4], TDOA and FDOA are attractive alternatives, since they can remove the ambiguity caused by unknown transmit time or unknown signal structure, and are somewhat more robust as biases caused by clutters tend to cancel each other out if the two receivers are relatively close to each other. Therefore, we focus on TDOA and FDOA measurements in this paper. In [3], we proposed an estimator using differential TDOA (DTDOA) and FDOA, where the location and velocity (collectively called the *state*) of every receiver are estimated using measurements from at least 5 beacons simultaneously in 2D space. In this paper, we consider a more practical situation where only one beacon is available per TDOA and FDOA measurement period, and the receiver state is estimated sequentially.

The most critical challenge for receiver state estimation using TDOA and FDOA measurements is synchronization between the two receivers. An offset between the local clocks of each receiver introduces biases into TDOA measurements, for which even a microsecond offset significantly degrades the overall estimation performance. Likewise, a relative clock skew between the two receivers distorts the FDOA measurements. In order to obtain reliable timing and frequency information, it is essential that receivers are time synchronized and achieve precise frequency alignment, and therefore most existing methods make this simplifying assumption [2]. However, clock synchronization is difficult to achieve and maintain in practice [5], [6]. Moreover, in order not to interfere with the existing operations of SOOP beacons, the navigation using SOOP often require that SOOP beacons do not need to be aware of the presence of the receivers using their signals, and will not actively synchronize with them or provide a common clock reference for the receivers.

In this paper, we consider a joint navigation and synchronization problem using SOOP beacons. We assume that a target receiver and a reference anchor receive signals from the same SOOP beacons, where the reference anchor is a receiver node with known location and velocity. We also

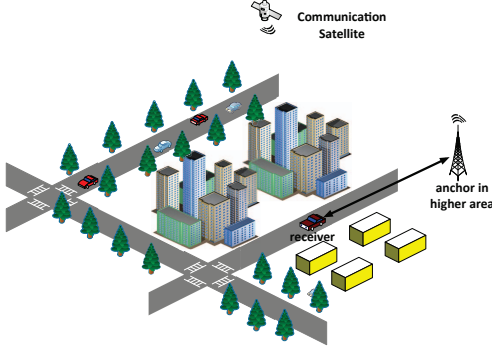


Fig. 1. Navigation using space-based SOOP beacons in urban environments.

assume that all devices, including the receiver, anchor, and beacons, are asynchronous. Using TDOA and FDOA measurements between the receiver and anchor, we propose a sequential estimator to jointly track the the location, velocity, and clock parameters of the receiver, with respect to (w.r.t.) the anchor. Empirical experiments using our software defined radio platform demonstrate that our proposed algorithm can correctly track the clock drift dynamics, with good accuracy for receiver location and velocity estimation performance.

## II. MEASUREMENT MODEL

We consider the problem of localizing and tracking a receiver  $R_1$  using SOOP from a set  $\mathcal{B}$  of non-navigation space-based beacons. The receiver performs self-localization and velocity estimation with the aid of a reference anchor  $R_0$  within communication range. An example scenario is shown in Figure 1, where a beacon  $b \in \mathcal{B}$  has known position  $\mathbf{p}_b$  and velocity  $\mathbf{v}_b$ , and broadcasts signals at a nominal carrier frequency  $f_b$ .

In order to infer its location, the target receiver  $R_1$  extracts TDOA and FDOA measurements by cross correlating the signals received by itself and the anchor  $R_0$ . Assume that the signal from beacon  $b$  is transmitted in bursts and each receiver makes sequential observations in  $L$  timeslots with an observation time  $T_e^{(l)}$  in the  $l$ -th timeslot, and we denote the TDOA and FDOA measurements obtained in the  $l$ -th timeslot as  $\{\hat{\tau}_b^{(l)}, \hat{\xi}_b^{(l)}\}$ . Since all receivers are asynchronous, the measurements will be distorted due to the local oscillator biases. Following a similar framework in [3], we can show that TDOA and FDOA measurements are modelled as follows,

$$\hat{\tau}_b^{(l)} \approx \left\| \mathbf{p}_1^{(l)} - \mathbf{p}_b^{(l)} \right\| - \left\| \mathbf{p}_0^{(l)} - \mathbf{p}_b^{(l)} \right\| + T_e^{(l)} \alpha^{(l)} + \theta^{(l)} + \varpi_b^{\tau}, \quad (1a)$$

$$\hat{\xi}_b^{(l)} \approx (\mathbf{v}_1^{(l)} - \mathbf{v}_b^{(l)})^T \mathbf{u}_{1,b}^{(l)} - (\mathbf{v}_0^{(l)} - \mathbf{v}_b^{(l)})^T \mathbf{u}_{0,b}^{(l)} + \alpha^{(l)} + \varpi_b^{\xi}, \quad (1b)$$

where  $\mathbf{u}_{j,b}^{(l)} = (\mathbf{p}_j^{(l)} - \mathbf{p}_b^{(l)}) / \left\| \mathbf{p}_j^{(l)} - \mathbf{p}_b^{(l)} \right\|$  is the relative direction from receiver  $j$  to beacon  $b$  in the  $l$ -th time slot, and  $\varpi_b^{\tau}$  and  $\varpi_b^{\xi}$  are corresponding measurement noises. The approximation in (1) is due to neglecting the small residual caused by the accumulation of clock skew during the observation, similar to that in [3]. The bias term  $\alpha^{(l)}$  in FDOA measurements is

a quantity depending on receivers' local clock skews, which describes the speed of receiver clock drift relative to that of the anchor and is typically related to the systematic and slowly varying frequency error due to ageing and environment. The bias term  $\theta^{(l)}$  in the TDOA measurement is a time-varying term that depends linearly on the clock offsets and clock skews of the receiver and anchor. In Section IV, empirical experiments using a software defined radio testbed and the Iridium satellites as SOOP beacons verifies the correctness of our measurement model in (1).

Stacking all unknowns and measurements into vectors as  $\mathbf{x}^{(l)} \triangleq [(\mathbf{p}_1^{(l)})^T, (\mathbf{v}_1^{(l)})^T, \theta^{(l)}, \alpha^{(l)}]^T$ ,  $\mathbf{y}^{(l)} \triangleq [\hat{\tau}_b^{(l)}, \hat{\xi}_b^{(l)}]^T$  and  $\varpi^{(l)} = [\varpi_b^{\tau}, \varpi_b^{\xi}]^T$ , we define the measurement model from (1) as,

$$\underbrace{\begin{bmatrix} \hat{\tau}_b^{(l)} \\ \hat{\xi}_b^{(l)} \end{bmatrix}}_{\mathbf{y}^{(l)}} = \underbrace{\begin{bmatrix} \left\| \mathbf{p}_1^{(l)} - \mathbf{p}_b^{(l)} \right\| - \left\| \mathbf{p}_0^{(l)} - \mathbf{p}_b^{(l)} \right\| + T_e^{(l)} \alpha^{(l)} + \theta^{(l)} \\ (\mathbf{v}_1^{(l)} - \mathbf{v}_b^{(l)})^T \mathbf{u}_{1,b}^{(l)} - (\mathbf{v}_0^{(l)} - \mathbf{v}_b^{(l)})^T \mathbf{u}_{0,b}^{(l)} + \alpha^{(l)} \end{bmatrix}}_{\triangleq \mathbf{g}_b(\mathbf{x}^{(l)})} + \varpi^{(l)}. \quad (2)$$

We assume that the measurement noise  $\varpi^{(l)}$  follows zero mean Gaussian with variance  $\mathbf{R}_l$ , i.e.,  $\varpi^{(l)} \sim \mathcal{N}(\mathbf{0}, \mathbf{R}_l)$ . The noise covariance matrix  $\mathbf{R}_l$  depends on the estimation accuracy for TDOA and FDOA measurements, and as a well-investigated problem, it has been shown that their Cramér-Rao bounds can be obtained in closed form and are fully determined by quantities related to signal characteristics like effective SNR, integration time, and signal bandwidth [7], [8].

## III. JOINT NAVIGATION AND SYNCHRONIZATION ALGORITHM

The target receiver then seeks to jointly estimate its state  $\{\mathbf{p}_1^{(l)}, \mathbf{v}_1^{(l)}\}$  and its clock parameters  $\{\theta^{(l)}, \alpha^{(l)}\}$  relative to the anchor  $R_0$ . To incorporate the dynamic information of the unknown state, we further derive the dynamic models to describe how  $\mathbf{x}^{(l)}$  could be updated from  $\mathbf{x}^{(l-1)}$ . The clock state in our case is relatively simple due to the fact that general oscillators can be characterized with a constant clock skew for a short period. For the the target maneuvering model, we assume that the receiver is moving with small variations in velocity, and in such cases it is common to model the acceleration as a continuous Wiener process with intensity  $\sigma_a$ . Let the observation interval from  $\mathbf{x}^{(l-1)}$  to  $\mathbf{x}^{(l)}$  be  $\Delta_l$ , the dynamic model is then given by,

$$\underbrace{\begin{bmatrix} \mathbf{p}_1^{(l)} \\ \mathbf{v}_1^{(l)} \\ \theta^{(l)} \\ \alpha^{(l)} \end{bmatrix}}_{\mathbf{x}^{(l)}} = \underbrace{\begin{bmatrix} \mathbf{I} & \Delta_l \mathbf{I} & \mathbf{0} & \mathbf{0} \\ \mathbf{0} & \mathbf{I} & \mathbf{0} & \mathbf{0} \\ \mathbf{0} & \mathbf{0} & 1 & \Delta_l \\ \mathbf{0} & \mathbf{0} & \mathbf{0} & 1 \end{bmatrix}}_{\triangleq \mathbf{H}_l} \begin{bmatrix} \mathbf{p}_1^{(l-1)} \\ \mathbf{v}_1^{(l-1)} \\ \theta^{(l-1)} \\ \alpha^{(l-1)} \end{bmatrix} + \boldsymbol{\nu}^{(l)}, \quad (3)$$

where  $\boldsymbol{\nu}^{(l)}$  represent the process noise following a zero mean Gaussian with variance  $\mathbf{Q}_l$ , i.e.,  $\boldsymbol{\nu}^{(l)} \sim \mathcal{N}(\mathbf{0}, \mathbf{Q}_l)$ . The covariance matrix  $\mathbf{Q}_l$  is a block diagonal matrix with its element  $\mathbf{Q}_a^{(l)}$  and  $\mathbf{Q}_c^{(l)}$  representing the noisy dispersion for

the target acceleration and the clock parameters, respectively. Specifically, we have,

$$\mathbf{Q}_a^{(l)} = \sigma_a^2 \begin{bmatrix} \frac{\Delta_l^5}{20} & 0 & 0 & \frac{\Delta_l^4}{8} & 0 & 0 \\ 0 & \frac{\Delta_l^5}{20} & 0 & 0 & \frac{\Delta_l^4}{8} & 0 \\ 0 & 0 & \frac{\Delta_l^5}{20} & 0 & 0 & \frac{\Delta_l^4}{8} \\ \frac{\Delta_l^4}{8} & 0 & 0 & \frac{\Delta_l^3}{3} & 0 & 0 \\ 0 & \frac{\Delta_l^4}{8} & 0 & 0 & \frac{\Delta_l^3}{3} & 0 \\ 0 & 0 & \frac{\Delta_l^4}{8} & 0 & 0 & \frac{\Delta_l^3}{3} \end{bmatrix}, \quad (4)$$

and

$$\mathbf{Q}_c^{(l)} = \begin{bmatrix} \sigma_\Omega^2 \Delta_l + \sigma_\beta^2 \frac{\Delta_l^3}{3} + \sigma_d^2 \frac{\Delta_l^5}{5} & \sigma_\beta^2 \frac{\Delta_l^2}{2} + \sigma_d^2 \frac{\Delta_l^4}{8} \\ \sigma_\beta^2 \frac{\Delta_l^2}{2} + \sigma_d^2 \frac{\Delta_l^4}{8} & \sigma_\beta^2 + \sigma_d^2 \frac{\Delta_l^3}{3} \end{bmatrix}, \quad (5)$$

where  $\sigma_\Omega$ ,  $\sigma_\beta$ , and  $\sigma_d$  are the diffusion coefficients for noise components of clock offset, clock skew, and clock drift respectively, and they describe the intensity of their corresponding noise.

We hereby approximate  $\mathbf{g}_b(\mathbf{x}^{(l)})$  by Taylor expansion with  $\mathbf{G}_l = \nabla_{\mathbf{x}} \mathbf{g}_b(\mathbf{x})|_{\mathbf{x}=\mathbf{x}^{(l)}}$ . Applying extended Kalman filter (EKF) to (2) and (3), it follows that

$$\mathbf{x}_{l|l-1} = \mathbf{H}_l \mathbf{x}_{l-1|l-1}, \quad (6a)$$

$$\mathbf{P}_{l|l-1} = \mathbf{Q}_l + \mathbf{H}_l \mathbf{P}_{l-1|l-1} \mathbf{H}_l^T, \quad (6b)$$

$$\mathbf{P}_{l|l} = \mathbf{P}_{l|l-1} - \mathbf{K}_l \mathbf{H}_l \mathbf{P}_{l|l-1}, \quad (6c)$$

$$\mathbf{x}_{l|l} = \mathbf{x}_{l|l-1} + \mathbf{K}_l (\mathbf{y}^{(l)} - \mathbf{g}_b(\mathbf{x}_{l|l-1})), \quad (6d)$$

where  $\mathbf{K}_l = \mathbf{P}_{l|l-1} \mathbf{G}_l (\mathbf{R}_l + \mathbf{G}_l^T \mathbf{P}_{l|l-1} \mathbf{G}_l)^{-1}$  represents the Kalman gain. Therefore, we implement the sequential tracking and synchronization algorithm based on (6), and the procedure starts with  $\mathbf{x}_{0|0} = \mathbf{x}^{(0)}$  and  $\mathbf{P}_{0|0} = \mathbf{P}^{(0)}$ , where  $\mathbf{x}^{(0)}$  is the initial guess for parameters and  $\mathbf{P}^{(0)}$  describes our confidence in the initial guess. Every time the target receiver obtains a new pair of TDOA and FDOA measurements, it updates  $\mathbf{x}_{l|l}$  and  $\mathbf{P}_{l|l}$  using (6), and obtains the estimate for the  $l$ -th time slot as  $\hat{\mathbf{x}}^{(l)} = \mathbf{x}_{l|l}$ .

#### IV. EMPIRICAL EXPERIMENTS

In order to evaluate the proposed measurement model (1) for TDOA and FDOA estimation and the proposed algorithm (6), several tests using real life data have been conducted. It should be noted that the tests presented in this section are only sample results and several additional experiments have been done with similar findings.

##### A. Experiment setup

The Iridium satellites are used as SOOP beacons due to its wide coverage and easy availability. Specifically, we make use of the broadcast signal at the ring alert channel whose downlink frequency is fixed at 1626.270833 MHz and is globally assigned to be the same known frequency for all Iridium satellites. One drawback is that this period lasts for 4.32 second and is relatively long for a fast manoeuvring target, and it may produce insufficient measurements to characterize the target movement. Generally, more signals, such as those from downlink traffic channel, message channel, and

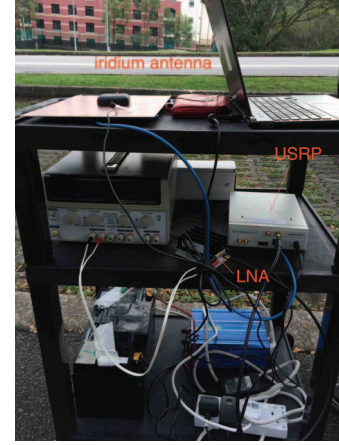


Fig. 2. A complete set of receiver used in the experiment.

synchronization channel, can be detected and used to achieve better performance. In this experiment, we focused on the ring alert signal for the proof of concept.

The receiver was implemented on a software-defined radio (SDR) testbed. The USRP-N210 SDR with WBX daughter-board [9] was used as the receiving device. The USRP is connected to and controlled by a standard PC with large and fast storage space. Other assisting components in one receiver set include one Iridium antenna, one low noise amplifier (LNA) ZHL-1217MLN, one standard DC power supply, and one portable battery. One complete set is shown in Figure 2.

The experiment was conducted across Singapore island with three sets of receivers. Their positions and trajectory are shown in Figure 3. Two receivers, *A* and *B*, are static, receiver *A* is placed on the rooftop of S2 building in NTU campus, receiver *B* is placed by the east coast near Changi village. Both places have open sky view so that two receivers can receive Iridium signals with relatively high SNR. The third receiver *C* is placed in a car and moves from Changi airport (on the east) to NTU (on the west). One separate GPS receiver is placed in the car so that the trajectory of receiver *C* can be recorded as a benchmark.

All three USRPs in the receivers are using free-running oscillators in the sense that no clock regulation was applied via any external sources during the recording. The USRPs are set to receive at frequency 1626.27 MHz with a sampling frequency 10 MHz. To guarantee that all receivers see the same satellite, we pre-calibrated the laptop clock before the experiment to an accuracy level of second, and we use the laptop time to initiate the recording at each receiver.

##### B. TDOA and FDOA measurements

The record lasts for about 48 minutes, and in total 8 Iridium satellites are observed. We use receiver *A* as the anchor, and TDOA/FDOA measurements are obtained for *B* and *C* w.r.t. the anchor respectively. The histograms for the corresponding measurement errors are plotted in Figure 4. The statistics are different for two pairs of receivers due to their different environments. The mean for both TDOA and FDOA are close

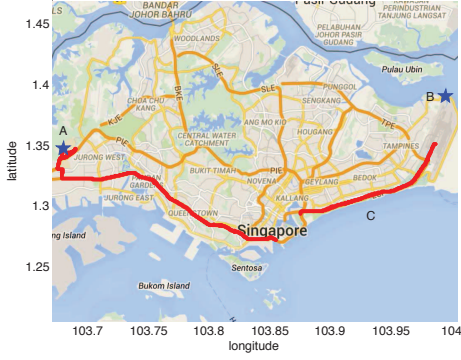
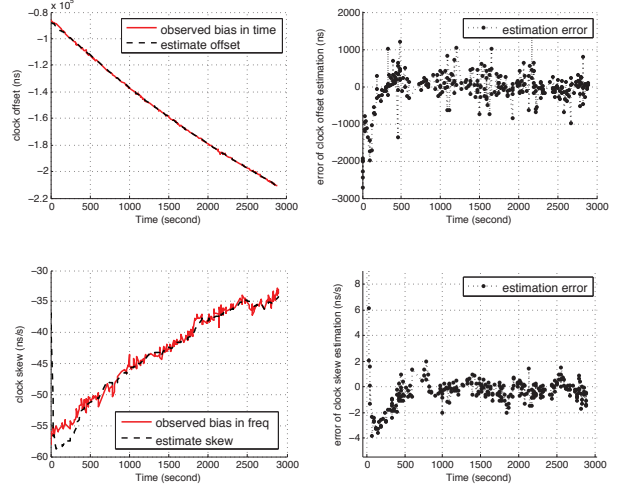


Fig. 3. Locations of receiver *A* and *B*; Trajectory of receiver *C*, where the discontinuity is caused by driving in a tunnel.



(a) Tracking clock drifting parameters

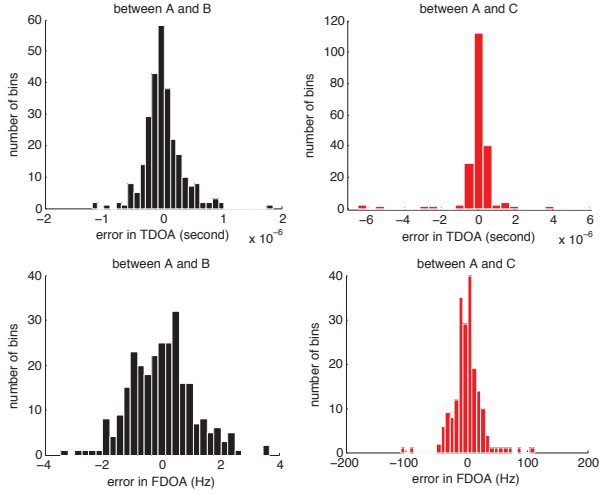
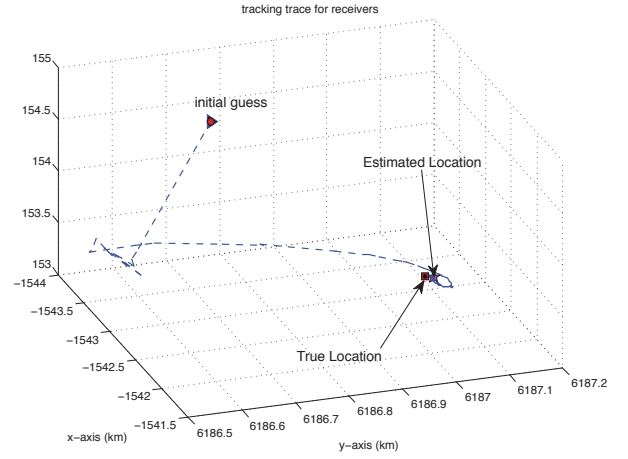


Fig. 4. Histogram for TDOA and FDOA measurement errors



(b) Trace for estimating the receiver location

to zero, the standard deviation for TDOA is 333.8 ns for the receiver pair *A-B* and 1.087  $\mu$ s for the receiver pair *A-C*, and the standard deviation for FDOA is 1.084 Hz for the receiver pair *A-B* and 24.12 Hz for the receiver pair *A-C*.

### C. Experiment results for localizing static receiver

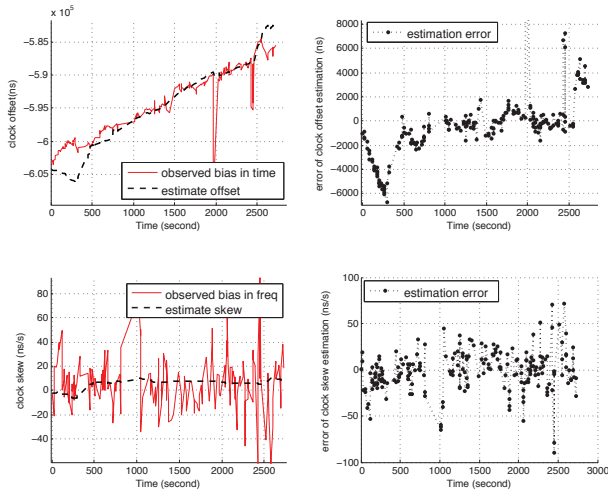
With the estimated TDOA and FDOA, we applied the proposed algorithm in (6) to jointly estimate the receiver *B*'s location and its clock parameters, where receiver *A* is taken as the anchor. The estimation results are shown in Figure 5. In our implementation, we set  $\mathbf{R}_l$  to be a diagonal matrix with its component standard deviation values following from the CRB of TDOA/FDOA estimation [7]. We set  $\sigma_\Omega = 10^{-10}$ ,  $\sigma_\beta = 10^{-9}$ , and  $\sigma_d = 10^{-8}$  for  $\mathbf{Q}_c^{(l)}$  in (5) according to the oscillator datasheet, we also set  $\sigma_a = 10^{-10}$  for  $\mathbf{Q}_s^{(l)}$  in (4) based on the fact that the receiver is static and the acceleration acts like a white noise term. Several tests have been conducted and it is shown that the proposed algorithm is robust to small variations in these covariance values.

The results for tracking relative clock parameters between two receivers are shown in Figure 5(a). In the left column,

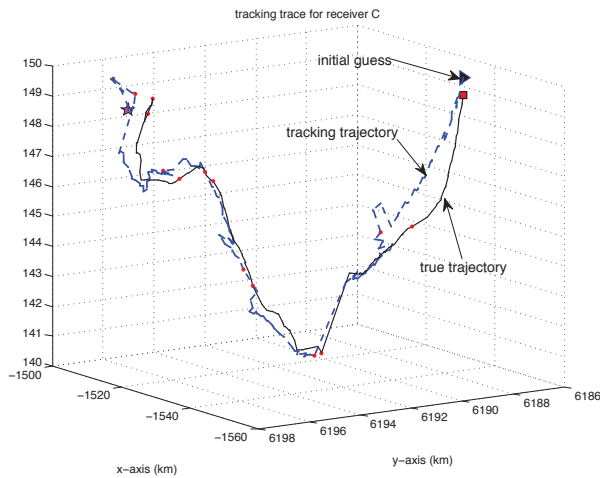
Fig. 5. The proposed algorithm for jointly estimating static receiver *B*'s location and clock parameters.

we show observed bias value and estimated value (in black dash line) for both clock offset  $\theta$  and clock skew  $\alpha$ . It can be seen that in the lower-left subfigure, the true clock skew is slightly increasing at the order of 10 ns/s, which conforms to the 0.01 ppm standard in the USRP N210 specification [9]. Accordingly, it results in a second order behaviour in the clock offset drifting, as shown in the upper-left subfigure, and our estimation of clock offset keeps a good track of the underlying clock offset. In the right column, we show estimation errors with respect to the observed bias, which shows a zero mean over time.

In Figure 5(b), we show the tracking trajectory of the receiver locations. The initial guess is a random point 5 km away from the true location, and our estimation of the receiver location achieves an error smaller than 50 meters within 5 minutes. At the end of 48 minutes, the error for the receiver location estimation is 36.86 m, which is close to the CRB value of 16.0 m. We have also observed that the error is



(a) Tracking clock drifting parameters



(b) Tracking the receiver state

Fig. 6. The proposed algorithm for tracking the manoeuvring receiver C.

dominated by the error from the x-axis. This is due to the fact that all satellite beacons are above in the sky and form an unfavourable geometry for the localization, and it is similar to the poor altitude resolution commonly seen in GPS navigation.

#### D. Experiment results for tracking manoeuvring receiver

With TDOA and FDOA measurements between receiver A and C, we applied the proposed algorithm to track the state of the receiver C and its relative clock parameters with respect to receiver A, and the results are shown in Figure 6. As observed in our experiment results, one key factor which affects the tracking performance is the correctness of the dynamic model. When the receiver is manoeuvring, e.g., taking turns and changing directions like receiver C in our experiment, the dynamic model (3) cannot accurately characterize the movement of the receiver especially when it is taking a sharp turn. In addition, as discussed in Section IV-A, the long periodicity of ring alert burst limits the number of measurements. Therefore, the estimation error accumulated

from previous time slots cannot be corrected timely during the manoeuvring period, and it results in larger deviations from the true locations when tracking the receiver state, as is clear from Figure 6(b). Furthermore, since we are tracking the receiver state and clock parameters simultaneously, the receiver position and clock offset are coupled in the sense that the estimation error in either component will be treated as a part of TDOA measurement resulting from the other component, and hence the estimation errors for both clock offset and receiver locations are further accumulated. From Figure 6(a), it shows a large error in the beginning and ending part for clock offset estimation, and this leads to a large localization error during the same period for tracking the receiver state.

#### V. CONCLUSION

In this paper, we have investigated the problem of joint navigation and synchronization using SOOP in GPS-denied environments. We assume two receivers have free-running oscillators, and we assume all beacons are unsynchronized with unknown clock offsets. Considering a general scenario where an anchor exists to share the received signal and the state information with the target receiver, we proposed a sequential algorithm to jointly estimate the receiver state and its clock parameters. Receivers were implemented on SDR testbed, and field experiments were conducted with Iridium satellites as SOOP beacons. Experimental results showed that our measurement model for TDOA and FDOA correctly describes the relationship between biases and clock parameters, and our proposed algorithm can track the receiver state and clock parameters with good accuracy when the dynamic model correctly characterize the change of the receiver state.

#### REFERENCES

- [1] K. A. Fisher, *The Navigation Potential of Signals of Opportunity-based Time Difference of Arrival Measurements*. Air Force Institute of Technology, 2005.
- [2] M. Bshara, U. Orguner, F. Gustafsson, and L. Van Biesen, "Robust tracking in cellular networks using HMM filters and cell-ID measurements," *IEEE Trans. Veh. Technol.*, vol. 60, no. 3, pp. 1016–1024, 2011.
- [3] M. Leng, W. P. Tay, C. M. S. See, and S. G. Razul, "Modified CRLB for cooperative geolocation of two devices using signals of opportunity," *IEEE Trans. Wireless Commun.*, vol. 13, no. 7, pp. 3636–3649, 2014.
- [4] N. Patwari, J. N. Ash, S. Kyperountas, A. O. H. III, R. L. Moses, and N. S. Correal, "Locating the nodes: cooperative localization in wireless sensor networks," *IEEE Signal Process. Mag.*, vol. 22, no. 4, pp. 54–69, 2005.
- [5] M. Leng and Y.-C. Wu, "Distributed clock synchronization for wireless sensor networks using belief propagation," *IEEE Trans. Signal Process.*, vol. 59, no. 11, pp. 5404–5414, 2011.
- [6] —, "Low-complexity maximum-likelihood estimator for clock synchronization of wireless sensor nodes under exponential delays," *IEEE Trans. Signal Process.*, vol. 59, no. 10, pp. 4860–4870, 2011.
- [7] S. Stein, "Algorithms for ambiguity function processing," *IEEE Trans. Acoust., Speech, Signal Process.*, vol. 29, no. 3, pp. 588–599, 1981.
- [8] N. Noels, H. Wymeersch, H. Steendam, and M. Moeneclaey, "True Cramer-Rao bound for timing recovery from a bandlimited linearly modulated waveform with unknown carrier phase and frequency," *IEEE Trans. Commun.*, vol. 52, no. 3, pp. 473–483, 2004.
- [9] USRP N210 datasheet. Hewlett-Packard Company. [Online]. Available: <http://www.ettus.com>

# Variational Bayesian PHD filter with Deep Learning Network Updating for Multiple Human Tracking

Pengming Feng<sup>1</sup>, Wenwu Wang<sup>2</sup>, Syed Mohsen Naqvi<sup>1</sup>, Jonathon A. Chambers<sup>1</sup>

1. Communications, Sensors, Signal and Information Processing Group, Newcastle University, UK

Emails: {p.feng2, s.m.r.naqvi, jonathon.chambers}@newcastle.ac.uk

2. Center for Vision Speech and Signal Processing, University of Surrey, UK

Email: w.wang@surrey.ac.uk

**Abstract**—We propose a robust particle probability hypothesis density (PHD) filter where the variational Bayesian method is applied in joint recursive prediction of the state and the time varying measurement noise parameters. The proposed particle PHD filter is based on forming variational approximation to the joint distribution of states and noise parameters at each frame separately; the state is estimated with a particle PHD filter and the measurement noise variances used in the update step are estimated with a fixed point iteration approach. A deep belief network (DBN) is used in the update step to mitigate the effect of measurement noise on the calculation of particle weights in each frame. The deep learning network is trained based on both colour and oriented gradient histogram (HOG) features and then used to mitigate the measurement noise from the particle selection step, thereby improving the tracking performance. Simulation results using sequences from the CAVIAR dataset show the improvements of the proposed DBN aided variational Bayesian particle PHD filter over the traditional particle PHD filter.

**Index Terms**—Multiple human tracking, PHD filter, deep learning, variational Bayesian

## I. INTRODUCTION

Unknown and varying number of targets cause the main problem in multiple target tracking (MTT); moreover the occlusion problem may occur which increases the challenge for reliable target tracking. A particular issue in MTT is that it is not always possible to associate measurements with particular targets and therefore false alarms and missed detections may be generated particularly in the presence of clutter, occlusion and noise [1], which can introduce detection in the number of targets and reduce the tracking accuracy in MTT.

Both the Kalman filter and particle filter have been widely used in tracking, however, in these approaches, the number of targets is assumed to be known and fixed. For a variable number of targets, the random finite set (RFS) [2] based probability hypothesis density (PHD) filter has been recently proposed for the MTT problem. The advantage of the PHD filter is that it can estimate both the number of targets and their locations, and thus avoids the need for data association techniques as part of the multiple target framework [3][4][5]. Moreover, it mitigates the computational complexity issue that often occurs in other multiple target tracking approaches such as the multiple hypothesis tracking (MHT) approach [5] by employing the intensity instead of the posterior distribution.

However, the limitation of the PHD filter is that its performance can be easily affected by estimation errors caused by noise.

The particle PhD filter often assumes a priori knowledge of the measurement and dynamic model parameters, including the noise statistics. However, such knowledge is not always available in practical applications [6]. Variational Bayesian (VB) methods on the other hand have been used for a wide range of models to perform approximate posterior inference at low computational cost in comparison with the sample methods [7], thereby establishing an analytically tractable form for the joint posterior distribution of the state and measurement parameters. Moreover, in human tracking, the VB method can be used with a factor-free form of distribution of the state and measurement noise model.

In this paper, we therefore propose a novel robust PHD filter for multiple human tracking where the VB method is used to approximate the joint posterior distribution of the state and the noise variance with a factorized free form distribution. The variance of the measurement noise is also updated by this VB approach, thereby providing more stable updates for the weights in the particle PHD filter. Since in an enclosed environment, only limited human features can be extracted when using a single camera and accurate measurement of the humans can be difficult to obtain due to illumination and posture changes, we employ a deep belief network (DBN) to aid in calculating the weights for the particle based PHD filter, which utilizes the colour and oriented gradient histogram features. The DBN has the advantage that it is robust to background noise in the measurement due to the difference between human target and noises features. To evaluate the performance of our proposed robust PHD filter, we employ sequences from the CAVIAR dataset [8] which include appearance, occlusion, and disappearance of humans in the field of view of a camera. Next we introduce the proposed particle PHD filter.

## II. PROPOSED PARTICLE PHD FILTER

### A. Optimal Bayesian filtering

We choose the particle filter to form the fundamental framework of the PHD filter so that the weight for each particle can be calculated via a DBN to improve the accuracy in human tracking. We approximate the PHD filter with a set of weighted

random samples using a sequential Monte Carlo method. The corresponding state and measurement model at time  $k$  can be written respectively as

$$\mathbf{x}_k = \mathbf{F}\mathbf{x}_{k-1} + \mathbf{w}_k \quad (1)$$

$$\mathbf{z}_k = \mathbf{H}\mathbf{z}_{k-1} + \mathbf{v}_k \quad (2)$$

where  $\mathbf{x}_k$  denotes the state vector at time  $k$  including the 2-D position of the target,  $\mathbf{z}_k$  is the measurement vector and  $\mathbf{w}_k \sim N(\mathbf{0}, \mathbf{P}_k)$  is the Gaussian process noise,  $\mathbf{v}_k \sim N(\mathbf{0}, \mathbf{R}_k)$  is the measurement noise with diagonal covariance matrix  $\mathbf{R}_k$ .  $\mathbf{F}$  and  $\mathbf{H}$  are respectively the state and measurement transition matrix.

We assume that the dynamic models of the states and the variance parameters within (1) and (2) are independent [9], and thus can be described as:

$$p(\mathbf{x}_k, \mathbf{R}_k | \mathbf{x}_{k-1}, \mathbf{R}_{k-1}) = p(\mathbf{x}_k | \mathbf{x}_{k-1})p(\mathbf{R}_k | \mathbf{R}_{k-1}) \quad (3)$$

The goal of Bayesian optimal filtering of the above model is to compute the posterior distribution  $p(\mathbf{x}_k, \mathbf{R}_k | \mathbf{Z}_k)$ , where  $\mathbf{Z}_k = \{\mathbf{z}_k, k = 1, \dots, N\}$ . As described in [6], the filtering problem consists of the following steps:

1. Initialization: The recursion starts from the initial prior distribution  $p(\mathbf{x}_0, \mathbf{R}_0)$ .

2. Prediction: The predictive distribution of the state  $\mathbf{x}_k$  and measurement noise covariance matrix  $\mathbf{R}_k$  is given by the Chapman-Kolmogorov equation:

$$p(\mathbf{x}_k, \mathbf{R}_k | \mathbf{Z}_{k-1}) = \int p(\mathbf{x}_k | \mathbf{x}_{k-1})p(\mathbf{R}_k | \mathbf{R}_{k-1}) \times p(\mathbf{x}_{k-1}, \mathbf{R}_{k-1} | \mathbf{Z}_{k-1}) d\mathbf{x}_{k-1} d\mathbf{R}_{k-1} \quad (4)$$

where the integral has the dimension equal to the sum of  $\dim(\mathbf{x}_k)$  and  $\dim(\mathbf{R}_k)$ .

3. Update: Given the next measurement  $\mathbf{z}_k$ , the predictive distribution above is updated to a posterior distribution by Bayes' rule:

$$p(\mathbf{x}_k, \mathbf{R}_k | \mathbf{Z}_k) \propto p(\mathbf{z}_k | \mathbf{x}_k, \mathbf{R}_k)p(\mathbf{x}_k, \mathbf{R}_k | \mathbf{Z}_{k-1}) \quad (5)$$

The integrations in the general solution are usually not analytically tractable [6]; in the following, the recursion steps are solved by using a variational Bayesian approximation for the posterior update.

### B. Variational approximation

As described in Section II-A, the goal of VB is to compute the posterior distribution  $p(\mathbf{x}_k, \mathbf{R}_k | \mathbf{Z}_k)$ . Given that the inverse-Gamma distribution is the conjugate prior distribution for the variance of a Gaussian distribution [10], a product of inverse-Gamma distributions can be adopted to approximate the posterior distribution of  $\mathbf{R}_k$ ; in this case, assuming the posterior distribution at time  $k-1$  can be represented by

$$p(\mathbf{x}_{k-1}, \mathbf{R}_{k-1} | \mathbf{Z}_{k-1}) = N(\mathbf{x}_{k-1}, \mu_{k-1}, \mathbf{P}_{k-1}) \prod_{i=1}^d \times IG(\sigma_{k-1,i}^2 | \alpha_{k-1,i}, \beta_{k-1,i}) \quad (6)$$

where  $d$  is the dimension of the measurement noise vector and  $N(\mathbf{x}_{k-1}, \mu_{k-1}, \mathbf{P}_{k-1})$  denotes a Gaussian probability density function for the random variable  $\mathbf{x}_{k-1}$  with mean  $\mu_{k-1}$  and covariance matrix  $\mathbf{P}_{k-1}$ , and  $IG(\sigma_{k-1,i}^2 | \alpha_{k-1,i}, \beta_{k-1,i})$  denotes the inverse-Gamma distribution, which has the degree of freedom parameter  $\alpha_{k-1,i}$  and the scalar parameter  $\beta_{k-1,i}$ . With the assumption that the dynamic models of the state and measurement noise variance are independent, the joint predictive distribution remains a factored form [9] of a Gaussian distribution and an inverse Gamma distribution

$$p_{k|k-1}(\mathbf{x}_k, \mathbf{R}_k | \mathbf{Z}_k) = p_{k|k-1}(\mathbf{x}_k | \mathbf{Z}_{k-1})p_{k|k-1}(\mathbf{R}_k | \mathbf{Z}_{k-1}) \\ = N(\mathbf{x}_{k|k-1}, \mu_{k|k-1}, \mathbf{P}_{k|k-1}) \prod_{i=1}^d IG(\sigma_{k|k-1,i}^2 | \alpha_{k|k-1,i}, \beta_{k|k-1,i}) \quad (7)$$

where in the joint posterior distribution, the state and measurement noise variance will be coupled with the likelihood function, which makes the exact posterior intractable.

The next step is to derive an analytical expression for the posterior distribution within the update equation; in order to make the computation tractable, an approximation to the posterior distribution is formed [7]. The standard VB approach is employed and a free form factored approximate distribution  $p(\mathbf{x}_k, \mathbf{R}_k | \mathbf{Z}_k)$  can be described as

$$p(\mathbf{x}_k, \mathbf{R}_k | \mathbf{Z}_k) \approx Q_{\mathbf{x}}(\mathbf{x}_k)Q_{\mathbf{R}}(\mathbf{R}_k) \quad (8)$$

where  $Q_{\mathbf{x}}(\mathbf{x}_k)$  and  $Q_{\mathbf{R}}(\mathbf{R}_k)$  are respectively a Gaussian distribution and inverse Gamma distribution as follows:

$$Q_{\mathbf{x}}(\mathbf{x}_k) = N(\mathbf{x}_k, \mu_k, \mathbf{P}_k) \quad (9)$$

$$Q_{\mathbf{R}}(\mathbf{R}_k) = IG(\sigma_{k,i}^2 | \alpha_{k,i}, \beta_{k,i}) \quad (10)$$

then the approximate posterior densities can be determined by minimizing the Kullback-Leibler(KL) divergence between the separable approximation and the true posterior density expressed as

$$KL\{Q_{\mathbf{x}}(\mathbf{x}_k)Q_{\mathbf{R}}(\mathbf{R}_k) || p(\mathbf{x}_k, \mathbf{R}_k | \mathbf{Z}_k)\} = \int Q_{\mathbf{x}}(\mathbf{x}_k)Q_{\mathbf{R}}(\mathbf{R}_k) \log \frac{Q_{\mathbf{x}}(\mathbf{x}_k)Q_{\mathbf{R}}(\mathbf{R}_k)}{p(\mathbf{x}_k, \mathbf{R}_k | \mathbf{Z}_k)} d\mathbf{x}_k d\mathbf{R}_k \quad (11)$$

In order to minimize the KL-divergence, methods from calculus of variations [6] are employed. Using the alternating optimisation, the probability densities  $Q_{\mathbf{x}}(\mathbf{x}_k)$  and  $Q_{\mathbf{R}}(\mathbf{R}_k)$  are calculated in turn, while keeping the other fixed, yielding:

$$Q_{\mathbf{x}}(\mathbf{x}_k) \propto E \left\{ \int \log p(\mathbf{z}_k, \mathbf{x}_k, \mathbf{R}_k | \mathbf{Z}_{1:k-1}) Q_{\mathbf{R}}(\mathbf{R}_k) d\mathbf{R}_k \right\} \quad (12)$$

$$Q_{\mathbf{R}}(\mathbf{R}_k) \propto E \left\{ \int \log p(\mathbf{z}_k, \mathbf{x}_k, \mathbf{R}_k | \mathbf{Z}_{1:k-1}) Q_{\mathbf{x}}(\mathbf{x}_k) d\mathbf{x}_k \right\} \quad (13)$$

Since the two equations are coupled, they cannot be solved directly, however, computing the expectation of the first equation yields the following equation

$$\int \log p(\mathbf{z}_k, \mathbf{x}_k, \mathbf{R}_k | \mathbf{Z}_{1:k-1}) Q_{\mathbf{R}}(\mathbf{R}_k) d\mathbf{R}_k = \\ -0.5(\mathbf{z}_k - \mathbf{H}_k \mathbf{x}_k)^T \langle \mathbf{R}_k^{-1} \rangle_{\mathbf{R}} (\mathbf{z}_k - \mathbf{H}_k \mathbf{x}_k) \\ -0.5(\mathbf{x}_k - \mathbf{F}_k \mathbf{x}_{k-1})^T \langle \mathbf{P}_k^{-1} \rangle (\mathbf{x}_k - \mathbf{F}_k \mathbf{x}_{k-1}) + C_1 \quad (14)$$

where  $\langle \cdot \rangle_{\mathbf{R}} = \int (\cdot) Q_{\mathbf{R}}(\mathbf{R}_k) d\mathbf{R}_k$  denotes the expected value with respect to the approximation distribution  $Q_{\mathbf{R}}(\mathbf{R}_k)$  and  $C_1$  denotes the terms independent of  $\mathbf{x}_k$ .

Similarly, the second expectation can be computed as follows

$$\begin{aligned} \int \log p(\mathbf{z}_k, \mathbf{x}_k, \mathbf{R}_k | \mathbf{Z}_{k-1}) Q_{\mathbf{x}}(\mathbf{x}_k) d\mathbf{x}_k &= - \sum_{i=1}^d \left( \frac{3}{2} + \alpha_{k,i} \right) \ln(\sigma_{k,i}^2) \\ &\quad - \sum_{i=1}^d \frac{\beta_{k,i}}{\sigma_{k,i}^2} - \frac{1}{2} \sum_{i=1}^d \frac{\langle (\mathbf{z}_k - \mathbf{H}_k \mathbf{x}_k)_i^2 \rangle_{\mathbf{x}_k}}{\sigma_{k,i}^2} + C_2 \end{aligned} \quad (15)$$

where  $\langle \cdot \rangle_{\mathbf{x}} = \int (\cdot) Q_{\mathbf{x}}(\mathbf{x}_k) d\mathbf{x}_k$ , and the parameters  $\mu_k, \mathbf{P}_k, \alpha_{k,i}$  and  $\beta_{k,i}$  are the solutions to the following coupled set of equations:

$$\begin{aligned} \mu_k &= \mu_{k-1} + \mathbf{P}_{k|k-1} \mathbf{H}_k^T (\mathbf{H}_k^T \mathbf{P}_{k|k-1} \mathbf{H}_k^T + \hat{\mathbf{R}}_k)^{-1} (\mathbf{z}_k - \mathbf{H}_k \mu_{k|k-1}) \\ \mathbf{P}_{k|k} &= \mathbf{P}_{k|k-1} - \mathbf{P}_{k|k-1} \mathbf{H}_k^T (\mathbf{H}_k^T \mathbf{P}_{k|k-1} \mathbf{H}_k^T + \hat{\mathbf{R}}_k)^{-1} \mathbf{H}_k \mathbf{P}_{k|k-1} \\ \alpha_{k,i} &= \hat{\alpha}_{k-1,i} + \frac{1}{2} \\ \beta_{k,i} &= \hat{\beta}_{k-1,i} + \frac{1}{2} [(\mathbf{z}_k - \mathbf{H}_k \hat{\mu}_k)_i^2 + (\mathbf{H}_k \mathbf{P}_k \mathbf{H}_k^T)_i] \end{aligned} \quad (16)$$

and the estimated covariance matrix  $\hat{\mathbf{R}}_k$  is

$$\hat{\mathbf{R}}_k = \text{diag} \left\{ \frac{\beta_{k,1}}{\alpha_{k,1}}, \dots, \frac{\beta_{k,m}}{\alpha_{k,m}} \right\} \quad (17)$$

where ‘ $\hat{\cdot}$ ’ denotes the estimate of the parameters. Following (16) and (17), the process of variational Bayes measurement parameter updating can be described as

1. Prediction: Compute the parameters of the predicted distribution as follows:

$$\begin{aligned} \hat{\alpha}_{k-1,i} &= \rho_i \alpha_{k-1,i} \\ \hat{\beta}_{k-1,i} &= \rho_i \beta_{k-1,i} \\ \hat{\mu}_{k|k-1} &= \mathbf{F}_{k-1} \hat{\mu}_{k-1|k-1} \\ \mathbf{P}_{k|k-1} &= \mathbf{F}_{k-1} \mathbf{P}_{k-1|k-1} \mathbf{F}_{k-1}^T + \mathbf{Q}_{k-1} \end{aligned} \quad (18)$$

where  $\rho_i \in (0, 1]$  is a scalar used for the extension of the noise fluctuations.

2. Update: In the update step, a fixed point iteration method is employed to achieve the best solution of the following equations. First set  $\mu_k^0 = \hat{\mu}_{k|k-1}$ ,  $\mathbf{P}_k^0 = \hat{\mathbf{P}}_{k|k-1}$ ,  $\alpha_{k,i}^0 = \frac{1}{2} + \hat{\alpha}_{k-1,i}$  and  $\beta_{k,i}^0 = \hat{\beta}_{k-1,i}$ , for  $i = 1, \dots, d$ . Then use the fixed-point iteration to achieve the solution of (16) and (17) for  $\ell$  steps: then set  $\beta_{k,i} = \beta_{k,i}^\ell$ ,  $m_k = m_k^\ell$  and  $P_k = P_k^\ell$ , after obtaining the optimal solution for the equations, the parameters are updated within the measurement model of the particle filter which thereby helps calculate the weights of each particle. In the next section, the VB aided particle filter is combined with the DBN to update the weights of the particles.

### C. Deep learning networks

Deep learning methods use a hierarchical learning method when training the classifier. As described in [11], hierarchical learning uses natural progression from low level to high level structure as seen in natural complexity, so it is easier to monitor what is being learnt and to guide the machine evolving to better subspaces. For example, when images are input into

the system, the first layer of the system represents the ‘edges’ of the feature; the second layer represents the ‘object parts’ of the feature and the third layer represents the objects in the features [11]. As described in [12], wherein a restricted Boltzmann machine (RBM) is employed, DBNs are graphical models which learn to extract deep hierarchical representations of the training data. DBNs provide the advantage of an intelligent method to use the limited information to train a classifier to calculate the weights of particles in human tracking, particularly with a single camera. The deep belief network we use is represented detailedly in [11], which is composed of one input layer, two RBMs based hidden layers and a one-class output layer. The process of training the RBM and DBN are described in [12] in detail. After training the DBNs following the process, the weight for each particle  $\mathbf{x}_k^i$  can be calculated as

$$p(\mathbf{x}_k^i) = e^{(c \cdot \mathbf{1} \cdot \mathbf{W}^{(m)})} \quad (19)$$

where  $\mathbf{1}$  is a  $(1 \times j)$  all-one vector,  $c$  is a constant we set for calculating the weights for the particles and  $\mathbf{W}^{(m)}$  is the weights from the last layer of DBN. In this way, the likelihood for each particle is obtained and these weights can then be taken as the input to the updating step of the PHD filter for MTT as discussed in the next section.

### D. Particle PHD implementation

To formulate the PHD filter the RFS framework is employed [13]. We denote  $\mathbf{D}_{k|k}(\mathbf{x})$  as the PHD filter at discrete time  $k$  associated with the multi-target posterior density  $p_{k|k}(\mathbf{X}_k | \mathbf{Z}_{1:k})$ , where  $\mathbf{X}_k = \{\mathbf{x}_k^m, m = 1, \dots, M\}$  includes the 2D position of all the human targets,  $\mathbf{x}_k^m$  denotes the state of the  $m^{\text{th}}$  target at time  $k$ ,  $M$  is the number of targets and  $\mathbf{Z}_{1:k}$  denotes the measurements up to time  $k$ . The PHD prediction step is defined as:

$$\mathbf{D}_{k|k-1}(\mathbf{x}_k^m) = \int \phi_{k|k-1}(\mathbf{x}_k^m, \xi) \mathbf{D}_{k-1|k-1}(\xi) d(\xi) + \Upsilon_k \quad (20)$$

where  $\Upsilon_k$  is the intensity function of the new target birth RFS,  $\phi_{k|k-1}(\mathbf{x}_k^m, \xi)$  is the analogue of the state transition probability in the single target case which is calculated from

$$\phi_{k|k-1}(\mathbf{x}_k^m, \xi) = e_{k|k-1}(\xi) f_{k|k-1}(\mathbf{x}_k^m | \xi) + \beta_{k|k-1}(\mathbf{x}_k^m | \xi) \quad (21)$$

in which  $f_{k|k-1}$  is the multi-target transition density,  $e_{k|k-1}(\xi)$  is the probability that the target still exists at time  $k$  and  $\beta_{k|k-1}(\mathbf{x}_k^m | \xi)$  is the intensity of the RFS that a target is spawned from the state  $\xi$ . The PHD update step is defined as [14]:

$$\mathbf{D}_{k|k}(\mathbf{x}_k^m) = \left[ p_M(\mathbf{x}_k^m) + \sum_{z \in \mathbf{Z}_k} \frac{\psi_{k,z}(\mathbf{x}_k^m)}{\kappa_k + \langle \psi_{k,z}, \mathbf{D}_{k|k-1} \rangle} \right] \mathbf{D}_{k|k-1}(\mathbf{x}_k^m) \quad (22)$$

where  $p_M$  is the missing detection probability,  $\psi_{k,z}(\mathbf{x}_k^m) = (1 - p_M) g_k(\mathbf{z} | \mathbf{x}_k^m)$  is the single-target likelihood defining the

probability that a measurement  $\mathbf{z}$  is generated by a target with state  $\mathbf{x}_k^m$ ,  $\kappa_k$  is the clutter intensity.

When the sequential Monte Carlo method is employed to approximate the PHD filter, two fundamental steps in the particle filter are sequential importance sampling and resampling. The basic principle of importance sampling is to represent a PDF  $p(\mathbf{X}_k)$  by a set of random particles associated with the weights, where  $\mathbf{X}_k^N = \{\mathbf{x}_k^i, i = 1, \dots, N\}$ , and  $N$  is the number of particles we employed in the particle filter. Given a set of particles [15]

$$\{w_{k-1}^i, \mathbf{x}_{k-1}^i\}_{i=1}^N \quad (23)$$

which are independently drawn from importance sampling density  $q(\mathbf{X}_k)$  [15], the weight of each particle can be calculated as

$$w_k^i = p(\mathbf{x}_k^i)/q(\mathbf{x}_k^i) \quad (24)$$

thus  $p(\mathbf{X}_k^N)$  can be approximated as

$$p(\mathbf{X}_k^N) \approx \sum_{i=1}^N w_k^i \delta(\mathbf{X}_k^N - \mathbf{x}_k^i) \quad (25)$$

where  $\delta(\cdot)$  denotes the Dirac delta function.

Assuming the particles for the PHD filter are independently drawn from the PDF  $p(\mathbf{X}_{k-1}^N | \mathbf{Z}_{1:k-1})$ , the particles  $\mathbf{x}_{k-1}^i, i = 1, \dots, N$  are propagated and updated by the Gaussian distribution, which are approximately distributed as  $p(\mathbf{X}_k^N | \mathbf{Z}_k)$  [16]. In this case, the proposed filter is an approximate implementation of the relationship between the prediction and updating step of the filter. The prediction and updating step can be described as follows.

1. Prediction: Draw particle  $\mathbf{x}_{k-1}^i$  from  $\mathbf{X}_{k-1}^N$  and feed it into the prediction step to obtain particles at time  $k$ . Thus the prediction model can be calculated as

$$p(\mathbf{X}_k^N | \mathbf{Z}_{k-1}) = \int p(\mathbf{X}_k^N | \mathbf{X}_{k-1}^N) p(\mathbf{X}_{k-1}^N | \mathbf{Z}_{k-1}) d\mathbf{X}_{k-1}^N \quad (26)$$

2. Measurement update: Upon the receipt of the measurement  $\mathbf{Z}_k$ , the likelihood of each prior sample  $\mathbf{x}_{k-1}^i, i = 1, \dots, N$ , can be evaluated and drawn independently from importance sampling density  $q(\mathbf{X}_k^N | \mathbf{Z}_k)$  [16]. The importance weight for each prior sample can be calculated as:

$$w_k^i = \frac{p(\mathbf{Z}_k | \mathbf{x}_{k-1}^i) p(\mathbf{X}_k^N | \mathbf{Z}_{k-1})}{q(\mathbf{x}_{k-1}^i | \mathbf{Z}_k)} \quad (27)$$

Equations (26) and (27) above form the basis of the proposed particle PHD filter. By introducing (26) into the PHD updating formula (22), we can obtain the particle PHD updating equation:

$$w_k^{(i)} = \left[ p_M(x_k^{(i)}) + \sum_{z \in \mathbf{Z}_k} \frac{\psi_{k,z}(x)}{\kappa_k(z) + C_k(z)} \right] w_{k-1}^{(i)} \quad (28)$$

where

$$C_k(z) = \sum_{j=1}^{L_{k-1} + J_k} \psi_{k,z}(\tilde{\mathbf{x}}_k^{(j)}) \tilde{w}_{k-1}^{(j)} \quad (29)$$

The above work underpins the proposed particle PHD filter for human tracking; in the next subsection, human features can be extracted to train a deep belief network in the utilization of particle selection and the updating part of the particle PHD filter to mitigate the noise from the environment.

When the variational Bayes method is applied within the particle PHD filter, an iteration for updating the measurement noise should be added before the updating step for the PHD filter, in this case, the recursive particle PHD filter follows the following process

---

**Algorithm 1** Processing of the variational Bayes particle PHD filter

---

At each time  $k$ , sample  $J_k$  particles for each new-born target from background subtraction, after setting the weight to the new-born target particles as  $1/J_k$ , we can obtain the particle set  $\{\mathbf{x}_k, w_k\}_{i=1}^N$  where  $J_k$  is the new-born target number and  $N$  is the number of particles at time  $k$ .

For each particle  $i = 1, \dots, N$

Initialize the state  $\mathbf{x}_k^i$  and hyper parameters:  $\alpha_k^i, \beta_k^i, \mathbf{P}_k^i, \mathbf{R}_k^i$ .

1 Predict the noise parameters using (18).

2 Sample the particles.

3 Update the measurement noise parameters using Variational Bayesian approach with fixed point iteration with (16) to (18) described in Section II-B.

4 Calculate the weights for each particle with DBN with (19) to aid the weights updating step.

5 Evaluate the weights using (22).

6 Resample the particles.

END

---

From the above process, we can obtain the Variational Bayes particle PHD filter; in the next section, simulation results and comparisons will be given.

### III. SIMULATION RESULTS

In order to evaluate the performance of the proposed robust particle PHD filter for multiple target tracking, we employed datasets from the EC Funded CAVIAR project [8], Video EnterExitCrossingPaths1cor and EnterExitCrossingPaths1front. There are four human targets appearing, occluding each other, and disappearing in the shopping mall environment. The number of particles is set to be 1000. When compared with the traditional PHD filter, our proposed PHD filter shows its improvement in reducing the mean of the error and standard deviation, where in scenario 1 which denotes the video EnterExitCrossingPaths1cor, the mean of the error is reduced from 13.45 to 11.89 with the standard deviation is reduced from 16.68 to 12.85; in scenario 2 which denotes the video EnterExitCrossingPaths1front, the mean of the error is reduced from 34.54 to 22.26 with the standard deviation is reduced from 19.87 to 11.85. To see this further the optimal subpattern assignment (OSPA) [17] is employed. The OSPA comparisons for both scenarios are shown in Figs. 1 and 2 respectively.

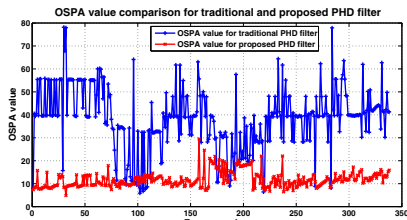


Fig. 1: Comparison of target OSPA value for scenario 1 between the proposed and the traditional PHD filter, where the blue line denotes the OSPA value for the traditional particle PHD filter with an average value of 38.25 and the red line denotes the OSPA value for the proposed particle PHD filter with an average value of 11.79.

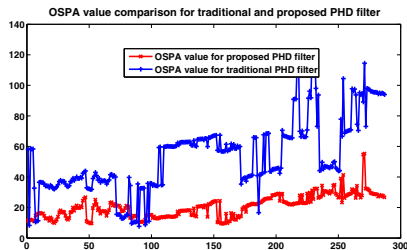


Fig. 2: Comparison of target OSPA value for scenario 2 between the proposed and the traditional PHD filter, where the blue line denotes the OSPA value for the traditional particle PHD filter with an average value of 53.55 and the red line denotes the OSPA value for the proposed particle PHD filter with an average value of 20.62.

To verify the performance improvement, a new performance metric for multiple target tracking based on optimal subpattern assignment, named OSPAMT [18] is employed, the OSPAMT includes both cardinality and localization errors versus time for the video 'EnterExitCrossingPaths1cor' are shown as From

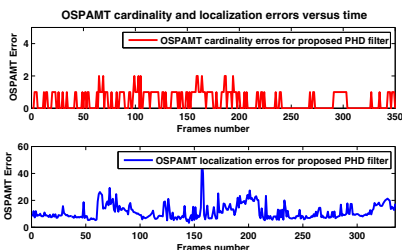


Fig. 3: OSPAMT cardinality and localization errors versus time for video 'EnterExitCrossingPaths1cor'.

the comparison of both OSPA and OSPAMT results, it can be observed that our proposed PHD filter performs much better than the baseline PHD filter since in both scenarios the OSPA value and OSPAMT are much reduced, which means false alarm and missing detection performance of our proposed PHD filter is likely to be much improved compared to the traditional PHD filter. The error for the PHD filter is mostly from the false alarm and miss detection caused by the noise from the background subtraction step, which can be mitigated by the DBN classifier in our proposed PHD filter. Both the mean of the error and the localization errors from OSPAMT are mitigated with the aid of our Variational Bayesian step for the update of the measurement parameters. This is because the parameters are adaptive to the posterior of the joint distribution of the measurements parameters and the state model. From the results, we can see that the proposed PHD filter improves the tracking accuracy over the traditional PHD filter.

## IV. CONCLUSIONS AND FUTURE WORK

In this paper, we have presented a new DBN aided variational Bayes particle PHD filter for human tracking, which is based on recursively forming separable approximations to the joint distribution of state and noise parameters by variational Bayesian methods and the noise mitigating step with the aid of DBN. The performance of the algorithm has been demonstrated by simulations. In our future work, more sequences will be used to evaluate the proposed PHD filter and an interaction model will be used to describe the state model of the targets.

## V. ACKNOWLEDGMENT

This work was supported by the Engineering and Physical Sciences Research Council (EPSRC) Grant number EP/K014307 and the MOD University Defence Research Collaboration in Signal Processing.

## REFERENCES

- [1] D. E. Clark, "Multiple target tracking with the probability hypothesis density filter." PhD thesis, Heriot-Watt University, 2006.
- [2] E. Maggio, M. Taj, and A. Cavallaro, "Efficient multi-target visual tracking using Random Finite Sets," *IEEE Transactions on Circuits and Systems for Video Technology*, vol. 10, pp. 1–12, 2008.
- [3] D. E. Clark and J. Bell, "Data association for the PHD filter." *The Second International Conference on Intelligent Sensors, Sensor Networks and Information Processing*, 2005, pp. 217–222.
- [4] K. Panta, B.-N. Vo, and S. Singh, "Novel data association schemes for the probability hypothesis density filter," *IEEE Transactions on Aerospace and Electronic Systems*, vol. 43, no. 2, pp. 556–570, 2007.
- [5] E. Maggio and A. Cavallaro, *Video Tracking*. John Wiley and Sons, Ltd, 2011.
- [6] S. Sarkka and A. Nummenmaa, "Recursive noise adaptive Kalman filtering by Variational Bayesian approximations," *IEEE Transactions on Automatic Control*, pp. 596–600, 2009.
- [7] T. S. Jaakkola, "Tutorial on variational approximation methods," *In Advanced Mean Field Methods: Theory And Practice*, M. Oper and D. Saad, Eds. Cambridge, MA: MIT Press, pp. 129–159, 2001.
- [8] R. Fisher. Caviar case scenarios. [Online]. Available: <http://groups.inf.ed.ac.uk/vision/CAVIAR/CAVIARDATA1/>
- [9] G. Zhang, F. Lian, C. Han, and S. Han, "An improved PHD filter based on Variational Bayesian method for multi-target tracking," *in Proc. IEEE 17th Conference on Information Fusion*, pp. 1–6, 2014.
- [10] J. Christmas and R. Everson, "Robust autoregression: Student-t innovation using variational Bayes," *IEEE Transactions on Signal Processing*, vol. 59, pp. 48–57, 2011.
- [11] P. Feng, M. Yu, S. M. Naqvi, and J. Chambers, "Deep learning for posture analysis in fall detection," *in Proc. IEEE 19th of the International Conference on Digital Signal Processing*, pp. 1–6, 2014.
- [12] G. Hinton and R. Salakhutdinov, "Reducing the dimensionality of data with neural networks," *Science*, pp. 504–507, 2006.
- [13] R. Mahler, "A theoretical foundation for the Stein-Winter Probability Hypothesis Density (PHD) multitarget tracking approach." DTIC Document, 2000.
- [14] A. Doucet, B. Vo, C. Andrieu, and M. Davy, "Particle filtering for multi-target tracking and sensor management." *The International Conference on Information Fusion, Annapolis, MD*, 2002, pp. 474–481.
- [15] M. S. Arulampalam, S. Maskell, N. Gordon, and T. Clapp, "A tutorial on particle filters for online nonlinear/non-Gaussian bayesian tracking." *IEEE Transactions on Signal Processing*, vol. 50, pp. 2454–2467, 2002.
- [16] S. Li, H. Wang, and T. Chai, "A t distribution based particle filter for target tracking." *Proceedings of the 2006 American Control Conference*, pp. 2191–2196, 2006.
- [17] B. Ristic, B. N. Vo, and D. Clark, "Performance evaluation of multi-target tracking using the OSPA metric," *in Proc. IEEE 13th Conference on Information Fusion*, pp. 1–7, 2010.
- [18] T. Vu and R. Evans, "A new performance metric for multiple target tracking based on optimal subpattern assignment," *in 17th IEEE International Conference on Information Fusion (FUSION)*, 2014, pp. 1–8.

# GPU-Accelerated Gaussian Processes for Object Detection

Calum Blair

Institute for Digital Communications  
University of Edinburgh  
Edinburgh, UK  
Email: c.blair@ed.ac.uk

John Thompson

Institute for Digital Communications  
University of Edinburgh  
Edinburgh, UK

Neil M. Robertson

Institute for Sensors, Signals and Systems  
Heriot-Watt University  
Edinburgh, UK

**Abstract**—Gaussian Process classification (GPC) allows accurate and reliable detection of objects. The high computational load of squared-error or radial basis function kernels limits the applications that GPC can be used in, as memory requirements and computation time are both limiting factors. We describe our version of accelerated GPC on GPU (Graphics Processing Unit). GPUs have limited memory so any GPC implementation must be memory-efficient as well as computationally efficient. Using a high-performance pedestrian detector as a starting point, we use its packed or block-based feature descriptor and demonstrate a fast matrix multiplication implementation of GPC which is also extremely memory efficient. We demonstrate a speed up of 3.7 times over a multicore, BLAS-optimised CPU implementation. Results show that this is more accurate and reliable than results obtained from a comparable support vector machine algorithm.

## I. INTRODUCTION

Gaussian Process Classification (GPC) is an emerging method of performing classification and regression for various machine learning tasks. It has been used for prediction of house prices, detection of various objects in multiple modalities, and behavioural analysis [1]–[3]. It works by approximating the underlying distribution of the variables under observation by using a set of Gaussian distributions.

Recent work has shown that GPCs provide similar levels of classification *accuracy*, while giving predictions which are more *reliable* [4] than other comparable classifiers. See the pedestrian detection example in Figure 1; false positives with high confidence values (green, from another algorithm) are treated less confidently by the GPC (red). In this case, *accuracy* refers to the proportion of samples which are classified correctly [5], while *reliability* is defined as how well a classifier’s probabilistic predictions match ground-truth observations. Classification algorithms are more likely to be trusted and used by operators if they behave in a predictable or well-understood manner [6]. Therefore, we argue that ranking classifiers based on reliability – and improving that metric where possible – allows more appropriate deployment of classification and object or anomaly detection algorithms.

The main problem encountered when applying GPCs for large-scale or extremely data-rich machine learning tasks is that the calculations involved are expensive, both in terms of processing time and memory use. General-Purpose Graphics Processing Units (GPUs) have been used for some time now

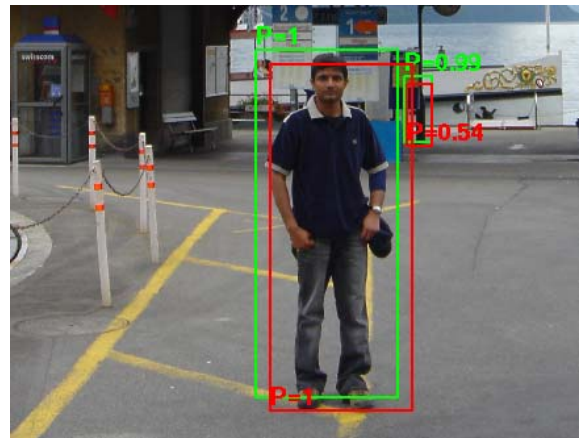


Fig. 1: Existing detector (ACF with Adaboost classifier, green) detects pedestrians and false positives with high confidence. Gaussian Processes classifier (red) assigns low confidence to false positives but maintains high confidence in true positives.

to speed up algorithm processing and evaluation due to the high levels of parallelism available. Other families of machine learning and classification algorithms such as support vector machines (SVMs) [7] and neural networks [8] have been accelerated on GPU, allowing the real-time classification of test images and use in large-scale machine learning tasks.

This paper describes our accelerated Gaussian Process classifier implementation focusing on one such problem; reliably detecting pedestrians in images using a state-of-the-art feature extraction pipeline. We then compare this to an accelerated SVM classifier to provide a baseline. Although we concentrate on detection of pedestrians here, this can be extended to any large-scale problem where features are extracted then stored in a memory-efficient manner.

In Section II we describe related work and existing algorithms and implementations. In Section III we describe the algorithm we use in detail, our accelerated implementation of it, and our testing methodology. We present timing, accuracy and reliability results in Section IV and discuss our conclusions and avenues for future work in Section V.



Fig. 2: Feature vector with multiple feature channels (three colour channels, pixel gradient magnitude, and gradient histograms in six angular bins) extracted from an image patch.

## II. RELATED WORK

Here we discuss feature extraction, GPCs and implementations.

### A. ACF Classifier

The ACF (Aggregate Channel Features) pedestrian detector is one of the top-performing classifiers on current object detection tasks [9]. It is based on one of the most well-known object detectors, histograms of oriented gradients (HOG) [10]. It depends on extracting multiple different feature channels from an image. The reference algorithm by Dollar *et al.* [9] uses ten channels. Starting with a colour image, ACF extracts LUV colour channels, pixel gradient magnitudes, and builds a six-bin histogram of pixel gradient orientations. This approach allows colour and shape features to be extracted. A set of features for an image patch is shown in Figure 2. This is then classified using an Adaboost classifier to give the final detection result. Given the sample resolution involved and the number of channels present, each feature vector has around 5000 entries. Large datasets therefore require large numbers of calculations during training and testing stages. This paper concentrates on acceleration of test-time calculations.

### B. Gaussian Process Classification

Here we concentrate on binary classification of samples with labels  $y \in \{0, 1\}$ . A high-level description of GPCs is given here, then we provide specific details of the approximation algorithm used in Section III. Gaussian Process Classifiers allow probabilistic prediction  $p(y = +1|\mathbf{x}_*)$  of a new data sample  $\mathbf{x}_*$ , after parameter learning on a set of training data  $\mathbf{X}$  and matching labels  $\mathbf{y}$ . This is done in two stages. The first involves defining a latent set of functions  $f(x)$ . This is assumed to have a Gaussian distribution and can be described by mean  $\mu(x)$  and covariance function  $k(\mathbf{X}, \mathbf{x}_*)$ . This can be a squared-error kernel:

$$k(x_i, x_j) = \sigma \exp\left(-\frac{(\mathbf{x}_i - \mathbf{x}_j)^2}{2\ell^2}\right). \quad (1)$$

where  $\sigma$  and  $\ell$  are hyperparameters learned in the training process. A common alternative is the linear kernel:

$$k(x_i, x_j) = \sigma \mathbf{x}_i \cdot \mathbf{x}_j. \quad (2)$$

To train a classifier, the distribution of the variable  $f_*$  corresponding to (i.e., which best fits)  $\mathbf{x}_*$  must first be estimated:

$$p(f_*|\mathbf{X}, \mathbf{y}, \mathbf{x}_*) = \int p(f_*|\mathbf{X}, \mathbf{x}_*, \mathbf{f})p(\mathbf{f}|\mathbf{X}, \mathbf{y})d\mathbf{f}. \quad (3)$$

where  $\mathbf{f}$  is the distribution of the latent function over  $\mathbf{X}$ . The second stage involves ‘squashing’  $f_*$  with an activation function with output range  $[0, 1]$ , such as:

$$\sigma(x) = \frac{1}{(1 + \exp(-f(x)))}. \quad (4)$$

This can then be used to calculate the final class membership probability:

$$\pi \triangleq p(y = +1|\mathbf{X}, \mathbf{y}, \mathbf{x}_*) = \int \sigma(f_*)p(f_*|\mathbf{X}, \mathbf{y}, \mathbf{x}_*)df_*. \quad (5)$$

The training process is  $\mathcal{O}(n^3)$ , while testing is  $\mathcal{O}(n^2)$ .

As a baseline we use the Support Vector Machine (a common classification approach) with a radial basis function (RBF) kernel. The SVM classification equation is given below, with  $\alpha$ ,  $\mathbf{w}$  and  $b$  learned during training.

$$f(\mathbf{x}) = \sum_{i=1}^N \alpha_i K(\mathbf{x}, \mathbf{w}_i) + b \quad (6)$$

The RBF kernel used is identical to that given in (1).

### C. Optimal Computation and Acceleration

Gaussian process regression and classification make extensive use of linear algebra. The standard library used for this is LAPACK (Linear Algebra Package). This relies heavily on BLAS (Basic Linear Algebra Subprograms); this includes vector, matrix and vector-matrix algorithms, such as fast multiplication of two matrices and tools for solution of simultaneous equations<sup>1</sup>. Heavily optimised versions of BLAS and LAPACK have been developed for a wide variety of high-performance processors, where the order of operations and amount of data stored in each level of the cache and memory are tweaked by machine or by hand to ensure optimal performance [11]. Two GPU versions are available, NVIDIA cuBLAS<sup>2</sup> and MAGMA [12].

Software packages such as MATLAB and Numpy rely on BLAS for optimised computation. High-level statements like  $C = AB$  are converted to calls to optimised libraries such as:

$$C = \text{sgermm}(A, B)$$

(i.e. single-precision, general matrix-matrix multiply). One of the limitations of using BLAS is that all operations must be reformulated to fit within the available subroutines provided by the library. When evaluated, the exponent term in (1) is expanded to:

$$(\mathbf{x}_i - \mathbf{x}_j)^2 = \mathbf{x}_i^2 + \mathbf{x}_j^2 - 2\mathbf{x}_i \cdot \mathbf{x}_j. \quad (7)$$

Three separate calls are then made to BLAS to calculate each right-hand-side expression, resulting in three separate passes over the data. Ideally, we would pass once over each matrix, making all required calculations simultaneously. There is considerable room for improvement here; for extremely large problems (matrices of  $> 1000 \times 1000$  in size), memory

<sup>1</sup><http://www.netlib.org/blas/>

<sup>2</sup><https://developer.nvidia.com/cuBLAS>

accesses as well as computations become a problem; datasets become too big to fit in any cache and must be stored in memory and traversed multiple times for any calculation. This is particularly apparent when working with GPUs, where overall throughput tends to be dominated by memory accesses rather than computational performance. Memory on GPUs is also much more limited than on conventional processors; 2GB or 4GB maximum limits are common. This presents a problem when very large  $\mathbf{X}$  matrices are generated by the training process.

The contribution of this paper is to document and make available as code our GPU-accelerated implementation of a GPC inference stage for large classification problems, and present timing, accuracy and reliability results. Although this is coded specifically for the feature extraction stage of the ACF algorithm, it can easily be adapted and used in any algorithm which relies on data extraction from local feature vectors stored in a data-efficient manner.

### III. METHOD

First we describe the algorithm which allows us to approximate the latent function as a Gaussian, then the extraction and storage in memory of ACF descriptors. Finally, we show how the former can be applied to the latter in a computationally and memory efficient manner.

#### A. GP Inference using Laplacian Approximation

Our goal is to produce an expression for the second term in (5) which we can evaluate analytically or numerically. This requires expressions for the predictive mean  $\mathbb{E}[\mathbf{f}_*|\mathbf{X}, \mathbf{y}, \mathbf{x}_*]$  and predictive variance  $\mathbb{V}[\mathbf{f}_*|\mathbf{X}, \mathbf{y}, \mathbf{x}_*]$ . The algorithm here is taken from [13, Ch.3]; see this reference for further details.

We start by defining the relationship between training and test samples:

$$\begin{bmatrix} \mathbf{f} \\ \mathbf{f}_* \end{bmatrix} \sim \mathcal{N}\left(\mathbf{0}, \begin{bmatrix} K(\mathbf{X}, \mathbf{X}) & K(\mathbf{X}, \mathbf{x}_*) \\ K(\mathbf{x}_*, \mathbf{X}) & K(\mathbf{x}_*, \mathbf{x}_*) \end{bmatrix}\right). \quad (8)$$

Where  $K$  describes the covariance matrix between training samples  $\mathbf{X}$  and test samples  $\mathbf{x}_*$ , and is calculated using a kernel function  $k(x_i, x_j)$  such as (1) or (2).

For notational convenience, we define  $K_X$  as  $K(\mathbf{X}, \mathbf{X})$ ,  $K_{X^*}$  as  $K(\mathbf{X}, \mathbf{x}_*)$  and  $K_*$  as  $K(\mathbf{x}_*, \mathbf{x}_*)$  throughout. Using [13, Ch.2] and [14, Ch.8, §9.3], we can define a conditional Gaussian on (8) as:

$$\begin{aligned} \mathbf{f}_*|\mathbf{X}, \mathbf{x}_*, \mathbf{f} &\sim \mathcal{N}(K(\mathbf{x}_*, \mathbf{X})K_X^{-1}\mathbf{f}, \\ &K_* - K(\mathbf{x}_*, \mathbf{X})K_X^{-1}, K_{X^*}). \end{aligned} \quad (9)$$

Evaluating this directly as in (3) is intractable [15], so we use a Laplacian approximation (from [13, Ch.3§4]), which allows the posterior over the training data and labels in (3) to be approximated as a Gaussian:

$$p(\mathbf{f}|\mathbf{X}, \mathbf{y}) \approx q(\mathbf{f}|\mathbf{X}, \mathbf{y}) = \mathcal{N}(\hat{\mathbf{f}}, A^{-1}), \quad (10)$$

where

$$\hat{\mathbf{f}} = \arg \max_{\mathbf{f}} p(\mathbf{f}|\mathbf{X}, \mathbf{y}), \quad (11)$$

**Require:**  $\mathbf{X}, \mathbf{y}, \mathbf{f}$ , kernel function  $k(x_i, x_j)$

- 1:  $\hat{\mathbf{f}} \triangleq \mathbb{E}_q[\mathbf{f}|\mathbf{X}, \mathbf{y}] = \operatorname{argmax}_{\mathbf{f}} p(\mathbf{f}|\mathbf{X}, \mathbf{y})$  // Using Newton's method
- 2:  $K_X = K(\mathbf{X}, \mathbf{X})$
- 3:  $W = -\nabla \nabla \log(p(\mathbf{y}|\hat{\mathbf{f}}))$
- 4:  $L = \operatorname{cholesky}(I + W^{\frac{1}{2}} K_X W^{\frac{1}{2}})$
- 5: **return**  $W, L, \hat{\mathbf{f}}, K_X$

Fig. 3: Prepare training posterior. This only needs to be done once and can be re-used during testing.

and (where  $\nabla$  represents differentiation):

$$A = -\nabla \nabla \log(p(\mathbf{f}|\mathbf{X}, \mathbf{y})|_{\mathbf{f}=\hat{\mathbf{f}}}). \quad (12)$$

$\hat{\mathbf{f}}$  can thus be found by applying Bayes' rule to the posterior distribution over the training variables,  $p(\mathbf{f}|\mathbf{X}, \mathbf{y}) = p(\mathbf{y}|\mathbf{f})p(\mathbf{f}|\mathbf{X})/p(\mathbf{y}|\mathbf{X})$ . Here,  $p(\mathbf{y}|\mathbf{X})$  can be discarded as we wish to maximise  $\mathbf{f}$ . Taking the log of  $p(\mathbf{f}|\mathbf{X}, \mathbf{y})$  and differentiating, we obtain the equation for the predictive mean:

$$\mathbb{E}_q[\mathbf{f}_*|\mathbf{X}, \mathbf{y}, \mathbf{x}_*] = K_{X^*}^T \nabla \log p(\mathbf{y}|\hat{\mathbf{f}}). \quad (13)$$

Similarly, we define predictive variance as:

$$\mathbb{V}_q[\mathbf{f}_*|\mathbf{X}, \mathbf{y}, \mathbf{x}_*] = K_* - K_{X^*}^T (K_X + W^{-1})^{-1} K_{X^*}. \quad (14)$$

With the diagonal matrix  $W \triangleq -\nabla \nabla \log(p(\mathbf{y}|\hat{\mathbf{f}}))$ .

Defining the symmetric positive definite matrix  $\mathbf{B}$  as  $\mathbf{B} = I + W^{\frac{1}{2}} K_X W^{\frac{1}{2}}$  and using a Cholesky decomposition  $\mathbf{L}\mathbf{L}^T = \mathbf{B}$  such that  $\mathbf{L} = \operatorname{cholesky}(\mathbf{B})$ , (14) can be simplified to:

$$\mathbb{V}_q[\mathbf{f}_*|\mathbf{X}, \mathbf{y}, \mathbf{x}_*] = K_* - K_{X^*}^T W^{\frac{1}{2}} (\mathbf{L}\mathbf{L}^T)^{-1} W^{\frac{1}{2}} K_{X^*} \quad (15)$$

$$\mathbb{V}_q[\mathbf{f}_*|\mathbf{X}, \mathbf{y}, \mathbf{x}_*] = K_* - \mathbf{v}^T \mathbf{v} \quad (16)$$

where:

$$\mathbf{v} = L \setminus (W^{\frac{1}{2}} K_{X^*}). \quad (17)$$

Finally, this allows the posterior in (5) to be approximated as a Gaussian  $q(\mathbf{f}_*|\mathbf{X}, \mathbf{y}, \mathbf{x}_*)$  with mean (13) and variance (16). This can then be used to calculate mean and variance values of new samples, and hence assign them a probabilistic prediction value. These are summarised in Figure 3 (generation of intermediate matrices, given training data) and Figure 4 (test-time prediction). Compute-heavy lines in the prediction stage are marked with  $\blacktriangleright$ ; it is these that we must consider accelerating. The usual method of calculating every line in Figure 4, and the one which is best supported by BLAS, is to store training and test data with one column for each sample.

#### B. Feature Extraction and Sliding-Window Classification

The ACF detector, as with many object detectors, works by the 'sliding window' approach; first a set of features for the whole image is generated, then a classification window is run over all the features representing the source image. All features inside the window are formed into a feature vector and classified. Then the window is moved a short distance (e.g. 8 pixels) in one direction, and this process is repeated. As a single image patch 'block' representing a small

**Require:**  $\mathbf{X}, \mathbf{x}_*, \mathbf{y}, \hat{\mathbf{f}}, W, L$ , kernel function  $k(x_i, x_j)$

- 1:  $K_{X_*} = K(\mathbf{X}, \mathbf{x}_*) \blacktriangleright$
- 2:  $K_* = K(\mathbf{x}_*, \mathbf{x}_*) \blacktriangleright$
- 3:  $\mathbb{E}_q[f_* | X, \mathbf{y}, \mathbf{x}_*] = K_{X_*}^\top \nabla \log(p(\mathbf{y} | \hat{\mathbf{f}}))$  // latent mean
- 4:  $\mathbf{v} = L \setminus (W^{\frac{1}{2}} K_{X_*}) \blacktriangleright$
- 5:  $\mathbb{V}_q[f_* | X, \mathbf{y}, \mathbf{x}_*] = K_* - \mathbf{v}^\top \mathbf{v}$  // latent variance
- 6:  $\bar{\pi}_* = \int \sigma(z) \mathcal{N}(z | E_q[f_*], \mathbb{V}_q[f_*]) dz$  // prediction
- 7: **return**  $\bar{\pi}$

Fig. 4: Calculate  $\pi$  at test time. Compute-heavy lines marked with  $\blacktriangleright$ .

pixel region can belong to many windows simultaneously, the memory-efficient way to do this is to store the features block by block, channel by channel, and iterate through them as they are classified at test time, only forming complete feature vectors as they are presented to the classification algorithm. This is incompatible with the BLAS approach; thus we can either duplicate image blocks many times over to form BLAS-compatible feature vectors, prioritising speed of computation at the expense of memory consumption (and, in practice, slow down calculations as we shuffle test vectors in and out of cache), or prioritise a lower memory footprint, but be unable to use the efficient BLAS routines. Here we combine the benefits of both approaches (low memory consumption and optimised processing).

### C. GPU Acceleration

We now consider GPU acceleration of the algorithm in Figure 4. The computationally expensive parts are the calculation of  $K_{X_*}$  and  $K_*$  in Figure 4, lines 1 and 2, and the calculation of  $\mathbf{v}$  on line 4. For  $K_{X_*}$  and  $K_*$ , we consider the work documented in [12]. Kurzak *et al.*, through extensive automated parameter space exploration, produced an optimised version of the  $C = AB$  matrix multiplication algorithm for a GPU [12]. Given  $A = m \times D$  and a  $B = D \times n$  matrices, each kernel walked along a vector of dimension  $D$ , loaded an optimal number of values from the  $A$  and  $B$  matrices into fast shared memory, then cross-multiplied and summed to produce a single entry in  $C$ .

In our case, the  $A$  matrix is arranged as we would expect (as the training matrix has one sample in each row). All samples are separate, as they represent discrete positive or negative training examples with no overlap. The  $B$  matrix, however, is packed as described in §III-B. We therefore build a per-block lookup table of  $B$  entries, then read the corresponding entry. As  $B$  is so densely packed, this greatly reduces the number of reads from slow global memory which must be done, and means the calculation is dominated by reading of  $A$  and writing of  $C$  (the resulting  $K_{X_*}$  matrix). As [12] proved, these are already well-arranged. Subsequent kernels take the result of (7) and apply the remaining steps in (1) to get  $K_{X_*}$  and  $K_*$ , which is then transferred to the host to continue with Figure 4. The solution of the division involving the lower triangular matrix  $L$  on line 4 requires too much

TABLE I: Time taken to perform matrix multiplication stage as part of classification algorithm in a  $640 \times 480$  image using baseline (CPU) and GPU-accelerated Gaussian Process Classification and RBF support vector machine classification.

Algorithm	Processor	Implementation	Time(s)	Speedup
GPC	CPU	MATLAB BLAS	10.28	
GPC	GPU	GPGPGPU	2.77	3.7×
SVM	CPU	LIBSVM	66.92	
SVM	GPU	cuSVM [17]	1.74	38.5×

memory to obtain any benefit from performing the calculation on a GPU. In our experiments it proved to be faster to execute this on the CPU; the memory limitations on the GPU meant that the test covariance matrix  $K_{X_*}$  had to be partitioned into very small batches, because of the large size of  $K_X$ . This decreased transfer-to-compute ratio eventually meant that GPU processing of (17) was slower than performing the calculation on CPU.

## IV. RESULTS

Here, to establish accuracy results, we consider detection performance on the INRIA pedestrians dataset, using the testing methodology in [16]. We compare this to a RBF (radial basis function) SVM classifier accelerated on GPU, as this is an accelerated detector which uses a similar approach [17]; the calculation in (6) is very similar to Figure 4 line 1, but this computation is the only step required for SVM prediction. Figure 5, using a ROC curve, shows the true positive rate (TPR) achieved for a given false positive rate (FPR). Similarly, Figure 6 shows a clearer separation between the two approaches when the rate of false positives per image is plotted against the miss rate. By both measurements, the GPC is more accurate than the SVM version. This is true whether the evaluations are run on CPU or GPU. The reliability diagram in Figure 7 plots the confidence scores of predicted samples against ground truth. Here, a ‘well-calibrated’ or perfectly reliable detector would lie on the black  $y = x$  line (i.e. of all the detections it predicts with 60% confidence, 60% will be evaluated as true. It shows that the GP classifier is more reliable, as it lies closer to the black line representing a ‘well-calibrated’ classifier.

Timing results are given in Table I. As a baseline we compare this to a MATLAB BLAS GPU-accelerated implementation. The CPU version used an Intel Xeon X5650, with 12 cores at 2.67GHz. The GPU results used a NVIDIA GeForce GTX 680 with 1536 cores and 2GB RAM. This shows a 3.7× speedup compared to an optimised CPU processor. However, every prediction also requires (17) to be applied. In contrast, the cuSVM implementation in Table I performs classification in a single step and runs faster. This is partly because the SVM requires fewer support vectors to be multiplied (3000 as opposed to all 14000 training vectors used by the GPC), and partly because the CPU SVM implementation is less optimised.

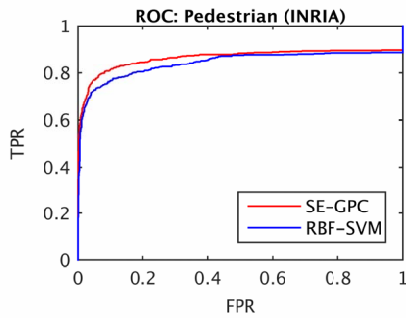


Fig. 5: GPC and SVM Receiver Operating Characteristic curve.

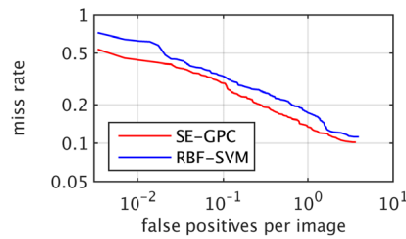


Fig. 6: GPC and SVM accuracy expressed as Detection Error Tradeoff curve. The GPC is always more accurate.

#### A. Discussion

This has speeded up the operation of the GPC method by a factor of 3.7. An alternative to this approach is to look at algorithmic methods for reducing the number of computations required to classify a new sample. Two methods can be used; reducing the quantity of training or test data which must be used in order to classify a sample, or simplifying the relatively expensive functions in the classification stage. Previous work [4] has considered the latter, showing that GPC with a linear kernel (2) performs significantly less well in both accuracy and reliability.

## V. CONCLUSIONS

This work has described the motivation behind customised GPU kernels for a common mathematical operation: the matrix version of the operation in (7), and their application to Gaussian Process Classification. This method demonstrates a speedup over the BLAS approach, where matrix multiplication operations are heavily optimised for a given processor. Therefore, when complex algorithms cannot be adequately represented by the available BLAS algorithms, a customised approach still offers a measurable benefit. However, as Table I shows, this approach is still slower than a SVM classifier with a similar kernel. Faster SVM predictions must be balanced against the increased accuracy and reliability available with GPCs. However, more efficient approaches are still needed to deliver real time performance. The code described here is available for download in [18].

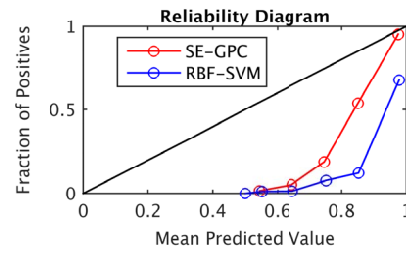


Fig. 7: GPC and SVM Reliability; classifiers closer to black line are more reliable.

## ACKNOWLEDGEMENT

This work was supported by the Engineering and Physical Sciences Research Council (EPSRC) Grant number EP/J015180/1 and the MOD University Defence Research Collaboration in Signal Processing.

## REFERENCES

- [1] R. Urtasun, D. J. Fleet, and P. Fua, "3D people tracking with Gaussian process dynamical models," in *Proc. IEEE Comput. Soc. Conf. Comput. Vis. Pattern Recognit.*, vol. 1. IEEE, 2006, pp. 238–245.
- [2] H. Grimmett, R. Paul, R. Triebel, and I. Posner, "Knowing When We Don't Know: Introspective Classification for Mission-Critical Decision Making," in *Proc. IEEE Int. Conf. Robot. Autom.*, May 2013.
- [3] S. Reece, S. Roberts, D. Nicholson, and C. Lloyd, "Determining intent using hard/soft data and Gaussian process classifiers," in *Inf. Fusion, Proc. 14th Int. Conf.*, 2011, pp. 1–8.
- [4] C. G. Blair, J. Thompson, and N. M. Robertson, "Introspective Classification for Pedestrian Detection," in *Sens. Signal Process. Def. (SSPD 2014)*, Edinburgh, 2014.
- [5] D. J. Hand, *Construction and Assessment of Classification Rules*. Wiley, 1997.
- [6] M. T. Dzindolet, S. A. Peterson, R. A. Pomranky, L. G. Pierce, and H. P. Beck, "The role of trust in automation reliance," *Int. J. Hum. Comput. Stud.*, vol. 58, no. 6, pp. 697–718, Jun. 2003.
- [7] A. Athanasopoulos, A. Dimou, V. Mezaris, and I. Kompatsiaris, "GPU acceleration for support vector machines," in *Proc. 12th Int. Work. Image Anal. Multimed. Interact. Serv. (WIAMIS 2011)*, no. April, 2011.
- [8] A. Coates, B. Huval, T. Wang, D. Wu, B. Catanzaro, and N. Andrew, "Deep learning with COTS HPC systems," in *Proc. 30th Int. Conf. Mach. Learn.*, 2013, pp. 1337–1345.
- [9] P. Dollár, R. Appel, S. Belongie, and P. Perona, "Fast feature pyramids for object detection," *IEEE Trans. Pattern Anal. Mach. Intell.*, vol. 36, no. 8, pp. 1532–1545, Aug. 2014.
- [10] N. Dalal and B. Triggs, "Histograms of Oriented Gradients for Human Detection," in *Proc. 2005 IEEE Conf. Comput. Vis. Pattern Recognit.* IEEE, 2005.
- [11] K. Goto and R. A. van de Geijn, "Anatomy of high-performance matrix multiplication," *ACM Trans. Math. Softw.*, vol. 34, no. 3, pp. 1–25, 2008.
- [12] J. Kurzak, S. Tomov, and J. Dongarra, "Autotuning GEMM kernels for the Fermi GPU," *IEEE Trans. Parallel Distrib. Syst.*, vol. 23, no. 11, pp. 2045–2057, 2012.
- [13] C. E. Rasmussen and C. K. I. Williams, *Gaussian Processes for Machine Learning*. University Press Group Limited, 2006.
- [14] R. von Mises, *Mathematical Theory of Probability and Statistics*. Academic Press, 1964.
- [15] C. Williams and D. Barber, "Bayesian classification with Gaussian processes," *IEEE Trans. Pattern Anal. Mach. Intell.*, vol. 20, no. 12, pp. 1342–1351, 1998.
- [16] P. Dollár, C. Wojek, B. Schiele, and P. Perona, "Pedestrian Detection: An Evaluation of the State of the Art," *IEEE Trans. Pattern Anal. Mach. Intell.*, vol. 34, no. 4, pp. 743–762, Jul. 2011.
- [17] A. Carpenter, "Cusvm: a cuda implementation of support vector classification and regression," 2009.
- [18] C. G. Blair, "GPGPGPU example," 2015. [Online]. Available: [http://homepages.ed.ac.uk/cblair2/code/gpgpgpu\\_example.zip](http://homepages.ed.ac.uk/cblair2/code/gpgpgpu_example.zip)

# Micro-Doppler based Recognition of Ballistic Targets using 2D Gabor Filters

Adriano Rosario Persico, Carmine Clemente, Christos V. Ilioudis,  
Domenico Gaglione, Jianlin Cao and John Soraghan

\*University of Strathclyde, CESIP, EEE, 204, George Street, G1 1XW, Glasgow, UK

E-mail: adriano.persico, carmine.clemente, c.ilioudis, domenico.gaglione, jianlin.cao, j.soraghan-@strath.ac.uk

**Abstract**—The capability to recognize ballistic threats, is a critical topic due to the increasing effectiveness of resultant objects and to economical constraints. In particular the ability to distinguish between warheads and decoys is crucial in order to mitigate the number of shots per hit and to maximize the ammunition capabilities. For this reason a reliable technique to classify warheads and decoys is required. In this paper the use of the micro-Doppler signatures in conjunction with the 2-Dimensional Gabor filter is presented for this problem. The effectiveness of the proposed approach is demonstrated through the use of real data.

## I. INTRODUCTION

The interest in recognition and classification of ballistic targets has grown in the last years. In particular, significant attention has been given to the challenge of distinguishing between warheads and decoys. The latter are objects of different shapes released by the missiles in order to introduce confusion in the interceptors. Since it is clear that warheads and decoys make specific micro-motions during their ballistic trajectory, the micro-Doppler effect analysis introduced in [1], and widely investigated in the last decade [2], may be used for the purpose of information extraction for target classification. Specifically, the warheads may be characterized by precession and nutation, while the decoys wobble, as described in [3] and [4]. Such different micro-motions generate different micro-Doppler signatures in the returned radar signal.

Classification based on the micro-Doppler signatures has been employed in [5] and [6] with feature extraction based on the Pseudo-Zernike moments.

In this paper, a novel algorithm for radar micro-Doppler classification based on the processing of the Cadence Velocity Diagram (CVD) with Gabor filter is presented. The Gabor filter has been successfully employed to extract reliable features in many different applications [7],[8],[9]. In particular, they have been usually used for texture and symbol classification, as in [7] and [10], and for face recognition in [11]. The scale, translation, rotation and illumination invariant properties of the filter have been utilised in these applications. The Gabor filter is capable of extracting local information from the micro-Doppler signature of the target of interest [12].

The remainder of the paper is organized as follows. Section II reviews the relevant 2D Gabor filter theory, while Section III describes the novel feature extraction algorithm. In Section IV the effectiveness of the proposed approach is demonstrated on real data. Section V concludes the paper.

## II. GABOR FILTER GLOBAL FEATURE

The 2D Gabor function is the product of a complex exponential representing a sinusoidal plane wave and an elliptical Gaussian in any rotation. The filter response in the continuous domain can be normalized to have a compact closed form [7],[11]

$$\psi(x, y) = \frac{f^2}{\pi\gamma\eta} e^{-\left(\frac{f^2}{\gamma^2}x'^2 + \frac{f^2}{\eta^2}y'^2\right)} e^{j2\pi f x'} \quad (1)$$

with

$$x' = x \cos(\theta) + y \sin(\theta), \quad y' = -x \sin(\theta) + y \cos(\theta) \quad (2)$$

where  $f$  is the central spatial frequency of the filter,  $\theta$  is the anti-clockwise rotation of the Gaussian envelope and the sinusoidal plane wave,  $\gamma$  is the spatial width of the filter along the plane wave, and  $\eta$  is the spatial width perpendicular to the wave. The sharpness of the filter is controlled on the major and the minor axes by  $\eta$  and  $\gamma$ , respectively, defining the aspect ratio of the Gaussian as  $\lambda = \eta/\gamma$ . The normalized filter harmonic response is [7]

$$\Psi(u, v) = e^{-\frac{\pi^2}{f^2}(\gamma^2(u-f)^2 + \eta^2v^2)} \quad (3)$$

where

$$u' = u \cos(\theta) + v \sin(\theta), \quad v' = -u \sin(\theta) + v \cos(\theta). \quad (4)$$

Figure 1 represents the real part of a Gabor filter response in the XY plane, with  $\eta = \gamma = 2\pi$ ,  $f = 4$  and for different orientation angles. In particular, from Figure 1a and Figure 1b, it is clear that the variation of the orientation angle leads to a rotation of the filter response.

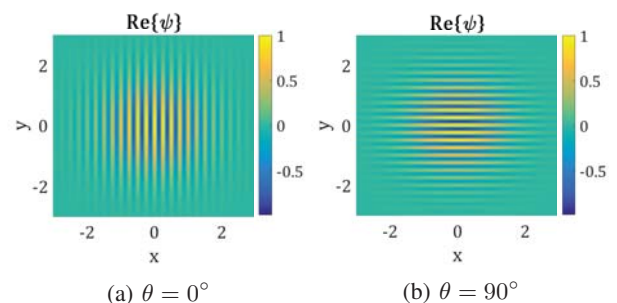


Figure 1: Real part of a Gabor filter response in the XY plane, with  $\eta = \gamma = 2\pi$  and  $f = 4$ .

Figure 2, instead, represents the magnitude of the Gabor filter harmonic response in the UV plane, obtained from the responses in Figure 1. The harmonic response is a pulse whose position depends on both  $f$  and  $\theta$ . Particularly, the pulse moves on a circumference centred in the origin and whose radius is defined by  $f$ , while  $\theta$  is the rotation angle in the anti-clockwise direction with respect to the  $\hat{u}$  axis, as shown in Figure 2a and Figure 2b. Hence, it is possible to extract local feature in the

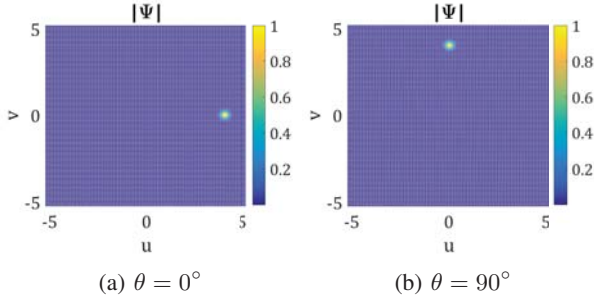


Figure 2: Magnitude of the Gabor filter harmonic response in the UV plane, with  $\eta = \gamma = 2\pi$  and  $f = 4$ .

Fourier domain by varying the filter parameters.

In the following subsection the classification algorithm based on features extracted with the Gabor filters is presented.

### III. FEATURE EXTRACTION ALGORITHM

The principal aim of the algorithm presented in this paper is to extract features based on the micro-Doppler by using 2D Gabor filters. For this reason, a fundamental step is to obtain a 2D image from the received radar signal scattered by the target of interest. A block diagram of the algorithm is shown in Figure 3. The starting point of the algorithm is the received

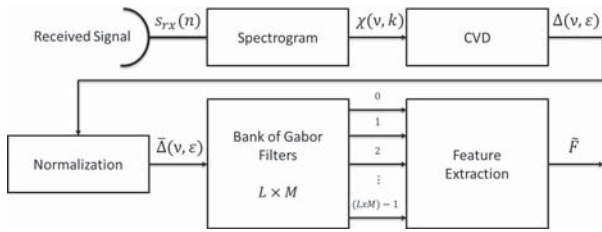


Figure 3: Block diagram of the proposed algorithm.

signal  $s_{rx}(n)$ , with  $n = 0, \dots, N - 1$ , containing the micro-Doppler components and where  $N$  is the number of signal samples. The first step is to evaluate the spectrogram through the computation of the modulus of the STFT (Short Time Fourier Transform) of the received signal  $s_{rx}(n)$  as follows:

$$\chi(\nu, k) = \left| \sum_{n=0}^{N-1} s_{rx}(n) w_h(n-k) \exp\left(-j2\nu \frac{n}{N}\right) \right| \quad (5)$$

$$k = 0, \dots, K - 1$$

where  $\nu$  is the normalized frequency and  $w_h(\cdot)$  is the smoothing window. The spectrogram is a time-frequency distribution that allows us to evaluate the signal frequency variation over the time and it is chosen for its robustness with respect to

the interference terms present in other time-frequency distributions. The next step consists of extracting the CVD (Cadence Velocity Diagram), that is defined as the Fourier Transform of the spectrogram along each frequency bin [5] and is given by

$$\Delta(\nu, \varepsilon) = \left| \sum_{k=0}^{K-1} \chi(\nu, k) \exp\left(-j2\nu \frac{k}{K}\right) \right| \quad (6)$$

where  $\varepsilon$  is the cadence frequency. The choice of the CVD is motivated by the possibility of extracting useful information such as the cadence of each frequency component and the maximum Doppler shift. Moreover, the CVD is more robust than the spectrogram since it does not depend on the initial position of the moving object. Thereafter, the CVD is normalized in order to obtain a matrix whose values lie in the range  $[0, 1]$  as follows

$$\bar{\Delta}(\nu, \varepsilon) = \frac{\Delta(\nu, \varepsilon) - \min_{\nu, \varepsilon} \Delta(\nu, \varepsilon)}{\max_{\nu, \varepsilon} [\Delta(\nu, \varepsilon) - \min_{\nu, \varepsilon} \Delta(\nu, \varepsilon)]} \quad (7)$$

Figure 4a and Figure 4b show an example of a normalized CVD and its 2D Fourier transform obtained from a signal scattered by a cylinder. Each element of the obtained matrix  $\bar{\Delta}$

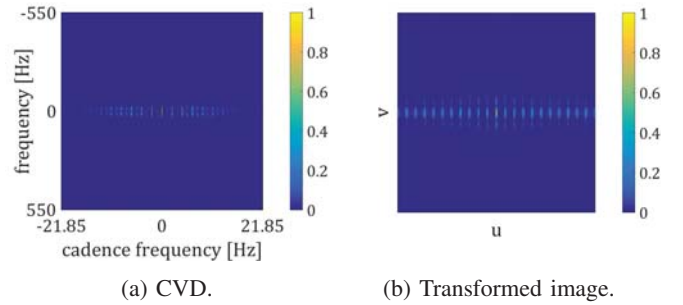


Figure 4: Example of a normalized CVD and its 2-D Fourier transform obtained from a signal scattered by a cylinder.

is considered as a pixel of a 2D image and this image is given as input to a bank of Gabor filters whose responses change by varying the orientation angle and the central frequency, as in (1). The value of each pixel of the output image is given by the convolution product of the Gabor function and the input image,  $\bar{\Delta}(\nu, \varepsilon)$ , and may be written as follows

$$g_{l,m}(\nu, \varepsilon; f_l, \theta_m) = \psi_{l,m}(\nu, \varepsilon; f_l, \theta_m) * \bar{\Delta}(\nu, \varepsilon) = \int_{-\infty}^{\infty} \int_{-\infty}^{\infty} \psi_{l,m}(\nu - \nu_\tau, \varepsilon - \varepsilon_\tau; f_l, \theta_m) \bar{\Delta}(\nu_\tau, \varepsilon_\tau) d\nu_\tau d\varepsilon_\tau \quad (8)$$

with  $l = 0, \dots, L - 1$  and  $m = 0, \dots, M - 1$ , where  $L$  and  $M$  are the numbers of central frequencies and orientation angles, respectively. The principal aim of the variation of  $f_l$  and  $\theta_m$  for each filter is to extract all the information contained in the CVD. Finally the output of the filters are processed to extract the feature vector used to classify the targets, which is the last step of proposed algorithm. In particular, a global feature is extracted from the output image of each filter by adding up the values of all the pixels, as follows

$$F_q = g_{l,m} = \sum_{\nu} \sum_{\varepsilon} |g_{l,m}(\nu, \varepsilon; f_l, \theta_m)| \quad (9)$$

where  $q = mL + l$ , with  $l = 0, \dots, L-1$ , and  $m = 0, \dots, M-1$ . Therefore, the obtained feature vector is given by

$$\mathbf{F} = [F_0 F_1 \dots F_{(L \times M) - 1}]. \quad (10)$$

Finally it is normalised as follows:

$$\tilde{\mathbf{F}} = \frac{\mathbf{F} - \eta_{\mathbf{F}}}{\sigma_{\mathbf{F}}} \quad (11)$$

where  $\eta_{\mathbf{F}}$  and  $\sigma_{\mathbf{F}}$  are the statistical mean and the standard deviation of the vector  $\mathbf{F}$ , respectively.

The benefit of the use of the proposed algorithm is clearer in the Fourier domain where the filtering is given by the multiplication of the harmonic response of the 2D Gabor filter and the transformed input. As shown above, the harmonic response of the Gabor filter is a pulse whose position depends on  $f$  and  $\theta$ . Since both the CVD and its 2D Fourier transform are characterized by vertical lines, as shown in Figure 4, the filter parameters can be tuned to match the lines, which are in different position for each class. This allows us to discriminate between different classes.

The classification performance of the extracted feature vectors is evaluated by using the  $k$ -Nearest Neighbour ( $k$ -NN) classifier, modified in order to account for the unknowns. Let  $\mathcal{N}$  be the set of nearest neighbour training vectors for the feature vector  $\mathbf{F}$ , that is:

$$\mathcal{N} = \left\{ \tilde{\mathbf{F}}_1, \dots, \tilde{\mathbf{F}}_k : \min_{\tilde{\mathbf{F}} \in \mathcal{T}} \|\tilde{\mathbf{F}} - \mathbf{F}\| \right\} \quad (12)$$

where  $\mathcal{T}$  is the training vectors set; moreover, let  $\rho = [\rho_1, \dots, \rho_k]$  be the labels of the vectors in  $\mathcal{N}$ , which can assume values in the range  $[1, \dots, V]$ , where  $V$  is the number of possible classes. The unknown class is made in two steps. First each label  $\rho_i, i = 1, \dots, k$  is updated as follows:

$$\rho_i = \begin{cases} 0 & \tilde{\mathbf{F}}_i \notin \mathcal{S}_{\mathbf{CM}_{\rho_i}}(\zeta_{\rho_i}) \\ \rho_i & \text{otherwise} \end{cases} \quad (13)$$

where  $\mathcal{S}_{\mathbf{CM}_v}(\zeta_v)$  is an hypersphere with centre  $\mathbf{CM}_v$  and radius  $\zeta_v$ , and  $\mathbf{CM}_v$  is the centre of mass of the training vectors belonging to the class  $v$ . Secondly, let  $\mathbf{s}$  be a  $(V+1)$ -dimensional score vector whose elements are the occurrences, normalised to  $k$ , of the integers  $[0, \dots, V]$  in the vector  $\rho$ ; eventually, the estimation rule is implemented as follows:

$$\hat{v} = \begin{cases} \arg \max \mathbf{s} & \text{if } \exists! (\max \mathbf{s}) > \frac{1}{2} \\ 0 & \text{otherwise} \end{cases} \quad (14)$$

where 0 is the unknown class.

Assuming that the feature vectors of each class are distributed uniformly around their mean vector, for all the analyses  $\zeta_v$  is chosen equal to  $\sigma_v \sqrt{12}/2$ , where  $\sigma_v = \text{tr}(\mathbf{C}_v)$  and  $\mathbf{C}_v$  is the covariance matrix of the training vectors which belong to the class  $v$ . The choice has been made according to the statistical proprieties of the uniform distribution. In fact, for an one dimensional uniform variable, the sum of the mean and the product between the standard deviation and the factor  $\sqrt{12}/2$ , gives the max possible value of distribution. Moreover, in order to consider the unknown class using a  $k$ -NN classifier,  $k$  has to be usually an integer greater than 1; then,  $k$  is set to 3. The choice of a  $k$ -NN classifier is justified for its low computational load and its capability of providing score values as an output. However, in general other classifiers with similar characteristics could also be selected.

## IV. EXPERIMENTAL RESULTS

In this section the effectiveness of the proposed algorithm is demonstrated using real data. The data has been realized using reproductions of the targets of interest. Particularly, two possible types of warhead have been considered, approximated by a simple cone and a cone with triangular fins at the base, while three are the possible decoys, approximated by a cylinder, a cone and a sphere.

According to the used model, the conical warhead has a diameter,  $d$ , of 1 m and a height,  $h$ , of about 0.75 m, while the fin's base,  $b_f$ , is 0.20 m and the height,  $h_f$ , is 0.50 m, as shown in Figure 5. The sizes of the decoys are usually

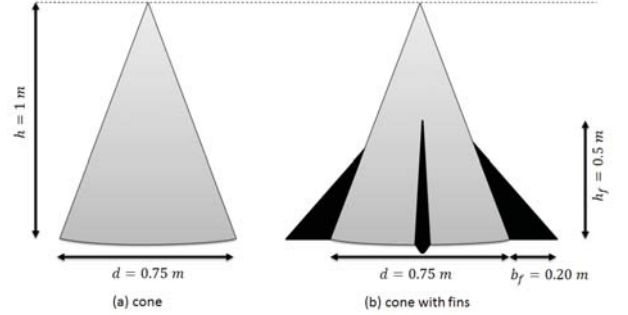


Figure 5: Model for two types of warhead.

comparable with the dimensions of the warheads in order to increase the number of false alarms. Therefore, according to the used model both the cylindrical and the conical decoys have diameter and height 0.75 m and 1 m respectively, while the sphere diameter is 1 m, as shown in Figure 6.

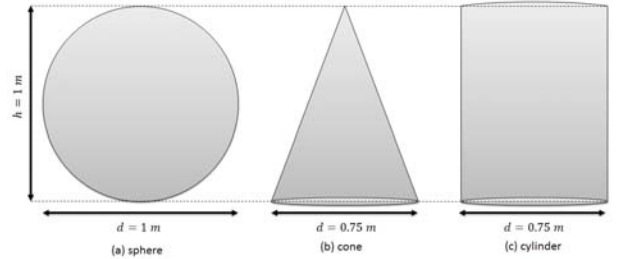


Figure 6: Model for three types of decoy.

The signals scattered by the replicas of the targets have been acquired by using a Continuous Wave (CW) radar, on varying the azimuth and the elevation angles. In particular, 10 acquisitions of 10 seconds have been made for each targets and for each possible couple of azimuth and elevation angles using three possible values for both of them, which are  $[0^\circ; 45^\circ; 90^\circ]$ . The different movements of the warheads and the decoys have been simulated by using a ST robotic manipulator R-17 and an added rotor motor [13].

### A. Results

In this section the proposed algorithm is compared with the Pseudo-Zernike (PZ) moments based feature vector approach,

presented in [5]. The targets of interest for the described analysis are divided in two classes which are *Warhead* and *Decoy*. Moreover, both of them are divided in sub-classes, and in particular the *Warhead* class comprises two sub-classes, one for warheads without the fins and the other one for those with fins, while *Decoy* class comprises three sub-classes each of them associated with one of the three different types of considered decoys.

In order to analyse the performance of the proposed algorithm, three figures of merit are considered which are the probabilities of *correct Classification* ( $P_C$ ), *correct Recognition* ( $P_R$ ) and *Unknown* ( $P_U$ ). In particular, according to the following definition of probability

$$\frac{\# \text{ number of occurrences}}{\# \text{ number of analysed cases}}, \quad (15)$$

$P_C$  is defined as the number of correct classified objects over the total number of analysed objects considering the two principal classes, while the second probability is calculated considering the classification on the five sub-classes; finally, the third figure of merit is given by the ratio of number of analysed objects for which the classifier does not take a decision and the total number of tests.

In order to statistically characterize the classifier and its performance, a Monte Carlo approach has been used, calculating the mean of the three figures of merit on several cases. In particular, 50 different runs have been carried out in which all the available signals have been divided randomly in 70% used for training and 30% for testing.

The spectrogram is computed by using a Hamming window with 75% overlap, and a varying number of points for the DFT,  $N_{bin}$ , which depends on both the used Hamming windows and the number of signal samples in order to obtain a square matrix for the spectrogram.

The algorithm is tested varying the observation time, which can be of 10, 5 and 2 seconds, the SNR and the dimension of the bank of filters, which depends on the chosen orientation angular pass  $\theta_{step}$ . Specifically, the number of filters,  $Q$ , is given by

$$Q = L \times \left( \left\lceil \frac{\pi/2}{\theta_{step}} \right\rceil + 1 \right) \quad (16)$$

where  $\lceil x \rceil$  is the ceiling function which gives the largest integer  $\geq x$ . The latter is fixed for the analysis, particularly 4 frequencies are used whose values are 0.5, 1, 1.5 and 2, while the integer values of  $\theta_{step}$  varies in the interval  $[3^\circ, 10^\circ]$ .

Figure 7 shows  $P_C$  and  $P_R$  versus the dimension of the bank of Gabor filters for different signal's duration. Analysing the results, it is possible to note that the average correct classification is greater than 0.98 for any value of  $Q$  and for both the signal's duration of 10 and 5 seconds; classification performance slightly decreases for the 2 seconds observation time case, due to the reduced amount of micro-Doppler information contained in the analysed signal. Moreover, the performance has shown that  $P_U$  is always under 0.02 for all the values of both the number of filters and the signal's duration. Figure 8a shows the performance on varying the SNR and with  $Q = 124$ . In particular, assuming that the noise is negligible for the acquired signals, the analysis over the SNR has been conducted by adding white Gaussian noise. It is clear that  $P_C$  and  $P_R$  slightly decrease as the signal's duration decreases while they improve by increasing the SNR, especially they are

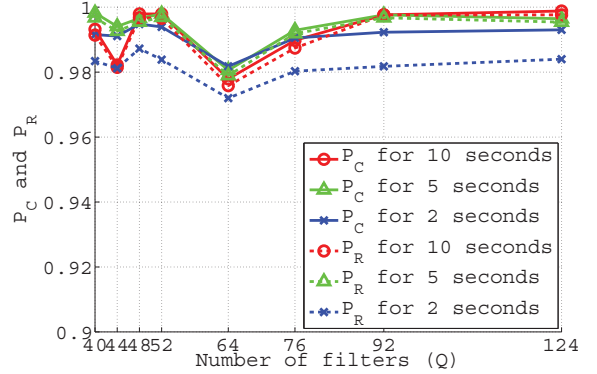


Figure 7: Probabilities of correct Classification,  $P_C$ , and correct Recognition,  $P_R$ , on varying  $Q$  and the duration of the observation.

greater than 0.99 when the SNR is above 0 dB. However, while for 10 seconds the performance remains almost constant, it decreases for signals of 5 and 2 seconds and for lower values of SNR. Figure 8b shows the performance of the PZ based algorithm for moments order of 10, which means that the length of the feature vector is  $(order + 1)^2 = 121$ . From the figure, it can be noted that for this algorithm the performance increases with the SNR. However,  $P_C$  and  $P_R$  are greater using the algorithm based on Gabor Filter for any value of SNR, when comparable dimensions of the feature vectors for the two approaches are considered.

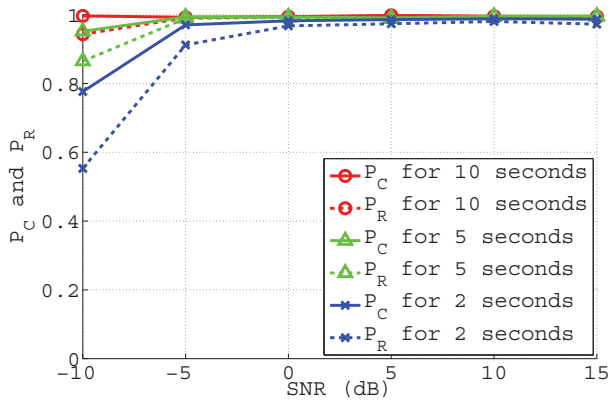
Finally, Figure 9 represents  $P_U$  for both the algorithms when the SNR and the observation time are varied. As shown, while for the proposed method  $P_U$  is smaller than 0.01 in any analysed case, for the PZ features the performance improves by increasing both the signal's duration and SNR.  $P_U$  becomes smaller than 0.01 for any analysed observation time when the SNR is greater than 5 dB, however it is worse compared to the performance obtained with the Gabor features.

## V. CONCLUSION

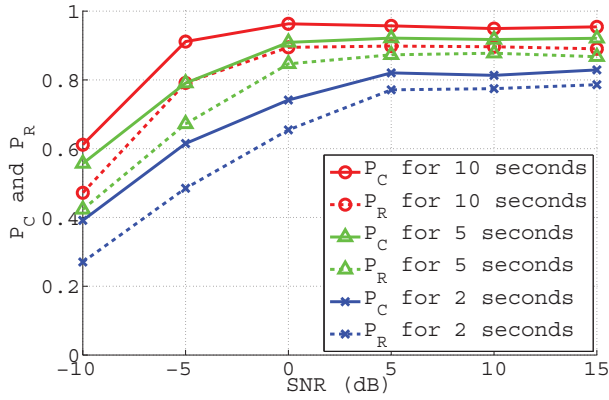
In this paper a novel algorithm used to extract robust feature based on micro-Doppler signature is presented. In particular, the algorithm takes advantage of the 2D Gabor filter applied on the normalized Cadence Velocity Diagram evaluated from the received signal. The reliability of the novel features has been demonstrated by testing them on real micro-Doppler data with the aim to classify between warheads and decoys. The performance has shown that these features generally ensure to correctly classify a ballistic target with a probability greater than 0.99 between different classes and, in particular, the performance is high also for low values of the SNR considering signals whose duration is bigger than 5 seconds. The proposed algorithm has been compared with the method which uses the Pseudo-Zernike moments based feature vector showing that the novel approach ensures better performance for the same number of features.

## ACKNOWLEDGMENT

This work was supported by the Engineering and Physical Sciences Research Council (EPSRC) Grant number EP/K014307/1.



(a) Gabor features,  $Q = 121$



(b) PZ feature, order 10

Figure 8: Probabilities of correct Classification,  $P_C$ , and correct Recognition,  $P_R$ , on varying the SNR and the signal's duration.

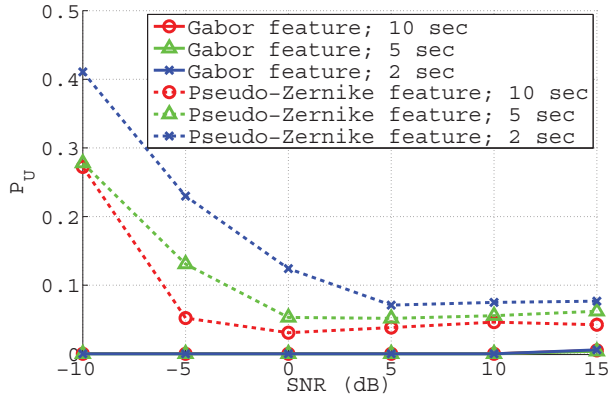


Figure 9: Unknown Probability,  $P_U$ , on varying the SNR and the signal's duration for the Gabor filter based and the Pseudo-Zernike moments based approaches.

## REFERENCES

[1] V. Chen, F. Li, S. Ho, and H. Wechsler, "Micro-Doppler effect in radar: Phenomenon, model, and simulation study," *IEEE Transactions on Aerospace and Electronic Systems*, vol. 42, no. 1, pp. 2–21, Jan 2006.

[2] C. Clemente, A. Balleri, K. Woodbridge, and J. Soraghan, "Developments in target micro-Doppler signatures analysis: radar imaging, ultrasound and through-the-wall radar," *EURASIP Journal on Advances in Signal Processing*, vol. 2013, no. 1, 2013.

[3] L. Liu, D. McLernon, M. Ghogho, W. Hu, and J. Huang, "Ballistic missile detection via micro-Doppler frequency estimation from radar return," *Digital Signal Processing*, vol. 22, no. 1, pp. 87–95, 2012.

[4] G. Hongwei, X. Liangui, W. Shuliang, and K. Yong, "Micro-Doppler signature extraction from ballistic target with micro-motions," *IEEE Transactions on Aerospace and Electronic Systems*, vol. 46, no. 4, pp. 1969–1982, Oct 2010.

[5] L. Pallotta, C. Clemente, A. De Maio, J. Soraghan, and A. Farina, "Pseudo-zernike moments based radar micro-doppler classification," in *Radar Conference, 2014 IEEE*, May 2014, pp. 0850–0854.

[6] C. Clemente, L. Pallotta, I. Proudler, A. De Maio, J. Soraghan, and A. Farina, "Pseudo-zernike-based multi-pass automatic target recognition from multi-channel synthetic aperture radar," *Radar, Sonar Navigation, IET*, vol. 9, no. 4, pp. 457–466, 2015.

[7] J.-K. Kamarainen, V. Kyrki, and H. Kalviainen, "Invariance properties of gabor filter-based features-overview and applications," *Image Processing, IEEE Transactions on*, vol. 15, no. 5, pp. 1088–1099, May 2006.

[8] J. Ilonen, J. Kämäräinen, and H. Kälviäinen, "Efficient computation of gabor."

[9] V. Kyrki, J.-K. Kamarainen, and H. Kälviäinen, "Simple gabor feature space for invariant object recognition," *Pattern recognition letters*, vol. 25, no. 3, pp. 311–318, 2004.

[10] N. Mittal, D. Mital, and K. L. Chan, "Features for texture segmentation using gabor filters," in *Image Processing And Its Applications, 1999. Seventh International Conference on (Conf. Publ. No. 465)*, vol. 1, Jul 1999, pp. 353–357 vol.1.

[11] J. Ilonen, J.-K. Kamarainen, and H. Kalviainen, "Fast extraction of multi-resolution gabor features," in *Image Analysis and Processing, 2007. ICIAP 2007. 14th International Conference on*, Sept 2007, pp. 481–486.

[12] J. Lei and C. Lu, "Target classification based on micro-doppler signatures," in *Radar Conference, 2005 IEEE International*, May 2005, pp. 179–183.

[13] S. A. P. Ltd., "Robotics within reach." Tech. Rep. [Online]. Available: <http://www.strobots.com/images/Brochure.pdf>

# Maximum Likelihood Signal Parameter Estimation via Track Before Detect

Murat Üney and Bernard Mulgrew

Institute for Digital Communications, School of Engineering,  
The University of Edinburgh,  
EH9 3JL, Edinburgh, UK  
Emails: {*M.Uney, B.Mulgrew*}@ed.ac.uk

Daniel Clark

School of Eng.& Physical Sciences,  
Heriot-Watt University  
EH14 4AS, Edinburgh, UK  
Email: *D.E.Clark@hw.ac.uk*

**Abstract**—In this work, we consider the front-end processing for an active sensor. We are interested in estimating signal amplitude and noise power based on the outputs from filters that match transmitted waveforms at different ranges and bearing angles. These parameters identify the distributions in, for example, likelihood ratio tests used by detection algorithms and characterise the probability of detection and false alarm rates. Because they are observed through measurements induced by a (hidden) target process, the associated parameter likelihood has a time recursive structure which involves estimation of the target state based on the filter outputs. We use a track-before-detect scheme for maintaining a Bernoulli target model and updating the parameter likelihood. We use a maximum likelihood strategy and demonstrate the efficacy of the proposed approach with an example.

## I. INTRODUCTION

Active sensors send energy packets towards a surveillance region in order to locate objects within from the reflections. For example, radars transmit radio frequency (RF) electromagnetic (EM) pulses and locate reflectors by searching for the pulse waveform in the spatio-temporal energy content of the received signal. This search is often performed using the matched filtering technique in which the received signal is projected onto versions of the transmitted waveform shifted so as to encode the desired reflector locations [1]. The more the energy a projection has, the more likely that it is due to the presence of a reflector.

In this work, we are interested in estimating parameters related to the signal at the output of the matched filters (MF) of a radar. This signal is composed of a distorted version of the waveform auto-correlation function in the presence of a reflector and additive thermal noise. Detection algorithms aim to decide on the existence of an object based on these outputs sampled at selected time instances so as to give the energy of the aforementioned projected signal [2]. These decisions are characterised by a probability of detection and a probability of false alarm which can be found given the energy of the reflected pulse at the receiver front-end  $E$ , and, the noise power  $\beta^2$  (or, the standard deviation of the noise process). These parameters also determine the signal-to-noise ratio which can be used to characterise the expected accuracy in further levels of processing [1].

Often only the noise power  $\beta^2$  is estimated using spatial windows over one snapshot of the outputs from MFs asso-

ciated with different range-bearing bins. These estimates are then used as design parameters in constant-false-alarm rate detection algorithms [3]. However, this approach is prone to errors due to incorrect identification of bins that contain only noise or signal-and-noise as a result of that this identification task requires the temporal information in the received signal which is ignored. Estimation of the signal energy  $E$  requires collection of temporal samples, as well. One way of doing this is to replace the MF bank in the basedband processing chain with iterative processing algorithms preferably working with high sampling rates (e.g., [4], [5]). This places requirements on the hardware architecture that are hard to satisfy in practice.

In this work, we use multiple snapshots from the MF bank collected across a time interval and perform spatio-temporal processing to jointly estimate  $E$  and  $\beta^2$ . We treat the problem as a parameter estimation problem in state space models. This allows us to integrate all the information in the measurements in a single likelihood function for both  $E$  and  $\beta^2$ . Such likelihood functions require the state distribution of the underlying (target) process given the measurement history, which can be found by the prediction stage of Bayesian filtering (or, tracking) recursions [6]. As the measurements are the MF outputs (as opposed to the outputs from a detection algorithm as in widely studied tracking scenarios), the corresponding recursions describe a track-before-detect algorithm.

In this framework, we derive explicit formulae for the parameter likelihood and its score function, i.e., the log-likelihood gradient. We use a maximum likelihood (ML) approach to design an unbiased and minimum variance estimator. In particular, we maximise the log-likelihood by using a coordinate ascent algorithm [7] in which we select the directions of increase based on the gradient and perform (golden section) line search along these directions.

This article is outlined as follows: We give the ML problem definition in Sec. II and detail the parameter likelihood in Sec. III. In Sec. IV, we derive the gradient of the objective function and detail an iterative optimisation procedure. We demonstrate the proposed approach with an example in Sec. V.

## II. PROBLEM DEFINITION

We consider a pulse transmitted towards a surveillance region which gets reflected if it interacts with an object at state

$x = [x_l^T, x_v^T]^T$  where  $x_l$  is the location,  $x_v = \dot{x}_l$  is the velocity of the object and  $(\cdot)^T$  denotes the transpose of a vector. These reflections are sought in the spatio-temporal energy content of the received signal by matched filtering [1]. Typically, the filter output is sampled with a period of the pulse length so as to compute the correlation of the transmitted waveform with the received signal corresponding to the  $i^{\text{th}}$  range bin of width  $\Delta r$  and  $j^{\text{th}}$  bearing bin of width  $\Delta\phi$ . Therefore, at time step  $k$ , the filter output for the bin  $(i, j)$  is given by

$$r_k(i, j) = \langle \mathbf{m}(i, j), \mathbf{r} \rangle \quad (1)$$

where  $\mathbf{r}$  is the (complex) received signal and  $\mathbf{m}(i, j)$  represents the transmitted waveform shifted to the  $(i, j)^{\text{th}}$  bin.

Let  $E_t$  represent the energy of the transmitted pulse, i.e.,  $E_t = \mathbf{m}^H \mathbf{m}$  where  $(\cdot)^H$  denotes the Hermitian transpose. In the presence of a reflecting object at state  $x_k$ , the inner product above leads to

$$r_k(i, j) = E_t e^{j\theta_k} h_{i,j}(x_k) + n_k \quad (2)$$

where  $n_k \sim \mathcal{N}(\cdot; 0, \beta^2)$  is circularly symmetric complex Gaussian noise with complex power  $\beta^2$ ,  $h_{i,j}(x_k)$  specifies the ratio of  $E$  that has been reflected from the  $(i, j)^{\text{th}}$  bin with (an unknown) phase  $\theta_k \sim \mathcal{U}(0, 2\pi]$ .

In this work, we assume a sensor resolution such that an object in the surveillance region affects only a single range-bearing bin, i.e.,

$$h_{i,j}(x_k) = H \delta_{C(x_k), (i,j)} \quad (3)$$

where  $\delta$  is the Kronecker's delta function,  $C: \mathcal{X} \rightarrow M \times N$  maps object states to range-bearing bins and  $H$  is the reflection coefficient.

We consider (2) and (3), and, are interested in estimating the received signal energy  $E \triangleq E_t H$ , and, the noise power  $\beta^2$ . These signal parameters determine the signal-to-noise ratio at the matched filter by

$$SNR = 10 \log_{10} \frac{E^2}{\beta^2}, \quad (4)$$

and are also required to compute false alarm rates and object detection probabilities of threshold rules [1].

We treat these parameters as (non-random) unknown constants and consider an ML solution. We now specify the arguments of the likelihood function: The reflection phase  $\theta_k$  in (2) models the ambiguity related to the exact position of the reflector within the  $(i, j)^{\text{th}}$  bin which cannot be mitigated. The modulus of (2), i.e.,

$$z_k(i, j) \triangleq |r_k(i, j)|$$

neglects the phase and is a sufficient statistic when testing whether  $r_k(i, j)$  is induced by a reflector at state  $x_k$  or noise alone. Therefore, we treat the intensity map given by  $z_k(i, j)$ s as measurements based on which the ML estimation will be relying upon.

Let us denote with  $\mathbf{z}_k$  the concatenation of  $z_k(i, j)$ s for all range-bearing bins, i.e., the intensity map. We would like to base the parameter likelihood on all measurements covering

time step 1 through  $k$ . Therefore, the ML estimation problem can be formulated as

$$(\hat{E}, \hat{\beta}^2) = \arg \max_{E, \beta^2} \log l(\mathbf{z}_1, \dots, \mathbf{z}_k | E, \beta^2), \quad (5)$$

the computation of which will be described next.

### III. THE SIGNAL PARAMETER LIKELIHOOD

Let us represent with a random set  $X_k$ , the events that there exists a reflector with state  $x_k$ , and, none, in which cases  $X_k = \{x_k\}$  and  $X_k = \emptyset$ , respectively.  $X_k$  is referred to as a Bernoulli random finite set (RFS) [8]. The likelihoods for  $z_k(i, j)$  given the signal parameters to be estimated  $E, \beta^2$  for the cases that  $X_k = \{x_k\}$  and  $X_k = \emptyset$  are well known results in the literature: After the uniformly distributed phase is marginalised-out, the modulus  $z_k(i, j)$  is distributed with a Rician distribution, i.e.,

$$\begin{aligned} l_1(z_k(i, j) | x_k; E, \beta^2) &\triangleq p(z_k(i, j) | X_k = \{x_k\}; E, \beta^2) \\ &= \frac{2z_k(i, j)}{\beta^2} \exp\left(-\frac{z_k(i, j)^2 + E^2}{\beta^2}\right) I_0\left(\frac{2z_k(i, j)E}{\beta^2}\right), \end{aligned} \quad (6)$$

if  $X_k = \{x_k\}$  and  $x_k \in C^{-1}(i, j)$ , where  $I_0$  is the zero order modified Bessel function of the first kind. Otherwise,  $z_k(i, j)$  follows a Rayleigh law given by [1, Chp.6]

$$\begin{aligned} l_0(z_k(i, j) | \beta^2) &\triangleq p(z_k(i, j) | X_k = \emptyset; E, \beta^2) \\ &= \frac{2z_k(i, j)}{\beta^2} \exp\left(-\frac{z_k(i, j)^2}{\beta^2}\right). \end{aligned} \quad (7)$$

Let us define the intensity map  $\mathbf{z}_k$  related quantities:

$$\begin{aligned} \Lambda(\mathbf{z}_k | x_k, E, \beta^2) &\triangleq l_1(z_k(C(x_k))) | x_k; E, \beta^2 \\ &\prod_{(i,j) \in \overline{C(x_k)}} l_0(z_k(i, j) | \beta^2), \end{aligned} \quad (8)$$

where  $\overline{C(x_k)}$  denotes the set of range-bearing bins complementing  $C(x_k)$ , and,  $l_0$  and  $l_1$  are given in (6) and (7), respectively. Similarly

$$\Lambda(\mathbf{z}_k | \beta^2) \triangleq \prod_{i,j} l_0(z_k(i, j) | \beta^2) \quad (9)$$

where the product is over all the range-bearing bins.

We assume that the noise processes for different bins and time steps are independent given the state of the object process  $X_k$ . Hence,

$$p(\mathbf{z}_k | X_k, E, \beta^2) = \begin{cases} \Lambda(\mathbf{z}_k | x_k, E, \beta^2), & \text{if } X_k = \{x_k\} \\ \Lambda(\mathbf{z}_k | \beta^2), & \text{if } X_k = \emptyset. \end{cases} \quad (10)$$

We would like to compute the parameter likelihood based on all measurements covering time step 1 through  $k$  which can be found as

$$\begin{aligned} l(\mathbf{z}_1, \dots, \mathbf{z}_k | E, \beta^2) &= \prod_{t=1}^k p(\mathbf{z}_t | \mathbf{z}_{1:t-1}, E, \beta^2) \\ &= l(\mathbf{z}_1, \dots, \mathbf{z}_{k-1} | E, \beta^2) \\ &\quad \times p(\mathbf{z}_k | \mathbf{z}_{1:k-1}, E, \beta^2) \end{aligned}$$

after using the chain rule of probabilities in the first line. The recursive structure revealed in the second line is typical to parameter estimation problems in state space models [9], [10], in which the update term is found by marginalising-out the underlying process  $X_k$ , i.e.,

$$p(\mathbf{z}_k|\mathbf{z}_{1:k-1}, E, \beta^2) = \int p(\mathbf{z}_k|X_k, E, \beta^2)p(X_k|\mathbf{z}_{1:k-1}, E, \beta^2)\delta X_k \quad (11)$$

where the right hand side is a set integral [8, Chp.11] as  $X_k$  is a set random variable. The first term inside the integral is the likelihood at  $k$  given by (10), and, the second term is the prediction of  $X_k$  based on the previous measurements.

The objective function for the ML solution in (5), hence, is given by

$$J(E, \beta^2; \mathbf{z}_{1:k}) = J(E, \beta^2; \mathbf{z}_{1:k-1}) + \log p(\mathbf{z}_k|\mathbf{z}_{1:k-1}, E, \beta^2). \quad (12)$$

Let us now consider the likelihood update term in (11). The computation of the predictive term inside the integral is detailed later in Section III-A. For our discussion on the likelihood update term, suppose that it is given by

$$p(X_k|\mathbf{z}_{1:k-1}, E, \beta^2) = \begin{cases} r_{k|k-1}s_{k|k-1}(x_k), & \text{if } X_k = \{x_k\} \\ 1 - r_{k|k-1}, & \text{if } X_k = \emptyset. \end{cases} \quad (13)$$

Then, (11) expands using the set integration rule in [8, Chp.11] with a Bernoulli RFS characterised by (13) and the likelihood in (10) as

$$\begin{aligned} p(\mathbf{z}_k|\mathbf{z}_{1:k-1}, E, \beta^2) &= p(\mathbf{z}_k|\emptyset, E, \beta^2)p(\emptyset|\mathbf{z}_{1:k-1}, E, \beta^2) \\ &+ \int p(\mathbf{z}_k|X_k = \{x_k\}, E, \beta^2)p(X_k = \{x_k\}|\mathbf{z}_{1:k-1}, E, \beta^2)dx_k \\ &= (1 - r_{k|k-1})\Lambda(\mathbf{z}_k|\beta^2) \\ &+ r_{k|k-1} \int \Lambda(\mathbf{z}_k|x_k, E, \beta^2)s_{k|k-1}(x_k)dx_k. \end{aligned} \quad (14)$$

After dividing both parts of the equation above by  $\Lambda(\mathbf{z}_k|\beta^2)$ , it can easily be shown that

$$\begin{aligned} \log p(\mathbf{z}_k|\mathbf{z}_{1:k-1}, E, \beta^2) &= \log \Lambda(\mathbf{z}_k|\beta^2) + \\ &\log(1 - r_{k|k-1} + \\ &r_{k|k-1} \int \frac{l_1(z_k(C(x_k))|x_k; E, \beta^2)}{l_0(z_k(C(x_k))|\beta^2)} s_{k|k-1}(x_k)dx_k) \end{aligned} \quad (15)$$

Therefore, the ML objective can be recursively evaluated using (15) in (12). Next, we discuss the computation of the predictive state distribution in (13) using Bernoulli track before detect.

#### A. Bernoulli track before detect

Recursive updating of a Bernoulli object model using measurements with likelihood models in the form of (10) can be carried out using the Bayesian recursive filtering principles [11], [12]. An important component of filtering with RFS models is the object appearance, or, birth model. The probability of object appearance at time  $k$  is given by  $P_b$  and the state of this object is distributed as  $b(x)$ . The probability of

an object that existed at  $k-1$  continuing to exist at time  $k$  is given by  $P_S$ . A Bernoulli model at time  $k-1$  characterised by  $(r_{k-1}, s_{k-1}(x_{k-1}))$ , then, leads to the following prediction:

$$\begin{aligned} r_{k|k-1} &= P_b(1 - r_{k-1}) + r_{k-1}P_S \\ s_{k|k-1}(x) &= \frac{P_b(1 - r_{k-1})}{r_{k|k-1}}b(x) \\ &+ \frac{r_{k-1}P_S}{r_{k|k-1}} \int \pi_{k|k-1}(x|x_{k-1})s_{k-1}(x_{k-1})dx_{k-1} \end{aligned} \quad (16)$$

where  $\pi_{k|k-1}$  is the state transition density [11].

Upon receiving  $\mathbf{z}_k$ , the posterior model is given by [11]

$$\begin{aligned} r_k &= \frac{r_{k|k-1} \int g_k(x_k|E, \beta^2)dx_k}{1 - r_{k|k-1} + r_{k|k-1} \int g_k(x_k|E, \beta^2)dx_k} \\ s_k(x_k) &= \frac{g_k(x_k|E, \beta^2)}{\int g_k(x_k|E, \beta^2)dx_k} \\ g_k(x_k|E, \beta^2) &\triangleq \frac{l_1(z_k(C(x_k))|x_k; E, \beta^2)}{l_0(z_k(C(x_k))|\beta^2)} s_{k|k-1}(x_k). \end{aligned} \quad (17)$$

As a result, the predictive term in (13) required for the parameter likelihood is found by iterating prediction and update cycles using (16) and (17).

The object birth model we use is selected so as to have a uniform distribution in the location component which is nonzero in the sensor field of view, and, a uniform distribution in the velocity component which is nonzero if the speed is between selected minimum and maximum values:

$$b([x_l^T, x_v^T]^T) = \mathcal{U}_{FOV}(x_l)\mathcal{U}_{v_{min} \leq |x_v| \leq v_{max}}(x_v). \quad (18)$$

#### IV. MAXIMUM LIKELIHOOD SIGNAL AMPLITUDE AND NOISE POWER ESTIMATION

The objective function of the ML solution in (5) is not straightforward to maximise partly because, in practice, only a noisy approximation of it can be obtained via particle methods, and, the term due to  $E$  in the right hand side (RHS) of (15) is dominated by the influence of  $\beta^2$  through the first term (see, e.g., the example in Section V).

Our ML realisation strategy is to apply coordinate ascent along the projections of the log-likelihood gradient. This can be viewed as a subgradient approach with the difference that we do not explicitly select step sizes to move along the selected subgradient direction. Instead, we perform (golden ratio) line search along the subgradient direction. The gradient equals the sum of the gradients of the log update term in (15) over time. Note that, the first term in the RHS of (15) is independent of  $E$ , hence,

$$\begin{aligned} \frac{\partial \log p(\mathbf{z}_k|\mathbf{z}_{1:k-1}, E, \beta^2)}{\partial E} &= \frac{r_{k|k-1} \int \frac{\partial \log l_1}{\partial E} \frac{l_1}{l_0} s_{k|k-1}}{1 - r_{k|k-1} + r_{k|k-1} \int \frac{l_1}{l_0} s_{k|k-1}} \\ &= \frac{r_{k|k-1} \int \frac{\partial \log l_1}{\partial E} g_k}{1 - r_{k|k-1} + r_{k|k-1} \int g_k} \end{aligned} \quad (19)$$

where the first line follows after differentiating the term inside the integral and using the identity  $\partial l_1 / \partial E = l_1 \times \partial \log l_1 / \partial E$ . The second line is obtained through the definition of  $g_k$  in (17).

The partial derivative of  $\log l_1$  with respect to  $E$  can easily be found [13] as

$$\frac{\partial \log l_1}{\partial E} = -\frac{2E}{\beta^2} + \frac{2z_k(C(x_k))}{\beta^2} \frac{I_1(2z_k(C(x_k))E/\beta^2)}{I_0(2z_k(C(x_k))E/\beta^2)} \quad (20)$$

where  $I_0$  and  $I_1$  are the modified Bessel functions of the first kind of order zero and one, respectively. After substituting (20) in (19), we get

$$\frac{\partial \log p(\mathbf{z}_k | \mathbf{z}_{1:k-1}, E, \beta^2)}{\partial E} = -\frac{2Er_k}{\beta^2} + \frac{2r_{k|k-1} \int \frac{z_k I_1}{\beta^2 I_0} g_k}{1 - r_{k|k-1} + r_{k|k-1} \int g_k}, \quad (21)$$

where  $r_k$  and  $g_k$  are given in (17).

Next, we consider the partial derivative of the log update term with respect to  $\beta^2$ :

$$\frac{\partial \log p(\mathbf{z}_k | \mathbf{z}_{1:k-1}, E, \beta^2)}{\partial \beta^2} = \sum_{i,j} \frac{\partial \log l_0}{\partial \beta^2} + \frac{r_{k|k-1} \int \left( \frac{\partial \log l_1}{\partial \beta^2} - \int \frac{\partial \log l_0}{\partial \beta^2} \right) g_k}{1 - r_{k|k-1} + r_{k|k-1} \int g_k} \quad (22)$$

The first partial derivative inside the integral above can be found [13] as

$$\frac{\partial \log l_1}{\partial \beta^2} = -\frac{1}{\beta^2} \left( 1 - \frac{z_k^2 + E^2}{\beta^2} + \frac{2z_k E}{\beta^2} \frac{I_1(2z_k E/\beta^2)}{I_0(2z_k E/\beta^2)} \right),$$

and the derivative of log-noise term with respect to the noise power is given by

$$\frac{\partial \log l_0}{\partial \beta^2} = -\frac{1}{\beta^2} + \frac{z_k^2}{\beta^4}.$$

Therefore, the first term inside the integral in (22) is given by

$$\frac{\partial \log l_1}{\partial \beta^2} - \frac{\partial \log l_0}{\partial \beta^2} = \frac{E^2}{\beta^4} - \frac{2Ez_k}{\beta^4} \frac{I_1}{I_0}. \quad (23)$$

As a result, the gradient of the log-likelihood function in (12) can be computed using (19)–(23) in the recursive form given by

$$\nabla J(E, \beta^2; \mathbf{z}_{1:k}) = \nabla J(E, \beta^2; \mathbf{z}_{1:k-1}) + \begin{bmatrix} \frac{\partial \log p(\mathbf{z}_k | \mathbf{z}_{1:k-1}, E, \beta^2)}{\partial E} \\ \frac{\partial \log p(\mathbf{z}_k | \mathbf{z}_{1:k-1}, E, \beta^2)}{\partial \beta^2} \end{bmatrix} \quad (24)$$

In order to maximise  $J$ , we adopt a coordinate ascent approach: Starting from an initial point  $(E_0, \beta_0^2)$ , at each iteration  $m$ , we find the gradient vector (24) and select a line search direction as follows:

$$d_m = \frac{\nabla J(E, \beta^2; \mathbf{z}_{1:k})^T e_m}{\|\nabla J(E, \beta^2; \mathbf{z}_{1:k})^T e_m\|} \quad (25)$$

$$e_m = \begin{cases} [0, 1]^T, & \text{if } m = 0, 2, 4, \dots \\ [1, 0]^T, & \text{if } m = 1, 3, 4, \dots \end{cases}$$

Then, we solve the following one dimensional problem

$$(E_{m+1}, \beta_{m+1}^2) = \arg \min_{\lambda \in [0, \lambda_{max}]} J([E_m, \beta_m^2]^T + \lambda d_m; \mathbf{z}_{1:k}) \quad (26)$$

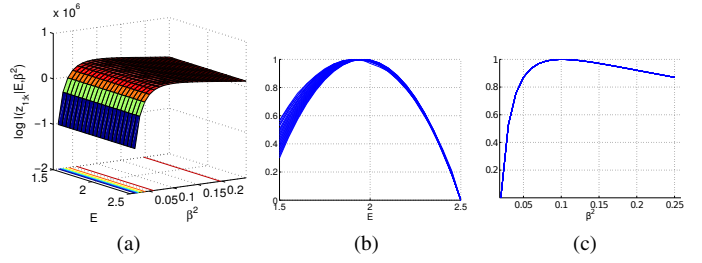


Fig. 1. (a) Log-likelihood surface for the example scenario evaluated over the grid  $1.5 \leq E \leq 2.5$  and  $0.01 \leq \beta^2 \leq 0.25$  with step sizes of 0.05 and 0.01, respectively. (b) The normalised profile of the surface along  $E$ -axis for varying  $\beta^2$ . (c) The normalised profile along  $\beta^2$  for varying  $E$ .

using golden section search [14].

The iterations terminate if two consecutive points are closer than a selected tolerance value. In other words, the solution to (5) is declared as  $(\hat{E}, \hat{\beta}^2) = (E_{m+1}, \beta_{m+1}^2)$  if

$$\|[E_{m+1}, \beta_{m+1}^2]^T - [E_m, \beta_m^2]^T\| < \delta.$$

The computations are carried out using particle methods: We sample from the predictive distribution in (13) using a Sequential Monte Carlo realisation [11] of the recursions given by (16) and (17). In order to sample from the birth model in (18), we find a grid of  $L$  samples for each bin  $C^{-1}(i, j)$  and concatenate with velocity components generated from  $\mathcal{U}_{v_{min} \leq |x_v| \leq v_{max}}$ . The integrals in (19)–(23) are estimated using samples generated from  $g_k$  during Bernoulli track before detect within the Monte Carlo method [15, Chp.3].

## V. EXAMPLE

Let us consider an example scenario consisting of an object with initial state  $x_0 = [-503.5, 4974.6, 5, 0]^T$  moving in accordance with a constant velocity motion model with a small process noise term and a sensor located at the origin with range and bearing resolutions of 10m and  $1^\circ$ , respectively. The sensor field of view is selected as the region bounded by 4800m and 5200m in range and  $\pm 10^\circ$  around the  $y$ -axis in order to restrict the size of the intensity map and hence the volume of computations needed. As a result, a  $40 \times 20$  intensity map is observed for  $k = 200$  time steps with signal amplitude  $E = 2$  and noise power  $\beta^2 = 0.1$ . The target signal, hence, has  $\sim 16$ dB SNR in the corresponding bin.

In Fig. 1(a), we present the ML objective surface evaluated for a given realisation of the measurement history  $\mathbf{z}_{1:200}$  and a grid of  $(E, \beta^2)$  values using the parameter likelihood detailed in Section III together with MC computations. For Bernoulli track before detect, we use  $L = 225$  uniform grid points for each of the 800 state bins given by  $C^{-1}(i, j)$  to represent  $b(x)$  in (16). Here,  $\pi$  is selected as a constant velocity motion model with a small additive process noise term. We maintain 10000 samples generated from  $s_k$  in (17) after resampling weighted samples from  $g_k$ . The probability of birth  $P_b = 0.01$  whereas the  $P_S = 0.99$ .

There are much less target associated measurements contributing to (15) compared to noise associated terms. This manifests itself in Fig. 1(a) as the significantly smaller curvature of the surface along  $E$  compared to that along  $\beta^2$ .

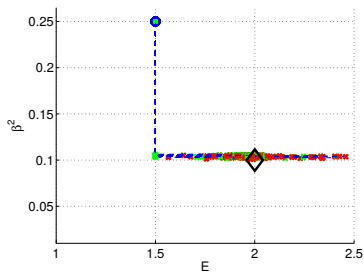


Fig. 2. Iterative maximisation of the parameter likelihood for 200 Monte Carlo runs: Initial point (blue circle), and converged estimates (red crosses) joined by estimates in the intermediate steps (green crosses and dashed lines). Diamond is the correct value of  $(E, \beta^2)$ .

Correspondingly, the Cramer-Rao lower bound (CRLB) for  $E$  is higher and estimates of  $E$  will be less accurate [16, App. 8A]. For a closer look to the log-likelihood objective function, we provide the normalised profiles of the surface along  $E$  and  $\beta^2$  axis in Fig. 1(b) and (c), respectively. Note that, for almost all values of  $E$  in the grid, it is possible to estimate  $\beta^2$  through maximising the objective along  $\beta^2$  direction.

Next, we use the proposed scheme described in Section IV starting from  $(E_0, \beta_0^2) = (1.5, 0.25)$ . After evaluating the gradient in (24), a golden section line search is performed along the direction selected using (25). The initial search interval length, i.e.,  $\lambda_{max}$  in (26), is selected to ensure that the resulting interval of uncertainty will be smaller than 0.001. For golden ratio search, this is given by  $\lceil \log(0.001 - 0.618) \rceil + 1$ . The tolerance  $\delta$  for checking convergence is selected as 0.001.

We repeat the proposed ML scheme for 200 Monte Carlo realisations of this scenario. The iterations are depicted in Fig. 2, in which the resulting estimates are shown by red crosses. The average number of iterations is 3.6. The average of  $(\hat{E}, \hat{\beta}^2)$  is  $(1.972, 0.104)$ , which is very close to the true value of  $(2, 0.1)$ . This indicates that the optimisation scheme is approximately unbiased. The variance of the estimation scheme as measured by the empirical average of the squared errors for  $\hat{E}$  and  $\hat{\beta}^2$  are found as  $1.78 \times 10^{-2}$  and  $1.7 \times 10^{-5}$ , respectively. The variance of  $\hat{E}$  is much higher than that for  $\hat{\beta}^2$ , as expected.

## VI. CONCLUSIONS AND FUTURE WORK

In this work, we proposed a ML scheme for jointly estimating the signal amplitude and noise power using the matched filter outputs of an active sensor. This likelihood involves track-before-detect in order predict the underlying target process which is modelled by a Bernoulli RFS. We derived explicit formulae for the score function and proposed an iterative maximisation procedure using a coordinate ascent approach.

It is possible to improve the optimisation step of the proposed algorithm. For example, Newtonian methods can be used after finding the Hessian of the log-likelihood. Such an approach would remove the need for line search and potentially provide more accurate estimates for fewer number of iterations and objective evaluations.

There is a tradeoff between the observation length and the accuracy in which  $E$  can be estimated (see, e.g., [17]). The relations between the Hessian, Fisher information and the associated Cramer-Rao lower bound can be explored in order to investigate this tradeoff. Another possible extension of this work is to accommodate multi-Bernoulli models in order to handle multiple moving objects via track-before-detect [18]. Estimation of parameters for other Swerling target types [1] within the proposed ML framework is also left as future work.

## ACKNOWLEDGMENT

This work was supported by the Engineering and Physical Sciences Research Council (EPSRC) grants EP/J015180/1 and EP/K014277/1, and the MOD University Defence Research Collaboration in Signal Processing.

## REFERENCES

- [1] M. A. Richards, *Fundamentals of Radar Signal Processing*. McGraw Hill, 2005.
- [2] S. Kay, *Fundamentals of Statistical Signal Processing: Detection Theory*. Prentice Hall, 1998, vol. II.
- [3] H. Rohling, "Radar cfar thresholding in clutter and multiple target situations," *IEEE Trans. on Aerospace and Elec. Sys.*, vol. AES-19, no. 4, pp. 608–621, July 1983.
- [4] R. C. Raup, R. A. Ford, G. R. Krumpolz, M. G. Czerwinski, and T. E. Clark, "The best approximation of radar signal amplitude and delay," *Lincoln Laboratory Journal*, vol. 3, pp. 311–327, 1990.
- [5] A. Sheikhi, M. Nayebi, and M. Aref, "Adaptive detection algorithm for radar signals in autoregressive interference," *IEE Proceedings - Radar, Sonar and Nav.*, vol. 145, no. 5, pp. 309–314, Oct 1998.
- [6] O. Cappé, S. J. Godsill, and E. Moulines, "An overview of existing methods and recent advances in sequential Monte Carlo," *Proceedings of the IEEE*, vol. 95, pp. 899–924, 2007.
- [7] D. P. Bertsekas, *Nonlinear Programming*. Athena Scientific, 1999.
- [8] R. P. S. Mahler, *Statistical Multisource Multitarget Information Fusion*. Springer, 2007.
- [9] M. Uney, B. Mulgrew, and D. Clark, "Cooperative sensor localisation in distributed fusion networks by exploiting non-cooperative targets," in *IEEE Stat. Sig. Proc. Workshop (SSP)*, 2014, June 2014, pp. 516–519.
- [10] —, "Target aided online sensor localisation in bearing only clusters," in *Sensor Sig. Proc. for Defence (SSPD)*, 2014, Sept 2014, pp. 1–5.
- [11] B. Ristic, B.-T. Vo, B.-N. Vo, and A. Farina, "A tutorial on bernoulli filters: Theory, implementation and applications," *Signal Processing, IEEE Transactions on*, vol. 61, no. 13, pp. 3406–3430, July 2013.
- [12] M. Rutten, N. Gordon, and S. Maskell, "Recursive track-before-detect with target amplitude fluctuations," *Radar, Sonar and Navigation, IEE Proceedings -*, vol. 152, no. 5, pp. 345–352, October 2005.
- [13] C. Carobbi and M. Cati, "The absolute maximum of the likelihood function of the rice distribution: Existence and uniqueness," *IEEE Trans. on Instrumentation and Meas.*, vol. 57, no. 4, pp. 682–689, April 2008.
- [14] M. S. Bazaraa, H. D. Sherali, and C. M. Shetty, *Nonlinear programming: Theory and algorithms*, 3rd ed. John Wiley & Sons, 2006.
- [15] G. Casella and C. P. Robert, *Monte Carlo Statistical Methods*, 2nd ed. Springer, 2005.
- [16] S. Kay, *Fundamentals of Statistical Signal Processing, Volume III: Practical Algorithm Development*. Pearson Education, 2013.
- [17] D. Clark, B. Ristic, B.-N. Vo, and B. T. Vo, "Bayesian multi-object filtering with amplitude feature likelihood for unknown object snr," *IEEE Trans. on Signal Proc.*, vol. 58, no. 1, pp. 26–37, Jan 2010.
- [18] B.-N. Vo, B.-T. Vo, N.-T. Pham, and D. Suter, "Joint detection and estimation of multiple objects from image observations," *IEEE Trans. on Signal Processing*, vol. 58, no. 10, pp. 5129–5141, Oct 2010.

# Direction of arrival estimation using a cluster of beams in a cone-shaped digital array radar

Micaela Contu, Marta Bucciarelli, Pierfrancesco Lombardo  
DIET Dept. University of Rome “La Sapienza”  
Rome, Italy  
contu@die.uniroma1.it, marta.bucciarelli@uniroma1.it,  
pierfrancesco.lombardo@uniroma1.it

Francesco Madia, Rossella Stallone, Marco Massardo  
Seastema S.p.A.  
Rome, Italy  
Francesco.Madia@fincantieri.it,  
rosella.stallone@seastema.it, marco.massardo@seastema.it

**Abstract**— In this paper some potential system and processing advantages of conformal cone shaped digital array radar have been investigated, in particular in relation to potential alternative approaches for angle estimation with respect to the traditional monopulse. First of all potential benefit in terms of reduction of the number of radiating elements is shown when a conical array is considered with respect to a traditional system formed by four planar arrays, if a coverage of  $360^\circ$  must be assured. Secondly, having in mind an innovative digital array system where the received signals are analog to digital converted at element level and the corresponding data are possibly transferred to a central elaboration unit, an alternative approach is investigated for angular estimation. In this paper we derive the theoretical expression of the Cramer Rao Lower Bound for elevation angle estimation using a cluster of beams; we compare the limit performance of the traditional approach for angle estimation based on Sum and Difference beams with the approach based on a crowded cluster of RX beams properly spaced. The approaches show approximately equivalent performance, making the second particularly interesting for those situations where monopulse is known to experience performance degradation, as low elevation angle estimation; in this particular case an example of cluster design is shown, where the direct signal from a low altitude target must compete with a specular multipath.

**Keywords**—Digital array radar, conformal array, angle estimation

## I. INTRODUCTION

It is well known that the basic characteristic on an array of radiating elements that makes it different with respect to traditional systems based on reflectors is the ability to form multiple beams with different characteristics and functionalities properly adjusting the phase or the delay of the signals received by each element in the array, [1].

In Phased Array Radars (PARs) this operation known as analog beamforming (ABF) is usually accomplished analogically through beamforming networks: in this case it is necessary to fix at design stage the number of the beams to be formed and their characteristics (beam steering direction, shape in terms of angular resolution and Peak to SideLobe Ratio - PSLR, etc...). As an example, when a typical searching mode is considered, the use of a PAR must allow the simultaneous detection and accurate Direction of Arrival (DoA) estimation of a target in all the search space; the system must be designed to contemporarily form the appropriate sum and difference

beams in each direction of interest for both applications, thus avoiding the necessity to re-irradiate to accurately estimate the targets' angle of arrival if detections occurred. As a consequence the beamforming network complexity increases with the number of directions to be monitored and the operative modes to be considered.

In Digital Array Radars (DARs) the analog to digital conversion at element or small sub-array level and the recording of all the amount of data for successive centralized processing allows completely changing the perspective with respect to operative modes based on analog beamforming, [1]-[8]. As an example the coverage required in the searching mode is accomplished by foreseeing a wide transmitting beam (up to nearly omnidirectional in the “Ubiquitous Radar” theory) covered in reception by clusters of simultaneous beams at least in one angular direction. This is a first evident difference with respect to PARs using ABF, that search in all the desired directions using pencil beams both in transmission and reception allowing the execution of multiple functionalities using a limited number of complex beamforming network. Moreover the early digitization of the received signals allows reducing the required dynamic range and the requirements of isolation with respect to near clutter returns. It is apparent how all these advantages can be achieved at the expense of the increased computational load and data transfer rate to a central elaboration unit where beamforming, DoA estimation, adaptive nulling for interference cancellation, etc. take place. An ultimate analysis highlights that DAR provide an increased flexibility with respect to PAR allowing to develop multiple functions simultaneously and to implement alternative processing schemes increasing the efficiency of the exploitation of the acquired radar signals. For example, it could be possible to form only the Sum beams for detection in all the search space and then synthesize Difference beam for accurate DoA estimation only for the resolution cells when detection occurred. Moreover an alternative approach to angle of arrival estimation could be achieved using a crowded cluster of beams properly steered according to the direction where detection occurred.

In the present paper the considered and simulated digital array is cone-shaped. This particular shape factor is very interesting since, while in the elevation dimension the coverage is achieved with beam scanning operations, a  $360^\circ$  azimuth coverage can be achieved using DBF without scanning but

only circularly shifting the weight matrix around the beam steering direction; this provides potential benefits with respect to a more traditional architecture, where four planar arrays are used each one to cover an horizontal sector of  $90^\circ$  with analogical or digital beam scanning. It has to be underlined that DBF not only allows a smart implementation of horizontal beamforming, but also provide an increased degree of technological feasibility to this conformal array, shifting the inherent criticalities from the analogic to the digital design, [8].

Having in mind an innovative array system like the one described, the aim of this paper is to investigate one of its numerous potentialities, comparing the performance of the traditional monopulse approach for DoA estimation, [9], possible both in a PAR and in a DAR architecture, and the approach feasible in a DAR based on a crowded cluster of RX beams properly spaced in an angular sector comprising the angular direction of the sum beam and for the resolution cell where a detection occurred. It is interesting to investigate this approach due to the fact that, as it is well known, [9], monopulse can suffer in particular situations where the investigated elevation angles are small and Sum and Difference beams can collect a great amount of land/sea clutter and multipath returns.

The paper is organized as follows. In section II the conical DAR system is described along with the reference operative scenario. In section III Cramer-Rao lower bound is derived for DoA estimation based on a cluster of beams and compared with the performance of the estimation based on Sum and Difference beams. An example of design for a cluster of beams to be employed for low altitude target DoA estimation is shown in IV. Finally we draw some conclusions in section V.

## II. SYSTEM DESCRIPTION AND POTENTIALITIES

In the present paper the considered receiving (RX) array is modelled as the “d.Radar”, [10], which is being studied and demonstrated by Fincantieri S.p.A. and Seastema S.p.A. It is formed by a set of columns of radiating elements placed over the surface of a truncated cone as shown in Fig. 1 in a xyz reference system. Each element is connected to a receiver so that received signals are analog to digital converted at element level and it is supposed that the corresponding data are sent to a central elaboration unit. The array is designed in such a way that each horizontal section is represented by a circular array with the same number of elements with different inter-element distance as the height of the considered section decreases, while the vertical inter-element distance is constant and equal in each column. The overall structure has approximately a height of 0.8 m and a major diameter of 1.42 meters.

As hinted in the introduction a cone-shaped structure supplied with DBF to provide  $360^\circ$  coverage can present advantages due to this conformal shape factor with respect to a traditional four-planar faces array, Fig. 2. Indeed in this case beamforming in every horizontal direction can be achieved by circularly shifting the weight matrix according to the beam steering direction that is by elaborating in the same way the signals digitized at element level received from a properly selected active sector of the array; in that way a beam with the same desired characteristics of width  $\delta\phi$  is achieved in every

direction without beam scanning (Fig. 2a). On the other hand when four planar arrays are used each one to cover an horizontal sector of  $90^\circ$  with analogical or digital beam scanning, degraded patterns are achieved off-boresight with maximum width equal to  $\delta\phi_{max}$  (Fig. 2b). Matching the approximate expressions of the beamwidth, in the hypothesis of equal element spacing, the ratio of the perimeters of both horizontal sections can be evaluated as a quality parameter showing the ratio between the number of elements required in the circular array with respect to the square array

$$\Delta N_{el} = \pi \sin(\phi_0) / 4 \cos(\alpha_0/2) \quad (1)$$

For sectors of active elements wider than  $120^\circ$ , the proposed coarse dimensioning suggests that using a conical array allows sparing radiating elements, mainly when the performance of the different configurations of the arrays are compared in the worst case, that is when the maximum beamwidth  $\delta\theta_{max}$  is taken into account.

One of the typical operative conditions of a radar is represented by the “searching mode”. In the considered system it is supposed that a transmitting (TX) antenna radiates with a beam which is narrow in the azimuth dimension and wide in elevation; therefore, using the conceived RX array with a properly dimensioned active sector and tapering functions specifically tailored to cope with a 3D displacement of the elements of the array, multiple Sum beams displaced in the vertical dimension must be formed to cover the nominal illuminated angular aperture along with the corresponding Difference beams; Fig. 4 shows the case of a TX aperture in elevation nearly equal to  $8^\circ$  covered by 3 RX beams for different steering directions of the central beam, in particular  $15^\circ$  in elevation and  $0^\circ$  in azimuth in Fig. 4a and  $5^\circ$  in elevation and  $0^\circ$  in azimuth in Fig. 4b. From this second case it is apparent how lower Sum and especially Difference beams in the cluster may suffer from clutter and multipath arising from low-height target. This may suggest the use of a different approach for DoA estimation, in particular for the elevation angle, which is not based on Difference beams as the monopulse. Indeed when detection occurs in a certain beam and at a certain resolution cell, if data acquired by all elements are available at a central elaboration unit before beamforming, accurate elevation angle estimation can be based on the exploitation of a crowded clusters of sum beams properly displaced in the angular area of interest. In the following section the feasibility of this approach is investigated.

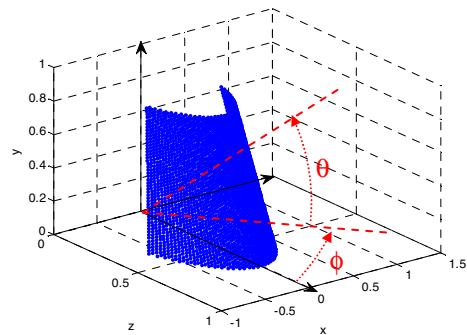


Fig. 1. Active sector ( $120^\circ$ ) of the considered cone-shaped array radar

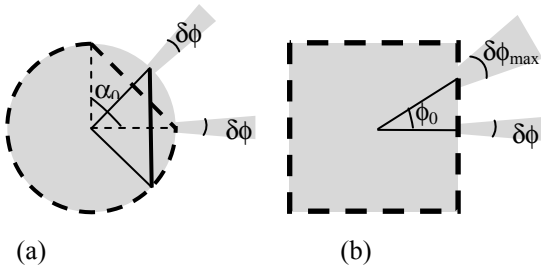


Fig. 2. Horizontal sections of (a) the cone and (b) the 4-planar faces arrays.

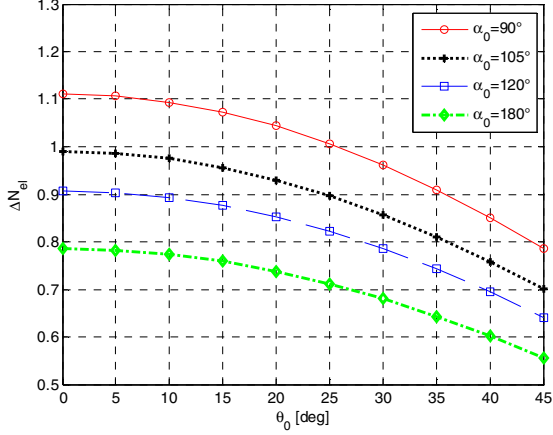


Fig. 3. Ratio between the number of elements required in circular DAR with respect to a square array as a function of the steering direction  $\theta_0$  for different widths of the active section  $\alpha_0$ .

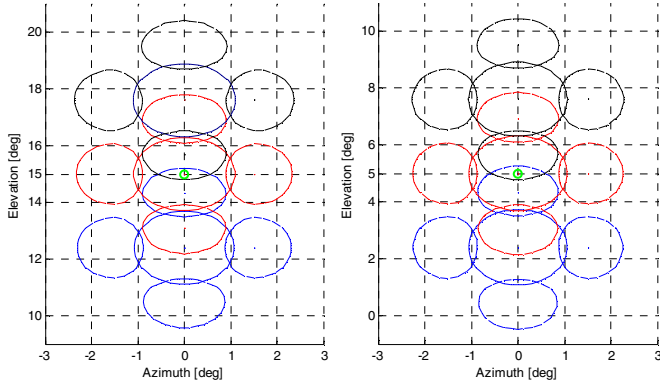


Fig. 4. Sum and Difference beam apertures for a central steering of (a) 15° in elevation and 0° in azimuth and (b) 5° in elevation and 0° in azimuth.

### III. CRAMER-RAO LOWER BOUND DERIVATION FOR DOA ESTIMATION BASED ON A CLUSTER OF BEAMS

In this paragraph the expression of the Cramer Rao Lower Bound (CRLB) is derived for the elevation DoA estimation using a cluster of beams. For this reason in the following the azimuth direction of the signal will be considered known and fixed to  $\phi_0=0$ .

The received signal  $\mathbf{x}$  is modelled as

$$\mathbf{x}(\theta) = A_0 G_{TX}(\theta, \theta_0) G_E(\theta) \mathbf{T} \mathbf{s}(\theta) + \mathbf{T} \mathbf{n} \quad (2)$$

$A_0$  is an amplitude factor depending on the signal path and on the radar equation,  $G_{TX}(\theta, \theta_0)$  is the gain at the direction  $\theta$  of the transmitting pattern steered towards  $\theta_0$ ,  $G_E(\theta)$  represents the gain provided by each antenna element to a signal  $\mathbf{s}(\theta)$  coming from the direction  $\theta$ ,  $\mathbf{T}$  is the transformation matrix that allows the switch from an element-wise to a cluster based representation and  $\mathbf{n}$  is the vector accounting for noise samples with null expected value and variance equal to  $\sigma_n$ .  $\mathbf{s}(\theta)$  is defined as

$$\mathbf{s}(\theta) = \begin{bmatrix} \exp(-j2\pi/\lambda \langle \mathbf{p}_1, \mathbf{u}(\theta) \rangle) \\ \vdots \\ \exp(-j2\pi/\lambda \langle \mathbf{p}_N, \mathbf{u}(\theta) \rangle) \end{bmatrix} \quad (3)$$

where  $\lambda$  is the wavelength,  $\mathbf{p}_i$  is the vector containing the xyz coordinates of the  $i$ th element in the array for  $i=1, \dots, N$ ,  $\mathbf{u}(\theta)$  is the direction cosine vector and the symbol  $\langle \cdot \rangle$  accounts for the inner product.

The transformation matrix  $\mathbf{T}$  can be written as

$$\mathbf{T} = \begin{bmatrix} \mathbf{W}_1 \mathbf{s}^*(\theta_1) \\ \vdots \\ \mathbf{W}_K \mathbf{s}^*(\theta_K) \end{bmatrix} \quad (4)$$

where  $K$  is the number of beams in the cluster, symbol  $*$  refers to the complex conjugate operation and  $\mathbf{W}_k$  is the diagonal matrix accounting for amplitude tapering.

The probability density function of  $\mathbf{x}(\theta)$  can be modelled as Gaussian and equal to

$$f[\mathbf{x}] = \frac{1}{2\pi \cdot \det(\mathbf{M})} \exp\left\{-[\mathbf{x} - A_0 \mathbf{v}]^H \mathbf{M}^{-1} [\mathbf{x} - A_0 \mathbf{v}]\right\} \quad (5)$$

where  $\mathbf{v}$  and  $\mathbf{M}$  are the expected value of  $\mathbf{x}$  and the covariance matrix of the disturbance

$$\mathbf{v}(\theta) = G_{TX}(\theta, \theta_0) G_E(\theta) \mathbf{T} \mathbf{s}(\theta) \quad (6)$$

$$\mathbf{M} = \sigma_n^2 \mathbf{T} \mathbf{T}^H \quad (7)$$

In the previous expression symbol  $H$  has been used to indicate complex conjugate and transpose operation, while  $\det(\mathbf{M})$  referred to the determinant of matrix  $\mathbf{M}$ .

The unknowns in (5) are the real and imaginary part of  $A_0$  and the elevation direction  $\theta$ . Therefore the Fisher information matrix can be written as

$$\mathbf{J} = -E \left\{ \left[ \frac{\partial}{\partial \boldsymbol{\eta}} \ln(f(\mathbf{x}|\boldsymbol{\eta})) \right]^T \left[ \frac{\partial}{\partial \boldsymbol{\eta}} \ln(f(\mathbf{x}|\boldsymbol{\eta})) \right] \right\} \quad (8)$$

where  $\boldsymbol{\eta}=[A_{OR} A_{OI} \theta]$  and apex T accounts for the transpose operation. The third element on the diagonal of the inverse of the matrix  $\mathbf{J}$  is the searched accuracy, equal to

$$\sigma_{\theta}^2 = \mathbf{J}^{-1}(3,3) = 2 \frac{|A_0|^2}{\sigma_n^2} \dot{\mathbf{v}}^H \left[ \mathbf{M}^{-1} - \frac{\mathbf{M}^{-1} \mathbf{v} \mathbf{v}^H \mathbf{M}^{-1}}{\mathbf{v}^H \mathbf{M}^{-1} \mathbf{v}} \right] \dot{\mathbf{v}} \quad (9)$$

where  $|A_0|^2 / \sigma_n^2$  is the signal to noise ratio at element level (SNR<sub>el</sub>) and  $\dot{\mathbf{v}}$  is the first derivative of the vector  $\mathbf{v}$  with respect to the direction  $\theta$ .

Fig. 5 shows the standard deviation of the estimation of  $\theta$  normalized with respect to the nominal beamwidth of a RX pattern in the elevation dimension as a function of the difference of the DoA  $\theta$  and the steering direction of the central beam in the cluster,  $\theta_r = 5^\circ$  in this case. All the sum beams have been formed considering properly modified Taylor windows both in azimuth and elevation with a PSLR of 42 dB and 36 dB respectively. The Difference beams in elevation are built using a Bayliss tapering with the same parameters. The signal to noise ratio at element level SNR<sub>el</sub> has been set equal to -20 dB, therefore a peak SNR on the central beam of nearly 13 dB is achieved: the gain of nearly 33 dB is provided by the coherent summation of the amplitude weighted signals received by nearly 3500 elements in the considered active sector.

Two different cases are considered: in the first case (Fig. 5a) we supposed an omnidirectional TX pattern, while in the second case (Fig. 5b) a directive transmission pattern has been considered with a -3dB aperture in elevation  $B_{TX-el} = 8^\circ$  nearly equal to three times the beamwidth of the generic RX pattern  $B_{RX-el}$ . In both cases omnidirectional elements have been considered and an active sector of  $120^\circ$  has been used for beamforming. Four curves are shown. The green one is related to the CRLB achieved considering a cluster formed by 3 Sum beams ( $3\Sigma$ ) and 3 Difference beams ( $3\Delta$ ) thus representing the lower bound for the monopulse accuracy in the covered area. The other curves refer to the cases of cluster of K uniformly spaced beams (K=5, 7, 13) covering the same elevation extent as the  $3\Sigma$  case, that is  $[\theta_T - B_{TX-el}/2, \theta_T + B_{TX-el}/2]$ . This means that as the number of beams in the cluster increases, the angular separation between beam steering directions decreases.

From Fig. 5 it is apparent how the limit performance of the  $3\Sigma+3\Delta$  configuration is equivalent to the limit performance of the DoA estimation based on cluster of crowded Sum beams, especially in the interval  $[-4^\circ, 4^\circ]$ ; as the number of beams increases, ripple's amplitude decreases since the coverage becomes uniform in the area of interest and the performance is less affected by pattern peaks with null derivative. In Fig. 5a it is apparent how a slight slope appears evidently as the number of beams increases; this effect arise from the asymmetry of the distribution of elements over the considered conical array surface, where higher elements are closer to each other than lower elements. In Fig. 5b the presence of a directive pattern in transmission is evident and shows itself as a tapering of the accuracy mainly due to the gain provided by the TX beam in each considered direction.

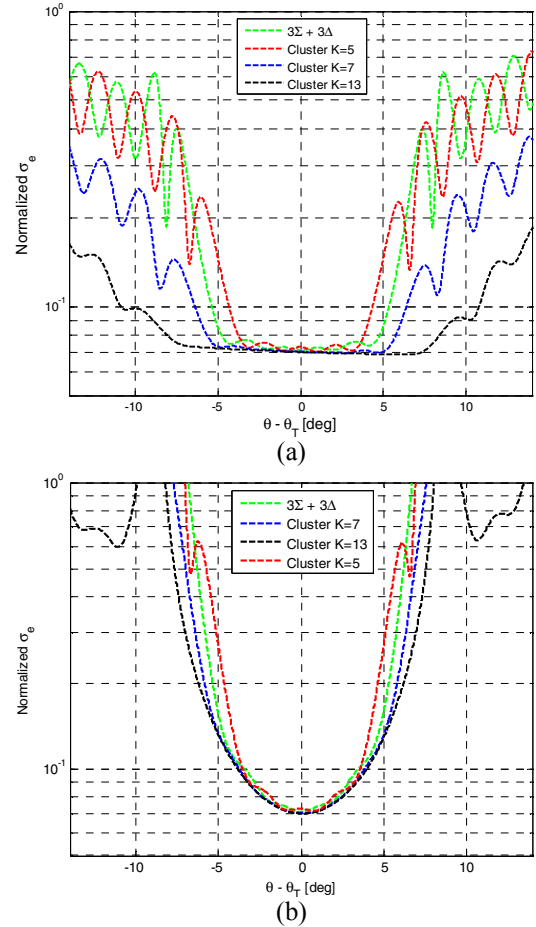


Fig. 5. Normalized Cramer Rao Lower Bound for the accuracy of the estimation of the DoA  $\theta$  (a) with omnidirectional pattern in TX and (b) for a directive pattern in TX.

Ultimately the derivation of the CRLB for the accuracy of elevation DoA estimation using a cluster of beams allowed us to compare the limit performance of an estimation approach which uses only Sum beams and the traditional approach using Sum and Difference beams and to assess an actual equivalence on the approaches. The main difference lies in the fact that although in both approaches all the Sum beams have positive tilts with respect to the horizon, Difference beams at very low elevation can heavily affect the estimation performance when significant land or sea clutter and multipath signals occur. Nevertheless also in the case of DoA estimation performed using a crowded cluster of Sum beams the design of the cluster needs to be accurate and to take into account the operative scenario, especially when target detection occurs at very low altitudes.

#### IV. EXAMPLE OF CLUSTER DESIGN

In this section an example of design of the cluster of Sum beams to be employed in DoA estimation is provided. It is based on an operative scenario where signals from a low altitude target are received through a direct and a specular reflected path in the flat earth model, Fig. 6.

## V. CONCLUSIONS

Some potential system and processing advantages of conformal conical DAR have been investigated, particularly in defining alternative approaches for DoA estimation.

A coarse dimensioning based on the matching of the pattern beamwidth in the azimuth dimension showed that the conical shape factor allows to guarantee without horizontal beam scanning  $360^\circ$  coverage using less elements with respect to the case of four planar arrays, each assuring a coverage of  $90^\circ$  with beam scanning. This result appeared to be valid as the sector of active elements used for beamforming in the conical array case increases for all the possible steering directions.

Having in mind an innovative digital array system like the one described, we derived the theoretical expression of the CRLB for elevation angle estimation using a cluster of beams and we compared the limit performance of the traditional approach based on sum and difference beams, possible both in a PAR and in a DAR architecture, and the approach feasible in a DAR based on a cluster of RX beams properly spaced according to the direction and for the resolution cell where a detection occurred. The approaches proved to be approximately equivalent, making the second particularly interesting for those situations where monopulse is known to experience performance degradation, as low elevation angle estimation. In this case an example of the design of the cluster of beams in presence of specular multipath has been provided

## ACKNOWLEDGMENT

The Authors thank Roberto Ronconi from Seastema S.p.A. for the useful discussion about the “d.Radar” system.

## REFERENCES

- [1] M. I. Skolnik, “Phased Array Radar Antennas,” in Radar Handbook, 3rd ed., McGraw-Hill Professional, 2008.
- [2] W. L. Melvin, J. A. Scheer, “Array Processing and Interference Mitigation techniques,” in Principles of Modern radar, Advanced Techniques, SciTech Publishing, 2012.
- [3] M. I. Skolnik, “Opportunities in radar-2002,” Electronics & Communication Engineering Journal, vol. 14, no. 6, pp. 263-272, 2002.
- [4] C. Tarran, “Advances in affordable Digital Array Radar,” 2008 IET Waveform Diversity and Digital Radar Conference, 8-9th December 2008, London, UK.
- [5] F. Le Chevalier, “Future concepts for electromagnetic detection from space-time-frequency resources management to wideband radars”, IEEE Aerosp. Electron. Syst. Mag., vol. 14, no. 10, pp. 9-17, 1999.
- [6] D. J. Rabideau, P. Parker, “Ubiquitous MIMO multifunction digital array radar”, 37<sup>th</sup> Asilomar Conference on Signals, Systems and Computers, 9-12 Nov. 2003, Pacific Grove, CA, USA.
- [7] B. Cantrell, J. de Graaf, F. Willwerth, G. Meurer; L. Leibowitz, C. Parris; R. Stapleton, “Development of a Digital Array Radar (DAR)”, IEEE Aerosp. Electron. Syst. Mag., vol. 17, no. 3, pp. 22-27, 2002.
- [8] J.H. Hunter, T.W. Miller, “Digital beamforming demonstration radar”, Antennas and Propagation Society International symposium, 7-11 May 1990, Dallas, Tx, USA.
- [9] S. M. Sherman, D. K. Barton, “Monopulse Principles and Techniques”, Artech House, 2011.
- [10] F. Madia, A. Maestrini, “Radar bistatico”, pending Italian patent N. RM2014A000005, Jan 9, 2014.

The steering direction of the lower beam in the cluster is selected to provide a gain of at least 3 dB to the direct signal from direction  $\theta$  with respect to the multipath signal received from the direction  $\theta_M$  in the worst condition of operation foreseen for the radar that is the minimum target height to take into account, experiencing the corresponding gain loss at the target direction  $\theta$ . The steering direction of the remaining beams in the cluster can be selected to uniformly cover the desired angular aperture. Assuming a specular reflection of the multipath signal, a distance  $D=20$  km and an antenna height of 15 m, as expected Fig. 7 shows how the design becomes more demanding as the target height decreases with a loss of -17 dB in the target direction for  $H_{tgt}=30$  m (Fig. 7a) and -7 dB for  $H_{tgt}=60$  m (Fig. 7b). In the previous example an omnidirectional TX pattern is taken into account; a further slight loss is expected when a directive pattern is employed in transmission.

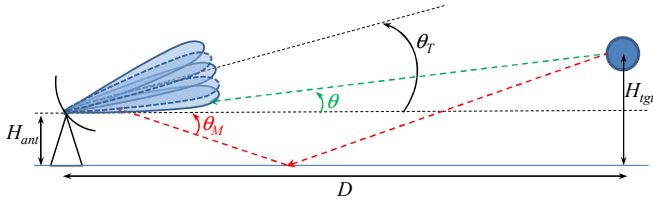


Fig. 6. Operative scenario

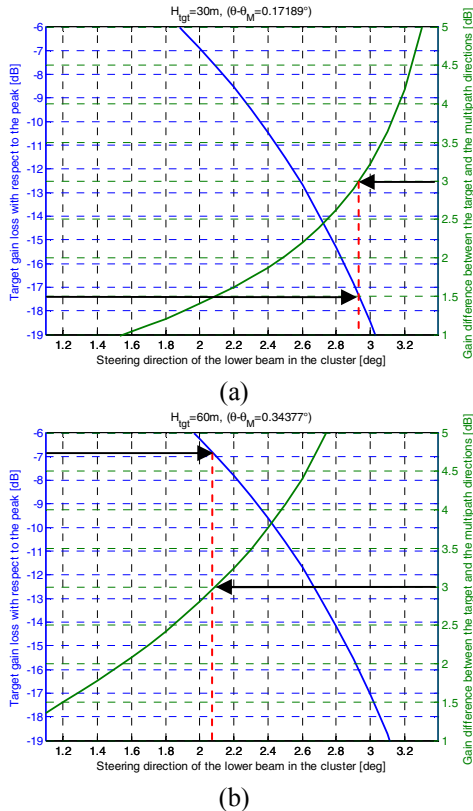


Fig. 7. Gain loss in the target direction (blue curve) and gain difference in the target and multipath directions (green curve) for a target height (a) of 30 m and (b) of 60 m.

# Low Complexity Parameter Estimation For Off-the-Grid Targets

Seifallah Jardak, Sajid Ahmed, and Mohamed-Slim Alouini

Computer, Electrical, and Mathematical Science and Engineering (CEMSE) Division

King Abdullah University of Science and Technology (KAUST)

Thuwal, Makkah Province, Saudi Arabia

Email: {seifallah.jardak, sajid.ahmed, slim.alouini}@kaust.edu.sa

**Abstract**—In multiple-input multiple-output radar, to estimate the reflection coefficient, spatial location, and Doppler shift of a target, a derived cost function is usually evaluated and optimized over a grid of points. The performance of such algorithms is directly affected by the size of the grid: increasing the number of points will enhance the resolution of the algorithm but exponentially increase its complexity. In this work, to estimate the parameters of a target, a reduced complexity super resolution algorithm is proposed. For off-the-grid targets, it uses a low order two dimensional fast Fourier transform to determine a suboptimal solution and then an iterative algorithm to jointly estimate the spatial location and Doppler shift. Simulation results show that the mean square estimation error of the proposed estimators achieve the Cramér-Rao lower bound.

**Keywords**—MIMO-radar, Reflection coefficient, Doppler, Spatial location, Cramér-Rao lower bound.

## I. INTRODUCTION

Using colocated multiple-input multiple-output (MIMO) radar, the locations and reflection coefficients of stationary targets are estimated using adaptive techniques (see e.g., [1], [2] and the references therein). To estimate the parameters of moving targets, different methods and models have been discussed in the literature. In the bistatic MIMO-radar case, the parameters of moving targets are estimated using maximum-likelihood (ML) estimator in [3]. The ML estimator yields the optimal performance, however, its computational complexity is very high, which prevents its use in practice. Reduced computational complexity algorithms, such as multiple-signal-classification (MUSIC) [4] and estimation-of-signal-parameters-via-rotational-invariant-techniques (ESPRIT) [5], have been used to estimate the parameters of moving targets in colocated MIMO-radar. These algorithms are suboptimal and, if the signal matrix is ill conditioned, their performance degrades significantly. Moreover, these algorithms can not optimally estimate the parameters if the targets are off-the-grid.

In this work, to estimate the parameters of a moving target using colocated MIMO-radar, a low complexity optimal algorithm based on the Capon estimator is proposed. In this algorithm, the problem of joint estimation of the target parameters is split into two estimation problems. The first part is a simple estimation problem, which yields the closed-form

solution for the reflection coefficient. Next, to jointly estimate the spatial location and Doppler shift, our manipulation of the cost function of the second estimation problem allows us to exploit two-dimensional fast-Fourier-transform (2D-FFT) [6]–[9]. To overcome the limited resolution of the 2D-FFT, the suboptimal solution is used as an initial point for a steepest descent algorithm in order to get off-the-grid estimates. To assess the performance of the estimators, we compared the mean-square-estimation-error (MSEE) of the parameters with the the Cramér-Rao-lower-bound (CRLB).

The organization of the paper is as follows. In the following section, the problem is formulated. The estimators of the different parameters are derived in Section III. In Section IV, the first order differentials required by the steepest descent algorithm are computed. Next, some insights regarding the derivation of the CRLB are given in Section V. Simulation results are presented in Section VI. Finally, conclusions are drawn in Section VII.

**Notation:** Bold upper case letters,  $\mathbf{X}$ , and lower case letters,  $\mathbf{x}$ , respectively denote matrices and vectors. The identity matrix of dimension  $n \times n$  is denoted by  $\mathbf{I}_n$  and  $\mathbf{D}_n^{n+m}$  denotes the diagonal matrix whose elements are  $[n \ n+1 \ \cdots \ n+m]$ . Transpose, conjugate and conjugate transposition of a matrix are respectively denoted by  $(\cdot)^T$ ,  $(\cdot)^*$ , and  $(\cdot)^H$ . The statistical expectation is denoted by  $E\{\cdot\}$ . The real, imaginary, and absolute value of a complex variable  $x$  are respectively represented by  $\Re(x)$ ,  $\Im(x)$ , and  $|x|$ .

## II. PROBLEM FORMULATION

Consider a narrowband MIMO radar system with uniform-linear-arrays (ULAs) at the transmitter and the receiver. Let  $d_T$  and  $d_R$  respectively denote the inter-element spacing between the  $n_T$  transmitting and  $n_R$  receiving antennas. A moving target of reflection coefficient  $\beta_t$  is located at an angle  $\theta_t$ , which produces a normalized Doppler shift of  $f_{dt}$ . Moreover, the angles  $\theta_1$  to  $\theta_L$  denote the location of the  $L$  static interferers, each of reflection coefficient  $\beta_i$ . If  $x_m(n)$  is the baseband signal transmitted from antenna  $m$ , the received signals after matched filter can be expressed in a vector form as

$$\mathbf{y}(n) = \beta_t e^{j2\pi f_{dt} n} \mathbf{a}_R(\theta_t) \mathbf{a}_T^T(\theta_t) \mathbf{x}(n) + \sum_{i=1}^L \beta_i \mathbf{a}_R(\theta_i) \mathbf{a}_T^T(\theta_i) \mathbf{x}(n) + \mathbf{v}(n), \quad n = 1, 2, \dots, N, \quad (1)$$

This paper is an extended version of the work presented in the International Radar Conference, Lille, France, Oct. 2014. This work was funded by a CRG grant from the KAUST Office of Competitive Research Fund (OCRF).

where  $N$  denotes the total number of symbols transmitted from each antenna while

$$\begin{aligned}\mathbf{a}_T(\theta_p) &= [1 \ e^{j\frac{2\pi}{\lambda}d_T \sin(\theta_p)} \ \dots \ e^{j\frac{2\pi}{\lambda}(n_T-1)d_T \sin(\theta_p)}]^T, \\ \mathbf{a}_R(\theta_p) &= [1 \ e^{j\frac{2\pi}{\lambda}d_R \sin(\theta_p)} \ \dots \ e^{j\frac{2\pi}{\lambda}(n_R-1)d_R \sin(\theta_p)}]^T, \\ \mathbf{x}(n) &= [x_1(n) \ x_2(n) \ \dots \ x_{n_T}(n)]^T, \\ \text{and } \mathbf{v}(n) &= [v_1(n) \ v_2(n) \ \dots \ v_{n_R}(n)]^T,\end{aligned}$$

are respectively the transmit and receive steering vectors corresponding to a location  $\theta_p$ , the vector of transmitted symbols at time index  $n$ , and the vector of complex white Gaussian noise samples each of zero mean and  $\sigma_n^2$  variance. Here,  $\lambda$  denotes the wavelength of the transmitted signals.

### III. PROPOSED PARAMETER ESTIMATION

In this work, the probing signals are linearly independent. To maximize the signal-to-interference-plus-noise-ratio (SINR), a beamformer weight vector,  $\mathbf{w}$ , is used at the receiver

$$\begin{aligned}\mathbf{w}^H \mathbf{y}(n) &= \beta_t e^{j2\pi f_{dt} n} \mathbf{w}^H \mathbf{a}_R(\theta_t) \mathbf{a}_T^T(\theta_t) \mathbf{x}(n) \\ &+ \sum_{i=1}^L \beta_i \mathbf{w}^H \mathbf{a}_R(\theta_i) \mathbf{a}_T^T(\theta_i) \mathbf{x}(n) + \mathbf{w}^H \mathbf{v}(n).\end{aligned}\quad (2)$$

If the covariance matrix of the interference plus noise term is denoted by  $\mathbf{R}_{in}$ , the SINR can be defined as

$$\text{SINR} = \frac{|\beta_t|^2 \mathbb{E} \left\{ |e^{j2\pi f_{dt} n} \mathbf{w}^H \mathbf{a}_R(\theta_t) \mathbf{a}_T^T(\theta_t) \mathbf{x}(n)|^2 \right\}}{\mathbf{w}^H \mathbf{R}_{in} \mathbf{w}},\quad (3)$$

where

$$\begin{aligned}\mathbf{R}_{in} &= \mathbb{E} \left\{ \left( \sum_{i=1}^L \beta_i \mathbf{a}_R(\theta_i) \mathbf{a}_T^T(\theta_i) \mathbf{x}(n) \right) \times \right. \\ &\quad \left. \left( \sum_{i=1}^L \beta_i \mathbf{a}_R(\theta_i) \mathbf{a}_T^T(\theta_i) \mathbf{x}(n) \right)^H \right\} + \sigma_n^2 \mathbf{I}_{n_R}.\end{aligned}$$

Using prior information of the interferers' parameters, the covariance matrix  $\mathbf{R}_{in}$  can be computed. Otherwise, the methods proposed in [10]–[12] can be used to reconstruct  $\mathbf{R}_{in}$ .

Using (3), the Capon beamformer [13] that maximizes the SINR can be derived as follows

$$\mathbf{w}(\theta) = \frac{\mathbf{R}_{in}^{-1} \mathbf{a}_R(\theta)}{\mathbf{a}_R^H(\theta) \mathbf{R}_{in}^{-1} \mathbf{a}_R(\theta)}.\quad (4)$$

Therefore, using (4), to estimate the value of  $f_{dt}$ ,  $\theta_t$ , and  $\beta_t$ , the cost-function to be minimized can be written as

$$\{f_{dt}, \theta_t, \beta_t\} = \underset{f_d, \theta, \beta}{\text{argmin}} \mathbb{E} \left\{ \left| \mathbf{w}^H(\theta) \mathbf{y}(n) - \beta e^{j2\pi f_{dt} n} \mathbf{a}_T^T(\theta) \mathbf{x}(n) \right|^2 \right\}.\quad (5)$$

By differentiating the above cost-function with respect to  $\beta^*$  and equating it to 0, the minimizing value  $\hat{\beta}$  can be found as

$$\hat{\beta}(f_d, \theta) = \frac{1}{n_T} \mathbb{E} \left\{ e^{-j2\pi f_{dt} n} \mathbf{w}^H(\theta) \mathbf{y}(n) \mathbf{x}^H(n) \mathbf{a}_T^*(\theta) \right\}.\quad (6)$$

Using (4) and (6) in (5), the cost function to be minimized in order to estimate  $f_{dt}$  and  $\theta_t$  becomes

$$\begin{aligned}J_1 &= \mathbf{w}^H(\theta) \mathbf{R}_y \mathbf{w}(\theta) \\ &= \frac{1}{n_T} \frac{\left| \mathbb{E} \left\{ e^{-j2\pi f_{dt} n} \mathbf{a}_R^H(\theta) \mathbf{R}_{in}^{-1} \mathbf{y}(n) \mathbf{x}^H(n) \mathbf{a}_T^*(\theta) \right\} \right|^2}{\left| \mathbf{a}_R^H(\theta) \mathbf{R}_{in}^{-1} \mathbf{a}_R(\theta) \right|^2}.\end{aligned}\quad (7)$$

In (7), it can be noticed that  $f_d$  intervenes only in the numerator of the second term of the right hand side expression. Moreover, in the absence of interferers, i.e.,  $\mathbf{R}_{in} = \sigma_n^2 \mathbf{I}_{n_R}$ , it can be proved that minimizing (7) is equivalent to maximizing the following simplified cost function (please see appendix)

$$J_2 = \left| \mathbb{E} \left\{ e^{-j2\pi f_{dt} n} \mathbf{a}_R^H(\theta) \mathbf{R}_{in}^{-1} \mathbf{y}(n) \mathbf{x}^H(n) \mathbf{a}_T^*(\theta) \right\} \right|^2.\quad (8)$$

Assuming  $\mathbf{r}(n) = \mathbf{R}_{in}^{-1} \mathbf{y}(n)$ , the term inside the expectation operator above can be written as

$$\begin{aligned}a(n) &= e^{-j2\pi f_{dt} n} \mathbf{a}_R^H(\theta) \mathbf{r}(n) \mathbf{x}^H(n) \mathbf{a}_T^*(\theta) \\ &= e^{-j2\pi f_{dt} n} \sum_{p=1}^{n_T} \sum_{q=1}^{n_R} r_q(n) x_p^*(n) e^{-j2\pi f_s (q-1 + \gamma(p-1))},\end{aligned}\quad (9)$$

where  $f_s = \frac{d_R}{\lambda} \sin(\theta)$  and  $\gamma = \frac{d_T}{d_R}$ . By combining the same frequency terms, we can write

$$\mathbb{E}\{a(n)\} = \frac{1}{N} \sum_{n=0}^{N-1} \sum_{m=0}^{n_R-1 + \gamma(n_T-1)} f(n, m) e^{-j2\pi f_{dt} n} e^{-j2\pi f_s m},\quad (10)$$

where  $f(n, m) = \sum_{i=1}^{n_T} x_i^*(n) r_{m+1-\gamma(i-1)}(n)$ .

Interestingly, the right hand side of (10) is similar to the famous expression of the 2D-FFT. Therefore, using a 2D-FFT, the spatial and Doppler frequencies can be jointly estimated as follows

$$\hat{f}_{dt}, \hat{f}_{st} = \underset{f_d, f_s}{\text{argmax}} \left| \sum_{n=0}^{N-1} \sum_{m=0}^{\gamma(n_T-1) + n_R-1} f(n, m) e^{-j2\pi f_{dt} n} e^{-j2\pi f_s m} \right|^2.\quad (11)$$

The second scenario takes into consideration the presence of interferers. In this case, since (11) exactly estimates  $\hat{f}_{dt}$ , a search method should be applied to find the estimate  $\hat{\theta}_t$  that minimizes the cost function  $J_1$  defined in (7). To reduce the computational cost, instead of evaluating the cost function  $J_1$  over all grid points, we can restrict the search method over the region centered around the maximum of  $J_2$ .

### IV. ITERATIVE METHOD

This method uses low resolution estimates  $\hat{f}_{dt}$  and  $\hat{f}_{st}$  as initial values to initialize the steepest decent algorithm and optimize the appropriate objective function. Thus, the first order derivatives with respect to  $\theta$  and  $f_d$  of the following two expressions

$$J_2(\theta, f_d) = \frac{\left| \sum_{n=0}^{N-1} e^{-j2\pi f_{dt} n} \mathbf{a}_R^H(\theta) \mathbf{r}(n) \mathbf{x}^H(n) \mathbf{a}_T^*(\theta) \right|^2}{N^2},\quad (12)$$

and

$$A(\theta) = \mathbf{a}_R^H(\theta) \mathbf{G} \mathbf{a}_R(\theta), \quad (13)$$

are required. Here,  $\mathbf{G}$  is a generic Hermitian positive semidefinite matrix of size  $n_R$ . It should be noted that the derivative (13) is only required when interferers are present.

Using matrix transformation, we can reformulate (12) as

$$J_2(\theta, f_d) = \frac{1}{N^2} \left| \sum_{n=0}^{N-1} e^{-j2\pi f_d n} \mathbf{x}^H(n) \mathbf{M}_r(n) \mathbf{a}_S^*(\theta) \right|^2, \quad (14)$$

where the  $i^{\text{th}}$  row of the  $n_T \times (n_R + \gamma(n_T - 1))$  matrix  $\mathbf{M}_r(n)$  is defined as

$$(\mathbf{M}_r(n))_i = \left[ \underbrace{0 \cdots 0}_{(i-1)\gamma} \quad \mathbf{r}^T(n) \quad 0 \cdots 0 \right], \quad i = 1, 2, \dots, n_T,$$

and

$$\mathbf{a}_S(\theta) = \left[ 1 \quad e^{j2\pi f_s} \quad \dots \quad e^{j2\pi f_s(n_R-1+\gamma(n_T-1))} \right]^T.$$

Hence, the first order derivatives of  $J_2(\theta, f_d)$  with respect to  $f_d$  and  $\theta$  are respectively

$$\frac{\partial J_2}{\partial f_d} = -\frac{4\pi}{N^2} \Im \left( \sum_{n=0}^{N-1} e^{-j2\pi f_d n} \mathbf{x}^H(n) \mathbf{M}_r(n) \mathbf{a}_S^*(\theta) \times \sum_{n=0}^{N-1} n e^{j2\pi f_d n} \mathbf{a}_S^T(\theta) \mathbf{M}_r^H(n) \mathbf{x}(n) \right), \quad (15)$$

and

$$\frac{\partial J_2}{\partial \theta} = -\frac{4\pi d_R \cos(\theta)}{\lambda N^2} \Im \left( \sum_{n=0}^{N-1} e^{-j2\pi f_d n} \mathbf{x}^H(n) \mathbf{M}_r(n) \mathbf{a}_S^*(\theta) \times \sum_{n=0}^{N-1} e^{j2\pi f_d n} \mathbf{a}_S^T(\theta) \mathbf{D}_0^{\gamma(n_T-1)+n_R-1} \mathbf{M}_r^H(n) \mathbf{x}(n) \right). \quad (16)$$

Next, to differentiate (13), we will take into consideration the symmetry of  $\mathbf{G}$  and reformulate it as follows

$$\begin{aligned} A(\theta) &= \sum_{l=1}^{n_R} \mathbf{G}_{l,l} + 2\Re \left( \sum_{l=1}^{n_R-1} \sum_{k>l}^{n_R} \mathbf{G}_{l,k} e^{j2\pi f_s(k-l)} \right) \\ &= 2\Re(\mathbf{g}^T \mathbf{a}_R(\theta)) \end{aligned} \quad (17)$$

where

$$\mathbf{g} = \left[ \frac{1}{2} \sum_{l=1}^{n_R} \mathbf{G}_{l,l} \quad \sum_{l=1}^{n_R-1} \mathbf{G}_{l,l+1} \quad \dots \quad \mathbf{G}_{1,n_R} \right]^T. \quad (18)$$

Consequently, the first order derivative with respect to  $\theta$  can be expressed as below

$$\frac{\partial A}{\partial \theta} = -4\pi \frac{d_R}{\lambda} \cos(\theta) \Im(\mathbf{g}^T \mathbf{D}_0^{n_R-1} \mathbf{a}_R(\theta)). \quad (19)$$

Thus, using (15), (16), and (19), the first order derivatives of the cost functions  $J_1$  and  $J_2$  defined in Section III can be derived.

## V. CRAMÉR-RAO LOWER BOUND

In this section, a brief insight on the derivation of the CRLB of the reflection coefficient  $\beta_t$ , the Doppler shift  $f_{dt}$ , and the spatial location  $\theta_t$  is presented. Let  $\boldsymbol{\eta} = [\Re(\beta_t) \quad \Im(\beta_t) \quad f_{dt} \quad \theta_t]$  be the vector of unknown parameters and  $\mathbf{y}$  be the vector where all received samples from time  $n$  to  $(n+N-1)$  are stacked. Similarly, by stacking the signal and noise samples in  $\mathbf{u}$  and  $\mathbf{v}$  respectively, the problem in (1) can be reformulated in a vector form as follows

$$\mathbf{y} = \mathbf{u} + \mathbf{v}, \quad (20)$$

where  $\mathbf{y} = [\mathbf{y}^T(n) \quad \mathbf{y}^T(n+1) \quad \dots \quad \mathbf{y}^T(n+N-1)]^T$ . Under the assumption that the noise samples are spatially uncorrelated, i.e., absence of interferers, the Fisher information matrix (FIM) for the estimation of  $\boldsymbol{\eta}$  can be found using the Slepian-Bangs formula [14]

$$\begin{aligned} \mathbf{F}(\boldsymbol{\eta}) &= \frac{2}{\sigma_n^2} \Re \left( \frac{\partial \mathbf{u}^H}{\partial \boldsymbol{\eta}} \frac{\partial \mathbf{u}}{\partial \boldsymbol{\eta}^T} \right) \\ &= \frac{2}{\sigma_n^2} \Re \left( \sum_{n=0}^{N-1} \left( \frac{\partial \mathbf{u}^H(n)}{\partial \boldsymbol{\eta}} \frac{\partial \mathbf{u}(n)}{\partial \boldsymbol{\eta}^T} \right) \right). \end{aligned} \quad (21)$$

Each entry of the vector  $\frac{\partial \mathbf{u}^H(n)}{\partial \boldsymbol{\eta}}$  can be expressed as follows

$$\begin{aligned} \frac{\partial \mathbf{u}(n)}{\partial \Re(\beta_t)} &= e^{j2\pi f_{dt} n} \mathbf{a}_R(\theta_t) \mathbf{a}_T^T(\theta_t) \mathbf{x}(n) = \frac{\mathbf{u}(n)}{\beta_t}, \\ \frac{\partial \mathbf{u}(n)}{\partial \Im(\beta_t)} &= j e^{j2\pi f_{dt} n} \mathbf{a}_R(\theta_t) \mathbf{a}_T^T(\theta_t) \mathbf{x}(n) = \frac{\mathbf{u}(n)}{-j\beta_t}, \\ \frac{\partial \mathbf{u}(n)}{\partial f_{dt}} &= j\beta_t 2\pi n e^{j2\pi f_{dt} n} \mathbf{a}_R(\theta_t) \mathbf{a}_T^T(\theta_t) \mathbf{x}(n) = (j2\pi n) \mathbf{u}(n), \end{aligned}$$

$$\begin{aligned} \text{and } \frac{\partial \mathbf{u}(n)}{\partial \theta_t} &= j\beta_t e^{j2\pi f_{dt} n} 2\pi \frac{d_R}{\lambda} \cos(\theta_t) \times \\ &(\gamma \mathbf{a}_T^T(\theta_t) \mathbf{D}_0^{n_T-1} \mathbf{x}(n) + \mathbf{a}_T^T(\theta_t) \mathbf{x}(n) \mathbf{D}_0^{n_R-1}) \mathbf{a}_R(\theta_t). \end{aligned}$$

Using simple calculations, it can be noticed that the FIM is independent of  $f_{dt}$ . The CRLB of the parameters can be found by simply inverting FIM. Since  $\mathbf{F}(\boldsymbol{\eta})$  is independent of  $f_{dt}$ , the CRLB will also be independent of  $f_{dt}$ . Due to the size limitation, derivations of the close form solution of the CRLB is not given in this work but can be found in the journal version of this paper [15].

## VI. SIMULATION RESULTS

In this section, three simulation results are presented to demonstrate the performance of the proposed estimators. In all simulations, we assumed perfect knowledge of the interference plus noise covariance matrix  $\mathbf{R}_{in}$  and used 10 transmit and 10 receive antennas with half-wavelength inter-element spacing, i.e.,  $d_R = d_T = \frac{\lambda}{2}$  and  $\gamma = 1$ . The results are averaged over 5,000 Monte Carlo realizations, the number of transmitted symbols is  $N = 32$  and the size of the 2D-FFT is 128. The target of interest is at an off-the-grid location  $\theta_t = 10^\circ$  and its reflection coefficient is  $\beta_t = -1 + 2j$ . Since the CRLB of the parameters is independent of the target's Doppler shift, for each realization,  $f_{dt}$  is generated from a Gaussian random variable with mean 0.25 and variance 0.001.

In the first simulation, we considered the case where there are no interferers. Thus, minimizing the cost function  $J_1$

becomes equivalent to maximizing  $J_2$ . Fig. 1 shows that, at very low SNR, the MSEE of all parameters fails to meet the CRLB. However, for SNR values higher than  $-20$  dB, the MSEE using only the 2D-FFT algorithm has an error floor while the MSEE of the iterative algorithm achieves the CRLB.

For the next simulations, we considered the presence of two interferers with reflection coefficients 100 times higher than the SNR and located at  $-10^\circ$  and  $30^\circ$ . Figure 2 shows the performance of the estimates, which minimize the cost function  $J_1$ . It can be seen that the MSEE of the Doppler shift exactly matches its CRLB. However, a 4dB gap is kept constant between the MSEE and the CRLB of the parameter  $\theta_t$ .

The last simulation offers a comparison between the performance of our algorithm and the Capon estimator derived in [2]. Contrarily to the first two scenarios where noise samples were drawn from a linearly independent Gaussian process, here a colored Gaussian noise with covariance matrix  $\mathbf{C}_{pq} = \frac{1}{SNR} 0.9^{|p-q|} e^{j\pi \frac{p-q}{2}}$  is used. Moreover, as the method in [2] only estimates the RCS and the location of stationary targets, the Doppler shift is set to zero. To estimate the parameters of a stationary target now located at  $\theta_t = 10.05^\circ$ , a 128 2D-FFT algorithm was used to initialize the iterative algorithm, whilst a  $0.1^\circ$  search grid is used for [2]. As shown in Fig. 3, the iterative algorithm outperforms the Capon algorithms as it generates optimal estimates of the target parameters.

## VII. CONCLUSION

In this work, a low resolution 2D-FFT is used to find an initial point for the steepest descent algorithm, which estimates the reflection coefficient, the Doppler shift, and the spatial location of an off-the-grid target. Moreover, simulation results showed that the MSEE of the derived estimators matches the CRLB and that the super resolution iterative algorithm outperforms the Capon method. Due to space limitation, the effect of  $\gamma$  on the performance of our algorithm was not discussed here but is covered in the journal version of this paper [15].

## VIII. APPENDIX

A two part proof will be derived to demonstrate that, in absence of interferers, minimizing the cost function  $J_1$  defined in (7) is equivalent to maximizing the cost function  $J_2$  introduced in (8). To this extent, we first need to prove that

$$\theta_t = \underset{\theta}{\operatorname{argmax}} \mathbf{w}^H(\theta) \mathbf{R}_y \mathbf{w}(\theta), \quad (22)$$

where  $\mathbf{w}(\theta)$  is as defined in (4).

In absence of interferers, i.e.,  $\mathbf{R}_{in} = \sigma_n^2 \mathbf{I}_{n_R}$ , using (4), we can write

$$\mathbf{w}^H(\theta) \mathbf{R}_y \mathbf{w}(\theta) = \frac{\mathbf{a}_R^H(\theta) \mathbf{R}_y \mathbf{a}_R(\theta)}{n_R^2}. \quad (23)$$

Moreover, as the independent waveforms  $\mathbf{x}(n)$  and the noise  $\mathbf{v}(n)$  are uncorrelated, the covariance matrix of the received signals  $\mathbf{R}_y$  can be expressed as below

$$\begin{aligned} \mathbf{R}_y &= \mathbb{E} \left\{ \left| \beta_t e^{j2\pi f_d n} \mathbf{a}_R(\theta_t) \mathbf{a}_T^T(\theta_t) \mathbf{x}(n) + \mathbf{v}(n) \right|^2 \right\} \\ &= |\beta_t|^2 n_T \mathbf{a}_R(\theta_t) \mathbf{a}_R(\theta_t)^H + \sigma_n^2 \mathbf{I}_{n_R}. \end{aligned} \quad (24)$$

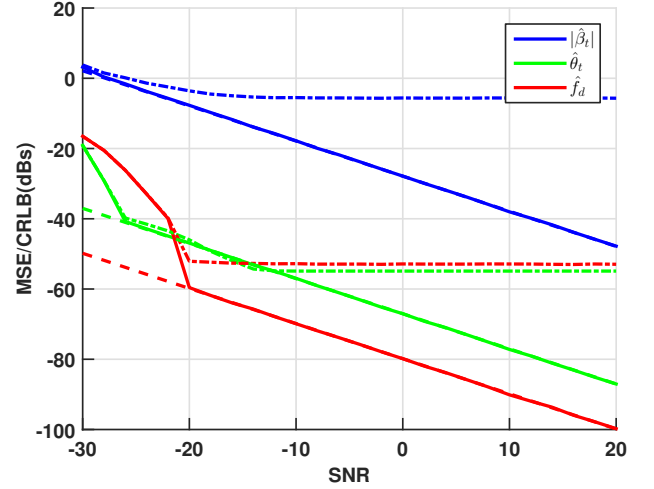


Fig. 1. Comparison of the 128 point 2D-FFT (dash-dot lines) and the iterative algorithm (solid lines) with the CRLB (dashed lines) of  $\beta_t$ ,  $f_d$ , and  $\theta_t$ . Here,  $\beta_t = -1 + 2j$  and  $\theta_t = 10^\circ$ .

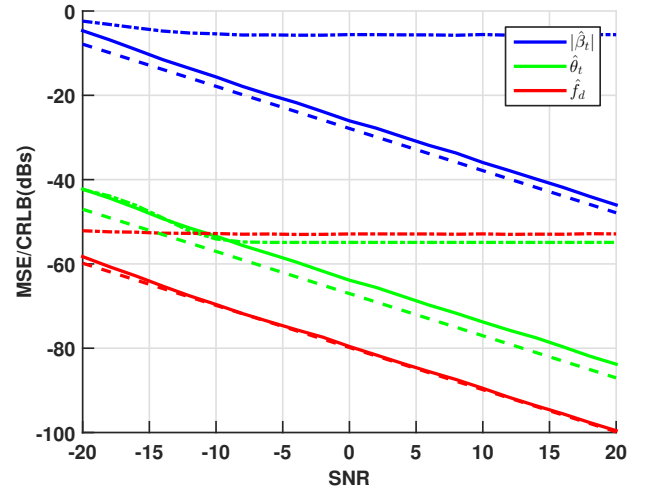


Fig. 2. Comparison of the 128 point 2D-FFT (dash-dot lines) and the iterative algorithm (solid lines) with the CRLB (dashed lines) of  $\beta_t$ ,  $f_d$ , and  $\theta_t$ . Here,  $\beta_t = -1 + 2j$ ,  $\theta_t = 10^\circ$ , and  $\text{INR} = 20$  dB.

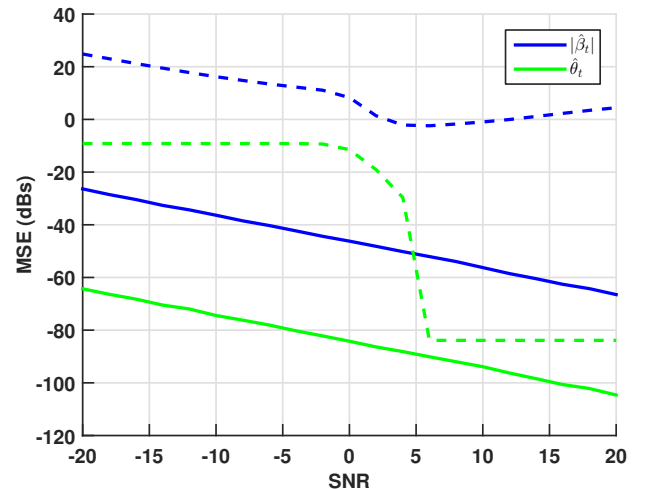


Fig. 3. Comparison of the iterative algorithm (solid lines) with the Capon (dashed lines) method derived in [2]. Here,  $\beta_t = -1 + 2j$ ,  $\theta_t = 10^\circ$ , and  $\text{INR} = 20$  dB.

Therefore, by combining (24) and (23), we can deduce that

$$\mathbf{w}^H(\theta)\mathbf{R}_y\mathbf{w}(\theta) = |\beta_t|^2 \frac{n_T}{n_R^2} \left| \mathbf{a}_R^H(\theta)\mathbf{a}_R(\theta_t) \right|^2 + \frac{\sigma_n^2}{n_R}, \quad (25)$$

which is clearly maximized at  $\theta = \theta_t$ .

In the second part of the demonstration, we will prove by contradiction that

$$\begin{aligned} f_{dt}, \theta_t &= \operatorname{argmax}_{f_d, \theta} \left| \mathbf{E} \left\{ e^{-j2\pi f_d n} \mathbf{w}^H(\theta) \mathbf{y}(n) \mathbf{x}^H(n) \mathbf{a}_T^*(\theta) \right\} \right|^2 \\ &= \operatorname{argmax}_{f_d, \theta} |\beta(f_d, \theta)|^2. \end{aligned} \quad (26)$$

Thus, let us assume that it exists a couple of variables  $(f_{de}, \theta_e)$  such that

$$|\beta(f_{de}, \theta_e)| > |\beta(f_{dt}, \theta_t)|. \quad (27)$$

Using (22), we can write

$$\mathbf{w}^H(\theta_e)\mathbf{R}_y\mathbf{w}(\theta_e) \leq \mathbf{w}^H(\theta_t)\mathbf{R}_y\mathbf{w}(\theta_t), \quad (28)$$

which leads to

$$\begin{aligned} \mathbf{w}^H(\theta_e)\mathbf{R}_y\mathbf{w}(\theta_e) - \frac{1}{n_T} |\beta(f_{de}, \theta_e)|^2 \\ < \mathbf{w}^H(\theta_t)\mathbf{R}_y\mathbf{w}(\theta_t) - \frac{1}{n_T} |\beta(f_{dt}, \theta_t)|^2. \end{aligned} \quad (29)$$

Because (29) contradicts (7), we can finally conclude that solving (7) is equivalent to solving (8) under the noise only assumption.

## REFERENCES

- [1] Jian Li and Petre Stoica, *MIMO Radar Signal Processing - Diversity Means Superiority*, John Wiley & Sons, Inc., Hoboken New Jersey, 2008.
- [2] Luzhou Xu, Jian Li, and Petre Stoica, "Target detection and parameter estimation for MIMO radar systems," *IEEE Transactions on Aerospace and Electronic Systems*, vol. 44, no. 3, pp. 927–939, July 2008.
- [3] A. Hassaniien, S.A. Vorobyov, and A.B. Gershman, "Moving target parameters estimation in noncoherent MIMO radar systems," *IEEE Transactions on Signal Processing*, vol. 60, no. 5, pp. 2354–2361, May 2012.
- [4] Ji Li, J. Conan, and Samuel Pierre, "Joint estimation of channel parameters for MIMO communication systems," in *2nd International Symposium on Wireless Communication Systems*, Sept. 2005, pp. 22–26.
- [5] Ming Jin, Guisheng Liao, and Jun Li, "Joint DOD and DOA estimation for bistatic MIMO radar," *Signal Processing*, vol. 89, no. 2, pp. 244 – 251, Feb. 2009.
- [6] Stephen R. Alty, Andreas Jakobsson, and Erik G. Larsson, "Efficient implementation of the time-recursive Capon and APES spectral estimators," in *12th European Signal Processing Conference*, Sept. 2004, pp. 1269–1272.
- [7] Torbjörn Ekman, Andreas Jakobsson, and Petre Stoica, "On efficient implementation of the capon algorithm," in *European Association Signal Processing Conference, Tampere, Finland*, Sept. 2000.
- [8] E.G. Larsson and Petre Stoica, "Fast implementation of two-dimensional APES and CAPON spectral estimators," *Multidimensional Systems and Signal Processing*, vol. 13, no. 1, pp. 35–53, 2002.
- [9] E.G. Larsson and Petre Stoica, "Fast implementation of two-dimensional APES and CAPON spectral estimators," in *IEEE International Conference on Acoustics, Speech, and Signal Processing*, 2001, vol. 5, pp. 3069–3072 vol.5.
- [10] Yujie Gu and A. Leshem, "Robust adaptive beamforming based on interference covariance matrix reconstruction and steering vector estimation," *IEEE Transactions on Signal Processing*, vol. 60, no. 7, pp. 3881–3885, July 2012.
- [11] Lei Huang, Jing Zhang, Xu Xu, and Zhongfu Ye, "Robust adaptive beamforming with a novel interference-plus-noise covariance matrix reconstruction method," *IEEE Transactions on Signal Processing*, vol. 63, no. 7, pp. 1643–1650, Apr. 2015.
- [12] MU PengCheng, LI Dan, YIN QinYe, and GUO Wei, "Robust mvdr beamforming based on covariance matrix reconstruction," *SCIENCE CHINA Information Sciences*, vol. 56, no. 4, pp. 42303, 2013.
- [13] J. Capon, "High-resolution frequency-wavenumber spectrum analysis," *Proceedings of the IEEE*, vol. 57, no. 8, pp. 1408–1418, Aug. 1969.
- [14] P. Stoica and R. Moses, *Introduction to Spectral Analysis*, Prentice Hall, Upper Saddle River, N.J., 1997.
- [15] S. Jardak, S. Ahmed, and M.-S. Alouini, "Low complexity MIMO-radar super resolution parameter estimation by exploiting 2D-FFT," *Submitted in IEEE Transactions on Signal Processing*, <http://archive.kaust.edu.sa/kaust/handle/10754/305796>.

# Normalised multi-stage clustering equaliser for underwater acoustic channels

Rangeet Mitra and Vimal Bhatia  
Signals and Software group  
Discipline of Electrical Engineering  
Indian Institute of Technology Indore  
Indore-453441, India

Email: phd1301202010@iiti.ac.in, vbhatia@iiti.ac.in

**Abstract**—Underwater communications systems are being increasingly used in defence, security service, oil exploration, ocean science and in many other applications. The underwater acoustic channel is characterised by the large delay spread, Doppler shifts, limited bandwidths and time variability. The channel is also affected by additive impulsive noise, which makes the underwater communication even more challenging. Since the channel and noise characteristics vary immensely, an adaptive equaliser at the communications receiver forms a viable solution for increasing the bit error rate of the communication link. The adaptive multistage clustering based equaliser is one such solution which provides high throughput. However, the performance of the multistage clustering equaliser degrades in the presence of impulsive noise. To improve the throughput and robustness, we propose an adaptive normalised multistage clustering based blind equaliser for underwater acoustic channel. From simulation results, it is observed that the proposed algorithm has better convergence and symbol error rate performance. Convergence analysis of the proposed algorithm is also presented in the paper.

## I. INTRODUCTION

In today's world there is an increasing research interest in underwater acoustic communication systems. This is due to their widespread use in systems for environmental monitoring, exploration, military missions [1], leisure and marine research, oceanography and defence [2]. Hence, in this paper, we focus on underwater acoustic channels. Underwater acoustic channels [3] are characterised by large delay spreads, large doppler shifts and are time varying in nature. The underwater communication channels are, in addition, further effected by impulsive noise caused by ice-cracking and, other natural and man-made sources. These communication channels and environmental conditions are more severe and thus require an adaptive equaliser at the communications receiver [2] for high throughput.

Most of the present day equalisers are optimised under the Gaussian noise assumption and their performance is degraded by the occurrence of impulsive noise [4]. Impulsive noise is more likely to exhibit sharp spikes or occasional bursts of outlying observations than one would expect from Gaussian distributed signals. A variety of impulsive noise models has been proposed in [5],[6]. However, a common model to represent impulsive phenomena is the family of  $\alpha$ -stable random variables [7]. Stable distributions share defining characteristics with the Gaussian distribution, such as the stability property and central limit theorems. The empirical data indicate that

the probability density functions (pdfs) of the impulsive noise processes exhibit a similarity to the Gaussian pdf, being bell shaped, smooth and symmetric, but at the same time having significantly heavier tails [8].

The outlook of a communications engineer in such scenarios, is to maximise the number of bits that are reliably be transmitted across the underwater communication channel. To this end, there are primarily three techniques can be used, namely: a) Equalisation, b) Diversity, and c) Channel Coding [9]. The scope of this paper is limited to channel equalisation. Equalisation can be broadly categorised as: a) blind based approaches, and b) training based approaches [9]. The blind based approaches do not require training data, and hence are spectrally efficient as the need for the bandwidth needed to send the pilot signals is saved. The training based approaches require a known sequence of labels of the data to be transmitted, which results in better performance but is not spectrally efficient. There are some adaptive equalisation approaches that utilise a combination of training-based and blind-based techniques for inference; they are called as semi-blind learning techniques [10], [11]. In this paper, we focus on blind equalisation techniques.

Constant modulus algorithm [12], one of the blind equalisation approaches, was applied in many channels including underwater acoustic channels [3] with some processing steps. It is observed in the literature that the class of multi-stage clustering based blind equalisers form a superior solution to the channel equalisation problem as described in [13], [14] as compared to other Busgang based algorithms. These algorithms rely on a stochastic gradient adaptation similar to the least mean squares (LMS) based algorithms and may converge slowly in severe conditions like underwater acoustic channels [3]. To this end normalised-LMS based approaches converge faster than most of LMS based approaches [15]. A normalised-CMA based approach is covered in [3] with some post processing steps so as to make the approach suitable for underwater acoustic channels.

In this paper, we propose a normalised - improved multi-stage clustering (IMSC) equaliser [14] and analyse its convergence. The proposed equaliser is compared against CMA based algorithms, and is observed to perform better in underwater acoustic channel in the presence of impulsive noise.

This paper is organised as follows: Section-II reviews the IMSC equaliser structure. The proposed algorithm is described

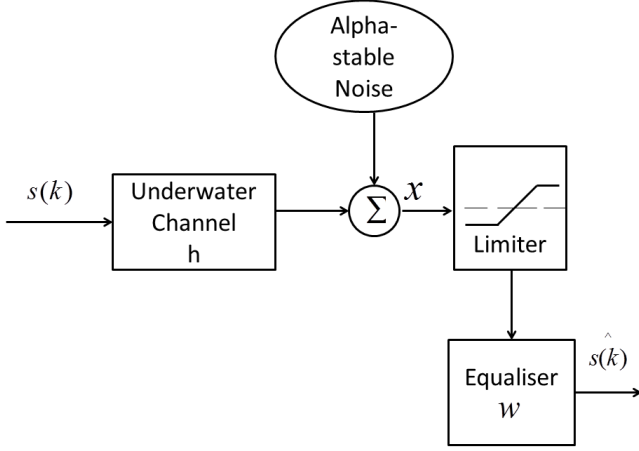


Fig. 1. Overall System Model

in section-III. Section-IV analyses the convergence of the proposed algorithm and section-V presents the simulation results. Conclusions from analysis and simulation results are drawn in section-VI.

## II. REVIEW OF IMPROVED MULTI-STAGE CLUSTERING (IMSC) BASED BLIND EQUALISATION

The system model assumed in this paper is depicted in Fig. 1, where  $s(k)$  is the input symbol,  $h$  is the underwater channel,  $w$  being the equaliser weights and  $\hat{s}(k)$  is estimated symbol at the output of the equaliser. In [14], a phase splitting equaliser was proposed for the multi-stage clustering problem in [13]. Instead of the assumption of a two dimensional Gaussian noise [13], two one dimensional Gaussian noises were assumed, one for each of the real and the imaginary part. In this scheme, two separate cost functions were defined as:

$$J_R(k) = \sum_{j=1}^Q \exp\left(\frac{-(y_R(k) - \mu_{Rj})^2}{2\rho}\right) \quad (1)$$

$$J_I(k) = \sum_{j=1}^Q \exp\left(\frac{-(y_I(k) - \mu_{Ij})^2}{2\rho}\right) \quad (2)$$

where  $\rho$  is the variance of the Gaussian noise,  $y_R(k)$  and  $y_I(k)$  are real and imaginary parts of the filtered output at  $k^{th}$  iteration and  $\{\mu_{Rj}\}_{j=1}^Q$ ,  $\{\mu_{Ij}\}_{j=1}^Q$  are the set of all possible real and imaginary parts of the symbols in the constellation. The equaliser weights are updated as:

$$\mathbf{w}_R(k+1) = \mathbf{w}_R(k) + \eta \nabla_{\mathbf{w}_R} J_R(k) \quad (3)$$

and

$$\mathbf{w}_I(k+1) = \mathbf{w}_I(k) + \eta \nabla_{\mathbf{w}_I} J_I(k) \quad (4)$$

where  $\eta$  is the step-size and the complex equaliser weight vector after the  $k^{th}$  iteration is

$$\mathbf{w}(k) = \mathbf{w}_R(k) + j\mathbf{w}_I(k) \quad (5)$$

The gradients of  $J_R$  and  $J_I$  with respect to  $\mathbf{w}_R$  and  $\mathbf{w}_I$  respectively are designated as  $\nabla_{\mathbf{w}_R} J_R$  and  $\nabla_{\mathbf{w}_I} J_I$ . The gradients can then be defined as:

$$\nabla_{\mathbf{w}_R} J_R(k) = \sum_{j=1}^Q \left( -\exp\left(\frac{-(y_R(k) - \mu_{Rj})^2}{2\rho}\right) (y_R(k) - \mu_{Rj}) \right) \mathbf{x} = e_{IMSC}^R(k) \mathbf{x} \quad (6)$$

and

$$\nabla_{\mathbf{w}_I} J_I(k) = \sum_{j=1}^Q \left( -\exp\left(\frac{-(y_I(k) - \mu_{Ij})^2}{2\rho}\right) (y_I(k) - \mu_{Ij}) \right) \mathbf{x} = e_{IMSC}^I(k) \mathbf{x} \quad (7)$$

where  $\mathbf{x}$  is the vector of past  $T$  samples. For the 16-quadrature amplitude modulation (QAM) case, in the first stage of clustering, each  $\mu_R$  and  $\mu_I$  equals  $\pm 2$  with  $Q = 2$ . In the second stage of clustering, there would be four possible values of  $\mu_R$  and  $\mu_I$  given by  $\pm 1$  and  $\pm 3$  with  $Q = 4$ .

For the 64-QAM case, this algorithm can be extended by the method given in [13]. In the first stage of clustering, each  $\mu_R$  and  $\mu_I$  equals  $\pm 2$  with  $Q = 2$ . In the second stage of clustering, there would be four possible values of  $\mu_R$  and  $\mu_I$  given by  $\pm 2$  and  $\pm 4$  with  $Q = 4$ . In the third stage, there will be eight possible values of moduli given by  $\{\pm 1, \pm 3, \pm 5, \pm 7\}$  with  $Q = 8$ . Even this can be extended similarly till 256-QAM as given in [13].

Similarly, a commonly used constellations used in underwater communications, like 3-pulse amplitude modulation (PAM) [16], the first stage of IMSC may have  $\mu_R = \{\pm 1\}$ , while the next stage of the IMSC will have  $\mu_R = \{0, \pm 3\}$ . As 3-PAM is a real constellation,  $\mu_I$  is zero for all stages.

## III. NORMALISED IMPROVED MULTI-STAGE CLUSTERING BASED BLIND EQUALISATION

In this section, the normalised improved multi-stage clustering equaliser is proposed. It is well known in the adaptive-filtering literature that normalised adaptive filtering based approaches converge faster than other stochastic gradient based variants of least mean squares (LMS) [15] like sign-error, sign-data and sign-sign algorithms. Therefore, we investigate for a normalised solution for the blind improved multi-stage clustering equaliser, and later confirm its robustness for impulsive noise effected communication channels.

In this section, we formulate the normalised IMSC cost function based equalisation. The normalised IMSC blind equaliser can be motivated as a solution to the following optimisation problem for real part of the constellation and then similarly extended to the imaginary part,

$$\begin{aligned} & \text{minimise}_{\mathbf{w}_R(k+1)} \quad \frac{\eta}{2} \|\mathbf{w}_R(k+1) - \mathbf{w}_R(k)\|_2^2 \\ & \text{subject to} \quad J_R = (1 - \epsilon) \\ & \quad \quad \quad \epsilon \rightarrow 0 \end{aligned}$$

Forming the Lagrangian  $\Lambda$ ,

$$\Lambda(\mathbf{w}_R, \lambda) = \frac{\eta}{2} \|\mathbf{w}_R(k+1) - \mathbf{w}_R(k)\|_2^2 - \lambda (J_R(k) - (1 - \epsilon)) \quad (8)$$

Solving for  $\mathbf{w}_R$ , we take gradient with respect to  $\mathbf{w}_R$  as follows:

$$\begin{aligned} \nabla_{\mathbf{w}_R} \Lambda(\mathbf{w}_R, \lambda) &= 0 \quad (9) \\ \implies \eta \mathbf{w}_R(k+1) - \eta \mathbf{w}_R(k) - \lambda e_{IMSC}^R(k) \mathbf{x} &= 0 \\ \implies \eta \mathbf{w}_R(k+1) &= \eta \mathbf{w}_R(k) + \lambda e_{IMSC}^R(k) \mathbf{x} \end{aligned}$$

Now solving for  $\lambda$  we assume  $\zeta$ -convergence of the weights and hence the output estimates,

$$\eta |y_R(k+1) - y_R(k)| = \lambda |e_{IMSC}^R(k)| \|\mathbf{x}\|_2^2 \quad (10)$$

Hence,

$$\lambda = \Gamma \frac{\eta}{\|\mathbf{x}\|_2^2} \quad (11)$$

where,

$$\Gamma = \frac{|y_R(k+1) - y_R(k)|}{|e_{IMSC}^R(k)|} \rightarrow 1 \quad (12)$$

as at convergence they both are very small, and lie to right hand limit of zero. Thus, the adaptation equation for the proposed normalised-IMSC is given as:

$$\mathbf{w}_R(k+1) = \mathbf{w}_R(k) + \lambda e_{IMSC}^R(k) \mathbf{x} \quad (13)$$

where,

$$\lambda = \frac{\eta}{\|\mathbf{x}\|_2^2} \quad (14)$$

A small penalty term  $\kappa$  may be added to the denominator to avoid misconvergence, as in common normalised adaptive filtering based approaches [17].

$$\lambda = \frac{\eta}{\kappa + \|\mathbf{x}\|_2^2} \quad (15)$$

The  $\lambda$  for imaginary part may be found out similarly and will equal  $\frac{\eta}{\kappa + \|\mathbf{x}\|_2^2}$ . As gradient descent directions are closed under scaling a constant [18], we adapt as follows till convergence:

$$\begin{aligned} \mathbf{w}_R(k+1) &= \mathbf{w}_R(k) + \eta e_{IMSC}^R(k) \frac{\mathbf{x}}{\kappa + \|\mathbf{x}\|_2^2} \quad (16) \\ \mathbf{w}_I(k+1) &= \mathbf{w}_I(k) + \eta e_{IMSC}^I(k) \frac{\mathbf{x}}{\kappa + \|\mathbf{x}\|_2^2} \end{aligned}$$

This gives a normalised version of IMSC, which performs better than IMSC as observed by simulations in section-V. However, this advantage would come at the cost of computing the norm of the observation vector at each instant and dividing by it.

#### IV. CONVERGENCE ANALYSIS

In this section, we analyse the convergence and prove that in well-conditioned channels, the proposed normalised based algorithm converges faster than the multi-stage clustering based approaches. The adaptation equation for normalised-IMSC are given in eq. (16). The adaptation equation for IMSC is given approximately as follows:

$$\begin{aligned} \mathbf{w}_R(k+1) &= (1 - \gamma) \mathbf{w}_R(k) + \eta \gamma e_{IMSC}^R(k) \mathbf{x} \quad (17) \\ \mathbf{w}_I(k+1) &= (1 - \gamma) \mathbf{w}_I(k) + \eta \gamma e_{IMSC}^I(k) \mathbf{x} \end{aligned}$$

where  $\gamma$  be assumed a positive constant close to zero. Assuming similar approximation for normalised-IMSC, we can write the approximate adaptation equation as:

$$\begin{aligned} \mathbf{w}_R(k+1) &= (1 - \gamma) \mathbf{w}_R(k) + \gamma \eta e_{IMSC}^R(k) \frac{\mathbf{x}}{\kappa + \|\mathbf{x}\|_2^2} \quad (18) \\ \mathbf{w}_I(k+1) &= (1 - \gamma) \mathbf{w}_I(k) + \gamma \eta e_{IMSC}^I(k) \frac{\mathbf{x}}{\kappa + \|\mathbf{x}\|_2^2} \end{aligned}$$

Let  $\mathbf{w}^{opt}$  be the optimal weight for eq. (5). Hence from the Banach contraction mapping theorem in [19], the deviation of the equaliser from the optimal weight for IMSC can be written as:

$$\|\mathbf{w}(k) - \mathbf{w}^{opt}\| \leq (1 - \gamma)^k \eta |e_{IMSC}(k)| \|\mathbf{x}\| \quad (19)$$

Similarly for the normalised-IMSC the deviation can be written as:

$$\|\mathbf{w}(k) - \mathbf{w}^{opt}\| \leq (1 - \gamma)^k \eta |e_{IMSC}(k)| \frac{\|\mathbf{x}\|}{\|\mathbf{x}\|_2^2} \quad (20)$$

where the weight  $\mathbf{w}(k)$  is defined in eq. (5). Clearly, it can be seen that normalised-IMSC has a lower deviation than IMSC as it is divided by the factor  $\|\mathbf{x}\|_2^2$  which can be assumed to be greater than unity for well-conditioned channels.

#### V. SIMULATIONS

In this section, to validate the performance of proposed algorithm, simulation results are presented for a variety of channels. We first describe the simulation conditions used to validate the performance of the proposed normalised-IMSC algorithm. The modulation scheme assumed is 3-PAM so as to generate a multi-level constellation. The IMSC based equaliser is compared with normalised-IMSC based equaliser in two underwater acoustic channels described in [3]. Step size  $\mu$  was considered as 0.02 for both equalisers. The first stage of the equaliser is given by first 700 iterations. For the second stage, in case of normalised-IMSC, equal weighting was given to both normalised-IMSC cost function and IMSC cost function after initial convergence.

To handle outliers/signals with higher amplitudes which are more tendentious to get affected by the tail of the Cauchy noise the techniques like clipping off the signal [20], [3] to its dynamic range and applying a tanh activation function on the error terms as discussed in [3] have been applied before the equaliser as in Fig. 1. The noise power for  $\alpha$ -stable distribution is calculated using the variance of the truncated distribution to account for the clipping preprocessing step which is done to remove samples affected by the heavy tails. In addition, this also aids in realisation of eq. (18) and eq. (20).

For the first impulsive noise affected channel, an underwater acoustic channel (channel (a) with impulse response given by [0.3132, -0.1040, 0.8908, 0.3143]) affected by Cauchy-distributed impulsive noise ( $\alpha = 1, \beta = 0$  in  $S\alpha S$  distribution) was considered from [3]. Firstly, its convergence is simulated in Fig. 2 at SNR of 22 dB. Faster convergence in case of the proposed algorithm from Fig. 2 is observed. We observe a significantly higher rate of decay in case of normalised-IMSC as compared to IMSC. Also, from Fig. 3, convergence to half a decade lower SER as a function of SNR can be observed. It is also observed that the CMA based equaliser weights take longer to converge than the proposed normalised IMSC based equaliser.

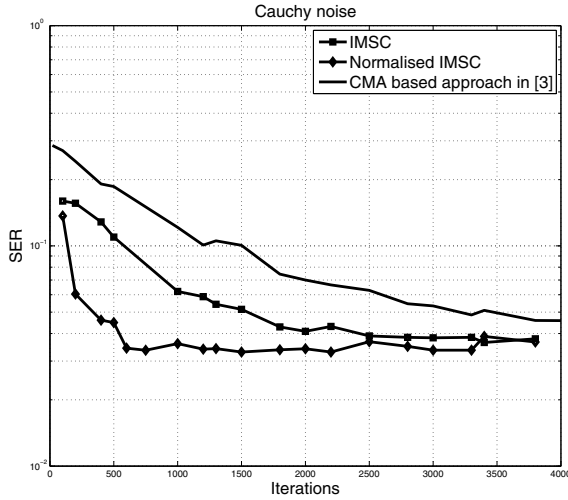


Fig. 2. Convergence plot comparison in first underwater acoustic channel (a) with impulse response given by  $[0.3132, -0.1040, 0.8908, 0.3143]$  at SNR of 22dB

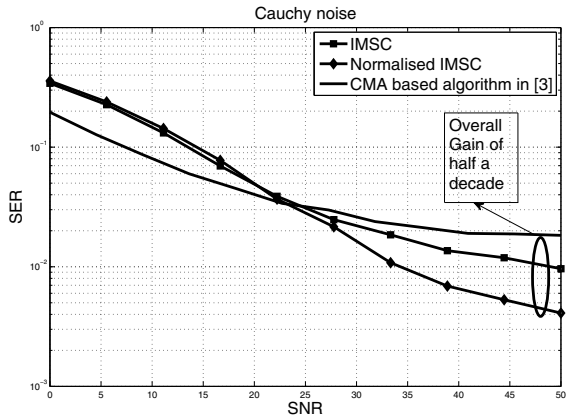


Fig. 3. SER vs SNR comparison in first underwater acoustic channel (a) with impulse response given by  $[0.3132, -0.1040, 0.8908, 0.3143]$

For the second impulsive noise affected channel, an underwater acoustic channel (channel (b) with impulse response given by  $[0.5849, -1, 0.2608, -0.1336, 0.0740, -0.0394, 0.0183, -0.0059, -0.0006, 0.0031]$ ) affected by Cauchy-distributed impulsive noise was considered from [3]. Significantly faster convergence to a lower SER at an SNR of 22 dB is observed in the convergence analysis plot in Fig. 4. SER vs SNR is plotted for the same channel in Fig. 5. An SNR gain of 10dB can be observed in the high SNR regime. While it can be seen that the SER vs SNR performance of IMSC and normalised-IMSC are almost identical, the normalised-IMSC converges much faster as compared to IMSC as can be seen from Fig. 4. We can also see that IMSC and normalised-IMSC outperform the work in [3] both in terms of convergence and SER vs SNR performance.

## VI. CONCLUSION

In this paper, a normalised-IMSC based blind equaliser is proposed for underwater acoustic communication channels.

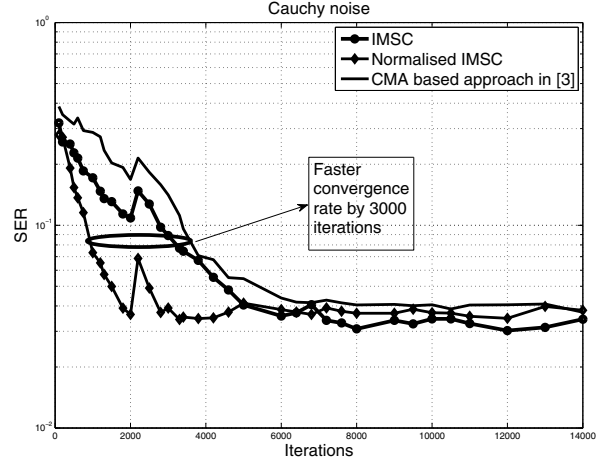


Fig. 4. SER convergence comparison in second underwater acoustic channel (b) with impulse response given by  $[0.5849, -1, 0.2608, -0.1336, 0.0740, -0.0394, 0.0183, -0.0059, -0.0006, 0.0031]$  at SNR of 22dB

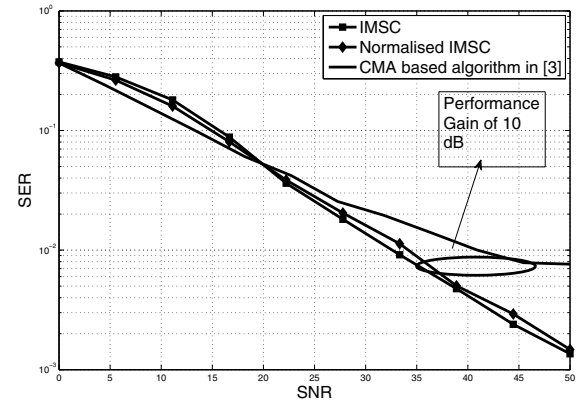


Fig. 5. SER vs SNR Comparison in second underwater acoustic channel (b) with impulse response given by  $[0.5849, -1, 0.2608, -0.1336, 0.0740, -0.0394, 0.0183, -0.0059, -0.0006, 0.0031]$

The proposed algorithm is observed to have faster convergence than IMSC and the CMA based algorithm. A lower SER is also observed for impulsive noise effected underwater acoustic communication channel for SNR greater than 20-25dBs. Convergence analysis was carried out and the proposed algorithm was analytically proven to be close to the optimal solution at a given iteration. Hence, the proposed algorithm is a viable solution to equalise an underwater acoustic channels in the presence of impulsive noise.

## ACKNOWLEDGMENT

The authors would like to thank IIT Indore for all the support.

## REFERENCES

[1] R. Otnes, A. Asterjadhi, P. Casari, M. Goetz, T. Husøy, I. Nissen, K. Rimstad, P. van Walree, and M. Zorzi, *Underwater acoustic networking techniques*. Springer Science & Business Media, 2012.

- [2] M. Chitre, S. Shahabudeen, and M. Stojanovic, "Underwater acoustic communications and networking: Recent advances and future challenges," *Marine technology society journal*, vol. 42, no. 1, pp. 103–116, 2008.
- [3] Z. Yin-bing, Z. Jun-wei, G. Ye-cai, and L. Jin-ming, "A constant modulus algorithm for blind equalization in  $\alpha$ -stable noise," *Applied Acoustics*, vol. 71, no. 7, pp. 653–660, 2010.
- [4] A. T. Georgiadis and B. Mulgrew, "Adaptive bayesian decision feedback equaliser for alpha-stable noise environments," *Signal Processing*, vol. 81, no. 8, pp. 1603–1623, 2001.
- [5] L. Lind and N. Mufti, "Efficient method for modelling impulse noise in a communication system," *Electronics Letters*, vol. 32, no. 16, pp. 1440–1441, 1996.
- [6] I. Mann, S. McLaughlin, W. Henkel, R. Kirkby, and T. Kessler, "Impulse generation with appropriate amplitude, length, inter-arrival, and spectral characteristics," *Selected Areas in Communications, IEEE Journal on*, vol. 20, no. 5, pp. 901–912, 2002.
- [7] M. Shao and C. L. Nikias, "Signal processing with fractional lower order moments: stable processes and their applications," *Proceedings of the IEEE*, vol. 81, no. 7, pp. 986–1010, 1993.
- [8] G. A. Tsihrintzis and C. L. Nikias, "Performance of optimum and suboptimum receivers in the presence of impulsive noise modeled as an alpha-stable process," *Communications, IEEE Transactions on*, vol. 43, no. 2/3/4, pp. 904–914, 1995.
- [9] J. G. Proakis, "Digital communications (ise)." 2001.
- [10] J. Choi, "Equalization and semi-blind channel estimation for space-time block coded signals over a frequency-selective fading channel," *Signal Processing, IEEE Transactions on*, vol. 52, no. 3, pp. 774–785., 2004.
- [11] V. Zarsoso and P. Comon, "Blind and semi-blind equalization based on the constant power criterion," *Signal Processing, IEEE Transactions on*, vol. 53, no. 11, pp. 4363–4375., 2005.
- [12] J. Treichler and B. Agee, "A new approach to multipath correction of constant modulus signals," *Acoustics, Speech and Signal Processing, IEEE Transactions on*, vol. 31, no. 2, pp. 459–472, 1983.
- [13] S. Chen, S. McLaughlin, P. M. Grant, and B. Mulgrew, "Multi-stage blind clustering equaliser," *Communications, IEEE Transactions on*, vol. 43, no. 234, pp. 701–705., 1995.
- [14] R. Mitra, S. Singh, and A. Mishra, "Improved multi-stage clustering-based blind equalisation," *IET Communications*, vol. 5, no. 9, pp. 1255–1261., 2011.
- [15] S. S. Haykin, *Adaptive filter theory*. Pearson Education India, 2007.
- [16] A. C. Singer, J. K. Nelson, and S. S. Kozat, "Signal processing for underwater acoustic communications," *Communications Magazine, IEEE*, vol. 47, no. 1, pp. 90–96, 2009.
- [17] S. S. Haykin and M. Moher, *Modern wireless communication*. Prentice Hall, 2004.
- [18] S. P. Boyd and L. Vandenberghe, *Convex optimization*. Cambridge university press., 2004.
- [19] T. W. Gamelin and R. E. Greene, *Introduction to topology*. Courier Corporation, 1999.
- [20] V. Bhatia, B. Mulgrew, and A. T. Georgiadis, "Stochastic gradient algorithms for equalisation in  $\alpha$ -stable noise," *Signal processing*, vol. 86, no. 4, pp. 835–845, 2006.

# Wideband CDMA waveforms for large MIMO sonar systems

Yan Pailhas, Yvan Petillot  
Ocean Systems Laboratory  
Heriot Watt University  
Edinburgh, UK, EH14 4AS  
Email: Y.Pailhas@hw.ac.uk

**Abstract**—Multiple Input Multiple Output (MIMO) sonar systems offer new perspectives for target detection and underwater surveillance. The inherent principle of MIMO relies on transmitting several pulses from different transmitters. The MIMO waveform strategy can vary from applications to applications. But among the waveform space, orthogonal waveforms are arguably the most important sub-space. Purely orthogonal waveforms do not exist, and several approximations have been attempted for MIMO radar applications. These approaches include separating the waveforms in the time domain, the frequency domain or using pseudo orthogonal codes. In this paper we discuss the different radar waveform approaches from a sonar point of view and propose a novel CDMA (code division multiple access) waveform design, more suitable for large wideband MIMO systems.

**Keywords**—MIMO sonar systems, MIMO waveform design, CDMA, wideband sonar.

## I. INTRODUCTION

MIMO stands for Multiple Inputs Multiple Outputs. It refers to a structure with spatially distributed transmitters and receivers. MIMO systems have been widely investigated during the last two decades for wireless communications. Such systems have then been developed for radar applications [1], [2]. MIMO have recently gained interest in the underwater acoustic community because of certain benefits over traditional systems such as increase resolution or increase in signal to clutter ratio to name a few.

The MIMO concept relies on multiple transmitters ( $N_t$ ) sending unique and orthogonal waveforms through the environment. Several receivers ( $N_r$ ) then capture the environment, the targets or the clutter response. At each receiver node, the total signal is filtered to separate the different transmitter signal contribution. Accessing the  $N_t \times N_r$  signals then requires the orthogonality of the waveform set. Purely orthogonal waveforms do not exist, and different approaches were developed to minimise the waveform cross-correlation. Such methods include TDMA (time division multiple access) where waveforms share the same frequency band, but at different times, FDMA (frequency division multiple access) where waveforms occupy different frequencies at the same time, or CDMA (code division multiple access) where waveforms share the same frequencies at the same time.

In this paper we review the three main classes of orthogonal waveforms proposed for radar applications. We examine their implications and restrictions for sonar systems. We finally propose a novel CDMA design: the IMCS (interlaced micro-chirp series) which suits large MIMO sonar systems and

transducer constraints. This paper is organised as follows: In section II we present the MIMO sonar formulation. We then demonstrate some of the MIMO sonar capabilities that can achieve using orthogonal waveforms: target recognition and super resolution. In section III we present an overview of the different strategy for radar MIMO waveform design and discuss their practicality for sonar applications. Finally in section IV, we propose the CDMA IMCS waveforms for sonar applications.

## II. MIMO SONAR SYSTEMS

### A. MIMO sonar formulation

We first present the MIMO formulation for the finite scatterer target model. A target is represented here with  $Q$  scattering points spatially distributed. Let  $\{X_q\}_{q \in [1, Q]}$  be their locations. The reflectivity of each scattering point is represented by the complex random variable  $\zeta_q$ . All the  $\zeta_q$  are assumed to be zero-mean, independent and identically distributed with a variance of  $E[|\zeta_q|^2] = 1/Q$ . Let  $\Sigma$  be the reflectivity matrix of the target,  $\Sigma = \text{diag}(\zeta_1, \dots, \zeta_Q)$ . By using this notation the average RCS of the target  $\{X_q\}$ ,  $E[\text{tr}(\Sigma\Sigma^H)]$ , is normalised to 1.

The MIMO system consists of a set of  $K$  transmitters and  $L$  receivers. Each transmitter  $k$  sends a pulse  $\sqrt{E/K}s_k(t)$ . We assume that all the pulses  $s_k(t)$  are normalised.  $E$  represents the total transmit energy of the MIMO system. Receiver  $l$  receives from transmitter  $k$  the signal  $z_{lk}(t)$  which can be written as:

$$z_{lk}(t) = \sqrt{\frac{E}{K}} \sum_{q=1}^Q h_{lk}^{(q)} s_k(t - \tau_{tk}(X_q) - \tau_{rl}(X_q)) \quad (1)$$

with  $h_{lk}^{(q)} = \zeta_q \exp(-j2\pi f_c[\tau_{tk}(X_q) + \tau_{rl}(X_q)])$ .  $f_c$  is carrier frequency,  $\tau_{tk}(X_q)$  represents the propagation time delay between the transmitter  $k$  and the scattering point  $X_q$ ,  $\tau_{rl}(X_q)$  represents the propagation time delay between the scattering point  $X_q$  and the receiver  $l$ . Note that  $h_{lk}^{(q)}$  represents the total phase shift due to the propagation and the reflection on the scattering point  $X_q$ . Assuming the  $Q$  scattering points are close together (*i.e.* within a resolution cell), we write:

$$\begin{aligned} s_k(t - \tau_{tk}(X_q) - \tau_{rl}(X_q)) &\approx s_k(t - \tau_{tk}(X_0) - \tau_{rl}(X_0)) \\ &= s_k^l(t, X_0) \end{aligned} \quad (2)$$

where  $X_0$  is the centre of gravity of the target  $\{X_q\}$ . Eq. (1) can then be rewritten as:

$$\begin{aligned} z_{lk}(t) &= \sqrt{\frac{E}{K}} s_k^l(t, X_0) \times \\ &\quad \left( \sum_{q=1}^Q \zeta_q \exp(-j2\pi f_c[\tau_{tk}(X_q) + \tau_{rl}(X_q)]) \right) \\ &= \sqrt{\frac{E}{K}} \left( \sum_{q=1}^Q h_{lk}^{(q)} \right) s_k^l(t, X_0) \end{aligned} \quad (3)$$

### B. Automatic target recognition capabilities

In this section we are interested in the MIMO intensity response of an object, *i.e.* the coefficient  $\sum_{q=1}^Q h_{lk}^{(q)}$  from Eq. (3). Lets assume that the reflectivity coefficients  $\zeta_q$  can be modelled by the random variable  $\frac{1}{\sqrt{Q}} e^{2i\pi U}$  where  $U \in [0, 1]$  is the uniform distribution. The central limit theorem then gives us the asymptotic behaviour of the target intensity response, and we can write:

$$\lim_{Q \rightarrow +\infty} \sqrt{\left| \sum_{q=1}^Q h_{lk}^{(q)} \right|^2} = \text{Rayleigh}(1/\sqrt{2}) \quad (4)$$

The convergence of Eq. (4) is fast. However for a small number of scatterers (typically  $Q \leq 5$ ), the target reflectivity PDF exhibits noticeable variations from the Rayleigh distribution.

Assuming that man-made targets can be effectively modelled by a small number of scatterers, we can take advantage of the dissimilarities of the reflectivity PDF functions to estimate the number of scattering points. Each observation is a realisation of the random variable  $\gamma_n = \sqrt{\left| \sum_{q=1}^Q h_{lk}^{(q)} \right|^2}$  with  $Q$  the number of scattering points. Each set of observations  $\Gamma = \{\gamma_n\}_{n \in [1, N]}$  where  $N$  is the number of views represents the MIMO output. Given  $\Gamma$ , we can compute the probability that the target has  $Q$  scatterers using Bayes rules:

$$P(T_Q|\Gamma) = \frac{P(\Gamma|T_Q)P(T_Q)}{P(\Gamma)} \quad (5)$$

where  $T_Q$  represents the event that the target has  $Q$  scatterers. Assuming independent observations, 4 target types and no *a priori* information about the target we have:

$$P(T_Q|\Gamma) = \frac{\prod_{n=1}^N P(\gamma_n|T_Q)}{\sum_{Q=2}^{5+} P(\Gamma|T_Q)} \quad (6)$$

The estimated target class corresponds to the class which maximises the conditional probability given by Eq. (6). Figure 1 draws the probability of correct classification for each class depending on the number of views based on  $10^6$  classification experiments. With only 100 views, the overall probability of correct classification is great than 92%.

### C. Super-resolution capabilities

Let  $r_l(t)$  be the total received signal at the receiver  $l$ . We can write  $r_l(t) = \sum_{k=1}^K z_{lk}(t)$ . The target response  $x_{lk}$  from the MIMO system is then the output of the filter bank  $s_k^*(t)$

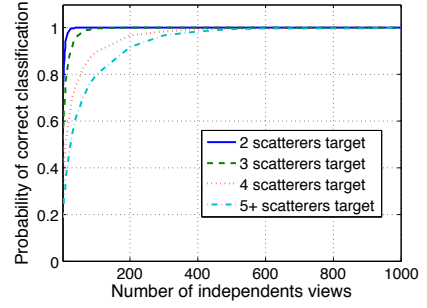


Fig. 1. Correct classification probability against the number of independent views for 4 classes of targets (2, 3, 4 and 5+ scattering points targets).

with  $k \in [1, K]$ . With our notations and assuming orthogonal waveforms, we arrive to:

$$x_{lk} = r_l \star s_k^*(t) = \sum_{q=1}^Q h_{lk}^{(q)} \quad (7)$$

The average target echo intensity from all the bistatic views is given by:

$$\mathcal{F}(\mathbf{r}) = \frac{1}{N} \sum_{l,k} \|x_{lk}\|^2 \quad (8)$$

Using the same target probability distribution stated in the model presented earlier (*cf.* section II-A), we deduce that  $\mathcal{F}(\mathbf{r})$  follows the probability distribution:

$$\mathcal{F}(\mathbf{r}) \sim \frac{1}{N} \sum_{n=1}^N \text{Rayleigh}^2(\sigma) \sim N \cdot \Gamma(N, 2\sigma^2) \quad (9)$$

where  $\Gamma$  is the Gamma distribution. Note that the second equivalence is given using the properties of the Rayleigh distribution. The asymptotic behaviour of  $\mathcal{F}(\mathbf{r})$  can be deduced from the following identity [3]:

$$\lim_{N \rightarrow +\infty} N \cdot \Gamma(Nx, N, 1) = \delta(1-x) \quad (10)$$

Eq. (10) shows that the MIMO mean target intensity  $\mathcal{F}(\mathbf{r})$  converges toward the RCS defined in section II-A. Physically speaking this result demonstrate that the scatterers within one resolution cell decorrelate between each other. MIMO systems then solve the speckle noise in the target response. This demonstrates why super-resolution can be achieved with large MIMO systems.

## III. WAVEFORM DESIGN FOR MIMO RADAR

### A. TDMA: Time Division Multiple Access

TDMA refers to Time Division Multiple Access. It refers to waveform sets sharing the same frequency band but not at the same time. Pulses are transmitted successively at regular interval  $\Delta_\tau$  called the pulse repetition interval (PRI). This strategy is by far the most commonly used for multi-static sonar systems. And as long as  $\Delta_\tau$  is large enough for the echo response to drop below the detection threshold, the TDMA waveforms are quasi-orthogonal. The intrinsic problem with TDMA is related to the dynamic of the scene. In an ASW (anti-submarine warfare) context for example, one may require to survey a large area. If the maximum distance is 40km, taking into account the relatively slow sound speed

in water, the PRI can be as high as 1 minute. A 15 knots target then could potentially move  $\frac{1}{2}$  km between pings. The tracking performance related to such system would then be diminished by the rapidly growing position uncertainty and the data association complexity.

### B. FDMA: Frequency Division Multiple Access

FDMA refers to Frequency Division Multiple Access. In this case, the waveform set occupies different frequency bands at the same time. As long as the frequency bands of each waveform are well separated, the waveforms are almost orthogonal. Different strategies have been explored to implement FDMA depending on the slicing of the available frequency band. Each pulse can occupy for example a different continuous frequency band or having finely interleaved frequency supports. For active sonar however, the bandwidth is a rare resource. Assuming identical transmitters, a FDMA approach results in dividing the full bandwidth by the number of transmitters and then potentially losing all benefit of wideband systems including SNR and resolution gain.

### C. CDMA: Code Division Multiple Access

Due to the restrictions of the two previous approaches, a lot of effort has been put in CDMA (code division multiple access) approaches. CDMA waveforms include polyphase code, pseudorandom phase codes, up and down chirps or codes such as Baker or Gold codes. The main criteria for MIMO waveform optimisation are the sidelobe level and cross correlation. Several optimisation solutions were proposed using SA (Simulated Annealing) algorithms [4], [5], Bee algorithms [6] or maximal length sequences [7]. In [8], Rabideau introduces another metric to measure the fitness of MIMO waveforms by considering the maximum amount of interference that can be cancelled. He then applied his metric for clutter reduction adaptive MIMO system. Another approach to CDMA waveform design is to relax the orthogonality hypothesis and optimising the waveform covariance matrix according to a given criterion. Forsythe in [9] for example computed the covariance matrix which maximises the image intensity. Li then proposed in [10] a cyclic algorithm to compute the covariance matrix under the constant amplitude constraint. In [11], Yang derives optimum waveform design to maximise MI (Mutual Information) and minimise mean-square error (MMSE) for the target response estimation.

## IV. ORTHOGONAL WAVEFORMS FOR MIMO SONAR

Radar designs and electronics impose a certain number of constraints on the waveform design. One of the most restrictive constraint is due to the non-linear amplifiers used for such systems and it imposes to the radar waveform a constant amplitude. Although the constant amplitude requirement maximises the pulse energy, it drastically reduces the degrees of freedom. The radar community then find efficient solutions to manipulate the signal phase including phase shift. Figure 2 provides an example of phased coded radar used in [7]. For active sonar system, pulse emission is the result of piezoelectric material excitation via linear amplifiers. Sonar systems are then not constraint to pulses with constant amplitude. The transducers however cannot handle drastic phase shifts and

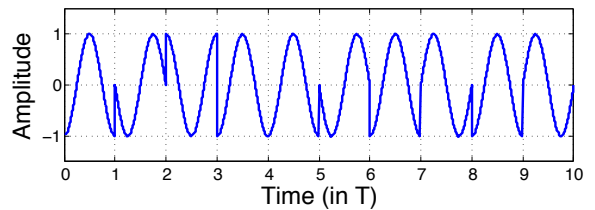


Fig. 2. Example of phased coded radar waveform.

phased coded waveforms may be extremely distorted through piezo ceramic PZT (Lead Zirconate Titanate) transducers.

Section II highlighted the importance of both orthogonality and independence of the MIMO signals for recognition tasks and/or for imagery purposes. Orthogonality is indeed needed in Eq. (5) to derive the target intensity function for each MIMO pair and in Eq. (7) to extract the target signal from a specific Tx/Rx pair. All derived results including MIMO autofocus algorithms [12] then depend on the waveform orthogonality assumption. So far only TDMA or FDMA waveforms have been tested for orthogonal waveform design. The only exception is the CDMA waveforms known as up and down chirps. The up and down chirp strategy however only provides two pseudo-orthogonal pulses and it is then inadequate for large MIMO systems. In this section we propose a CDMA strategy which fits the requirements of wideband large MIMO sonar systems:

- 1) wideband width covered by every pulses
- 2) 'good' auto- and cross-correlation functions
- 3) possibility to generate a large number of orthogonal waveforms
- 4) waveforms with smooth phase transition
- 5) waveforms with relative constant amplitude

Note that if sonar amplifier electronics relax the strict constant amplitude constraint, a relative constant amplitude helps to maintain a high energy pulse and then maximise the signal to noise ratio. To fulfil the requirements previously stated, we propose to build the MIMO sonar waveforms using interlaced micro-chirp series (IMCS) with constant bandwidth. The waveform is the summation of two concatenations of micro-chirps series. Each micro-chirp has the same duration  $\tau$ . The second micro-chirps series is time shifted relative to the first one by a factor of  $\frac{\tau}{2}$ . Figure 3(a) draws the envelopes of interlaced two micro-chirp series.

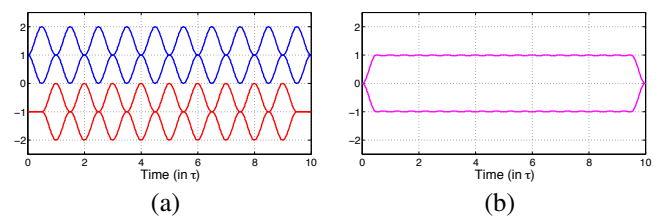


Fig. 3. (a) envelopes of the first and second concatenated micro-chirps series (respectively blue and red curves). (b) full IMCS waveform envelop.

Each micro-chirp has the same duration  $\tau$  and the same windowing. In this paper we chose the Hann tapering window. The windowing function has a threefold purpose:

- it smoothes the phase transition between each consecutive micro-chirp
- it ensures a relatively constant amplitude for the overall waveform (as shown in Fig. 3(b))
- it constrains the micro-chirp to a constant bandwidth

The full available bandwidth  $B$  is divided into  $N_B$  equal sub-bandwidth. The size of the minimal sub-bandwidth is given by the micro-pulse duration  $\tau$  and the windowing function and can be approximated in our case by  $1/\tau$ .  $N_B$  can then be approximated by  $B\tau$ .

The duration of the full waveform is  $\tau N_\tau$  where  $N_\tau$  is the number of micro-chirps of the first  $\mu$ -chirp series. Each  $\mu$ -chirp is chosen randomly between the  $N_B$  sub-bands with a random up or down chirp structure. The randomised up or down structure minimised the cross-correlation as well as the sidelobes in the auto-correlation function. Figure 4 draws an example of IMCS waveform structure in the time-frequency plane. Blue and red segments represent respectively the  $\mu$ -chirp structure of the first and second  $\mu$ -chirp series in the time-frequency plane.

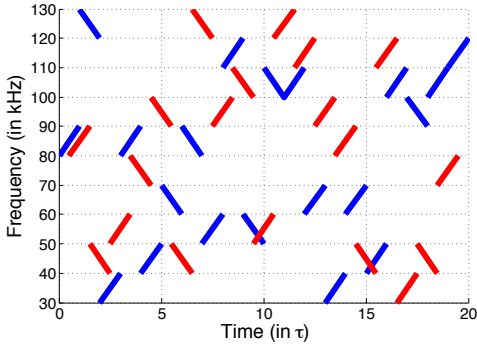


Fig. 4. Example of an IMCS waveform structure in the time-frequency domain. The blue segments represent the micro-chirps of the first series, the red ones represent the second series.

Theoretically there are  $(2N_B)^{2N_\tau-1}$  different waveforms. We computed 100 different waveforms for  $B = [30 \text{ kHz} - 130 \text{ kHz}]$ ,  $\tau = 10^{-4}\text{s}$ ,  $N_B = 10$  and  $N_\tau = 90$ . Figure 5(a) displays the waveform covariance matrix. For perfectly orthogonal waveforms, we expect the covariance matrix being the identity matrix  $I_N$ . Figure 5(b) shows the auto-correlation function and very low cross-correlation function of one particular waveform.

## V. CONCLUSION

In paper we explore the diverse strategies for orthogonal waveforms proposed for MIMO radar applications. Because most of the strategies are based on phase coded signals, they proved to be inadequate for sonar transducers. We proposed a novel CDMA waveform: the IMCS which fits the requirement for large wideband MIMO sonar systems. The IMCS combines the coverage of the full frequency band for each waveform, very low cross-correlation functions and minimal sidelobes for the auto-correlation functions. The signal phase varies slowly and is suitable for piezo-electric transducers. Future work includes the testing of the IMCS waveforms in real environments to assess their robustness against noise, clutter or multi-path.

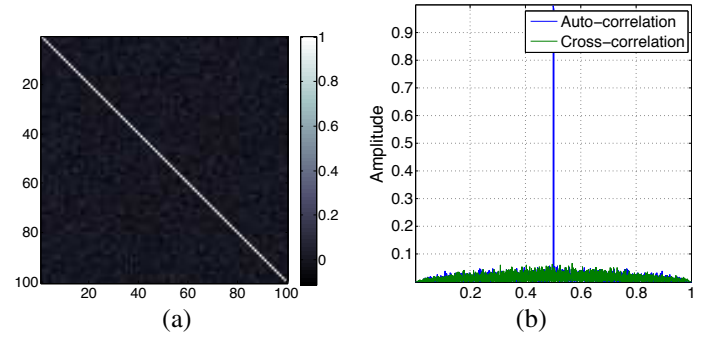


Fig. 5. (a) Waveform covariance matrix. (b) Example of auto-correlation (blue curve) and cross-correlation (green curve) functions of the proposed waveforms.

## ACKNOWLEDGEMENT

This work was supported by the Engineering and Physical Sciences Research Council (EPSRC) Grant number EP/J015180/1 and the MOD University Defence Research Collaboration in Signal Processing.

## REFERENCES

- [1] D. Bliss and K. Forsythe, "Multiple-input multiple-output (mimo) radar and imaging: Degrees of freedom and resolution," in *Proc. 37th Asilomar Conf. Signals, Systems and Computers*, 2003.
- [2] E. Fishler, A. Haimovich, R. S. Blum, D. Chizhik, L. J. Cimini, and R. A. Valenzuela, "Mimo radar: An idea whose time has come," in *Proc. IEEE Int. Conf. Radar*, 2004.
- [3] Y. Pailhas, "Sonar systems for objects recognition," Ph.D. dissertation, Heriot-Watt University, 2012.
- [4] H. Deng, "Polyphase code design for orthogonal netted radar systems," *Signal Processing, IEEE Transactions on*, vol. 52, no. 11, pp. 3126–3135, Nov 2004.
- [5] A. Aubry, M. Lops, A. Tulino, and L. Venturino, "On mimo waveform design for non-gaussian target detection," in *Radar Conference - Surveillance for a Safer World, 2009. RADAR. International*, Oct 2009, pp. 1–6.
- [6] M. Malekzadeh, A. Khosravi, S. Alighale, and H. Azami, "Optimization of orthogonal poly phase coding waveform based on bees algorithm and artificial bee colony for mimo radar," in *Intelligent Computing Technology*, ser. Lecture Notes in Computer Science, D.-S. Huang, C. Jiang, V. Bevilacqua, and J. Figueroa, Eds. Springer Berlin Heidelberg, 2012, vol. 7389, pp. 95–102.
- [7] M. H. Rao, G. V. K. Sharma, and K. R. Rajeswari, "Orthogonal phase coded waveforms for mimo radars," *International Journal of Computer Applications*, vol. 63, no. 6, pp. 31–35, February 2013.
- [8] D. J. Rabideau, "Adaptive mimo radar waveforms," in *Radar Conference, 2008. RADAR '08. IEEE*, May 2008, pp. 1–6.
- [9] K. Forsythe and D. Bliss, "Waveform correlation and optimization issues for mimo radar," in *Signals, Systems and Computers, 2005. Conference Record of the Thirty-Ninth Asilomar Conference on*, October 2005, pp. 1306–1310.
- [10] J. Li, P. Stoica, and X. Zhu, "Mimo radar waveform synthesis," in *Radar Conference, 2008. RADAR '08. IEEE*, May 2008, pp. 1–6.
- [11] Y. Yang and R. Blum, "Mimo radar waveform design based on mutual information and minimum mean-square error estimation," *Aerospace and Electronic Systems, IEEE Transactions on*, vol. 43, no. 1, pp. 330–343, January 2007.
- [12] Y. Pailhas and Y. Petillot, "Synthetic aperture imaging and autofocus with coherent mimo sonar systems," in *Synthetic aperture sonar & synthetic aperture radar conference*, 2014.

# Performance Analysis of Polynomial Matrix SVD-based Broadband MIMO Systems

André Sandmann, Andreas Ahrens and Steffen Lochmann

Hochschule Wismar, University of Applied Sciences: Technology, Business and Design

Philipp-Müller-Straße 14, 23966 Wismar, Germany

Email: andreas.ahrens@hs-wismar.de

**Abstract**—Singular-value decomposition (SVD) is well-established in multiple-input multiple-output (MIMO) signal processing where a broadband MIMO channel is transformed into a number of weighted single-input single-output (SISO) channels. However, applying SVD to frequency-selective MIMO channels results in unequally weighted SISO channels requiring complex resource allocation techniques for optimizing the channel performance. Therefore, a different approach utilizing polynomial matrix singular-value decomposition (PMSVD) for removing the MIMO interference is studied, outperforming conventional SVD-based MIMO systems in the analyzed channel scenarios. As shown by the bit-error rate (BER) simulation results as well as the obtained spectral efficiencies, the proposed PMSVD-based solution seems to be a good alternative to conventional SVD-based MIMO systems.

## I. INTRODUCTION

The strategy of placing multiple antennas at the transmitter and receiver sides, well-known as multiple-input multiple-output (MIMO), improves the performance of wireless systems by the use of the spatial characteristics of the channel. MIMO systems have become the subject of intensive research over the past 20 years as MIMO is able to support higher data rates and shows a higher reliability compared with single-input single-output (SISO) systems [1], [2]. Singular-value decomposition (SVD) is well-established in MIMO signal processing where the whole MIMO channel is transferred into a number of weighted SISO channels. The unequal weighting of the SISO channels has led to intensive research to reduce the complexity of the required bit and power allocation techniques [2]. The polynomial matrix singular-value decomposition (PMSVD) is a signal processing technique which decomposes the MIMO channel into a number of independent frequency-selective SISO channels so called layers [1]. The remaining layer-specific interferences, as a result of the PMSVD-based signal processing, can be easily removed by further signal processing such as zero-forcing equalization as demonstrated in this work.

The novelty of our contribution is that we demonstrate the benefits of amalgamating a suitable choice of MIMO layers activation and number of bits per layer along with the appropriate allocation of the transmit power under the constraint of a given fixed data throughput. Here, bit- and power-loading in both SVD- and PMSVD-based MIMO transmission systems are elaborated. Assuming a fixed data rate, which is required in many applications (e.g., real time video applications), a two stage optimization process is proposed. Firstly, the allocation of bits to the number of SISO channels is optimized and secondly, the allocation of the available total

transmit power is studied when minimizing the overall bit-error rate (BER) at a fixed data rate. Our BER and spectral efficiency results, obtained by computer simulation, show that PMSVD could be an alternative signal processing approach compared to conventional SVD-based MIMO approaches in frequency-selective MIMO channels.

The remaining part of this paper is structured as follows: Section II introduces the state of the art SVD-based MIMO system model. The polynomial matrix singular-value decomposition is analyzed in section III. The quality criteria are briefly reviewed and the proposed power allocation solutions are discussed in section IV, while the associated BER performance results are presented and interpreted in section V. Moreover, in section VI the achievable spectral efficiency for SVD as well as PMSVD systems are discussed. Finally, section VII provides some concluding remarks.

## II. STATE OF THE ART

A frequency selective MIMO link, composed of  $n_T$  transmit and  $n_R$  receive antennas is given by  $\mathbf{u} = \mathbf{H} \cdot \mathbf{c} + \mathbf{n}$ . Here,  $\mathbf{c}$  is the  $(N_T \times 1)$  transmit data signal vector containing the complex input symbols transmitted over  $n_T$  transmit antennas in  $K$  consecutive time slots, i.e.,  $N_T = K n_T$ . The vector  $\mathbf{u}$  describes the  $(N_R \times 1)$  receive signal vector of length  $N_R = (K + L_c) n_R$  [2]. The number of non-zero elements of the resulting symbol rate sampled overall channel impulse response between the  $\mu$ th transmit and  $\nu$ th receive antenna is given by  $(L_c + 1)$ . Finally, the  $(N_R \times 1)$  vector  $\mathbf{n}$  describes the noise term. The  $(N_R \times N_T)$  system matrix  $\mathbf{H}$  of the block-oriented system model results in

$$\mathbf{H} = \begin{bmatrix} \mathbf{H}_{11} & \cdots & \mathbf{H}_{1n_T} \\ \vdots & \ddots & \vdots \\ \mathbf{H}_{n_R 1} & \cdots & \mathbf{H}_{n_R n_T} \end{bmatrix} \quad (1)$$

and consists of  $n_R n_T$  SISO channel matrices  $\mathbf{H}_{\nu\mu}$  (with  $\nu = 1, \dots, n_R$  and  $\mu = 1, \dots, n_T$ ). The system description, called spatio-temporal vector coding, was introduced by Raleigh [3]. Using SVD the system is transformed into

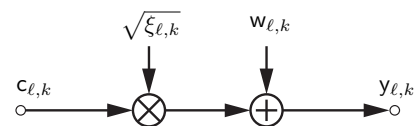


Fig. 1. Resulting layer-specific SVD-based broadband MIMO system model (with  $\ell = 1, 2, \dots, L$  and  $k = 1, 2, \dots, K$ )

independent, non-interfering layers having unequal gains [2]. The SVD-based equalization leads to a different number of MIMO layers  $\ell$  (with  $\ell = 1, 2, \dots, L$ ) at the time  $k$  (with  $k = 1, 2, \dots, K$ ) as shown in Fig. 1. Here it is worth noting that the number of parallel transmission layers  $L$  at the time-slot  $k$  is limited by  $\min(n_T, n_R)$ . The complex-valued data symbol  $c_{\ell,k}$  to be transmitted over the layer  $\ell$  at the time  $k$  is now weighted by the corresponding positive real-valued singular-value  $\sqrt{\xi_{\ell,k}}$  of the matrix  $\mathbf{H}^H \mathbf{H}$  and further disturbed by the additive noise term  $w_{\ell,k}$  after SVD post-processing [2].

### III. POLYNOMIAL MATRIX FACTORIZATION

The polynomial matrix factorization exploits a description of the channel impulse responses in the  $z$ -domain. Thus, each frequency-selective channel impulse response  $h_{\nu\mu}(k)$  of a  $(n_R \times n_T)$  broadband MIMO system is given by

$$\underline{h}_{\nu\mu}(z) = \sum_{k=0}^{L_c} h_{\nu\mu}[k] z^{-k}, \quad (2)$$

where the underscore denotes a polynomial and  $z^{-k}$  is the unit delay operator. Consecutively, the broadband MIMO channel is formed by grouping these impulse responses into the channel matrix as follows

$$\underline{\mathbf{H}}(z) = \begin{bmatrix} \underline{h}_{11}(z) & \cdots & \underline{h}_{1n_T}(z) \\ \vdots & \ddots & \vdots \\ \underline{h}_{n_R1}(z) & \cdots & \underline{h}_{n_Rn_T}(z) \end{bmatrix}, \quad (3)$$

with  $\underline{\mathbf{H}}(z) \in \mathbb{C}^{n_R \times n_T}$  being the MIMO channel matrix in polynomial notation. Using this polynomial description the MIMO system is defined as  $\underline{\mathbf{u}}(z) = \underline{\mathbf{H}}(z) \underline{\mathbf{c}}(z) + \underline{\mathbf{n}}(z)$ , where  $\underline{\mathbf{c}}(z)$  is the  $(n_T \times 1)$  transmit signal vector,  $\underline{\mathbf{u}}(z)$  is the  $(n_R \times 1)$  receive signal vector and  $\underline{\mathbf{n}}(z)$  describes the  $(n_R \times 1)$  additive white Gaussian noise vector in polynomial notation. This system is orthogonalized by using the polynomial matrix singular-value decomposition (PMSVD) applying the second-order sequential best rotation (SBR2) algorithm as presented in [1], [4]. The layer-based discrete-time description of the system orthogonalized by using PMSVD is expressed as

$$y_{\ell}(k) = v_{\ell}(k) * c_{\ell}(k) + w_{\ell}(k), \quad (4)$$

where  $*$  denotes discrete convolution and  $w_{\ell}(k)$  is the noise after PMSVD post-processing. The corresponding layer-specific model is depicted in Fig. 2, where at each layer the input symbols  $c_{\ell}(k)$  are influenced by a finite impulse response filter  $v_{\ell}(k) = (v_{\ell,0}, v_{\ell,1}, \dots, v_{\ell,L_v})$ , and hence intersymbol

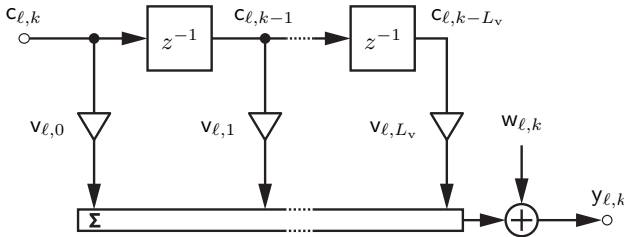


Fig. 2. Layer-specific PMSVD-based broadband MIMO system model assuming  $(L_v + 1)$  non-zero coefficients of the layer-specific impulse response

interference (ISI) occurs on each layer. In order to fully remove the ISI a layer-specific T-spaced Zero Forcing equalizer  $f_{\ell}(k)$  is applied to the received signal  $y_{\ell}(k)$ . Thus the equalized receive signal results in

$$z_{\ell}(k) = y_{\ell}(k) * f_{\ell}(k) = c_{\ell}(k) + w_{\ell}(k) * f_{\ell}(k), \quad (5)$$

where the transmitted symbols  $c_{\ell}(k)$  are received unchanged and the noise  $w_{\ell}(k)$  is weighted by the equalizer coefficients  $f_{\ell}(k)$ . The PMSVD-based broadband MIMO system model with layer-specific T-spaced equalization is henceforth referred to as T-PMSVD system model.

### IV. RESOURCE ALLOCATION

In general, the quality criterion for transmission systems can be expressed by using the signal to noise ratio (SNR) at the detector input as follows

$$\rho = \frac{(\text{half vertical eye opening})^2}{\text{noise power}} = \frac{(U_A)^2}{P_R}, \quad (6)$$

where  $U_A$  and  $P_R$  correspond to one quadrature component. Considering a layer-based MIMO system with a given SNR  $\rho^{(\ell,k)}$  for each layer  $\ell$  and time  $k$  and a  $M$ -ary quadrature amplitude modulation (QAM), the bit-error rate (BER) probability is given in [5] by

$$P_{\text{BER}}^{(\ell,k)} = \frac{2}{\log_2 M_{\ell}} \left( 1 - \frac{1}{\sqrt{M_{\ell}}} \right) \text{erfc} \left( \sqrt{\frac{\rho^{(\ell,k)}}{2}} \right). \quad (7)$$

This BER is averaged over all time slots and activated layers taking different modulation sizes at each layer into account. Finally, the overall BER is obtained by taking the changes in the BER characteristic into consideration. For QAM modulated signals the average transmit power per layer can be expressed as  $P_{s,\ell} = 2/3 U_{s,\ell}^2 (M_{\ell} - 1)$ . Intuitively the total available transmit power  $P_s$  is equally split between the  $L$  activated layers, and hence the layer-specific transmit power is given by  $P_{s,\ell} = P_s/L$ , influencing the half-level transmit amplitude  $U_{s,\ell}$  for each MIMO layer.

#### A. SVD-based Resource Allocation

Considering the SVD layer model, the noise power is unchanged at the receiver. However, the half vertical eye opening  $U_A$  at each time slot  $k$  and layer  $\ell$  is influenced by the singular values so that  $U_A^{(\ell,k)} = \sqrt{\xi_{\ell,k}} U_{s,\ell}$  holds and the corresponding SNR values are given by

$$\rho_{\text{SVD}}^{(\ell,k)} = \frac{\xi_{\ell,k} U_{s,\ell}^2}{P_R} = \frac{3 \xi_{\ell,k}}{L (M_{\ell} - 1)} \frac{E_s}{N_0}, \quad (8)$$

with  $E_s$  being the transmit symbol energy and the parameter  $N_0$  is describing the noise power spectral density. The overall bit-error rate of the uncoded MIMO system is largely determined by the layer with the highest BER. In order to balance the bit-error rates on all layers, the mean of choice is to equalize the SNR values  $\rho^{(\ell,k)}$  over all layers. This is clearly not the optimal solution for minimizing the overall BER but it is easy to implement and not far away from the optimum as shown in [2]. Therefore, the half-level transmit amplitude  $U_{s,\ell}$  is adjusted on each layer by multiplying it with  $\sqrt{p_{\ell,k}}$  in order

to apply the power allocation (PA) scheme. Consequently, the half vertical eye opening of the received symbols becomes

$$U_{A,PA}^{(\ell,k)} = \sqrt{p_{\ell,k}} \sqrt{\xi_{\ell,k}} U_{s,\ell} . \quad (9)$$

With this adjustment the SNR values are resulting in

$$\rho_{PA}^{(\ell,k)} = p_{\ell,k} \rho^{(\ell,k)} . \quad (10)$$

The respective system model for SVD equalization including PA is depicted in Fig. 3. In order to achieve the above mentioned equal SNR PA considering the limited total transmit power, the PA factors  $p_{\ell,k}$  can be calculated as follows [2]

$$p_{\ell,k}^{(SVD)} = \frac{(M_\ell - 1)}{\xi_{\ell,k}} \frac{L}{\sum_{\lambda=1}^L \frac{(M_\lambda - 1)}{\xi_{\lambda,k}}} . \quad (11)$$

Using the equal-SNR criterion nearly the same BER can be obtained on all activated layers.

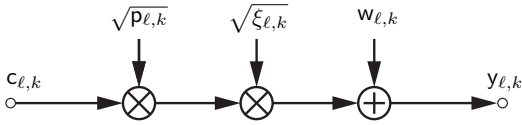


Fig. 3. Resulting layer-specific SVD-based model with PA

### B. T-PMSVD-based Resource Allocation

By applying T-PMSVD the ISI is fully removed by the equalizer and thus for each layer the half vertical eye opening  $U_{A,\ell}$  of the receive signal equals the half-level amplitude of the transmitted symbol  $U_{s,\ell}$ . The drawback of T-PMSVD is that the noise is weighted differently on each layer by the equalizer coefficients expressed by the factor  $\theta_\ell$  and therefore the noise power on each layer results in

$$P_{R,\ell} = \theta_\ell P_R , \quad \text{where} \quad \theta_\ell = \sum_{\forall k} |f_{\ell,k}|^2 . \quad (12)$$

Equalizing the SNRs on all layers is achieved by varying the half-level transmit amplitude with the PA factor in analogy to (10), where the factor is calculated as follows

$$p_\ell^{(T-PMSVD)} = \theta_\ell (M_\ell - 1) \frac{L}{\sum_{\lambda=1}^L \theta_\lambda (M_\lambda - 1)} . \quad (13)$$

The layer-specific T-PMSVD model with power allocation is shown in Fig. 4

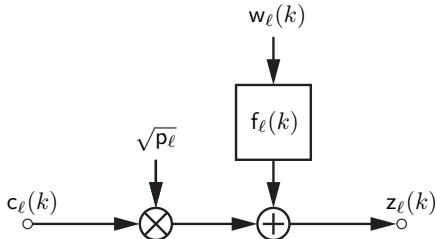


Fig. 4. Resulting layer-specific T-PMSVD-based model with PA

## V. BIT-ERROR RATE PERFORMANCE

In this work, the BER quality is studied by using fixed transmission modes with a spectral efficiency of 8 bit/s/Hz. The analyzed QAM constellations, equivalent to how many bits are allocated to each layer, are shown in Tab. I. It has to be

TABLE I. TRANSMISSION MODES

throughput	layer 1	layer 2	layer 3	layer 4
8 bit/s/Hz	256	0	0	0
8 bit/s/Hz	64	4	0	0
8 bit/s/Hz	16	16	0	0
8 bit/s/Hz	16	4	4	0
8 bit/s/Hz	4	4	4	4

noted that all calculated BER curves for the different PMSVD systems are lower bounds, because the small off-diagonal elements after the diagonalization process of  $\underline{H}(z)$  applying PMSVD, based on the SBR2 algorithm, have been neglected. In order to study the BER performance of PMSVD-based as well as SVD-based MIMO systems, a time-variant wireless channel is analyzed. Here, a two path ( $4 \times 4$ ) MIMO channel without a line-of-sight component is analyzed ( $L_c = 1$ ), with the amplitudes being modeled as Rayleigh distributed. The BER results are shown in Fig. 5 and 6. Here the (16,16,0,0)

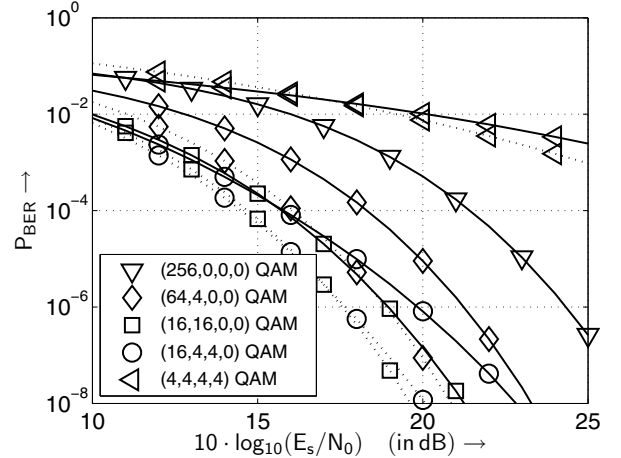


Fig. 5. SVD-based BER with PA (dotted line) and without PA (solid line) when transmitting over a Rayleigh distributed ( $4 \times 4$ ) MIMO two path channel with 8 bit/s/Hz using the transmission modes introduced in Table I

QAM transmission mode performs best for SVD as well as for T-PMSVD equalization. Thus, not all layers have to be activated for achieving the best BER performance results. Applying equal SNR PA results in a significant improvement of the BER. The BER performance comparison depicted in Fig. 7 shows that the T-PMSVD BER quality is superior to the SVD BER quality.

In order to further maximize the BER performance of PMSVD-based MIMO systems a layer-specific maximum likelihood sequence estimation (MLSE) is carried out over applying the T-spaced equalization. The name V-PMSVD is suggested to refer to PMSVD-based MIMO systems with layer-specific Viterbi detection. In order to analyze the BER performance with Viterbi detection on all PMSVD layers, a

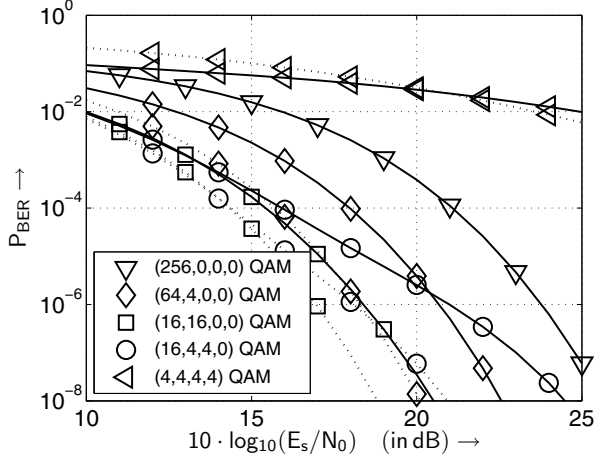


Fig. 6. T-PMSVD-based BER with PA (dotted line) and without PA (solid line) when transmitting over a Rayleigh distributed  $(4 \times 4)$  MIMO two path channel

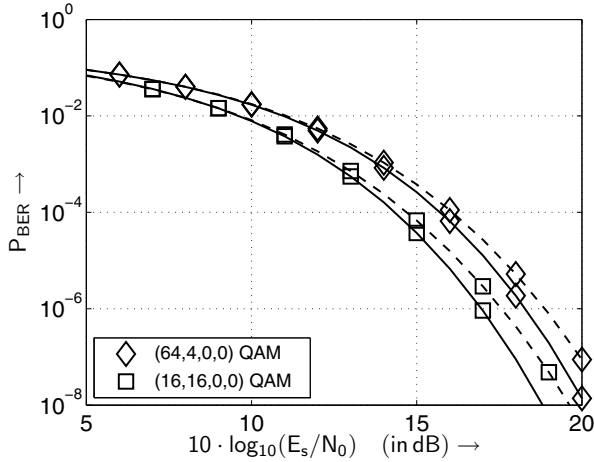


Fig. 7. BER comparison between the SVD-based (dashed line) and T-PMSVD-based equalization results (solid line) when transmitting over a Rayleigh distributed  $(4 \times 4)$  MIMO two path channel with 8 bit/s/Hz applying equal SNR PA

two-path time-invariant  $(4 \times 4)$  MIMO system is investigated. The polynomial channel matrix is chosen as

$$\underline{\mathbf{H}}(z) = \mathbf{H}_0 + \mathbf{H}_1 z^{-1} \quad \text{with} \quad \mathbf{H}_1 = \frac{\mathbf{H}_0}{2} \quad (14)$$

and

$$\mathbf{H}_0 = \sqrt{\frac{8}{15}} \begin{bmatrix} 1 & 0.6 & 0.5 & 0.3 \\ 0.5 & 0.8 & 0.6 & 0.4 \\ 0.4 & 0.5 & 0.7 & 0.5 \\ 0.3 & 0.4 & 0.5 & 0.6 \end{bmatrix}. \quad (15)$$

The calculated BER results are shown in Fig. 8 comparing the best constellations of conventional SVD and PMSVD processing, where PMSVD is combined with a T-spaced equalizer (T-PMSVD) or Viterbi detection (V-PMSVD). Similar to the Rayleigh BER performance, T-PMSVD processing is superior to conventional SVD processing. By replacing the sub-optimum T-spaced equalizer with an optimal Viterbi detector on each PMSVD layer the BER performance is significantly

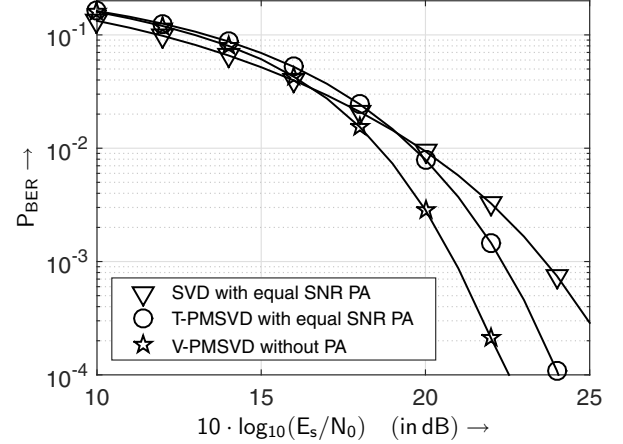


Fig. 8. Comparing the BER performance of different equalization techniques using the winning  $(64,4,0,0)$  QAM constellation when transmitting over the time-invariant  $(4 \times 4)$  MIMO channel

improved despite not using a specific power allocation scheme for V-PMSVD. Thus, it is expected that the performance can be improved further by applying an appropriate power allocation scheme.

## VI. SPECTRAL EFFICIENCY

In this section the achievable spectral efficiency in dependency on the applied processing type is evaluated. By using the spatio-temporal vector coding description and applying SVD processing (see Fig. 1) a frequency selective MIMO channel is transformed into independent frequency non-selective MIMO layers. Accordingly, the achievable spectral efficiency  $\eta$  can be calculated separately at each time slot  $k$  for all MIMO layers  $\ell$  as follows

$$\eta_k = \sum_{\ell=1}^{L_w} \log_2 \left( 1 + \rho^{(\ell,k)} \right) \quad [\text{bit/s/Hz}] , \quad (16)$$

with  $\rho^{(\ell,k)}$  being the corresponding SNR defined as

$$\rho^{(\ell,k)} = \frac{P_{s,\ell}^{(k)}}{P_R} \xi_{\ell,k} . \quad (17)$$

Applying spatio-temporal vector coding,  $\sqrt{\xi_{\ell,k}}$  are the non-zero singular values of  $\mathbf{H}$  easily extractable by using SVD. Since PMSVD-based systems have frequency selective layers, spatio-temporal vector coding with SVD, including the appropriate pre- and post-processing, is used on each single PMSVD layer to obtain frequency non-selective conditions. In this way, the PMSVD-based singular values are determined. The average achievable spectral efficiency is obtained by applying the expectation functional  $E\{\cdot\}$  to all time slots  $k$  resulting in

$$\eta = E\{\eta_k\} \quad \forall k \quad [\text{bit/s/Hz}] . \quad (18)$$

In order to find the optimal power distribution for each MIMO layer, water-filling is used. By applying water-filling, the transmit power is assigned according to

$$P_{s,\ell}^{(k)} = \max \left\{ 0, P_w - \frac{P_R}{\xi_{\ell,k}} \right\} , \quad (19)$$

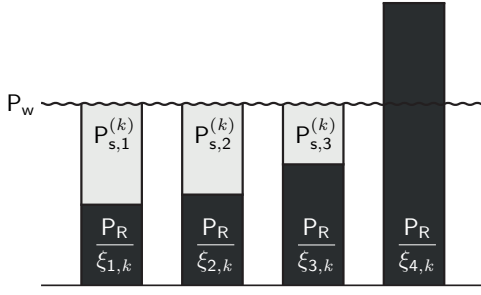


Fig. 9. Water filling principle: Visualizing the amount of transmit power  $P_{s,\ell}^{(k)}$  allocated to the corresponding layers  $\ell$  depending on the noise power to eigenvalue level  $P_R/\xi_{\ell,k}$  at the  $k$ th time slot

with  $P_w$  being the water-filling threshold ensuring

$$\sum_{\ell=1}^{L_w} P_{s,\ell}^{(k)} = P_s \quad \forall k. \quad (20)$$

That implies, if  $P_w - P_R/\xi_{\ell,k}$  is negative, no power will be allocated to this specific layer. The threshold  $P_w$  depends on the used number of MIMO layers  $L_w$  at the corresponding time slot  $k$  and results in

$$P_w = \frac{P_s}{L_w} + \frac{P_R}{L_w} \sum_{\ell=1}^{L_w} \frac{1}{\xi_{\ell,k}}. \quad (21)$$

The water filling technique is illustrated in Fig. 9. The achievable spectral efficiencies calculated for the time-invariant  $(4 \times 4)$  MIMO channel given by (14) are depicted in Fig. 10. The graph shows the benefit when applying water-filling-based power allocation over equally splitting the total available transmit power across all layers. Our results show that the efficiencies achievable with PMSVD are nearly identical to the ones achievable with conventional SVD processing. This signifies that there is no drawback applying PMSVD over SVD processing in terms of spectral efficiency. The same

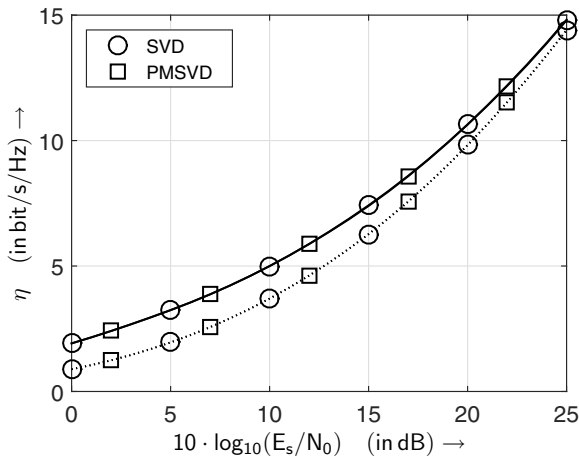


Fig. 10. Achievable spectral efficiencies with water-filling (solid line) and with equal distributed power allocation (dotted line) of the time-invariant  $(4 \times 4)$  MIMO two path channel

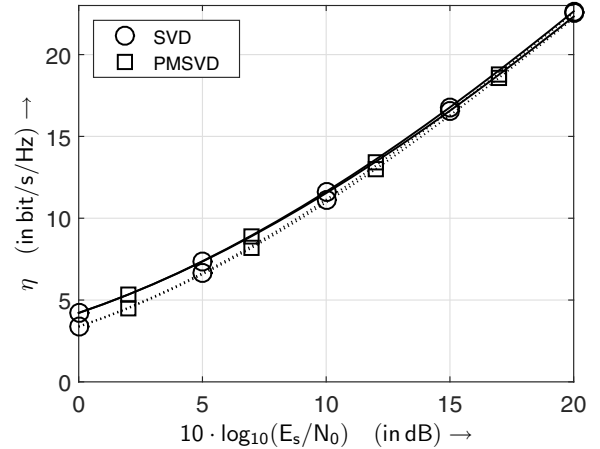


Fig. 11. Achievable spectral efficiencies with water-filling (solid line) and with equal distributed power allocation (dotted line) of the  $(4 \times 4)$  MIMO two path Rayleigh channel

conclusions can be made considering the achievable spectral efficiencies obtained for the  $(4 \times 4)$  Rayleigh channel shown in Fig. 11.

## VII. CONCLUSION

In this contribution broadband MIMO systems have been analyzed using polynomial matrix factorization. In order to remove the MIMO channel interference a particular singular-value decomposition algorithm for polynomial matrices (PMSVD) including layer-specific T-spaced equalization for eliminating the remaining intersymbol interference has been studied. This T-PMSVD technique has been compared in terms of the bit-error rate performance with the well-known spatio-temporal vector coding description applying SVD equalization. Using T-PMSVD equalization the BER performance is superior compared with conventional SVD. For both equalization types bit loading schemes have been combined with equal SNR power allocation so as to optimize the BER performance. Furthermore, it has been shown that there is some room for improving the PMSVD BER performance by utilizing Viterbi detection. The results for the achievable spectral efficiencies emphasize that there is no loss applying PMSVD over conventional SVD processing in the analyzed channel scenarios.

## REFERENCES

- [1] J. McWhirter, P. Baxter, T. Cooper, S. Redif, and J. Foster, "An EVD Algorithm for Para-Hermitian Polynomial Matrices," *IEEE Transactions on Signal Processing*, vol. 55, no. 5, pp. 2158–2169, May 2007.
- [2] A. Ahrens and C. Benavente-Peces, "Modulation-Mode and Power Assignment in Broadband MIMO Systems," *Facta Universitatis (Series Electronics and Energetics)*, vol. 22, no. 3, pp. 313–327, December 2009.
- [3] G. G. Raleigh and J. M. Cioffi, "Spatio-Temporal Coding for Wireless Communication," *IEEE Transactions on Communications*, vol. 46, no. 3, pp. 357–366, March 1998.
- [4] A. Sandmann, A. Ahrens, and S. Lochmann, "Modulation-Mode and Power Assignment in SVD-Assisted Broadband MIMO Systems using Polynomial Matrix Factorization," *Przegląd Elektrotechniczny*, no. 04, pp. 10–13, April 2015.
- [5] J. G. Proakis, *Digital Communications*. Boston: McGraw-Hill, 2000.

# LOW-COMPLEXITY ROBUST ADAPTIVE BEAMFORMING ALGORITHMS EXPLOITING SHRINKAGE FOR MISMATCH ESTIMATION

*Hang Ruan \* and Rodrigo C. de Lamare\*#*

\*Department of Electronics, The University of York, England, YO10 5BB

#CETUC, Pontifical Catholic University of Rio de Janeiro, Brazil

Emails: hr648@york.ac.uk, delamare@cetuc.puc-rio.br \*

## ABSTRACT

This paper proposes low-complexity robust adaptive beamforming (RAB) techniques based on shrinkage methods. We firstly briefly review a Low-Complexity Shrinkage-Based Mismatch Estimation (LOCSME) batch algorithm to estimate the desired signal steering vector mismatch, in which the interference-plus-noise covariance (INC) matrix is also estimated with a recursive matrix shrinkage method. Then we develop low complexity adaptive robust version of the conjugate gradient (CG) algorithm to both estimate the steering vector mismatch and update the beamforming weights. A computational complexity study of the proposed and existing algorithms is carried out. Simulations are conducted in local scattering scenarios and comparisons to existing RAB techniques are provided.

*Index Terms*— robust adaptive beamforming, shrinkage methods, low complexity methods.

## 1. INTRODUCTION

Sensor array signal processing techniques and their applications to wireless communications, sensor networks and radar have been widely investigated in recent years. Adaptive beamforming is one of the most important topics in sensor array signal processing which has applications in many fields. However, adaptive beamformers may suffer performance degradation due to small sample data size or the presence of the desired signal in the training data. In practical environments, desired signal steering vector mismatch problems like signal pointing errors [13], imprecise knowledge of the antenna array, look-direction mismatch or local scattering may even lead to more significant performance loss [2].

### 1.1. Prior and Related Work

In order to address these problems, robust adaptive beamforming (RAB) techniques have been developed in recent years. Popular approaches include worst-case optimization [2], diagonal loading [3, 4], and eigen-decomposition

[12, 13]. However, general RAB designs have some limitations such as their ad hoc nature, high probability of subspace swap at low SNR and high computational cost [5].

Further recent works have looked at approaches based on combined estimation procedures for both the steering vector mismatch and interference-plus-noise covariance (INC) matrix to improve RAB performance. The worst-case optimization methods in [2] solve an online semi-definite programming (SDP) while using a matrix inversion to estimate the INC matrix. The method in [8] estimates the steering vector mismatch by solving an online Sequential Quadratic Program (SQP) [6], while estimating the INC matrix using a shrinkage method [8]. Another similar method which jointly estimates the steering vector using SQP and the INC matrix using a covariance reconstruction method [9] has outstanding performance compared to other RAB techniques. However, their main disadvantages include the high computational cost associated with online optimization programming, the matrix inversion or reconstruction process, and slow convergence. In [11] and [15] we have introduced a Low-Complexity Shrinkage-Based Mismatch Estimation (LOCSME) method and a reduced-cost adaptive version [15] for robust beamforming, which estimate the steering vector mismatch by exploiting the cross-correlation vector between the sensor array data and the beamformer output.

### 1.2. Contributions

In this work, we develop an adaptive version of the LOCSME technique in [11] based on conjugate gradient (CG) adaptive algorithm, resulting in the proposed LOCSME-CG algorithm. Different from the approach of LOCSME-SG, the LOCSME-CG algorithm not only updates the beamforming weights, but can also estimate the mismatched steering vector, which sequentially performs the estimation of the mismatched vector by LOCSME in every snapshot. An analysis shows that LOCSME-CG requires lower complexity than the original LOCSME and has comparable complexity to LOCSME-SG. Simulations also show an excellent performance which benefits from the precise estimation of the steering vector.

The paper is organized as follows. The system model and problem statement are described in Section II. A review of the

---

\*This work was supported in part by The University of York

LOCSME method is provided in Section III whereas Section IV presents the proposed LOCSME-CG algorithm. Section V presents the simulation results. Section VI gives the conclusion.

## 2. SYSTEM MODEL AND PROBLEM STATEMENT

Consider a linear antenna array of  $M$  sensors and  $K$  narrow-band signals which impinge on the array. The data received at the  $i$ th snapshot can be modeled as

$$\mathbf{x}(i) = \mathbf{A}(\boldsymbol{\theta})\mathbf{s}(i) + \mathbf{n}(i), \quad (1)$$

where  $\mathbf{s}(i) \in \mathbb{C}^{K \times 1}$  are uncorrelated source signals,  $\boldsymbol{\theta} = [\theta_1, \dots, \theta_K]^T \in \mathbb{R}^K$  is a vector containing the directions of arrival (DoAs),  $\mathbf{A}(\boldsymbol{\theta}) = [\mathbf{a}(\theta_1) + \mathbf{e}, \dots, \mathbf{a}(\theta_K)] \in \mathbb{C}^{M \times K}$  is the matrix which contains the steering vector for each DoA and  $\mathbf{e}$  is the steering vector mismatch of the desired signal,  $\mathbf{n}(i) \in \mathbb{C}^{M \times 1}$  is assumed to be complex Gaussian noise with zero mean and variance  $\sigma_n^2$ . The beamformer output is

$$y(i) = \mathbf{w}^H \mathbf{x}(i), \quad (2)$$

where  $\mathbf{w} = [w_1, \dots, w_M]^T \in \mathbb{C}^{M \times 1}$  is the beamformer weight vector, where  $(\cdot)^H$  denotes the Hermitian transpose. The optimum beamformer is computed by maximizing the SINR given by

$$SINR = \frac{\sigma_1^2 |\mathbf{w}^H \mathbf{a}|^2}{\mathbf{w}^H \mathbf{R}_{i+n} \mathbf{w}}. \quad (3)$$

where  $\sigma_1^2$  is the desired signal power,  $\mathbf{R}_{i+n}$  is the INC matrix. Assuming that the steering vector  $\mathbf{a}$  is known precisely ( $\mathbf{a} = \mathbf{a}(\theta_1)$ ), then problem (3) can be cast as an optimization problem

$$\begin{aligned} & \underset{\mathbf{w}}{\text{minimize}} && \mathbf{w}^H \mathbf{R}_{i+n} \mathbf{w} \\ & \text{subject to} && \mathbf{w}^H \mathbf{a} = 1, \end{aligned} \quad (4)$$

which is known as the MVDR beamformer or Capon beamformer [1]. The optimum weight vector is given by  $\mathbf{w}_{opt} = \frac{\mathbf{R}_{i+n}^{-1} \mathbf{a}}{\mathbf{a}^H \mathbf{R}_{i+n}^{-1} \mathbf{a}}$ . Since  $\mathbf{R}_{i+n}$  is usually unknown in practice, it can be estimated by the sample covariance matrix (SCM) of the received data as

$$\hat{\mathbf{R}}(i) = \frac{1}{i} \sum_{k=1}^i \mathbf{x}(k) \mathbf{x}^H(k), \quad (5)$$

which results in the Sample Matrix Inversion (SMI) beamformer  $\mathbf{w}_{SMI} = \frac{\hat{\mathbf{R}}^{-1} \mathbf{a}}{\mathbf{a}^H \hat{\mathbf{R}}^{-1} \mathbf{a}}$ . However, the SMI beamformer requires a large number of snapshots to converge and is sensitive to steering vector mismatches [8, 9]. The problem we are interested in solving is how to design low-complexity robust adaptive beamforming algorithms that can preserve the SINR performance in the presence of uncertainties in the steering vector of a desired signal.

## 3. LOCSME ROBUST BEAMFORMING ALGORITHM

The basic idea of LOCSME [11] is to obtain a precise estimate of the desired signal steering vector by exploiting cross-correlation vector between the beamformer output and the array observation data and then computing the beamforming weights.

### 3.1. Steering Vector Estimation

The cross-correlation between the array observation data and the beamformer output can be expressed as  $\mathbf{d} = E\{\mathbf{x}y^*\}$ . With assumptions that  $|\mathbf{a}_m \mathbf{w}| \ll |\mathbf{a}_1 \mathbf{w}|$  for  $m = 2, \dots, K$  and that the signal sources and that the system noise have zero mean while the desired signal is independent from the interferers and the noise,  $\mathbf{d}$  can be rewritten as  $\mathbf{d} = E\{\sigma_1^2 \mathbf{a}_1^H \mathbf{w} \mathbf{a}_1 + \mathbf{n} \mathbf{n}^H \mathbf{w}\}$ . By projecting  $\mathbf{d}$  onto a predefined subspace [7], which collects all possible information from the desired signal, the unwanted part of  $\mathbf{d}$  can be eliminated. LOCSME also exploits prior knowledge which amounts to choosing an angular sector in which the desired signal is located, say  $[\theta_1 - \theta_e, \theta_1 + \theta_e]$ . The subspace projection matrix  $\mathbf{P}$  is given by

$$\mathbf{P} = [\mathbf{c}_1, \mathbf{c}_2, \dots, \mathbf{c}_p][\mathbf{c}_1, \mathbf{c}_2, \dots, \mathbf{c}_p]^H, \quad (6)$$

where  $\mathbf{c}_1, \dots, \mathbf{c}_p$  are the  $p$  principal eigenvectors of the matrix  $\mathbf{C}$ , which is defined by [6]

$$\mathbf{C} = \int_{\theta_1 - \theta_e}^{\theta_1 + \theta_e} \mathbf{a}(\theta) \mathbf{a}^H(\theta) d\theta. \quad (7)$$

In order to achieve a better estimation of the steering vector, an extension of the oracle approximating shrinkage (OAS) ([10]) technique is employed to obtain a more accurate estimate of the vector  $\mathbf{d}$ . Let us define the sample correlation vector (SCV) in snapshot  $i$  as

$$\hat{\mathbf{1}}(i) = \frac{1}{i} \sum_{k=1}^i \mathbf{x}(k) y^*(k), \quad (8)$$

and its mean value as

$$\hat{\nu}(i) = \sum \hat{\mathbf{1}}(i) / M. \quad (9)$$

Then we aim to shrink the SCV towards its mean value  $\hat{\nu}(i)$ , which yields

$$\hat{\mathbf{d}}(i) = \hat{\rho}(i) \hat{\nu}(i) + (1 - \hat{\rho}(i)) \hat{\mathbf{1}}(i), \quad (10)$$

where  $\hat{\rho}(i)$  represents the shrinkage coefficient ( $\hat{\rho}(i) \in (0, 1)$ ). To find out the optimum  $\hat{\rho}(i)$ , we minimize the mean square

error (MSE) of  $E[\|\hat{\mathbf{d}}(i) - \hat{\mathbf{d}}(i-1)\|^2]$ , which leads to

$$\hat{\rho}(i) = \frac{(1 - \frac{2}{M})\hat{\mathbf{d}}^H(i-1)\hat{\mathbf{l}}(i-1) + \sum \hat{\mathbf{d}}(i-1) \sum^* \hat{\mathbf{d}}(i-1)}{(i - \frac{2}{M})\hat{\mathbf{d}}^H(i-1)\hat{\mathbf{l}}(i-1) + (1 - \frac{i}{M}) \sum \hat{\mathbf{d}}(i-1) \sum^* \hat{\mathbf{d}}(i-1)}.$$

Once the correlation vector  $\hat{\mathbf{d}}$  is obtained, the steering vector is estimated by

$$\hat{\mathbf{a}}_1(i) = \frac{\mathbf{P}\hat{\mathbf{d}}(i)}{\|\mathbf{P}\hat{\mathbf{d}}(i)\|_2}. \quad (12)$$

### 3.2. Signal Power Estimation and Beamforming Weights

Following the description in [11], the desired signal power  $\sigma_1^2$  is estimated by

$$\hat{\sigma}_1^2(i) = \frac{|\hat{\mathbf{a}}_1^H(i)\mathbf{x}(i)|^2 - |\hat{\mathbf{a}}_1^H(i)\hat{\mathbf{a}}_1(i)|\sigma_n^2}{|\hat{\mathbf{a}}_1^H(i)\hat{\mathbf{a}}_1(i)|^2}, \quad (13)$$

which has a linear complexity  $\mathcal{O}(M)$ .

Once the steering vector and power of the desired signal are obtained, the INC matrix is also estimated by a matrix shrinkage method [11] and the weight vector is computed by

$$\hat{\mathbf{w}}(i) = \frac{\hat{\mathbf{R}}_{i+n}^{-1}(i)\hat{\mathbf{a}}_1(i)}{\hat{\mathbf{a}}_1^H(i)\hat{\mathbf{R}}_{i+n}^{-1}(i)\hat{\mathbf{a}}_1(i)}, \quad (14)$$

which has a computationally costly matrix inversion  $\hat{\mathbf{R}}_{i+n}^{-1}(i)$ .

## 4. PROPOSED LOCSME-CG ALGORITHM

In this section, we develop a CG adaptive strategy based on LOCSME. We employ the same recursions as in LOCSME to estimate the steering vector and the desired signal power, whereas the estimation procedure of the beamforming weights is different. In order to avoid costly inner recursions, we let only one iteration be performed per snapshot[14]. Here we denote the CG-based weights and steering vector updated by snapshots as

$$\hat{\mathbf{a}}_1(i) = \hat{\mathbf{a}}_1(i-1) + \alpha_{\hat{\mathbf{a}}_1}(i)\mathbf{p}_{\hat{\mathbf{a}}_1}(i), \quad (15)$$

$$\mathbf{v}(i) = \mathbf{v}(i-1) + \alpha_{\mathbf{v}}(i)\mathbf{p}_{\mathbf{v}}(i). \quad (16)$$

As can be seen, the subscripts of all the quantities for inner iterations are eliminated. Then, we employ the degenerated scheme to ensure  $\alpha_{\hat{\mathbf{a}}_1}(i)$  and  $\alpha_{\mathbf{v}}(i)$  satisfy the convergence bound [14] given by

$$0 \leq \mathbf{p}_{\hat{\mathbf{a}}_1}^H(i)\mathbf{g}_{\hat{\mathbf{a}}_1}(i) \leq 0.5\mathbf{p}_{\hat{\mathbf{a}}_1}^H(i)\mathbf{g}_{\hat{\mathbf{a}}_1}(i-1), \quad (17)$$

$$0 \leq \mathbf{p}_{\mathbf{v}}^H(i)\mathbf{g}_{\mathbf{v}}(i) \leq 0.5\mathbf{p}_{\mathbf{v}}^H(i)\mathbf{g}_{\mathbf{v}}(i-1). \quad (18)$$

Instead of updating the negative gradient vectors  $\mathbf{g}_{\hat{\mathbf{a}}_1}(i)$  and  $\mathbf{g}_{\mathbf{v}}(i)$  in iterations, now we utilize the forgetting factor to re-express them in one snapshot as

$$\mathbf{g}_{\hat{\mathbf{a}}_1}(i) = (1 - \lambda)\mathbf{v}(i) + \lambda\mathbf{g}_{\hat{\mathbf{a}}_1}(i-1) + \hat{\sigma}_1^2(i)\alpha_{\hat{\mathbf{a}}_1}(i)\mathbf{v}(i)\mathbf{v}^H(i)\mathbf{p}_{\hat{\mathbf{a}}_1}(i) - \mathbf{x}(i)\mathbf{x}^H(i)\hat{\mathbf{a}}_1(i), \quad (19)$$

$$\mathbf{g}_{\mathbf{v}}(i) = (1 - \lambda)\hat{\mathbf{a}}_1(i) + \lambda\mathbf{g}_{\mathbf{v}}(i-1) - \alpha_{\mathbf{v}}(i)(\hat{\mathbf{R}}(i) - \hat{\sigma}_1^2(i)\hat{\mathbf{a}}_1(i)\hat{\mathbf{a}}_1^H(i))\mathbf{p}_{\mathbf{v}}(i) - \mathbf{x}(i)\mathbf{x}^H(i)\mathbf{v}(i-1). \quad (20)$$

Pre-multiplying (19) and (20) by  $\mathbf{p}_{\hat{\mathbf{a}}_1}^H(i)$  and  $\mathbf{p}_{\mathbf{v}}^H(i)$ , respectively, and taking expectations we obtain

$$E[\mathbf{p}_{\hat{\mathbf{a}}_1}^H(i)\mathbf{g}_{\hat{\mathbf{a}}_1}(i)] = E[\mathbf{p}_{\hat{\mathbf{a}}_1}^H(i)(\mathbf{v}(i) - \mathbf{x}(i)\mathbf{x}^H(i)\hat{\mathbf{a}}_1(i))] + \lambda E[\mathbf{p}_{\hat{\mathbf{a}}_1}^H(i)\mathbf{g}_{\hat{\mathbf{a}}_1}(i-1)] - \lambda E[\mathbf{p}_{\hat{\mathbf{a}}_1}^H(i)\mathbf{v}(i)] + E[\alpha_{\hat{\mathbf{a}}_1}(i)\mathbf{p}_{\hat{\mathbf{a}}_1}^H(i)\hat{\sigma}_1^2(i)\mathbf{v}(i)\mathbf{v}^H(i)\mathbf{p}_{\hat{\mathbf{a}}_1}(i)], \quad (21)$$

$$E[\mathbf{p}_{\mathbf{v}}^H(i)\mathbf{g}_{\mathbf{v}}(i)] = \lambda E[\mathbf{p}_{\mathbf{v}}^H(i)\mathbf{g}_{\mathbf{v}}(i-1)] - \lambda E[\mathbf{p}_{\mathbf{v}}^H(i)\hat{\mathbf{a}}_1(i)] - E[\alpha_{\mathbf{v}}(i)\mathbf{p}_{\mathbf{v}}^H(i)(\hat{\mathbf{R}}(i) - \hat{\sigma}_1^2(i)\hat{\mathbf{a}}_1(i)\hat{\mathbf{a}}_1^H(i))\mathbf{p}_{\mathbf{v}}(i)], \quad (22)$$

where in (22) we have  $E[\hat{\mathbf{R}}(i)\mathbf{v}(i-1)] = E[\hat{\mathbf{a}}_1(i)]$ . After substituting (22) back into (18) we obtain the bounds for  $\alpha_{\mathbf{v}}(i)$  as follows

$$\frac{(\lambda - 0.5)E[\mathbf{p}_{\mathbf{v}}^H(i)\mathbf{g}_{\mathbf{v}}(i-1)] - \lambda E[\mathbf{p}_{\mathbf{v}}^H(i)\hat{\mathbf{a}}_1(i)]}{E[\mathbf{p}_{\mathbf{v}}^H(i)(\hat{\mathbf{R}}(i) - \hat{\sigma}_1^2(i)\hat{\mathbf{a}}_1(i)\hat{\mathbf{a}}_1^H(i))\mathbf{p}_{\mathbf{v}}(i)]} \leq E[\alpha_{\mathbf{v}}(i)] \leq \frac{\lambda E[\mathbf{p}_{\mathbf{v}}^H(i)\mathbf{g}_{\mathbf{v}}(i-1)] - \lambda E[\mathbf{p}_{\mathbf{v}}^H(i)\hat{\mathbf{a}}_1(i)]}{E[\mathbf{p}_{\mathbf{v}}^H(i)(\hat{\mathbf{R}}(i) - \hat{\sigma}_1^2(i)\hat{\mathbf{a}}_1(i)\hat{\mathbf{a}}_1^H(i))\mathbf{p}_{\mathbf{v}}(i)]}. \quad (23)$$

Then we can introduce a constant parameter  $\eta_{\mathbf{v}} \in [0, 0.5]$  to restrict  $\alpha_{\mathbf{v}}(i)$  within the bounds in (23) as

$$\alpha_{\mathbf{v}}(i) = \frac{\lambda(\mathbf{p}_{\mathbf{v}}^H(i)\mathbf{g}_{\mathbf{v}}(i-1) - \mathbf{p}_{\mathbf{v}}^H(i)\hat{\mathbf{a}}_1(i)) - \eta_{\mathbf{v}}\mathbf{p}_{\mathbf{v}}^H(i)\mathbf{g}_{\mathbf{v}}(i-1)}{\mathbf{p}_{\mathbf{v}}^H(i)(\hat{\mathbf{R}}(i) - \hat{\sigma}_1^2(i)\hat{\mathbf{a}}_1(i)\hat{\mathbf{a}}_1^H(i))\mathbf{p}_{\mathbf{v}}(i)}. \quad (24)$$

Similarly, we can also obtain the bounds for  $\alpha_{\hat{\mathbf{a}}_1}(i)$ . For simplicity let us define  $E[\mathbf{p}_{\hat{\mathbf{a}}_1}^H(i)\mathbf{g}_{\hat{\mathbf{a}}_1}(i-1)] = A$ ,  $E[\mathbf{p}_{\hat{\mathbf{a}}_1}^H(i)\mathbf{v}(i)] = B$ ,  $E[\mathbf{p}_{\hat{\mathbf{a}}_1}^H(i)\mathbf{x}(i)\mathbf{x}^H(i)\hat{\mathbf{a}}_1(i)] = C$  and  $E[\mathbf{p}_{\hat{\mathbf{a}}_1}^H(i)\hat{\sigma}_1^2(i)\mathbf{v}(i)\mathbf{v}^H(i)\mathbf{p}_{\hat{\mathbf{a}}_1}(i)] = D$ . Substituting equation (21) into (17) gives

$$\frac{\lambda(B - A) - B + C}{D} \leq E[\alpha_{\hat{\mathbf{a}}_1}(i)] \leq \frac{\lambda(B - A) - B + C + 0.5A}{D}, \quad (25)$$

in which we can introduce another constant parameter  $\eta_{\hat{\mathbf{a}}_1} \in [0, 0.5]$  to restrict  $\alpha_{\hat{\mathbf{a}}_1}(i)$  within the bounds in (25) as

$$E[\alpha_{\hat{\mathbf{a}}_1}(i)] = \frac{\lambda(B - A) - B + C + \eta_{\hat{\mathbf{a}}_1}A}{D}, \quad (26)$$

**Table 1.** Complexity Comparison

RAB Algorithms	Flops
LOCSME [11]	$4M^3 + 3M^2 + 20M$
LOCSME-SG	$15M^2 + 30M$
Algorithm of [8]	$M^{3.5} + 7M^3 + 5M^2 + 3M$
LOCME [7]	$2M^3 + 4M^2 + 5M$
LCWC [12]	$100M^2 + 350M$
LOCSME-CG	$13M^2 + 77M$

or

$$\begin{aligned} \alpha_{\hat{\mathbf{a}}_1}(i) = & [\lambda(\mathbf{p}_{\hat{\mathbf{a}}_1}^H(i)\mathbf{v}(i) - \mathbf{p}_{\hat{\mathbf{a}}_1}^H(i)\mathbf{g}_{\hat{\mathbf{a}}_1}(i-1)) - \mathbf{p}_{\hat{\mathbf{a}}_1}^H(i)\mathbf{v}(i) \\ & + \mathbf{p}_{\hat{\mathbf{a}}_1}^H(i)\mathbf{x}(i)\mathbf{x}^H(i)\hat{\mathbf{a}}_1(i) + \eta_{\hat{\mathbf{a}}_1}\mathbf{p}_{\hat{\mathbf{a}}_1}^H(i)\mathbf{g}_{\hat{\mathbf{a}}_1}(i-1)] \\ & / [\hat{\sigma}_1^2(i)\mathbf{p}_{\hat{\mathbf{a}}_1}^H(i)\mathbf{v}(i)\mathbf{v}^H(i)\mathbf{p}_{\hat{\mathbf{a}}_1}(i)]. \quad (27) \end{aligned}$$

Then we can update the direction vectors  $\mathbf{p}_{\hat{\mathbf{a}}_1}(i)$  and  $\mathbf{p}_{\mathbf{v}}(i)$  by

$$\mathbf{p}_{\hat{\mathbf{a}}_1}(i+1) = \mathbf{g}_{\hat{\mathbf{a}}_1}(i) + \beta_{\hat{\mathbf{a}}_1}(i)\mathbf{p}_{\hat{\mathbf{a}}_1}(i), \quad (28)$$

$$\mathbf{p}_{\mathbf{v}}(i+1) = \mathbf{g}_{\mathbf{v}}(i) + \beta_{\mathbf{v}}(i)\mathbf{p}_{\mathbf{v}}(i), \quad (29)$$

where  $\beta_{\hat{\mathbf{a}}_1}(i)$  and  $\beta_{\mathbf{v}}(i)$  are updated by

$$\beta_{\hat{\mathbf{a}}_1}(i) = \frac{[\mathbf{g}_{\hat{\mathbf{a}}_1}(i) - \mathbf{g}_{\hat{\mathbf{a}}_1}(i-1)]^H \mathbf{g}_{\hat{\mathbf{a}}_1}(i)}{\mathbf{g}_{\hat{\mathbf{a}}_1}^H(i-1)\mathbf{g}_{\hat{\mathbf{a}}_1}(i-1)}, \quad (30)$$

$$\beta_{\mathbf{v}}(i) = \frac{[\mathbf{g}_{\mathbf{v}}(i) - \mathbf{g}_{\mathbf{v}}(i-1)]^H \mathbf{g}_{\mathbf{v}}(i)}{\mathbf{g}_{\mathbf{v}}^H(i-1)\mathbf{g}_{\mathbf{v}}(i-1)}. \quad (31)$$

Finally we can update the beamforming weights by

$$\mathbf{w}(i) = \frac{\mathbf{v}(i)}{\hat{\mathbf{a}}_1^H(i)\mathbf{v}(i)}, \quad (32)$$

To reproduce the proposed LOCSME-CG algorithm, equations (9)-(12),(13),(15),(16),(19),(20),(24),(27)-(32) are required. The forgetting factor  $\lambda$  and constant  $\eta$  for estimating  $\alpha(i)$  need to be adjusted to give its best performance.

A complexity analysis in terms of flops (total number of additions and multiplications) required by the proposed LOCSME-CG algorithm and the existing ones is compared in Table 1. The proposed LOCSME-CG algorithm avoids costly matrix inversion and multiplication procedures, which are unavoidable in the existing RAB algorithms. The LCWC algorithm of [12] requires  $N$  inner iterations per snapshot, which significantly varies in different snapshots (here we take  $N = 50$  as an averagely evaluated value). It is clear that LOCSME-CG has lower complexity in terms of the number of sensors  $M$ , dominated by  $\mathcal{O}(M^2)$ , resulting in great advantages when  $M$  is large.

## 5. SIMULATION RESULTS

The simulations are carried out under both coherent and incoherent local scattering mismatch [4] scenarios. A uniform

linear array (ULA) of  $M = 12$  omnidirectional sensors with half wavelength spacing is considered. 100 repetitions are executed to obtain each point of the curves and a maximum of  $i = 300$  snapshots are observed. The desired signal is assumed to arrive at  $\theta_1 = 10^\circ$  while there are other two interferers impinging on the antenna array from directions  $\theta_2 = 30^\circ$  and  $\theta_3 = 50^\circ$ . The signal-to-interference ratio (SIR) is fixed at 0dB. For our proposed algorithm, the angular sector in which the desired signal is assumed to be located is chosen as  $[\theta_1 - 5^\circ, \theta_1 + 5^\circ]$  and the number of eigenvectors of the subspace projection matrix  $p$  is selected manually with the help of simulations. The results focus on the beamformer output SINR performance versus the number of snapshots, or a variation of input SNR (-10dB to 30dB).

### 5.1. Mismatch due to Coherent Local Scattering

The steering vector of the desired signal affected by a time-invariant coherent local scattering effect is modeled as

$$\mathbf{a}_1 = \mathbf{p} + \sum_{k=1}^4 e^{j\varphi_k} \mathbf{b}(\theta_k), \quad (33)$$

where  $\mathbf{p}$  corresponds to the direct path while  $\mathbf{b}(\theta_k)$  ( $k = 1, 2, 3, 4$ ) corresponds to the scattered paths. The angles  $\theta_k$  ( $k = 1, 2, 3, 4$ ) are randomly and independently drawn in each simulation run from a uniform generator with mean  $10^\circ$  and standard deviation  $2^\circ$ . The angles  $\varphi_k$  ( $k = 1, 2, 3, 4$ ) are independently and uniformly taken from the interval  $[0, 2\pi]$  in each simulation run. Notice that  $\theta_k$  and  $\varphi_k$  change from trials while remaining constant over snapshots.

Fig. 1 illustrate the performance comparisons of SINR versus snapshots and SINR versus SNR regarding the mentioned RAB algorithms in the last section under coherent scattering case. Specifically to obtain the SINR versus snapshots results, we select  $\lambda = 0.95$ ,  $\eta = 0.2$  for LOCSME-CG. However, selection of these parameters may vary according to different input SNR as in the SINR versus SNR results. LOCSME-CG outperforms the other algorithms and is very close to the standard LOCSME.

### 5.2. Mismatch due to Incoherent Local Scattering

In the incoherent local scattering case, the desired signal has a time-varying signature and the steering vector is modeled by

$$\mathbf{a}_1(i) = s_0(i)\mathbf{p} + \sum_{k=1}^4 s_k(i)\mathbf{b}(\theta_k), \quad (34)$$

where  $s_k(i)$  ( $k = 0, 1, 2, 3, 4$ ) are i.i.d zero mean complex Gaussian random variables independently drawn from a random generator. The angles  $\theta_k$  ( $k = 0, 1, 2, 3, 4$ ) are drawn independently in each simulation run from a uniform generator with mean  $10^\circ$  and standard deviation  $2^\circ$ . This time,  $s_k(i)$  changes both from run to run and from snapshot to snapshot.

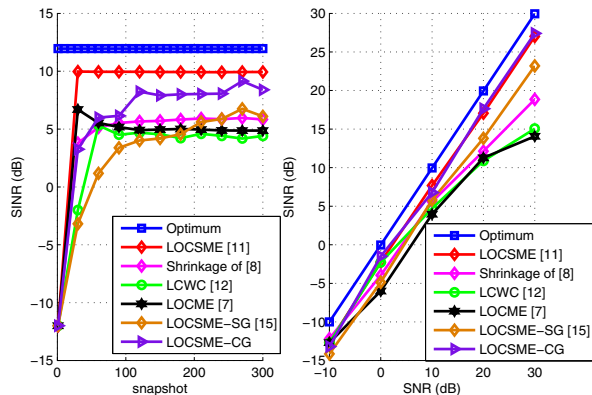


Fig. 1. coherent local scattering

Fig. 2 illustrate the performance comparisons of SINR versus snapshots and SINR versus SNR regarding the mentioned RAB algorithms in the last section under incoherent scattering case. To obtain the SINR versus snapshots results, we select  $\lambda = 0.95$ ,  $\eta = 0.3$  for LOCSME-CG. However, we have optimized the parameters to give the best possible performance at different input SNRs.

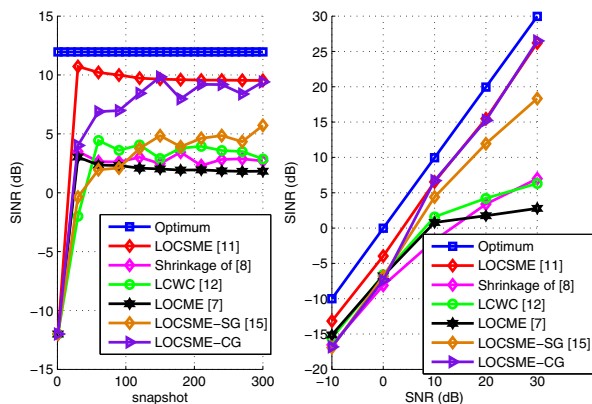


Fig. 2. incoherent local scattering

Different from the coherent scattering results, all the algorithms have a certain level of performance degradation due to the effect of incoherent local scattering model, in which case we have the extra system dynamics with the time variation, contributing to more environmental uncertainties in the system. However, over a wide range of input SNR values, LOCSME-CG still outperforms the other RAB algorithms. One point that needs to be emphasized is, most of the existing RAB algorithms experience significant performance degradation when the input SNR is high (i.e. around or more than 20dB), which is explained in [9] that the desired signal always

presents in any kind of diagonal loading technique. However, LOCSME-CG improves the estimation accuracy, so that the high SNR degradation is successfully avoided as can be seen in Fig. 1 and Fig. 2.

## 6. CONCLUSION

This work proposed a low-complexity adaptive RAB algorithm, LOCSME-CG, developed from the LOCSME RAB method. We have derived recursions for the weight vector update with low complexity. We also have enabled the estimation for the mismatch steering vector inside the CG recursions to enhance the robustness. Simulation results have shown that LOCSME-CG achieves excellent output SINR performance and is suitable for operation in high input SNR.

## 7. REFERENCES

- [1] H. L. Van Trees, *Optimum Array Processing*, New York: Wiley, 2002.
- [2] S. A. Vorobyov, A. B. Gershman and Z. Luo, "Robust Adaptive Beamforming using Worst-Case Performance Optimization: A Solution to Signal Mismatch Problem," *IEEE Trans. Sig. Proc.*, Vol. 51, No. 4, pp 313-324, Feb 2003.
- [3] J. Li, P. Stoica and Z. Wang, "On Robust Capon Beamforming and Diagonal Loading," *IEEE Trans. Sig. Proc.*, Vol. 57, No. 7, pp 1702-1715, July 2003.
- [4] D. Astely and B. Ottersten, "The effects of Local Scattering on Direction of Arrival Estimation with Music," *IEEE Trans. Sig. Proc.*, Vol. 47, No. 12, pp 3220-3234, Dec 1999.
- [5] A. Khabbazi-basmenj, S. A. Vorobyov and A. Hassanien, "Robust Adaptive Beamforming Based on Steering Vector Estimation with as Little as Possible Prior Information," *IEEE Trans. Sig. Proc.*, Vol. 60, No. 6, pp 2974-2987, June 2012.
- [6] A. Hassanien, S. A. Vorobyov and K. M. Wong, "Robust Adaptive Beamforming Using Sequential Quadratic Programming: An Iterative Solution to the Mismatch Problem," *IEEE Sig. Proc. Letters.*, Vol. 15, pp 733-736, 2008.
- [7] L. Landau, R. de Lamare, M. Haardt, "Robust Adaptive Beamforming Algorithms Using Low-Complexity Mismatch Estimation," *Proc. IEEE Statistical Signal Processing Workshop*, 2011.
- [8] Y. Gu and A. Leshem, "Robust Adaptive Beamforming Based on Jointly Estimating Covariance Matrix and Steering Vector," *Proc. IEEE International Conference on Acoustics Speech and Signal Processing*, pp 2640-2643, 2011.
- [9] Y. Gu and A. Leshem, "Robust Adaptive Beamforming Based on Interference Covariance Matrix Reconstruction and Steering Vector Estimation," *IEEE Trans. Sig. Proc.*, Vol. 60, No. 7, July 2012.
- [10] Y. Chen, A. Wiesel and A. O. Hero III, "Shrinkage Estimation of High Dimensional Covariance Matrices," *Proc. IEEE International Conference on Acoustics Speech and Signal Processing*, pp 2937-2940, 2009.
- [11] H. Ruan and R. C. de Lamare, "Robust Adaptive Beamforming Using a Low-Complexity Shrinkage-Based Mismatch Estimation Algorithm," *IEEE Sig. Proc. Letters.*, Vol. 21, No. 1, pp 60-64, 2013.
- [12] A. Elnashar, "Efficient implementation of robust adaptive beamforming based on worst-case performance optimization," *IET Signal Process.*, Vol. 2, No. 4, pp. 381-393, Dec 2008.
- [13] J. Zhuang and A. Manikas, "Interference cancellation beamforming robust to pointing errors," *IET Signal Process.*, Vol. 7, No. 2, pp. 120-127, April 2013.
- [14] L. Wang and R. C. de Lamare, "Constrained adaptive filtering algorithms based on conjugate gradient techniques for beamforming," *IET Signal Process.*, Vol. 4, No. 6, pp. 686697, Feb 2010.
- [15] H. Ruan and R. C. de Lamare, "Low-Complexity Robust Adaptive Beamforming Based on Shrinkage and Cross-Correlation," *19th International ITG Workshop on Smart Antennas*, pp 1-5, March 2015.

# Sparsity based Ground Moving Target Imaging via Multi-Channel SAR

Di Wu, Mehrdad Yaghoobi and Mike Davies

School of Engineering  
University of Edinburgh  
UK, EH9 3JL

Email: {D.Wu, m.yaghoobi-vaighan, mike.davies}@ed.ac.uk

**Abstract**—State-of-the-art Ground Moving Target Indicator (GMTI) schemes include the Displaced Phase Center Antenna (DPCA) and Along Track Interferometry (ATI) which are commonly used image-based dual-channel techniques for moving target detection. In the present paper, we provide a different perspective for solving GMTI tasks by generalising the ground moving targets imaging as a parameter estimation and an optimisation problem. A sparsity based ground target imaging approach is described to improve the image quality for moving targets and estimate their states. By exploiting the fact that moving targets are highly sparse in the observed scene and feasible velocity space, the proposed method constructs a velocity map for the illuminated region, and combines this map with a sparsity based optimisation algorithm to realise the image formation. The performance of the presented method is demonstrated through GOTCHA airborne SAR data set.

**Index Terms**—SAR, GMTI, sparsity, compressed sensing, velocity map

## I. INTRODUCTION

One of the basic principles of SAR is to assume a stationary scene. Therefore moving targets will induce displacement and blurring in the image. Ground Moving Target Indicator (GMTI) aims to detect the moving targets in the SAR image and estimate their velocities which are of great value for the battlefield awareness and information gathering. The entire SAR/GMTI systems often consist of several signal processing steps such as pre-processing, range compression, clutter cancellation, target detection, geo-location, motion parameters estimation and SAR image formation [1][2][3].

Displaced Phase Center Antenna (DPCA), Along Track Interferometry (ATI) and Space-time Adaptive Processing (STAP) are the multi-channel methods which have been widely used in the SAR community. DPCA and ATI [4][5] attempt to expose the moving targets from the SAR images of different channels with magnitudes and interference phases respectively. However the target radial velocities can be derived from the ATI results directly and DPCA is not capable of doing that. STAP [6] is well known to be computationally expensive, and it is hampered by the false alarm rates especially in non-homogeneous urban environments. Also in 2012, Prunte proposed to indicate moving targets based on multi-channel SAR using compressed sensing [7]. The proposed method is utilising the sparsities pixel-wise in the image domain.

In this paper, we present a model to link up certain parts of the processing chain in multi-channel SAR/GMTI and

represent them as a generalised optimisation problem. By introducing the sparsities in the proposed model, i.e. the number of moving targets is reasonably small compared to the size of the observed scene, ground moving targets can be mapped and their motion parameters can be estimated. We hope this novel model can provide an alternative perspective for viewing SAR/GMTI problems.

The remainder of this paper is organized as follows. Section two describes the signal model in a typical dual-channel SAR system. In section three, the sparsity based moving target imaging model is presented. We first discuss the channel balancing techniques to co-register different channels. Then, we present the mechanism of traditional SAR imaging and clutter cancellation algorithms, and finally introduce the sparse regularized optimisation model to realise simultaneous SAR/GMTI. In section four, the real airborne SAR data is utilised to demonstrate the performances of the proposed model. Conclusions and future work are presented in section five.

## II. SIGNAL MODELING

The proposed framework is presently demonstrated through a typical dual-channel SAR system in this paper, but it can be generalised to the scenarios with more than two channels. The geometry with a moving target in the observed scene is shown in Fig. 1. The phase centres of the fore-antenna and aft-antenna are spatially separated by a distance  $d$  on the flight path of the platform. The Cartesian velocity components of the moving target are denoted as  $(v^{(x)}, v^{(y)}, v^{(z)})$  which can be converted to  $(v^{(az)}, v^{(r)})$  in the azimuth and radial directions. Here positive  $v^{(r)}$  represents its speed away from the platform in the 3-D physical space and  $v^{(az)}$  denotes its velocity component in the  $x - y$  space which is orthogonal to  $v^{(r)}$ . Let the azimuth time of the transmitted pulses be  $\tau_n$  where  $n = \{1, 2, \dots, N\}$  is the pulse number. Then  $\mathbf{r}(\tau_n)$  is the position of the target at  $\tau_n$ ,  $r_i^{(t)}(\tau_n)$  and  $r_i^{(o)}(\tau_n)$  represent the distance from the moving target to the  $i$ -th antenna and the distance from the scene origin to the corresponding antenna position. Also the platform velocity within a short sub-aperture is approximated by a constant  $v_p$ , and  $f_{PRF}$  is the pulse repetition frequency (PRF).

In the remainder of the paper, we apply the stop-and-hop approximation which assumes that the targets and platform

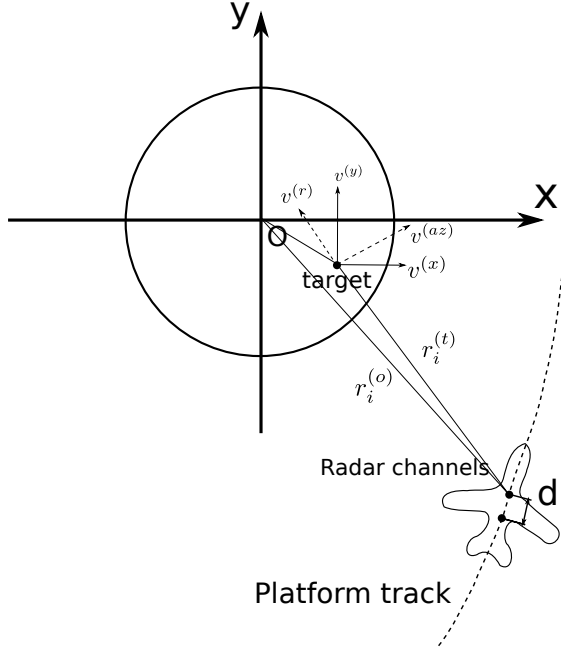


Fig. 1. The geometry of a dual-channel SAR system with a moving target in the observed scene.

have constant positions during the RF propagation of one pulse unless otherwise stated. After the de-chirping process, in which the platform motion has been compensated with reference to the scene origin, the channel 1 (fore-antenna) and 2 (aft-antenna) discrete received signals of a single moving target located at  $\mathbf{r}(\tau_n)$  are:

$$Y_i(f_k, \tau_n) = A_i \sigma(\mathbf{r}(\tau_n)) \exp\left(-\frac{j4\pi f_k u_i(\tau_n)}{c}\right) \quad (1)$$

where  $\{f_k | k = 1, 2, \dots, K\}$  denotes the range frequencies;  $A_i$  is the nominal factor of the received signal for the  $i$ -th channel which accounts for the beam pattern and energy loss;  $\sigma(\mathbf{r}(\tau_n))$  is the complex reflectivity of this moving target;  $c$  represents the speed of light and  $u_i(\tau_n)$  denotes the differential range  $r_i^{(t)}(\tau_n) - r_i^{(o)}(\tau_n)$ .

We assume that the moving target has constant velocity during the sub-aperture time, then the instantaneous spatial location of the target  $\mathbf{r}(\tau_n)$  can be expressed as  $(x_0 + \tau_n v^{(x)}, y_0 + \tau_n v^{(y)}, z_0 + \tau_n v^{(z)})$  where  $(x_0, y_0, z_0)$  stands for the initial position of the target. The goal of SAR/GMTI is to estimate the target states including the geolocation  $\mathbf{r}(\tau_n)$  and velocities  $(v^{(x)}, v^{(y)}, v^{(z)})$  given the received signals  $Y_1(f_k, \tau_n)$  and  $Y_2(f_k, \tau_n)$ .

### III. SPARSITY BASED MOVING TARGET IMAGING

Based on the dual-channel SAR system we describe the proposed sparsity based moving target imaging approach and its relationship with commonly used SAR/GMTI techniques.

#### A. Pre-processing and Channel Balancing

For subtractive GMTI methods such as ATI and DPCA, the differences between channels are exploited to detect targets

and suppress the clutter. Thus, it is crucial to equalise the channel transfer functions in the pre-processing step. With channel balancing techniques, we attempt to retrieve the same responses for stationary targets between different channels.

Since the baseline  $d$  in the SAR system is along the platform track, the received echo of the aft-antenna can be viewed as the delayed received signal of the fore-antenna, if the observed region does not change over time. We can illustratively assume that  $\mathbf{r}_1^{(c)}(\tau_n) = \mathbf{r}_2^{(c)}(\tau_n + \Delta)$  where  $\mathbf{r}_i^{(c)}(\tau_n)$  denotes the location of the  $i$ -th antenna at  $\tau_n$  and  $\Delta = d/v_p$  represents the delay between two channels. Here  $\tau_n + \Delta$  may not correspond to an exact pulse time. Then the differential range  $u_2(\tau_n + \Delta)$  can be rewritten as

$$\begin{aligned} u_2(\tau_n + \Delta) &= r_2^{(t)}(\tau_n + \Delta) - r_2^{(o)}(\tau_n + \Delta) \\ &= \|\mathbf{r}_2^{(c)}(\tau_n + \Delta) - \mathbf{r}(\tau_n + \Delta)\| - \|\mathbf{r}_2^{(c)}(\tau_n + \Delta)\| \\ &= \|\mathbf{r}_1^{(c)}(\tau_n) - \mathbf{r}(\tau_n + \Delta)\| - \|\mathbf{r}_1^{(c)}(\tau_n)\| \end{aligned} \quad (2)$$

If the targets are isotropic and their reflectivities keep the same over time then we can derive from (1) that

$$\begin{aligned} Y_1(f_k, \tau_n) &= A_1 \sigma(\mathbf{r}(\tau_n)) \times \\ &\exp\left(-\frac{j4\pi f_k (\|\mathbf{r}_1^{(c)}(\tau_n) - \mathbf{r}(\tau_n)\| - \|\mathbf{r}_1^{(c)}(\tau_n)\|)}{c}\right) \end{aligned} \quad (3)$$

$$\begin{aligned} Y_2(f_k, \tau_n + \Delta) &= A_2 \sigma(\mathbf{r}(\tau_n)) \times \\ &\exp\left(-\frac{j4\pi f_k (\|\mathbf{r}_1^{(c)}(\tau_n) - \mathbf{r}(\tau_n + \Delta)\| - \|\mathbf{r}_1^{(c)}(\tau_n)\|)}{c}\right) \end{aligned} \quad (4)$$

where  $Y_2(f_k, \tau_n + \Delta)$  is the time-shifted version of  $Y_2(f_k, \tau_n)$  which can be estimated by the multiplication in the frequency domain with a  $\Delta$ -induced phase shift term. We denote this as  $\tilde{Y}_2(f_k, \tau_n) = Y_2(f_k, \tau_n + \Delta)$ .

It can be seen that the velocity and position information of the moving targets are fully described by the last exponential terms in (3) and (4). We also need to balance the channels to equalise  $A_1$  and  $A_2$  as done for example in [8]. In this way,  $Y_1(f_k, \tau_n)$  and  $\tilde{Y}_2(f_k, \tau_n)$  are supposed to be the same for stationary targets. We will employ this channel balancing technique to pre-process the SAR data in the remainder of the paper.

#### B. SAR Imaging and Clutter Cancellation

Numerous algorithms have been proposed for SAR image formation by investigating the trade-off between complexity and image quality. For simplicity we will focus on matched filter based techniques.

Let the discrete grid on which the image is formed be  $\mathbb{G}_{ml} = (x_m, y_l, 0)$  and  $d_{mln} = \|\mathbf{r}_1^{(c)}(\tau_n) - \mathbb{G}_{ml}\| - \|\mathbf{r}_1^{(c)}(\tau_n)\|$ , where  $m = \{1, 2, \dots, M\}$  and  $l = \{1, 2, \dots, L\}$ . Then the observed scene can be viewed as the collection of the targets in this grid. Here the elevation is assumed to be

zero for the convenience of subsequent analysis. The formed SAR images with the matched filter method are

$$X_1(m, l) = \sum_{k=1}^K \sum_{n=1}^N Y_1(f_k, \tau_n) \exp\left(\frac{j4\pi f_k d_{mln}}{c}\right) \quad (5)$$

$$X_2(m, l) = \sum_{k=1}^K \sum_{n=1}^N \tilde{Y}_2(f_k, \tau_n) \exp\left(\frac{j4\pi f_k d_{mln}}{c}\right) \quad (6)$$

Typical clutter suppression methods such as DPCA and ATI exploit the differences between (5) and (6) to reveal the moving targets. Specifically, DPCA is achieved by subtracting (6) from (5), and ATI is realised by multiplying (5) with the conjugate of (6). For DPCA, we have that

$$\begin{aligned} & X_1(m, l) - X_2(m, l) \\ &= \sum_{k=1}^K \sum_{n=1}^N Y_1(f_k, \tau_n) \exp\left(\frac{j4\pi f_k d_{mln}}{c}\right) \left(1 - \exp\left(-\frac{j4\pi f_k (w_{mln})}{c}\right)\right) \end{aligned} \quad (7)$$

where  $w_{mln} = \|\mathbf{r}_1^{(c)}(\tau_n) - \mathbf{r}_{ml}(\tau_n + \Delta)\| - \|\mathbf{r}_1^{(c)}(\tau_n) - \mathbf{r}_{ml}(\tau_n)\|$ . At azimuth time  $\tau_n$ , the position of the target, which was initially located at  $(x_m, y_l, 0)$ , is denoted as  $\mathbf{r}_{ml}(\tau_n)$ .  $w_{mln}$  can then be approximated by  $v_{ml}^{(r)}\Delta$  where  $v_{ml}^{(r)}$  is the radial velocity of this target. Also  $\exp(-j4\pi f_k w_{mln}/c)$  can be approximated with a constant if the target remains in the same range resolution cell during the time interval  $\Delta$  [9]. Then equation (7) can be rewritten as:

$$X_1(m, l) - X_2(m, l) \approx X_1(m, l) \left(1 - \exp\left(-\frac{j4\pi f_0 (v_{ml}^{(r)}\Delta)}{c}\right)\right) \quad (8)$$

where  $f_0$  is denoted as the centre frequency of the transmitted signal chirps. Similarly for ATI we have that

$$X_1(m, l) \times X_2^*(m, l) \approx |X_1(m, l)|^2 \exp\left(\frac{j4\pi f_0 (v_{ml}^{(r)}\Delta)}{c}\right) \quad (9)$$

It can be seen that (8) and the phase of (9) are zero for stationary targets ( $v_{ml}^{(r)} = 0$ ). Particularly the DPCA results are approximately the velocity-scaled reflectivities of the moving targets. Hence, clutter suppression techniques such as DPCA and ATI enable us to project out stationary targets. Also the radial velocities  $\{v_{ml}^{(r)} | m = 1, 2, \dots, M; l = 1, 2, \dots, L\}$  can be estimated directly based on the phase of (9).

### C. Sparse Regularized SAR/GMTI

There has been a number of SAR imaging algorithms with super-resolution effects by utilising the image sparsity [10][11]. The proposed approaches can mitigate the sidelobes in SAR images and reconstruct the bright image elements. In GMTI applications the whole observed scene is not sparse but the moving targets are often sparse. In this way, if we can build up the linear projection from the raw data to the moving targets and its inverse projection, the techniques which are commonly

used in compressed sensing [12] can then be leveraged to form the image of these sparse targets.

Let  $\mathbf{X}_i = \{X_i(m, l)\} \in \mathbb{C}^{M \times L}$  be the SAR image of the  $i$ -th channel;  $\mathbf{Y}_1 = \{Y_1(f_k, \tau_n)\} \in \mathbb{C}^{K \times N}$  and  $\tilde{\mathbf{Y}}_2 = \{\tilde{Y}_2(f_k, \tau_n)\} \in \mathbb{C}^{K \times N}$  be the received phase history of the 1st channel and the balanced phase history of the 2nd channel respectively. Based on (1) we can write the signal model in matrix-vector form as  $\mathbf{Y}_1 = \Phi_F(\mathbf{X}_1)$  where  $\Phi_F$  is the forward projection operator.

Note that DPCA is essentially the linear projection from  $\mathbf{Y}_1 - \tilde{\mathbf{Y}}_2$  to  $\mathbf{X}_1 - \mathbf{X}_2$ , thereby all stationary scatterers are removed. Therefore a simple sparsity based GMTI could exploit the following optimisation problem:

$$\begin{aligned} & \min_{\mathbf{X}} \|\mathbf{Y}_1 - \tilde{\mathbf{Y}}_2 - \Phi_F(\mathbf{X})\|_F^2 + \lambda \|\mathbf{X}\|_1 \\ & \text{s.t. } \mathbf{X} \in \mathbb{C}^{M \times L} \end{aligned} \quad (10)$$

where  $\|\cdot\|_F$  represents the Frobenius norm,  $\lambda$  is a positive tuning parameter, and  $\mathbf{X}$  is the sparsified image of moving targets and sparsity in  $\mathbf{X}$  is encouraged through the inclusion of the  $L_1$  norm penalty function. Note that this formulation still takes no account of the velocity effect at this stage, and the moving targets will be displaced and blurred in the resulting  $\mathbf{X}$ .

A more advanced sparsity based SAR/GMTI formulation can also be derived that simultaneously takes into account the sparsity of the moving targets and estimates their velocities. Let  $\mathbf{V} = (\mathbf{V}^{(x)}, \mathbf{V}^{(y)}, 0)$  denote the velocity maps for a specific observed scene  $\mathbf{X}$  (here  $\mathbf{X}$  includes stationary and moving targets) where  $\mathbf{V}^{(x)} = \{v_{ml}^{(x)}\} \in \mathbb{R}^{M \times L}$  and  $\mathbf{V}^{(y)} = \{v_{ml}^{(y)}\} \in \mathbb{R}^{M \times L}$  are the velocity components of  $\mathbb{G}_{ml}$  in  $x$  and  $y$  directions. The velocity map  $\mathbf{V}$  can be interpreted as granting each image element with specific velocity components. With reference to the geometry Fig. 1, the velocity map can be directly converted to the corresponding azimuth velocity  $\mathbf{V}^{(az)} = \{v_{ml}^{(az)}\} \in \mathbb{R}^{M \times L}$  and radial velocity  $\mathbf{V}^{(r)} = \{v_{ml}^{(r)}\} \in \mathbb{R}^{M \times L}$ .

In this model, we make the reasonable assumption that there is only one dominant velocity for each image element. This assumption makes the reconstructions for a specific physical position  $(m, l)$  to be 1-sparse along the  $\mathbf{V}$  axis. Incorporating the velocities into the signal model it can be shown that:

$$Y_1(f_k, \tau_n) = \sum_{m=1}^M \sum_{l=1}^L X(m, l) \exp\left(-\frac{j4\pi f_k d'_{1mln}}{c}\right) \quad (11)$$

$$\begin{aligned} & \tilde{Y}_2(f_k, \tau_n) \\ &= \sum_{m=1}^M \sum_{l=1}^L X(m, l) \exp\left(-\frac{j4\pi f_k d'_{1mln}}{c}\right) \exp\left(-\frac{j4\pi f_k v_{ml}^{(r)}\Delta}{c}\right) \end{aligned} \quad (12)$$

where  $d'_{1mln} = \|\mathbf{r}_1^{(c)}(\tau_n) - \mathbb{G}_{ml}(-\tau_n v_{ml}^{(x)}, \tau_n v_{ml}^{(y)}, 0)\| - \|\mathbf{r}_1^{(c)}(\tau_n)\|$ .

Given a velocity map  $\mathbf{V}$ , we can denote the projection operator from the physical space  $\mathbf{X}$  to the phase history  $\mathbf{Y}_1$  and

$\tilde{\mathbf{Y}}_2$  as  $\Phi_F^{\mathbf{V}}$  and  $\tilde{\Phi}_F^{\mathbf{V}}$  respectively. The following model is hereby introduced to simultaneously estimate the target's states and form the SAR images:

$$\begin{aligned} & \min_{\mathbf{X}, \mathbf{V}} \|\mathbf{Y}_1 - \Phi_F^{\mathbf{V}}(\mathbf{X})\|_F^2 + \|\tilde{\mathbf{Y}}_2 - \tilde{\Phi}_F^{\mathbf{V}}(\mathbf{X})\|_F^2 + \lambda \|\mathbf{V}^{(x)}\|_0 + \lambda \|\mathbf{V}^{(y)}\|_0 \\ & s.t. \quad \mathbf{X} \in \mathbb{C}^{M \times L}, \mathbf{V}^{(x)} \in \mathbb{R}^{M \times L}, \mathbf{V}^{(y)} \in \mathbb{R}^{M \times L} \\ & \quad \text{supp}(\mathbf{V}^{(x)}) = \text{supp}(\mathbf{V}^{(y)}) \end{aligned} \quad (13)$$

where  $\lambda$  is a positive tuning parameter. The resulting  $\mathbf{X}$  represents the reflectivities of the observed scene including both stationary and moving targets. Practically solving (13) is challenging and therefore in the next section we will explore a solution based on a partial formulation of (13) that further leverages the ATI technique.

#### IV. PROCESSING RESULTS OF THE GOTCHA DATA

The sparsity method is demonstrated through the AFRL GOTCHA data set [13]. The described scope contains an X-band SAR system with three phase centers and a number of moving vehicles in an urban environment. The ground truth data of one vehicle is provided. To be specific, the transmitted chirp is centred at 9.6 GHz, the phase history is collected over 71 seconds interval, and the PRF is 2.17 kHz. Furthermore, as presented in [13], the data was range-gated from 5400 range samples to 384 sub bins to decrease the required storage. The scenario can be found in Fig. 2 which is synthesized with eight range-gated images. Based on the ground truth data, the target trajectory is illustrated by the red path. With reference to the streets and roads, the target trajectory is displaced along the  $x$  direction for about 20 meters. These displacements result from the elevation variations of the observed terrain. In this section, we consider the data from first two channels at the 46-th second snapshot of the scenario with 200 pulses (about 0.1 second interval).

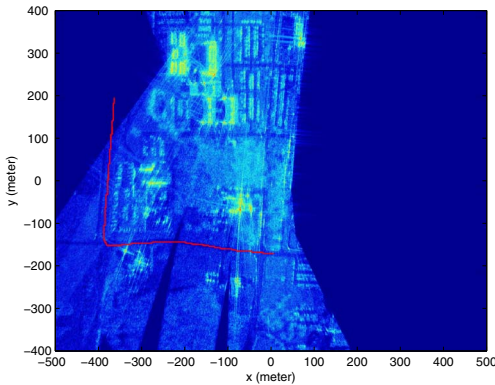


Fig. 2. The reconstructed SAR image in dB with partial data to show the GMTI scenario. Here we assume a flat terrain and the accelerated version of (5) is employed. The red path stands for the target trajectory based on the ground truth data.

To preprocess the data, we first run the inverse operation of the range gating and replace the unknown range gates with

zero. The phase histories are reorganized into data matrices  $\mathbf{Y}_1 \in \mathbb{C}^{5400 \times 200}$  and  $\mathbf{Y}_2 \in \mathbb{C}^{5400 \times 200}$ . We then apply the 2D channel balancing technique [8] to the first two channels and the calibrated phase histories are  $\mathbf{Y}_1$  and  $\tilde{\mathbf{Y}}_2$ . To decrease the computational complexity, here we approximately crop the phased history with a hamming windowed band-pass filter (29 points in range and 5 points in azimuth directions) to focus on the known target. The cropped phase histories are denoted as  $\mathbf{Y}_1^{(t)} \in \mathbb{C}^{5400 \times 200}$  and  $\tilde{\mathbf{Y}}_2^{(t)} \in \mathbb{C}^{5400 \times 200}$ . The formed image of  $\mathbf{Y}_1^{(t)}$  with (5) can be found in Fig. 3.

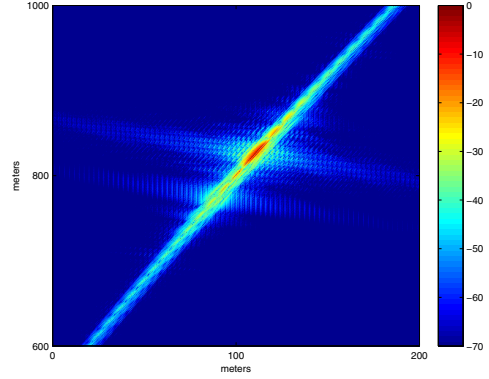


Fig. 3. The corresponding SAR image of the cropped phase history. The image is displayed in -70~0 dB. No velocity is assumed in this image. The target appears to be displaced and blurred.

It is well known that the radial velocities can be estimated from the phase information using ATI. Therefore, to simplify the problem, based on ATI, we still estimate the radial velocity  $\mathbf{V}^{(r)}$  by  $c\Theta/(4\pi f_0 \Delta)$  given that the phases of the ATI results are  $\Theta$ . Here the baseline  $d = 0.238m$  can be estimated in the preprocessing [2] and the radial velocity is chosen to be the mean value of nonzero  $\mathbf{V}^{(r)}$ . Once we have  $\mathbf{V}^{(r)}$ , it is straight forward to map  $\mathbf{V}^{(r)}$  and  $\mathbf{V}^{(az)}$  to  $\mathbf{V}$  based on the geometry, and we denote this as  $\mathbf{V} = \Upsilon(\mathbf{V}^{(az)}, \mathbf{V}^{(r)})$ . We now have the following model:

$$\begin{aligned} & \min_{\mathbf{X}, \mathbf{V}^{(az)}} \|\mathbf{Y}_1^{(t)} - \tilde{\mathbf{Y}}_2^{(t)} - \Phi_F^{\mathbf{V}}(\mathbf{X})\|_F^2 + \lambda \|\mathbf{X}\|_1 \\ & s.t. \quad \mathbf{X} \in \mathbb{C}^{M \times L}, \mathbf{V}^{(az)} \in \mathbb{R}^{M \times L}, \mathbf{V} = \Upsilon(\mathbf{V}^{(az)}, \mathbf{V}^{(r)}) \\ & \quad \text{supp}(\mathbf{X}) = \text{supp}(\mathbf{V}^{(az)}) \end{aligned} \quad (14)$$

As  $\mathbf{Y}_1^{(t)}$  and  $\tilde{\mathbf{Y}}_2^{(t)}$  are focusing on the target, the elements in  $\mathbf{V}^{(az)}$  can be assigned to a single  $v^{(az)}$  throughout the image. Here a naive method to solve (14) is implemented. We first compute (14) using five iterations of FISTA algorithm [14] ( $\lambda$  is about  $0.015 \cdot 2 \|\Phi_F^{\mathbf{V}^H}(\mathbf{Y}_1^{(t)} - \tilde{\mathbf{Y}}_2^{(t)})\|_\infty$ ) with different  $v^{(az)}$  independently. The objective value of (14) with each specific  $v^{(az)}$  is recorded. Fig. 4 shows the objective value against  $v^{(az)}$  plot, and the optimal  $v^{(az)}$  and  $\mathbf{X}$  are chosen to correspond with the minimised objective value. The estimated  $\mathbf{X}$  gives the relocated and refocused image of the moving target, which is shown in Fig. 5.

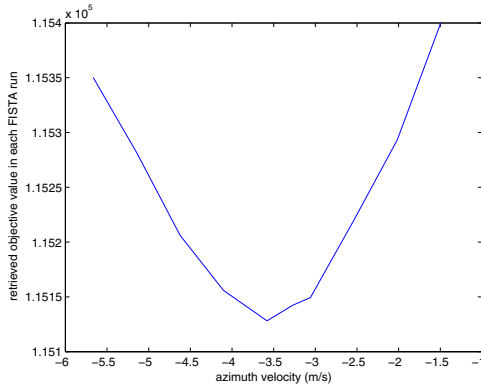


Fig. 4. Resulting objective values with respect to different  $v^{(az),s}$  after five iterations of FISTA algorithm.

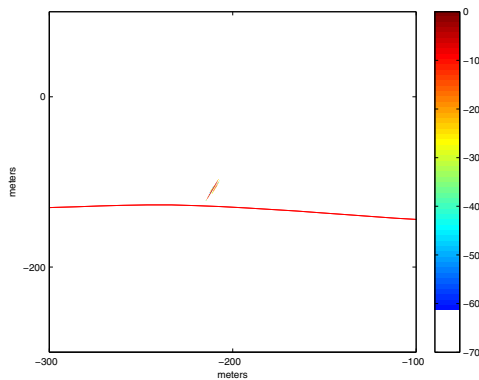


Fig. 5. The reconstructed image in dB of the moving target. Five iteration FISTA is employed for the 46 – th second with 200 pulses. The red line indicates the ground truth data, and the corresponding position of the moving target can be found in Table I.

The estimation results are concluded in Table I. The ground truth data has been corrected with a GPS time offset term, which is provided in the dataset, to better align the ground truth to the SAR image. It can be seen from Fig. 2 that the ground truth trajectory has deviations in the formed image due to the terrain elevation. The range distance ground truth coincides with the estimation result in Table I, and the error in target position estimation results from the radial velocity estimation error and scene elevation. Note that all the estimations are based on a very short sub-aperture, a larger sub-aperture is likely to increase the accuracy as long as the constant velocity assumptions still hold.

## V. CONCLUSION

This paper presents a sparse regularized model for multi-channel SAR/GMTI. Specifically we show how the SAR/GMTI task can be generalised as an optimisation problem and how the sparsity can be used to estimate targets' state and form SAR images. The experimental results based on real GOTCHA GMTI data illustrate the effectiveness of the proposed model. In practice, SAR/GMTI is likely to encounter

TABLE I  
COMPARISONS BETWEEN THE GROUND TRUTH AND ESTIMATIONS

	Ground Truth	Estimations
x (m)	-206.7	-211
y (m)	-129.0	-110
z (m)	-3.2	0
range distance to the platform (m)	1.0375e4	1.0380e4
$v^{(r)}$ (m/s)	9.588	9.82
$v^{(az)}$ (m/s)	-2.14	-3.58
overall v (m/s)	13.63	14.32

the problems such as the imperfections in channel balancing, the ambiguities in velocity estimations and the demand on computational power. These will be investigated in the future work.

## ACKNOWLEDGMENT

This work was supported by the Engineering and Physical Sciences Research Council (EPSRC) grants [EP/K014277/1]; and the University Defence Research Collaboration (UDRC).

## REFERENCES

- [1] R. Deming, M. Best, and S. Farrell, "Simultaneous SAR and GMTI using ATI/DPCA," *Proc. SPIE*, vol. 9093, pp. 90 930U–90 930U–19, 2014.
- [2] B. Guo, D. Vu, L. Xu, M. Xue, and J. Li, "Ground moving target indication via multichannel airborne SAR," *IEEE T. Geoscience and Remote Sensing*, vol. 49, no. 10, pp. 3753–3764, 2011.
- [3] J. Yang, C. Liu, and Y. Wang, "Detection and imaging of ground moving targets with real SAR data," *IEEE T. Geoscience and Remote Sensing*, vol. 53, no. 2, pp. 920–932, 2015.
- [4] S. Chiu and C. Livingstone, "A comparison of displaced phase centre antenna and along-track interferometry techniques for RADARSAT-2 ground moving target indication," *Canadian Journal of Remote Sensing*, vol. 31, no. 1, pp. 37–51, 2005.
- [5] I. Sikaneta and C. Gierull, "Ground moving target detection for along-track interferometric SAR data," in *Aerospace Conference, 2004. Proceedings, 2004 IEEE*, vol. 4, March 2004, pp. 2227–2235 Vol.4.
- [6] J. Ward, "Space-time adaptive processing for airborne radar," in *Space-Time Adaptive Processing (Ref. No. 1998/241), IEE Colloquium on*, Apr 1998, pp. 2/1–2/6.
- [7] L. Prunte, "GMTI from multichannel SAR images using compressed sensing," in *Synthetic Aperture Radar, 2012. EUSAR. 9th European Conference on*, April 2012, pp. 199–202.
- [8] C. Gierull, "Digital channel balancing of along-track interferometric SAR data," in *Technical Memorandum DRDC Ottawa TM 2003-024*. Defence R&D, Ottawa, Canada, March 2003.
- [9] R. W. Deming, "Along-track interferometry for simultaneous SAR and GMTI: application to gotcha challenge data," *Proc. SPIE*, vol. 8051, pp. 80 510P–80 510P–18, 2011.
- [10] S. Kelly and M. Davies, "RFI suppression and sparse image formation for UWB SAR," in *Radar Symposium (IRS), 2013 14th International*, vol. 2, June 2013, pp. 655–660.
- [11] M. Cetin and R. L. Moses, "SAR imaging from partial-aperture data with frequency-band omissions," *Proc. SPIE*, vol. 5808, pp. 32–43, 2005.
- [12] M. Fornasier and H. Rauhut, "Compressive sensing," in *Handbook of Mathematical Methods in Imaging*. Springer, 2011, pp. 187–228.
- [13] S. M. Scarborough, C. H. Casteel, Jr., L. Gorham, M. J. Minardi, U. K. Majumder, M. G. Judge, E. Zelnio, M. Bryant, H. Nichols, and D. Page, "A challenge problem for SAR-based GMTI in urban environments," *Proc. SPIE*, vol. 7337, pp. 73 370G–73 370G–10, 2009.
- [14] A. Beck and M. Teboulle, "A Fast Iterative Shrinkage-Thresholding Algorithm for Linear Inverse Problems," *SIAM Journal on Imaging Sciences*, vol. 2, no. 1, pp. 183–202, Mar. 2009.

# A Location Scale Based CFAR Detection Framework for FOPEN SAR Images

Marco Liguori\*, Alessio Izzo\*, Carmine Clemente<sup>†</sup>,  
Carmela Galdi\*, Maurizio Di Bisceglie\* and John J. Soraghan<sup>†</sup>  
\* Department of Engineering, University of Sannio, 82100 Benevento, Italy

E-mail: marco\_494@hotmail.it, alessiodiesel@hotmail.it,  
galdi@unisannio.it, dibisceg@unisannio.it

<sup>†</sup> University of Strathclyde, CeSIP, EEE, 204, George Street, G1 1XW, Glasgow, UK  
E-mail: carmine.clemente@strath.ac.uk, j.soraghan@strath.ac.uk

**Abstract**—The problem of target detection in a complex clutter environment, with Constant False Alarm Ratio (CFAR), is addressed in this paper. In particular an algorithm for CFAR target detection is applied to the context of FOliage PENetrating (FOPEN) Synthetic Aperture Radar (SAR) imaging. The extreme value distributions family is used to model the data and exploiting the location-scale property of this family of distributions, a multi-model CFAR algorithm is derived. Performance analysis on real data confirms the capability of the developed framework to control the false alarm probability.

## I. INTRODUCTION

Among the different applications of Synthetic Aperture Radar Imaging, FOliage PENetrating (FOPEN) is one of the most challenging [1]. The fundamental characteristic of FOPEN Radars is the capability to collect returns from scatterers under foliage. This goal is achieved by using relatively low frequencies for typical radar systems (UHF and VHF) that are able to penetrate the vegetating layer. The ability to “see” through foliage canopies makes FOPEN radar a powerful tool for military purposes, in particular, if SAR techniques are used a FOPEN SAR sensor becomes capable to detect, track and recognize vehicles hiding in forests [1].

However, due to the nature of the imaged scene, several issues are still present for the complete and reliable exploitation of such a sensor. In particular, canopies and hidden vehicles are not the only possible reflecting targets in a forest scene; trunks are present and contribute significantly to the intensity of the signal returned to the radar.

Reflections from trunks result in detection if an accurate strategy of control of false alarms is not adopted. Solutions or partial solutions to this problem have been provided in literature. In particular, clutter modelling has been identified as a viable solution to mitigate tree trunks detections: physical, statistical and the combination of the two approaches were used to model forest clutter in FOPEN SAR [2], [3], [4], [5], [6]. The models proposed in [2], [3], [4] consider electromagnetic modelling of forests to extract deterministic clutter models. These models are useful in terms of understanding of the scattering phenomenology, but are not applicable in statistical detection frameworks. The model in [5], introduce statistical properties in the model in [3], however this model is not robust with respect to presence of tree trunks dominating a scene.

In [6] a model for VHF clutter generation was proposed, integrating both background scatterers and large-amplitude discrete clutter (trees). Despite the flexibility and the model proposed in [6], unfortunately, it is not available in a closed form and is not suitable to derive detectors with false alarm rate control.

Starting from a statistical modelling of the FOPEN SAR clutter, in this paper we introduce a novel framework for CFAR detection in FOPEN SAR images. In our approach, the clutter is statistically modelled and exploits distributions that belongs to the location-scale family of distributions. The heavy-tailed distributions are used due physical

considerations of the forest scene [1], [6], while the location-scale (LS) family is a requirement of the CFAR detection algorithm [7] that is exploited in this work.

After modelling the forest clutter as location-scale distributed, the CFAR detection algorithm introduced in [8], [9] and applied to high resolution SAR images in [7] can be embedded in a framework that is able to select the best heavy-tailed location-scale distribution to be used to compute the adaptive threshold and that will ensure the Constant False Alarm Rate in the highly inhomogeneous FOPEN SAR image environment.

The reminder of the paper is organized as follows, Section II introduces the multi-Model CFAR detection framework, addressing the specific cases of Gumbel Maximum and Weibull distributed background. The performance in terms of distribution fitting of the two above mentioned models are assessed and discussed in Section III using real VHF FOPEN SAR data. Section IV discusses the CFAR detection algorithm performance analysis on real data, demonstrating the capability of the proposed approach to control the false alarm probability.

## II. MULTI-MODEL CFAR DETECTOR IN LS ENVIRONMENT

The architecture of the proposed algorithm is detailed, with particular focus on the amendments applied the algorithm in [7] to deal with the specific FOPEN challenge. The selection of this algorithm is motivated by the fact that it is flexible and reliable, allowing different statistical models and using an adaptive threshold setting aimed to control the false alarm probability.

The proposed framework has been designed in order to ensure a major robustness and reliability of the results, with respect to the single model approach performed in [7], by considering  $K$  possible statistical distributions of the background. Hence, it has the capability to automatically adapt with respect to the distribution that fits better the real data in a specific reference window, introducing robustness with respect to inaccurate a-priori knowledge of trees density in a spatial window under test.

Its final goal is to perform the binary hypothesis test:

$$\begin{cases} H_B : X'_i < \hat{T}(\gamma_i, \hat{\theta}_{L,i}, \hat{\theta}_{S,i}) \\ H_T : X'_i \geq \hat{T}(\gamma_i, \hat{\theta}_{L,i}, \hat{\theta}_{S,i}) \end{cases} \quad (1)$$

where  $H_B$  is the hypothesis of no target present (background only) and  $H_T$  is the hypothesis of the presence of target,  $X'_i$  is the set of samples associated to  $i$ -th selected distribution and  $\hat{T}(\gamma_i, \hat{\theta}_{L,i}, \hat{\theta}_{S,i})$  is the threshold value function of the distribution parameters selected on the statistical characterization stage. Finally  $i = 1, 2, \dots, K$ , identifies the output index of the distribution selected in the statistical distribution stage. Moreover, a data transformation block is used in order to consider both genuine Location-Scale (LS) distributions and

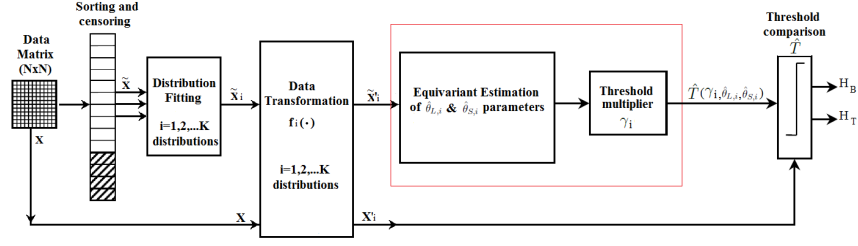


Figure 1: Architecture of the Multi-Model CFAR system in LS environment.

transformable into LS type. Without loss of generality the case  $K = 2$  is considered in this work.

The algorithm architecture is illustrated in Figure 1.

- The starting point is a window under analysis, composed of  $N \times N$  samples of intensity obtained from the complex SAR image.
- the data are organized into a vector  $X$  then sorted and censored obtaining the vector  $\tilde{X}$ . The censoring consists in the removal of  $r$  (censoring depth) pixels of data with the highest intensity values from the set used to estimate the distribution parameters representing the  $H_B$  hypothesis. This is required in order to avoid self masking of targets, meaning that the presence of target pixels in the background parameters estimation would lead to a higher threshold that would produce detection misses.
- the statistical characterization of the background starts with the evaluation of the empirical cumulative distribution function (ECDF) of the real censored data. The aim is to find a statistical distribution that fits well the real data. To achieve this goal, a test on the goodness of fit is required. Among the approaches used to verify if a set of data is compatible with a design distribution  $F(x)$ , in this work the Kolmogorov Smirnov (KS) test [10] is selected. The outcome of the KS test is defined by:
  - $H_0$ : the selected distribution shows a good fit compared to the real data;
  - $H_1$ : the null hypothesis is rejected, hence the selected distribution does not fit well the real data.

For the case in hand, data are extremely inhomogeneous due to the presence of trees in the scenario [6]. Hence, distributions with heavy tail characteristics are required. Several LS distributions have been considered, but for conciseness in this section we discuss only the two distributions that resulted to provide better performance in terms of goodness of fit on real data and that are then exploited in this paper:

- the Gumbel for maximum distribution, with CDF

$$F(\mathbf{x}; \theta_L, \theta_S) = \exp \left[ -\exp \left( -\frac{x - \theta_L}{\theta_S} \right) \right] \quad (2)$$

with  $\theta_L \in \mathbb{R} \quad \theta_S > 0$

which belongs to location-scale family;

- the Weibull distribution, with CDF

$$F(\mathbf{x}; \kappa, \lambda) = \begin{cases} 1 - e^{-\left(\frac{x}{\lambda}\right)^\kappa}, & \text{if } x \geq 0, \\ 0, & \text{if } x < 0. \end{cases}$$

whose natural logarithm is LS.

These two distributions are particularly suitable for the case in hand as they provide good fitting on the tail and are LS, thus allowing the application of the desired algorithm. Performing a hypothesis test on a statistic, a  $p$ -value helps to determine the significance of the results, exploiting a threshold value called

the significance level of the test and denoted as  $\alpha$ . In other words, if  $p$ -value is equal to or smaller than the significance level  $\alpha$ , it suggests that the observed data are inconsistent with the assumption that the null hypothesis is true, and thus that hypothesis must be rejected and the alternative hypothesis is accepted as true.

Let  $\rho_i$  be  $p$ -value associated to  $i$ -th distribution  $D_i$ , and  $\alpha$  set to 5%, for each reference window the distribution selection rule is:

$$D_i : i = \arg \max_{i=1,2,\dots,K} \rho_i \quad (3)$$

- the Multi-Model CFAR algorithm is applied exploiting, for each reference window, the parameters  $(\gamma_i, \hat{\theta}_{L,i}, \hat{\theta}_{S,i})$  of the specific  $i$ -th distribution. In this work, two kind of background distributions will be analyzed in order to design the CFAR detector, Gumbel for maximum distribution ( $i = 1$ ) and Weibull distribution ( $i = 2$ ). If the first distribution belongs to the Location-Scale family, the second one do not. In the latter case, using a log-transformation, the Weibull distribution can be transformed in a log-Weibull distribution, which belongs to the Location-Scale family. For the case in hand the data transformation block follows the following rule:

$$f_i(\cdot) = \begin{cases} 1 \times (\cdot) & \text{with } i = 1 \\ \ln(\cdot) & \text{with } i = 2 \end{cases} \quad (4)$$

Thus, the Best Linear Unbiased (BLU) estimates of the Location and Scale parameters are used to obtain the distribution parameters. By minimizing the variance, subject to the constraints of unbiasedness, the BLU estimators can be obtained [9] as:

$$\begin{pmatrix} \hat{\theta}_{L,i} \\ \hat{\theta}_{S,i} \end{pmatrix} = \left( \mathbf{H}_i^T \mathbf{C}_{0,i}^{-1} \mathbf{H}_i \right)^{-1} \mathbf{H}_i^T \mathbf{C}_{0,i}^{-1} \tilde{\mathbf{X}}_i' \quad (5)$$

where  $\mathbf{H}_i = (\mathbf{1} \mu_{0,i})$ , while  $\mu_{0,i}$  and  $\mathbf{C}_{0,i}$  are the mean vector and the covariance matrix of the standardized vector  $\tilde{\mathbf{X}}_{0,i}'$ , respectively. Letting  $G_i^{(m)}$  be the  $m$ -th order derivative of the inverse cumulative distribution function  $G_i(\cdot) = F_i^{-1}(\cdot)$ , the approximate expressions of mean and covariance matrix of the ordered samples are [7]:

$$\begin{aligned} \mu_{0(k),i} &\approx G_{k,i} + \frac{p_k q_k}{2(n+2)} G_{k,i}^{(2)} + \frac{p_k q_k}{(n+2)^2} \\ &\quad \times \left( \frac{1}{3} (q_k - p_k) G_{k,i}^{(3)} + \frac{1}{8} p_k q_k G_{k,i}^{(4)} \right), \\ C_{0(k,h),i} &\approx \frac{p_k q_h}{(n+2)} G_{k,i}^{(1)} G_{h,i}^{(1)} + \frac{p_k q_h}{(n+2)^2} \\ &\quad \times [(q_k - p_k) G_{k,i}^{(2)} G_{h,i}^{(1)} + (q_h - p_h) G_{h,i}^{(2)} G_{k,i}^{(1)} \\ &\quad + \frac{1}{2} p_k q_k G_{k,i}^{(3)} G_{h,i}^{(1)} + \frac{1}{2} p_h q_h G_{h,i}^{(3)} G_{k,i}^{(1)} \\ &\quad + \frac{1}{2} p_k q_h G_{k,i}^{(2)} G_{h,i}^{(2)}], \quad k \leq h \end{aligned} \quad (6)$$

with  $p_k = k/(n + 1)$  and  $q_k = (1 - p_k)$  and  $G_{k,i} = G(p_k)$ . The moments in (6) can be evaluated with reference to a specific reduced distribution by direct substitution of the derivatives, until the fourth order, of its quantile function (inverse CDF). Let  $G_{i=1}(x)$  be the quantile function associated with the reduced extreme value distribution of type I for maximum (Gumbel for maximum), the set of equations to substitute in (6), and containing the four derivatives under test include:

$$\begin{aligned} G_1(x) &= -\ln(-\ln(x)); \\ G_1^{(1)}(x) &= -\left(\frac{1}{x \ln(x)}\right); \\ G_1^{(2)}(x) &= \left(\frac{\ln(x) + 1}{x^2 \ln^2(x)}\right) \\ G_1^{(3)}(x) &= -\left(\frac{2 \ln^2(x) + 3 \ln(x) + 2}{x^3 \ln^3(x)}\right) \\ G_1^{(4)}(x) &= \left(\frac{6 \ln^3(x) + 11 \ln^2(x) + 12 \ln(x) + 6}{x^4 \ln^4(x)}\right) \end{aligned} \quad (7)$$

The same procedure has been done for the quantile function associated to the reduced extreme value distribution of type I for minimum (Log-Weibull) and the results are reported in (8).

$$\begin{aligned} G_2(x) &= \ln(-\ln(1-x)); \\ G_2^{(1)}(x) &= \left(\frac{1}{(x-1) \ln(1-x)}\right); \\ G_2^{(2)}(x) &= -\left(\frac{\ln(1-x) + 1}{(x-1)^2 \ln^2(1-x)}\right) \\ G_2^{(3)}(x) &= \left(\frac{2 \ln^2(1-x) + 3 \ln(1-x) + 2}{(x-1)^3 \ln^3(1-x)}\right) \\ G_2^{(4)}(x) &= -\left(\frac{6 \ln^3(1-x) + 11 \ln^2(1-x) + 12 \ln(1-x) + 6}{(x-1)^4 \ln^4(1-x)}\right) \end{aligned} \quad (8)$$

It follows that, by using (6) with either (7) or (8), Location and Scale parameters related to the specific distribution under test can be estimated through (5). The adaptive threshold can be computed as:

$$\hat{T}(\gamma_i, \hat{\theta}_{L,i}, \hat{\theta}_{S,i}) = \hat{\theta}_{S,i}(\tilde{X}'_i) \gamma_i + \hat{\theta}_{L,i}(\tilde{X}'_i) \quad (9)$$

However, the evaluation of the adaptive threshold in (9) requires also the knowledge of the constant  $\gamma_i$ , called *threshold multiplier*: this constant is evaluated according to the desired false alarm probability.

The threshold multiplier is the solution of the equation:

$$P_{FA} = Pr \left\{ \frac{\tilde{X}'_i - \hat{\theta}_{L,i}}{\hat{\theta}_{S,i}} > \gamma_i | H_B \right\}, \quad (10)$$

which is the  $(1 - P_{FA})$ -quantile of the normalized test statistic  $((\tilde{X}'_i - \hat{\theta}_{L,i})/\hat{\theta}_{S,i})$ . Obviously, if the statistical distribution of the test statistic is known, then  $\gamma_i$  can be determined. Unfortunately, this distribution cannot be evaluated in a closed form because it requires the knowledge of the joint distribution of the variable  $\tilde{X}'_i$  and of the location and scale estimators. In order to overcome this problem, the value of the quantile  $\gamma_i$  has been computed via Monte Carlo simulation,  $N_p$  realizations of the test statistic have been generated and the threshold multiplier level has been estimated from the empirical CDF. In order to improve the estimators reliability, a suitable number of trials is needed. Precisely, it has been set to  $N_p \cong \frac{10^2}{P_{FA}}$ .

Summarizing, once the location and scale parameters have been estimated with (5), and the threshold multiplier,  $\gamma_i$ , has been computed via Monte Carlo simulation, all the requirements to extract the adaptive threshold in (9) are met.

- the decision rule is applied using the threshold value  $\hat{T}(\gamma_i, \hat{\theta}_{L,i}, \hat{\theta}_{S,i})$  associated to the specific distribution;

We can conclude that the algorithm automatically adapts with respect to the distribution that fits better the real data in a specific reference window, independently from an a-priori knowledge of trees density. Finally, exploiting the decision rule in (11), which compares each data pixel with the adaptive threshold just extracted

$$X'_i \underset{H_B}{\overset{H_T}{\gtrless}} \hat{T}(\gamma_i, \hat{\theta}_{L,i}, \hat{\theta}_{S,i}) \quad (11)$$

the detection problem can be solved and the detector's false alarm rate can be assessed.

### III. STATISTICAL CHARACTERIZATION OF BACKGROUND: PERFORMANCE ANALYSIS

In this section we present the results obtained in terms of goodness of fit to justify the selection of the statistical distributions for the  $H_B$  hypothesis. The dataset used in this work has been acquired using the Swedish low frequency SAR system *CARABAS-II VHF SAR* [11]. The system transmits HH-polarized radio waves between 20-90 MHz, corresponding to wavelengths between 3.3 m and 15 m. In the imaged areas 25 military vehicles are concealed by forest, in four different deployment (for reader's convenience see [11]). Due to the presence of trees in the scenario, we deal with extremely inhomogeneous data. Hence, we have to consider different distributions, including heavy tailed and also light tailed distributions. Among the several distributions with these features, we have analyzed Log-Normal, Weibull, Extreme Value Distributions, Gamma, as well as more usual distributions like Rayleigh and Normal. However, not all result to provide good fitting with the data. For example, the Log-Normal distribution in low density forest results to be rejected in the 42.33% of the cells analysed. Weibull Distribution and the Gumbel for Maximum Distribution result to provide the best results for low and high density forests respectively. For this reason, and for conciseness of the paper, these two distributions have been selected and the results will be discussed in this section.

In order to analyze the performance of statistical characterization we consider an homogeneous area in forest 1 and 2 from Fredrik and Sigismund set of acquisitions respectively [11]. For these areas, a set of  $29 \times 29$  reference windows is considered (841 in total), each window is composed of  $16 \times 16$  pixels producing a set of 256 samples. For each reference window, it is performed a KS test of the area under test to verify the compatibility of data into a cell with a specific distribution. In high density forest cases the Gumbel Maximum distribution is considered, while Weibull distribution is selected for the low density case.

In the high density area the  $H_0$  hypothesis has been rejected 12 times, while the Gumbel Maximum distribution fits the data with the percentage of  $P_{H_0} = 98.57\%$ . For the low density case, the  $H_0$  hypothesis has been rejected 7 times; meaning that the Weibull Distribution provide a fit percentage of  $P_{H_0} = 99.17\%$ .

Finally, similar analysis has been done changing the reference window dimensions of both forests under test. These results are reported in Tables I and II. In particular, increasing the number of pixels for each cell a slight performance degradation was found. Specifically, a reference window dimension  $16 \times 16$  provides the best fitting, for both Weibull and Gumbel Maximum distributions.

Table I: KS test outcomes for high density forests: percentage of  $H_0$  hypothesis using Gumbel Maximum distribution.

Fredrik Mission	Gumbel Maximum Distribution
16 × 16	<b>98.57%</b>
24 × 24	<b>98.06%</b>
32 × 32	<b>95.92%</b>

Table II: KS test outcomes for low density forests: percentage of  $H_0$  hypothesis using Weibull distribution.

Sigismund Mission	Weibull Distribution
16 × 16	<b>99.17%</b>
24 × 24	<b>98.06%</b>
32 × 32	<b>96.64%</b>

Further performances improvement are achieved through the implementation of a multi model fitting approach, as described in Section II.

For the high density case, from a percentage  $P_{H_0} \{GUM\} = 98.57\%$  of  $H_0$  hypothesis associated to the Gumbel Maximum single model, the multi-model approach allows to achieve  $P_{H_0} \{MM\} = 99.28\%$ . Similarly, in the low density forest case, from a percentage  $P_{H_0} \{WBL\} = 99.17\%$  of  $H_0$  hypothesis associated to the Weibull single model, the multi-model approach provides  $P_{H_0} \{MM\} = 99.89\%$ .

In conclusion, for each reference window, the combination of Weibull and Gumbel models enable to choose the statistical distribution that fits better the data, providing robustness in the model selection.

#### IV. CFAR DETECTOR: PERFORMANCE ANALYSIS

In this section the performance of the proposed framework in terms of false alarm control and detection are analysed. In order to assess the performance of the CFAR detector, the variation of 3 parameters is considered:

- dimension of the reference window;
- censoring depth;
- type of statistical distribution.

The CFAR detector requires choosing the dimension of the reference window and the depth of censoring. A reasonable rule is to take the number of samples in the reference window much greater than the maximum expected object dimension and, at the same time, to discard a number of samples that is at least equal to the overall size of the objects.

The algorithm's efficiency has been tested for different reference windows, censoring depth values and false alarm rates. For reader's convenience, among all the cases analyzed, the attention will be focused on the flight pass number 1 of each flight mission/target deployment [11] with design  $P_{FA}=10^{-4}$ ,  $N = 16$  and  $r = [0 \ 32 \ 64 \ 96 \ 115 \ 128]$ .

##### A. False alarm rate performance

The main purpose of this section is to assess the false alarm rate when the designed CFAR algorithm is applied to a specific area within forests 1 and 2, in absence of targets. The single-model CFAR detector for high density forest is performed using a Gumbel for maximum distribution for forest 1 and Weibull distribution for forest 2.

Considering the same areas used for the distribution fitting, the multi-model approach is also evaluated. False alarm probabilities for single

and multi-model CFAR detector are reported in Tables III and IV, for a nominal false alarm rate equal to  $10^{-4}$  and for different values of the censoring depth. The estimated  $P_{FA}$  after detection is compatible with the design  $P_{FA}$ , hence the CFAR property is ensured for both. From Table III,  $P_{FA}$  values are comparable, even if the multi-model approach ensures major robustness, hence a major reliability of the results is obtained. Moreover, in the low-density case (Table IV), the Multi-Model CFAR algorithm achieves better performance in terms of false alarm probabilities than the Weibull CFAR algorithm, for each of the considered censoring depths.

Table III: False alarm probabilities: single-model (Gumbel Max) vs multi-model CFAR detector for various values of the censoring depth.

Censoring Depth $r$	$P_{FA\_MM}$	$P_{FA\_GUM}$
0	$5.08 \times 10^{-5}$	$5.55 \times 10^{-5}$
32	$6.75 \times 10^{-4}$	$0.97 \times 10^{-4}$
64	$1.20 \times 10^{-4}$	$1.20 \times 10^{-4}$
96	$2.91 \times 10^{-4}$	$1.66 \times 10^{-4}$
115	$1.29 \times 10^{-4}$	$1.99 \times 10^{-4}$
128	$1.75 \times 10^{-4}$	$2.40 \times 10^{-4}$

Table IV: False alarm probabilities: single-model (Weibull) vs multi-model CFAR detector for various values of the censoring depth.

Censoring Depth $r$	$P_{FA\_MM}$	$P_{FA\_WBL}$
0	$5.55 \times 10^{-5}$	$1.11 \times 10^{-4}$
32	$9.25 \times 10^{-5}$	$3.00 \times 10^{-4}$
64	$2.77 \times 10^{-4}$	$4.53 \times 10^{-4}$
96	$1.39 \times 10^{-5}$	$5.87 \times 10^{-4}$
115	$1.39 \times 10^{-5}$	$4.81 \times 10^{-4}$
128	$1.39 \times 10^{-5}$	$5.97 \times 10^{-4}$

##### B. Detection Probability Performance

The detection capability of the CFAR detector is performed in an area within forests 1 and 2 in the presence of targets. Precisely, the Fredrik deployment has been tested in forest 1 while the Sigismund deployment has been considered for forest 2. In both cases the performance are evaluated for both the single and multi-model approaches. The single-model CFAR detector performance have been assessed setting the  $P_{FA}$  to  $10^{-4}$  and with different censoring depths, in order to avoid self-masking problem. When no censoring is applied the targets are not detected, due to a self-masking effect of the targets. Increasing  $r$  up to 128 samples, the detection capability of the algorithm improves remarkably. Further increasing the depth of censoring does not introduce additional features to the targets detection but, otherwise, generate underestimation of the distribution parameters. In Table V the probabilities of detection for a single - model CFAR Gumbel for maximum detector with  $P_{FA}$  set to  $10^{-4}$  are reported along with the probabilities of detection of a multi-model CFAR detector referred to the same area under test. Precisely, they have been extracted with respect to the target ground truth of Fredrik deployment. From the results in Table V, the Multi-Model CFAR algorithm achieves equivalent performance in terms of detection probabilities to the Single-Model CFAR algorithm. In Table VI the probabilities of detection for a single - model CFAR Weibull detector with  $P_{FA}$  set to  $10^{-4}$  are reported along with the probabilities of detection of a multi-model CFAR detector referred to the same area under test. For both cases a good probability of detection is achievable with both the single and multi-model approaches, with the latter providing higher reliability in terms of  $P_{FA}$  control. Finally, an example detection maps for Multi-Model CFAR detector are reported in Figure 2 together with the original SAR image and the considered

Table V: Detection probabilities for a single-model CFAR Gumbel for maximum detector vs multi-model CFAR detector for Fredrik targets' deployment.

Censoring Depth $r$	$P_{D\_GUM}$	$P_{D\_MM}$
0	0.076	0.068
32	0.124	0.122
64	0.170	0.236
96	0.209	0.225
115	0.220	0.221
128	0.233	0.233

Table VI: Detection probabilities for a single-model CFAR Weibull detector vs multi-model CFAR detector for Sigismund targets' deployment.

Censoring Depth $r$	$P_{D\_WBL}$	$P_{D\_MM}$
0	0.045	0.101
32	0.121	0.169
64	0.277	0.281
96	0.396	0.359
115	0.434	0.373
128	0.468	0.397

#### Empirical Ground Truth.

In these results it can be appreciated that increasing  $r$  more detections are obtained, moreover the capability of the algorithm to detect extended targets as demonstrated in [7] is confirmed.

### V. CONCLUSION

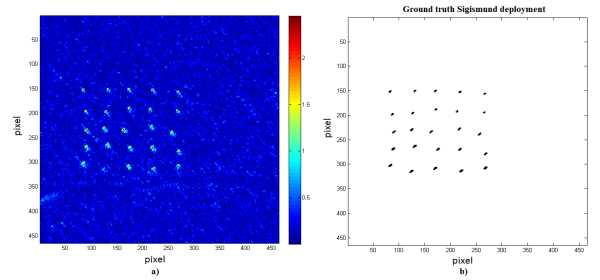
In this paper a novel framework for CFAR detection in FOPEN SAR images has been proposed exploiting a multi-model approach. The novel framework exploits a CFAR detection algorithm based on location-scale and heavy-tailed distributions. The proposed framework is able to control the False Alarm Probability in the FOPEN SAR scenario, adapting the best heavy-tailed location-scale distribution fitting the secondary data. The effectiveness of the proposed approach has been demonstrated on real data, demonstrating that the framework able to adapt both the model and the threshold provides a high level of reliability. Future work will deal with the generalization of the statistical model of the background, exploiting the existing relationship between the extreme value distributions and the forest densities.

#### ACKNOWLEDGMENT

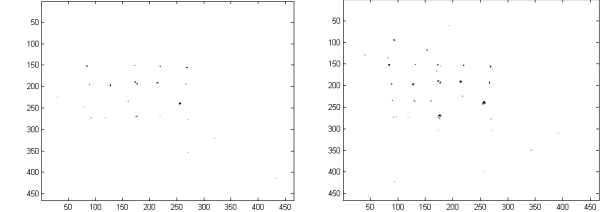
This work was supported by the Engineering and Physical Sciences Research Council (EPSRC) Grant number EP/K014307/1 and the MOD University Defence Research Collaboration in Signal Processing and the University of Sannio.

#### REFERENCES

- [1] Davis, M. E., *Foliage Penetration Radar. Detection and Characterization of Objects Under Trees*, Scitech Publishing, 2012.
- [2] Fransson, J., Walter, F., Ulander, L., "Estimation of forest parameters using CARABAS-II VHF SAR data," *IEEE Transactions on Geoscience and Remote Sensing*, vol. 38, no. 2, pp. 720–727, Mar 2000.
- [3] Smith, G. Ulander, L., "A model relating VHF-band backscatter to stem volume of coniferous boreal forest," *IEEE Transactions on Geoscience and Remote Sensing*, vol. 38, no. 2, pp. 728–740, Mar 2000.
- [4] Williams, M., Manninen, T., Kellomaki, S., Ikonen, V.-P., Sievanen, R., Lehtonen, M., Nikinmaa, E., Vesala, T., "Modeling the SAR response of pine forest in Southern Finland," in *Proceedings. 2003 IEEE International Geoscience and Remote Sensing Symposium, 2003. IGARSS '03.*, July 2003, vol. 2, pp. 1350–1352 vol.2.

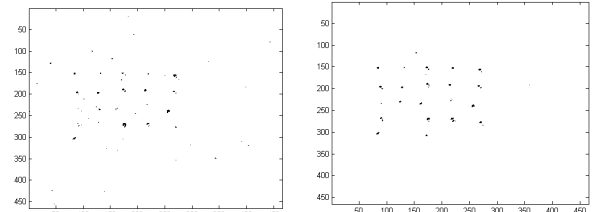


(a) Original SAR Image and Ground Truth.



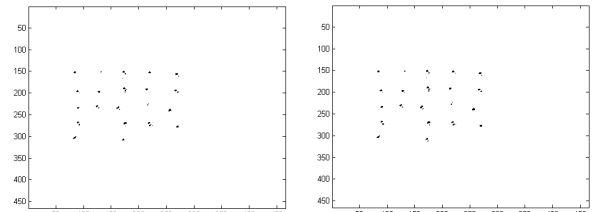
(b)  $r=0$ .

(c)  $r=32$ .



(d)  $r=64$ .

(e)  $r=96$ .



(f)  $r=115$ .

(g)  $r=128$ .

Figure 2: Original SAR image, Empirical Ground Truth and detection maps for multi-model CFAR detector, for the Sigismund deployment (Forest 2), with various censoring depths,  $P_{FA} = 10^{-4}$  and the cell size to  $16 \times 16$ .

- [5] Kononov, A. Ka, M.-H., "Model-Associated Forest Parameter Retrieval Using VHF SAR Data at the Individual Tree Level," *IEEE Transactions on Geoscience and Remote Sensing*, vol. 46, no. 1, pp. 69–84, Jan 2008.
- [6] Jackson, J. A. Moses, R. L., "A Model for Generating Synthetic VHF SAR Forest Clutter Images," *IEEE Transactions on Aerospace and Electronic Systems*, vol. 45, no. 3, pp. 1138 – 1152, 7 2009.
- [7] Bisceglie, M. D. Galdi, C., "CFAR Detection of Extended Objects in High-Resolution SAR Images," *IEEE Transaction on Geoscience and Remote Sensing*, 2005.
- [8] Longo, M., Guida, M., Lops, M., "Biparametric linear estimation for CFAR against Weibull clutter," 1992.
- [9] Conte, E., Lops, M., Tulino, A., "Hybrid procedure for cfar in non-gaussian clutter," *IEE Proceedings Radar, Sonar and Navigation*, vol. 144, no. 6, pp. 361–369, Dec 1997.
- [10] D'Agostino, R. B. Stephens, M. A., *Goodness of fit techniques*, Marcel Dekker Inc., 1986.
- [11] Hellsten, H., Ulander, L., Gustavsson, A., Larsson, B., *Development of VHF CARABAS II SAR*, Proc. SPIE vol. 2747, Radar Sensor Technology, held in Orlando, FL, 8-9 April 1996, pag. 48-60, 1996.

# *Velocity Estimation of moving ships using C-band SLC SAR data*

Andrea Radius

Instituto de Telecomunicações – Polo de Lisboa, ISEL  
Lisbon, Portugal  
aradius@deetc.isel.ipl.pt

Paulo Marques

Instituto de Telecomunicações – Polo de Lisboa, ISEL  
Lisbon, Portugal  
pmarques@isel.ipl.pt

**Abstract**—A new algorithm for the velocity vector estimation of moving ships using Single Look Complex (SLC) SAR data in strip map acquisition mode is proposed. The algorithm exploits both amplitude and phase information of the Doppler decompressed data spectrum, with the aim to estimate both the azimuth antenna pattern and the backscattering coefficient as function of the look angle. The antenna pattern estimation provides information about the target velocity; the backscattering coefficient can be used for vessel classification. The range velocity is retrieved in the slow time frequency domain by estimating the antenna pattern effects induced by the target motion, while the azimuth velocity is calculated by the estimated range velocity and the ship orientation. Finally, the algorithm is tested on simulated SAR SLC data.

**Keywords**—SAR, Doppler spectrum, azimuth antenna pattern, velocity estimation

## I. INTRODUCTION

Synthetic Aperture Radar (SAR) is a very important sensor for Earth surface monitoring, due to its interaction capability with man-made moving targets, as cars and ships, in day and night in virtually any weather conditions and its capability to retrieve the kinematic parameters of the observed targets.

This paper presents a novel technique for moving target velocity estimation based on the synergy between Doppler history analysis and estimation of the antenna pattern effects induced in the slow-time frequency domain.

In the recent years the interest for multi-channel SAR systems has increased, mainly due to their applicability on moving target processing in strong clutter [1].

Unfortunately, multi-channel SAR systems are not typically available for civilian applications. For this reason we focus the attention on the single-Channel SAR systems, optimizing the available informative content.

When only a single channel SAR system is available, the velocity estimation is more difficult than in multi-channel systems, because is necessary to exploit all the informative content of the target migration during the integration time, generating many difficulties for the clutter separation and the accurate estimation of the motion parameters.

It is well known, that the moving targets cause a variation of the Doppler history that can be approximated as a quadratic

function for low squint angles [2]; the variation of quadratic and linear terms cause, respectively, the energy smearing and the peak displacement in azimuth, due to the reference function mismatching and wrong range migration compensation.

A typical approach for azimuth velocity estimation consists in using Doppler rate filters to select the velocity that better focuses the target [3]; another classical technique for the azimuth velocity estimation uses matching criteria on the displacement vector obtained from the spatial shift of the moving target from sub-apertures [4].

Unfortunately, the aforementioned azimuth velocity estimation techniques using a velocity filters bank or the displacement calculation from sequential sub-apertures only works well in presence of point-like scatterers. For extended targets, such as ships, these estimates become severely degraded since these kind of targets are constituted by many scatterers.

A recently proposed technique for range velocity estimation uses sub-aperture images, applying maximum-likelihood criterion to estimate the linear range migration correction on the look spectrum of the range compressed data [5]. Other recently proposed techniques with the same purpose use a maximum-likelihood criterion to estimate the motion parameters in the spatial frequency domain [6], or compute the skew of the bi-dimensional spectral signature of the target [7].

This paper presents an algorithm for ship velocity estimation using SLC data, which exploits the Doppler decompressed data spectrum of the moving target to estimate the range velocity and uses the orientation information for the azimuth velocity estimation. In fact, the range velocity component is estimated by analyzing the amplitude of the range compressed moving target signature before the azimuth compression in the Doppler spectrum domain, while the azimuth velocity is calculated from both the estimated range velocity and the ship orientation.

Finally, the velocity estimation algorithm will be tested using synthetic SLC SAR data generated with the simulator presented in [8] and [9].

## II. MOVING TARGET SPECTRAL SIGNATURE: THEORETICAL MATHEMATICAL EXPRESSIONS

Let  $f_\eta$ ,  $f_{Dc}$  and  $f_R$  denote, respectively, the Doppler frequency, the Doppler centroid and the Doppler rate. The

range compressed data of a point-like scatterer in the Doppler frequency domain before azimuth compression are [2]:

$$G(f_D, t) = D(f_D) \cdot \sigma(f_D) \exp[-j4\pi R(f_D)/\lambda] \cdot \text{sinc}\left\{\pi B \left[ t - 2R(f_D)/c \right]\right\} \quad (1)$$

where  $f_D = f_\eta - f_{Dc}$  is the Doppler frequency centred around the Doppler centroid,  $t$  denotes the range time,  $\sigma$  the backscattering coefficient,  $D$  the azimuth antenna pattern,  $\lambda$  the radar wavelength,  $c$  the light speed,  $R$  the range migration and  $B$  the bandwidth of the transmitted signal.

For low squint angle the range migration is given by:

$$R(f_D) = \sqrt{R_0^2 + V_R^2 \left(\frac{f_D}{f_R}\right)^2} \approx R_0 + \frac{V_R^2}{2R_0} \left(\frac{f_D}{f_R}\right)^2 \quad (2)$$

where  $R_0$  and  $V_R$  are respectively the slant range at the synthetic aperture centre and the relative velocity between antenna and the target. From (1), the range migration causes a variation of the amplitude term and of the phase term, respectively  $\text{sinc}\left\{\pi B \left[ t - 2R(f_D)/c \right]\right\}$  and  $\exp(-j4\pi R(f_D)/\lambda)$ ; the first term is related to the locus of energy of a single target in the bi-dimensional data domain, which varies during the azimuth time. This term must be compensated through the range migration compensation step, performed through interpolation. Mathematically, it corresponds to select the range time:

$$t(f_D, R'_0) = \frac{2R(f_D)}{c} = \frac{2}{c} \left[ R'_0 + \frac{V_R^2}{2R'_0} \left(\frac{f_D}{f_R}\right)^2 \right] \quad (3)$$

For  $t = (f_D, R'_0 = R_0)$  the dependence on the range variable in (3) was removed and the range compressed data became therefore a mono-dimensional vector.

The expressions (1)-(2) are valid for a stationary target. If the target is moving with ground range velocity and azimuth velocity  $V_{rg}$  and  $V_{az}$ , the Doppler history is modified. In fact, the range velocity causes the variation mainly of the linear term of (2), while the azimuth velocity modifies only the quadratic term.

Therefore the range migration expression becomes:

$$R'(f_D) \approx R_0^{MT} + \frac{(V_R^{MT})^2}{2R_0^{MT}} \left(\frac{f_D - f_{Dc}^{MT}}{f_R^{MT}}\right)^2 \quad (4)$$

$$\text{with: } \begin{cases} R_0^{MT} = R_0 + V_{rg} \frac{f_D}{f_R} \sin \theta \\ V_R^{MT} = V_R - V_{az} \\ f_{Dc}^{TOT} = f_{Dc} + \frac{2V_{rg}}{\lambda} \sin \theta = f_{Dc} + f_{Dc}^{MT} \\ f_R^{MT} \approx -\frac{2(V_R - V_{az})^2}{\lambda \left( R_0 + V_{rg} \frac{f_D}{f_R} \sin \theta \right)} \end{cases} \quad (5)$$

where  $\theta$  is the incidence angle and  $f_{Dc}^{MT} = 2V_{rg} \sin \theta / \lambda$  the Doppler frequency due to the radial motion.

After the range migration compensation operated using (3) for a stationary target, the range compressed data in the Doppler frequency domain become:

$$G(f_D, t) = D(f_D - f_{Dc}^{MT}) \sigma(f_D - f_{Dc}^{MT}) \exp\left[-j4\pi \frac{R'(f_D)}{\lambda}\right] \cdot \text{sinc}\left\{\frac{2\pi B}{c} \left[ t - 2 \frac{R'(f_D)}{c} \right]\right\} = D(f_D - f_{Dc}^{MT}) \cdot \sigma(f_D - f_{Dc}^{MT}) \cdot \exp\left[-j \frac{4\pi R_0^{MT}}{\lambda}\right] \cdot \exp\left[-j \frac{2\pi (V_R^{MT})^2}{\lambda R_0^{MT}} \left(\frac{f_D - f_{Dc}^{MT}}{f_R^{MT}}\right)^2\right] \cdot \text{sinc}\left\{-\frac{2\pi B}{c} [R'_0 - R_0^{MT} + g(f_D)]\right\} \quad (6)$$

with  $g(f_D) = \frac{V_R^2}{2R_0} \left(\frac{f_D}{f_R}\right)^2 - \frac{(V_R^{MT})^2}{2R_0^{MT}} \left(\frac{f_D - f_{Dc}^{MT}}{f_R^{MT}}\right)^2$ .

The argument of the *sinc* term corresponds to the residual range migration due to a mismatch in the compensation.

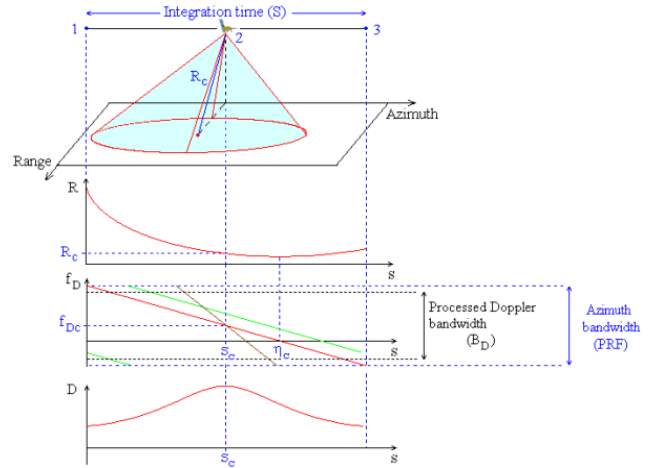


Fig. 1. Relation between the motion and the target spectral signature in the synthetic aperture.

Fig. 1 shows the motion effects in the time frequency domain. The graphic on the top shows the acquisition plane, where the integration time determines the synthetic aperture length; the second graphic represents the slant range depending on the azimuth time for a stationary target; the third graphic shows the time-frequency plane, and the spectral signature is shown for stationary target (in red), moving target in the range direction (in green) and moving target in the azimuth direction (in brown). Finally, the graphic at the bottom represents the azimuth antenna pattern.

From the figure it is possible to observe that the azimuth velocity causes an expansion/contraction of the two-way antenna radiation pattern  $D$ , while the range velocity generates the Doppler frequency shift  $f_{Dc}^{MT}$ .

### III. VELOCITY ESTIMATION ALGORITHM

The proposed algorithm for the estimation of the complete velocity vector is based on two main steps. The first step consists in estimating the range velocity using the amplitude information in (6). The second step uses the range velocity, obtained previously, combined with the orientation of the ship, to estimate the azimuth velocity component.

The range velocity component is estimated using the amplitude information of (6), as in [10] where the velocity estimation is performed for point-like targets, resulting:

$$A(f_D, t) = |G(f_D)| = D(f_D - f_{Dc}^{MT}) \cdot \left| \sigma(f_D - f_{Dc}^{MT}) \right| \cdot \text{sinc} \left\{ 2\pi B/c \left[ t - 2R^{MT}(f_D)/c \right] \right\} \quad (7)$$

For the sake of simplicity, let us assume that the backscattering coefficient is independent on the look angle, i.e.  $\sigma$  is constant. The *sinc* function represents the residual range migration. The principle of the methodology is to take the spectral signature of the moving target represented by the azimuth antenna pattern along the energy trajectory.

In C-band strip map acquisitions, the residual range migration is typically very small; in fact, for velocities lower than 20 m/s the residual range migration is lower than 2 range pixels. For this reason, the spectral signal energy is obtained by calculating the mean of two sub-apertures in sub-sampled range direction such that the spectral energy is concentrated along the same azimuth line. The range sub-aperture processing allows the compensation of the residual range migration, represented by the *sinc* term in (7). This means that only the azimuth antenna pattern term is remaining after the range sub-aperture processing step.

The azimuth antenna pattern is represented by:

$$D(f_D - f_{Dc}^{MT}) \approx \text{sinc}^2 \left[ \frac{kL_a}{2} \tan^{-1} \left( \frac{V_R - V_{az} f_D - f_{Dc}^{MT}}{R_0 f_R} \right) \right] \quad (7)$$

where  $k$  is the wave vector and  $L_a$  the antenna length.

The azimuth antenna pattern is centred in the Doppler frequency  $f_{Dc}^{MT}$ . The algorithm purpose is the estimation of the spectral signature peak position, which is related without ambiguity to the range velocity of the target.

The main problem is that the spectral signature is not always visible, due to the clutter presence. The algorithm needs a pre-filtering step with the aim to filter the sea clutter in order to synthetically increase the Signal to Clutter Ratio (SCR).

The pre-filtering is performed using a dedicated azimuth sub-aperture combination [9], in which three partially overlapped sub-apertures are combined through interferometric processing. The filtered data amplitude is used to weight the original SLC data to preserve the phase information.

Finally, differently from [10], the azimuth velocity is calculated using the previously estimated range velocity and the ship orientation  $\Phi$ , where  $\Phi$  is the trigonometric angle, starting to the x-axis and counter clockwise oriented.  $\Phi$  was

estimated here using the Matlab function *regionprops*, dedicated function used to compute properties for image regions which, among other properties, is able to measure the shape orientation.

Fig. 2 shows the sinc-type antenna pattern which is estimated from the filtered azimuth spectrum of the moving target. In this example, the moving target is a small boat.

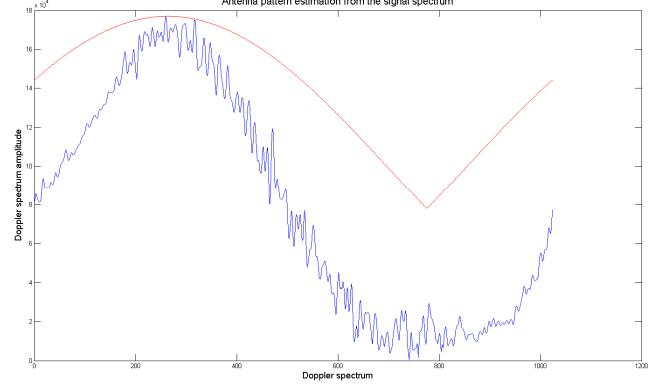


Fig. 2. Antenna pattern estimation (in red) from the azimuth spectrum profile of a moving ship.

Starting from SLC data, the velocity estimation algorithm is based on the following steps.

#### A. Data filtering

- Data flip to obtain the image in the original acquisition geometry.
- Use of dedicated sub-aperture processing proposed in [9] to filter the SLC data. The filtered data are shifted to the Doppler centroid.

#### B. Range velocity estimation

- Digital spotlight of the ship as described in [6].
- Spectrum calculation of the filtered data and azimuth decompression, with removal of the smoothing window used to weight the azimuth reference filter.
- Mean computation of two not overlapped range sub-apertures generated using 50% of the range bandwidth and a subsampling factor of 2.
- Amplitude profile fitting of the spectral signature using the sinc function  $\text{sinc}^2[a \cdot (x-b)]$ , with the aim to estimate the spectrum maximum expressed by the term  $b$ .
- Retrieval of the Doppler Centroid of the target from the amplitude profile maximum position and range velocity estimation using (7):

$$V_{rg} = \lambda \cdot f_{Dc}^{MT} / 2 \cdot \sin \theta \quad (8)$$

#### C. Azimuth velocity estimation

- The azimuth velocity is calculated by:

$$V_{az} = V_{rg} \cdot \tan \Phi \quad (9)$$

The azimuth velocity sign is defined univocally from the orientation and the range sign.

#### IV. RESULTS

The test and preliminary validation of the velocity estimation algorithm was done using the SLC data simulator proposed in [9], which injects moving targets in real SLC images by defocusing the data in range and azimuth inserting the target raw data through the overlapping and sum principle and refocusing the image. The used SLC data is a fine mode Radarsat-2 image.

Table 1 shows some results obtained with simulated data. The results are relative to a simulated ship which is characterized by length  $L$ , orientation  $\Phi$ , Signal to Clutter Ratio SCR, range velocity  $V_{rg}$  and azimuth velocity  $V_{az}$ .  $\bar{\Phi}$ ,  $\bar{V}_{rg}$  and  $\bar{V}_{az}$  are, respectively, the estimated orientation, range velocity and azimuth velocity.

TABLE I. PRELIMINARY RESULTS OF THE VELOCITY ESTIMATION

$L$ (m)	SCR (dB)	$\Phi$ (°)	$V_{rg}$ (m/s)	$V_{az}$ (m/s)	$\bar{\Phi}$ (°)	$\bar{V}_{rg}$ (m/s)	$\bar{V}_{az}$ (m/s)
30	31.6	90	10	0	90	10.3	0
30	24.8	49.1	7.6	6.5	45	6.7	6.7
50	33.7	67.3	7.4	3.1	72.3	6.2	3.8
50	28.3	67.3	11.1	4.6	60.6	10.7	6
50	28.7	112.7	10.1	-4.3	120.8	8.8	-5.3
50	29.8	117.7	10.3	-7.9	116.7	7.9	-5.9
35	21.9	112.5	12.7	-8.1	130.8	10.6	-12.3
45	30.7	124.3	12.4	-8.4	112.7	11.1	-7.1

From the results, the mean square errors of the range velocity, azimuth velocity and orientation are respectively 11.5%, -11.3% and 16.3%.

Note that an estimation error on  $V_{rg}$  and on the ship orientation is propagated on the azimuth velocity, as demonstrated for the penultimate result in Table 1. In fact, if the ship is composed by several scatterers that interact with constructive or destructive interference, the orientation and the azimuth antenna pattern could be difficult to estimate accurately.

The presented algorithm presents some limitations. In fact, the proposed methodology does not work when the ship is moving only in the azimuth direction, and it could produce high estimation errors in the presence of very small range velocity components, due to the stationary sea clutter which overlaps the moving target spectral signature.

Finally, the algorithm can fail- when the vessels are small, and the algorithm is not able to calculate their orientation.

#### V. CONCLUSIONS AND FUTURE WORK

The proposed algorithm is able to estimate the full velocity vector of a moving target using SLC data which is commonly available for civilian applications.

The velocity estimation error increases for low SCR, because the spectral signature is difficult to reconstruct, when

the velocity is low, because the target spectrum maximum is in the same band of the sea clutter, when the backscattering coefficient varies during the integration time and when multiple scatterers interact with destructive interference.

Even if the algorithm is limited by the aforementioned problems, it produced very encouraging results also taking into account the classification capabilities. In fact, if the azimuth antenna pattern in (7) is estimated, the backscattering coefficient depending on the look angle can be calculated for classification purposes.

The activities foreseen in the next future for the algorithm improvement are the following:

- Fitting processing optimization.
- Improvement of the ship orientation estimation using alternative methods, as the Radon transform.
- Calculation of the backscattering coefficient variation during the integration time for classification purposes.
- Algorithm extension to high residual range migration situations (X-band high resolution SAR systems).
- Extended validation on simulated and real data and comparison with other existing algorithms.

#### References

- [1] J. H. G. Ender, P. Berens, A. R. Brenner, L. Rossing, U. Skupin, "Multi-channel SAR/MTI system development at FGAN: from AER to PAMIR", Proc. of IEEE Int. Geoscience Remote Sensing Symposium, IGARSS, 24-28 June 2002.
- [2] I.G. Cumming, F.H. Wong, "Digital Signal Processing of Synthetic Aperture Radar Data: Algorithms and Implementation", Artech House, January 2005.
- [3] S.Hinz, F.Meyer, A.Laika, R.Bamler, "Spaceborne traffic monitoring with Dual Channel Synthetic Aperture Radar – Theory and Experiments", Proc. of IEEE, Computer Society Conference on, Vol.3, pp. 7-7, 20-26 June 2005.
- [4] M.Kirscht, Detection and velocity estimation of moving objects in a sequence of single-look SAR images, Proc. of IEEE Int. Geoscience Remote Sensing Symposium, IGARSS, 27-31 May 1996.
- [5] M. Kirscht, "Detection and imaging of arbitrarily moving targets with single-channel SAR", Proc. of IEE Radar, Sonar and Navigation, Vol. 150, Issue 1, pp. 7-11, Feb 2003.
- [6] J. Dias, P. Marques, "Multiple moving target detection and trajectory estimation using a single SAR sensor", IEEE Trans. on Aerospace and Electronic Systems, Vol. 39, Issue 2, pp. 604–624, April 2003.
- [7] P. Marques, J. Dias, "Velocity estimation of fast moving targets using a single SAR sensor", IEEE Trans. on Aerospace and Electronic Systems, Vol. 41, Issue 1, pp. 75–89, Jan 2005.
- [8] A. Radius, P. Marques, "Synthetic Aperture Radar Raw Data Simulator for Sea Environment dedicated to Moving Ship Detection", Sensor Signal Processing for Defence (SSPD) Conference, pp. 1–4, 25-27 Sept 2012.
- [9] A. Radius, J. Ferreira, P. Carmo, P. Marques, "Advanced Ship Detection for Spaceborne based Maritime Awareness", Living Planet Symposium, pp. 1–4, 09-13 Sept 2013.
- [10] A. Radius, P. Marques, "Velocity Vector Estimation of Moving Targets using C-band SLC Strip Map SAR data", Proceedings of the 7<sup>th</sup> European Conference on Synthetic Aperture Radar, EUSAR'14, 3-5 June 2014.

# On the Target Detection in OFDM Passive Radar Using MUSIC and Compressive Sensing

Watcharapong Ketpan, Seksan Phonsri, Rongrong Qian and Mathini Sellathurai  
Institute of Sensors, Signals and Systems,  
School of Engineering and Physical Sciences,  
Heriot-Watt University, Edinburgh, The United Kingdom EH14 4AS  
Email: wk1@hw.ac.uk

**Abstract**—The passive radar also known as *Green Radar* exploits the available commercial communication signals and is useful for target tracking and detection in general. Recent communications standards frequently employ Orthogonal Frequency Division Multiplexing (OFDM) waveforms and wideband for broadcasting. This paper focuses on the recent developments of the target detection algorithms in the OFDM passive radar framework where its channel estimates have been derived using the matched filter concept using the knowledge of the transmitted signals. The MUSIC algorithm, which has been modified to solve this two dimensional delay-Doppler detection problem, is first reviewed. As the target detection problem can be represented as sparse signals, this paper employs compressive sensing to compare with the detection capability of the 2-D MUSIC algorithm. It is found that the previously proposed single time sample compressive sensing cannot significantly reduce the leakage from the direct signal component. Furthermore, this paper proposes the compressive sensing method utilizing multiple time samples, namely  $l_1$ -SVD, for the detection of multiple targets. In comparison between the MUSIC and compressive sensing, the results show that  $l_1$ -SVD can decrease the direct signal leakage but its prerequisite of computational resources remains a major issue. This paper also presents the detection performance of these two algorithms for closely spaced targets.

## I. INTRODUCTION

The passive radar, which employs the commercial broadcasting signals, has gained a great deal of interest. Having the separate transmitter and receiver, the bistatic radar can be handled more economically than the monostatic counterparts, and their concept can be perfectly combined with the passive paradigm, namely, Passive Bistatic Radar [1]. Due to the fact that the operated signals are not distinct from the commercial signals, the activity of passive radar may not need additional transmit power. Currently, wireless internet and mobile communications are functioned with the Orthogonal Frequency Division Multiplexing (OFDM) signals, whose orthogonal characteristic between subcarriers is used to reduce the intersymbol interference and increase the bandwidth efficiency. Further, the OFDM signals can be generated efficiently with the Discrete Fourier Transform. As a result, passive radar equipped with OFDM signal has become an area of significant interest within the target detection research.

However, the OFDM signal along with multipath channel estimates produces high complexity at the receiver. In this context, Palmer et al. [2] has proposed the ambiguity function analysis for the passive radar employing Digital Video Broadcasting signals as well as the mismatched filtering to

estimate the channels and reduce the effect of the clutters. Moving-target detection via moving platform can be found in [3] using Space Time Adaptive Processing. There are also some interesting applications of the OFDM passive radar demonstrated on a passive Synthetic Aperture Radar [4] and the employment of Probability Hypothesis Density filter in the OFDM passive radar for multi-target tracking is demonstrated in [5]. To emphasize target detection problem, this paper reviews the OFDM passive radar developed by Berger et al. [6], where the channel estimates are efficiently implemented as fast Fourier transform and can be used directly for target detection. Berger et al. claimed a novel matched filter which is generally employed in radar systems by correlating the transmitted and received signal to determine the peak of delay-matched power. The first proposed signal extraction method is the Multiple Signal Classification (MUSIC) algorithm, which is normally used to identify the direction of arrivals (DOA). Chan et al.[7] has employed the MUSIC for DOA detection of ground moving objects. The other recently proposed detection method is compressive sensing which can achieve recovery of sparse signals along with a slower sampling rate than Nyquist's sampling theorem.

In order to compare the target detection performance of the MUSIC and compressive sensing methods, this paper simulates the scenario of a static OFDM passive radar capturing the reflections from the moving targets and stationary clutters along with the direct signals to be able to test various detection algorithms proposed within the recent literature including 2-D MUSIC and compressive sensing. The MUSIC algorithm which is implemented by modifying the pseudo-code presented in [6] is able to identify the target parameters; however, many snapshots of the incoming signals should have been applied. On the other hand, the basis pursuit presented in [6] with a single snapshot may not be sufficient to recover signals in noise. This paper also proposes a method employing multiple time samples compressive sensing called  $l_1$ -SVD and compares its performance with the MUSIC algorithm as well as with its single sample counterpart compressive sensing. The paper also displays the comparison between the MUSIC and compressive sensing for very close targets in order to understand the resolution provided by these methods.

The rest of this paper is organized as follows. Section II presents the system model of the OFDM passive radar. The MUSIC algorithm and compressive sensing for target detection in the OFDM passive radar are given in Section III, and then the simulation results and the discussions are presented in

Section IV, Finally, Section V concludes this work.

## II. SYSTEM AND PROBLEM MODEL

### A. Signal and Channel Model

The passive radar uses the OFDM signal which is a multicarrier modulation scheme with  $N$  subchannels. Suppose that  $M$ -ary QAM is used, then on the  $n$ th subcarrier, the signal is declared as

$$\begin{aligned} u_n(t) &= s_{ni} \cos 2\pi f_n t - s_{nq} \sin 2\pi f_n t \\ &= S_n e^{j\theta_n} e^{j2\pi f_n t} \\ &= s[n] e^{j2\pi f_n t}, \end{aligned} \quad (1)$$

where  $S_n = \sqrt{s_{ni}^2 + s_{nq}^2}$  and  $\theta_n = \tan^{-1}(\frac{s_{nq}}{s_{ni}})$  are amplitude and phase of a complex data symbol  $s[n]$  respectively. The orthogonality of each symbol is achieved by periodically expanding the transmitted waveform with a cyclic prefix (CP). Let  $T_{cp}$  denote the time interval for a CP, and a rectangular window  $q(t)$  can be define with the range  $t \in [-T_{cp}, T]$ , where  $T$  is the data symbol length and is equal to  $\frac{1}{\Delta f}$  when  $\Delta f$  is the subcarrier spacing. This results in the following  $i$ th symbol of the transmitted signal

$$x_i(t) = \sum_{n=-\frac{N}{2}}^{\frac{N}{2}-1} s_i[n] e^{j2\pi n \Delta f t} q(t), \quad (2)$$

where  $f_n = n\Delta f$ . Each symbol has a duration of  $T'$  which is equal to  $T + T_{cp}$ . It is obvious that the operation in (2) is similar to the  $N$ -point Inverse Discrete Fourier Transform (IDFT) of  $s[n]$ . Therefore, the OFDM signal can be generated efficiently with the DFT functions. Moreover, to construct the OFDM symbol, the last CP-length values in each symbol can be employed as a cyclic prefix and appended before the arrival of each data symbol. The signals impinging on the receiver consist of both direct signal and target reflections. The echo either from a cluster or a target is described by a delay and a Doppler shift. Given the center frequency  $f_c$ , the existing Doppler shift is given as  $f_D = a f_c$  for  $a$  is a quotient of range-rate divided by speed of light. Suppose that there are  $N_p$  arrival paths, and let  $A_p$  and  $\tau_p$  respectively be the attenuation and delay for the  $p$ -th path,  $p \in \{1, \dots, N_p\}$ , and assume that  $w(t)$  is additive white noise. The received signal can be expressed as [6]

$$y(t) = \sum_p A_p e^{j2\pi a_p f_c t} x(t - \tau_p) + w(t), \quad (3)$$

where  $x(t) = \sum_{i=-\infty}^{\infty} x_i(t - iT')$ .

### B. Matched Filter

The matched filter is a choice of receiver filter applied for the maximization of the output SNR, when the transmitted and received waveform is matched. The impulse response of the matched filter is realized by time-reversing and conjugating the transmitted waveform,  $h(\hat{\tau}) = \alpha x^*(T_{max} - \hat{\tau})$  for an arbitrary time  $T_{max}$  which is at the point of maximum SNR. Given an

input signal to the filter  $y(t)$ , then the output can be derived by the convolution as

$$z(\hat{\tau}) = \int_{-\infty}^{\infty} y(t) h(\hat{\tau} - t) dt \quad (4)$$

$$= \alpha \int_{-\infty}^{\infty} y(t) x^*(t + T_{max} - \hat{\tau}) dt. \quad (5)$$

As seen from (5), the matched filter can be implemented as a correlator for the cross-correlation between the transmitted and received signals. Following the derivation in [6], the output of the overall matched filter can be shown as

$$|z_k(\hat{\tau})| = \left| \sum_{i=1}^L \sum_{n=-\frac{N}{2}}^{\frac{N}{2}-1} e^{-j2\pi(i\hat{a}_k f_c T' - n\Delta f \hat{\tau})} H_n^{(i)} \right|, \quad (6)$$

where

$$H_n^{(i)} \approx A_0 T |s[n]|^2 e^{j2\pi(i a_0 f_c T' - n\Delta f \tau_0)}. \quad (7)$$

It is shown that the matched filter output (6) can be effectively generated using a 2-D discrete Fourier transform of the channel estimates (7). The result of this implementation will be displayed in section IV.

### C. Problem Formulation

As spatial smoothing technique required in this paper, the target detection problem starts with defining the steering vector  $\mathbf{b}$  from the  $\text{vec}\{\cdot\}$ -operation of a subarray matrix  $\mathbf{B}_{n',i'}(\hat{\tau}, \hat{a})$  where its elements  $b_{n',i'}(\hat{\tau}, \hat{a}) = e^{j2\pi(i\hat{a} f_c T' - n\Delta f \hat{\tau})}$  are described as the feedback of one array element to a wave of  $(\hat{\tau}, \hat{a})$ . The  $\text{vec}\{\cdot\}$ -operation is to acquire a matrix column-wise in favour of generating a new vector so  $\mathbf{b}_{n',i'}(\hat{\tau}, \hat{a}) = \text{vec}\{\mathbf{B}_{n',i'}(\hat{\tau}, \hat{a})\}$ . New dimensions  $N'$  and  $L'$  are of the subarray matrix which are lower than of the total channel estimates. As the consequences, the channel estimates in (7) which is perfectly analogous to the one of  $N_p$  wavefronts impinging on a grid of sensors, where the steering vectors have amplitudes  $A_p$  [6], can be assembled by piling up the columns of each subarray matrix on top of each other and the vectors can be shown as

$$\mathbf{h}_{n',i'} = \sum_{p=1}^{N_p} A_p \mathbf{b}_{n',i'}(\hat{\tau}_p, \hat{a}_p). \quad (8)$$

## III. TARGET DETECTION ALGORITHMS FOR OFDM PASSIVE RADAR

### A. The MUSIC Algorithm

The MUSIC is the technique employed to estimate the parameters of multiple signals arriving at an antenna array, exploiting the measurements of the received waveforms. Assuming that the number of incident signals is not larger than the number of array elements, the subspace algorithm can be used. Involving to signal and noise eigenvectors subspace, the 1-dimensional MUSIC algorithm is developed by Schmidt in [8]. On the other hand, as mentioned in section II-B, the target detection problem for the passive radar is a 2-dimensional (2-D) problem, which involves the Doppler frequency and time

delay. Berger et al. [6] have illustrated the derivation of the 2-D MUSIC as

$$f_{MUSIC}(\hat{\tau}, \hat{a}) = \left( |\mathbf{b}^H(\hat{\tau}, \hat{a}) \mathbf{E}_N|^2 \right)^{-1} \quad (9)$$

$$= \left( N' L' - |\mathbf{b}^H(\hat{\tau}, \hat{a}) \mathbf{E}_S|^2 \right)^{-1}. \quad (10)$$

Implementations exploiting noise subspace and signal subspace are shown in (9) and (10) respectively. Berger et al. claimed that the interpretation of either (9) or (10) can be achieved with 2-D FFT, see [6]. This key concept has also been applied in this paper including the pseudo-code mentioned in Berger's paper. To implement the 2-D MUSIC algorithm, first, the direct signal should be eliminated from the observation matrix by using high-pass filter or least-squares fitting the received data to a template assuming no time variation of a very limited degree of change as suggested in [6]. This paper assumes that this step has been completed rather perfectly as the cancellation algorithm is beyond the scope of this paper. Secondly, there is an observation matrix  $\mathbf{R} = [\mathbf{h}_1, \dots, \mathbf{h}_M]$  where  $\mathbf{h}$  is from (8) and  $M$  is the number of snapshots. An eigen-decomposition is calculated as shown

$$\mathbf{R}^H \mathbf{R} = \mathbf{U} \mathbf{\Sigma} \mathbf{U}^H. \quad (11)$$

The matrix of eigenvectors  $\mathbf{U}$  has been sorted according to the eigenvalue in  $\mathbf{\Sigma}$ . The number of eigenvectors and eigenvalues are then selected as the number of impinging signal paths  $N_p$  and  $\mathbf{U}_p$  can be generated as  $\mathbf{U}_p = [\mathbf{R} \mathbf{U}(:, 1 : N_p) \mathbf{\Sigma}(1 : N_p)]^{\frac{1}{2}}$ . Next, the channel estimates  $\mathbf{h}$  is projected on the space orthogonal to the stationary components as the following

$$\mathbf{h}_m = (\mathbf{I} - \mathbf{U}_p \mathbf{U}_p^H) \mathbf{h}. \quad (12)$$

The steering vector  $\mathbf{b}$  is created from the resulted  $\mathbf{h}_m$  and then formulate another observation matrix  $\mathbf{R}_s = [\mathbf{b}^{(1)}, \dots, \mathbf{b}^{(K)}]$ . The eigen-decomposition is applied to the subarray-version matrix before finding the matrix  $\mathbf{B}_s = [\mathbf{U}_s(:, 1 : N_p) \mathbf{\Sigma}_s(1 : N_p)]^{\frac{1}{2}}$ . The MUSIC spectrum is finally computed by applying 2D-FFT on the multiplication between  $\mathbf{R}_s$  and each column of  $\mathbf{B}_s$  and then calculate the summation over all transformed results.

### B. Compressive Sensing with a Single Time Sample

According to the problem (8), the basic narrowband observation model can be expressed as [9]

$$\mathbf{h}(t) = \mathbf{B}(\hat{\tau}, \hat{a}) \mathbf{a}(t) + \mathbf{w}(t), \quad t \in \{t_1, \dots, t_M\}. \quad (13)$$

In order to focus on a single sample, the number of snapshots  $M$  is equal to 1. The objective of this problem is determining the delay( $\hat{\tau}$ ) and the Doppler frequency( $\hat{a}$ ) of the impinging signals. The sparse representation problem begins with creating an overcomplete representation  $\mathbf{B}$  in terms of all possible delays and Doppler frequencies which are  $\hat{\tau} = 0, \frac{T}{N'}, \dots, (N' - 1) \frac{T}{N'}$  and  $\hat{a} = 0, \frac{1}{f_c T' L'}, \dots, \frac{(L' - 1)}{f_c T' L'}$ . In this case, the matrix  $\mathbf{B}$  is known and can be the same as mentioned in section II-C.  $\mathbf{a}(t)$  can be described as an  $(N' \cdot L') \times 1$  vector, where there are  $N_p$  nonzero elements. Without the knowledge of the  $N_p$  pairs of  $(\hat{\tau}_p, \hat{a}_p)$ , this problem can be realized as

$l_1$ -norm regularization in Basis Pursuit(BP) [6] which can be evolved into,

$$\text{minimize } \|\mathbf{h} - \mathbf{B} \mathbf{a}\|_2^2 + \lambda \|\mathbf{a}\|_1 \quad (14)$$

regarding that  $\mathbf{a}$  is sparse. In this case, however,  $\mathbf{a}$  is a complex vector where its  $l_1$ -norm can be calculated by  $\|\mathbf{a}\|_1 = \sum_{i=1}^n (\mathbf{Re}\{\mathbf{a}_i\}^2 + \mathbf{Im}\{\mathbf{a}_i\}^2)^{\frac{1}{2}}$ . The problem in (14) is reformulated as,

$$\text{minimize } \|\tilde{\mathbf{h}} - \tilde{\mathbf{B}} \begin{bmatrix} \mathbf{Re}\{\mathbf{a}\} \\ \mathbf{Im}\{\mathbf{a}\} \end{bmatrix}\|_2^2 + \lambda \mathbf{1}^T \mathbf{u}$$

$$\text{subject to } \sqrt{\mathbf{Re}\{\mathbf{a}_i\}^2 + \mathbf{Im}\{\mathbf{a}_i\}^2} \leq u_i, \quad i = 1, \dots, n \quad (15)$$

which is a second-order cone program(SOCP) problem[10].

### C. Compressive Sensing with Multiple Time Samples

In order to compare with the MUSIC, the expression introduced above may not be enough due to only one time sample. To realize the real system, multiple time samples technique is required. This comes to the application of  $l_1$ -SVD which is proposed in [9]. In this context, the cost function is

$$\min \|\mathbf{H}_{SV} - \mathbf{B} \mathbf{A}_{SV}\|_f^2 + \lambda \|\tilde{\mathbf{a}}^{(l_2)}\|_1 \quad (16)$$

where the Singular Value Deposition (SVD) is applied to the matrix  $\mathbf{H} = [\mathbf{h}(t_1), \dots, \mathbf{h}(t_M)]$ . The objective is to decompose the matrix into the signal and noise subspaces. This algorithm deals with the reduced dimensions regarding the signal subspace only. Decreasing the dimension of  $\mathbf{H}$  to  $(N' \cdot L') \times N_p$ , it results in  $\mathbf{H}_{SV} = \mathbf{U} \mathbf{L} \mathbf{D}_{N_p} = \mathbf{H} \mathbf{V} \mathbf{D}_{N_p} = \mathbf{B} \mathbf{A}_{SV} + \mathbf{N}_{SV}$ .  $\mathbf{D}_{N_p} = [\mathbf{I}_{N_p} \mathbf{0}']$  where  $\mathbf{I}_{N_p}$  is an identity matrix with the dimension  $N_p \times N_p$  and  $\mathbf{0}$  is a matrix of zeros with the dimension  $N_p \times (M - N_p)$ .  $\mathbf{A}_{SV}$  and  $\mathbf{N}_{SV}$  can be defined as  $\mathbf{A} \mathbf{V}_{N_p}$  and  $\mathbf{N} \mathbf{V}_{N_p}$  respectively given that the matrix  $\mathbf{U}, \mathbf{L}$  and  $\mathbf{V}$  resulted from the SVD of  $\mathbf{H}$ . The operation  $\|\cdot\|_f$  is the Frobenius norm and more details in SOCP implementation of  $l_1$ -SVD can be found in [9].

## IV. SIMULATION RESULTS

Regarding the realization of the system, standard Digital Audio Broadcasting (DAB) specifications are applied with some modifications. The carrier frequency used in this simulation is 227.36 MHz along with 1 kHz spacing between the subcarriers. This makes the symbol length to be 1 ms. In contrast to the configuration (Table I of [6]), this simulation uses 128 subchannels along with 64 blocks per frame due to the computational constraints. Hence, the amount of bandwidth is reduced as well as the size of the cyclic prefix which is normally equal to a quarter of symbol time.

The parameters above have been used for illustrating the matched filter (6) as displayed in Fig. 1. The number of impinging signals on the array elements is 5 which are 1) a direct signal, 2) two cluster reflection signals and 3) two moving-target reflection signals. The power of the direct signal is approximately 50-dB higher than of the targets. The direct signal path possesses a shortest delay while the targets' path delays are longer. The first target velocity is about 591 m/s whereas the second travels around 887 m/s. When the power of the direct component is much higher, the results are not sufficiently apparent as shown in Fig. 2 when using MUSIC

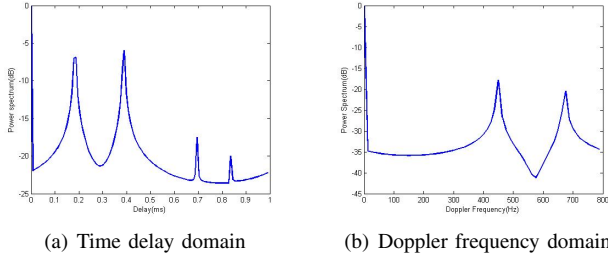


Fig. 1. Simulation results from the output of the matched filter with 5 multipath components detected

algorithm. In order to overcome this issue, direct signal cancellation must be applied before trying to detect targets. In the following simulation results, the direct signal power is set to be lower but still greater than zero as the cancellation method might not be perfect enough to cancel the direct signal completely.

Fig. 3 illustrates the ability of detection from the MUSIC compared to a single time sample compressive sensing. There are 5 components, all with the same amount of power. Both algorithms are able to display 5 peaks of delay values and 3 Doppler frequencies (one at zero and two for the targets) at the correct locations as in Fig. 1. The MUSIC results process 500 snapshots as well as 3200 subarrays. Regarding the compressive sensing, the regularization parameter ( $\lambda$ ) in (14) is selected employing the formula in [10] which is  $\lambda \geq \lambda_{max} = \|2B^T h\|_\infty$ .

The other two simulations utilize  $l_1$ -SVD where the peaks are clearer than that of the one time sample CS or the MUSIC outputs. For the clarity of the comparison and the problem of computational size, the number of wavefronts are decreased to 3 which are only a single direct transmission and two moving-target illuminations. Fig. 4 determines the targets with their parameters consistent with the former simulations while the other, Fig. 5, determines the closest parameter values which are able to be distinguished by these two methods. The simulations illustrate that two targets that are separated by 0.0408 ms (12.24 km) in delay and 64 Hz (84.45 m/s) in Doppler frequency. The resolution of this system is poor because (i) the size of the channel estimates (the number subchannels  $N$  and symbols  $L$ ) is limited by the computational cost of compressive sensing and matrix multiplication for the MUSIC algorithm. This size is less than the standard DAB configuration. This leads to (ii) smaller dimensions of the subarray matrix which cause the separation between the receiver grid arrays to be wider. Nevertheless, there is no evidence of the maximum subarray size can be computed which might be determined in the future work. The last figure (Fig. 6) exhibits the simulation when applying a single time sample compressive sensing onto 5 paths of signals (with additional cluster signals) involving two close targets. It is able to detect the targets but the simulation results display unwanted signal peaks. From the figures, it can be predicted that compressive sensing methods are possible to work with higher power of direct signal and  $l_1$ -SVD can eliminate interference even though many snapshots are included. Computational time for each algorithm when applying 3-multipath scenario (same as Fig. 4 and Fig. 5) is shown in Table I.

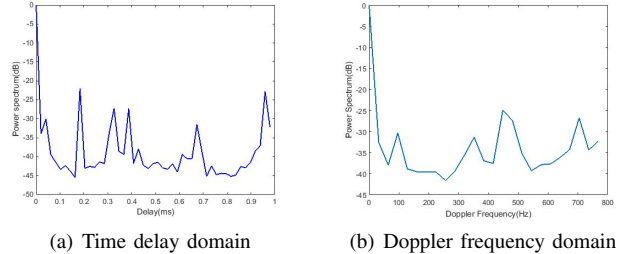


Fig. 2. The MUSIC algorithm results with the 50-dB stronger direct path

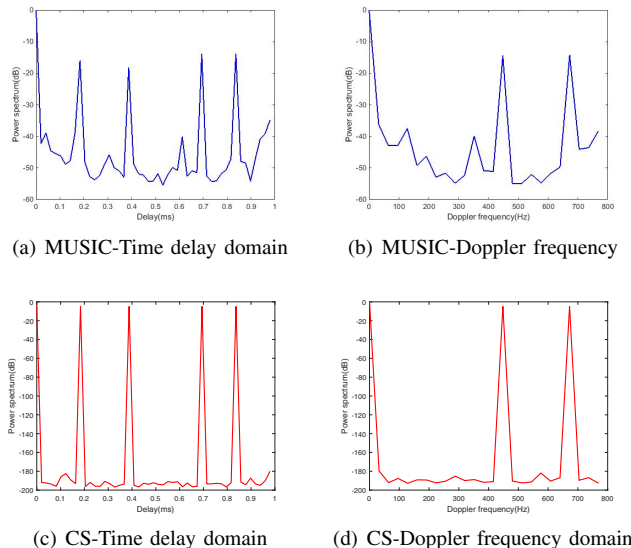


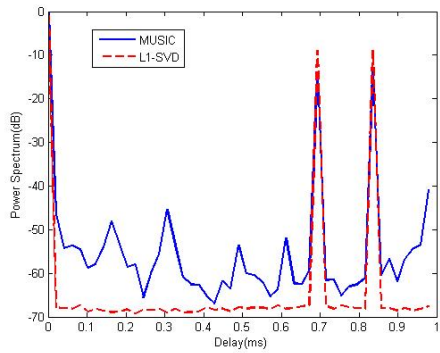
Fig. 3. The results from the MUSIC algorithm and single time-sample compressive sensing (with the same level of power among the paths)

TABLE I. CPU TIME FOR TARGET DETECTION ALGORITHMS

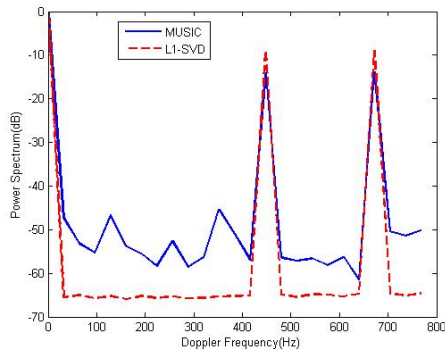
Methods	Elapsed time (sec)
MUSIC	96.81
One time sample CP	15488.94
$l_1$ -SVD	9367.13

## V. CONCLUSION AND FUTURE WORK

This paper studied the target detection ability of MUSIC and compressive sensing. The MUSIC algorithm is found to work very well except that there is a requirement for a large number of snapshots as well as it produces some interference from the direct signals. A single time sample compressive sensing which consumes the highest CPU time is not able to eradicate the unexpected signal. Therefore, this paper has suggested the  $l_1$ -SVD which has an impressive capability of targets detection in the passive radar paradigm. Regarding the further work, this paper does not study the computational efficiency of the algorithms in terms of the number of detected targets as increasing multipath components can cause complexity issues. Furthermore, the profiles of the target parameters can be made closer if there is a revision on the overcomplete matrix (e.g. multiresolution grid in [9]). This means that it is possible to increase the resolution of compressive sensing detector while it is unlikely for the MUSIC algorithm. Finally, the modifications of sensing scenarios such



(a) Time delay domain



(b) Doppler frequency domain

Fig. 4. The comparison between the results from the MUSIC algorithm and  $l_1$ -SVD with multiple time samples with 3 multipath components detected

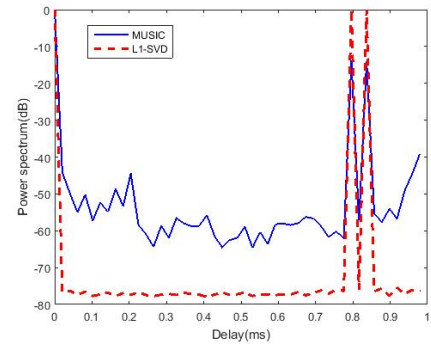
as multiple transceivers or non-static receiving platform are also challenging interesting issues to solve.

#### ACKNOWLEDGEMENT

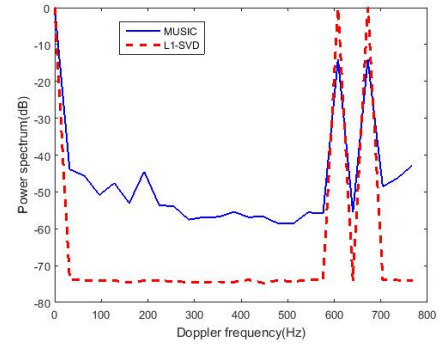
The authors would like to thank the anonymous reviewers and acknowledge the Royal Thai Air Force for financial support. This project is also funded by EPSRC Project EP/M014126/1, Large Scale Antenna Systems Made Practical: Advanced Signal Processing for Compact Deployments [LSAS-SP].

#### REFERENCES

- [1] M. Cherniakov, *Bistatic radar: emerging technology*. Sussex: John Wiley & Sons, Inc., 2008.
- [2] J. E. Palmer, H. A. Harms, S. Member, S. J. Searle, L. M. Davis, and S. Member, "DVB-T Passive Radar Signal Processing," *IEEE Transactions on Signal Processing*, vol. 61, no. 8, pp. 2116–2126, 2013.
- [3] B. Dawidowicz, P. Samczynski, M. Malanowski, J. Misiurewicz, and K. S. Kulpa, "Detection of moving targets with multichannel airborne passive radar," *IEEE Aerospace and Electronic Systems Magazine*, vol. 27, no. November, pp. 42–49, 2012.
- [4] D. Gromek, P. Samczy, K. Kulpa, J. Misiurewicz, and A. Gromek, "Analysis of Range Migration and Doppler History for an Airborne Passive Bistatic SAR Radar," in *15th International Radar Symposium (IRS)*, 2014, pp. 1–6.
- [5] G. Battistelli, L. Chisci, C. Fantacci, A. Farina, and A. Graziano, "Distributed Multitarget Tracking for Passive Multireceiver Radar Systems," in *14th International Radar Symposium (IRS)*, Dresden, Germany, 2013, pp. 337–342.

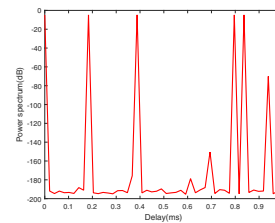


(a) Time delay domain

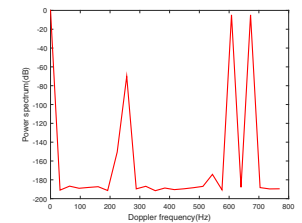


(b) Doppler frequency domain

Fig. 5. The comparison between the results from the MUSIC algorithm and  $l_1$ -SVD on the very close targets with 3 multipath components detected



(a) Time delay domain



(b) Doppler frequency domain

Fig. 6. The compressive sensing with a single time sample experiments on two close targets with 5 multipath components detected

- [6] C. R. Berger, B. Demissie, J. Heckenbach, and P. Willett, "Signal Processing for Passive Radar Using OFDM Waveforms," *IEEE Journal on Selected Topics in Signal Processing*, vol. 4, no. 1, pp. 226–238, 2010.
- [7] T. Chan, Y. Kuga, and S. Roy, "Combined Use of Various Passive Radar Techniques and Angle of Arrival using MUSIC for the Detection of Ground Moving Objects," in *IEEE International Symposium on Antennas and Propagation (APSURSI)*, 2011, pp. 2561–2564.
- [8] R. Schmidt, "Multiple emitter location and signal parameter estimation," *IEEE Transactions on Antennas and Propagation*, vol. 34, no. 3, pp. 276–280, 1986.
- [9] D. Malioutov, M. Çetin, and a. S. Willsky, "A sparse signal reconstruction perspective for source localization with sensor arrays," *IEEE Transactions on Signal Processing*, vol. 53, no. 8, pp. 3010–3022, 2005.
- [10] S. J. Kim, K. Koh, M. Lustig, S. Boyd, and D. Gorinevsky, "An Interior-Point Method for Large-Scale  $l_1$ -Regularized Least Squares," *IEEE Journal of Selected Topics in Signal Processing*, vol. 1, no. 4, pp. 606–617, 2007.

# Radar Imaging With Quantized Measurements Based on Compressed Sensing

Xiao Dong, Yunhua Zhang

The Key Laboratory of Microwave Remote Sensing, Chinese Academy of Sciences  
National Space Science Center, Chinese Academy of Sciences  
Beijing, China  
dongxiao@mirslab.cn

**Abstract**—In this paper, we consider the problem of radar imaging with quantized data. The quantized CS (QCS) method is used to reconstruct the radar image of sparse targets from quantized data. The reconstruction problem is derived in the maximum *a posteriori* (MAP) estimation framework and formulated as a convex optimization problem. We compare the proposed method with the traditional  $l_1$ -regularization method using 1-D simulated data with different quantization bits. For coarse quantization with 1 or 2 bits, the simulation results show that the QCS method outperforms the  $l_1$ -regularization method in high SNR situations. For high-resolution quantization with more bits, we derive the conditions under which the  $l_1$ -regularization method and the QCS method are equivalent. This statement is explained theoretically and confirmed by simulation results.

**Keywords**—compressed sensing (CS); maximum *a posteriori* (MAP); quantization; radar imaging; sparsity.

## I. INTRODUCTION

Practical radar systems usually use large bandwidth waveforms to achieve high resolution. According to the Shannon sampling theory, a high-rate analog-to-digital converter (ADC) is needed for acquiring the echo data from the output of the radar receiver, which brings two challenges for modern imaging radar. First, generally speaking, the dynamic range of ADC degrades as a function of the sampling rate. A high-rate ADC with high-resolution quantization is expensive and energy-inefficient. Second, the large volumes of data produced by high-rate ADC bring many difficulties to storing and transmission devices, especially for spaceborne synthetic aperture radar (SAR) systems.

The recently developed compressed sensing (CS) theory indicates that a sparse signal can be recovered from a small number of linear measurements [1-4]. CS has been successfully applied to radar imaging of sparse targets using sub-sampled data [5-7]. Classic CS theory does not consider the issue of quantization accuracy. However, in real applications, measurements are always quantized with a finite number of bits, thus the quantization error should be considered. Several works discussed the issue of quantized CS (QCS) [8-11]. In [8], Laska *et al.* proposed two approaches to deal with the saturation errors. Soon after he proposed the quantized iterative hard thresholding algorithm in [9], which exhibited better performance over classic CS algorithms with quantized measurements. In [10], two convex optimization

methods, i.e. the  $l_1$ -regularized maximum likelihood method and the  $l_1$ -regularized least squares method, were proposed for CS with quantized measurements. In [11], a variational Bayesian inference based CS algorithm is proposed for QCS. An extreme case of QCS is the so-called 1-bit CS where only the sign information of each measurement is preserved. The 1-bit CS problem was first discussed by Boufounos and Baraniuk [12], and their results show that accurate recovery can be achieved using 1-bit measurements. Various algorithms have been proposed for 1-bit CS, e.g., binary iterative hard thresholding (BIHT) [13], renormalized fixed point iteration (RFPI) [12], adaptive outlier pursuit (AOP) [14], etc.

Very recently, we applied 1-bit CS in SAR imaging of sparse targets [15], where the SAR imaging problem with 1-bit measurements was formulated as a convex optimization problem in the Bayesian maximum *a posteriori* (MAP) estimation framework [15]. It has been shown that the radar image can be recovered from 1-bit quantized data provided the targets are sufficiently sparse. However, the application of 1-bit quantization in radar imaging still faces two problems. First, the loss of amplitude information makes the estimation of radar cross-section impossible. Second, as pointed in [15, 16], 1-bit quantization would cause ghost targets. It has shown in [15] that, for a small number of targets, the ghost targets can be well suppressed by the sparse optimization method. However, as will be shown in the following experiments, it is hard to eliminate the ghost targets or other artifacts while in the meantime preserve the weak targets in 1-bit radar imaging.

In this paper, we consider the problem of radar imaging with low-bit quantized data. The quantized CS (QCS) is used to reconstruct the 1-D radar image. We extend our previous work on 1-bit CS radar imaging to handle quantized measurements at arbitrary bits. The reconstruction of radar images from quantized measurements is formulated as a convex problem based on MAP estimation. We also compare the proposed method with the classic CS reconstruction method under different bits of quantization and noise levels.

The next section presents the mathematical model of radar imaging based on QCS. Section IV conducts numerical simulations and Section V concludes the paper.

## II. QCS FOR RADAR IMAGING

In this section, we start from the classic CS model for radar imaging without quantization error, then we formulate

the reconstruction of radar images from quantized measurements as a MAP estimation problem.

### A. Classic CS Radar Imaging

Under the Born approximation, the received radar signal is the output of a linear operator performed on the target reflectivity. After discretization, we have

$$\mathbf{s} = \mathbf{U}\mathbf{f} + \mathbf{e}, \quad (1)$$

where  $\mathbf{f} \in \mathbb{C}^N$  represents the target reflectivity vector,  $\mathbf{s} \in \mathbb{C}^M$  represents the received complex baseband signal after quadrature demodulation,  $\mathbf{e} \in \mathbb{C}^M$  represents the additive noise vector, and  $\mathbf{U} \in \mathbb{C}^{M \times N}$  represents the measuring process.

When the illuminated scene only contains a small number of strong-scattering targets, it can be regarded as sparse. This could happen in cases of imaging ships on sea surface, airplanes in sky, or moving targets in a stationary background. Based on the CS theory, if  $\mathbf{f}$  is sparse enough, near perfect reconstruction from a small number of measurements can be achieved by solving the  $l_1$ -regularization problem

$$\min \frac{1}{2} \|\mathbf{U}\mathbf{f} - \mathbf{s}\|_2^2 + \lambda \|\mathbf{f}\|_1, \quad (2)$$

Assuming  $\mathbf{n}_i$  are independent identically distributed (iid) Gaussian random variables, then the above  $l_1$ -regularization has the same form of MAP estimator under the Laplace prior. It should be noted that, although  $l_1$ -regularization has been proved capable of recovering sparse or compressible vectors, it offers no guarantees for the recovery of vectors drawn iid from a Laplace distribution [17]. In fact, it has been shown that Laplace distributed data is not compressible [17].

Note that in the complex-valued domain, the  $l_1$ -regularization problem can be solved in the real-valued domain after the following transformation

$$\begin{aligned} \mathbf{y} &= \begin{bmatrix} \mathcal{R}\{\mathbf{s}\} \\ \mathcal{I}\{\mathbf{s}\} \end{bmatrix}, \quad \mathbf{A} = \begin{bmatrix} \mathcal{R}\{\mathbf{U}\} & -\mathcal{I}\{\mathbf{U}\} \\ \mathcal{I}\{\mathbf{U}\} & \mathcal{R}\{\mathbf{U}\} \end{bmatrix}, \\ \mathbf{x} &= \begin{bmatrix} \mathcal{R}\{\mathbf{f}\} \\ \mathcal{I}\{\mathbf{f}\} \end{bmatrix}, \quad \mathbf{n} = \begin{bmatrix} \mathcal{R}\{\mathbf{e}\} \\ \mathcal{I}\{\mathbf{e}\} \end{bmatrix}. \end{aligned} \quad (3)$$

then (1) becomes

$$\mathbf{y} = \mathbf{A}\mathbf{x} + \mathbf{n}, \quad (4)$$

Using the fact that  $\|\mathbf{f}_i\| = \sqrt{\mathbf{x}_i^2 + \mathbf{x}_{i+N}^2}$ , we can rewrite (2) as

$$\min \frac{1}{2} \|\mathbf{A}\mathbf{x} - \mathbf{y}\|_2^2 + \lambda \sum_{i=1}^N [\mathbf{x}_i^2 + \mathbf{x}_{i+N}^2]^{1/2}, \quad (5)$$

### B. QCS Radar Imaging

In radar system, quantization is performed separately on the I and Q channels of the radar signal, i.e.,

$$\mathbf{r} = Q(\mathcal{R}\{\mathbf{s}\}) + jQ(\mathcal{I}\{\mathbf{s}\}), \quad (6)$$

where  $\mathcal{R}\{\cdot\}$  and  $\mathcal{I}\{\cdot\}$  denote the real part operator and the imaginary part operator, respectively, and  $Q$  denote the quantizer function. Given a scalar  $\eta \in \mathbb{R}$ , we have

$$Q(\eta) = \begin{cases} \eta_0, & \text{if } \eta \in (\tau_0, \tau_1), \\ \eta_1, & \text{if } \eta \in [\tau_1, \tau_2), \\ \dots, & \dots, \\ \eta_{L-1}, & \text{if } \eta \in [\tau_{L-1}, \tau_L), \end{cases} \quad (7)$$

where  $\tau_0 < \tau_1 < \dots < \tau_L$  are the quantization thresholds and  $\eta_0 < \eta_1 < \dots < \eta_{L-1}$  are the quantization levels, respectively. The number of the quantization levels satisfies  $L = 2^B$ , where  $B$  denotes the number of bits. In the extreme case  $B = 1$ , i.e., 1-bit quantization, only the sign information of the measurements is preserved.

Let  $\mathbf{q} = \begin{bmatrix} \mathcal{R}\{\mathbf{r}\} \\ \mathcal{I}\{\mathbf{r}\} \end{bmatrix}$ , then we can rewrite (6) as

$$\mathbf{q} = Q(\mathbf{A}\mathbf{x} + \mathbf{n}). \quad (8)$$

In the following, we use  $\mathbf{l} \in \mathbb{R}^{2M}$  and  $\mathbf{u} \in \mathbb{R}^{2M}$  to denote the lower and upper thresholds associated with the quantized measurement vector  $\mathbf{q}$ , i.e.,

$$Q^{-1}(\mathbf{q}_i) = [\mathbf{l}_i, \mathbf{u}_i), \quad (9)$$

for  $i = 1, 2, \dots, 2M$ .

Using (9), we can rewrite (8) as,

$$\mathbf{l} \leq \mathbf{A}\mathbf{x} + \mathbf{n} \leq \mathbf{u} \quad (10)$$

Assuming  $\mathbf{n}_i$  are iid Gaussian random variables with mean zero and variance  $\sigma^2$ , the conditional probability density function (pdf) of  $\mathbf{q}$  under  $\mathbf{x}$  is [10]

$$p(\mathbf{q}|\mathbf{x}) = \prod_{i=1}^{2M} \left[ \Phi\left(\frac{-\mathbf{a}_i^T \mathbf{x} + \mathbf{u}_i}{\sigma}\right) - \Phi\left(\frac{-\mathbf{a}_i^T \mathbf{x} + \mathbf{l}_i}{\sigma}\right) \right], \quad (11)$$

where  $\mathbf{a}_i^T$  is the  $i$ th row of  $\mathbf{A}$ , and

$$\Phi(z) = \frac{1}{\sqrt{2\pi}} \int_{-\infty}^z \exp\left(-\frac{t^2}{2}\right) dt \quad (12)$$

is the cumulative distribution function (CDF) of the standard normal distribution.

In the following, we solve (8) or (10) using the Bayesian maximum *a posteriori* (MAP) estimation. The objective of MAP estimation is to maximize the *a posteriori* pdf  $p(\mathbf{x}|\mathbf{q})$ , or equivalently, to minimize  $-\ln p(\mathbf{x}|\mathbf{q})$ . Using Bayes rule, we can formulate the MAP problem as

$$\min_{\mathbf{x} \in \mathbb{R}^{2N}} -\ln p(\mathbf{q}|\mathbf{x}) - \ln p(\mathbf{x}). \quad (13)$$

When the target reflectivity vector  $\mathbf{f}$  is sparse, we can use the  $l_1$ -norm of  $\mathbf{f}$  to enforce the sparsity. Specifically, we choose the prior as

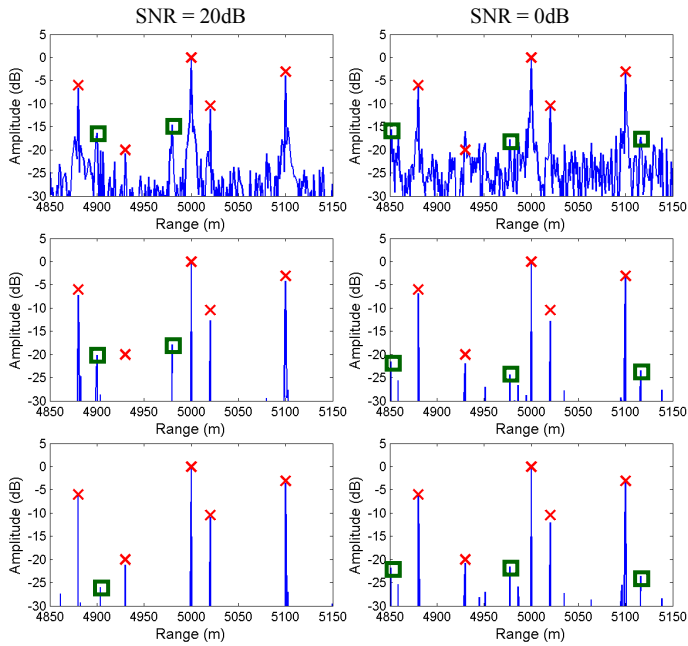


Fig. 1. Simulated 1-D radar range profiles with 1-bit quantized data under SNRs of 20 and 0dB. The first row shows the results obtained by MF, the second row shows the results obtained by  $l_1$ -regularization, and the third row shows the results obtained by QCS-MAP. Ghost targets and artifacts are marked with green boxes.

$$-\ln p(\mathbf{x}) \propto \|\mathbf{f}\|_1 = \sum_{i=1}^N \sqrt{\mathbf{x}_i^2 + \mathbf{x}_{i+N}^2} \quad (14)$$

By substituting (11) and (14) into (13) and omitting the constant, we have

$$\min_{\mathbf{x} \in \mathbb{R}^{2N}} - \sum_{i=1}^{2M} \ln \left[ \Phi \left( \frac{-\mathbf{a}_i^T \mathbf{x} + \mathbf{u}_i}{\sigma} \right) - \Phi \left( \frac{-\mathbf{a}_i^T \mathbf{x} + \mathbf{l}_i}{\sigma} \right) \right] + \lambda \sum_{i=1}^N \sqrt{\mathbf{x}_i^2 + \mathbf{x}_{i+N}^2}. \quad (15)$$

Hereafter, we shall call the problem (15) as QCS-MAP.

The QCS-MAP formulation has the same form of MAP estimator under Laplace prior. However, we do not assume the target reflectivity vector  $\mathbf{f}$  is iid Laplace distributed because the Laplace distribution is not compressible [17]. Here the  $l_1$ -norm is used to recover sparse or compressible vectors.

When only one bit is used in the quantization, the formulation in (15) turns to

$$\min_{\mathbf{x} \in \mathbb{R}^{2N}} - \sum_{i=1}^{2M} \ln \Phi \left( \frac{\mathbf{q}_i \mathbf{a}_i^T \mathbf{x}}{\sigma} \right) + \lambda \sum_{i=1}^N \sqrt{\mathbf{x}_i^2 + \mathbf{x}_{i+N}^2}, \quad (16)$$

which is the same as the 1-bit radar imaging model in [15].

The problem (15) is a convex, unconstrained optimization problem which can be solved by general purpose convex optimization algorithms. Among these algorithms, first order algorithms are more suitable for large scale problems because

they can incorporate fast matrix-vector multiplication into the optimization process. In [15], we solved the 1-bit radar imaging problem (16) using the first-order primal-dual algorithm proposed by Chambolle and Pock [18]. In [10], the authors solved the QCS problem which is similar to (15) using the first-order fixed-point method. An accelerated version based on Nesterov's gradient method is presented in [19].

### III. EXPERIMENTAL RESULTS

In this section, we conduct several experiments to evaluate the QCS method using 1-D simulated radar data. We first point out the limitation of 1-bit quantization. Then we show that, by adding one-bit of the amplitude information (i.e., using 2-bit quantization), the recovery can be significantly improved. In addition, a theoretical comparison between  $l_1$ -regularization and QCS using high quantization bits is presented in the end of this section.

#### A. Set up

In the simulations, a chirp waveform of 100 MHz bandwidth and  $6\mu\text{s}$  time duration is used as the transmitted signal. The received signal is backscattered by five targets. Generally, there are two ways for pulse compression of the chirp waveform, i.e., matched filtering (MF) and stretch processing. The MF approach requires the received signal sampled at a rate higher than the bandwidth of the transmitted signal and it is suitable for arbitrary waveforms. The stretch approach can reduce the sampling rate of the received signal but it is only suitable for the chirp waveform. Besides, the low sampling rate of the stretch approach also restricts the size of the observed scene, thus stretch processing is only suitable for imaging small areas like ISAR or spotlight SAR applications. In this simulation, we consider the MF approach with the sampling rate at 120 MHz.

#### B. 1-bit Quantization

In the first experiment, we aim to reconstruct the range profile using only the sign information of the received radar signal. We compare the results of traditional MF,  $l_1$ -regularization and QCS-MAP under different SNRs. The  $l_1$ -regularization problem is solved using the fast iterative shrinkage-thresholding algorithm (FISTA) in [20] and the QCS-MAP is solved using the algorithm proposed in [19]. In the  $l_1$ -regularization problem, we chose the regularization parameter  $\lambda$  after trying several different values and comparing the performances. In the QCS-MAP algorithm, we use the true value of the noise variance  $\sigma$  and chose  $\tau$  after several tries. Fig. 1 presents the reconstructed range profiles with 1-bit quantized data under different SNRs. The first row of Fig. 1 shows the results obtained by MF, the second row shows the results obtained by  $l_1$ -regularization, and the third row shows the results obtained by QCS-MAP.

When  $\text{SNR} = 20\text{dB}$ , we can clearly see the ghost targets located at 4900m and 4980m in the MF image, and their amplitudes are even larger than the true target located at 4930m. This phenomenon is caused by the loss of amplitude information of 1-bit measurements [16]. The  $l_1$ -regularization method suppress the noisy background, but the ghost targets

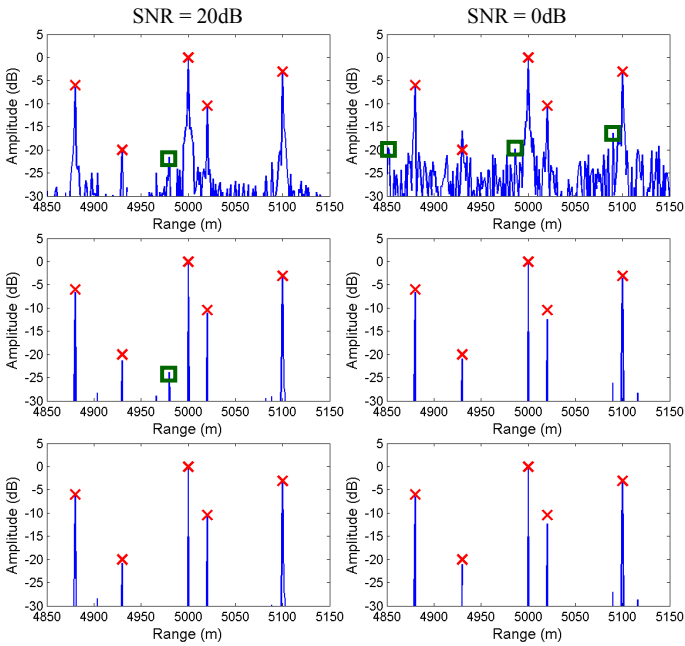


Fig. 2. Simulated 1-D radar range profiles with 2-bit quantized data under SNRs of 20 and 0dB. The first row shows the results obtained by MF, the second row shows the results obtained by  $l_1$ -regularization, and the third row shows the results obtained by QCS-MAP. Ghost targets and artifacts are marked with green boxes.

are still visible and the target at 4930m is totally lost. The QCS-MAP method can suppress the ghost targets to a certain extent and recover all the targets, but still introduces some artifacts. By decreasing the value of  $\tau$  in (15), although the artifacts can be eliminated, the true targets are also suppressed. When SNR = 0dB, the high level noise introduces many artifacts in the recovered images, and the amplitudes of some artifacts are comparable to the true target at 4930m. We also notice that the results of  $l_1$ -regularization method and QCS-MAP are quite similar with each other in this case.

This simulation demonstrates the limitation of 1-bit quantization in radar imaging. The loss of amplitude information makes us difficult to distinguish the true weak-scattering targets from the ghost targets and other artifacts. Note that the true amplitude of the target at 4930m is 20dB lower than the largest target. This is not uncommon for radar applications since the RCS of realistic targets may vary by as much as 20 or 30dB [21].

### C. 2-bit Quantization

Previous simulation shows that it is difficult to recover the targets from 1-bit quantized data, which is mainly because the amplitude information is totally lost in 1-bit quantization. In this experiment, we evaluate the performance of 2-bit QCS in radar imaging. Compared with 1-bit quantization, 2-bit quantization gets one additional bit to record the amplitude information aside from the sign bit. The quantization thresholds and levels are generated using Lloyd-Max optimization. Fig. 2 shows the reconstructed range profiles with 2-bit quantized data. Compared with the results of 1-bit

quantization, the number of the ghost targets and artifacts are much smaller. When SNR=20dB, the ghost target at 4980 is still visible in the MF and  $l_1$ -regularization images. On the contrary, the QCS-MAP method recover all the targets accurately and suppress the ghost targets well. When SNR=10dB, both  $l_1$ -regularization and QCS-MAP produce good results in respect of accurately recovery of amplitude information and increased target-to-background ratio.

From Figs. 1 and 2, we can conclude that, the main advantage of QCS-MAP over  $l_1$ -regularization is its ability to suppress the ghost targets in high SNR situations. When SNR is low,  $l_1$ -regularization and QCS-MAP produce similar results.

### D. High Quantization Bits

Before we proceed to the experiments with 3 or more quantization bits, we first compare QCS-MAP and  $l_1$ -regularization theoretically. We rewrite the objective functions of QCS-MAP and  $l_1$ -regularization (i.e., (5) and (15), respectively) in a general form,

$$\min_{\mathbf{x} \in \mathbb{R}^{2N}} \sum_{i=1}^{2M} f_i(\mathbf{a}_i^T \mathbf{x}) + g(\mathbf{x}). \quad (17)$$

where  $g(\mathbf{x}) = \text{Const} \cdot \sum_{i=1}^N \sqrt{\mathbf{x}_i^2 + \mathbf{x}_{i+N}^2}$ , and  $f_i: \mathbb{R} \rightarrow \mathbb{R}$  is the data fidelity term making the target signal consistent with the measured data.

For  $l_1$ -regularization,

$$f_i(z) = \frac{1}{2}(z - \mathbf{y}_i)^2, \quad (18)$$

Note that in our experiments, we choose the quantized measurement vector as the measured data, i.e.,  $\mathbf{y} = \mathbf{q}$ , where  $\mathbf{q}$  is defined in (8).

For QCS-MAP

$$f_i(z) = -\ln \left[ \Phi\left(\frac{-z + \mathbf{u}_i}{\sigma}\right) - \Phi\left(\frac{-z + \mathbf{l}_i}{\sigma}\right) \right], \quad (19)$$

where  $\mathbf{u}$  and  $\mathbf{l}$  are defined in (9).

By substituting  $\Phi(z)$  with (12), we can rewrite (19) as

$$f_i(z) = -\ln \left[ \frac{1}{\sqrt{2\pi}} \int_{\frac{-z + \mathbf{l}_i}{\sigma}}^{\frac{-z + \mathbf{u}_i}{\sigma}} \exp\left(-\frac{t^2}{2}\right) dt \right] \quad (20)$$

Based on the mean value theorem of integrals, there exists some  $c$  in  $[\mathbf{l}_i, \mathbf{u}_i]$  such that

$$\begin{aligned} f_i(z) &= -\ln \left\{ \frac{1}{\sqrt{2\pi}} \frac{\mathbf{u}_i - \mathbf{l}_i}{\sigma} \exp \left[ -\frac{1}{2} \left( \frac{-z + c}{\sigma} \right)^2 \right] \right\} \\ &= -\ln \left( \frac{\mathbf{u}_i - \mathbf{l}_i}{\sqrt{2\pi}\sigma} \right) + \frac{1}{2\sigma^2} (z - c)^2 \end{aligned} \quad (21)$$

When the number of quantization bits is large, the interval of  $[\mathbf{l}_i, \mathbf{u}_i]$  is small (here we assume neither  $\mathbf{l}_i$  or  $\mathbf{u}_i$  approaches infinity), thus

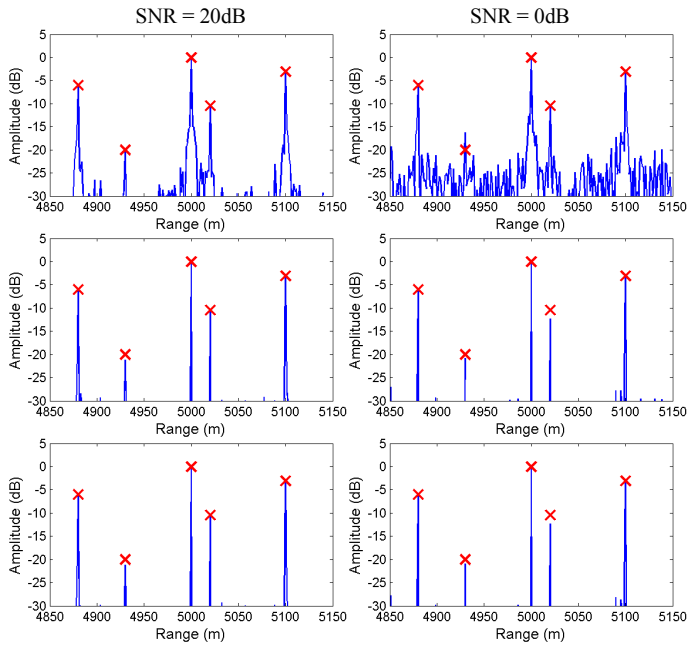


Fig. 3. Simulated 1-D radar range profiles with 3-bit quantized data under SNRs of 20 and 0dB. The first row shows the results obtained by MF, the second row shows the results obtained by  $l_1$ -regularization, and the third row shows the results obtained by QCS-MAP.

$$f_i(z) \approx -\ln\left(\frac{\mathbf{u}_i - l_i}{\sqrt{2\pi}\sigma}\right) + \frac{1}{2\sigma^2}(z - \mathbf{q}_i)^2 \quad (22)$$

which has the same form as (18) except for a constant (i.e., the first term) and a scaling factor (i.e.,  $\sigma^{-2}$ ). If the measurement is out of the range of the quantizer, then the interval of  $[l_i, \mathbf{u}_i]$  is infinity and the approximation in (22) does not hold any longer.

In conclusion,  $l_1$ -regularization and QCS-MAP is approximately equivalent to each other provided the following two conditions are met: first, the number of quantization bits is large; second, the saturation error is small, which requires most of the measurements lie in the range of the quantizer. Fig. 3 shows the results of 3-bit quantization. We can see from fig. 3 that the results of  $l_1$ -regularization and QCS-MAP are nearly the same, which further justifies the above analysis.

#### IV. CONCLUSION AND DISCUSSION

In this paper, we have studied radar imaging with low-bit quantized data based on QCS. The QCS radar imaging model is derived in the MAP estimation framework. We also compare the proposed method with  $l_1$ -regularization method under different bits of quantization and noise levels. For coarsely quantized data like 1-bit and 2-bit quantization, the simulation results show that the QCS method outperforms the  $l_1$ -regularization method in high SNR situations. Under high resolution quantization situation, both theoretical analysis and simulation results show that, when the saturation error is small, QCS and  $l_1$ -regularization are approximately equivalent.

#### REFERENCES

- [1] D. L. Donoho, "Compressed sensing," *IEEE Trans. Inf. Theory*, vol. 52, pp. 1289-1306, 2006.
- [2] E. J. Candes and T. Tao, "Near-Optimal Signal Recovery From Random Projections: Universal Encoding Strategies?," *IEEE Trans. Inf. Theory*, vol. 52, pp. 5406-5425, 2006.
- [3] E. J. Candes, J. Romberg, and T. Tao, "Robust uncertainty principles: exact signal reconstruction from highly incomplete frequency information," *IEEE Trans. Inf. Theory*, vol. 52, pp. 489-509, 2006.
- [4] E. J. Candes, "The restricted isometry property and its implications for compressed sensing," *C. R. Math. Acad. Sci. Paris, Ser. I*, vol. 346, pp. 589-592, May 2008.
- [5] J. Ender, "A brief review of compressive sensing applied to radar," in 2013 14th International Radar Symposium (IRS), 2013, pp. 3-16.
- [6] M. Tello Alonso, Lo, x, P. pez-Dekker, Mallorqui, and J. J., "A Novel Strategy for Radar Imaging Based on Compressive Sensing," *IEEE Trans. Geosci. Remote Sens.*, vol. 48, pp. 4285-4295, 2010.
- [7] V. M. Patel, G. R. Easley, D. M. Healy, and R. Chellappa, "Compressed Synthetic Aperture Radar," *IEEE J. Sel. Top. Appl. Earth Observ.*, vol. 4, pp. 244-254, 2010.
- [8] J. N. Laska, P. T. Boufounos, M. A. Davenport, and R. G. Baraniuk, "Democracy in action: Quantization, saturation, and compressive sensing," *Appl. Comput. Harmon. Anal.*, vol. 31, pp. 429-443, 2011.
- [9] L. Jacques, K. Degraux, and C. De Vleeschouwer, "Quantized Iterative Hard Thresholding: Bridging 1-bit and High-Resolution Quantized Compressed Sensing," arXiv preprint arXiv:1305.1786, 2013.
- [10] A. Zymnis, S. Boyd, and E. Candes, "Compressed Sensing With Quantized Measurements," *IEEE Signal Process. Lett.*, vol. 17, pp. 149-152, 2010.
- [11] Y. Zai, X. Lihua, and Z. Cishen, "Variational Bayesian Algorithm for Quantized Compressed Sensing," *IEEE Trans. Signal Process.*, vol. 61, pp. 2815-2824, 2013.
- [12] P. T. Boufounos and R. G. Baraniuk, "1-Bit compressive sensing," in 42nd Annual Conference on Information Sciences and Systems, 2008. CISS 2008., 2008, pp. 16-21.
- [13] L. Jacques, J. N. Laska, P. T. Boufounos, and R. G. Baraniuk, "Robust 1-Bit Compressive Sensing via Binary Stable Embeddings of Sparse Vectors," *IEEE Trans. Inf. Theory*, vol. 59, pp. 2082-2102, 2013.
- [14] Y. Ming, Y. Yi, and S. Osher, "Robust 1-bit Compressive Sensing Using Adaptive Outlier Pursuit," *IEEE Trans. Signal Process.*, vol. 60, pp. 3868-3875, 2012.
- [15] X. Dong and Y. Zhang, "A MAP Approach for 1-bit Compressive Sensing in Synthetic Aperture Radar Imaging," *IEEE Geosci. Remote Sens. Lett.*, vol. 12, pp. 1237-1241, 2015.
- [16] G. Alberti, G. Franceschetti, G. Schirinzi, and V. Pascasio, "Time-domain convolution of one-bit coded radar signals," *Proc. Inst. Elect. Eng. F.*, vol. 138, pp. 438-444, 1991.
- [17] R. Gribonval, V. Cevher, and M. E. Davies, "Compressible Distributions for High-Dimensional Statistics," *IEEE Trans. Inf. Theory*, vol. 58, pp. 5016-5034, 2012.
- [18] A. Chambolle and T. Pock, "A First-Order Primal-Dual Algorithm for Convex Problems with Applications to Imaging," *J. Math. Imag. Vis.*, vol. 40, pp. 120-145, 2011.
- [19] D. E. Bellasi, L. Bettini, C. Benkeser, T. Burger, H. Qiuting, and C. Studer, "VLSI Design of a Monolithic Compressive-Sensing Wideband Analog-to-Information Converter," *IEEE J. Emerg. Sel. Top. Circuits Syst.*, vol. 3, pp. 552-565, 2013.
- [20] A. Beck and M. Teboulle, "A Fast Iterative Shrinkage-Thresholding Algorithm for Linear Inverse Problems," *SIAM Journal on Imaging Sciences*, vol. 2, pp. 183-202, 2009.
- [21] M. Skolnik, *Radar Handbook*, Third Edition: McGraw-Hill Education, 2008.

# Traffic Scheduling Algorithm for Wireless Mesh Networks based Defense Networks Incorporating Centralized Scheduling Architecture

Sidharth Shukla and Vimal Bhatia

Signals and Software group

Discipline of Electrical Engineering

Indian Institute of Technology, Indore

Indore – 453441, India

Email: [shukla.sidharth@gmail.com](mailto:shukla.sidharth@gmail.com), [vbhatia@iiti.ac.in](mailto:vbhatia@iiti.ac.in)

**Abstract-** Wireless mesh networks (WMN) are the networks of the future which are flexible, easy to deploy and can support high data rate triple play (voice, video and data) services. WMNs are ideal for future defense networks. WMN can operate on multi protocols ranging from WiFi, WiMax and LTE. To enable the support of high data rate services WMN should incorporate optimum traffic scheduling algorithms which will improve the performance of the WMN in highly loaded traffic scenarios for a combat communication network. In this paper, we propose an efficient traffic scheduling algorithms to improve the overall blocking probability of the WMN employed for defense networks and the same is substantiated by the simulation results.

**Keywords-** WiFi, WiMax, LTE, NGN, TE, CoS.

## 1. INTRODUCTION

Future wireless networks will incorporate technologies like WiFi, WiMax and Long Term Evolution (LTE) in the form of Wireless Mesh Networks (WMNs) to provide Next Generation Networks (NGN) which will be flexible, easy to deploy and which will guarantee high data rates to the end users to support triple play services. WMNs are self-configured and self-organized in a dynamic manner, automatically establishing an ad-hoc network with the nodes in the network and also maintains connectivity in the mesh. The advantages offered by WMNs are easy network maintenance, low up-front cost, reliable service coverage, robustness, etc. WMNs comprises of mesh routers and mesh clients [1]. Because of multi-hop communication, a mesh router achieves more coverage with low transmission power. Since the mobility is minimal, mesh routers constitute mesh backbone which is needed by the mesh clients. Mesh router's function of behaving as bridge/gateway results in desegregation of WMNs with various other types of networks. Mesh routers are also responsible for networking in a mesh amidst mesh clients and mesh routers [1]. Wireless Network Interface Cards (NICs) are used by the established nodes to get connected to WMNs in a direct manner through wireless mesh routers.

WMNs have undergone and are also undergoing rapid commercialization in other application scenarios such as community networking, metropolitan high speed area networks, building automation, enterprise networking and broadband home networking. WMN are ideal and can be used for defense networks.

The entire paper is divided into six sections. The section II deals with WMN based Defense networks. Traffic scheduling in WMN is explained in section III. Section IV explains the proposed TSA in detail. Simulation results and their analysis is given in section V.

## II. WMN BASED DEFENSE NETWORKS

The inherent requirement for defense networks is to be reliable, flexible, mobile and should be able to transport real time voice, data and video services. Further due to tactical communication requirements of defense operations, the network should be adaptive to changes in the defense operations and should be established in no time. Due to the above, WMN based defense networks are the ideal networks for deployment in defense communication. To support high data rates the WMN based defense networks incorporate futuristic technologies like LTE. Such networks can provide failsafe communication for defense networks. However, during the time of actual operations we may find overloading of user traffic in these networks and these networks may be prone to congestion in certain subnets.

The primary aim of WMN based defense networks is to ensure that these networks deliver at critical junctures of defense operations and to optimally utilize the bandwidth during overloaded traffic conditions. Further there is an inherent requirement of WMN based defense networks to prioritize traffic according to the requirement of defense operations, which may be a problem dynamic in nature. The above requirement can be fulfilled by incorporating a new traffic scheduling algorithm which should optimally utilize the limited bandwidth of WMN based defense networks. The proposed Traffic Scheduling Algorithm (TSA) in this paper shall effectively incorporate class of service quantization of connection requests and prioritization of service requests to ensure lesser blocking probability in WMN based defense networks. A brief overview of traffic scheduling in WMN is given in the next section for completeness.

## III. TRAFFIC SCHEDULING IN WMN

The most challenging and the important issue in WMN at the MAC (Media Access Control) layer is transmission scheduling. Efficient utilization of the channel is determined

by the scheduling of transmission of traffic at the MAC layer. In a scheme of scheduling, a mechanism of scheduling is regarded to attain a goal, e.g., maximizing the throughput of the network [1].

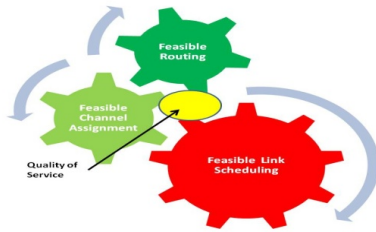


Fig. 1. Integrated Problem of Scheduling in WMN

However, scheduling in case of wireless networks (which are multi-hop) is a problem which is highly integrated, as shown in Figure 1, having many sub-problems such as finding communication path (problem of feasible routing), efficient usage of wireless channels which are available (feasible assignment of channel) and activation of link which are free of interference (feasible scheduling of links). The scheduling problem may have to take into account application constraints, like providing Quality of Service (QoS).

There has been various research works in scheduling algorithms proposed recently. The Cluster Header Load Balancing (CHLB) algorithm has been proposed that guarantees the QoS for different data streams through cross-layer design to accomplish the load balance without bringing heavy extra-load [2]. RAILoB in WMNs is set out to improve traffic performance. This algorithm aims at providing traffic migration without the need for the mesh router migration [3]. In a typical scheduling scheme, a scheduling mechanism for WMN is considered to achieve a goal, i.e. maximizing the network throughput [4]. A multi-channel WMN architecture (called Hyacinth) [5] equips each mesh network node with multiple 802.11 NICs. Differentiated Services (DiffServ) to the wireless mesh backbone has been researched [6]. Studies on classification of scheduling algorithms in WMN have also been done [7]. The strategy to optimize the radio resource allocation process in LTE Advance networks to improve network throughput has also been researched [8].

The proposed Traffic Scheduling Algorithm utilizes the parameters Class of Service (CoS), number of Hops, Data rate required and Tolerable Delay required by a traffic request, in a simplistic but effective manner as explained in next section.

#### IV. TSA ALGORITHM

Wireless networks require efficient scheduling algorithms to maximize network throughput. The various parameters affecting the performance are described in details, followed by the proposed TSA architecture and functionality is presented below.

##### A. Differentiated Services for Wireless Mesh Backbone

Scalability of WMN is a concern due to the per-flow reservation information and heavy signalling overhead. In edge

WMN routers for DiffServ, packets can be classified into a limited number of service classes. In a core router, packets from different classes are aggregately differentiated by different Per-Hop Behaviours (PHBs). Hence, no per-flow information is kept in the core network, which makes differentiated services scalable. Research on DiffServ has mainly focused on the wireline Internet. DiffServ in wireline networks is well researched and introduction of DiffServ in wireless mesh backbone is available [6].

##### B. Class of Service Quantization of Traffic

The aim is to prioritize service traffic into various classes of service so as to guarantee Service Level Agreement (SLA). This prioritization will ensure that during congestion of subnet of the wireless network the lower priority service traffic is dropped and the higher priority service traffic is transported. To achieve the above the proposed algorithm classifies the service/user traffic into the following three classes:-

- a) EF traffic (S = 3): for real time traffic (for voice and live video applications).
- b) AF traffic (S = 2): for non real time traffic (for compressed video and transactional data traffic).
- c) BE traffic (S = 1): for delay tolerant traffic (transfer of files).

The values of the CoS ranges from 3 to 1 as defined above, 3 being the highest value and 1 being the lowest value. The SLAs with the user will be based on the above type of classification of traffic and will provide the necessary Guarantee of Service (GoS). The above classification functionality will be performed by a traffic prioritizer called “CoS Prioritizer” which will be present at each user/service interface in the network.

##### C. Algorithm Architecture

The various components of the architecture are Request Handler, CoS Quantizer, Request Prioritizer, bidirectional wireless links and control links. The detailed architecture for the above components for implementation of the TSA algorithm is shown in Figure 2.

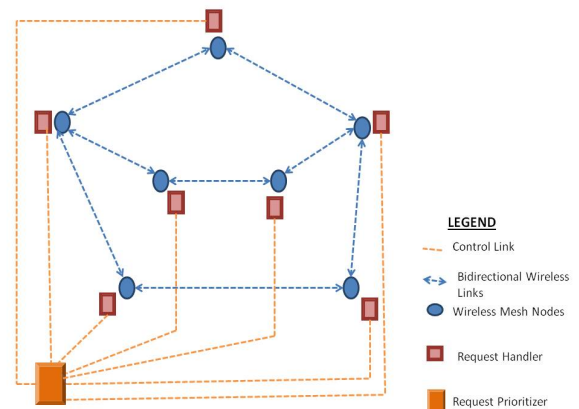


Fig. 2. Architecture for TSA.

#### D. Algorithm Functionality

An algorithm has been proposed to improve the utilization of network resources by scheduling of requests in WMN. The proposed scheduling algorithm will involve the following processes as described below:

1) Handling of Requests: Various metrics of service requests directed towards a WMN node will be extracted by a Request Handler present at every node. The following metrics will be extracted from each service request, for further providing this information to a central Request Prioritizer.

- a) Hop count (H): Initially the source and destination WMN node id no's of service request is extracted. Thereafter, from the network graph, created by existed routing algorithm like Djisktra / Bellman Ford, the number of Hops required to traverse in a WMN by each service request can be found out.
- b) Tolerable Delay (D): The delay in time a request can tolerate inside the WMN for the service to be accepted at the destination without the degradation in QoS.
- (c) Required Data Rate (DR): The minimum data rate required by the service requests throughout all links in the WMN.
- (d) Service Priority (S): This is a classification of the type of service request that a client to the WMN is desirous to transmit. The various types of service classification will be as given in sub section B of section IV.

The above four metric parameters will be provided by the Request Handler located at each WMN node to the central Request Prioritizer module of the WMN on control channel for further processing according to following steps:

**Step-1:** Create a requirement matrix for all the requests in the network as shown in Table 1.a.

TABLE 1.A: REQUIREMENT MATRIX

Ser No	Source Id	Destination Id	No of Hops (H)	Data Rate Req. (in Mbps)	CoS Req. (S)	Tolerable Delay (in msec)
1	001	003	2	0.2	2	0.45
2	002	005	3	0.3	1	0.30
3	001	004	3	0.4	3	0.50
4	002	006	4	0.5	2	0.40
5	003	006	3	0.6	2	0.35
6	005	002	3	0.7	1	0.25

**Note:** The values given in the matrix are arbitrary to demonstrate the functionality of the algorithm.

**Step-2:** After obtaining the above requirement matrix, the Request Prioritizer will calculate the weight (W) for each request by using the eq. (1) below:-

$$W = H/H_{max} + 1/S + DR / M_d + D \quad (1)$$

The eq. (1) has been devised with the logic that the weight of a request (W) is directly proportional to the fraction of network resources used, assuming that the request is serviced. This

capacity utilization factor, which is coined as Weight (W) of the request, is calculated with the summation of terms in eq. (1). The explanation of the terms in eq. (1) is as given below:

- a) **First term of eq. (1)** – gives the ratio of number of hops used (H) by the request with respect to the maximum number of hops in the network (Hmax).
- b) **Second term of eq. (1)** – gives the value of CoS (S) assigned to the request with respect to the highest value of CoS, which is 3 as explained in sub section B of section IV.
- c) **Third term of eq. (1)** - Fraction of Data Rate (DR) utilized by the request with respect to the maximum data rate engineered in the network ( $M_d$ ), which has been assumed to be 7 megabits per second.
- d) **Fourth term of eq. (1)** – The delay in time a request can tolerate inside the WMN for the service to be accepted at the destination without the degradation in the required QoS.

At each node the weighted service requests will be arranged in the order of increasing weights in the form of a queue and the requests with lower Weights will be serviced first. The Weight (W) values for all the entries in the requirement matrix in Table 1.a will be calculated and a new weighted requirement matrix will be created as shown in Table 1.b.

TABLE 1.B: WEIGHTED REQUIREMENT MATRIX

Ser No	Source Id	Destination Id	No of Hops (H)	Data Rate Req. (in Mbps)	CoS Req. (S)	Delay tolerant (in msec)	Weight (W)
1	001	003	2	0.2	2	0.45	1.55
2	002	005	3	0.3	1	0.30	2.20
3	001	004	3	0.4	3	0.50	1.79
4	002	006	4	0.5	2	0.40	2.15
5	003	006	3	0.6	2	0.35	1.90
6	005	002	3	0.7	1	0.25	2.35

Note: Hmax has been chosen to be 4 hops and  $M_d$  has been chosen as 7 megabits per second (Mbps) to demonstrate the functionality of the algorithm.

**Step-3:** The entries in the weighted requirement matrix at Table 1.b will be rearranged in ascending order of the Weights (W), such that light weighted requests are higher on the table and heavier weighted requests are at the bottom of the table. Resulting that a new table will be created, which will be called as Prioritized Queuing Table as shown in Table 2.

TABLE 2: PRIORITIZED QUEUEING TABLE (FOR NODE 1)

Ser No	Source Id	Destination Id	No of Hops (H)	Data Rate Req. (in Mbps)	CoS Req. (S)	Delay tolerant (in sec)	Weight (W)
1	001	003	2	0.2	2	0.45	1.55
3	001	004	3	0.4	3	0.50	1.79
5	003	006	3	0.6	2	0.35	1.90
4	002	006	4	0.5	2	0.40	2.15
2	002	005	3	0.3	1	0.30	2.20
6	005	002	3	0.7	1	0.25	2.35

**Step-4:** The Prioritized Queuing Table (for each node), Table 2 from Step 3 will be used by the Request Prioritizer for assignment of requests to the available links. The top entry of Table 2 will be assigned a channel for the destination node if available. This process will be repeated for the next entry of Table 2 till there are no entries left in Table 2. Step-4 will be followed for all the nodes in the network architecture. The complexity of the Algorithm is of the order  $O(1)$ .

## V. RESULTS AND ANALYSIS

The architecture for simulation of TSA is in the geographical area near our research lab and is given as Figure 3.

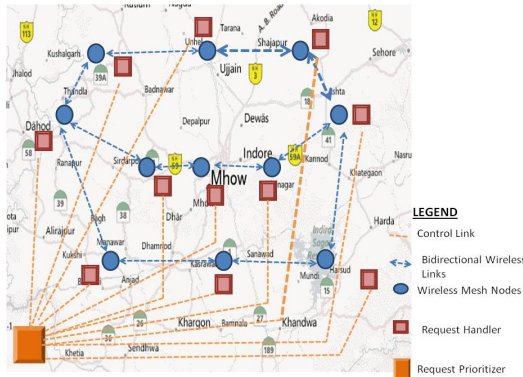


Fig. 3. Architecture for simulation of TSA

The architecture consists of 11 wireless nodes which form part of a WMN based Defense network and 14 bidirectional wireless links which connect the wireless nodes as given in Figure 3. The architecture has one central Request Prioritizer connected to each wireless node by a control link to the Request Handler collocated at each wireless node. The control link is used for transmission of control signals from Request Prioritizer to Request Handler and vice versa. Each node is provided with a Request Handler, which regularly updates its state information to the central Request Prioritizer via the control link. A single Routing Controller is co-located with the central Request Prioritizer and is responsible for routing of requests in the WMN based Defense network. The following assumptions have been made for the simulation process:

- The connection requests are random in nature and are established on a process which is Poisson in nature. The times of arrival between two events of connection requests in succession, follow a distribution which is exponential in nature.
- The maximum data rate of each of the bidirectional wireless link has been assumed to be 7 megabits per second. The data rate requests have been chosen as multiples of 0.1 megabits per second.
- The packets are generated randomly among all possible source – destination pairs and a request for connection is said to be not serviced or rejected if it is not dispensed with the available network resources.
- The performance of the proposed TSA is measured in terms of Blocking Probability (BP) where lower the BP, better

the performance of the network. The BP [9] has been plotted with respect to increasing Traffic Intensity (TI) measured in Erlangs [9], both in linear scale. TI is calculated for the entire wireless network and is directly proportional to increase in number of users of the network. BP is directly proportional to the number of packets lost in the network.

e) The number of packets generated by each node into the network has been slowly increased in the simulation process to upto 5000 packets, generated from each node into the network. Hence the resulting overall increase in the TI of the WMN based Defense network.

(f) The simulations have been done taking into consideration the LTE eNodeB as a wireless node. The TSA algorithm has been evaluated taking into consideration a LTE based WMN.

The simulation has been carried out in two phases as described below:

### A. PHASE I

In the first phase of the simulation process, the functionality and performance of TSA algorithm was evaluated in isolation, without incorporating any routing algorithm. The simulation has been carried out in the LTE based WMN Defense network architecture, which is the geographical area in the neighborhood of our research lab, as shown in Figure 3. The simulation was carried out in two parts. In the first part, the network was simulated with ordinary traffic (without incorporating any traffic grooming / Traffic Engineering (TE) algorithm). In the second part, the simulation in the WMN based Defense network architecture of Figure 3 has been carried out incorporating the TSA. The BP has been plotted with respect to increasing TI, for a single frequency per bidirectional wireless link. The simulation was next carried out with two, three and four frequencies in each of the bidirectional wireless links. The simulation plots of BP with respect to TI for one, two, three and four frequency per bidirectional links for both ordinary traffic and groomed traffic (incorporating TSA) is shown as a composite figure in Figure 4.

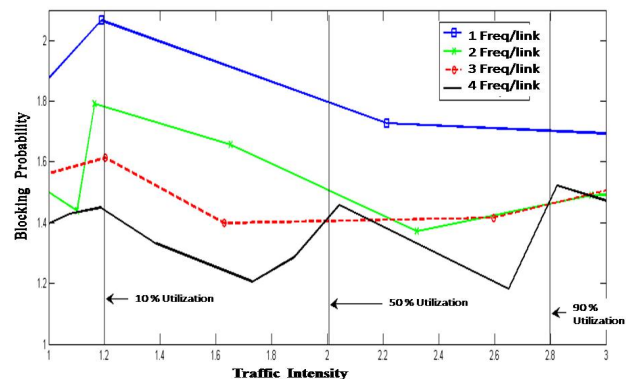


Fig. 4. Comparison of BP v/s TI curves for 1/2/3/4 Frequencies/ Bidirectional link of non-TSA with TSA normalized to X- Axis.

From the simulation results of Figure 4 we can infer the following:

a) In Figure 4, the TSA curve has been kept in the X-axis that is given a value of 1, and the non-TSA curves are plotted to this normalized TSA case (X-Axis). Hence we see that there are four curves for frequencies ranging from 1, 2, 3 and 4. The improvement can be seen as how many times the BP of non-TSA case is higher than TSA case kept at a value of 1 for increasing frequency values of 1, 2, 3 and 4 frequencies per bidirectional link in the simulation architecture of Figure 4.

b) We observe that when the frequency is 1 per bidirectional link the non-TSA case has nearly 2 times higher BP than TSA case. Further for 2 frequencies per bidirectional link the non-TSA case has nearly 1.8 times higher BP than TSA case. For 3 frequencies per bidirectional the non-TSA case has nearly 1.6 times higher BP than TSA case and for 4 frequencies per bidirectional the improvement value comes down to 1.4.

c) There is a substantial improvement in the connection BP performance of the network while incorporating TSA algorithm. The improvement reduces as the number of frequencies increase in each bidirectional wireless link. This is in accordance to the established fact, that TE is less effective when the network is underutilized [10].

## B. PHASE 2

In the second phase of the simulation process, the TSA has been combined with the dynamic OSPF-TE routing algorithm and its performance evaluated by comparing it with a dynamic OSPF-TE routing model without TSA. The BP has been plotted with respect to increasing TI for four frequencies per bidirectional wireless link in the simulation architecture of Figure 3, and the result is shown in Figure 5.

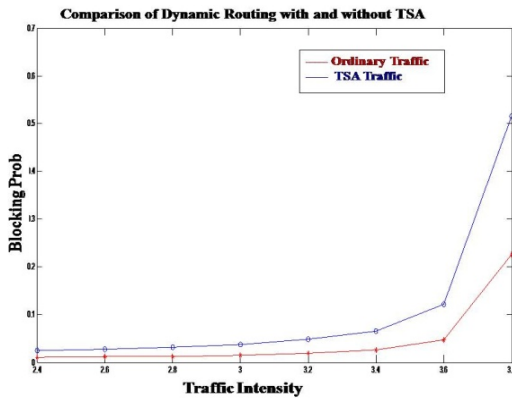


Fig. 5. Comparison of Dynamic Routing with and without TSA, BP v/s TI

From the simulation result of Figure 5, we can infer the following:

a) Dynamic routing (OSPF-TE) incorporating TSA has a better performance in terms of connection BP when compared to dynamic routing (OSPF-TE) with ordinary traffic (without TSA). There is a substantial improvement in connection BP using TSA algorithm.

b) The improvement in connection BP is most effective when the WMN based defense network is loaded with greater than 90% of input user traffic.

## VI. CONCLUSION

Wireless networks of the future are anticipated as a convergence of various kinds of technologies which are wireless, for example Cellular Technologies (LTE), Wireless Metropolitan Area Networks (WMANs), Wireless Local Area Networks (WLANs), Wireless Sensor Networks (WSNs), and conventional wired networks. WMN based Defense networks will incorporate such high data rate wireless technologies to ensure effective and adaptive robust communication. Though the users will be unknown to the particular underlying network which is being utilized by the users' applications, the networks must be capable of providing the users with assured Quality of Service (QoS) even in high traffic conditions. The simulation results and their analysis in Section V have clearly demonstrated that the proposed TSA has substantially improved the BP performance of the WMN based Defense network. Hence, there is a requirement to incorporate efficient traffic scheduling algorithm like the proposed TSA in such networks to facilitate the utilization of wireless resources optimally. The efficient TSA tends to reduce delay, packet loss and promote the efficient usage of available bandwidth, even at high traffic scenarios, in the WMN based Defense network.

## ACKNOWLEDGEMENT

We thank IIT Indore for all the support for this research work.

## REFERENCES

- [1] I. F. Akyldiz, X. Wang, and Kiyon, "A Survey on Wireless Mesh Networks" *IEEE Radio Communications*, vol. 43, pp. S23-S30, September 2005.
- [2] J. Zhong, R. Hu, X. Zhu, "A Novel Load-balancing Algorithm for QoS Provisionings over 802.11s Wireless Mesh Networks" *WiCOM*, pp. 1-4, 2010.
- [3] V.C.M. Borges, E. Dimitrov, M. Cuervo and E. Monteiro, "RAILOB - A Routing Algorithm for Inter-cluster Load Balancing in Wireless Mesh Networks" *IEEE Consumer Communications and Networking Conference*, pp. 904-909, 2012
- [4] V. Gabale, B. Raman, P. Dutta, and S. Kalyanraman, "A Classification Framework for Scheduling Algorithms in Wireless Mesh Networks", *IEEE Communications Surveys & Tutorials*, vol. 15, no. 1, pp. 199-222, 2013.
- [5] A. Raniwala, T. Chiueh, "Architecture and Algorithm for an IEEE 802.11- Based Multichannel Wireless Mesh Network", *INFOCOM*, vol. 3, pp. 2223-2234, 2005.
- [6] H. Jiang, W. Zhuang, X. Shen, A. Abdrabou, and P. Wang, "Differentiated Services for Wireless Mesh Backbone", *IEEE Communications Magazine*, vol. 44, no. 7, pp. 113-119, July 2006.
- [7] V. Gabale, B. Raman, P. Dutta, and S. Kalyanraman, "A Classification Framework for Scheduling Algorithms in Wireless Mesh Networks", *IEEE Communications Surveys & Tutorials*, vol. 15, no. 1, first quarter 2013.
- [8] A. Tassi, C. Khirallah, D. Vukobratovic, F. Chiti, J. S. Thompson, R. Fantassi, "Resource Allocation Strategies for Network-Coded Video Broadcasting Services Over LTE-Advanced", *IEEE Transactions of Vehicular Technology*, vol. 64, no. 5, pp. 2186-2192, Jan 2015.
- [9] D. P. Bertsekas, R. G. Gallager, "Data Networks", 2nd edition, Prentice Hall, 1992.
- [10] A. Farrel and I. Bryskin, *GMPLS Architecture and Applications*, Elsevier, 2006.

# Outage Analysis of OFDM based AF Cooperative Systems in Selection Combining Receiver over Nakagami- $m$ fading channels with Nonlinear Power Amplifier

Nagendra Kumar and Vimal Bhatia  
Signals and Software group  
Discipline of Electrical Engineering  
Indian Institute of Technology Indore, India  
Email: phd1301202008@iiti.ac.in, vbhatia@iiti.ac.in

**Abstract**—In this paper, we investigate the performance of orthogonal frequency division multiplexing (OFDM) based amplify-and-forward (AF) cooperative relaying systems over independent and identically distributed (i.i.d) Nakagami- $m$  fading channels. Specifically, we derive a closed-form expression for lower bound of outage probability by using selection combining (SC) scheme at the receiver. A nonlinear power amplifier (PA) is considered at the relay which introduces the nonlinear distortions. We present simulation and numerical results to validate the theoretical analysis, and demonstrates the impact of nonlinearity of PA parameters over outage probability for different values of threshold signal-to-noise ratio (SNR) at various mean SNR levels.

## I. INTRODUCTION

In today's world, the demand from wireless communications to provide high bit rate and coverage in hostile environments/terrains is of prime importance for defence and natural security. Cooperative communication systems have ability to enhance the coverage and to increase the capacity of wireless communication link by exploiting the spatial diversity without the need of multiple antennas [1]. The basic idea of cooperative communication is studied in details in [2], [3], [4]. Several cooperative relaying protocols have been presented in literature, of which two are most common, namely; decode-and-forward (DF) where each relay forwards the detected version of incoming signal, and amplify-and-forward (AF) where each relay forwards the amplified version of incoming signal [5]. The use of AF scheme is widespread due to its low complexity and it provides better end-to-end performance than other relaying schemes. When the relays have limited signal processing resources, the AF is more preferred relaying protocol. The performance of AF relaying technique is studied extensively in [6], [7], [8], [9]. There are different kinds of diversity combining technique, used at the receiver to combine the multiple replicas of the signal to improve the strength of the signal. In literature, maximal ratio combining (MRC), equal gain combining and selection combining (SC) are basically used, of which last one is the least complex technique that maintain the full diversity gain by using less amount of required resources [10], [11], [12].

On the other hand, the orthogonal frequency division multiplexing (OFDM) plays an important role in broadband

communications due to its ability to mitigate the intersymbol interference (ISI), intercarrier interference (ICI) and provide high spectral efficiency [13]. OFDM is the key element of many wireless communication standards such as IEEE 802.11a, IEEE 802.16, IEEE 802.22, third generation project (3GPP) long-term evolution (LTE) and digital video broadcasting [14].

High peak-to-average power ratio (PAPR) is characterized as one of the major drawback of the signals at the output of the OFDM block [14], [15]. If a high input back-off (IBO) is not used, a high PAPR level is the main reason for introducing nonlinearities in the received signals, which come from the saturated operation of PAs [16]. These nonlinear distortions severely affect the receiver performance.

In non-cooperative communications, high PAPR is an important issue in uplink due to cheaper equipments and power constraints of the user equipments. However, in cooperative relay systems, high PAPR becomes more significant issue in the downlink due to the presence of nonlinear power amplifier at the relay, when relay nodes may be mobile users or small stations [16], [17], [18], [19].

Currently, there is a growing interest in OFDM based AF cooperative relaying systems in which most of the work focuses on the performance analysis of linear PA at relay nodes. Only few works have investigated the effects of nonlinear distortion of the PA on the performance of cooperative communication systems. In [17] and [18], performance of outage probability in AF cooperative OFDM system with nonlinear PA have been derived for MRC and relay selection, respectively. In [19], the cancellation techniques of nonlinear PA distortion in cooperative OFDM based AF relay networks are proposed. In [16], closed-form expressions of the outage probability and ASER in OFDM based AF relaying system with nonlinear PA has been investigated. Bit error rate (BER) probability expressions are derived for an OFDM based AF cooperative relaying networks in [20], assuming nonlinear PAs at both of the base station and relay node. In [21], performance of the BER in OFDM based AF cooperative systems is proposed, considering Doppler effect impairments and high PA effects at both of the base stations and relay. In [22], a closed-form expression of the outage probability

is derived with the effects of nonlinear PA distortions in AF cooperative OFDM system using moment generating function (MGF) approach.

To the best of authors knowledge, in literature, only frequency selective Rayleigh fading channel has been considered for performance analysis in the case of nonlinear PA. In this paper, we consider a more general distribution model as frequency selective Nakagami- $m$  fading channels to derive a closed-form expression for the lower bound of outage probability approximating the instantaneous SNR at the SC receiver output.

Rest of the paper is organized as follows: In section II, system model considered for the analysis is described. The analysis of outage probability is presented in section III. In section IV, numerical and simulation results are discussed. Conclusions are provided in section V.

## II. SYSTEM MODEL

In this paper, we consider a cooperative OFDM system model with AF relaying scenario which is shown in Fig. 1. This system model consists of source node ( $S$ ) that communicates with the destination node ( $D$ ) through the direct link  $S \rightarrow D$  and an indirect link  $S \rightarrow R \rightarrow D$  where  $R$  denotes the relay. Source, relay and destination node, each consists of one transmitting and one receiving antenna. All communication between nodes operate in half-duplex mode and all the nodes are synchronized at symbol level. The communication occurs in two orthogonal times slots. In first time slot,  $S$  transmits the signal towards the  $R$  and  $D$ , simultaneously, and in the second time slot,  $R$  amplify the received signal and send it towards  $D$ . At the receiver, one signal is selected by using SC scheme which have higher SNR.

All the wireless channels are assumed as independent frequency selective Nakagami- $m$  fading channels and the length of the OFDM cyclic prefix is higher than or equal to the maximum multipath delay of all the wireless channels. All the subcarriers of the source and relay consists of same transmission power  $P_s$  and  $P_r$ , respectively. For downlink transmission, the source comprise of a linear PA while the relay comprise of a nonlinear PA. This consideration is done, since the source is a base station which have much less power constraint and the relay is a small station which have higher power constraint. It is also assumed that the channel state information (CSI) of all links is present at  $D$ , and CSI for SR link is present at  $R$ .

In this paper, we consider the system model which consists of a nonlinear PA at the relay node and this PA is modeled by a soft clipper as discussed in [17], [16], [23]. Accordingly, the end-to-end SNR at the SC receiver is given as

$$\gamma_n^{SC} = \max(\gamma_n^{SD}, \gamma_n^{SRD}), \quad 1 \leq n \leq N \quad (1)$$

in which  $N$  represents the number of subcarriers,  $\gamma_n^{SD} = |h_n^{SD}|^2 P_s / \sigma_\eta^2$  is the instantaneous SNR of the  $n^{th}$  subcarrier of  $S \rightarrow D$  link, where  $h_n^{SD}$  and  $\sigma_\eta^2$  represent the channel frequency response and variance of the corresponding link, respectively. Further, the instantaneous SNR of the  $n^{th}$  subcarrier for  $S \rightarrow R \rightarrow D$  link is given in [17] as

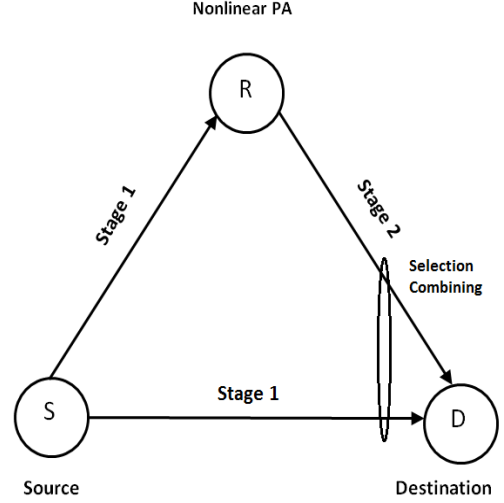


Fig. 1. Cooperative system model

$$\gamma_n^{SRD} = \frac{\gamma_n^{SR} \gamma_n^{RD} \gamma^{PA}}{\gamma_n^{SR} \gamma_n^{RD} + \gamma_n^{SR} \gamma^{PA} + \gamma_n^{RD} \gamma^{PA} + \gamma_n^{RD} + \gamma^{PA}} \quad (2)$$

with  $\gamma_n^{SR} = |h_n^{SR}|^2 P_s / \sigma_\eta^2$  and  $\gamma_n^{RD} = |h_n^{RD}|^2 P_r / \sigma_\eta^2$  are the instantaneous SNRs of the  $n^{th}$  subcarrier of  $S \rightarrow R$  and  $R \rightarrow D$  links, respectively,  $h_n^{SR}$  and  $h_n^{RD}$  stands for channel frequency response of the corresponding links. Also  $\gamma^{PA} = |K_0^R|^2 P_r / \sigma_{dR}^2$  is the instantaneous SNR at the output of the PA, where  $K_0^R$  and  $\sigma_{dR}^2$  are the complex-valued constant gain and the variance of frequency domain nonlinear distortion (where 'd' represents distortion) respectively. The closed-form expressions for  $K_0^R$  and  $\sigma_{dR}^2$  are presented in [17], [20] as

$$K_0^R = 1 - e^{(-A_{sat}^2/P_s)} + \frac{\sqrt{\pi} A_{sat}}{2\sqrt{P_s}} \operatorname{erfc}\left(\frac{A_{sat}}{\sqrt{P_s}}\right)$$

and

$$\sigma_{dR}^2 = P_s \left(1 - e^{(-A_{sat}^2/P_s)} - |K_0^R|^2\right)$$

where  $\operatorname{erfc}(\cdot)$  denotes the complementary error function and  $A_{sat}$  is the amplifier saturation amplitude.

Further, the approximated upper bound value of instantaneous SNR for  $S \rightarrow R \rightarrow D$  link given in (2) can be expressed as [17]

$$\gamma_n^{SRD} \leq \min(\gamma_n^{SR}, \gamma^{PA}, \gamma_n^{RD}) \quad (3)$$

Hence, we can write the upper bound of end-to-end SNR at SC receiver as

$$\gamma_n^{SC} = \max(\gamma_n^{SD}, \gamma_n^{\min}) \quad (4)$$

where  $\gamma_n^{\min} = \min(\gamma_n^{SR}, \gamma^{PA}, \gamma_n^{RD})$ . This approximation is reasonably accurate for low and high values of SNRs, as found in literature [6], [9].

### III. OUTAGE PROBABILITY ANALYSIS

In this section, we derived closed-form expressions for lower bound of outage probability in considered OFDM based AF relaying system with selection combining scheme. Here, the outage probability for  $n^{\text{th}}$  subcarrier can be defined as the probability that the end-to-end SNR ( $\gamma_n^{\text{SC}}$ ) falls below a predefined threshold SNR ( $\gamma_{\text{th}}$ ). Thus,

$$P_n^{\text{out, LB}}(\gamma_{\text{th}}) = \Pr(\gamma_n^{\text{SC}} < \gamma_{\text{th}}) \quad (5)$$

where  $\gamma_n^{\text{SC}} = \max(\gamma_n^{\text{SD}}, \gamma_n^{\text{min}})$ , is the upper bound SNR at the SC receiver. After substituting the value of  $\gamma_n^{\text{SC}}$  from (4) into (5), it can be also rewritten as

$$\begin{aligned} P_n^{\text{out, LB}}(\gamma_{\text{th}}) &= \Pr\{\max(\gamma_n^{\text{SD}}, \gamma_n^{\text{min}}) < \gamma_{\text{th}}\} \\ &= F_{\gamma_n^{\text{SD}}}(\gamma_{\text{th}})F_{\gamma_n^{\text{min}}}(\gamma_{\text{th}}) \end{aligned} \quad (6)$$

where  $F_X(\cdot)$  denote the cumulative distribution function (CDF) of the corresponding random variable. Here, we consider Nakagami- $m$  distribution for all channels, hence, the CDF for the  $S \rightarrow D$  link is given as  $F_{\gamma_n^{\text{SD}}}(\gamma_{\text{th}}) = \left[1 - \frac{\Gamma(m, \frac{m\gamma_{\text{th}}}{\bar{\gamma}^{\text{SD}}})}{\Gamma(m)}\right]u(\gamma_{\text{th}})$ . Also  $F_{\gamma_n^{\text{min}}}(\gamma_{\text{th}})$  can be calculated as

$$\begin{aligned} F_{\gamma_n^{\text{min}}}(\gamma_{\text{th}}) &= 1 - \left[1 - F_{\gamma_n^{\text{SR}}}(\gamma_{\text{th}})\right] \times \\ &\quad \left[1 - F_{\gamma_n^{\text{PA}}}(\gamma_{\text{th}})\right] \left[1 - F_{\gamma_n^{\text{RD}}}(\gamma_{\text{th}})\right] \end{aligned} \quad (7)$$

where  $F_{\gamma_n^{\text{SR}}}(\gamma_{\text{th}}) = \left[1 - \frac{\Gamma(m, \frac{m\gamma_{\text{th}}}{\bar{\gamma}^{\text{SR}}})}{\Gamma(m)}\right]u(\gamma_{\text{th}})$  and  $F_{\gamma_n^{\text{RD}}}(\gamma_{\text{th}}) = \left[1 - \frac{\Gamma(m, \frac{m\gamma_{\text{th}}}{\bar{\gamma}^{\text{RD}}})}{\Gamma(m)}\right]u(\gamma_{\text{th}})$  because of considering Nakagami- $m$  distributed link. Moreover, assuming PA has fixed SNR, so  $\bar{\gamma}^{\text{PA}} = \gamma^{\text{PA}}$  then its CDF is given by  $F_{\gamma_n^{\text{PA}}}(\gamma_{\text{th}}) = u(\gamma_{\text{th}} - \bar{\gamma}^{\text{PA}})$ . Also  $\Gamma(\cdot, \cdot)$  represents the incomplete gamma function [24] and  $u(\cdot)$  represents unit step function. The  $\bar{\gamma}^{\text{SD}}, \bar{\gamma}^{\text{SR}}$  and  $\bar{\gamma}^{\text{RD}}$  represent the statistical expectation of  $\gamma_n^{\text{SD}}, \gamma_n^{\text{SR}}$  and  $\gamma_n^{\text{RD}}$  respectively. Substituting the values of CDF for each link, (7) can be rewritten as

$$\begin{aligned} F_{\gamma_n^{\text{min}}}(\gamma_{\text{th}}) &= u(\gamma_{\text{th}}) - \frac{\Gamma(m, \frac{m\gamma_{\text{th}}}{\bar{\gamma}^{\text{SR}}})}{\Gamma(m)} \times \frac{\Gamma(m, \frac{m\gamma_{\text{th}}}{\bar{\gamma}^{\text{RD}}})}{\Gamma(m)} \\ &\quad u(\gamma_{\text{th}})u(\bar{\gamma}^{\text{PA}} - \gamma_{\text{th}}) \end{aligned} \quad (8)$$

Further, using CDF of  $S \rightarrow D$  link and substituting (8) into (6), we can derived the tight lower bound of outage probability for OFDM based AF cooperative system as given in (9). This expression can further be simplified as in (10). This analytical expression is used to find the numerical values of outage probability.

### IV. NUMERICAL AND SIMULATION RESULTS

This section provides the numerical results obtained from (10) and simulation results to verify correctness of our analytical approach. An OFDM based AF cooperative system is considered, where we use QPSK modulated signals,  $N = 64$  subcarriers, cyclic prefix length is 16 and frequency selective Nakagami- $m$  fading channels with 16 independent taps. Furthermore, a nonlinear PA at relay is modeled by a soft clipper (soft limiter) with  $A_{\text{sat}} = 1$  and  $P_s = P_r = 1$  which leads  $\bar{\gamma}^{\text{PA}} = 12$  dB. All channels are considered as

identical and independent with equal noise variances, hence  $\bar{\gamma}^{\text{SR}} = \bar{\gamma}^{\text{RD}} = \bar{\gamma}^{\text{SD}} = \bar{\gamma}$ .

Fig. 2 shows the comparison between lower bound and simulation results of outage probability versus mean SNR,  $\bar{\gamma}$  over Nakagami- $m$  fading channel with fading parameter,  $m = 1$  (Rayleigh fading). The outage probability being obtained for various values of threshold SNR,  $\gamma_{\text{th}}$ . It can be observed that the lower bound curves from (10) and simulation curves are very close to each other (gap less than 1 dB) for most of the cases. When  $\gamma_{\text{th}} = 10$ dB, gap between the curves is increased due to the reason that for equal values of  $\gamma_{\text{th}}$  and  $\bar{\gamma}^{\text{PA}}$ , (3) does not give good approximation [17]. By the slopes of the curves, we can observe that the system diversity gain is higher when  $\gamma_{\text{th}} < \bar{\gamma}^{\text{PA}}$ . This is due to the fact the nonlinear distortion is more significant at high SNRs than low SNRs.

Fig. 3 shows the comparison between lower bound and simulation results of outage probability versus mean SNR,  $\bar{\gamma}$  over Nakagami- $m$  fading channel with non-integral fading parameter,  $m = 1.5$ . These curves show similar behavior as in Fig. 2, but the outage probability performance is improved for higher values of fading parameter, as expected. Hence, conclusions for Fig. 2 (when  $m = 1$ ) are also applicable for Fig. 3 when fading parameter is non-integer.

Fig. 4 shows the comparison between lower bound and simulation results of outage probability versus mean SNR,  $\bar{\gamma}$  over Nakagami- $m$  fading channel with fading parameter,  $m = 2$ . These curves show similar behavior as in Fig. 2 and Fig. 3, but the outage probability is further improved, as expected. Hence, conclusions for Fig. 2 (when  $m = 1$ ) and Fig. 3 (when  $m = 1.5$ ) are also applicable for Fig. 4 (when  $m = 2$ ).

Fig. 5 describes the comparison between lower bound and simulation results of outage probability versus mean SNR,  $\bar{\gamma}$  over Nakagami- $m$  fading channel with fading parameter,  $m = 2$ , considering linear and nonlinear PAs, for various values of threshold SNR. It can be observed that for  $\gamma_{\text{th}} < \bar{\gamma}^{\text{PA}}$ , nonlinear PA behaves like linear PA, however when  $\gamma_{\text{th}} > \bar{\gamma}^{\text{PA}}$ , the impact of nonlinearity is increased over outage probability. The difference between the outage probability curves of linear and nonlinear PAs is further increased by increasing the value of  $\gamma_{\text{th}}$ . Hence, it can be conclude that the nonlinearity of PA affects the system outage probability only for high values of  $\gamma_{\text{th}}$ .

### V. CONCLUSION

We have analyzed the performance of orthogonal frequency division multiplexing (OFDM) based amplify-and-forward (AF) cooperative relaying scheme over i.i.d Nakagami- $m$  fading channels. We derived a closed-form expression for lower bound of outage probability with SC receiver. The comparison of numerical and simulation results demonstrated that the derived expression of outage probability has good approximation in most of the cases, specially at low and high SNRs. It can also be observed that PA nonlinearity degrades the outage probability performance only at high threshold SNRs. At low threshold SNR, nonlinear PA behaves like linear PA.

$$P_n^{out, LB}(\gamma_{th}) = \left[ 1 - \frac{\Gamma\left(m, \frac{m\gamma_{th}}{\bar{\gamma}^{sd}}\right)}{\Gamma(m)} \right] \left[ 1 - \frac{\Gamma\left(m, \frac{m\gamma_{th}}{\bar{\gamma}^{sr}}\right) \Gamma\left(m, \frac{m\gamma_{th}}{\bar{\gamma}^{rd}}\right)}{\Gamma(m) \Gamma(m)} u(\bar{\gamma}^{PA} - \gamma_{th}) \right] u(\gamma_{th}) \quad (9)$$

$$P_n^{out, LB}(\gamma_{th}) = \left[ 1 - \frac{\Gamma\left(m, \frac{m\gamma_{th}}{\bar{\gamma}^{sd}}\right)}{\Gamma(m)} - \frac{\Gamma\left(m, \frac{m\gamma_{th}}{\bar{\gamma}^{sr}}\right) \Gamma\left(m, \frac{m\gamma_{th}}{\bar{\gamma}^{rd}}\right)}{\Gamma(m) \Gamma(m)} u(\bar{\gamma}^{PA} - \gamma_{th}) + \frac{\Gamma\left(m, \frac{m\gamma_{th}}{\bar{\gamma}^{sd}}\right) \Gamma\left(m, \frac{m\gamma_{th}}{\bar{\gamma}^{sr}}\right)}{\Gamma(m) \Gamma(m)} \frac{\Gamma\left(m, \frac{m\gamma_{th}}{\bar{\gamma}^{rd}}\right)}{\Gamma(m)} u(\bar{\gamma}^{PA} - \gamma_{th}) \right] u(\gamma_{th}) \quad (10)$$

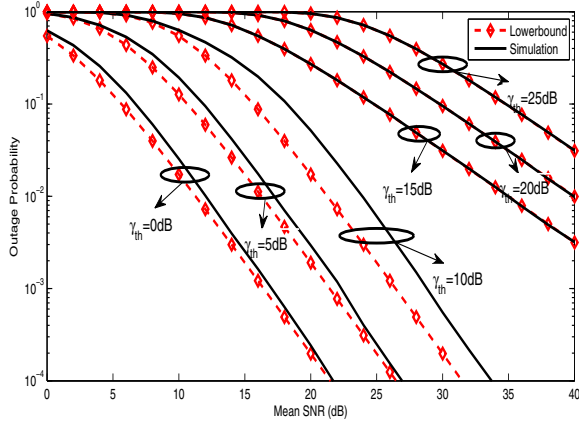


Fig. 2. Comparison between lower bound and simulation results of outage probability versus mean SNR over Nakagami- $m$  channel with  $m = 1$  (Rayleigh) and various values of  $\gamma_{th}$

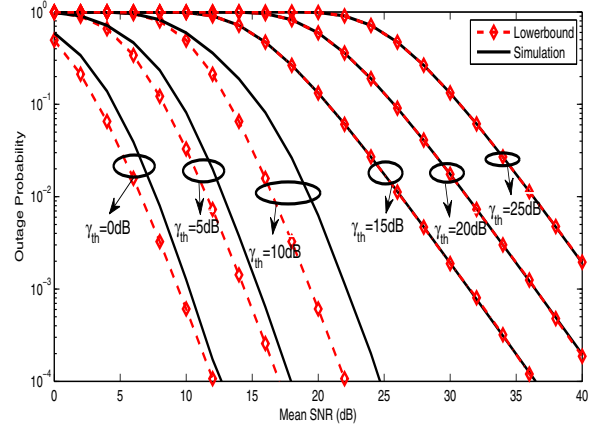


Fig. 4. Comparison between lower bound and simulation results of outage probability versus mean SNR over Nakagami- $m$  channel with  $m = 2$  and various values of  $\gamma_{th}$

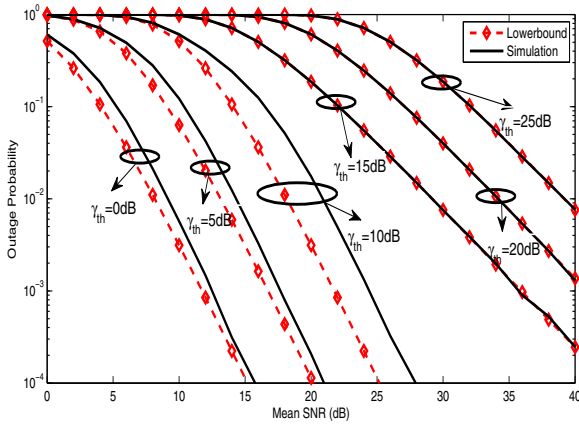


Fig. 3. Comparison between lower bound and simulation results of outage probability versus mean SNR over Nakagami- $m$  channel with  $m = 1.5$  and various values of  $\gamma_{th}$

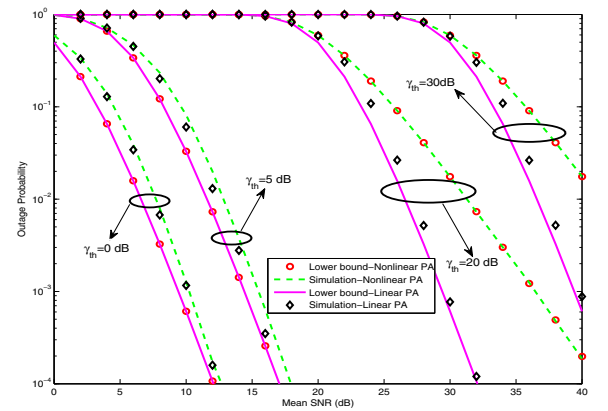


Fig. 5. Comparison between lower bound and simulation results of outage probability versus mean SNR over Nakagami- $m$  channel with  $m = 2$ , various values of  $\gamma_{th}$  and linear and nonlinear PAs

## ACKNOWLEDGMENT

The authors would like to thank IIT Indore for all the support and research facilities.

## REFERENCES

- [1] J. N. Laneman, D. N. Tse, and G. W. Wornell, "Cooperative diversity in wireless networks: Efficient protocols and outage behavior," *Information Theory, IEEE Transactions on*, vol. 50, no. 12, pp. 3062–3080, 2004.
- [2] J. N. Laneman and G. W. Wornell, "Energy-efficient antenna sharing and relaying for wireless networks," in *Wireless Communications and Networking Conference, 2000. WCNC. 2000 IEEE*, vol. 1. IEEE, 2000, pp. 7–12.
- [3] —, "Distributed space-time coded protocols for exploiting cooperative diversity in wireless networks," in *Global Telecommunications Conference, 2002. GLOBECOM'02. IEEE*, vol. 1. IEEE, 2002, pp. 77–81.
- [4] A. Nosratinia, T. E. Hunter, and A. Hedayat, "Cooperative communication in wireless networks," *Communications Magazine, IEEE*, vol. 42, no. 10, pp. 74–80, 2004.
- [5] H. Zhu, B. Farhang-Boroujeny, and C. Schlegel, "Pilot embedding for joint channel estimation and data detection in MIMO communication systems," *Communications Letters, IEEE*, vol. 7, no. 1, pp. 30–32, 2003.
- [6] M. O. Hasna and M.-S. Alouini, "End-to-end performance of transmission systems with relays over Rayleigh-fading channels," *Wireless Communications, IEEE Transactions on*, vol. 2, no. 6, pp. 1126–1131, 2003.
- [7] T. Tsiftsis, G. Karagiannidis, S. Kotsopoulos, and F.-N. Pavlidou, "BER analysis of collaborative dual-hop wireless transmissions," *Electronics Letters*, vol. 40, no. 11, pp. 679–681, 2004.
- [8] P. A. Anghel and M. Kaveh, "Exact symbol error probability of a cooperative network in a Rayleigh-fading environment," *Wireless Communications, IEEE Transactions on*, vol. 3, no. 5, pp. 1416–1421, 2004.
- [9] S. Ikki and M. H. Ahmed, "Performance analysis of cooperative diversity wireless networks over Nakagami- $m$  fading channel," *Communications Letters, IEEE*, vol. 11, no. 4, pp. 334–336, 2007.
- [10] N. Kong, "Performance comparison among conventional selection combining, optimum selection combining and maximal ratio combining," in *Communications, 2009. ICC'09. IEEE International Conference on*. IEEE, 2009, pp. 1–6.
- [11] S. S. Ikki and M. H. Ahmed, "Exact error probability and channel capacity of the best-relay cooperative-diversity networks," *Signal Processing Letters, IEEE*, vol. 16, no. 12, pp. 1051–1054, 2009.
- [12] Y. Lei, W. Cheng, and Z. Zeng, "Performance analysis of selection combining for amplify-and-forward cooperative diversity networks over Weibull fading channels," in *Communications Technology and Applications, 2009. ICCTA'09. IEEE International Conference on*. IEEE, 2009, pp. 648–651.
- [13] A. Pandharipande, "Principles of OFDM," *Potentials, IEEE*, vol. 21, no. 2, pp. 16–19, 2002.
- [14] T. Hwang, C. Yang, G. Wu, S. Li, and G. Y. Li, "OFDM and its wireless applications: a survey," *Vehicular Technology, IEEE Transactions on*, vol. 58, no. 4, pp. 1673–1694, 2009.
- [15] R. Prasad, *OFDM for wireless communications systems*. Artech House, 2004.
- [16] C. A. R. Fernandes, D. B. da Costa, and A. L. de Almeida, "Performance analysis of cooperative amplify-and-forward orthogonal frequency division multiplexing systems with power amplifier nonlinearity," *IET Communications*, vol. 8, no. 18, pp. 3223–3233, 2014.
- [17] C. A. R. Fernandes, "Outage performance of cooperative amplify-and-forward OFDM systems with nonlinear power amplifiers," in *Signal Processing Advances in Wireless Communications (SPAWC), 2012 IEEE 13th International Workshop on*. IEEE, 2012, pp. 459–463.
- [18] C. A. R. Fernandes, D. B. da Costa, and A. L. F. d. Almeida, "Outage analysis of cooperative OFDM systems with nonlinear amplifiers and relay selection." *Simpósio Brasileiro de Telecomunicações*, 2012.
- [19] V. Del Razo, T. Riihonen, F. Gregorio, S. Werner, and R. Wichman, "Nonlinear amplifier distortion in cooperative amplify-and-forward OFDM systems," in *Wireless Communications and Networking Conference, 2009. WCNC 2009. IEEE*. IEEE, 2009, pp. 1–5.
- [20] T. Riihonen, S. Werner, F. Gregorio, R. Wichman, and J. Hamalainen, "BEP analysis of OFDM relay links with nonlinear power amplifiers," in *Wireless Communications and Networking Conference (WCNC), 2010 IEEE*. IEEE, 2010, pp. 1–6.
- [21] H. A. Ahmed, A. I. Sulyman, and H. Hassanein, "BER performance of OFDM systems in mobile multi-hop relaying channels," in *Proceedings of the 6th International Wireless Communications and Mobile Computing Conference*. ACM, 2010, pp. 905–910.
- [22] S. L. Silva and C. A. R. Fernandes, "Outage analysis of af OFDM relaying systems with power amplifier nonlinearity," in *Telecommunications Symposium (ITS), 2014 International*. IEEE, 2014, pp. 1–5.
- [23] D. Dardari, V. Tralli, and A. Vaccari, "A theoretical characterization of nonlinear distortion effects in OFDM systems," *Communications, IEEE Transactions on*, vol. 48, no. 10, pp. 1755–1764, 2000.
- [24] A. Jeffrey and D. Zwillinger, *Table of integrals, series, and products*. Academic Press, 2007.

# A Novel Self Localization Approach for Sensors

Dogan Yildiz, Serap Karagol,  
Okan Ozgonenel  
Ondokuz Mayis University  
Electrical-Electronic Dept.  
Samsun, TURKEY  
serap.karagol@omu.edu.tr

Satish Tadiparthi  
Prolifics  
New York, NY, USA  
satish.tadiparthi@gmail.com

Marwan Bikdash  
Computational Science and Eng.  
North Carolina A&T State  
University  
Greensboro, NC, USA  
bikdash@ncat.edu

**Abstract**— This paper presents a modification of 3N Time of Arrival (TOA) and a reliable Time Difference of Arrival (TDOA) based localization algorithms. TDOA is formulated using the parametric equations of the hyperbolas whose intersections are candidate locations for the nodes to be localized. The TDOA algorithm is guaranteed to find all possible relevant solutions, even when implemented on a computational node with limited capability. Monte-Carlo simulations were used to assess the performance for both algorithms.

**Keywords**— *Hyperbolic Position Estimation, TOA, TDOA, Sensors, Parametric Equations.*

## I. INTRODUCTION

Technology has enabled the creation of many smart environments based on a network of tiny sensors employed in a variety of applications, such as environmental monitoring, disaster management, surveillance, security systems, a biological environment and an information technology (IT) structure [1]. Sensor networks include sensor nodes that are strewn haphazardly or systematically over a large area to sense a physical fact. Basic tasks of the sensor nodes are sensing, information collection, and redirection [2-3].

One of the most important topics for the application of wireless sensor networks is sensor localization. If sensor location is known, various sensor data can be used efficiently and premeditate resource routing exigencies to help forward network service or carry out supervision efficaciously [4]. In other words, the signals are most useful when correlated with their locations. Moreover, interaction between the sensors enables the construction of an environment description that non-interacting sensors are incapable of creating, and their flexibility enables the support of a wide variety of real world applications. This is a stepping-stone towards the emergence of ambient intelligence, pervasive control, and ubiquitous sensing.

A number of localization schemes, localization algorithms and distance estimate measurement techniques are proposed in the literature to solve localization problems. The classification of localization schemes depends on the measurement techniques utilized. They are generally categorized as range-based, which utilize point-to-point distance measurements to produce an output, or range-free, which utilize proximity and connectivity information to generate an output [5-6].

Localization algorithms are divided into three classes. These are centralized algorithms, which collect measurements at a central processor prior to calculation, localized or otherwise called distributed algorithms, which require the nodes to share the data to their one hop neighbors [7], and hybrid algorithms, which utilize the capabilities of centralized and localized algorithms [8].

Distance estimate measurement techniques are generally categorized as direction finding systems and range finding systems. In the position location concept, Direction Finding Systems (DFS) use the direction bearing of the signal in the calculation of the position location. Some methods of Radio Frequency Position Location Systems use directions as a measure in calculating the Angle of Arrival (AOA) and Received Signal Strength Indicator (RSSI). Range finding systems utilize a point-to-point distance measure as an input measure to calculate. In TOA, the distance between the two nodes is estimated by measuring the duration of signal propagation between the two nodes. This requires clock-synchronized nodes that utilize well-known parameters known as the TOA technique, such as the speed of the signal and the carrier frequency. Balogh et al. [9] utilized the TOA data of muzzle blast to eliminate the multi-path effects and resolve multiple simultaneous acoustic sources in the source localization scheme, which is used in a wireless sensor network based counter-sniper system. Srirangarajan and Tewfik propose a sensor node localization scheme that utilizes spatial domain Quasi-Maximum Likelihood (QML) [10] based on a TOA algorithm. Their algorithm uses the orientational domain quasi maximum likelihood approach to detect the essential sensor. They showed that their system achieved a high accuracy output. A signal-circle analogy used by Barbeau et al. [11] is generally used analogous to the TOA distance measurement technique.

Time Difference of Arrival (TDOA) is a measurement technique widely used for the passive localization of a target by determining its position from the measurements of time differences of arrival of the emitter signals at a set of receivers, where  $N-1$  linearly independent TDOA equations can be formulated from a system of  $N$  receivers [12]. A direct and short derivation of an algorithm is presented in [11] based on the closed-form solution of the nonlinear equations for emitter location using TDOA measurements from  $N+1$  receivers, where  $N \geq 3$ . Arnold and Bean [13] compared traditional techniques on a small number of measurement

probes with known locations to investigate the efficacy of TDOA measurements for accurate localization, over long ranges and under noisy propagation conditions, and showed improved performance. Yangy and Luo [14] showed the efficiency and superior performance of the convex relaxation approach, based on TDOA measurements, as compared to the least squares based approach in a robust target localization problem using semi-definite programming and unknown sensor locations.

Lastly, Bian et al. [15] proposed a scheme that utilizes the hyperbola-based method for event localization and a normal distribution for estimation error modeling and gauging. The performance of their scheme demonstrates clear progress over the mostly used circle-based least squares location estimation. Kaune et al. [16] proposed a method for optimizing sensor trajectories, based on the Cramér Rao Lower Bound (CRLB), such that quick and exact localization of the emitter is performed. The online trajectory administration submitted in this article is especially helpful for TDOA measurements because of its dependence on geometry. Wu and Lu [17] proposed a method called Modified Asymptotic Linear Solver to locate the emitters by solving the intersections of hyperbolas described by measured TDOA.

The proposed algorithm solves the nonlinearity problem in hyperbolic localization simply and provides computational efficiency. This paper is organized as follows: Section II introduces a modification of the 3N Time of Arrival (TOA) based algorithm and presents its performance using a comprehensive quantitative Monte-Carlo simulations study; Section III proposes a reliable Time Difference of Arrival (TDOA) based localization algorithm using parametric equation of the hyperbola. Monte-Carlo simulations were used to assess the performance. Conclusions are presented in Section IV.

## II. TIME OF ARRIVAL BASED LOCALIZATION

Time of Arrival (TOA) is a method used to estimate the location of a target node based on the correlation of the signals. This method calculates the distance from each anchor to the target by multiplying the speed of the signal and the time at which the signal is received. This method requires knowledge of the precise starting time of the signal transmitted, as well as precise maintenance and synchronization of the clocks at the target and all anchor nodes involved.

### A. Resolution of ambiguity in the sparse field of sensor nodes

The field of sensor nodes is generally sparse in the sense that some nodes may have less than neighboring anchors to fully localize. In fact, they may have less than 3 neighbors. A well-known 3 Neighbor algorithm is as follows: each node that is not equipped with a position-awareness device sends a position request message; a node that knows or can compute its position sends it to all its neighbors; a node that receives position messages from three different nodes, say  $A_1$ ,  $A_2$ , and  $A_3$ , can calculate its position, as shown in Fig. 1 (a). However, this algorithm exhibits a deficiency: where a target node receives only two anchor nodes ( $A_1$ ,  $A_2$ ), locations and two

distance measurements, the target node fails to find its own location, due to the obvious ambiguity, as shown in Fig. 1(b) [11].

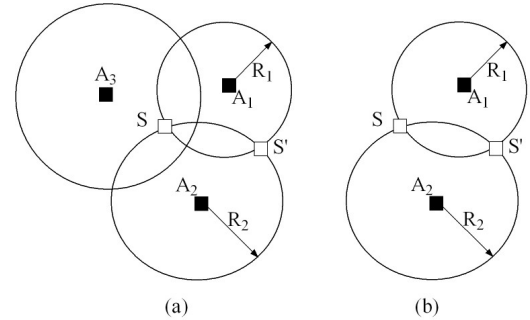


Fig. 1. (a) three anchors (b) two anchors

### B. Modified 3N algorithm

We propose the following modification for 3N Time of Arrival (TOA) based localization algorithm. While the algorithm is being run, the target nodes that are localized are now position-aware and possess the capability to share their positions. This newly found position-aware node is introduced into the pseudo anchor list, the neighboring network is intimated of this change, and the gradual increase of the position-aware nodes in the network enable an enhanced localization performance. The following steps are added to the 3N algorithm:

1. While there are target nodes
  - a) if maximum number of iterations is exceeded, stop (some targets are not located)
  - b) if less than three anchor nodes are in range, skip this node and go to step 1 to consider another target node
  - c) if there are three or more anchor nodes in range, find the closest three anchor nodes and use them to locate the target node
  - d) Add the localized target node into the pseudo-anchor list and remove it from target list
2. go to step 1, consider the next in target list.

### C. Design of simulation environment

The simulation environment is designed for the quantitative performance study of the proposed modified 3 Neighbor algorithm. A heterogeneous node network containing a mix of anchor nodes has the capabilities of ascertaining their own locations and the target nodes, which are not position-aware, are generated. A pseudo-anchor list is created that serves as a dynamic anchor list while the simulation is being run. As the new target nodes are localized, they are added to the list of pseudo-anchors and the whole network is made aware of these newly localized nodes in order to enhanced performance of localizing other target nodes with the help of this new knowledge. The simulation creates a distance matrix that is generated using the euclidean method of calculation of the distance between the anchor nodes. This forms the basis for the generation of other modules needed,

such as adjacency lists. From this adjacency list, each target node determines its neighbors. An approximated circle is constructed using the distance from the anchor node to the target node as the radius and the absolute position of the anchor as the center. The intersection of circles gives a location estimate of the target node.

#### D. Analysis of time of arrival simulations

This section presents the localization capability of the TOA based localization algorithm with exhaustive Monte-Carlo simulations, where the effect of the input parameters determine the self-localization environment. The simulation environment to test the performance of the algorithm on all combinations of the context parameters is formulated. Each Monte-Carlo simulation is generated for a particular set of input parameters and run 100 times with different fields and randomly located nodes. The results are then averaged. The input parameters include the percentage of anchor nodes (position-aware and initially synchronized nodes), the number of target nodes, and the range of communication. With the number of nodes varying from 50 to 400, the percentage of available nodes is localized in a square field dimension of 100x100 units. Fig. 2 is produced by varying the percentage of anchor nodes for a constant communication range of 8% of the field dimension, the point where the localization performance of the algorithm shows a substantial gain moves toward the lower density of nodes. Fig. 3 shows the effect of input parameters on the localization performance due to the increased communication range. The performance dramatically increases even with much lower node densities.

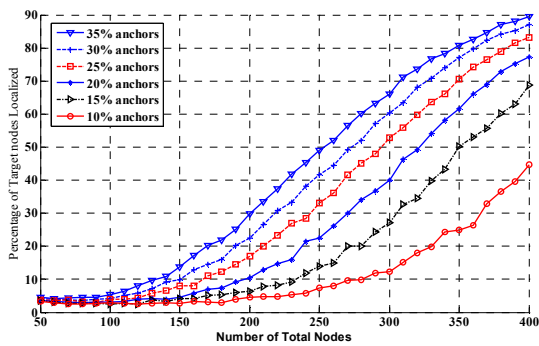


Fig. 2. At communications range 8% of the field dimension.

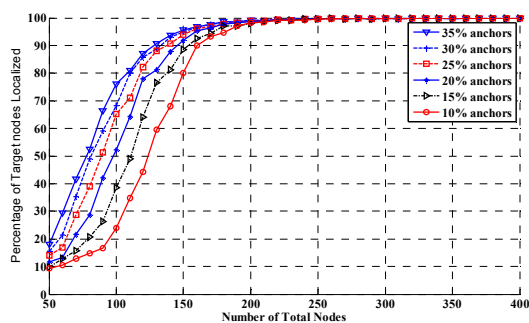


Fig. 3. At communications range 15% of the field dimension.

### III. HYPERBOLIC POSITION LOCATION ALGORITHM

A position can be defined in different ways, such as absolute position on geoid, GPS, location relative to fixed beacons, LORAN, and location relative to a starting point such as inertial platforms. For most applications, range and resolution of the position location needs to be proportionate to the scale of the objects being located. Estimation of position uses the range differences to the three nodes or beacons. Given two foci at  $p$  and  $q$ , and a target  $s$ , the TDOA measurement is computed as

$$m = \|s - p\| - \|s - q\| \quad (1)$$

where a negative measurement  $m$  indicates that the target is closer to the first focus  $p$ . This will specify the branch of the hyperbola needed. A measurement of  $-m$  indicates the other branch. The center of the hyperbola is at the point  $(p+q)/2$ .

#### A. Parametric Method for Hyperbolic Location

The parametric equation of the hyperbola is given by

$$\begin{aligned} x &= a \operatorname{sect} \\ y &= b \tan t \end{aligned} \quad (2)$$

where  $-\pi/2 < t < \pi/2$ . Moreover

$$\frac{y}{x} = \frac{b \tan t}{a \operatorname{sect}} \xrightarrow{t \rightarrow \frac{\pi}{2}} \frac{b}{a} \quad (3)$$

The parametric equation of a rotated and translated hyperbola is

$$\begin{bmatrix} x \\ y \end{bmatrix} = \begin{bmatrix} \cos \theta & -\sin \theta \\ \sin \theta & \cos \theta \end{bmatrix} \begin{bmatrix} a \operatorname{sect} \\ b \tan t \end{bmatrix} + \begin{bmatrix} h \\ k \end{bmatrix} \quad (4)$$

Here, the hyperbola is rotated clockwise by an angle  $\theta$ , and

the center of the hyperbola is then shifted to  $\begin{bmatrix} h \\ k \end{bmatrix}$ .

The rotation matrix is

$$R(\theta) = \begin{bmatrix} \cos \theta & -\sin \theta \\ \sin \theta & \cos \theta \end{bmatrix} \quad (5)$$

A mathematical model is developed for the hyperbolic position estimator based on parametric equations.

The equation of the rotated first hyperbola is

$$\begin{bmatrix} x_1 \\ y_1 \end{bmatrix} = \begin{bmatrix} \cos \theta_1 & -\sin \theta_1 \\ \sin \theta_1 & \cos \theta_1 \end{bmatrix} \begin{bmatrix} a_1 \operatorname{sect}_1 \\ b_1 \tan t_1 \end{bmatrix} + \begin{bmatrix} h_1 \\ k_1 \end{bmatrix} \quad (6)$$

where  $t_1 \in (-\pi/2, \pi/2)$ ,  $\theta_1$  is the orientation angle of the first hyperbola,  $(h_1, k_1)$  is the center of the first hyperbola.

The equation of the rotated second hyperbola is

$$\begin{bmatrix} x_2 \\ y_2 \end{bmatrix} = \begin{bmatrix} \cos \theta_2 & -\sin \theta_2 \\ \sin \theta_2 & \cos \theta_2 \end{bmatrix} \begin{bmatrix} a_2 \operatorname{sect}_2 \\ b_2 \tan t_2 \end{bmatrix} + \begin{bmatrix} h_2 \\ k_2 \end{bmatrix} \quad (7)$$

where  $t_2 \in (-\pi/2, \pi/2)$ ,  $\theta_2$  is the orientation angle of the second hyperbola,  $(h_2, k_2)$  is the center of the second hyperbola.

Equating  $x_1(t_1) = x_2(t_2)$  leads to

$$\begin{aligned} 0 &= a_1 \cos \theta_1 \operatorname{sect}_1 - b_1 \sin \theta_1 \tan t_1 + h_1 \\ &\quad - a_2 \cos \theta_2 \operatorname{sect}_2 + b_2 \sin \theta_2 \tan t_2 - h_2. \end{aligned} \quad (8)$$

Equating  $y_1(t_1) = y_2(t_2)$  leads to

$$0 = a_1 \sin \theta_1 \sec t_1 + b_1 \cos \theta_1 \tan t_1 + k_1 - a_2 \sin \theta_2 \sec t_2 - b_2 \cos \theta_2 \tan t_2 - k_2. \quad (9)$$

The two equations to be solved are (8) and (9).

Multiplying (8) with  $\cos \theta_1$  leads to

$$0 = a_1 \cos^2 \theta_1 \sec t_1 - b_1 \sin \theta_1 \cos \theta_1 \tan t_1 + h_1 \cos \theta_1 - a_2 \cos \theta_1 \cos \theta_2 \sec t_2 + b_2 \cos \theta_1 \sin \theta_2 \tan t_2 - h_2 \cos \theta_1. \quad (10)$$

Multiplying (9) with  $\sin \theta_1$  leads to

$$0 = a_1 \sin^2 \theta_1 \sec t_1 + b_1 \sin \theta_1 \cos \theta_1 \tan t_1 + k_1 \sin \theta_1 - a_2 \sin \theta_1 \sin \theta_2 \sec t_2 - b_2 \sin \theta_1 \cos \theta_2 \tan t_2 - k_2 \sin \theta_1. \quad (11)$$

Adding (10) to (11) results in

$$-a_1 \sec t_1 = e_1 + e_2 \sec t_2 + e_3 \tan t_2 \quad (12)$$

where

$$\begin{aligned} e_1 &= (h_1 - h_2) \cos \theta_1 + (k_1 - k_2) \sin \theta_1, \\ e_2 &= -a_2 (\cos \theta_1 \cos \theta_2 + \sin \theta_1 \sin \theta_2), \\ e_3 &= b_2 (\cos \theta_1 \sin \theta_2 - \sin \theta_1 \cos \theta_2). \end{aligned} \quad (13)$$

Similarly multiplying (8) with  $\sin \theta_1$  to obtain

$$0 = a_1 \sin \theta_1 \cos \theta_1 \sec t_1 - b_1 \sin^2 \theta_1 \tan t_1 + h_1 \sin \theta_1 - a_2 \sin \theta_1 \cos \theta_2 \sec t_2 + b_2 \sin \theta_1 \sin \theta_2 \tan t_2 - h_2 \sin \theta_1 \quad (14)$$

and (9) with  $-\cos \theta_1$  to obtain

$$0 = -a_1 \sin \theta_1 \cos \theta_1 \sec t_1 - b_1 \cos^2 \theta_1 \tan t_1 - k_1 \cos \theta_1 + a_2 \cos \theta_1 \sin \theta_2 \sec t_2 + b_2 \cos \theta_1 \cos \theta_2 \tan t_2 + k_2 \cos \theta_1 \quad (15)$$

and adding (14) to (15) results in

$$b_1 \tan t_1 = f_1 + f_2 \sec t_2 + f_3 \tan t_2 \quad (16)$$

where

$$\begin{aligned} f_1 &= (h_1 - h_2) \sin \theta_1 + (k_1 - k_2) \cos \theta_1, \\ f_2 &= -a_2 (\sin \theta_1 \cos \theta_2 - \cos \theta_1 \sin \theta_2), \\ f_3 &= b_2 (\sin \theta_1 \sin \theta_2 + \cos \theta_1 \cos \theta_2). \end{aligned} \quad (17)$$

The equations (12) and (16) are two equations in two unknowns  $t_1$  and  $t_2$ . Note that both  $t_1$  and  $t_2$  must belong to  $[-\pi/2, \pi/2]$ . To eliminate ambiguities due to multivaluedness, one can use

$$\begin{aligned} t_1 &= \tan^{-1} \left( \frac{f_1 + f_2 \sec t_2 + f_3 \tan t_2}{b_1} \right), \\ F &= \sec(t_1) - \left( \frac{e_1 + e_2 \sec t_2 + e_3 \tan t_2}{-a_1} \right), \\ t_{\text{int}} &= t_1(\text{find}(\text{diff}(\text{sign}(F)))) \quad t_1 \in (-\pi/2, \pi/2) \end{aligned} \quad (18)$$

where the values of  $t_{\text{int}}$  are the required intersection values of  $t_1 \in (-\pi/2, \pi/2)$ . These values are substituted into

$$\begin{bmatrix} x_1 \\ y_1 \end{bmatrix} = \begin{bmatrix} \cos \theta_1 & -\sin \theta_1 \\ \sin \theta_1 & \cos \theta_1 \end{bmatrix} \begin{bmatrix} a_1 \sec t_{\text{int}} \\ b_1 \tan t_{\text{int}} \end{bmatrix} + \begin{bmatrix} h_1 \\ k_1 \end{bmatrix} \quad (19)$$

and into

$$\begin{bmatrix} x_2 \\ y_2 \end{bmatrix} = \begin{bmatrix} \cos \theta_2 & -\sin \theta_2 \\ \sin \theta_2 & \cos \theta_2 \end{bmatrix} \begin{bmatrix} a_2 \sec t_{\text{int}} \\ b_2 \tan t_{\text{int}} \end{bmatrix} + \begin{bmatrix} h_2 \\ k_2 \end{bmatrix} \quad (20)$$

These  $(x_1, y_1)$  and  $(x_2, y_2)$  will result on the same points as the intersections of both hyperbolas.

### B. Analysis of parametric-equation based TDOA localization algorithm

This section presents the simulation results of the performance of the proposed hyperbolic location estimator. The performance of the algorithm applied to varied parameters is studied. The test scenario is Ad-Hoc and the experiment work flow is designed selecting only the most widely accepted assumptions, such as all nodes are homogeneous, i.e all the nodes have similar capabilities and node placement in the environment is completely random. Ideal environment is assumed where no channel is noise free and all the input metrics are error free. The simulation includes a square field area of 100x100 units. Here, three anchors or pseudo-anchors are needed to completely locate a target node s, including the resolution of ambiguity as shown in Fig. 4. In essence  $D_2$ - $D_1$ ,  $D_3$ - $D_1$  are used to find 1, 2 or 3 candidates, then the measurement  $D_3$ - $D_2$  is used to resolve the ambiguity.

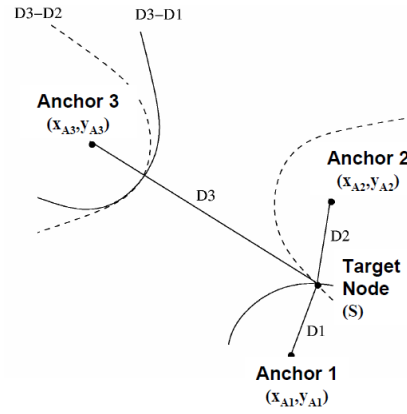


Fig.4. Hyperbolic lines of position

In Fig. 5 the anchor percentage is varied from 10% of the total nodes to 35%. The communications range is kept constant at 8% of the field dimension. At this set of parameters, the density of nodes increases from 50 nodes to 400 nodes and the localization performance shows that even with 35% anchor nodes present and the density at 400 nodes, the localized nodes reach around 88% nodes localized. With low anchor nodes percentage (10%) and a density of 400 nodes present in the field, the localization reaches only 50% of nodes localized. In Fig. 6, the communications range is kept constant at 15% of the field dimension. The localization performance of the algorithm with the parameters at 10% nodes reaches almost 100% nodes localized at the density of around 200 nodes. At anchor percentage of 35%, the performance reaches almost 90% nodes localized at around 125 nodes.

It is deduced that the anchor percentage and the density have a limited effect on performance, that the communication range is tightly connected to performance, and that the algorithm shows a dramatic improvement with a minimal increase in the communication range.

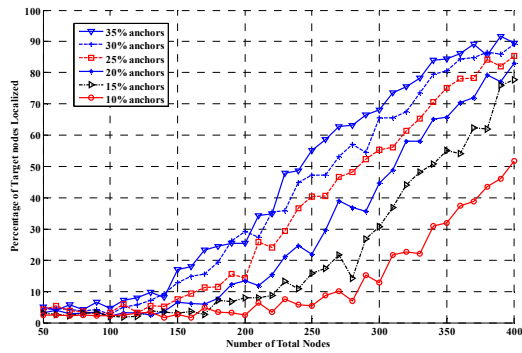


Fig. 5. At communications range 8% of the field dimension.

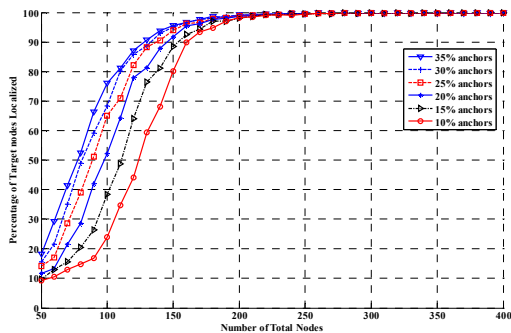


Fig. 6. At communication range 15% of the field dimension.

#### IV. CONCLUSIONS

This work is a step towards a better understanding of the effects of different designs, measurements, contexts, and parameters of Wireless Sensor Networks. Another challenge addressed here is the resolution of ambiguity in position estimates in anchor-sparse environments where the density of anchors in the network is very low.

A modified 3N localization algorithm was developed and tested. It immediately uses the knowledge of newly localized nodes for the enhanced performance of the localization of other target nodes. The simulations conducted have shown that the introduction of the knowledge of newly localized nodes into the network enhances its localization capability, but that if the nodes cannot be located by the 3N algorithm because of the limitations on range and sparsity of the anchors, then those nodes will not be localized by the modified algorithm either. We showed through extensive Monte-Carlo simulation that the communication range is a crucial context parameter that is found to be tightly coupled with the localization performance.

A parametric-equation based TDOA localization algorithm is developed and studied. This algorithm is guaranteed to find all the candidate locations even when the hyperbolas are degenerate. Monte-Carlo simulations of the proposed algorithm showed that the intersections are guaranteed to be found when they exist, and that the TDOA effectiveness in localizing nodes in a network is similar to that of TOA. Since TDOA is the less demanding of the hardware,

requiring less synchronization for instance, one can argue that TDOA is the best alternative especially that the algorithm here is not significantly more expensive computationally.

#### REFERENCES

- [1] P. A. Boncz, A. Bonifati et al, "P2P, Ad Hoc and Sensor Networks - All the Different or All the Same?", in *Proceedings of the Dagstuhl Seminar*, 2007.
- [2] K. Sohrawy, D. Minoli, T. Znati, "Wireless Sensor Networks: Technology, Protocols, and Applications," Wiley-Interscience, 1<sup>st</sup> edition.
- [3] S. Pandey, P. Prasad, P. Sinha and P. Agrawal, "Localization of Sensor Networks Considering Energy Accuracy Tradeoffs," in *Proc. of the 1st International Conference on Collaborative Computing: Networking, Applications and Worksharing*, SanJose, CA, USA, December 19-21, 2005.
- [4] K. Langendoen and N. Reijers, "Distributed localization in wireless sensor networks: a quantitative comparison", *Computer Networks*, Vol. 43, pp. 499-518, 2003.
- [5] A. Pal, "Localization Algorithms in Wireless Sensor Networks: Current Approaches and Future Challenges," *Network Protocols and Algorithms*, Vol. 2, no. 1, pp. 45-73, 2010.
- [6] B. Zhang, F. Yu, "An event-triggered localization algorithm for mobile wireless sensor networks," *Future Computer and Communication (ICFCC), 2010 2nd International Conference on*, vol.1, no., pp.V1-250-253, 21-24 May 2010.
- [7] N. Patwari, J. N. Ash, S. Kyperountas, A. O. III Hero, R. L. Moses, N. S. Correal, "Locating the nodes: cooperative localization in wireless sensor networks", *IEEE Signal Processing Magazine*, vol. 22, no. 4, pp. 54-69, July 2005.
- [8] S. Tully, M. Hyungpil, D. Morales, G. Kantor, H. Choset, "Hybrid localization using the hierarchical atlas", in *Proc. 2007 IEEE/RSJ International Conference on Intelligent Robots and Systems*, pp. 2857 - 2864.
- [9] G. Balogh, A. Ledeczi, M. Maroti, and G. Simon, "Time of arrival data fusion for source localization", In *Proc. of The WICON Workshop on Information Fusion and Dissemination in Wireless Sensor Networks (SensorFusion 2005)*, July 2005.
- [10] S. Sriangarajan and A. H. Tewfik, "Sensor Node Localization via Spatial Domain Quasi-Maximum Likelihood Estimation", *14th European Signal Processing Conference*, Florence, Italy, Sep 2006.
- [11] M. Barbeau, E. Kranakis, et al., "Improving Distance Based Geographic Location Techniques in Sensor Networks," *3rd International Conference on Ad-Hoc Networks & Wireless*, 2004.
- [12] S. R. Drake, K. Dogancay, "Geolocation by time difference of arrival using hyperbolic asymptotes", *IEEE International Conference on Acoustics, Speech, and Signal Processing*, vol. 2, 17-21 May 2004, pp. ii - 361 - 364.
- [13] J. Arnold, and N. Bean, "Node localization in wireless ad hoc networks using Time Difference Of Arrival", *2nd International Conference on Signal Processing and Communication Systems*, 15-17 Dec. 2008, pp.1-10.
- [14] K. Yangy, Z. Luo, "Robust target localization with multiple sensors using time difference of arrivals", *Radar Conference, 2008. RADAR '08. IEEE*, pp. 1 - 6, 26-30 May 2008.
- [15] T. Bian, R. Venkatesan, and C. Li, "Design and Evaluation of a New Localization Scheme for Underwater Acoustic Sensor Networks," *Global Telecommunications Conference, 2009. GLOBECOM 2009. IEEE*, vol., no., pp.1-5, 2009
- [16] R. Kaune, A. Charlish, "Online Optimization of Sensor Trajectories for Localization using TDOA Measurements", *16th International Conference on Information Fusion Istanbul*, Turkey, July 9-12, 2013.
- [17] H. Wu; I.-T. Lu, "A simple and accurate linear solver for hyperbolic localization," *Wireless Communications and Networking Conference, 2005 IEEE*, vol.3, no., pp.1733,1736 Vol. 3, 13-17 March 2005.

# Quadrature Filters for Underwater Passive Bearings-Only Target Tracking

Rahul Radhakrishnan

Department of Electrical Engineering  
Indian Institute of Technology Patna  
Email: rahul.pee13@iitp.ac.in

Abhinoy Kumar Singh

Department of Electrical Engineering  
Indian Institute of Technology Patna  
Email: abhinoy@iitp.ac.in

Shovan Bhaumik

Department of Electrical Engineering  
Indian Institute of Technology Patna  
Email: shovan.bhaumik@iitp.ac.in

Nutan Kumar Tomar

Department of Mathematics  
Indian Institute of Technology Patna  
Email: nktomar@iitp.ac.in

**Abstract**—A typical underwater passive bearings-only target tracking problem is solved using nonlinear filters namely cubature Kalman filter (CKF), Gauss-Hermite filter (GHF) and sparse-grid Gauss-Hermite filter (SGHF). The performance of the filters is compared in terms of estimation accuracy, track-loss count and computational time. Theoretical Cramer-Rao lower bound (CRLB) is used to determine the maximum achievable performance and to compare the error bounds of various filters used.

## I. INTRODUCTION

The problem of bearings-only tracking finds its application in many real-life scenarios like aircraft surveillance [1], underwater tracking [2] *etc.* The problem is often referred to as target motion analysis (TMA), where the objective is to find the kinematics of a moving target such as range, speed *etc.*, using noise corrupted bearings-only measurements. If the measurements are obtained using a single observer, as in the case described in this paper, the problem is referred to as autonomous TMA [2]. For underwater scenarios, bearing measurements are obtained using a passive sonar mounted on an ownship. Since the identity of the observer is not revealed in passive mode, it can be considered as a tactical advantage for scenarios involved in defence applications [1]. Tracking an enemy submarine using a passive sonar mounted on a warship is an example of one such application. Here, the output of the tracker will be uploaded to a torpedo for engaging the target. More accurate estimates from the tracker help the guidance law to successfully guide the torpedo to its desired destination.

BOT problems have been widely discussed in literature. Most of the research in this field have concentrated on autonomous TMA for tracking nonmanoeuvring targets [3], [4]. The resulting dynamic model becomes unobservable when the observer follows a constant velocity model, *i.e.* without any manoeuvre [5]. So in most of the situations, observer manoeuvre is required which makes the states

observable [6]. Observer manoeuvre is often modeled in straight line segments, where each segment is a phase of the autonomous TMA problem. Therefore, to estimate target states from noisy bearing measurements require at least two phases of observer data. Tracking of a manoeuvring target using bearings-only noisy measurements has also been explored [7], [8], [9].

BOT problems are usually solved in the Bayesian framework, where the posterior probability density of the target kinematics is computed using the predicted motion of the target and the likelihood of the obtained passive angle measurements. But, the solution becomes mathematically intractable due to the highly nonlinear nature of the measurement model [2], [3], [4]. The first suboptimal algorithm for nonlinear estimation which came into existence in literature was the extended Kalman filter (EKF). But it resulted in poor track accuracy and track divergence due to the linearisation of the measurement model [10]. Succeeding EKF, a variety of nonlinear filtering algorithms were introduced such as the unscented Kalman filter (UKF) [11], cubature Kalman filter (CKF) [12] *etc.*

The unscented Kalman filter is based on the unscented transformation in which the posterior probability density is approximated using a set of deterministic sample points and weights. The accuracy of UKF was much higher than the EKF. However, for state dimensions greater than three, some weights turn negative. This may lead to potential numerical problems. CKF uses spherical radial cubature rule for numerically computing the multivariate moment integrals encountered in the nonlinear Bayesian filtering framework. Using spherical radial transformation, the integrals encountered in filtering are decomposed into spherical and radial integrals, which are then numerically computed using the spherical cubature rule and the Gaussian quadrature rule respectively. CKF proved to be more numerically stable with comparable accuracy levels with the UKF.

In a quest to achieve more accuracy, Gauss-Hermite

filter (GHF) was introduced [13], [14]. GHF makes use of Gauss-Hermite quadrature rule for univariate systems. This univariate quadrature rule is extended to multidimensional domain by using the product rule, which in turn results in an exponential rise in multivariate quadrature points and hence, suffers from the *curse of dimension* problem. This hinders the practical applicability of the filter for on-board systems dealing with higher dimensional problems. Sparse-grid Gauss-Hermite filter (SGHF) achieves similar accuracy levels as compared to GHF, with reduced computational load [15]. In this technique, the univariate quadrature rule is extended to multivariate with the help of the Smolyak rule [16]. This theory remarkably reduces the computational load of the algorithm. Instead of using the moment matching method for defining the univariate quadrature points as described in [15], Golub's technique can also be used [17].

In this paper, performance of CKF, GHF and SGHF for a typical underwater BOT problem is studied in terms of estimation accuracy, percentage of track-loss and computational time. To compare the estimation accuracy and the theoretical lower bound of error, Cramer-Rao lower bound (CRLB) is also plotted.

## II. PROBLEM FORMULATION

The target-observer dynamics is developed using cartesian coordinates. Our motive is to estimate the position vector,  $r_t = [x^t \ y^t]^T$  and the velocity vector  $v_t = [\dot{x}^t \ \dot{y}^t]^T$  of the target from noise corrupted passive angle measurements. Hence, the state vector denoting target dynamics can be defined as  $\mathbf{x}_k^t = [x_k^t \ y_k^t \ \dot{x}_k^t \ \dot{y}_k^t]^T$ . Similarly, observer state dynamics can be defined as  $\mathbf{x}_k^o = [x_k^o \ y_k^o \ \dot{x}_k^o \ \dot{y}_k^o]^T$ . Now, we introduce a relative state vector  $\mathbf{x}_k \triangleq \mathbf{x}_k^t - \mathbf{x}_k^o = [x_k \ y_k \ \dot{x}_k \ \dot{y}_k]^T$ .

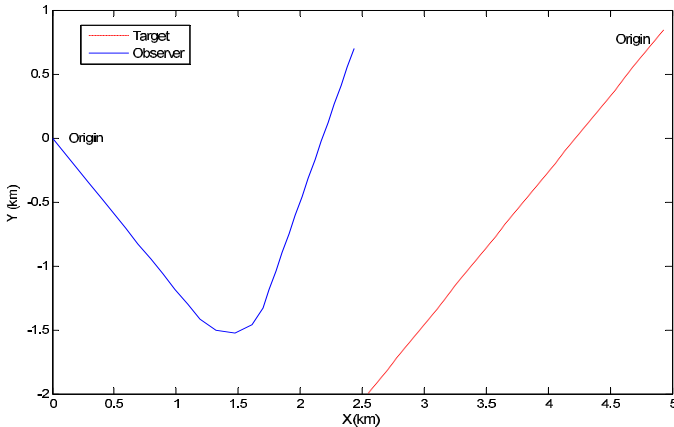


Fig. 1: Nonlinear BOT scenario

The discrete time state equation for the target dynamics, where it is assumed to follow a near constant velocity motion model can be expressed as [18]:

$$\mathbf{x}_k = F\mathbf{x}_{k-1} + v_{k-1} - U_{k-1,k}. \quad (1)$$

$F$  is the state transition matrix defined as:

$$F = \begin{bmatrix} 1 & 0 & T & 0 \\ 0 & 1 & 0 & T \\ 0 & 0 & 1 & 0 \\ 0 & 0 & 0 & 1 \end{bmatrix}$$

and  $v_{k-1}$  is a zero mean Gaussian process noise vector with covariance matrix

$$Q = \begin{bmatrix} \frac{T^3}{3} & 0 & \frac{T^2}{2} & 0 \\ 0 & \frac{T^3}{3} & 0 & \frac{T^2}{2} \\ \frac{T^2}{2} & 0 & T & 0 \\ 0 & \frac{T^2}{2} & 0 & T \end{bmatrix} \bar{q},$$

where  $\bar{q}$  is the process noise intensity and  $T$ , the sampling interval. To consider observer accelerations in the target dynamics,  $U_{k-1,k}$  is defined which is a vector of observer inputs given by

$$U_{k-1,k} = \begin{bmatrix} u_1 \\ u_2 \\ u_3 \\ u_4 \end{bmatrix} = \begin{bmatrix} x_k^o - x_{k-1}^o - T\dot{x}_{k-1}^o \\ y_k^o - y_{k-1}^o - T\dot{y}_{k-1}^o \\ \dot{x}_k^o - \dot{x}_{k-1}^o \\ \dot{y}_k^o - \dot{y}_{k-1}^o \end{bmatrix}.$$

These observer values are often determined by an on-board inertial navigation system powered by a Global Positioning System (GPS).

The measurement equation can be represented as:

$$z_k = \gamma(\mathbf{x}_k) + \eta_k, \quad (2)$$

where  $\eta_k$  is a zero mean Gaussian noise with standard deviation  $\sigma_\theta$ . From this model, the only available measurement, which is the noise corrupted passive bearings are obtained. Measurements are obtained from the observer's platform to the target with a reference clockwise positive to the y-axis. The true bearing measurements are defined as:

$$\gamma(\mathbf{x}_k) = \tan^{-1} \left( \frac{x_k}{y_k} \right). \quad (3)$$

Now, the problem of bearings-only tracking boils down to estimating the states of the relative state vector  $\mathbf{x}_k$ , defined by (1), for a set of measurements,  $z_i$ , for  $i = 1, 2, \dots, k$ , as defined in (2).

## III. FILTERING METHODS

### A. Cubature Kalman filter

Cubature Kalman Filter (CKF) is a nonlinear filter which uses spherical radial cubature rule for numerically computing the multivariate moment integrals encountered in the nonlinear Bayesian filtering framework [12]. In this technique, the intractable integrals encountered in nonlinear Bayesian filtering are decomposed into spherical

and radial integrals. This is achieved using a spherical-radial transformation. The spherical and radial integrals are then numerically computed by the spherical cubature rule and the Gaussian quadrature rule. Transformation has been done in such a way that the surface integral can be calculated over a unit hyper-sphere of dimension  $n$ .

For an arbitrary function  $f(\mathbf{x})$ ,  $\mathbf{x} \in R^n$ , the integral

$$I(f) = \frac{1}{\sqrt{|\Sigma|(2\pi)^n}} \int_{R^n} f(\mathbf{x}) \exp \frac{-1}{2} (\mathbf{x}-\mu)^T \Sigma^{-1} (\mathbf{x}-\mu) d\mathbf{x}$$

can be expressed in spherical coordinate system as

$$I(f) = \frac{1}{\sqrt{(2\pi)^n}} \int_{r=0}^{\infty} \int_{U_n} [f(CrZ + \mu) ds(Z)] r^{n-1} e^{-r^2/2} dr,$$

where  $\mathbf{x} = CrZ + \mu$ ,  $C$  is the cholesky decomposition of  $\Sigma$ ,  $\|Z\| = 1$ ,  $U_n$  is the surface of unit hyper-sphere. To compute the integral  $I(f)$ , first we need to compute

$$\int_{U_n} f(CrZ + \mu) ds(Z).$$

This integral can be approximately calculated by third degree fully symmetrical spherical radial cubature rule. By considering zero mean and unity variance, it can be approximated as

$$\int_{U_n} f(rZ) ds(Z) = \frac{2\sqrt{\pi^n}}{2n\Gamma(n/2)} \sum_{i=1}^{2n} f[ru]_i,$$

where  $[u]_i$  ( $i = 1, 2, \dots, 2n$ ) are the cubature points located at the intersections of unit hyper-sphere and it's axes.

### B. Gauss-Hermite filter

In GHF, the single dimensional quadrature points are generated by utilizing the Golub's technique. The single dimensional quadrature rule could be extended to multi-dimension by applying the product rule [14].

Let us consider a multidimensional random variable  $\mathbf{x}$  and the weight function as the standard normal distribution, hence the integral of interest will be:

$$I_N = \int_{-\infty}^{\infty} f(\mathbf{x}) \aleph(\mathbf{x}; 0, I_n) d\mathbf{x}.$$

By applying the product rule, the integral  $I_N$  could be approximated as:

$$I_N \approx \sum_{i_1}^m \dots \sum_{i_n}^m f(q_{i_1}, q_{i_2}, \dots, q_{i_n}) w_{i_1} w_{i_2} \dots w_{i_n}.$$

To evaluate the expected value of an  $n$  dimensional integral with  $m$ -point GHF,  $m^n$  number of multivariate quadrature points and corresponding weights are required. For an example, for a three dimensional system and three point GHF, twenty-seven quadrature points and weights are required which may be expressed as  $\{q_i, q_j, q_k\}$  and  $\{w_i w_j w_k\}$  respectively for  $i = 1, 2, 3$ ;  $j = 1, 2, 3$ ; and  $k = 1, 2, 3$ . As the number of quadrature points increases exponentially with increasing dimension, the GHF suffers from *the curse of dimension* problem.

### C. Sparse-grid Gauss-Hermite filter

In SGHF, the single dimensional quadrature rule is extended to multidimension by using the Smolyak rule [16]. Although Smolyak rule was available in literature for a long time, it was introduced to filtering very recently in [15]. It can reduce the computational load considerably when compared to product rule.

*Smolyak rule:*

Any integral of the form

$$I_{n,L}(f) = \int_{\mathbb{R}^n} f(\mathbf{x}) \aleph(\mathbf{x}; 0, I_n) d\mathbf{x}$$

can be approximated numerically as:

$$I_{n,L}(f) \approx \sum_{q=L-n}^{L-1} (-1)^{L-1-q} C_{L-1-q}^{n-1} \sum_{\Xi \in \mathbf{N}_q^n} (I_{l_1} \otimes I_{l_2} \otimes \dots \otimes I_{l_n}), \quad (4)$$

where  $I_{n,L}$  represents the numerical evaluation of  $n$ -dimensional integral with the accuracy level  $L$ , meaning that the approximation is exact for all the polynomials having degree upto  $(2L - 1)$ .  $C$  stands for the binomial coefficient, *i.e.*  $C_k^n = n!/k!(n-k)!$ ,  $I_{l_j}$  is the single dimensional quadrature rule with accuracy level  $l_j \in \Xi$  *i.e.*  $\Xi \triangleq (l_1, l_2, \dots, l_n)$ ,  $\otimes$  stands for the tensor product and  $\mathbf{N}_q^n$  is set of possible values of  $l_j$  given as:

$$N_q^n = \begin{cases} \Xi : \sum_{j=1}^n l_j = n + q & \text{for } q \geq 0 \\ \emptyset & \text{for } q < 0. \end{cases} \quad (5)$$

Equation (4) can be written as:

$$I_{n,L}(f) \approx \sum_{q=L-n}^{L-1} (-1)^{L-1-q} C_{L-1-q}^{n-1} \sum_{\Xi \in \mathbf{N}_q^n} \sum_{q_{s_1} \in X_{l_1}} \sum_{q_{s_2} \in X_{l_2}} \dots \sum_{q_{s_n} \in X_{l_n}} f(q_{s_1}, q_{s_2}, \dots, q_{s_n}) w_{s_1} w_{s_2} \dots w_{s_n}, \quad (6)$$

where  $X_{l_j}$  is the set of quadrature points for the single dimensional quadrature rule  $I_{l_j}$ ,  $[q_{s_1}, q_{s_2}, \dots, q_{s_n}]^T$  is a sparse-grid quadrature point *i.e.*  $q_{s_j} \in X_{l_j}$  and  $w_{s_j}$  is the weight associated with  $q_{s_j}$ . Some quadrature points may occur multiple times, which could be counted only once and by adding their weights. The final set of the SGQ points can be represented as:

$$X_{n,L} = \bigcup_{q=L-n}^{L-1} \bigcup_{\Xi \in \mathbf{N}_q^n} (X_{l_1} \otimes X_{l_2} \otimes \dots \otimes X_{l_n}),$$

where  $\bigcup$  represents union of the individual SGQ points.

### D. Cramer-Rao lower bound (CRLB)

For the bearings-only tracking problem discussed in this paper, the posterior CRLB is computed, which gives the best possible performance that can be attained. The approach mentioned in [19] is followed in which it is defined

that for a nonlinear discrete time system, the covariance of the estimated states follow the condition:

$$\mathbb{E}[(\hat{x}_k - x_k)(\hat{x}_k - x_k)^T] \geq J_k^{-1}.$$

$J_k$ , termed as the information matrix, can be recursively calculated using the equation

$$J_k = D_{k-1}^{22} - D^{21}(J_{k-1} + D^{11})^{-1}D^{12},$$

where, for the additive Gaussian noise models considered in this paper, the matrices mentioned above can be defined as:

$$D^{11} = F^T Q^{-1} F, \quad D^{12} = -F^T Q^{-1},$$

$$D^{21} = (D^{12})^T, \quad D_{k-1}^{22} = Q^{-1} + \mathbb{E}[H_k^T R_k^{-1} H_k],$$

where  $R_k = \sigma_\theta^2$  and  $H_k$  is given by the Jacobian of the measurement function.

$$H_k = \frac{\partial \gamma(\mathbf{x}_k)}{\partial \mathbf{x}_k}$$

$$= \begin{bmatrix} \frac{y_k}{x_k^2 + y_k^2} & \frac{-x_k}{x_k^2 + y_k^2} & 0 & 0 \end{bmatrix}.$$

Finally, the CRLB for the RMS position error can be defined as:

$$CRLB_k = \sqrt{J_k^{-1}(1,1) + J_k^{-1}(2,2)},$$

where  $J(i,j)$  denotes the element in the  $i^{th}$  row and the  $j^{th}$  column and  $J_k$  is initialised as  $J_0 = \mathbb{E}[P_0^{-1}]$ ,  $P_0$  being the initial covariance matrix as defined in (8).

#### IV. SIMULATIONS

The performance of GHF and SGHF is compared with the performance of CKF for a number of 500 Monte Carlo runs. The target-observer dynamics is represented in Fig. 1. For each Monte Carlo run, the target starts at the same target state and is subjected to a process noise intensity  $\bar{q} = 1.944 \times 10^{-6} km^2/min^3$ . The parameters used in the tracking scenario is mentioned in Table I.

TABLE I: Tracking scenario parametrs

Parameters	values
Initial range ( $r$ )	5 km
Target speed ( $s$ )	4 knots
Target course	-140°
Observer speed	5 knots
Observer initial course	140°
Observer final course	20°
Observer manoeuver	From 13 <sup>th</sup> to 17 <sup>th</sup> min

##### A. Filter Initialisation

The filters are all initialised using the method given in [2]. The position estimates of the relative vector,  $[\bar{x} \ \bar{y}]^T$  is initialised based on the prior range estimate of the target and on the first bearing measurement. The prior range estimate of the target is defined to be  $\bar{r} \sim N(r, \sigma_r^2)$ , where  $r$  is the true initial range of the target from the

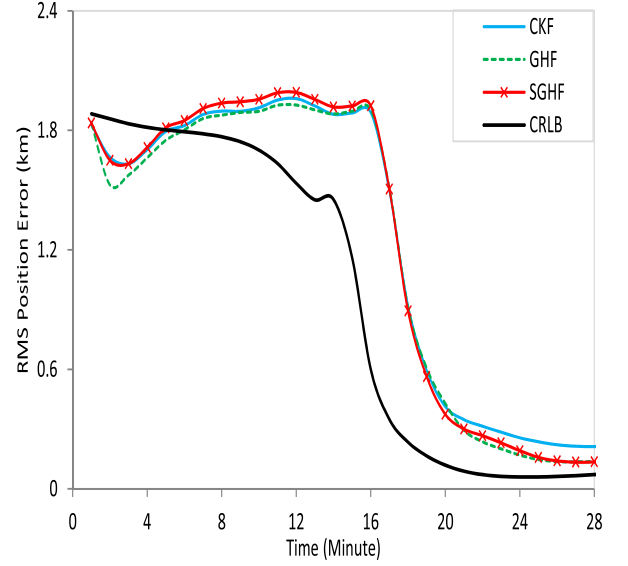


Fig. 2: RMS position error of different filters

observer. For initial bearing measurement estimate, the true initial bearing  $\theta$  with an accuracy  $\sigma_\theta$  is used such as  $\theta_0 \sim N(\theta, \sigma_\theta^2)$ . Assuming the prior knowledge of target speed,  $s$  is known, the initial speed estimate of the target is defined as  $\bar{s} \sim N(s, \sigma_s^2)$ . Inferring that the target is closing in on the observer, the initial course estimate is defined as  $\bar{c} = \theta_0 + \pi$ . The values of  $\sigma_r$ ,  $\sigma_s$ ,  $\sigma_\theta$  and  $\sigma_c$  used in this study are 2 km, 2 knots, 1.5° and  $\pi/\sqrt{12}$ , respectively.

Now, the initial state estimate for the relative state vector  $\hat{\mathbf{x}}$  can be defined as:

$$\hat{\mathbf{x}}_0 = \begin{bmatrix} \bar{x} \\ \bar{y} \\ \bar{x} \\ \bar{y} \end{bmatrix} = \begin{bmatrix} \bar{r} \sin(\theta_0) \\ \bar{r} \cos(\theta_0) \\ \bar{s} \sin(\bar{c}) - \dot{x}_0^o \\ \bar{s} \cos(\bar{c}) - \dot{y}_0^o \end{bmatrix}. \quad (7)$$

Here,  $(\dot{x}_0^o, \dot{y}_0^o)$  is the initial velocity component of observer state vector. Similarly, the initial covariance is calculated as:

$$P_0 = \begin{bmatrix} P_{xx} & P_{xy} & 0 & 0 \\ P_{yx} & P_{yy} & 0 & 0 \\ 0 & 0 & P_{\dot{x}\dot{x}} & P_{\dot{x}\dot{y}} \\ 0 & 0 & P_{\dot{y}\dot{x}} & P_{\dot{y}\dot{y}} \end{bmatrix}, \quad (8)$$

where

$$P_{xx} = \bar{r}^2 \sigma_\theta^2 \cos^2(\theta_0) + \sigma_r^2 \sin^2(\theta_0)$$

$$P_{yy} = \bar{r}^2 \sigma_\theta^2 \sin^2(\theta_0) + \sigma_r^2 \cos^2(\theta_0)$$

$$P_{xy} = P_{yx} = (\sigma_r^2 - \bar{r}^2 \sigma_\theta^2) \sin \theta_0 \cos \theta_0$$

$$P_{\dot{x}\dot{x}} = \bar{s}^2 \sigma_c^2 \cos^2 \bar{c} + \sigma_s^2 \sin^2 \bar{c}$$

$$P_{\dot{y}\dot{y}} = \bar{s}^2 \sigma_c^2 \sin^2 \bar{c} + \sigma_s^2 \cos^2 \bar{c}$$

$$P_{\dot{x}\dot{y}} = P_{\dot{y}\dot{x}} = (\sigma_s^2 - \bar{s}^2 \sigma_c^2) \sin \bar{c} \cos \bar{c}.$$

The sampling interval is taken as  $T = 1 \text{ min}$  and the observation period lasts for 28 min. Performance analysis was done by plotting the root mean square position error

TABLE II: Track-loss and computational time of different filters

Filters	% Track-loss	Computational time (sec)
CKF	5.6	5.04
GHF	4.6	9.48
SGHF	5	6.9

of different filters as shown in Fig. 2. For the particular target-observer scenario discussed in this paper, it can be found that the results given by quadrature filters GHF and SGHF are comparable and is much better than CKF. Better or more accurate estimates means higher probability in successfully tracking and engaging the target. For a submarine torpedo engagement scenario, more precise estimates imply higher probability in neutralising the enemy submarine. As a reference to the theoretical lower bound of error that can be achieved, the posterior CRLB is also plotted. For simulations, a 2-point GHF was considered and the accuracy level of SGHF was taken as 2.

The RMSE was calculated considering a stringent track-loss condition. A track was defined divergent when the position error at any time index exceeds a predefined value, set as 5 km in our simulations. The number of divergent tracks for various filters were counted and is listed in Table. II. It can be observed that divergent tracks counted for GHF is less than all other filters. Table. II also mentions the computational time for the different filters. As CKF uses less number of points, it takes less time for tracking the target. GHF, which suffer from the *curse of dimension* problem takes more time for estimating the target track. SGHF on the other hand gives better performance by consuming less computational time with comparable track-loss counts.

## V. CONCLUSION

In this paper, the performance of nonlinear filters namely CKF, GHF and SGHF were studied for a typical underwater passive BOT problem. Filter performance was validated using RMS position error plot, number of track-loss incurred and computational time. Eventhough the track-loss counts were comparable, accuracy levels of the GHF and SGHF proved to be better than the CKF. Better computational efficiency of SGHF when compared to GHF and high accuracy levels than CKF, makes it's performance superior to both the filters, GHF and CKF. Hence, SGHF can be proposed as an alternate filtering algorithm for the kind of BOT problem discussed in this work.

## REFERENCES

[1] R. Karlsson and F. Gustafsson, "Recursive bayesian estimation: bearings-only applications," in *IEE Proceedings-Radar, Sonar and Navigation*, vol. 152, no. 5. IET, 2005, pp. 305–313.

[2] B. Ristic, S. Arulampalam, and N. Gordon, *Beyond the Kalman filter: Particle filters for tracking applications*. Artech house Boston, 2004, vol. 685.

[3] V. J. Aidala, "Kalman filter behavior in bearings-only tracking applications," *IEEE Transactions on Aerospace and Electronic Systems*, no. 1, pp. 29–39, 1979.

[4] A. Farina, "Target tracking with bearings-only measurements," *Signal processing, Elsevier*, vol. 78, no. 1, pp. 61–78, 1999.

[5] S. C. Nardone and V. J. Aidala, "Observability criteria for bearings-only target motion analysis," *IEEE Transactions on Aerospace and Electronic Systems*, no. 2, pp. 162–166, 1981.

[6] T. L. Song, "Observability of target tracking with range-only measurements," *IEEE Journal of Oceanic Engineering*, vol. 24, no. 3, pp. 383–387, 1999.

[7] B. Ristic and M. S. Arulampalam, "Tracking a manoeuvring target using angle-only measurements: algorithms and performance," *Signal processing*, vol. 83, no. 6, pp. 1223–1238, 2003.

[8] M. S. Arulampalam, B. Ristic, N. Gordon, and T. Mansell, "Bearings-only tracking of manoeuvring targets using particle filters," *EURASIP Journal on Applied Signal Processing*, vol. 2004, pp. 2351–2365, 2004.

[9] L. q. Li and W. x. Xie, "Bearings-only maneuvering target tracking based on fuzzy clustering in a cluttered environment," *AEU-International Journal of Electronics and Communications*, vol. 68, no. 2, pp. 130–137, 2014.

[10] S. J. Julier and J. K. Uhlmann, "A new extension of the kalman filter to nonlinear systems," in *Int. symp. aerospace/defense sensing, simul. and controls*, vol. 3, no. 26. Orlando, FL, 1997, pp. 3–2.

[11] —, "Unscented filtering and nonlinear estimation," *Proceedings of the IEEE*, vol. 92, no. 3, pp. 401–422, 2004.

[12] I. Arasaratnam and S. Haykin, "Cubature kalman filters," *IEEE Transactions on Automatic Control*, vol. 54, no. 6, pp. 1254–1269, 2009.

[13] K. Ito and K. Xiong, "Gaussian filters for nonlinear filtering problems," *Automatic Control, IEEE Transactions on*, vol. 45, no. 5, pp. 910–927, 2000.

[14] G. Chalasani and S. Bhaumik, "Bearing only tracking using gauss-hermite filter," in *7th IEEE Conference on Industrial Electronics and Applications (ICIEA)*. IEEE, 2012, pp. 1549–1554.

[15] B. Jia, M. Xin, and Y. Cheng, "Sparse-grid quadrature nonlinear filtering," *Automatica*, vol. 48, no. 2, pp. 327–341, 2012.

[16] S. A. Smolyak, "Quadrature and interpolation formulas for tensor products of certain classes of functions," in *Dokl. Akad. Nauk SSSR*, vol. 4, no. 240-243, 1963, p. 123.

[17] G. H. Golub and J. H. Welsch, "Calculation of gauss quadrature rules," *Mathematics of Computation*, vol. 23, no. 106, pp. 221–230, 1969.

[18] P. H. Leong, S. Arulampalam, T. A. Lamahewa, and T. D. Abhayapala, "A gaussian-sum based cubature kalman filter for bearings-only tracking," *IEEE Transactions on Aerospace and Electronic Systems*, vol. 49, no. 2, pp. 1161–1176, 2013.

[19] P. Tichavsky, C. H. Muravchik, and A. Nehorai, "Posterior cramer-rao bounds for discrete-time nonlinear filtering," *Signal Processing, IEEE Transactions on*, vol. 46, no. 5, pp. 1386–1396, 1998.

# Fusion of radar and secondary sensor data using kinematic models of multiple simultaneous targets

Brian L. Karlsen, Esben Nielsen, Morten T. Pedersen  
Processing, Technology & Innovation, Terma A/S  
Hovmarken 4, DK-8520 Lystrup  
Phone: +45 8743 6000  
Denmark

**Abstract**—We present a method for fusion of radar and secondary sensor data, e.g. AIS (Automatic Identification System), ADS-B (Automatic Dependent Surveillance Broadcast) or IFF (Identification, Friend or Foe) data. The method is based on fusion of kinematic models of target trajectories from the two sensors into kinematic models of the associations. The method can handle several hundred simultaneous targets (shown for 529 x 529 targets + 1600 clutter plots). It does not require several iterations through the data set in order to find associations, and it includes track history from the two sensors. The mathematical framework of the method is based on Kalman filters, maximum likelihood and probability theory as well as kinematics.

## I. INTRODUCTION

In this paper, we will investigate such a specialized method applied to tracking of multiple moving physical objects. The sensors employed are a monostatic primary radar and AIS (Automatic Identification System)<sup>1</sup>, but other sensors like ADS-B (Automatic Dependent Surveillance - Broadcast)<sup>2</sup> or IFF (Identification, Friend or Foe)<sup>3</sup> registering object movement might be used as well.

Fusing data from radar and AIS have been reported previously in e.g. [1], [2], [3]. In [1], Stateczny and Lisaj proposed to fuse the estimates of  $n$  kinematic models through a linear combination of the model estimates. The coefficients of the linear combination were weight matrices computed from the covariance matrices of the different sensor models. Suo and Liu proposed a different method in [2], where the fusion of the data is based on a fuzzy C-mean clustering algorithm. This algorithm is capable of handling multiple simultaneous targets. AIS trajectories are treated as the center of a cluster and an “adaptive correlation-detecting function” is derived from the trajectories of the two sensors. Habtemariam [3] advocates a measure-level approach to generate a single fused track estimate based on a kinematic model.

Our method resembles very closely that of multiple-hypothesis tracking with pruning introduced by Blackman [5]. However, instead of applying it to data from a single sensor, we apply it to data from two types of sensors and after tracking. In our method we will only be using knowledge about the position of each object and the uncertainty in position

<sup>1</sup>AIS is a short range coastal tracking system used on ships and search-and-rescue units for identifying and locating these by e.g. vessel traffic services.

<sup>2</sup>A cooperative surveillance technology in which an aircraft determines its position via satellite navigation and periodically broadcasts it

<sup>3</sup>Interrogation system for identifying aircraft, vehicles or forces as friendly and to determine their bearing and range from the interrogator

to build kinematic models, however the method could easily be extended to include velocity and other features as well. The kinematic models are based on a variant of a standard Kalman filter [4]. All objects detected by a sensor will get a kinematic model assigned. Included in the kinematic model is a likelihood signifying how well the given kinematic model fits the data as well as a covariance matrix denoting uncertainty. The models from the two sensors are fused based on these two measures as well as the Mahalanobis distance. This will generate many different potential associations between models from the two sensors. Each association is ranked according to its probability when compared to all conflicting associations. The best association for each set of conflicting associations will be compared to an association probability threshold and published if above this threshold. If the probability of a given association drops below a minimum probability limit, the association will be ignored.

In the following sections, our method will be presented, starting with track building, going through track fusion and ending with the model selection. We will then present some simulations showing the performance of the method, and finally we will discuss the results and present our conclusions.

## II. METHOD

### A. Track building

This section presents the framework for forming all kinds of tracks including fused tracks from observations. The kinematic model is based solely on positional observation data and their uncertainty. These observations are used to derive velocity estimates using the kinematic model. For our investigation, we are using a constant characteristic acceleration and a Kalman filter variant as the kinematic model [4]. For each detected target of a sensor, at least one kinematic model is assigned, i.e. all radar targets will get a kinematic model and all AIS targets will get a kinematic model.

Some definitions:

- A *track* is a series of 2D observations which might be a set of real observations from a target.
- A *target* is a physical object which can be detected by a sensor. A target might have several possible tracks.
- Two tracks are *conflicting* if they share an observation.
- A *kinematic model* is built on all or some of the observations in a *track* and can be used to predict

where the *target* related to the *track* is going to be in 2D space at a particular point in time.

1) *Track likelihood*: Each track  $\tau$  has a likelihood  $L_\tau \in [0; \infty[$  of being a real track disregarding other possible tracks (see below). The likelihood is proportional to the value of the continuous probability density function of  $\tau$  for a given observation. Assuming there are only two possibilities, either the track is correct or there are no tracks at all, the probability of the track being correct is defined as

$$P(\tau) = \frac{L_\tau}{1 + L_\tau}$$

when no tracks at all has a likelihood  $L(\emptyset) = 1$ . The likelihood is updated as follows: If an observation  $o$  associates with a track  $\tau$ ,

$$\begin{aligned} L_{\tau+o} &= \frac{P(o \text{ is an observation of target of } \tau)}{P(o \text{ is clutter or noise})} L_\tau \\ &= P_g P_{d,\tau} \frac{\Lambda(o, \tau)}{\Lambda(o, 0)} L_\tau, \end{aligned}$$

where  $P_{d,\tau}$  is the probability of detection for the track  $\tau$ ,  $P_g$  is the gating probability (see below), and  $\Lambda(o, \tau)$  is the association probability density between the observation  $o$  and the track  $\tau$ . The probability density  $\Lambda(o, \tau) = \mathcal{N}[\Delta\zeta; \mathbf{0}, \rho_d]$  originates from the Kalman filter of  $\tau$  and is normally distributed with a mean of  $\mathbf{0}$  and residual filter covariance  $\rho_d$  (see Eq. 2) evaluated at the observation residual  $\Delta\zeta$  (see Eq. 1).  $\Lambda(o, 0)$  is the association probability density that  $o$  does not belong to any track, i.e. the density of clutter and noise. The gating probability  $P_g$  is defined in terms of the acceleration number of sigmas [4, p. 109]:  $g_a = \frac{a_{\max}}{\sigma_a} = \sqrt{-2 \ln(1 - P_g)}$ , where  $\sigma_a$  is the standard deviation of the acceleration and  $a_{\max}$  is the characteristic acceleration in any direction. If a track does not associate with any observations, the track likelihood is updated according to

$$L_{\tau'} = (1 - P_g P_{d,\tau}) L_\tau.$$

Now we call a track for which  $L_\tau > L_c$  confirmed.  $L_c \geq 1$  is a parameter with a typical value of 10.

2) *Detecting observation overlap of tracks*: Now consider a track originating from a two-dimensional sensor such as radar or AIS. We assume that each predicted track position according to the kinematic model and individual observations represents bivariate normal distributions in latitude and longitude with a mean represented by the  $2 \times 1$  column vector

$$\zeta = \begin{bmatrix} x \\ y \end{bmatrix}$$

in latitude  $x$  and longitude  $y$  and with a  $2 \times 2$  positional covariance  $\rho$  in the same latitude-longitude coordinate system. The use of a cartesian coordinate system here takes place under the assumption of high resolution in radar azimuth ( $< 1^\circ$  beamwidth) and it serves as a first order approximation to the range-bearing coordinate system of the radar.

To detect overlap between an observation and a track in terms of similarity, location and uncertainties, a merge probability  $P_m$  is used. The merge probability should for a radar have a value close to one, for instance 0.999. This merge

probability is converted to a maximum Mahalanobis distance  $D_M^{\max}$  between the two tracks as follows

$$[D_M^{\max}]^2 = -2 \ln(1 - P_m).$$

The observation residual, i.e. the difference between an observation and a predicted track position is

$$\Delta\zeta = \zeta_\tau - \zeta_o, \quad (1)$$

with a residual filter covariance of

$$\rho_d = \rho_\tau + \rho_o \quad (2)$$

where  $\rho_\tau$  is the covariance of the Kalman filter for predicted position and  $\rho_o$  is the covariance of the observation. The Mahalanobis distance  $D_M(o, \tau)$  is then found as

$$D_M^2(o, \tau) = \Delta\zeta^T \cdot \rho_d^{-1} \cdot \Delta\zeta. \quad (3)$$

The criterion for overlap is then

$$D_M^2(o, \tau) \leq [D_M^{\max}]^2. \quad (4)$$

Any observations  $o$  satisfying this criterion will be eligible for inclusion in the track  $\tau$ .

Using the likelihood formulas of II-A1 and the overlap criterion of Eq. (4) it can be determined if a particular observation belongs to a particular track. Using this membership makes it possible to build kinematic models based on the observations selected for a particular track.

## B. Fusion of tracks

Assuming that all radar tracks and all AIS tracks have kinematic models assigned to them, we can now consider how to fuse these two sets of data. Furthermore we assume that:

- AIS is always valid: Each AIS message contains correct position (with some uncertainty), time and identifier. If an AIS transmitter is switched off the target is still present.
- The radar tracker tracks the target correctly given the observations.
- A *hypothesis* is a set of associations assumed to be correct in the sense that each observation of each association originated from the suggested targets.

Let us say an AIS track consists of a list of AIS messages:  $a = \{m_1, \dots, m_k\}$ , and a radar track is a list of observations (plots):  $\tau = \{o_1, \dots, o_k\}$ . We can assume a hypothesis of association as a set of pairs  $H = \{(a_1, \tau_1), \dots\}$ . Notice that  $H = \emptyset$  denotes the hypothesis that no radar tracks and AIS tracks are associated.

We assume there is at most one correct AIS track for each radar track and vice versa, i.e. there are no overlapping pairs in  $H$ . So if  $(a, \tau), (a', \tau') \in H$  then  $\tau$  and  $\tau'$  must not overlap in time, but can originate from track fragments.

At any given time, we can ascribe a hypothesis with a probability  $p(H)$ . We assign each hypothesis a unit-less likelihood  $L(H)$  such that

$$p(H) = \frac{L(H)}{\sum_{H'} L(H')}$$

where  $H'$  includes the empty hypothesis and fix the scale by  $L(\emptyset) = 1$ . This is realized by setting  $L(H) = p(H)/p(\emptyset)$ .

Because the AIS messages and radar observations do not have the same time stamps, we need to inter- and extrapolate in time. Thus, we need a kinematic filter to give an estimate of how well an update fits the previous update, e.g. a Kalman filter. This kinematic model (see II-A) of the association is built using both the radar observations and the AIS messages.

Given an AIS message  $m$ , we get association densities  $\Lambda(m, a)$  and  $\Lambda(m, (a, \tau))$ , where  $\Lambda(m, (a, \tau))$  is the association probability density between the message  $m$  and the association  $(a, \tau)$  and  $\Lambda(m, a)$  is the association probability density that  $m$  belongs to the AIS track  $a$ . Both densities have the dimension of inverse of the dimension of the message  $m$ , i.e.  $m^{-2}$  and the densities are still normally distributed and based on filter properties (see II-A1). Similarly, from a radar observation  $o$  in a track update we get association densities  $\Lambda(o, \tau)$  and  $\Lambda(o, (a, \tau))$  with the dimension of inverse area i.e.  $m^{-2}$ .

1) *AIS update*: Let us say an AIS track  $a$  is updated with a new message  $m$ , i.e.

$$a' = a \cup \{m\} .$$

The hypothesis  $H$  containing  $(a, \tau)$  will be updated to  $H'$  containing  $(a', \tau)$ . Notice that the original hypothesis containing  $(a, \tau)$  will no longer be relevant because we assume the full AIS track is correct. For any practical applications,  $H' = H$  and will be denoted as such. Using this in a Bayesian update model, we have:

$$p(H|m) = \frac{p(m|H)}{p(m)} p(H) .$$

If a given hypothesis contains the association  $(a, \tau)$ , then  $p(m|H) \propto \Lambda(m, (a, \tau))$ . If a given hypothesis does not contain an association then  $p(m|H) \propto \Lambda(m, a)$ . Setting the proportionality factor to  $p(m)/\Lambda(m, a)$  the likelihood can be derived:

$$\begin{aligned} L(H|m) &= \frac{p(H|m)}{p(\emptyset)} = L(H) \frac{p(m|H)}{p(m)} \\ \Downarrow \\ L(H|m) &= L(H) \begin{cases} \frac{\Lambda(m, (a, \tau))}{\Lambda(m, a)} & \text{for } (a, \tau) \in H \\ 1 & \text{for no } (a, \tau) \in H . \end{cases} \end{aligned}$$

Notice that by dividing by  $\Lambda(m, a)$  in both conditions, the dimension of  $L(H)$  remains unchanged. If  $m$  represents a new AIS target, i.e.  $a = \{m\}$ , then for each radar track  $\tau$ , a new hypothesis can be spawned, namely the one where  $\tau$  associates to  $a$ :

$$H \leftarrow \begin{cases} H \\ H \cup \{(a, \tau)\} . \end{cases}$$

We must apply the same Bayesian type update

$$\begin{aligned} p(H|m) &\propto \Lambda(m, 0)p(H) \\ p(H \cup \{(a, \tau)\}|m) &\propto \Lambda(m, \tau)p(H) \end{aligned}$$

where  $\Lambda(m, 0)$  is a constant signifying the density of previously non-existent AIS tracks. This leads to

$$\begin{aligned} L(H|m) &= L(H) \\ L(H \cup \{(a, \tau)\}|m) &= \frac{\Lambda(m, \tau)}{\Lambda(m, 0)} L(H) . \end{aligned}$$

2) *Radar update*: Let us say radar track  $\tau$  is updated with a new observation  $o$ , i.e.

$$\tau \leftarrow \tau \cup \{o\} .$$

For a hypothesis  $H$  containing  $(a, \tau)$

$$p(H|o) \propto \Lambda(o, (a, \tau))p(H) ,$$

whereas for a hypothesis where  $\tau$  is not associated

$$p(H|o) \propto \Lambda(o, \tau)p(H) .$$

I.e.

$$L(H|o) = L(H) \begin{cases} \frac{\Lambda(o, (a, \tau))}{\Lambda(o, \tau)} & \text{for } (a, \tau) \in H \\ 1 & \text{for no } (a, \tau) \in H . \end{cases}$$

If a new track arrives from the radar tracker let us consider the first observation, i.e.  $\tau = \{o\}$ : For each AIS track a new hypothesis can be spawned

$$H \leftarrow \begin{cases} H \\ H \cup \{(a, \tau)\} \end{cases}$$

$$\begin{aligned} p(H|o) &\propto \Lambda(o, 0)p(H) \\ p(H \cup \{(a, \tau)\}|o) &\propto \Lambda(o, a)p(H) \end{aligned}$$

where  $\Lambda(o, 0)$  is a number describing the density of previously non-existent tracks. Or formulated as likelihood

$$\begin{aligned} L(H|o) &= L(H) \\ L(H \cup \{(a, \tau)\}|o) &= \frac{\Lambda(o, a)}{\Lambda(o, 0)} L(H) . \end{aligned}$$

3) *Association likelihood*: Let us define the association likelihood  $\tilde{L}(a, \tau)$ . When a new AIS track  $a$  arrives with message  $m$ , for each radar track  $\tau$  we initialize  $(a, \tau)$  with

$$\tilde{L}(a, \tau) = \frac{\Lambda(m, \tau)}{\Lambda(m, 0)} .$$

When a new radar track appears, for each AIS track  $a$  we initialize  $(a, \tau)$  on the first observation  $o$  with

$$\tilde{L}(a, \tau) = \frac{\Lambda(o, a)}{\Lambda(o, 0)} .$$

When a new message,  $m$ , for AIS track  $a$  arrives:

$$\tilde{L}(a, \tau) \leftarrow \frac{\Lambda(m, (a, \tau))}{\Lambda(m, a)} \tilde{L}(a, \tau) .$$

When a new radar track update with observation  $o$  arrives, calculate

$$\tilde{L}(a, \tau) \leftarrow \frac{\Lambda(o, (a, \tau))}{\Lambda(o, \tau)} \tilde{L}(a, \tau) .$$

It can now be seen that for any hypothesis,  $H$ ,

$$L(H) = \prod_{(a, \tau)} \tilde{L}(a, \tau) .$$

Determining if a particular observation or message from the radar track or the AIS track should be included in the kinematic model of the association is handled by re-using Eq. (4) and the framework presented in Sec. II-A. If the overlap criterion is not met, the association in question is removed from the pool of candidate associations.

### C. Model selection

Once a number of potentially conflicting hypotheses for associating AIS tracks with radar tracks (or vice versa) have been found, we need to select which hypothesis will be accepted. Put in other terms, we need to determine which associations should be part of the accepted hypothesis.

A simple way is to set up the association cost as

$$c(a, \tau) = -\ln \tilde{L}(a, \tau),$$

and then use a standard 2D assignment algorithm such as Auction [4, p. 648]. Alternatively, this selection can be performed by calculating the probability of associating an AIS track  $a$  with a radar track  $\tau$  as

$$p((a, \tau)) \equiv \frac{\tilde{L}(a, \tau)}{1 + \sum_{(a', \tau')} \tilde{L}(a', \tau')},$$

i.e.  $(a', \tau')$  iterates over all the conflicting associations of  $(a, \tau)$  including itself. The criterion for acceptance of an association is then

$$\max_{(a', \tau')} p((a', \tau')) > p_T$$

where  $p_T$  is a probability threshold usually set to 0.9. Thus we maximize the probability across all conflicting associations, and if the maximum is higher than  $p_T$  we accept the association. The unaccepted associations will remain unaccepted candidates for association as long as their probabilities stay above a minimum probability  $p_{\min}$ , usually set to 0.1. If their probabilities drop below  $p_{\min}$ , the associations in question will be removed from the pool of candidate associations.

## III. SIMULATIONS

The simulations will show how our fusion method performs with several hundred simulated targets from radar and from AIS. The intention behind the simulations is to provide a clear and concise evaluation of the method. We will not be providing real-world data, since such data may be more ambiguous and open for interpretation. However, the method is ready for implementation in real-world scenarios.

### A. Baseline

This scenario forms the baseline of the following simulations. The scenario is composed of 529 radar targets and 529 AIS targets superimposed on top of the radar targets. The radar data are generated using 2 sec updates with a maximum range of 33 nmi ( $\approx 61$  km). There are 1600 noise plots present. The targets are arranged radially with 23 circles of 23 targets each. The range to each circle increases in steps of 2667 m from 1341 m to 60015 m. Each target has an azimuthal course and the speeds vary from 2.0 kt to 89 kt from the innermost circle to the outermost circle. The AIS targets are updated in random sequence with 1-5 sec intervals. An overview of the scenario can be seen in Fig.1. We will be employing two measures for evaluating the quality of the fusions. The fraction of correct fusions has previously been promoted by [4, p. 472]. This is defined in terms of the number of tracks with purity equal to 1 relative to the total number of tracks. The data for the baseline scenario can be seen in Fig.2. Correct fusions start to appear after two AIS updates of the slowest updating targets. After

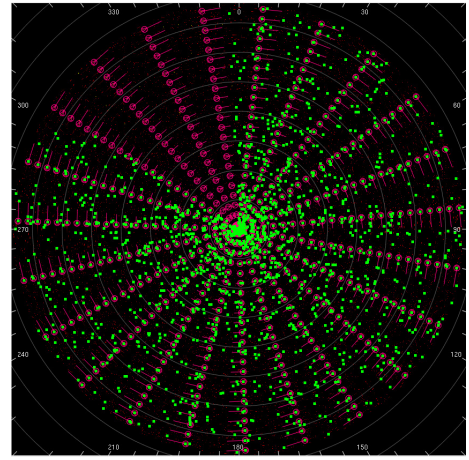


Fig. 1. Baseline scenario with 529 AIS targets superimposed on top of 529 radar targets. Also shown are a part of the 1600 radar noise plots with random intensity. The picture is captured with 5/6 of a sweep and all plots are shown in green. Note: The red color in this picture shows fused targets.

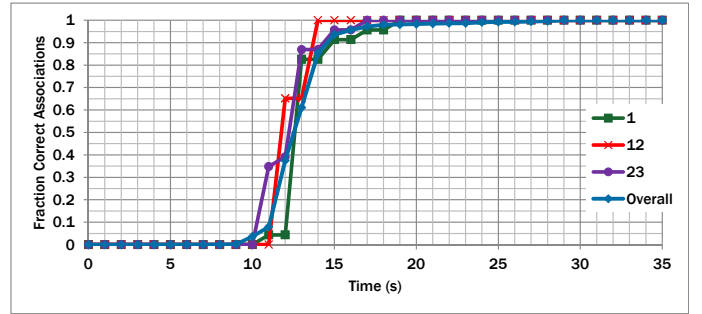


Fig. 2. Fraction of correct fusions over time in the baseline scenario. Data are shown for both the first radius (1), the mid radius (12), the final radius (23) and the overall value.

28 s all targets have been correctly fused. The total maximum rate of fusion is on the order of 120 targets/s, but the overall rate of fusion is only 28 targets/s.

The average Mahalanobis distance (see Eq. 3) can be used to determine how well the kinematic fusion model fits the fused data. The Mahalanobis distance data for the baseline scenario are shown in Fig.3. As can be seen from the figure

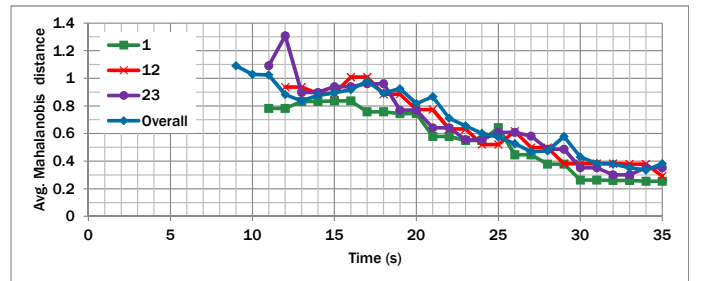


Fig. 3. Average Mahalanobis distance over time in the baseline scenario. Data are shown for both the first radius (1), the mid radius (12), the final radius (23) and the overall value.

the Mahalanobis distance is high in the beginning of the

fusion process (after the initial phase). This is naturally due to several incorrect associations and hence suboptimal kinematic models are assigned leading to large Mahalanobis distances. The overall average Mahalanobis distance drops rapidly to acceptable level below 0.2 as the correct associations are formed.

### B. Displacement

The baseline scenario is modified displacing AIS targets from radar targets. The distance between the two targets increases from 0 to 500 m as we move from the radius with index 1 to the radius with index 23. The resulting fraction of correct fusions and average Mahalanobis distance can be seen in Fig.4 and Fig.5. As expected, our method has more

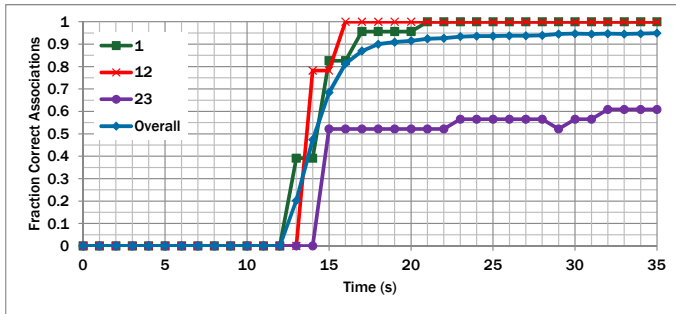


Fig. 4. Fraction of correct fusions over time in the displaced scenario. Data are shown for both the first radius (1), the mid radius (12), the final radius (23) and the overall value.

difficulty converging on a steady state of associations when the two types of targets are displaced from each other. For the targets on the 23rd radius, it converges very slowly since these targets are displaced by 500 m. However, the maximum rate of association is still on the order 120 targets/s. After 35 s, the situation is as can be seen in Fig.6, where the fraction of correct associations clearly falls as the distance between the targets reaches 450 m. The Mahalanobis distance

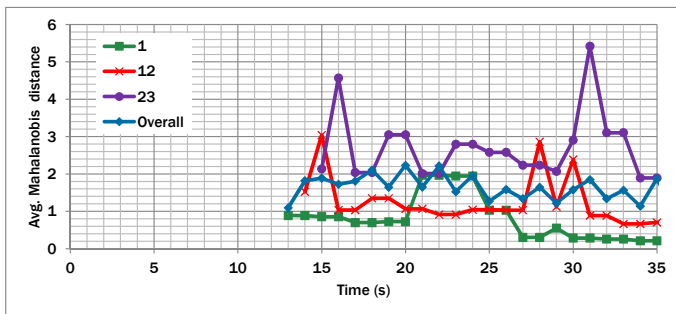


Fig. 5. Average Mahalanobis distance over time in the displaced scenario. Data are shown for both the first radius (1), the mid radius (12), the final radius (23) and the overall value.

shows significant jumps across time. These jumps occur when a suboptimal association is accepted. Notice that the displayed average Mahalanobis distances include Mahalanobis distances of unaccepted associations. Also, no obvious convergence can be observed.

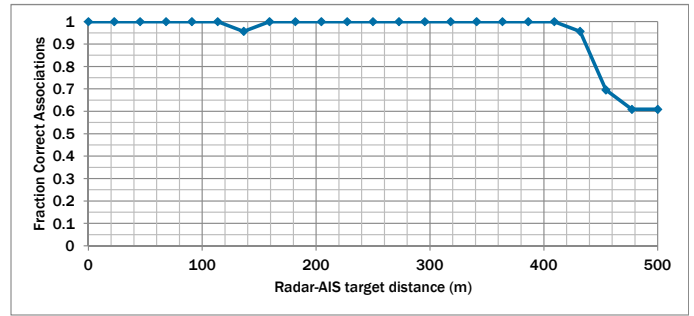


Fig. 6. Fraction of correct fusions over target displacement at a time of 35 s.

## IV. DISCUSSION

Comparing the results of Sec. III-A with the results of Sec. III-B, it is clear that although the overall maximum rate of association is roughly the same, the convergence is much slower for the displaced scenario. After 35 s, it is clear that large displacements beyond 450 m inhibit association. This is fully as expected. When tracks move this far apart, we would not expect them to originate from the same target.

The Mahalanobis distance of the displaced scenario clearly shows significantly larger values than for the baseline scenario and there is not really any traceable convergence in these data. This is also as expected since the distance between the two types of targets will force the kinematic model to make compromises in order to accommodate all the data.

## V. CONCLUSIONS

We have presented a method for fusion of radar data and AIS data. The method shows expected behaviour in terms of track distance dependency. The method is able to fuse data from highly complex scenarios with several hundred tracks from both sensors in real time (demonstrated for 529 tracks from each + 1600 clutter plots). The method is based on kinematic models of the tracks from each sensor, which are fused into kinematic models of the associations between the sensor tracks. The selection of the accepted associations is made using likelihoods and probability theory. The method is fast and scalable and includes the history of the underlying tracks.

## REFERENCES

- [1] A. Staczny and A. Lisaj, *Radar and AIS Data Fusion for the Needs of the Maritime Navigation*, International Radar Symposium, 2006. IRS 2006, pp. 1-4, 2006
- [2] Suo J. and Liu. X., *Fusion of radar and AIS data*, 7th International Conference on Signal Processing, 2004. Proceedings. ICSP '04, pp. 2604 - 2607 vol.3, 2004
- [3] B. Habtemariam, *Effective Data Association Algorithms for Multitarget Tracking*, Ph.D. Thesis, Department of Electrical and Computer Engineering, McMaster University, Canada, 2014
- [4] Y. Bar-Shalom and X. Rong Li and T. Kirubarajan, *Estimation with Applications to Tracking and Navigation*, Wiley, 2001, New York
- [5] S. S. Blackman, *Multi-Hypothesis Tracking for Multiple Target Tracking*, IEEE A&E Systems Magazine Vol. 19, no. 1, pp. 5-18, January 2004

# Improved high-degree cubature Kalman filter

Abhinoy Kumar Singh  
 Department of Electrical Engineering  
 Indian Institute of Technology Patna  
 Patna, Bihar, India  
 Email: abhinoy@iitp.ac.in

Shovan Bhaumik  
 Department of Electrical Engineering  
 Indian Institute of Technology Patna  
 Patna, Bihar, India  
 Email: shovan.bhaumik@iitp.ac.in  
 Telephone: +91 612 255 2049  
 Fax: +91-612-227 7383

**Abstract**—In this paper, an improved filter has been proposed for solving the nonlinear estimation problem. The intractable integral appeared while solving the nonlinear estimation problem is decomposed into two parts, namely the surface and the line integrals. The surface integral is solved by using the arbitrary odd degree spherical cubature rule and the line integral is solved with any order Gauss-Laguerre quadrature rule. The proposed filter is named as Improved high-degree cubature Kalman filter (IHCKF). The filter is applied to estimate the states of a nonlinear system and it shows enhanced accuracy compared to the cubature Kalman filter (CKF), the cubature quadrature Kalman filter (CQKF) and the high-degree cubature Kalman filter (HDCKF).

**Index Terms**—Nonlinear filtering, Spherical cubature rule, Gauss-Laguerre Quadrature rule.

## I. INTRODUCTION

Unavailability of optimal estimator for nonlinear systems, necessitates to develop an accurate and computationally efficient estimator. In this paper, Bayesian framework of filtering is used. A system could be described with

$$\text{state model} \quad x_{k+1} = \phi(x_k) + \eta_k \quad (1)$$

$$\text{measurement model} \quad y_k = \gamma(x_k) + v_k \quad (2)$$

where  $x_k \in \mathbb{R}^n$  denotes the state of the system and  $y_k \in \mathbb{R}^p$  is the measurement at the instant  $k$  where  $k \in \{0, 1, 2, 3, \dots, N\}$ .  $\phi(x_k)$  and  $\gamma(x_k)$  are known nonlinear functions of  $x_k$ . The process noise  $\eta_k \in \mathbb{R}^n$  and measurement noise  $v_k \in \mathbb{R}^p$  are assumed to be uncorrelated and normally distributed with zero mean and covariance  $Q_k$  and  $R_k$  respectively.

The Bayesian framework of nonlinear consists of two major steps

### Prediction step

Prior probability density function can be given by Chapman-Kolmogorov equation

$$p(x_k|y_{1:k-1}) = \int p(x_k|x_{k-1})p(x_{k-1}|y_{1:k-1})dx_{k-1} \quad (3)$$

### Update step

Posterior probability density function is given by Baye's rule

$$p(x_k|y_{1:k}) = \frac{p(y_k|x_k)p(x_k|y_{1:k-1})}{p(y_k|y_{1:k-1})} \quad (4)$$

where the normalizing constant

$$p(y_k|y_{1:k-1}) = \int p(y_k|x_k)p(x_k|y_{1:k-1})dx_k \quad (5)$$

The integrals given in equation (3) and (4) are intractable, which need to be solved for filtering. Initially, the extended Kalman filter (EKF)[1], [2] is introduced in literature where the state and measurement equations are linearized. But the EKF suffers with several limitations like smoothness requirement of functions, noise Gaussian restriction and lack of convergence for highly nonlinear systems[1]. To overcome these limitations, several filtering techniques like the unscented Kalman filter (UKF)[3], [4], the Gauss-Hermite filter (GHF)[5], [6], the central difference filter (CDF)[7], the particle filter (PF) [8] etc. have been developed, where the intractable integrals are approximated with deterministically chosen points and their corresponding weights.

Among all the above mentioned filters, the UKF is most popular, because of its high accuracy at very less computational cost. But research continues to develop more accurate filter at reasonable computational cost. Recently Arasratnam introduced cubature Kalman filter (CKF)[9] and claimed higher accuracy. In CKF, the intractable integral is first decomposed in surface and radial integrals and then solved by using the  $3^{rd}$ -degree spherical-radial rule.

For enhanced accuracy, CKF has been modified to cubature quadrature Kalman filter (CQKF)[10],[11] and the high-degree cubature Kalman filter (HDCKF)[12]. In CQKF, the surface integral has been solved by using  $3^{rd}$ -degree spherical cubature rule, while arbitrary ordered Gauss-Laguerre quadrature rule is applied for solving the radial integral.

In HDCKF, the surface integral is approximated by using arbitrary odd degree spherical cubature rule and moment matching method is applied for approximating the line integral. The method used to evaluate the line in-

tegral is ambiguous and does not provide the best possible solution.

In this paper, the Gauss-Laguerre quadrature method is applied for solving the line integral, while higher degree cubature rule is adopted from [12],[13] to approximate the spherical integral. The proposed filter is named as Improved high-degree cubature Kalman filter (IHDKF). The ambiguity appeared in HDCKF with moment matching method could be avoided with IHDKF. The developed filter shows higher accuracy than the CKF, CQKF and HDCKF.

## II. HIGHER DEGREE CUBATURE QUADRATURE EVALUATION

### A. Approach

To compute the integrals appeared in (3) and (4), we decompose them into a surface integral and a line integral. We incorporate the higher order quadrature rule with arbitrary but odd degree spherical cubature rule in Bayesian framework of filtering.

Bin Jia *et al.* proposed method to evaluate the line integral is ambiguous and the solution is neither unique nor the best available. In this paper, we propose to use the Gauss-Laguerre quadrature rule [14], [15] of any order to solve the radial integral.

*Theorem 1:* For any arbitrary function  $f(X)$ ,  $X \in \mathbb{R}^n$  the integral

$$I(f) = \frac{1}{\sqrt{|\Sigma|} (2\pi)^n} \int_{\mathbb{R}^n} f(X) e^{-(1/2)(X-\mu)^T \Sigma^{-1} (X-\mu)} dX \quad (6)$$

can be decomposed to two integrals as given below:

$$I(f) = \frac{1}{\sqrt{(2\pi)^n}} \int_{r=0}^{\infty} \int_{U_n} [f(CrZ + \mu) d\sigma(Z)] r^{n-1} e^{-r^2/2} dr \quad (7)$$

where  $X = CrZ + \mu$ ,  $C$  is the Cholesky decomposition of covariance matrix  $\Sigma$ ,  $\|Z\| = 1$ ,  $\mu$  is the mean of Gaussian distribution and  $U_n$  is the surface of a unit hyper-sphere.

The proof for this theorem is given in [11].  $\square$

The integral

$$\int_{U_n} f(CrZ + \mu) d\sigma(Z) \quad (8)$$

is to be calculated over the surface of a unit hyper-sphere of dimension  $n$ . Without loss of generality, if we assume zero mean and unity covariance, equation (8) can be represented as

$$\int_{U_n} f(rZ) d\sigma(Z) \quad (9)$$

The integral described in (9) has been solved using arbitrary odd degree of spherical cubature rule.

### B. Higher degree cubature rule

To solve a multidimensional integral numerically, various types of cubature rule exist in literature [16], [17]. In this paper, we adopt a generalized spherical cubature rule of arbitrary but odd degree. The method is first proposed by Genz [13] later utilized by Bin Jia and others [12] in the nonlinear filtering context. In a sentence, we could say that the spherical cubature rule of degree  $(2m+1)$ , where  $m$  is any positive integer, is used to evaluate the integral (9) over the surface of a unit hyper sphere.

*Theorem 2:* [12] The surface integral of the form  $I_{U_n}(f_{rZ}) = \int_{U_n} f(rZ) d\sigma(Z)$  can be evaluated numerically for arbitrarily selected but odd degree as:

$$I_{U_n, 2m+1}(f_{rZ}) = \sum_{|p|} w_p f\{ru_p\} \quad (10)$$

where  $I_{U_n, (2m+1)}(f_{rZ})$  represents spherical integration of the function  $f(rZ)$  with  $(2m+1)$ th degree spherical cubature rule, where  $m$  is any positive integer.  $ru_p$  and  $w_p$  are cubature points and corresponding weights whose expressions are given by

$$w_p \triangleq 2^{-n_z(u_p)} \left( I_{U_n} \left( \prod_{i=1}^n \prod_{j=0}^{p_i-1} \frac{z_i^2 - u_j^2}{u_i^2 - u_j^2} \right) \right) \quad (11)$$

$$\{ru_p\} \triangleq \bigcup (\beta_1 ru_{p_1}, \beta_2 ru_{p_2}, \dots, \beta_n ru_{p_n}) \quad (12)$$

where  $p$  is a set of non-negative numbers *i.e.*  $p = [p_1, p_2, \dots, p_n]$ , and  $|p| = p_1 + p_2 + \dots + p_n$ ;  $u_p$  is also a set of non-negative numbers (not necessarily an integer);  $n_z(u_p)$  gives the number of non-zero elements in  $u_p$ ;  $\beta_i = \pm 1$  and  $u_{p_i} = \sqrt{p_i/m}$ .

The proof of this theorem is provided in [12], [13] and omitted here.  $\square$

The intermediate weights,  $w_p$ , expressed in equation (11) can be evaluated using the following theorem

*Theorem 3:* [12] The spherical integration of the form  $\int_{U_n} z_1^{\delta_1} z_2^{\delta_2} \dots z_n^{\delta_n} d\sigma(Z)$  where  $Z = [z_1, z_2, \dots, z_n]^T$  and  $\sigma(Z)$  is the surface of unit hyper sphere  $U_n$ , can be evaluated as [14]

$$\int_{U_n} z_1^{\delta_1} z_2^{\delta_2} \dots z_n^{\delta_n} dZ \approx \frac{2^{\Gamma((\delta_1+1)/2)\Gamma((\delta_2+1)/2)\dots\Gamma((\delta_n+1)/2)}}{\Gamma((|\delta|+n)/2)} \quad (13)$$

Where  $\Gamma(\cdot)$  represents the Gamma function and  $|\delta| = \delta_1 + \delta_2 + \dots + \delta_n$ .

For proof, we recommend to follow [12], [13].  $\square$

### C. Gauss-Laguerre quadrature rule

Any integral of a function  $f(\cdot)$  in the form of

$$\int_{\lambda=0}^{\infty} f(\lambda) \lambda^\alpha e^{-\lambda} d\lambda \quad (14)$$

can be approximately evaluated using quadrature points and weights associated with them. The quadrature points can be determined from the roots of the  $n'$  order of Chebyshev-Laguerre polynomial equation [14], [15].

$$L_{n'}^\alpha(\lambda) = (-1)^{n'} \lambda^{-\alpha} e^\lambda \frac{d^{n'}}{d\lambda^{n'}} \lambda^{\alpha+n'} e^{-\lambda} = 0 \quad (15)$$

Let the quadrature points be  $\lambda_{i'}$ . The weights can be determined as

$$\omega_{i'} = \frac{n'! \Gamma(\alpha + n' + 1)}{\lambda_{i'} [\dot{L}_{n'}^\alpha(\lambda_{i'})]^2} \quad (16)$$

So the integral (14) can be approximated as

$$\int_{\lambda=0}^{\infty} f(\lambda) \lambda^\alpha e^{-\lambda} d\lambda \approx \sum_{i'=1}^{n'} \omega_{i'} f(\lambda_{i'}) \quad (17)$$

#### D. Higher degree cubature quadrature rule

*Theorem 4:* Any integral in the form of equation (7) can be approximately evaluated as

$$\begin{aligned} I(f) &= \frac{1}{\sqrt{(2\pi)^n}} \int_{r=0}^{\infty} \int_{U_n} [f(CrZ + \mu) d\sigma(Z)] r^{n-1} e^{-r^2/2} dr \\ &= \frac{1}{2\sqrt{\pi^n}} \sum_{i'=1}^{n'} \omega_{i'} \left[ \sum_{|p|} w_p f \left\{ \sqrt{2\lambda_{i'}} u_p \right\} \right] \end{aligned} \quad (18)$$

*Proof:* Considering zero mean and unity covariance, the above integral becomes

$$I(f) = \frac{1}{\sqrt{(2\pi)^n}} \int_{r=0}^{\infty} \int_{U_n} [f(rZ) d\sigma(Z)] r^{n-1} e^{-r^2/2} dr \quad (19)$$

Substituting equation (10) into equation (19)

$$I(f) = \frac{1}{\sqrt{(2\pi)^n}} \int_{r=0}^{\infty} \left[ \sum_{|p|} w_p f \{ r u_p \} \right] r^{n-1} e^{-r^2/2} dr \quad (20)$$

Now to integrate the rest of the term, we use the Gauss-Laguerre quadrature formula described above. To cast the integration in the form of (14), let us substitute  $t = r^2/2$ . With this transformation, the above integral becomes

$$I(f) = \frac{1}{2\sqrt{\pi^n}} \int_{t=0}^{\infty} \left[ \sum_{|p|} w_p f \left\{ \sqrt{2t} u_p \right\} \right] t^{n/2-1} e^{-t} dt \quad (21)$$

Now, the above integral is a radial integral which is exactly in the form, as given in equation (14) for  $\alpha = n/2 - 1$ . Hence Gauss-Laguerre quadrature rule can be applied for solving this integral. For  $i'$  number of quadrature points denoted as  $\lambda_{i'}$  the integral (21) becomes

$$I(f) = \frac{1}{2\sqrt{\pi^n}} \sum_{i'=1}^{n'} \omega_{i'} \left[ \sum_{|p|} w_p f \left\{ \sqrt{2\lambda_{i'}} u_p \right\} \right] \quad (22)$$

□

### III. SIMULATION RESULTS

The proposed estimator has been applied to estimate the states of the following nonlinear system [18].

$$\text{state model} \quad x_{k+1} = 20 \cos(x_k) + \eta_k \quad (23)$$

$$\text{measurement model} \quad y_k = \sqrt{1 + x_k^T x_k} + v_k \quad (24)$$

The initial truth states are considered as  $x_0 = 0.1 \times 0_{n \times 1}$ . The filter is initialized with a value of  $\hat{x}_0$  and  $P_0$ , where  $\hat{x}_0 = 0_{n \times 1}$  and  $P_0 = I_n$ . The error covariance matrices are given as  $Q = I_n$  and  $R = 1$ . The states are estimated using the CKF, the CQKF, the HDCKF, and the IHDCKF. The CQKF is implemented with second order Gauss-Laguerre quadrature. The HDCKF is implemented with fifth degree of cubature rule [13], and IHDCKF is implemented with fifth degree cubature and second order Gauss-Laguerre quadrature rule.

The accuracy of the estimators is compared in terms of the root mean square error (RMSE) using 500 Monte Carlo runs. Fig. 1 shows the RMSE plots for the first states. From the figures it is clear that the RMSE value for the proposed IHDCKF is less compared to the other existing filters in cubature family.

### IV. DISCUSSIONS AND CONCLUSION

In this paper, a new method has been developed for solving the nonlinear filtering problems. The proposed filter is named as Improved high-degree cubature Kalman filter. The intractable integrals appeared during the filtering are decomposed into a surface and a line integrals. The surface integral is solved by using generalized spherical cubature rule of arbitrary but odd degree, while the line integral is solved by any ordered Gauss-Laguerre quadrature rule. The accuracy of the proposed filter is found to be better than the CKF, the CQKF, and the HDCKF. However, rises at the cost of computational burden. Due to enhanced accuracy the proposed filter may become promising to the practitioners.

### REFERENCES

- [1] B. D. O. Anderson and J.B. Moore, *Optimal filtering* New York: Dover, INC., Mineola, 2005.
- [2] Y. Bar-Shalom, X. R. Li and T. Kirubarajan, *Estimation with application to tracking and navigation* New York: Wiley-Interscience, John Wiley and Sons, INC., 2001.
- [3] J. Simon, J. Uhlmann and H. F. Durrant-Whyte, "A new Method for the nonlinear transformation of means and covariances in filters and estimators," *IEEE Trans. Auto. Control*, vol. 45, no. 3, Mar. 2000, pp. 477-482.
- [4] S. Bhaumik, S. Sadhu and T. K. Ghoshal, "Risk-sensitive formulation of unscented Kalman filter," *IET Control Theory Appl.*, vol. 3, no. 4, Apr. 2009, pp. 375-382.

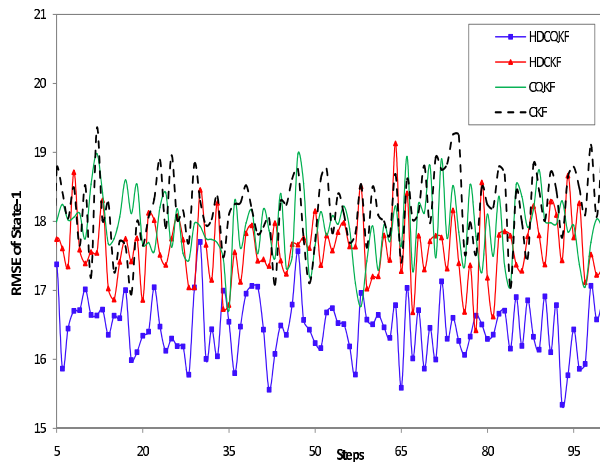


Fig. 1: RMSE plot for 100 steps

- [5] I. Arasaratnam, S. Haykin and R.J. Elliott, "Discrete-time nonlinear filtering algorithms using Gauss-Hermite quadrature," *Proc. IEEE*, vol. 95, no. 5, July 2007, pp. 953-977.
- [6] A. K. Singh and S. Bhaumik, "Nonlinear estimation using transformed Gauss-Hermite quadrature points," *IEEE intern. conf. signal process., comput. control*, Solan, India, 2013, pp. 1-4.
- [7] K. Ito and K. Xiong, "Gaussian filters for nonlinear filtering problems," *IEEE Trans. Auto. Control*, vol. 45, no. 5, Aug. 2000, pp. 910-927.
- [8] M. S. Arulampalam, S. Maskell, N. Gordon and T. Clapp, "A tutorial on particle filters for online nonlinear/non-gaussian bayesian tracking," *IEEE Trans. signal process.*, vol. 50, no. 2, Feb. 2002, pp. 174-188.
- [9] I. Arasaratnam and S. Haykin, "Cubature Kalman filter," *IEEE Trans. Auto. Control*, vol. 54, no.6, Jun. 2009, pp. 1254-1269.
- [10] Swati and S. Bhaumik, "Nonlinear estimation using cubature quadrature points," *Proc. Conf. Energy Auto. Signal*, India, 2011, pp. 1-6.
- [11] S. Bhaumik and Swati, "Cubature quadrature Kalman filter," *IET Signal Process.*, vol. 7, no. 7, Sep. 2013, pp. 1-9.
- [12] B. Jia, M. Xin and Y. Cheng, "High-degree cubature Kalman filter," *Automatica*, vol. 49, No. 5, Feb. 2013, pp. 510-518.
- [13] A. Genz, "Fully symmetric interpolatory rules for multiple integrals over hyper-spherical surfaces," *Jr. Compt. Appl. Maths*, vol. 157, No. 1, Aug. 2003, pp. 187-195.
- [14] I. V. Krylov, *Approximate calculation of integrals*, New York, Dover, 2005.
- [15] B. F. Hildebrand, *Introduction to Numerical Analysis*, New York, Dover, 2nd edn, 2008.
- [16] S. B. Stoyanova, "Cubature formulae of the seventh degree of accuracy for the hypersphere," *Jr. Compt. Appl. Maths*, vol. 84, no. 1, Oct. 1997, pp. 15-21.
- [17] A. Genz, "Monomial cubature rules since Stroud: a compilation," *Jr. Compt. and Appl. Maths*, vol. 48, No. 3, Nov. 1993, pp. 309-326.
- [18] L. Chang, B. Hu, A. Li, and F. Qin, "Transformed unscented Kalman filter," *IEEE Trans. Autom. Control*, vol. 58, no. 1, Dec. 2013, pp. 252-257.

# Shortening of Paraunitary Matrices Obtained by Polynomial Eigenvalue Decomposition Algorithms

Jamie Corr\*, Keith Thompson\*, Stephan Weiss\*, Ian K. Proudler†, and John G. McWhirter‡

\*Department of Electronic & Electrical Engineering, University of Strathclyde, Glasgow, Scotland

†School of Electrical, Electronics and Systems Engineering, Loughborough University, Loughborough, UK

‡School of Engineering, Cardiff University, Cardiff, Wales, UK

{jamie.corr,keith.thompson,stephan.weiss}@strath.ac.uk

**Abstract**—This paper extends the analysis of the recently introduced row-shift corrected truncation method for paraunitary matrices to those produced by the state-of-the-art sequential matrix diagonalisation (SMD) family of polynomial eigenvalue decomposition (PEVD) algorithms. The row-shift corrected truncation method utilises the ambiguity in the paraunitary matrices to reduce their order. The results presented in this paper compare the effect a simple change in PEVD method can have on the performance of the paraunitary truncation. In the case of the SMD algorithm the benefits of the new approach are reduced compared to what has been seen before however there is still a reduction in both reconstruction error and paraunitary matrix order.

## I. INTRODUCTION

Broadband array processing problems are often formulated with a space-time covariance matrix  $\mathbf{R}[\tau]$ , which in addition to a spatial component contains an explicit lag  $\tau$ . Its  $z$ -transform,  $\mathbf{R}(z) \bullet\text{---}\circ \mathbf{R}[\tau]$ , yields a polynomial cross-spectral density (CSD) matrix, which extends the symmetric or Hermitian property known from standard matrix algebra to the parahermitian case as  $\mathbf{R}(z) = \tilde{\mathbf{R}}(z)$ , whereby the parahermitian operator  $\{\cdot\}$  consists of a Hermitian transposition  $\{\cdot\}^H$  and time reversal i.e.  $\tilde{\mathbf{R}}(z) = \mathbf{R}^H(z^{-1})$ .

Since the eigenvalue decomposition (EVD) of a covariance matrix provides an optimal factorisation for numerous signal processing problems, its extension from the narrowband to the broadband case has led to polynomial EVD (PEVD) as proposed in [1]. For a parahermitian matrix  $\mathbf{R}(z)$ ,

$$\mathbf{R}(z) \approx \tilde{\mathbf{Q}}(z)\mathbf{D}(z)\mathbf{Q}(z) \quad (1)$$

factorises  $\mathbf{R}(z)$  into a paraunitary  $\mathbf{Q}(z)$ , such that  $\mathbf{Q}(z)\tilde{\mathbf{Q}}(z) = \mathbf{I}$ , and a diagonal parahermitian  $\mathbf{D}(z)$ ,

$$\mathbf{D}(z) = \text{diag}\{D_0(z) D_1(z) \dots D_{M-1}(z)\} \quad (2)$$

Extending the idea of an ordered EVD [2], the polynomial eigenvalues in  $\mathbf{D}(z)$  are spectrally majorised, i.e. their power spectral densities  $D_m(e^{j\Omega}) = D_m(z)|_{z=e^{j\Omega}}$  satisfy

$$D_{m+1}(e^{j\Omega}) \geq D_m(e^{j\Omega}) \quad \forall \Omega \quad m = 0 \dots (M-1) \quad (3)$$

For FIR paraunitary matrices, the equality in (1) is not guaranteed [1] but likely valid in close approximation for high orders of  $\mathbf{Q}(z)$  [3].

The PEVD enables a number of applications spanning from filter bank-based channel coding [4], to the design of

broadband precoding and equalisation of MIMO systems [5], subband coding [6], broadband angle of arrival estimation [7], and others. A number of these applications are directly influenced by the order of the paraunitary matrix  $\mathbf{Q}(z)$ , such as polynomial subspace decomposition techniques [4], [5], [7], and paraunitary matrices of low order therefore can be crucial.

A number of iterative algorithms have been developed to approximate (1). For example, an approximate PEVD (APEVD) algorithm with fixed order has been reported in [8], but has not been proved to converge. Other algorithms have been proven to converge towards a diagonalised  $\mathbf{D}(z)$  and can achieve better diagonalisation than APEVD, including the family of second order sequential best rotation (SBR2) algorithms [1], [6] and the family of sequential matrix diagonalisation (SMD) algorithms [9], [10]. Although guaranteed to diagonalise  $\mathbf{R}(z)$ , the SBR2 and SMD algorithms [1], [6], [9], [10] are unconstrained in their order and therefore the polynomial degrees of both  $\mathbf{D}(z)$  and  $\mathbf{Q}(z)$  grow with the number of iterations.

The growing order of the diagonal parahermitian matrix causes difficulties, as its increase is responsible for the rising complexity of iterative PEVD algorithms such as [1], [6], [9], [10] as iterations go on. To this end, trimming small coefficients at the ends of this matrix has been suggested in [1], [11] in order to reduce the complexity of iterative PEVD algorithms. However, the paraunitary matrix also grows with the number of iterations; while its increase does not impact on the complexity during iterations, the application cost of the finally extracted paraunitary matrix can be high for polynomial subspace-based applications as mentioned above. Therefore, reducing the order of the paraunitary matrix has been suggested in [12], whereby similarly to [1], [11] small outer matrix coefficients are truncated.

In addition to the trimming approach in [12], an enhanced alternative method has been suggested in [13] and applied to SBR2. The aim of this paper therefore is to investigate the so-called shift-corrected version in [13] for both SBR2 and SMD families of iterative PEVD algorithms. To accomplish this, Sec. II reviews the PEVD algorithms that will be used to generate paraunitary matrices. Sec. III provides an overview of the two paraunitary truncation approaches to be compared. The results from applying the different truncation methods to the paraunitary matrices produced by the two PEVD methods are presented in Sec. IV and conclusions are given in Sec. V.

## II. PEVD ALGORITHMS

### A. General Approach

Starting from the parahermitian matrix  $\mathbf{R}(z)$ , all PEVD algorithms apply a series of elementary paraunitary matrices in order to iterate towards an approximately diagonal polynomial matrix  $\mathbf{D}(z)$ . At the  $i$ -th iteration, building on a partially diagonalised parahermitian matrix  $\mathbf{S}^{(i-1)}(z)$ , PEVD algorithms build an elementary paraunitary matrix  $\mathbf{Q}^{(i)}(z)$  from two components: a shift matrix  $\mathbf{\Lambda}^{(i)}(z)$  which transfers large off-diagonal elements of  $\mathbf{S}^{(i-1)}(z)$  onto the zero lag, followed by a rotation  $\mathbf{Q}^{(i)}$  which moves the transferred elements' energy onto the diagonal. Thus, for the  $i$ th iteration we have

$$\mathbf{Q}^{(i)}(z) = \mathbf{Q}^{(i)} \mathbf{\Lambda}^{(i)}(z) \quad (4)$$

While various PEVD algorithms share this same general approach, both  $\mathbf{\Lambda}^{(i)}(z)$  and  $\mathbf{Q}^{(i)}$  are algorithm dependent. The delay matrix,  $\mathbf{\Lambda}^{(i)}(z)$ , is determined by the search strategy, while the rotation  $\mathbf{Q}^{(i)}$  is defined by the family of algorithms used. The  $i$ th iteration of any iterative PEVD algorithm is then implemented as

$$\mathbf{S}^{(i)}(z) = \mathbf{Q}^{(i)} \mathbf{S}^{(i-1)}(z) \tilde{\mathbf{Q}}^{(i)} \quad (5)$$

The algorithm is stopped after  $I$  iterations if either the off-diagonal energy of  $\mathbf{S}^{(i)}(z)$  falls below a predefined threshold or  $I$  reaches a selected limit. Thereafter  $\hat{\mathbf{D}}(z) = \mathbf{S}^{(I)}(z)$  and

$$\hat{\mathbf{Q}}(z) = \prod_{i=1}^I \mathbf{Q}^{(i)} \mathbf{\Lambda}^{(i)}(z) \quad (6)$$

Generally, (6) can be calculated after the algorithm has been executed, as storing the parameters of  $\mathbf{Q}^{(i)}$  and  $\mathbf{\Lambda}^{(i)}(z)$  is more efficient than storing and updating the whole paraunitary matrix. Based on the PEVD outline above the following subsections will go into the unique details for both PEVD algorithms utilised in the results section.

### B. Second Order Sequential Best Rotation

The second order sequential best rotation (SBR2) algorithm is an extension of the classical Jacobi algorithm for scalar matrices to the polynomial case [1]. Like the Jacobi algorithm, SBR2 starts with a search for the maximum off diagonal element but this now extends to all lags of the polynomial matrix. Starting from  $\mathbf{S}^{(0)}(z) = \mathbf{R}(z)$ , at the  $i$ -th iteration the maximum off diagonal element is found using

$$\{k^{(i)}, \tau^{(i)}\} = \arg \max_{k, \tau} \|\hat{\mathbf{s}}_k^{(i-1)}[\tau]\|_\infty, \quad i = 1 \dots I \quad (7)$$

With the transform pair  $\mathbf{S}^{(i-1)}[\tau] \circ \bullet \mathbf{S}^{(i-1)}(z)$ , the modified  $k^{(i)}$ th column vector,  $\hat{\mathbf{s}}_k^{(i-1)}[\tau]$ , contains only off diagonal elements. The delay matrix  $\mathbf{\Lambda}^{(i)}(z)$  is then constructed using

$$\mathbf{\Lambda}^{(i)}(z) = \text{diag}\left\{ \underbrace{1 \dots 1}_{k^{(i)}-1} z^{-\tau^{(i)}} \underbrace{1 \dots 1}_{M-k^{(i)}} \right\}, \quad (8)$$

where the parameters  $k^{(i)}$  and  $\tau$  are used to advance or delay the  $k^{(i)}$ th column and row, shifting the maximum element

by  $\tau^{(i)}$  lags onto the zerolag. Finally, the energy from the maximum element is transferred onto the diagonal using the Jacobi transformation

$$\mathbf{Q}^{(i)} = \begin{bmatrix} \mathbf{I}_1 & & & & \\ & \cos \varphi^{(i)} & \dots & e^{j\vartheta^{(i)}} \sin \varphi^{(i)} & \\ & \vdots & & \vdots & \\ -e^{-j\vartheta^{(i)}} \sin \varphi^{(i)} & & \mathbf{I}_2 & & \\ & & \dots & \cos \varphi^{(i)} & \\ & & & & \mathbf{I}_3 \end{bmatrix}, \quad (9)$$

where the rotation angles  $\varphi^{(i)}$  and  $\vartheta^{(i)}$  are determined by the value of the maximum element. The dimensions of the identities in (9),  $\mathbf{I}_n$ ,  $n = 1, 2, 3$ , are  $(\min\{m^{(i)}, k^{(i)}\} - 1)$ ,  $(|m^{(i)} - k^{(i)}| - 1)$  and  $(M - \max\{m^{(i)}, k^{(i)}\} + 1)$  respectively. Although (9) has to be applied to all lags of the parahermitian matrix its sparse nature means that only two rows and columns are modified when proceeding from  $\mathbf{S}^{(i-1)}(z)$  to  $\mathbf{S}^{(i)}(z)$ .

### C. Sequential Matrix Diagonalisation

In addition to the three main PEVD steps described above the sequential matrix diagonalisation (SMD) [9] algorithm includes an additional initialisation step that brings all off diagonal zerolag energy onto the diagonal prior to any shift operations. This results in

$$\mathbf{S}^{(0)}(z) = \mathbf{Q}^{(0)} \mathbf{R}(z) \mathbf{Q}^{(0)H}, \quad (10)$$

where  $\mathbf{Q}^{(0)}$  is the modal matrix for the EVD of the zerolag of  $\mathbf{R}(z)$ .

The search step of the SMD is also different in that the  $l_\infty$  norm in (7) is replaced by an  $l_2$  norm, thereby changing the search from maximum element to maximum column norm

$$\{k^{(i)}, \tau^{(i)}\} = \arg \max_{k, \tau} \|\hat{\mathbf{s}}_k^{(i-1)}[\tau]\|_2 \quad (11)$$

Using the same modified column vector,  $\hat{\mathbf{s}}_k^{(i-1)}[\tau]$ , the parameters  $k^{(i)}$  and  $\tau^{(i)}$  are again used in (8). For the SMD algorithm, an energy transfer matrix,  $\mathbf{Q}^{(i)}$ , that clears all zero lag off-diagonal elements can be found by an EVD at zero lag.

In general, the SMD algorithm transfers more energy per iteration than the SBR2 algorithm. Due to the full EVD being non-sparse and requiring a full matrix multiplication for each lag in the parahermitian matrix, each SMD iteration is more computationally costly than a similar SBR2 iteration. Therefore, SMD overall has a higher complexity than SBR2 to compute an approximate PEVD, but is capable of producing paraunitary matrices of lower order [9], making operations involving  $\hat{\mathbf{Q}}(z)$  less costly to apply once the PEVD is calculated.

## III. PARAUNITARY MATRIX TRUNCATION METHODS

To reduce the cost of applying the paraunitary matrix  $\hat{\mathbf{Q}}(z)$ , two different truncation methods have been proposed in [12], [13], which are reviewed below.

### A. Lag Based Truncation

The truncation approach specified in [12] reduces the order of the paraunitary matrix by removing the  $N_1$  leading and  $N_2$  trailing lags, unlike the method for parahermitian truncation in [1], [11] this is done asymmetrically. The trim function for paraunitary matrices can be defined as

$$f_{\text{trim}}(\hat{\mathbf{Q}}[n]) = \begin{cases} \hat{\mathbf{Q}}[n + N_1] & 0 \leq n < N - N_2 - N_1 \\ \mathbf{0} & \text{otherwise} \end{cases} .$$

The proportion of energy removed in the  $N_1$  leading and  $N_2$  trailing lags of  $\hat{\mathbf{Q}}[n]$  by the  $f_{\text{trim}}(\cdot)$  operation is given by

$$\begin{aligned} \gamma_{\text{trim}} &= 1 - \frac{\sum_n \|f_{\text{trim}}(\hat{\mathbf{Q}}[n])\|_{\text{F}}^2}{\sum_n \|\hat{\mathbf{Q}}[n]\|_{\text{F}}^2} \\ &= 1 - \frac{1}{M} \sum_n \|f_{\text{trim}}(\hat{\mathbf{Q}}[n])\|_{\text{F}}^2 , \end{aligned}$$

where  $\|\cdot\|_{\text{F}}$  is the Frobenius norm. To control the impact of the truncation operation on the paraunitary matrix, the parameter  $\mu$  is used as an upper bound for the proportion of energy removed,  $\gamma_{\text{trim}}$ . Here we want to maximise the number of lags removed,  $N_1 + N_2$ , whilst keeping the energy removed below  $\mu$ , hence the constrained optimisation problem:

$$\text{maximise } (N_1 + N_2) \quad (12)$$

$$\text{s.t. } \gamma_{\text{trim}} \leq \mu . \quad (13)$$

The implementation of  $f_{\text{trim}}(\cdot)$  is as simple as sequentially removing the outermost matrix coefficients of polynomial  $\mathbf{Q}(z)$ , at either leading or trailing lags, which possess the smallest Frobenius norm whilst ensuring (13) is satisfied.

### B. Row-Shift Corrected Truncation

The row-shift corrected truncation method [13] exploits the ambiguity in paraunitary matrices [13], [14]. The ambiguity permits  $\mathbf{Q}(z)$ , from (1), to be replaced by  $\tilde{\mathbf{Q}}(z)$  where  $\tilde{\mathbf{Q}}(z) = \mathbf{\Gamma}(z)\mathbf{Q}(z)$ . As argued in [13], the only viable option for the polynomial matrix  $\mathbf{\Gamma}(z)$  takes the form

$$\mathbf{\Gamma}(z) = \text{diag}\{z^{-\tau_1} \ z^{-\tau_2} \ \dots \ z^{-\tau_M}\} \quad (14)$$

which consists of  $M$  row shifts by  $\tau_m$  samples, where  $m = 1 \dots M$ , i.e. for each row of the paraunitary matrix. These row shifts can now be used to align the maximum values in each row so that the overall paraunitary matrix can be truncated further.

We can subdivide the paraunitary matrix,  $\hat{\mathbf{Q}}(z)$ , into its  $M$  row vectors  $\hat{\mathbf{q}}_m(z)$ ,  $m = 1 \dots M$ ,

$$\tilde{\mathbf{Q}}(z) = [\hat{\mathbf{q}}_1(z) \ \dots \ \hat{\mathbf{q}}_M(z)] . \quad (15)$$

For the row-shift corrected method each row is truncated individually using

$$f_{\text{shift}}(\hat{\mathbf{q}}_m[n]) = \begin{cases} \hat{\mathbf{q}}_m[n + N_{1,m}] & 0 \leq n < T_m \\ \mathbf{0} & \text{otherwise} \end{cases} , \quad (16)$$

where the overall length of the truncated vector is  $T_m = N - N_{2,m} - N_{1,m}$ . The row shifts,  $\tau_m$ , in (14) are then set equal

to  $N_{1,m} \ \forall m = 1 \dots M$ . As each vector has unit energy the proportion of energy to be removed from each row, using the vector-valued truncation,  $f_{\text{shift}}(\hat{\mathbf{q}}_m[n])$ , becomes

$$\gamma_{\text{shift},m} = 1 - \sum_n \|f_{\text{shift}}(\hat{\mathbf{q}}_m[n])\|_2^2 . \quad (17)$$

Similar to the lag-based method, this presents us with the following constrained optimisation problem for  $f_{\text{shift}}(\cdot)$ :

$$\text{maximise } \min_m (N_{1,m} + N_{2,m}) \quad (18)$$

$$\text{s.t. } \gamma_{\text{shift},m} \leq \frac{\mu'}{M} \ \forall m = 1 \dots M . \quad (19)$$

The length of resulting paraunitary matrix will be  $\max_m T_m$  and the maximum proportion of energy removed will be  $\mu'$ . The process outlined above is equivalent to truncating each row of  $\hat{\mathbf{Q}}(z)$  with the lag based truncation method in Sec. III-A and [12].

## IV. RESULTS

To compare the performance of the different truncation approaches on the two PEVD methods, performance metrics for this are first defined, followed by a number of simulation scenarios.

### A. Performance Metrics

*Reconstruction Error.* When the paraunitary matrix,  $\hat{\mathbf{Q}}(z)$ , is truncated, the paraunitary property is lost. The paraunitary property states  $\hat{\mathbf{Q}}(z)\tilde{\mathbf{Q}}(z) = \mathbf{I}$  therefore the difference from paraunitary is

$$\mathbf{E}(z) = \mathbf{I}_{M \times M} - \hat{\mathbf{Q}}_{\text{T}}(z)\tilde{\mathbf{Q}}_{\text{T}}(z) . \quad (20)$$

with  $\hat{\mathbf{Q}}_{\text{T}}(z)$  being the truncated matrix, and the transform  $\mathbf{E}[\tau] \circ \bullet \mathbf{E}(z)$ . When  $\hat{\mathbf{Q}}(z)$  is a filter bank, the loss in paraunitarity can be measured as the reconstruction error [15]

$$\xi = \frac{1}{M} \sum_{\tau} \|\mathbf{E}[\tau]\|_{\text{F}}^2 . \quad (21)$$

*Diagonalisation.* The goal of the PEVD algorithms is to iteratively approximate a diagonal parahermitian matrix. Therefore, a second performance criterion measures the reduction in off-diagonal energy calculated as

$$E_{\text{norm}}^{(i)} = \frac{\sum_{\tau} \sum_{k=1}^M \|\hat{\mathbf{s}}_k^{(i)}[\tau]\|_2^2}{\sum_{\tau} \|\mathbf{R}[\tau]\|_{\text{F}}^2} , \quad (22)$$

where  $\hat{\mathbf{s}}_k^{(i)}[\tau]$  is the modified column vector from (7) containing only off-diagonal elements.

### B. Simulation Scenario

For the following results, the PEVD algorithms are run for 100 iterations recording the performance metrics from Sec. IV-A along with the paraunitary matrix order at each iteration. All results apart from those shown in Sec. IV-E have been averaged over an ensemble of  $10^3$  instantiations. The initial parahermitian matrix,  $\mathbf{R}(z)$ , for all of the simulations below was generated using the source model described in [9], which

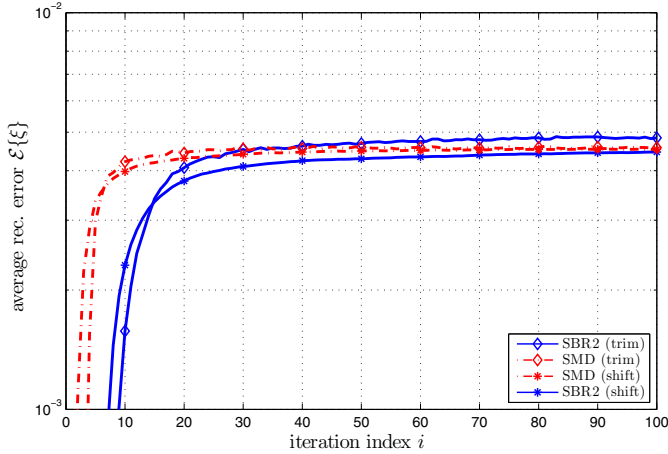


Fig. 1. Ensemble reconstruction error  $\mathcal{E}\{\xi\}$  vs. PEVD iterations for the different truncation approaches and PEVD methods.

is randomised to produce a unique  $\mathbf{R}(z)$  for each instantiation. The paraunitary matrix produced is  $\mathbf{R}(z) \in \mathbb{C}^{6 \times 6}$  for all of the simulations excluding Sec. IV-E where the dimensions are reduced to  $\mathbf{R}(z) \in \mathbb{C}^{4 \times 4}$  with the number of lags for all  $\mathbf{R}(z)$  set at 47.

### C. Reconstruction Error

In [13], one of the major benefits of the row-shift corrected truncation was the drastic reduction in reconstruction error. With the row-shift corrected method it was found that the amount of energy removed from the paraunitary matrix could be increased by a factor of 5 whilst maintaining a similar level of reconstruction error to the lag based truncation. Here for comparison, the truncation parameters across the PEVD methods remain the same with  $\mu = 10^{-4}$  and  $\mu' = 5\mu$ . Fig. 1 shows the reconstruction error for the different PEVD methods, here the SBR2 algorithm using the row-shift corrected method performs the best with an error of  $4.5 \times 10^{-4}$  and SBR2 using the original truncation is worst with an error of  $4.8 \times 10^{-4}$  after 100 iterations. Initially the error curves start very low but they quickly increase as the outer elements become smaller and the truncation algorithms begin to remove their full quota of energy, be it  $\mu$  or  $\mu'$ . Even with the compensation of  $\mu' = 5\mu$ , the row-shift correction method still tends to have a slightly lower error for both PEVD methods despite being permitted to remove five times the energy.

### D. Truncated Order and Diagonalisation

As previously shown in [13], the row-shift corrected method has a significant effect on reducing the paraunitary order for the SBR2 method, however with the SMD algorithm the same reduction in paraunitary order is not apparent for the selected source model. There is still a slight benefit to using the row-shift corrected truncation but due to the nature of the SMD algorithm there tends to be fewer outliers which need to be corrected by the row-shift truncation.

Fig. 3 shows the diagonalisation measure vs. paraunitary order for the different PEVD algorithms and truncation methods. As with the previous figures these results are over 100

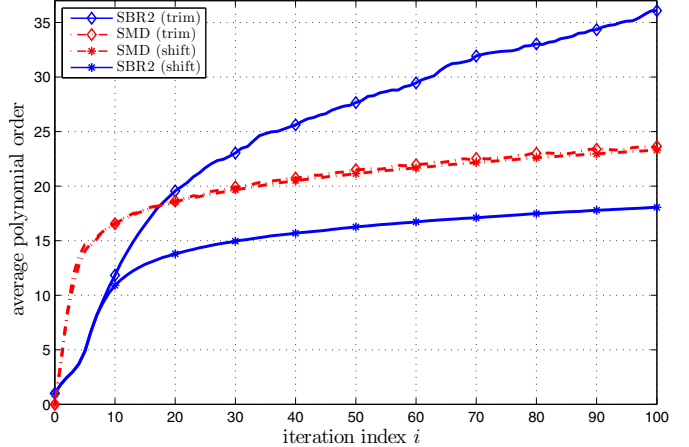


Fig. 2. Average order after truncation of  $\hat{\mathbf{Q}}(z)$  vs. PEVD iterations for the different truncation approaches.

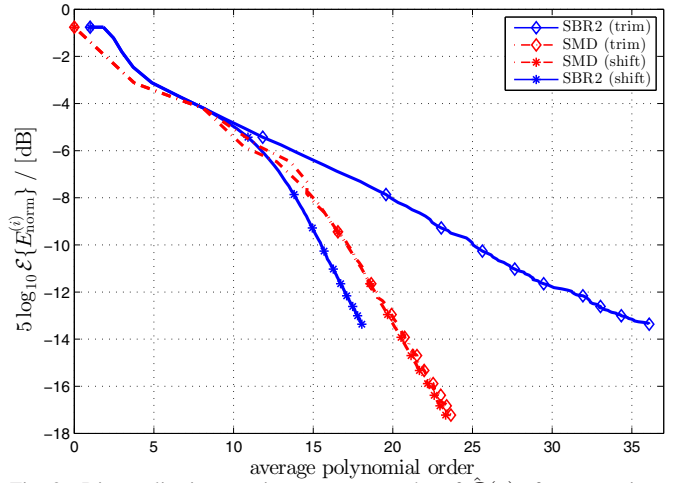


Fig. 3. Diagonalisation metric vs. average order of  $\hat{\mathbf{Q}}(z)$  after truncation.

iterations with the diagonalisation recorded after each iteration. In Fig. 3 there is a similar trend to Fig. 2, with the row-shift corrected method SBR2 outperforming the SMD equivalent. Crucially for a set level of diagonalisation, SBR2 with the row-corrected truncation generates a paraunitary matrix of lower cost than SMD, thereby negating one of the benefits of the SMD approach identified in Sec. II and in [9] for this particular source model.

### E. Examples of Truncated Paraunitary Matrices

Figs. 4 and 5 illustrate the differences in the paraunitary matrices for both the lag-based truncation method with the row-corrected results overlaid. For clarity of the figures, the initial parahermitian matrix has been reduced to  $\mathbf{R}(z) \in \mathbb{C}^{4 \times 4}$  with all other simulation parameters remaining the same. Clearly in the SBR2 paraunitary matrix the row shift corrected approach has more of an effect than it does for SMD. Whereas the maxima in the rows of the SBR2 paraunitary matrix are delayed and spread out with respect to one another, the SMD paraunitary maxima are clustered and delayed by a similar amount. With SMD, the row-shift correction does not aid in reducing the paraunitary matrix length. For the examples

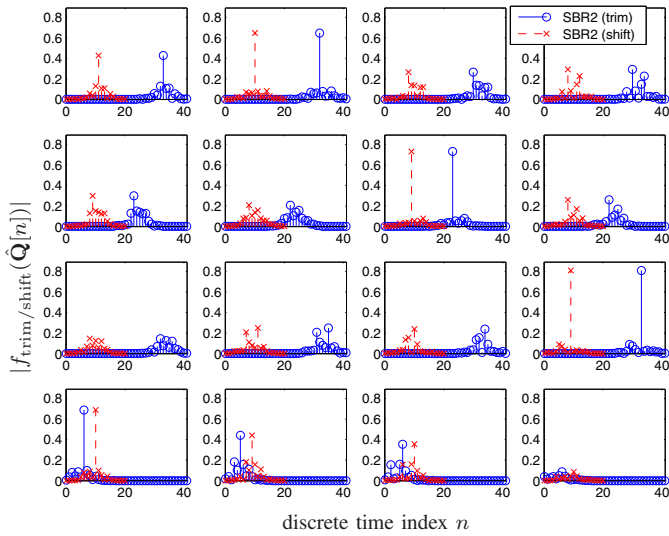


Fig. 4. SBR2 paraunitary matrix truncated with  $\mu = 10^{-4}$  using the lag based [12] and row-shift corrected [13] truncation methods.

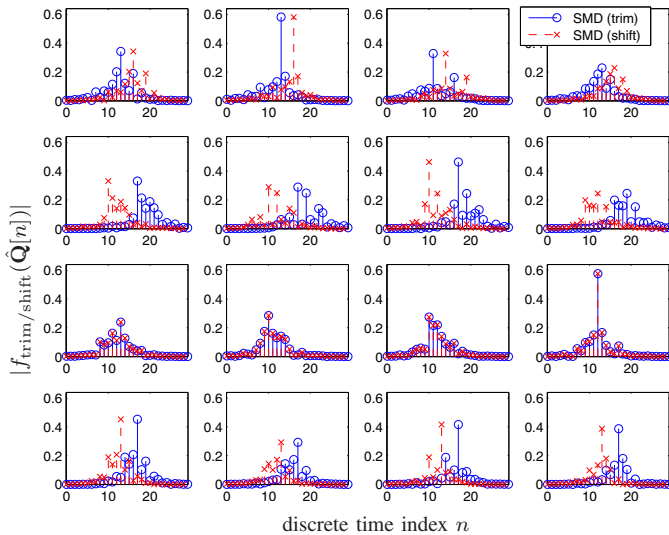


Fig. 5. SMD paraunitary matrix truncated with  $\mu = 10^{-4}$  using the lag based [12] and row-shift corrected [13] truncation methods.

shown in Figs. 4 and 5 the reduction in order for the row-corrected method is 21 for the SBR2 paraunitary matrix but only 1 for SMD, and the total row corrected lengths are 21 and 29 respectively.

## V. CONCLUSION

This paper has investigated the application of the newly developed row-shift corrected truncation to paraunitary matrices produced by both the SBR2 and SMD PEVD algorithms. Previously the SMD algorithm has been shown to generate paraunitary matrices of lower order than SBR2.

Using the row-shift corrected truncation method the simulation results show only a marginal improvement in both reconstruction error and paraunitary order with SMD. For the SBR2 algorithm we see a larger benefit to using the new truncation approach to the extent that the SBR2 algorithm has now been shown to produce lower order paraunitary matrices

than SMD for a set level of diagonalisation. Based on the results presented here, to minimise the order for an application that extracts the paraunitary matrix, the best approach is to use the SBR2 PEVD method combined with the recently developed row-shift corrected truncation.

## ACKNOWLEDGEMENT

This work was supported by the Engineering and Physical Sciences Research Council (EPSRC) Grant number EP/K014307/1 and the MOD University Defence Research Collaboration in Signal Processing.

## REFERENCES

- [1] J.G. McWhirter, P.D. Baxter, T. Cooper, S. Redif, J. Foster. An EVD Algorithm for Para-Hermitian Polynomial Matrices. *IEEE Trans. SP*, 55(5):2158–2169, May 2007.
- [2] G.H. Golub, C.F. Van Loan. *Matrix Computations*. John Hopkins, 3rd ed., 1996.
- [3] S. Icart, P. Comon. Some Properties of Laurent Polynomial Matrices. In *Conf. Math. Signal Proc.*, Birmingham, UK, Dec. 2012.
- [4] S. Weiss, S. Redif, T. Cooper, C. Liu, P.D. Baxter, J.G. McWhirter. Paraunitary Oversampled Filter Bank Design for Channel Coding. *J. Applied SP*, 2006.
- [5] C.H. Ta, S. Weiss. A Design of Precoding and Equalisation for Broadband MIMO Systems. In *15th Int. Conf. DSP*, pp. 571–574, Cardiff, UK, July 2007.
- [6] S. Redif, J. McWhirter, S. Weiss. Design of FIR Paraunitary Filter Banks for Subband Coding using a Polynomial Eigenvalue Decomposition. *IEEE Trans. SP*, 59(11):5253–5264, Nov. 2011.
- [7] M. Almah, S. Weiss, S. Lambotharan. An Extension of the MUSIC Algorithm to Broadband Scenarios using Polynomial Eigenvalue Decomposition. In *EUSIPCO*, pp. 629–633, Barcelona, Spain, Aug. 2011.
- [8] A. Tkachenko. Approximate Eigenvalue Decomposition of Para-Hermitian Systems through Successive FIR Paraunitary Transformations. In *IEEE ICASSP*, pp. 4074–4077, Dallas, TX, Mar. 2010.
- [9] S. Redif, S. Weiss, J. McWhirter. Sequential Matrix Diagonalization Algorithms for Polynomial EVD of Parahermitian Matrices. *IEEE Trans. SP*, 63(1):81–89, Jan. 2015.
- [10] J. Corr, K. Thompson, S. Weiss, J. McWhirter, S. Redif, I. Proudler. Multiple Shift Maximum Element Sequential Matrix Diagonalisation for Parahermitian Matrices. In *IEEE SSP*, pp. 312–315, Gold Coast, Australia, June 2014.
- [11] J. Foster, J.G. McWhirter, J. Chambers. Limiting The Order of Polynomial Matrices within the SBR2 Algorithm. In *IMA Math. Signal Proc.*, Cirencester, UK, Dec. 2006.
- [12] C.H. Ta, S. Weiss. Shortening the Order of Paraunitary Matrices in SBR2 Algorithm. In *Int. Conf. Inf. Comm. & SP*, pp. 1-5, Singapore, Dec. 2007.
- [13] J. Corr, K. Thompson, S. Weiss, I. Proudler, and J. McWhirter. Row-Shift Corrected Truncation of Paraunitary Matrices for PEVD Algorithms. In *European Signal Processing Conference*, Nice, France, September 2015. (submitted).
- [14] A. Jafarian, J. McWhirter. A Novel Method for Multichannel Spectral Factorization. In *EUSIPCO*, pp. 1069–1073, Bucharest, Romania, Aug. 2012.
- [15] P.P. Vaidyanathan. *Multirate Systems and Filter Banks*. Prentice Hall, 1993.

# Observing the dynamics of waterborne pathogens for assessing the level of contamination

Isabella McKenna, Francesco Tonolini, Rachael Tobin, Jeremie Houssineau, Helen Bridle, Craig McDougall, Isabel Schlangen, John S. McGrath, Melanie Jimenez and Daniel E. Clark

**Abstract**—In environments of scarce hygiene it is of primary importance to detect potentially harmful concentrations of pathogens in drinking water. In many situations, however, accurate analysis of water samples is prohibitively complex and often requires highly specialised apparatuses and technicians. In order to overcome these limitations, a method to employ video processing to assist microfluidics water filtering apparatuses is proposed. Through the automated analysis of videos captured at the output of such devices it is possible to extract useful information that could control an autonomous calibration, hence eliminating the need of an expert and possibly leading to the construction of readily employable water quality assessing devices.

**Index Terms**—Waterborne pathogens, microfluidics, tracking, water contamination, detection, classification.

## INTRODUCTION

Often during major combat situations hygiene can be poor and access to potable water limited. Additionally, military personnel can also be exposed to potentially contaminated water during other scenarios, e.g., training and relaxation or deployment for humanitarian aid. Illness evidently reduces operational capability and is highly undesirable. During the 1990s norovirus outbreaks on US aircraft carriers affected up to 44% of the crews [1]. Other waterborne pathogens, e.g., protozoa such as *Cryptosporidium* and *Giardia* [2], [3], [4], are also potential risk factors though much less is known about their prevalence in military disease outbreaks. However, these pathogens are resistant to disinfection by chlorine and have extremely low infectious doses explaining why these have been responsible for major outbreaks of waterborne gastroenteritis in Europe and the US [5].

Water quality monitoring methods [6], [7], [8], especially those which are automated and easy to use, could play a significant role in reducing the risk of disease in military scenarios. Water utilities regularly monitor water quality to ensure the safety of supply. However, existing methods are time consuming and require highly trained microbiologists [9].

In this article new approaches to water monitoring, focussing on the use of automated microfluidic systems are being developed. Microfluidics is an emerging area of focus for waterborne pathogen sample processing and detection [10].

Within microfluidics devices observing the position and flow behaviour of pathogens is critical to the optimisation of designs and operating parameters as well as in the development of early warning approaches where the presence of a particle of a particular size or shape at a certain channel location could indicate a pathogen.

The method of pathogen observation proposed hereafter exploits video processing techniques to first detect and then classify particles in the output flow of a microfluidics apparatus. A digital camera positioned at the outlet of the device records the flow of particles. In the detection stage, the video frames are individually processed to retrieve position coordinates and size estimation. The obtained data is then fed into a Hypothesised filter for Independent Stochastic Populations (HISP) [11] which returns particle tracks and velocity information and which is able to classify particles according to their dynamic behaviour.

## I. MICROFLUIDICS DEVICES

To properly assess the level of water contamination, an efficient detection system should be able to screen out other particles present in the water, evaluate the concentration of pathogens in the water sample and give the means to determine species and viability of the organisms.

Retrieving and correctly interpreting the output of such devices could make the engineering of automated calibration schemes possible. Miniaturised fluidic devices in which the output can be directly observed and recorded with a camera are optimally suited to achieve automation. Given their means of particle segregation and the ease of recording the output flow with a digital camera, we identify two suitable set-ups. Passive hydrodynamic focussing, which exploits the geometries of microchannels to sort particles, and dielectrophoresis devices, in which an applied electric field segregates the particles of interest by viability and/or species, thus indicating infectivity. Preliminary results have been obtained for these two set-ups for particles as small as bacteria.

### A. Passive hydrodynamics

As part of the Aquavalens project, Jimenez et al. have developed a sample processing microfluidics device based on a passive hydrodynamic method<sup>1</sup>. By controlling the flow rate in a carefully designed channel, chosen particles can be focused along certain streams within the channel, see Figure 1. Viable and non-viable pathogens and different species of pathogens usually show dissimilarities in size and deformability, which determines their behaviour and final lateral channel position. Therefore, they can be collected into different outlets as required.

Detection methods applied to the output streams of the device could determine the effectiveness of the approach and

<sup>1</sup>further design details cannot be given due to a pending patent application.

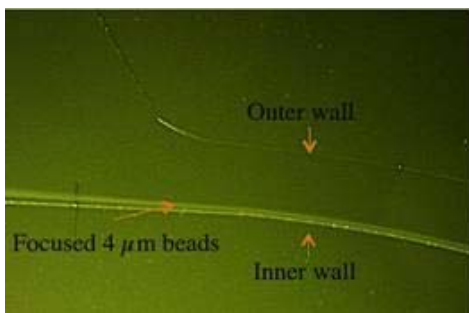


Fig. 1. Image of the device working with a high concentration of beads of a particular size. The image illustrates how particles of a particular size are sorted into a narrow size band, relative to the width of the channel, and can therefore be concentrated and collected by appropriate design of the outlet area. Different size particles will be located at different points across the channel.

produce a quantitative analysis of the outlet flows. These detections could also act as an early warning system for pathogen presence.

### B. Dielectrophoresis

Polarisable particles such as biological cells can be trapped and manipulated by applying an inhomogeneous electric field in a phenomenon called dielectrophoresis (DEP) [5].

The direction and magnitude of the force acting on the particles depend on the polarisability of the particles with respect to the medium. Viable and non-viable pathogen oocysts have been shown to behave differently under the force of the same electric field [12].

Figure 2 shows the output of a DEP electroration device. A set of carefully positioned electrodes creates a pattern of electric fields to trap particles in the centre of the device and allow them to rotate. In the case of pathogen filtering, it has been shown that organisms behave differently according to their viability. In particular, their rate and direction of rotation differ; non-viable oocysts tend to rotate clockwise and faster than viable ones.

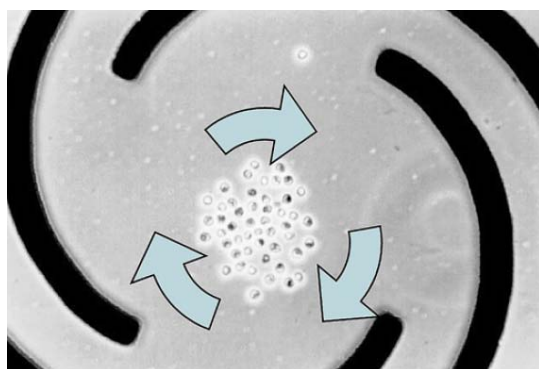


Fig. 2. Image of the output of a DEP electroration device. The electrodes (in black) generate an electric field such that the particles are kept in a specific area, but can rotate within it [12].

A continuous flow system has recently been developed utilising DEP to direct oocysts to different outlets, see Figure 3.



Fig. 3. The images on the left indicate the device design. Top picture shows the central channel where electrodes are located. The bottom picture shows the outlets where particles influence by the DEP have moved to the top half of the channel and are collected through the top outlet. The right image shows two different particle trajectories indicating how the degree of separation between them increases along the channel..

Video processing techniques can be applied to characterise the performance at different flow rates and electric fields, in order to assist in determining optimal operating parameters.

## II. ANALYSIS

The aim of an automated video analysis in this context is that of extracting meaningful information associated with each of the observed particles individually, such as their position, size and velocity, as time evolves. The obtained data can then be made use of in constructing indicators of statistical behaviour that are descriptive of the system and readily provide useful knowledge for contamination level assessment or apparatus calibration response.

To perform such information extraction, the procedure consists of two main steps; a detection step, which retrieves position coordinates and related uncertainty and estimated size for each particle at each video frame, and a classification step, which exploits a multi-object filter to obtain tracks of the detected objects and classify them according to their appearance or behaviour.

### A. Detection

To perform tracking of objects in microfluidics videos it is necessary to first obtain accurate detections of such objects for each video frame. In other words, it is necessary to extrapolate an estimate of the position and associated uncertainty for each object in every frame. An important condition on the retrieved information is that the positions and deviations obtained from the video frames are independent from one another. This is because the tracker relies on the assumption that observations at different time steps are not correlated with each other.

The problem is to recognise objects of interest in an image according to the known features that make them distinguishable from the rest of the image. The objects that are processed through different microfluidics set-ups can be of varied nature and generally the features that make them recognisable have to be chosen depending on the specific situation [13], [5].

In most biological applications of microfluidics particle sorting, however, the particles of interest tend to present a roughly spherical shape and it is precisely this feature, along

with their intensity difference with the immediate surrounding, that was largely exploited in the hereafter described detection method.

Prior to any recognition algorithm, a binary image is generated from the video frame under analysis via thresholding. This operation needs to be applied either to the image or to its negative, depending whether the particles to be detected are darker or brighter than the background.

To seek for circles in the binary image, with conditions imposed on the possible radii, the first part of the algorithm employed uses the circular Hough transform. Such method takes all pixels of high intensity gradient as candidate perimeter pixels  $p_i$ . Each candidate pixel is then made to cast a vote on the pixels that trace out a circular perimeter of different potential radii  $r_g$  around it and if a particular combination of pixel location and guess radius has a vote over a certain threshold that pixel location and guess radius determine a detected circle [14], [15]. That is, given an image  $I \in \mathbb{R}^{n \times m}$ , a votes array  $V_g \in \mathbb{R}^{n \times m}$  for each guess radius  $r_g$  is computed as follows

$$V_g = \sum_{i=1}^k C(p_i, r_g), \quad (1)$$

where  $C(p_i, r_g) \in \mathbb{R}^{n \times m}$  is an array of ones on the perimeter of a circle with center  $p_i$  and radius  $r_g$  and zeros everywhere else.  $k$  is the number of perimeter candidate pixels. In every vote array  $V_g$ , those elements that are over a certain threshold determine a detected circle in the image  $I$  with the coordinates of such an element as its center and  $r_g$  as its radius.

It is worth noting that this first step provides not only the position of the detected objects, but also their radius and hence their surface area. It is therefore possible to classify particles according to their size and group them in categories that have approximately the same mean area.

The above described method proved to be quite successful at recognising and locating single particles with limited flow rate. However, in microfluidics channels, particles occasionally move at faster rates or agglomerate in small clusters.

To address such situations, the second step in the detection algorithm considers all objects within a given area interval as candidate high speed objects or agglomerates. Their surface area is then compared with the mean area of each of the previously detected spheres groups. Objects which are found to have an area equal to that of a particular category within a certain tolerance are classified as belonging to that category. Objects which are found to be significantly smaller than any of the previously observed sizes are discarded as unimportant features in the image. Objects which are found to have an area significantly bigger than the area of any of the categories are labelled as agglomerates.

To locate objects within an estimated agglomerate, a small subsection of the image containing the agglomerate is convolved with different circles, each having the mean size of a particular category. The position and radius that yields the highest value in the convolved image are taken as center and radius of a detected object. The detected object is then

subtracted from the image and the process is repeated until the remaining agglomerate has an area which is considerably less than that of any category.

### B. Classification

Tracking and classification are performed jointly in order to provide a full probabilistic picture of the situation. This has been made possible with the introduction of a tracking framework modelling partially distinguishable populations [11]. This level of generality is required to perform principled multi-object estimation where specific information about objects, referred to as track, is propagated. This, in turn, allows for performing classification by distinguishing objects with different behaviours. The multi-object estimation algorithm that is used in this article is called the Hypothesised filter for Independent Stochastic Populations, or HISP filter [11], [16], [17], and is an approximated but tractable version of a multi-object Bayes filter. Joint tracking and classification has already been performed with the HISP filter for different applications such as harbour surveillance [18]. The principle of the approach is to perform multi-object estimation on a population that is composed of two or more sub-populations. In order to obtain information on this additional aspect, each sub-population should have distinct characteristics such as different motion models or different trajectories. In this article, we consider both location- and motion-based classification.

This way of classifying particles do not rely on visual features that could be obtained from the video. In consequence, the quality of the images acquired by the digital camera does not affect the performance of the classification algorithm as long as the detection technique described in Section II-A can be applied.

## III. EXPERIMENT

In order to demonstrate the proposed detection algorithm in a controlled environment, it was necessary to simulate a flow of particles in a microfluidic channel in vitro.

This was achieved by using spherical beads of diameters 7 microns and 10 microns suspended in a mixture of water and liquid detergent in a flow channel 300 microns in diameter. Adjustable flow paths were set up prior to the particles entering the channel using an acoustical sorting process which created resonant conditions using an ultrasonic transducer and a reflective boundary.

The standing wave that arose due to these resonant conditions created nodes which behave as pressure maxima and minima with axial forces drawing particles towards them; the particles were then drawn together by lateral forces and particle-particle interactions, resulting in precise flow streams.

The particles then entered the channel until displaced approximately 150 microns orthogonal to the direction of travel through laser controlled optical tweezing. The beam power and waist were chosen for optimal performance based on the desired particle size and density.

The video was captured with a Prosilica EC1280 firewire camera imaging the outlet of the above described apparatus

and was shot at 23 frames per second; a captured frame can be viewed in Figure 4.

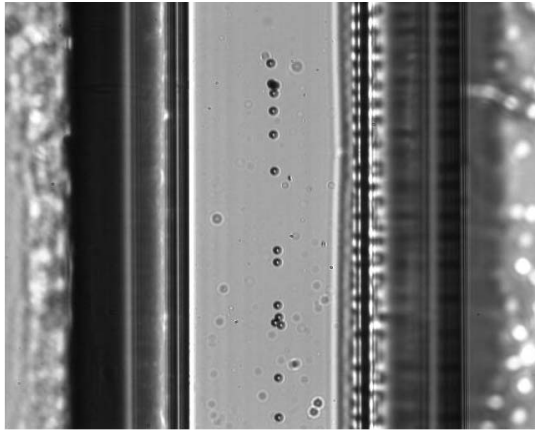


Fig. 4. Image of the output of a DEP electrorotation device. The electrodes (in black) generates an electric field such that the particles are kept in a specific area, but can rotate within it.

#### A. Detection

The detection method was found to be very effective provided the particles to be detected do not differ by more than a factor of two in radius from each other and that the speed at which they move is still sufficiently low such that the particle does not move by more than twice its size in the acquisition time of one frame. These assumption may not always hold for every particle sorting apparatus and the method might need to be modified to accommodate certain situations. In the particle sorting data that were processed and are reported here, however, these assumption mostly held true and the detection was found to be quite accurate. Results of the detection method described above are shown for one particular frame taken from a sorting microfluidics video in Figure 5, where the particles detected by the first part and the second part of the algorithm are highlighted in different colours.

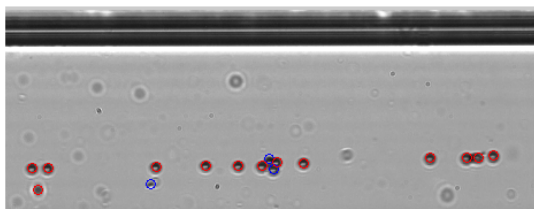


Fig. 5. Detected locations of particles overlaid on the video frame they have been extracted from. The detections highlighted in red are obtained as a result of the circular Hough transform filtering and the detections highlighted in blue are obtained employing the second section of the algorithm. It can be seen how, although the circular Hough transform is successful at recognising most of the particles, it misses particles which are part of a cluster and a particle that moves faster than the others. The second section of the algorithm effectively compensates for such missed detections.

As for the deviations associated with the retrieved positions, these were taken to be symmetric and the ones related to particles detected through the first step were set to roughly

their retrieved diameter and those obtained from the second step were set to twice their diameter. This is because successful detection through the circular Hough transform resulted to be very precise in this context, whereas detection of fast moving particles and clustered particles yields less precise estimates of their centre positions.

In order to assess the proposed detection method, the performance of the algorithm in terms of cardinality and localisation has been evaluated using the OSPA distance [19] on simulated data. For the simulation to be sufficiently representative of the real problem, an average number of 12 synthetic beads of different sizes have been added to a real background in 40 different configurations including agglomerates. The average OSPA distance, with a 2-norm and a cut-off of 10 px, is found to be equal to 0.64 with a standard deviation of 0.0818. This result indicates that most of the beads are found in the image without creating many false positives and that these beads are accurately localised.

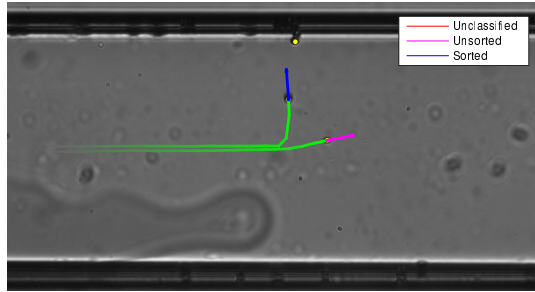
#### B. Classification

We consider the experiment described in Section III and perform the classification with the following parameters: sorted and unsorted beads both have a motion model based on a constant velocity up to the position of the laser. The unsorted beads are unaffected by the laser whereas the sorted ones are diverted by it, which is modelled as a force applied orthogonally. In the latter model, two additional forces are considered: the first one is the friction due to the viscosity of the fluid and the second one is a trapping effect due to the laser, which compensates for the motion of the fluid along the channel. The uncertainty on each motion model is characterised by an additive noise on the acceleration. A location-based classification is utilised for counting the number of beads that exit the field of view of the camera through the far end of the channel and the number of beads that are stopped on the border of the channel around the location of the laser. The obtained numbers are indicated in the titles of Figures 6(a) and 6(b). Two examples are given in these figures where tracks corresponding to beads with different behaviours are displayed with various colours. To handle the fact that all beads have the same motion model up to the position of the laser, an additional class named "Unclassified" is created and associated to beads for which the classification is too uncertain. Specifically, the probability for one bead to be part of a given class has to be above 75% for the corresponding track to be displayed with the associated colour.

## IV. CONCLUSION

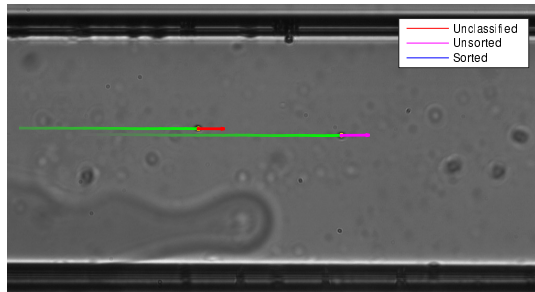
The employment of video processing techniques to assist the operation of microfluidic devices could allow for the production of portable, readily employable and extremely accurate water contamination assessing tools, ideally suited for the needs of military operations. The detection method presented here allowed efficient detection of differently sized microspheres flowing through the outlet of a microfluidic device. The two techniques described in section II-A proved to be

Classification for microfluidics: number of unsorted: 20 # sorted: 2



(a) Time step 606: one bead is being diverted by the laser (blue) while the other one has not been affected (magenta)

Classification for microfluidics: number of unsorted: 22 # sorted: 3



(b) Time step 673: one bead is not classified yet (red) and the other one has not been affected by the laser (magenta)

Fig. 6. Examples of classification with the HISP filter. Observations are indicated in yellow, tracks are displayed with different colours depending on their classification, and the trajectory for each track is shown in fading green.

effective at obtaining accurate estimates of particle positions and sizes in every video frame with tolerable amounts of false alarms and missed detections.

The classification of the observed particles was carried out employing the HISP filter. Such algorithm was able to extract particle tracks and associated velocity along with the related uncertainties. The obtained information was then used to classify the objects into sorted and unsorted particles. Having such detailed information for every single particle flowing through the outlet of a microfluidic channel gives a complete measure of the apparatus state of operation and hence can be used as a reliable and automated feedback for the calibration of the device through the optimisation of its many parameters.

As in most cases the relationship between output particle behaviour and system parameters is known, the data retrieved by the classification can be used to control a proper automated response. For instance, if a stream of particles appears clustered and poorly focused at the outlet of a spiral channel device, it can be deduced that the flow rate through the channel is too low. From the autonomously obtained data it is then possible to quantify these characteristics of the stream and trigger an appropriate increase of flow rate. In many cases pathogen size and dynamic behaviour are also indicators of species and viability, hence a measure of the level of contamination of the sample can be deduced from a classification method analogous to that described above.

## ACKNOWLEDGMENTS

Helen Bridle, John McGrath and Melanie Jimenez are supported by STFC, the EU Aquavalens project and Scottish Water. Jeremie Houssineau and Daniel E. Clark are supported by DSTL Task ED TIN 2-3. Isabel Schlangen has a PhD scholarship from the Edinburgh Super-resolution Imaging Consortium (ESRIC). Craig McDougall is supported by the EPSRC as a post doctoral researcher. Daniel Clark is supported by the EPSRC/Dstl University Defence Research Centre on Signal Processing (UDRC) Phase 2 (EP/K014227/1).

## REFERENCES

- [1] J. J. Wijnker and H. de Man, "Assessing the waterborne risk of a norovirus infection for military personnel in the netherlands," *Nederlands militair geneeskundig tijdschrift*, vol. 67, no. 1, pp. 16–18, 2014.
- [2] M. Smith and K. C. Thompson, *Cryptosporidium: the analytical challenge*. Royal Society of Chemistry, 2001, vol. 1.
- [3] F. Chen, K. Huang, S. Qin, Y. Zhao, and C. Pan, "Comparison of viability and infectivity of cryptosporidium parvum oocysts stored in potassium dichromate solution and chlorinated tap water," *Veterinary parasitology*, vol. 150, no. 1, pp. 13–17, 2007.
- [4] C. C. Tam, L. C. Rodrigues, L. Viviani, J. P. Dodds, M. R. Evans, P. R. Hunter, J. J. Gray, L. H. Letley, G. Rait, D. S. Tompkins *et al.*, "Longitudinal study of infectious intestinal disease in the uk (iid2 study): incidence in the community and presenting to general practice," *Gut*, vol. 61, no. 1, pp. 69–77, 2012.
- [5] H. Bridle, M. Kersaudy-Kerhoas, B. Miller, D. Gavriilidou, F. Katzer, E. A. Innes, and M. P. Y. Desmulliez, "Detection of cryptosporidium in miniaturised fluidic devices," *Water research*, vol. 46, no. 6, pp. 1641–1661, 2012.
- [6] T. M. Straub and D. P. Chandler, "Towards a unified system for detecting waterborne pathogens," *Journal of Microbiological Methods*, vol. 53, no. 2, pp. 185–197, 2003.
- [7] P. T. Monis, S. Giglio, A. R. Keegan, and R. A. Thompson, "Emerging technologies for the detection and genetic characterization of protozoan parasites," *Trends in parasitology*, vol. 21, no. 7, pp. 340–346, 2005.
- [8] H. V. Smith and R. A. Nichols, "Cryptosporidium: detection in water and food," *Experimental parasitology*, vol. 124, no. 1, pp. 61–79, 2010.
- [9] H. Bridle, *Waterborne Pathogens: Detection Methods and Applications*. Newnes, 2013.
- [10] H. Bridle, B. Miller, and M. P. Y. Desmulliez, "Application of microfluidics in waterborne pathogen monitoring: A review," *water research*, vol. 55, pp. 256–271, 2014.
- [11] J. Houssineau, "Representation and estimation of stochastic populations," Ph.D. dissertation, Heriot-Watt University, 2015.
- [12] A. D. Goater, J. P. H. Burt, and R. Pethig, "A combined travelling wave dielectrophoresis and electrorotation device: applied to the concentration and viability determination of cryptosporidium," *Journal of Physics D-Applied Physics*, vol. 30, no. 18, p. L65, 1997.
- [13] J. C. Mountford and M. Turner, "In vitro production of red blood cells," *Transfusion and Apheresis Science*, vol. 45, no. 1, pp. 85–89, 2011.
- [14] H. Rhody, "Hough circle transform," *Chester F. Carlson Center for Imaging Science. Rochester Institute of Technology*, 2005.
- [15] S. Kaur and M. Shukla, "Reversible data hiding in images using circular hough transform," *International Journal of Computer Science & Information Technologies*, vol. 5, no. 5, 2014.
- [16] J. Houssineau, P. Del Moral, and D. E. Clark, "General multi-object filtering and association measure," in *Computational Advances in Multi-Sensor Adaptive Processing (CAMSAP), 5th IEEE Workshop on*, 2013.
- [17] J. Houssineau, D. E. Clark, and P. Del Moral, "A sequential Monte Carlo approximation of the HISP filter," in *European Signal Processing Conference (EUSIPCO)*, 2015.
- [18] Y. Pailhas, J. Houssineau, E. Delande, Y. Petillot, and D. E. Clark, "Tracking underwater objects using large MIMO sonar systems," in *International Conference on Underwater Acoustic*, 2014.
- [19] D. Schuhmacher, B.-T. Vo, and B.-N. Vo, "A consistent metric for performance evaluation of multi-object filters," *Signal Processing, IEEE Transactions on*, vol. 56, no. 8, pp. 3447–3457, 2008.

# Distributed Implementation for Person Re-identification

Saurav Sthapit\*, John Thompson\*, James R. Hopgood\* and Neil M. Robertson†

\*Institute of Digital Communications, School of Engineering, University of Edinburgh

Emails: {s.sthapit, john.thompson, james.hopgood}@ed.ac.uk

†Vision Lab, School of Engineering and Physical Sciences, Heriot-Watt University

Email: n.m.robertson@hw.ac.uk

**Abstract**—Person re-identification is to associate people across different camera views at different locations and time. Current computer vision algorithms on person re-identification mainly focus on performance, making it unsuitable for distributed systems. For a distributed system, computational complexity, network usage, energy consumption and memory requirement are as important as the performance. In this paper, we compare the merits of current algorithms. We consider three key algorithms, Keep It Simple and Straightforward Metric (KISSME), Symmetry-Driven Accumulation of Local Features (SDALF) and Unsupervised Saliency Matching (USM). The advantage of SDALF, and USM is that they are unsupervised methods so training is not required but computationally many time expensive than KISSME. The Saliency based method is superior in performance but also has the largest feature size. As the features needs to be transmitted from one camera to other in distributed system, this mean higher energy consumption and longer time delay. Among these three, KISSME offers a balance between performance, complexity and feature lengths and hence more suitable for distributed systems.

## I. INTRODUCTION

Person re-identification refers to associating people across camera views at different locations and times [1]. It can have huge impact on surveillance and security because manual identification is not only tedious and costly but the results may also be received too late. The main challenges it faces is that the Field Of View (FOV) of the cameras can be non-overlapping, background and pose can change, as well as the occurrence of occlusion. A particular individual can look dissimilar in different views, while different individuals can look similar from different angles. Figure1 shows some sample pedestrian images from the VIPeR dataset [2] taken by two cameras illustrating these difficulties.



Fig. 1. Samples of pedestrian images from VIPeR dataset [2]

Person re-identification algorithms can broadly be classified into supervised and unsupervised algorithms. Supervised methods include algorithms like Mid-level features [3], Keep It Simple and Straightforward Metric (KISSME) [4], Locally Aligned Feature Transform (LAFT) [5], Information Theoretic Metric Learning (ITML) [6]. They mostly focus on metric learning, whereas unsupervised algorithms focus on feature

design. Some of the unsupervised methods include Symmetry-Driven Accumulation of Local Features (SDALF) [7], Bio-inspired Covariance based features (BiCov) [8] and spatio-temporal [9]. For a more detailed review of recent approaches, refer to these papers [1], [10], [11], [12].

Current research in this area, however, focusses on implementing their algorithm on a single system [7], [4], [13], [3]. Implementing person re-identification on a distributed system has numerous benefits which will be illustrated with the example shown in Fig. 2. The system comprises of multiple smart cameras which may be static or moving. They are shown in the Fig. 2 by black and white camera icons respectively. The cameras are connected to each other and their field of view may be non-overlapping. The targets 1 and 2 are moving along the path shown by the arrows.

In a centralised system, all the sensor nodes would have been connected to a single computer with immediate access to data from all the sensor nodes. But on the downside, it has to process the data itself, which may be challenging particularly in real-time applications. In the distributed case, each sensor node has access to its own data only but offers more flexibility for signal processing. Running it on wireless embedded platform such as smartphone could be possible, which means the cameras could be deployed and scaled easily. In a military context, this means the camera may be embedded within a soldier's uniform to monitor targets without raising suspicion in conflict zones. We can think of light cameras in Fig.2 as these soldiers monitoring target 2. however, along with the algorithm's accuracy, there are several other factors to think about such as feature data length, computational complexity etc.

In this paper, we discuss the advantages and the disadvantages of current person re-identification algorithms when implemented on a distributed platform. The paper is structured as follows. Section II describes the basic workflow in person re-identification. Then we analyse various algorithms in section III. Section IV describes the experiments carried out and their results. Finally section V discusses the results and concludes the paper.

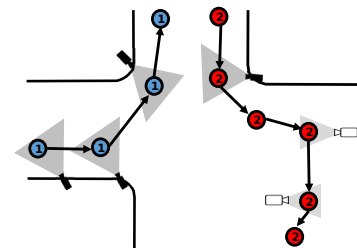


Fig. 2. Scenario of multi-camera person re-identification. Shaded cameras are fixed, white cameras are moving and grayed area represent Field of View (FOV)

## II. SYSTEM DESCRIPTION

Person re-identification algorithms generally follow the basic workflow depicted in Fig. 3. Images are taken from each camera and preprocessed. The pre-processing step may include background subtraction and a person detection algorithm. To create a unique signature of each person, features are extracted. Popular features include combination of low level features such as colour histograms, Local Binary Patterns (LBP) [14], Scale Invariant Feature Transform (SIFT) [15] and Histogram of Gradient(HOG) [16]. Metric distance between signatures is calculated to verify if the images belong to the same individual or not. Alternatively, the test signature may be compared with the gallery set containing signatures of a seen individual to find the correct match. Some researchers have defined the person identification problem as a ranking problem [17].

In the distributed case, the signature has to be communicated from one camera to another as shown in the Fig. 3. Very often, these camera are connected with wireless networks such as Wi-Fi or cellular system. We know that the time taken and energy required to send the data across the network is directly proportional to the length of the data [18]. We conduct an experiment to quantize the energy and time required for such system in section IV-A.

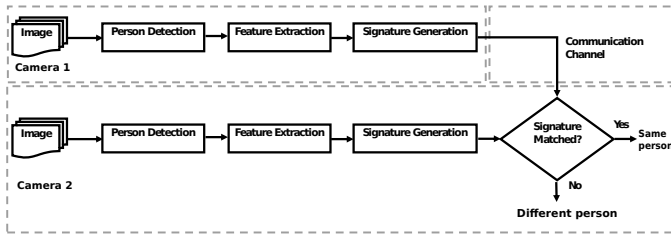


Fig. 3. Person Re-identification workflow.

Depending upon the number of images used, algorithms can be classified into single-shot and multi-shot algorithms. Single-shot algorithms take into account only one image per person (class) whereas multiple-shot algorithms uses multiple images. Multi-shot algorithms tries to keep the signature data size low and keep the matching considerably fast by throwing away redundant information.

### A. Distributed Scenario

For implementing the re-identification system on a distributed system, let us assume each camera in Fig.3 has its own processing capability. So each sensor node can generate signature for the people in its FOV. For signature matching, one device has to send their signature to its neighbour so that it can be matched with its camera views. These are often battery powered devices, such as a smartphone, so longevity of the battery is desired. As it is desirable to keep the signature size as small as possible, we analyse the size of descriptors of the algorithms in consideration. Distributed systems are equipped with less powerful processors and have less memory resources, so the complexity of the algorithm is desired to be as low as possible. In order to measure complexity, we measure the time taken to run. For this paper, we have run our experiments on a desktop computer.

### B. Datasets

Popular publicly available datasets for person re-identification are listed in Table.I. VIPeR is the most widely used and challenging dataset, one of the reason being limited samples per subject. We have used the VIPeR dataset in our

experiments because many published algorithm comparisons are available.

## III. PERSON RE-IDENTIFICATION ALGORITHMS

Among many algorithms, we have selected three key ones owing to their significance in person re-identification and availability of their source code. We go through them very briefly here.

### A. KISS METric Learning

Keep It Simple and Straightforward Metric (KISSME) [4] focusses on learning the metric rather than complicated descriptor design. For the descriptor, images are divided into overlapping blocks and histograms are extracted in HSV and LAB colour-space. Local Binary Patterns (LBP) [14] are extracted to capture the texture information. For the VIPeR dataset, based on the code and data<sup>1</sup> provided by authors [4], each image has 22154 dimension features. Principal Component Analysis (PCA) is used by the authors to shorten the length of the descriptor to 34 experimentally chosen dimensions.

The Mahalanobis Metric learning is a widely used method in classification and in computer vision. It is defined as the squared distance between two points  $x_i$  and  $x_j$  as

$$d_M^2(x_i, x_j) = (x_i - x_j^T)M(x_i - x_j) \quad (1)$$

where  $M \succeq 0$  is a positive semi-definite matrix. The main approach of Mahalanobis based algorithms is to define and learn the matrix  $M$  such that distance between images of same class is minimised and distance between images of different classes are maximised. KISSME [4], ITML, [6], LDML [21] and LAFT [5] are based on these methods. A detailed review of Mahalanobis based methods can be found in Roth et al's paper [22]. KISSME tries to address the metric learning approach from a statistical inference point of view. They test the hypothesis  $H_0$  that the pair is dissimilar versus the alternative hypothesis  $H_1$  that the pair is similar.

$$\delta(\mathbf{x}_{ij}) = \log \left( \frac{p(\mathbf{x}_{ij}|H_0)}{p(\mathbf{x}_{ij}|H_1)} \right) = \log \left( \frac{f(\mathbf{x}_{ij}|\theta_0)}{f(\mathbf{x}_{ij}|\theta_1)} \right) \quad (2)$$

where  $\mathbf{x}_{ij} = \mathbf{x}_i - \mathbf{x}_j$  is the pairwise difference with zero mean. A high value of  $\delta(\mathbf{x}_{ij})$  means the pair are dissimilar and vice-versa. Assuming a Gaussian structure of the difference space, Eq. 2 can be written as

$$\delta(\mathbf{x}_{ij}) = \log \left( \frac{\frac{1}{\sqrt{2\pi|\Sigma_{y_{ij}=0}|}} \exp(-1/2 \mathbf{x}_{ij}^T \Sigma_{y_{ij}=0}^{-1} \mathbf{x}_{ij})}{\frac{1}{\sqrt{2\pi|\Sigma_{y_{ij}=1}|}} \exp(-1/2 \mathbf{x}_{ij}^T \Sigma_{y_{ij}=1}^{-1} \mathbf{x}_{ij})} \right) \quad (3)$$

where,

$$\Sigma_{y_{ij}=0,1} = \sum_{y_{ij}=0,1} (\mathbf{x}_i - \mathbf{x}_j)(\mathbf{x}_i - \mathbf{x}_j)^T \quad (4)$$

They arrive at the Mahalanobis distance metric in Eqn.1 that reflects the properties of the log-likelihood ratio test by re-projecting  $\hat{M} = \left( \Sigma_{y_{ij}=1}^{-1} - \Sigma_{y_{ij}=0}^{-1} \right)$  onto the cone of positive semi-definite matrices.

<sup>1</sup>accessible from <https://irs.icg.tugraz.at/research/kissme/>

TABLE I. POPULAR PERSON RE-IDENTIFICATION DATASETS

Dataset	No. of Person	No. of Images	Features
VIPeR [2]	632	1264	pose, background, only 1 image per subject per camera
CAVIAR4REID [19]	72	1220	pose, background, varying resolution, multiple images per subject per camera
CUHK01 [20]	971	3884	pose, background, multiple images per subject per camera

### B. Symmetry-Driven Accumulation of Local Features(SDALF)

SDALF [7] is suitable for single-shot and multi-shot images. The pedestrian image is divided into the head, torso and leg region and three types of features Weighted Color Histograms(WHSV), Maximally Stable Color Region(MSCR) and Recurrent High-Structured Patches (RHSP) are extracted. Each of these features are extracted from the torso and leg region and optionally from the head region. The histograms feature is built with 12 bins channel per region, totalling to  $12 \times 3 \times 3 = 108$  dimensions<sup>2</sup>. The MSCR feature of a blob is represented by 9 dimensional feature but these blobs per image is variable. Similarly, the feature length of RHSP features is variable as well. Similarity between two images is calculated as weighted sum of euclidean distance between their features. As the algorithm is unsupervised, it doesn't require any training and is also scalable to videos.

### C. Unsupervised Saliency

*Saliency* is defined as “distinct features that 1) are *discriminative* in making a person standing out from their companions, and 2) are *reliable* in finding the same person across different views” [23]. Zhao et al. have developed a few variants of supervised and unsupervised methods using saliency [13], [23], [3] but we will mostly focus on Unsupervised Saliency Matching [13]. Each image is densely divided into overlapping patches. For each patch, 32 bin LAB colour histograms are computed in three scales for three channels. So the colour feature is of length  $32 \times 3 \times 3 = 288$ . Similarly for SIFT features, each patch is further divided into  $4 \times 4$  cells to obtain  $4 \times 4 \times 8 = 128$  dimensional feature per channel. So total feature length for each patch is  $288 + 128 \times 3 = 672$  dimensions. For an image, these DenseFeats features is represented as  $X^{A,u} = \{x_{m,n}^{A,u} | m = 1, \dots, M, n = 1, \dots, N\}$  where  $(A, u)$  denotes the  $u^{th}$  image in camera A,  $(m, n)$  denotes the patch centred at the  $m^{th}$  row and the  $n^{th}$  column of the image. Total size of feature for an image is  $M \times N \times 672$ .

Once, the features are extracted for each patch, the key steps of the algorithm is briefly listed in Table II. Fig.4 illustrates the adjacency constrained search set of the patch in yellow box which is used in computing the Nearest Neighbour set. One of the two approaches is based nearest neighbour distances. A score is assigned for each patch using Eq. 5.

$$\text{score}_{knn}(x_{m,n}^{A,u}) = D_k(X_{NN}(x_{m,n}^{A,u})) \quad (5)$$

where  $D_k$  denotes the distance of the  $k$ -th nearest neighbour. Similarity between two images is calculated using Eq.6

$$\text{Sim}(\mathbf{x}^{A,u}, \mathbf{x}^{B,v}) = \sum_{m,n} \frac{\text{score}_{knn}(x_{m,n}^{A,u}) \cdot s(x_{m,n}^{A,u}, x_{i,j}^{B,v}) \cdot \text{score}_{knn}(x_{i,j}^{B,v})}{\alpha_{sdc} + |\text{score}_{knn}(x_{m,n}^{A,u}) - \text{score}_{knn}(x_{i,j}^{B,v})|} \quad (6)$$

## IV. SIMULATION RESULTS

In the ideal scenario, the algorithms would be implemented on a real distributed system such as Android smartphone



Fig. 4. Illustration of adjacency constrained search. Green region represents the adjacency constrained search set of the patch in yellow box. The patch in red box is the target match [23]

TABLE II. ALGORITHM FOR UNSUPERVISED HUMAN SALIENCY LEARNING

Algorithm for learning Unsupervised Human saliency
<b>Input:</b> image $X^{A,u}$ and a reference image set $\mathbb{R} = \{X^{B,v}, v = 1, \dots, N_r\}$
<b>Output:</b> saliency probability map $P(l_{m,n}^{A,u} = 1   x_{m,n}^{A,u})$
<b>for</b> each patch $x_{m,n}^{A,u}$ <b>do</b>
compute Nearest Neighbour (NN) set $X_{NN}(x_{m,n}^{A,u})$
compute $\text{score}_{knn}(x_{m,n}^{A,u})$ based on NN distances,
<b>end for</b>

and results could be measured. However, the algorithms are initially written in MATLAB to simulate a distributed system scenario and the simulations were carried out on MATLAB running on a desktop PC. In future, we can experiment with implementing the algorithms on embedded device to check their performance.

Experiments were carried out on a desktop PC with an Intel Xeon processor (X5650) with 12 cores and 24 gigabytes of RAM running Scientific Linux 6.5 unless specified. Some of the algorithms have parallel implementation as well but we have turned it off for these experiments for two reasons. 1) To make the comparisons fair, 2) Parallel MATLAB instances run within their own Java Virtual Machine (JVM) environments accounting for increased memory allocations. This caused some algorithms to fill the RAM to fill quickly and slowing down the execution.

For the experiments, the VIPeR dataset was randomly split into two sets of 316 image pairs each. One set was used for training and other for testing. We do this following the testing conventions in these papers [7], [4], [13].

### A. Cost of sending data in wireless network

In the distributed case, the signature of a person extracted in one camera has to be transmitted to another via a communication channel as shown in Fig. 3. The implication of transferring data to a neighbour node has a cost in terms of energy and time, particularly in the case of wireless transmission. We conducted simple experiment to analyse how much energy and time is required in order to data to other nodes. We developed a simple application(app) for the Android platform which sends files of various sizes to the server using WiFi or mobile data (see Fig.5). The application was built using Google's Android Development Kit (ADK) and Android Studio. The experiments were conducted in a LG G2 smartphone. Time is measured using the system clock. Initial time is noted when data sending commences. The final time is noted after an acknowledgement is received from the server and the time taken

<sup>2</sup>reduced to 72 if head region is not used

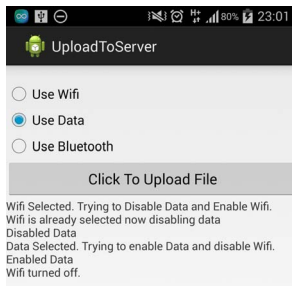


Fig. 5. Android application for calculating time and energy cost of transmitting data

is the difference of these two. Measuring energy consumed is however complicated than measuring time, because by default Android reports battery level in percentage only. It is too crude for our purpose and also as many processes are running simultaneously in background, it's hard to calculate the exact energy consumed for the communication. We used a third party application called Treprn profiler [24]. It is developed by Qualcomm for their Snapdragon processors and has access to hardware counters in the processor which are not available for public use. It isolates the energy used by an application, by collecting baseline energy consumption before starting the test application. Similar to the counter for measuring time, we flag the start and the end of the communication event to the Treprn application using Android Intent. Treprn then logs the energy consumption for each event.

As expected, the evaluations show in Fig.6 that the cost rises as the size of data goes up. WiFi has generally lower energy consumption than the phone networks. The difference becomes notable as the size of data goes up. Surprisingly, the speed of 4G was even faster than the WiFi albeit at higher energy cost. The test were done in Edinburgh with the WiFi provided by router connected to the Virgin Network and 4G by Everything Everywhere (EE) Network. But we didn't take into account many factors such as the load on the network, Signal strength etc.

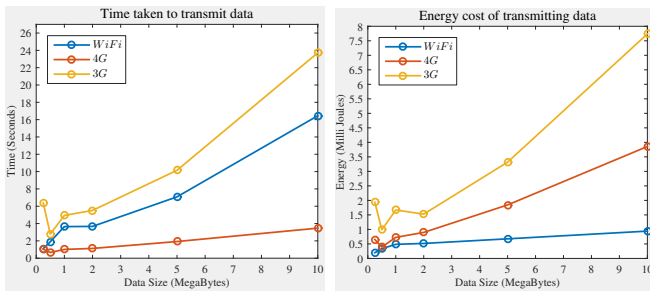


Fig. 6. Time and energy required to send data across the network

## B. Runtime and Feature Length

1) *KISSME*: Among all the methods, KISSME was the fastest to train and learn the metric and it performed well too. The length of the feature before and after dimensionality reduction was determined from the source code and feature dataset provided. However, to calculate the time taken for feature extraction, we wrote the code as per their paper [4]. We divide the image into overlapping blocks of size  $8 \times 16$  and stride of  $8 \times 8$  to get 105 patches. We took histograms of 24 bins per channel and uniform LBP of 59 bins. So in total, the feature size is  $105 \times 3 \times 2 \times 24 + 105 \times 59 = 21315$  dimensions. The histogram extraction of HSV and LAB and LBP features

TABLE III. SDALF EXECUTION TIME

Step	Time(sec)
Division into 3 parts	162.15
MSCR Extraction	138.21
WHSV Extraction	123.17
RHSP Extraction	4824.6
MSCR Matching	6095.3
WHSV Matching	214.74
RHSP Matching	423.00
Total	11981.17

TABLE IV. FEATURE LENGTH, RUNTIME AND RANK 1 RESULTS.

Algorithm	Feature Length(PCA)	Time(sec)	Rank 1
KISSME	22154(34)	260.05	18.03
SDALF	5359	11981.00	19.80
Unsupervised Saliency	201600	11737.90	27.22

took approximately 260 seconds, which is very high compared to its training time of around 0.05 seconds. But still, feature extraction per image would take about  $260/1264 \approx 0.2$  seconds. After dimensionality reduction, the feature dimension is reduced to just 34 which is highly desirable.

2) *SDALF*: As discussed in section III, the feature length of SDALF is not fixed but dependent on the number of RHSP patches and MSCR regions found in the image. Table III shows the breakdown of average time spent per step for the VIPeR dataset. RHSP features took the longest to compute so we experimented with removing it. The result showed there was only marginal degradation of performance. It can be seen in Fig. 7. But as the test has been done only in one dataset, it may not be true for all.

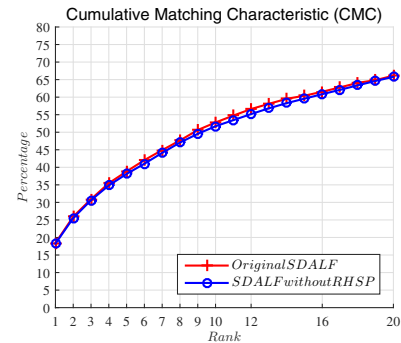


Fig. 7. Performance of SDALF with and without RHSP

3) *Saliency*: Saliency learning has the highest feature size per image. Each feature is of 201600 dimensions, if we suppose it is of MATLAB double precision, it's size is approximately 1.5 Megabytes which is not huge. However, each probe patch has its own adjacency search area for each image in the gallery set. If we assume 10 patches per row and constrained search area to be  $\pm 2$  rows, and there are 100 images in the gallery then. For each patch, we need to calculate the distance between itself and  $10 \times 5 = 5000$  patches<sup>3</sup>. If there are 300 patches per image, it amounts to  $5000 \times 300 = 1,500,000$  distances per image, which is more than 11 Megabytes in MATLAB double precision. In terms of running on embedded devices, memory is often a limited resource.

## C. Cumulative Matching Characteristics (CMC) curves

Cumulative Matching Characteristics(CMC) [25] is widely used in person re-identification performance evaluation. It treats person re-identification as a ranking problem. Rank-1

<sup>3</sup>except for two top and two bottom rows

implies that the correct match has been found whereas Rank- $k$  implies there were  $k - 1$  wrong classes ahead of the correct class.  $CMC(k)$  measures the probability that the correct match has a rank equal or higher than  $k$  [10]. Table IV shows Rank-1 score of various algorithms. It shows Saliency has better performance although it is computationally expensive and high data size. KISSME on the other hand looks the best to be implemented on distributed system as it is shown to be fast and computationally inexpensive as well.

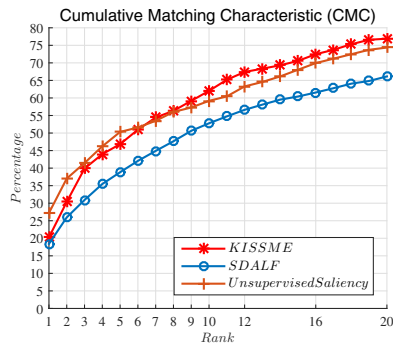


Fig. 8. Performance of the algorithms in VIPeR dataset

## V. CONCLUSION

In this paper, we explored the possibilities of implementing person re-identification algorithms on distributed systems. We studied KISSME, SDALF and Unsupervised Saliency matching in terms of their runtime, size of descriptor, along with their person re-identification performance. We also looked at time and energy cost of communicating with neighbouring systems using various wireless technologies. Unsupervised Saliency has better Rank-1 result but it is computationally the most expensive and the memory requirement is also the highest. Even though we did not mention the energy cost for computing on the distributed platform, this would also consume high amount of energy. SDALF on the other hand has smallest signature before dimensionality reduction and potentially could be made even smaller by removing RHSP features. In theory at least, SDALF and Saliency features may be reduced using dimensionality reduction as well. But based on our experiments, without any modifications, KISSME is the best algorithm for a distributed system owing to its low complexity and shortest signature length. The only drawback is that it has to be trained and the large covariance matrices has to be computed and communicated to the neighbours.

This paper explored only the consequences of using distributed systems for person re-identification systems where communication between the sensor nodes is a requirement. But in some cases there might be a question between communicating or processing on its own. Even with communicating between nodes, there is a question of which node to communicate to when multiple nodes are available. In future, we are interested in answering these questions.

## VI. ACKNOWLEDGEMENT

This work was supported by the Engineering and Physical Sciences Research Council (EPSRC) [EP/K014277/1] and the MOD University Defence Research Centre (UDRC) on Signal Processing

## REFERENCES

[1] S. Gong, M. Cristani, S. Yan, and C. C. Loy, *Person Re-Identification, Advance in Computer Vision and Pattern Recognition*. 2014.

[2] D. Gray, S. Brennan, and H. Tao, "Evaluating appearance models for recognition, reacquisition, and tracking," *Perform. Eval. Track. Surveill. (PETS), 10th Int. Work.*, vol. 3, pp. 41–47, 2007.

[3] R. Zhao, W. Ouyang, and X. Wang, "Learning Mid-level Filters for Person Re-identification," *2014 IEEE Conf. Comput. Vis. Pattern Recognit.*, pp. 144–151, June 2014.

[4] M. Kostinger, M. Hirzer, P. Wohlhart, P. M. Roth, and H. Bischof, "Large scale metric learning from equivalence constraints," *Proc. IEEE Comput. Soc. Conf. Comput. Vis. Pattern Recognit.*, no. Ldml, pp. 2288–2295, 2012.

[5] Z. Li, S. Chang, F. Liang, T. S. Huang, L. Cao, and J. R. Smith, "Learning Locally-Adaptive Decision Functions for Person Verification," *2013 IEEE Conf. Comput. Vis. Pattern Recognit.*, pp. 3610–3617, June 2013.

[6] J. V. Davis, B. Kulis, P. Jain, S. Sra, and I. S. Dhillon, "Information-theoretic metric learning," *ICML*, pp. 209–216, 2007.

[7] M. Farenzena, L. Bazzani, a. Perina, V. Murino, and M. Cristani, "Person re-identification by symmetry-driven accumulation of local features," *Proc. IEEE Comput. Soc. Conf. Comput. Vis. Pattern Recognit.*, pp. 2360–2367, 2010.

[8] H. Ma, C. Zeng, and C. X. Ling, "A Reliable People Counting System via Multiple Cameras," *ACM Trans. Intell. Syst. Technol.*, vol. 3, pp. 1–22, Feb. 2012.

[9] T. B. T. Sebastian, P. H. Tu, J. Rittscher, R. Hartley, and N. Gheissari, "Person Reidentification Using Spatiotemporal Appearance," in *2006 IEEE Comput. Soc. Conf. Comput. Vis. Pattern Recognit. - Vol. 2*, vol. 2, pp. 1528–1535, IEEE, 2006.

[10] X. Wang and R. Zhao, "Person Re-Identification: System Design and Evaluation Overview," in *Pers. Re-Identification* (S. Gong, M. Cristani, S. Yan, and C. C. Loy, eds.), London: Springer London, 2014.

[11] M. H. M. Saad, H. B. Zaman, M. A. Saghaif, and A. Hussain, "Review of person re-identification techniques," *IET Comput. Vis.*, pp. 1–20, Feb. 2014.

[12] A. Bedagkar-Gala and S. K. Shah, "A survey of approaches and trends in person re-identification," *Image Vis. Comput.*, vol. 32, pp. 270–286, 2014.

[13] R. Zhao, W. Ouyang, and X. Wang, "Unsupervised Saliency Learning for Person Re-identification," *2013 IEEE Conf. Comput. Vis. Pattern Recognit.*, pp. 3586–3593, June 2013.

[14] T. Ojala, M. Pietikäinen, T. Maenpää, T. Mäenpää, and T. Maenpää, "Multiresolution gray-scale and rotation invariant texture classification with local binary patterns," *Pattern Anal. Mach. Intell. IEEE Trans.*, vol. 24, no. 7, pp. 971–987, 2002.

[15] D. G. Lowe, "Distinctive image features from scale-invariant keypoints," *Int. J. Comput. Vis.*, vol. 60, pp. 91–110, 2004.

[16] N. Dalal and B. Triggs, "Histograms of Oriented Gradients for Human Detection," *IEEE Comput. Soc. Conf. Comput. Vis. Pattern Recognit.*, vol. 1, pp. 886–893, 2005.

[17] B. Prosser, W.-S. Zheng, S. Gong, and T. Xiang, "Person Re-Identification by Support Vector Ranking," *Proceedings Br. Mach. Vis. Conf. 2010*, vol. 1, pp. 21.1–21.11, 2010.

[18] K. Kumar and Y.-H. Lu, "Cloud Computing for Mobile Users: Can Off-loading Computation Save Energy?," *Computer (Long. Beach. Calif.)*, vol. 43, no. 4, pp. 51–56, 2010.

[19] L. B. Dong Seon Cheng, Marco Cristani, Michele Stoppa and V. Murino, "Custom Pictorial Structures for Re-identification," *Proc. Br. Mach. Vis. Conf.*, pp. 68.1–68.11, 2011.

[20] W. Li and X. Wang, "Locally aligned feature transforms across views," *Proc. IEEE Comput. Soc. Conf. Comput. Vis. Pattern Recognit.*, pp. 3594–3601, 2013.

[21] M. Guillaumin, J. Verbeek, and C. Schmid, "Is that you? Metric learning approaches for face identification," *2009 IEEE 12th Int. Conf. Comput. Vis.*, pp. 498–505, 2009.

[22] P. M. Roth, M. Hirzer, M. Köstinger, C. Beleznaï, and H. Bischof, "Mahalanobis Distance Learning for Person Re-identification," in *Pers. Re-Identification*, pp. 247–267, Springer London, 2014.

[23] R. Zhao, W. Ouyang, and X. Wang, "Person Re-identification by Saliency Matching," *2013 IEEE Int. Conf. Comput. Vis.*, pp. 2528–2535, 2013.

[24] Q. Technologies, "Trepn Profiler Starter Edition User Guide." 2014.

[25] J. R. Beveridge, D. S. Bolme, B. A. Draper, and M. L. Teixeira, "The CSU face identification evaluation system - Its purpose, features, and structure," *Mach. Vis. Appl.*, vol. 16, no. April 2003, pp. 128–138, 2005.

# Extraction of Pulse Repetition Interval Based on Incomplete, Noisy TOA Measurements by the Moving Passive Receiver

Yang Liu\*, Fucheng Guo\*, Min Zhang\* and Wenli Jiang\*

\*College of Electronic Science and Engineering,

National University of Defense Technology, Changsha,410073, Hunan, P.R.China.

Email: ruben052013@126.com

**Abstract**—This paper investigates the problem of extracting the pulse repetition interval (PRI) of stationary pulsed radar emitter from noisy time of arrival(TOA) measurements with missing observations (incomplete) by the moving receiver. The relative motion between the receiver and emitter induces the large estimation bias to estimate PRI, we first discuss the conditions on which identifying the period integer numbers under the circumstance of relative movement, then propose two robust algorithms based on compensating delay of each observations on emitter's status space grids. The proposed algorithms can efficiently reduce the estimation bias introduced by model mismatch without the requirement of specific emitter location information. Simulation studies indicates that the proposed solutions can improve the PRI estimation accuracy.

## I. INTRODUCTION

Pulse repetition interval (PRI) analysis is important for electronic intelligence (ELINT) or electronic support measures (ESM) systems [1]-[2]. Extracting PRI is a typical period estimation problem. In fact, period estimate from the incomplete (some observations are missing),noisy periodic time of arrival(TOA) measurements has been investigated for many years and various estimation algorithms have been developed. Modified Euclidean algorithm (MEA) was proposed in [3]-[4]. The separable least squares line search (SLS2-ALL) was proposed in [5]. Clarkson proposed a lattice line search (LLS) algorithm [6] based on lattice theory. McKilliam developed a maximum likelihood (ML) estimate called the integer lattice line search (ZnLLS) of the PRI in [7]. Recently, several fast algorithms were proposed [8]-[9].

The above works modeled the PRI estimation problem as a periodic point process model and the ML estimate of PRI, which requires that there is no relative movement between the passive receiver and the emitters. However, in some practical applications, receivers are often equipped on moving platforms. Relative movement results in that the TOA measurements does not satisfy the static observation model and mismatch model generates large PRI estimation bias, which is even much larger than the estimation error caused by the TOA measurement noise. As we know, this problem does not attract much attention. Ye analyzed the bias induced by the relative movement and proposed an algorithm that calibrating the observations using the geolocation result in [10]. The conclusion of [10] shows that improved PRI estimation accuracy depends on the high geolocation accuracy which is constrained by many practical factors including the numbers

of receivers, measurement accuracy and geometry between the receivers and emitter. And [10] ignored a problem that identifying period integer numbers requires to satisfy certain conditions when there exists missing observations and relative movement between the receiver and emitter.

In this paper, we propose two robust PRI estimation algorithms. Different from the idea in [10], the delay of each pulse TOA measurement can be compensated using 'hypothesis' emitter locations which are the grid points of the emitter's location space. The grid points near the true emitter location could generate the high accuracy period estimate. The proposed solutions improve the period accuracy without the requirement of geolocation. The moving observation model is introduced in section II. The proposed solutions are presented and the observability conditions of period integer numbers are analyzed in section III. The performance is corroborated by simulation studied in section 4, followed by the conclusions in the last section.

## II. OBSERVATION MODEL

In this section, we discuss period estimation instead of PRI estimation throughout the paper because extracting PRI is a typical period estimation problem.

Considering in a two dimensional plane, a moving receiver  $s$ , whose location at time  $i$  is  $\mathbf{s}_i = [x_i, y_i]^T$ , collects the pulsed transmitted by a stationary source located at  $\mathbf{u} = [x_t, y_t]^T$ , whose period (PRI) is denoted as  $T$ , the receiver measures TOA of each pulse along its trajectory. Some observations are missing. The noise-free TOA measurement at time  $j$  can be formulated as

$$t_j = t_1 + k_j T + \frac{d_j - d_0}{c} + \delta_j, \quad j = 2, 3, \dots, M \quad (1)$$

where,  $t_1$  denotes the TOA measurement of the first received pulse,  $d_j$  is the distance between the source and receiver location at time  $j$  and  $d_j = \|\mathbf{u} - \mathbf{s}_j\|$ ,  $\|\cdot\|$  denotes Euclidean vector norm.  $M$  is the total number of received pulses.  $c$  is the propagation speed of the signal,  $\frac{d_j}{c}$  represents the delay that the  $j$ th pulse transmits from the source to the receiver.  $k_j$  denotes the period integer number between the  $j$ th pulse and the first received pulse and  $k_j$  is discontinuous due to incomplete observations.  $\delta_j$  is the measurement noise which is modeled as a zero-mean Gaussian white noise with the variance  $\sigma_t^2$ .

Note that in (1),  $\mathbf{u}, T, k_j$  are all unknown. If we do not consider missing observations and relative movement,  $k_j$  can be obtained by counting the pulses. However, identifying  $k_j$  requires known period and should satisfy certain conditions under the circumstance of missing observations and relative movement, which will be discussed later. We proceed to finish the formulation. For simplicity, multiply  $c$  on both sides of (1) yields

$$r_{j1} = d_{j1} + N_j R_T + \delta_{rj1}, j = 2, 3 \dots M \quad (2)$$

where  $d_{j1} = d_j - d_1$  and  $R_T$  denotes  $cT$ . All measurements can be written as a vector form

$$\mathbf{r} = \mathbf{r}^o + \mathbf{n}. \quad (3)$$

where  $\mathbf{r}^o$  is noise-free range difference measurements,  $(*)^o$  denotes true value of the variable  $(*)$  and

$$\mathbf{r}^o = \mathbf{d} + \mathbf{N}R_T \quad (4)$$

where  $\mathbf{r} = [r_{21}, r_{31}, \dots, r_{M1}]^T$ ,  $\mathbf{r}^o = [r_{21}^o, r_{31}^o, \dots, r_{M1}^o]^T$ ,  $\mathbf{d} = [d_{21}, d_{31}, \dots, d_{M1}]^T$  and  $\mathbf{N} = [k_2, k_3, \dots, k_M]^T$ ,  $\mathbf{n} = [\delta_{21}, \delta_{31}, \dots, \delta_{M1}]^T$  and the covariance of  $\mathbf{n}$  is  $\mathbf{Q}$  whose diagonal elements are  $2c^2\sigma_t^2$  and others are  $c^2\sigma_t^2$ .

### III. ALGORITHM

In this section, we develop two period estimation algorithms according to different identification methods of period integer numbers, which lead to different observability conditions of period integer numbers. First, the period estimation algorithms are introduced and then different observability conditions of period integer numbers are analyzed.

Both are based on dividing location spaces of the emitter into several grids. *Zn-LLS* algorithm is ML estimate of the period under the condition where there is no relative motion between the receiver and emitter or it will give a biased period estimation result  $\hat{T}_{ini}$ .  $\hat{T}_{ini}$  involves the bias introduced by the receiver movement, if the bias  $c\mathbf{N}(\hat{T}_{ini} - T^o)$  is not compensated, it will become larger as the time increases.

The improved idea is compensating the delay of each TOA observation. For avoiding source localization, we can divide the area in which the emitter may locates into several grids and assume each grid is the source location, the hypothesis source location is used to compensate the delay of the TOA measurements. When the grid is near the true source location, the period estimate becomes more precise and others maybe become worse. Define the cost value as

$$C(\mathbf{p}, T) = (\mathbf{r} - \mathbf{r}^p)^T (\mathbf{r} - \mathbf{r}^p) \quad (5)$$

where  $\mathbf{r}^p$  is the predicted measurement utilizing the source location grid  $\mathbf{p}$ . Our aim is to find the source location and  $T$  to minimize  $C(\mathbf{p}, T)$ .

#### A. Grid-based period estimation with identifying period integer numbers from original TOA measurements

The first algorithm identifies the period integer number  $k_j$  from original TOA measurement sequence  $\{t\}_{i=1}^M$ . Identifying  $k_j$  requires known period but the period is unknown. However, a biased period estimate result, which is denoted as  $\hat{T}$ , can be obtained by MEA algorithm or other period estimators

from original TOA measurement sequence although  $k_j$  is unknown.  $k_j$  can be estimated from incomplete and noisy TOA measurement sequence according to

$$k_j = k_{21} + k_{32} + k_{i(i-1)} \dots k_{j(j-1)}, i = 2, 3 \dots j, j = 2, 3 \dots M \quad (6)$$

where  $k_{i(i-1)} = k_i - k_{i-1}$ ,  $k_{j1}$  implies that identifying  $k_j$  is equivalent to identify each  $k_{i(i-1)}$ , which can be estimated according to adjacent TOA measurements and estimated period by

$$k_{i(i-1)} = \left\lfloor \frac{t_i - t_{i-1}}{\hat{T}} \right\rfloor \quad (7)$$

where  $\lfloor * \rfloor$  denotes the operation of finding the nearest integer. The procedures of the first algorithm are summarized as:

---

#### Algorithm 1 Grid-Based Period Estimation 1

---

Divide the area in which the source located into  $N$  grids

$\{p_i\}_{i=1:N}$ ;

Estimate period  $\hat{T}_i$  from  $\{t_j\}_{j=1:M}$  by Zn-LLS algorithm;

Estimate  $\hat{\mathbf{N}}$  according to (6) and (7);

**for**  $i = 1$  to  $N$  **do**

Compensating the delay of each TOA measurement by  $t_j^c = t_j - (||p_i - s_j|| - ||p_i - s_1||)/c, j = 2, 3, \dots M$ .

Repeatedly estimate period  $\hat{T}_i^c$  from  $\{t_j\}_{j=1:M}^c$ ;

**for**  $k = 1$  to  $M - 1$  **do**

Evaluate  $\mathbf{r}^p(k) = ||\mathbf{p}_i - \mathbf{s}_k|| - ||\mathbf{p}_i - \mathbf{s}_1|| + c\hat{\mathbf{N}}(k)\hat{T}_i^c$ ;

**end for**

Evaluate  $C(\mathbf{p}_i, \hat{T}_i^c)$  according to (5);

**end for**

Finding the grid to minimize  $C$ , the corresponding  $\hat{T}_i^c$  represents the period estimation result.

---

#### B. Grid-based period estimation with identifying period integer numbers from compensated TOA measurements

The second algorithm considers to identify the period integer number  $k_{i(i-1)}$  from compensated TOA measurement sequence  $\{t^c\}_{i=1}^M$ .

$$k_{i(i-1)} = \left\lfloor \left( \frac{t_i^c - t_{i-1}^c}{\hat{T}} \right) \right\rfloor. \quad (8)$$

The procedures of the second algorithm are as follows:

#### C. Observability Conditions Analysis

The different methods of identifying period integer numbers leads to different observability conditions of period integer numbers. In fact, identifying period integer numbers from (7) and (8) is not always correct, it requires to satisfy certain conditions. The conditions on which estimating period integer numbers from (7) and (8) are analyzed respectively. The former case is discussed first. Denote the initial period estimation result by  $\hat{T} = T^o + \Delta T$  where  $\Delta T$  is estimation error. Putting  $\hat{T}$  into (7), mathematically, we have

$$\begin{aligned} \alpha &= \frac{t_i - t_{i-1}}{\hat{T}} \\ &= \frac{k_i T^o + d_{i(i-1)}/c + \delta_{i(i-1)}}{T^o + \Delta T} \\ &= \frac{1}{\left(1 + \frac{\Delta T}{T^o}\right)} \left( \frac{d_{i(i-1)}}{cT^o} + k_j + \frac{\delta_{i(i-1)}}{T^o} \right) \end{aligned} \quad (9)$$

---

**Algorithm 2** Grid-Based Period Estimation 2
 

---

Divide the area in which the source located into  $N$  grids  $\{p_i\}_{i=1:N}$ ;  
**for**  $i = 1$  to  $N$  **do**  
 Compensating the delay of each TOA measurement by  $t_j^c = t_j - (||p_i - s_j|| - ||p_i - s_1||)/c, j = 2, 3, \dots, M$ .  
 Estimate period  $\hat{T}_i^c$  from  $\{t_j\}_{j=1:M}^c$  according to Zn-LLS algorithm;  
 Estimate  $\hat{N}$  from  $\hat{T}_i^c$  according to (6) and (8);  
**for**  $k = 1$  to  $M - 1$  **do**  
 Evaluate  $r^p(k) = ||p_i - s_k|| - ||p_i - s_1|| + c\hat{N}(k)\hat{T}_i^c$ ;  
**end for**  
 Evaluate  $C(p_i, \hat{T}_i^c)$  according to (5);  
**end for**  
 Finding the grid to minimize  $C$ , the corresponding  $\hat{T}_i^c$  represents the period estimation result.

---

where  $\delta_{i(i-1)} = \delta_i - \delta_{i-1}$ ,  $k_{i(i-1)} = \lfloor \alpha \rfloor$  gives the correct estimate of  $k_{i(i-1)}$  under two conditions:

Condition A:  $\Delta T$ , satisfies  $\Delta T/T \ll 1$  and  $\delta_{i(i-1)}/T$  is sufficient small;

Condition B: arbitrary  $d_{i(i-1)} < 0.5cT$ , Denote the maximum range difference among the  $d_{i(i-1)}$  as  $d_{i(i-1)}^{max}$ , condition B means if  $T > d_{i(i-1)}^{max}/2c$ , arbitrary  $d_{i(i-1)} < 0.5cT$  and calculating  $k_j$  from  $\{t_i\}_{i=1}^M$  is unambiguous.

Condition B is often satisfied commonly when the source is in the far field and deviates from the direction of the receiver's trajectory. Condition B indicates that if the observations miss continuously,  $d_{i(i-1)}^{max}$  will become large so that the observability condition of period integer numbers will become worse.

When the above two conditions mentioned above are satisfied,  $N$  is estimated correctly in algorithm 1 Section.III-A.

We proceed to discuss conditions on which estimating period integer numbers from (7) correctly. From (9), the analysis of condition A is also applicable to the second algorithm, we just discuss condition B. Denote the nearest grid point as  $\hat{\mathbf{u}} = \mathbf{u} + \Delta\mathbf{u}$ ,  $\Delta\mathbf{u}$  is the distance between the grid and the true emitter location. We expand the maximum range difference  $d_{i(i-1)}^{max}$  at  $\hat{\mathbf{u}}$  utilizing Taylor-series expansion technique

$$d_{i(i-1)}^{max} \approx d_{i(i-1)}^{max,o} + \underbrace{(\rho_{\hat{\mathbf{u}},s_i} - \rho_{\hat{\mathbf{u}},s_{i-1}})^T}_{\mathbf{H}} \Delta\mathbf{u} \quad (10)$$

where,  $\rho_{\mathbf{a},\mathbf{b}}$  is the unit directional vector from  $\mathbf{a}$  to  $\mathbf{b}$  and  $\rho_{\mathbf{a},\mathbf{b}} = (\mathbf{a} - \mathbf{b})/||\mathbf{a} - \mathbf{b}||$ . Subtract  $d_{i(i-1)}^{max}/cT^o$  from (9), we have

$$\alpha - \frac{d_{i(i-1)}^{max}}{cT^o} = k_j + \underbrace{\frac{\mathbf{H}\Delta\mathbf{u}}{cT^o}}_{\Delta\alpha}. \quad (11)$$

In (11), if  $\Delta\alpha < 0.5$ ,  $\lfloor \alpha - \frac{d_{i(i-1)}^{max}}{cT^o} \rfloor$  gives the correct estimate of  $k_{m,j}$ . Taking expectation of  $\Delta\alpha$ , we have

$$E[\Delta\alpha\Delta\alpha^T] = \frac{\mathbf{H}E[\Delta\mathbf{u}\Delta\mathbf{u}^T]\mathbf{H}^T}{c^2T^{o2}} = \frac{\sigma_{\mathbf{u}}^2}{c^2T^{o2}}\mathbf{H}\mathbf{H}^T \quad (12)$$

where,  $E[*]$  is taking expectation of the random variable  $(*)$  and  $\sigma_{\mathbf{u}}^2$  represents the variance of the grid error. From  $\Delta\alpha < 0.5$  and (9), the observability condition is

$$T^2 > \frac{\sigma_{\mathbf{u}}^2}{4c^2}\mathbf{H}\mathbf{H}^T. \quad (13)$$

(13) indicates that the closer to the true emitter location the grid is, the better the observability condition of  $N$  is.

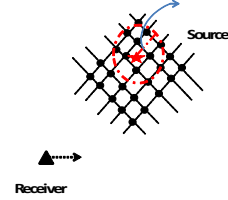


Fig. 1. Illustration of observation condition B in algorithm 2

In fact, as can be seen in Fig.1, there always exists the grids near the true emitter location if the resolution of the grid is sufficient fine, it means the observability condition of period integer numbers in the second algorithm is always satisfied theoretically.

#### IV. SIMULATION RESULTS AND ANALYSIS

In this section, simulation studies are performed to validate the performance of the proposed two algorithms. Simulation scenario is configured as follows: Consider the receiver locates at  $s_1 = [0, 0]^T$  at the start time, and moves along the x-axis with a constant velocity  $v = 300$  m/s and measure the TOA of each pulse transmitted by a stationary source located at  $u = [3, 10]^T$  km. The source transmitting a sequence of periodic pulses, whose PRI is 50 millisecond(ms). Two simulation studies are performed. One compared the performances of the proposed solutions and the biased period estimators when the total observation time  $T_a$  is set to be 30s and 60s, another compares the the performances of these algorithms when the  $T_a = 30s$ ,  $\delta_t = 30ns$  and the speed of the receiver varies from 50m/s to 350m/s. We assume some pulses will be lost randomly with 80 percent lost rate. Both x-axis and y-axis range of the interested area are 1 ~ 30 km, Because the area is large, practically two level grids are used. the resolution of the first level is 3km. In the second level, the area reduces to  $3 \times 3$  km around the source location estimate of the first level and the resolution is set to be 100m. The number of Monte Carlo test is 500 times and the root mean square error(RMSE) is compared with the biased estimation result. RMSE is calculated according to

$$\text{RMSE}(T) = \sqrt{\frac{1}{M} \sum_{i=1}^M ||\hat{T}_i - T^o||^2}. \quad (14)$$

As shown in Fig.2, it is obvious that receiver movement leads to large bias of the PRI estimate. The RMSE curve of biased PRI estimator varies slowly as the TOA measurement noise increases because the bias caused by the receiver dominates and is larger than the estimation error caused by TOA measurement noise, which is identical to the conclusion in

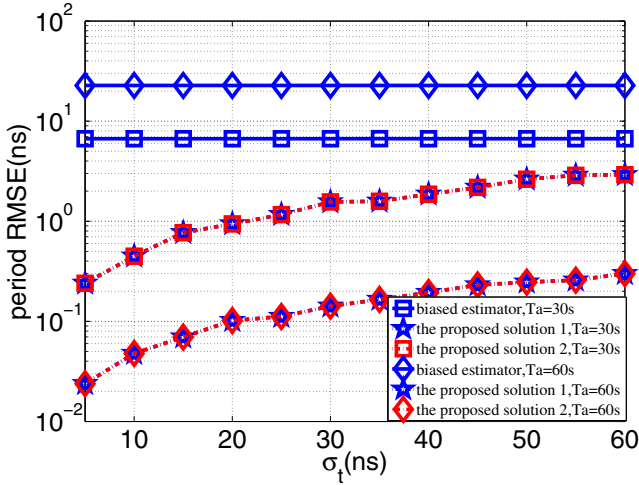


Fig. 2. Period estimation error comparisons when the observation time  $T_a$  equals 30s and 60s

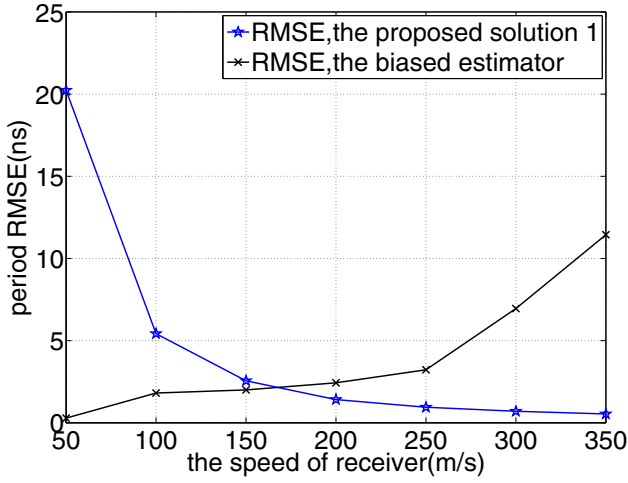


Fig. 3. Period estimation error comparisons when the speed of the receiver varies from 50 to 350 m/s

[10]. Moreover, the comparisons of the period estimation error when the observation time is 30s and 60s indicate that the bias caused by receiver movement accumulates as the observation time increases. Inversely, both the two proposed solutions can effectively reduce the bias and improve the period estimate accuracy. And the PRI estimation accuracy of the two proposed solutions becomes better as the observation time increases.

Fig.3 compares the period estimation performances of biased period estimator and the proposed solution 1 when the speed of the receiver varies from 50m/s to 350m/s. As the speed of receiver becomes larger, the bias caused by the relative motion will become larger. But when the speed is smaller than about 170m/s, the performance of the biased estimator is better than the proposed solutions. From Fig.2 and Fig.3, whether the bias caused by the relative movement can be ignored depends on the speed of the receiver and the collecting time.

It is necessary to point out the two proposed solutions

give the same performance because their kernel procedures are the same and the difference is just the observability conditions of the period integer numbers. In the above scenario, condition A is satisfied, we calculate the condition B of two algorithms according to Section III-C. For algorithm 1, if the  $PRI > O(10^{-5})$  s, the period integer numbers can be identified correctly. For algorithm 2, we assume the  $\Delta u$  equals the resolution of grids 100 m, if the  $PRI > O(10^{-7})$  s, the period integer numbers can be identified correctly. The better the grid resolution is, the better the observation condition is. For small PRI, the second algorithm is a better choice.

In this paper, we just consider the case of the missing pulses and a single emitter. If the pulses of multiple emitters are mixed, the TOA measurements should be separated (deinterleaved) using the PRI pattern [11] or other approaches first. The more complex cases such as multipath or joint source localization and period estimation will be examined in the further work.

## V. CONCLUSION

In this paper, we develop two algorithms to extract PRI from a incomplete, noisy timing data when there exists relative movement between the receiver and emitter. Simulation study indicates that the proposed solutions effectively reduce the bias of the period estimators due to the receiver movement. The advantage of the proposed solutions is that there is no requirement to source localization although the two algorithms increase the computational complexity.

## REFERENCES

- [1] P. J. Ware and J. B. Mcdowall, "The application of pulse analyzers in passive sensor systems," in *Proc. IEEE 28th European Microwave Conference*, pp. 560–565, 1998.
- [2] "New trends in esm/elint airborne sensors," in *Proc. IEEE 28th European Microwave Conference*, pp. 552–559, 1998.
- [3] S.D.Casey and B.M.Sadler, "Modifications of the euclidean algorithm for isolating periodicities from a sparse set of noisy measurements," *IEEE Trans. Signal Process.*, vol. 44, no. 9, pp. 2260–2272, Sep. 1996.
- [4] B. Sadler and S. Casey, "On periodic pulse interval analysis with outliers and missing observations," *IEEE Trans. Signal Process.*, vol. 46, no. 11, pp. 2990–3002, Nov. 1998.
- [5] N. D. Sidiropoulos, A. Swami, and B. M. Sadler, "Quasi-ml period estimation from incomplete timing data," *IEEE Trans. Signal Process.*, vol. 53, no. 2, pp. 733–739, Feb. 2005.
- [6] I. V. L. Clarkson, "Approximate maximum-likelihood period estimation from sparse, noisy timing data," *IEEE Trans. Signal Process.*, vol. 56, no. 5, pp. 1779–1787, May 2008.
- [7] R. G. McKilliam and I. V. L. Clarkson, "Maximum-likelihood period estimation from sparse, noisy timing data," in *Proc. Int. Conf. Acoust. Spe. Signal Process.*, pp. 3697–3700, Mar. 2008.
- [8] H. Ye, Z. Liu, and W. Jiang, "Fast approximate maximum likelihood period estimation from incomplete timing data," *Chin. J. Aeronautics*, vol. 26, no. 2, pp. 435–441, Aug. 2013.
- [9] R. G. McKilliam, I. V. L. Clarkson, and B.G.Quinn, "Fast sparse period estimation," *IEEE Signal Processing Letter*, vol. 22, no. 1, pp. 62–66, Jan. 2015.
- [10] H.Ye, Z.Liu, and W.Jiang, "Pulse repetition interval estimation in moving passive sensors based on observation calibration," *Progr. Electromagn. Res.C*, vol. 28, pp. 257–270, 2012.
- [11] Y. Chan and J. Towers, "New techniques for the deinterleaving of repetitive sequences," *Radar and Signal Processing, IEE Proceedings F*, vol. 28, no. 4, pp. 183–198, Oct. 1992.

# Removing Speckle Noise by Analysis Dictionary Learning

Jing Dong, Wenwu Wang  
Centre for Vision, Speech and Signal Processing  
University of Surrey, Guildford GU 7XH  
United Kingdom  
Email: {j.dong, w.wang}@surrey.ac.uk

Jonathon Chambers  
School of Electrical and Electronic Engineering  
Newcastle University, Newcastle upon Tyne NE1 7RU  
United Kingdom  
Email: Jonathon.Chambers@newcastle.ac.uk

**Abstract**—Speckle noise inherently exists in images acquired by coherent systems, for example, synthetic aperture radar (SAR) and sonar images. Removal of speckle noise is a challenging problem because the noise multiplies (rather than adds to) the original image and it does not follow a Gaussian distribution. In this paper, we focus on the speckle noise removal problem and propose a method using analysis dictionary learning. In our proposed method, the image recovery is addressed in the logarithmic transform domain, thereby converting the multiplicative model to an additive model. Our formulation consists of a data fidelity term derived from the distribution of the speckle noise and a regularization term using the learned analysis dictionary. Experimental results on synthetic speckled images and real SAR images demonstrate the promising performance of the proposed method.

## I. INTRODUCTION

Speckle noise arises in many images, such as synthetic aperture radar (SAR) and sonar (SAS) images, due to the coherent nature of their acquisition processes. Removing speckle noise is different from the traditional image denoising problem of removing additive Gaussian noise for two reasons. First, speckle noise is multiplicative noise which multiplies (rather than adds to) the original image. Besides, the widely used Gaussian distribution in image denoising is not suitable to describe the statistical properties of speckle noise; the Gamma distribution is one of the most commonly used models for the description of speckle noise [1], [2], [3].

Many methods proposed to remove speckle noise formulate this task as an optimization problem consisting of a data fidelity term and regularization terms. The method of Aubert-Aujol (AA) [4] uses the classical maximum *a posteriori* (MAP) estimate, leading to a data fidelity term and a total variation (TV) regularization term which is applied to the image in the original domain. However, this model is not convex, which raises difficulties from an optimization point of view. In [5], Shi and Osher (SO) eliminate this non-convex issue by applying the TV of the image in the log-domain as the regularization. The multiplicative image denoising by augmented Lagrangian (MIDAL) algorithm [2] addresses the same formulation of SO using a different optimization method, showing advantages in terms of speed and denoising performance. Duran, Fadili and Nikolova (DFN) [1] apply the shrinkage of the curvelet transform coefficients and the TV in the log-domain as the regularization terms. Recently,

dictionary learning techniques in sparse representation have also been used to address the speckle noise removal problem. The method proposed in [3] introduces a regularization term using a dictionary learned based on the synthesis model and obtains better denoising results as compared with some existing methods.

In recent years, the analysis model for sparse representation, as a counterpart of the synthesis model, has drawn much attention [6], [7]. For a signal  $\mathbf{y} \in \mathbb{R}^m$ , this model assumes that the product of  $\mathbf{\Omega} \in \mathbb{R}^{p \times m}$  and  $\mathbf{y}$  is sparse, i.e.  $\mathbf{x} = \mathbf{\Omega}\mathbf{y}$  with  $\|\mathbf{x}\|_0 = p - l$ , where the  $\ell_0$ -norm  $\|\cdot\|_0$  counts the number of non-zero elements of its argument and  $0 \leq l \leq p$  is the co-sparsity of  $\mathbf{y}$ . The matrix  $\mathbf{\Omega}$  is usually referred to as an analysis dictionary [8], with each row of  $\mathbf{\Omega}$  being an atom. The vector  $\mathbf{x} \in \mathbb{R}^p$  is the analysis representation of the signal  $\mathbf{y}$  with respect to  $\mathbf{\Omega}$ . In this model, the analysis dictionary  $\mathbf{\Omega}$  plays an important role in the analysis representation of the signal  $\mathbf{y}$ , and the dictionaries learned from a set of training signals show some advantages compared with pre-defined dictionaries [8]. Some algorithms for learning an analysis dictionary have been proposed [8], [9], [10]. The learned analysis dictionaries have been shown to be useful in denoising additive Gaussian noise, but their employment to removing speckle noise has not been investigated yet.

In this work, we propose a new method for removing speckle noise using analysis dictionary learning. The remainder of the paper is as follows. In Section II, the speckle noise removal task is formulated as a regularized convex optimization problem. Section III introduces our proposed method. The experimental results with synthetic speckled images and real SAR images are presented in Section IV, and Section V concludes the paper.

## II. PROBLEM FORMULATION

Mathematically, the observed image  $\mathbf{w} \in \mathbb{R}^N$ , contaminated by speckle noise  $\mathbf{u} \in \mathbb{R}^N$ , can be represented as [2], [3]

$$\mathbf{w} = \mathbf{g} \circ \mathbf{u} \quad (1)$$

where  $\mathbf{g} \in \mathbb{R}^N$  denotes the image to be restored. The symbol  $\circ$  calculates the Hadamard product (i.e. entry-wise product) of two matrices/vectors. Each entry of  $\mathbf{u}$  is assumed to be a random variable following the Gamma distribution whose

probability density function is [2], [3], [1]

$$f_u(u) = \frac{L^L}{\Gamma(L)} u^{L-1} e^{-Lu} \quad (2)$$

where  $L$  is a positive integer reflecting noise level and  $\Gamma(\cdot)$  is the classical Gamma function defined by  $\Gamma(L) = (L-1)!$ . A smaller  $L$  indicates stronger noise.

An additive noise model is obtained by taking the (element-wise) logarithm of both sides of (1), that is

$$\underbrace{\log \mathbf{w}}_{\mathbf{z}} = \underbrace{\log \mathbf{g}}_{\mathbf{y}} + \underbrace{\log \mathbf{u}}_{\mathbf{v}}. \quad (3)$$

The probability distribution of each entry of  $\mathbf{v}$  is given by

$$\begin{aligned} f_v(v) &= f_u(e^v) \cdot e^v \\ &= \frac{L^L}{\Gamma(L)} e^{L(v-e^v)}. \end{aligned} \quad (4)$$

Under the independent and identically distributed (i.i.d.) assumption of the entries of  $\mathbf{v}$ , the probability density of  $\mathbf{v}$  is given by

$$f_{\mathbf{v}}(\mathbf{v}) = \prod_{i=1}^N \frac{L^L}{\Gamma(L)} e^{L(v_i - e^{v_i})} \quad (5)$$

where  $v_i$  denote the entries of the vector  $\mathbf{v}$  with  $i = 1, 2, \dots, N$ . Thus, the maximum log-likelihood (ML) estimation of  $\mathbf{y}$  is given by the optimal point of the following problem [2]

$$\hat{\mathbf{y}} = \arg \min_{\mathbf{y}} \sum_{i=1}^N (y_i + e^{z_i - y_i}), \quad (6)$$

which is employed as the data fidelity term in our formulation.

We assume log-image  $\mathbf{y}$  to be sparse with respect to an analysis dictionary. Since adaptive analysis dictionaries usually have the potential to fit signals better than pre-defined dictionaries [8] as mentioned in Section I, the analysis dictionary learning technique is applied in our proposed method. The details for dictionary learning will be presented in Section III-A. For now, suppose a dictionary  $\Omega \in \mathbb{R}^{p \times m}$  has been learned with log-image patches. In order to apply  $\Omega$  to the restored log-image  $\mathbf{y}$ , the image patches of the same size are extracted from  $\mathbf{y}$  and concatenated as the columns of a matrix  $\mathbf{Y} \in \mathbb{R}^{m \times n}$ , where  $n$  denotes the number of patches. Thus, the co-sparsity of  $\mathbf{y}$  can be measured by  $\|\Omega \mathbf{Y}\|_0$ . Using  $\|\Omega \mathbf{Y}\|_0$  as the regularization term, the speckle noise removal problem is formulated as

$$\mathbf{Y}^* = \arg \min_{\mathbf{Y}} \sum_{i=1}^m \sum_{j=1}^n (\mathbf{Y}_{i,j} + e^{\mathbf{Z}_{i,j} - \mathbf{Y}_{i,j}}) + \lambda \|\Omega \mathbf{Y}\|_0 \quad (7)$$

where  $\lambda$  is the Lagrangian multiplier. The subscript  $i, j$  denote the element locating in the  $i$ th row and  $j$ th column of a matrix. Notice that the matrix  $\mathbf{Z} \in \mathbb{R}^{m \times n}$  is obtained with the observed log-image  $\mathbf{z}$  by the same approach as generating  $\mathbf{Y}$  from  $\mathbf{y}$ . This formulation (7) combines the data fidelity term obtained via the ML estimation, based on the Gamma distribution, with the regularization term based on the learned dictionary  $\Omega$ . However, it is non-convex due to the combinatorial nature of the  $\ell_0$ -norm, which brings about difficulties

for optimization. The  $\ell_0$ -norm is thus relaxed as the  $\ell_1$ -norm to construct a convex approximation of (7), that is

$$\mathbf{Y}^* = \arg \min_{\mathbf{Y}} \sum_{i=1}^m \sum_{j=1}^n (\mathbf{Y}_{i,j} + e^{\mathbf{Z}_{i,j} - \mathbf{Y}_{i,j}}) + \lambda \|\Omega \mathbf{Y}\|_1. \quad (8)$$

This is the formulation of our approach to removing speckle noise based on a learned analysis dictionary.

### III. PROPOSED METHOD

In general, our proposed method consists of two stages: analysis dictionary learning and image recovery. In the first stage, an analysis dictionary is learned with some image data in the log-domain. The goal of the image recovery stage is to obtain the restored image by solving the optimization problem (8). Our proposed method is referred to as removing speckle noise by analysis dictionary learning (RSN-ADL).

#### A. Analysis Dictionary Learning Stage

Given a set of training data  $\mathbf{A}$ , the analysis dictionary learning problem can be written as [11]

$$\begin{aligned} \{\Omega^*, \mathbf{X}^*\} &= \arg \min_{\{\Omega, \mathbf{X}\}} \|\mathbf{X} - \Omega \mathbf{A}\|_F^2 \\ \text{s.t. } &\|\mathbf{X}_{:,i}\|_0 = p - l, \forall i, \end{aligned} \quad (9)$$

where  $\mathbf{X}_{:,i}$  represents the  $i$ th column of  $\mathbf{X} \in \mathbb{R}^{p \times n}$ . This is a general formulation without any additional constraint on  $\Omega$  apart from the co-sparsity constraints  $\|\mathbf{X}_{:,i}\|_0 = p - l, \forall i$ . However, this formulation has ambiguities caused by scaling [10]. In order to avoid these ambiguities, unit  $\ell_2$ -norm constraints on the rows of  $\Omega$  are applied, leading to the following formulation of the Analysis SimCO algorithm [10]

$$\begin{aligned} \{\Omega^*, \mathbf{X}^*\} &= \arg \min_{\{\Omega, \mathbf{X}\}} \|\mathbf{X} - \Omega \mathbf{A}\|_F^2 \\ \text{s.t. } &\|\mathbf{X}_{:,i}\|_0 = p - l, \forall i \\ &\|\Omega_{j,:}\|_2 = 1, \forall j, \end{aligned} \quad (10)$$

where  $\Omega_{j,:}$  denotes the  $j$ th row of  $\Omega$ . The Analysis SimCO algorithm alternates between two stages: analysis sparse coding and dictionary update, as summarized in Algorithm 1.

---

#### Algorithm 1 Analysis SimCO

---

**Input:**  $\mathbf{A}, p, l$

**Output:**  $\Omega^*$

**Initialization:**

Initialize the iteration counter  $t = 1$  and the analysis dictionary  $\Omega^{(t)}$ . Perform the following steps.

**Main Iterations:**

- 1) Analysis sparse coding: Compute the representations  $\mathbf{X}^{(t)}$  with the fixed dictionary  $\Omega^{(t)}$  and the training signals in  $\mathbf{A}$ , based on equations (11) and (12).
  - 2) Dictionary update: Update the dictionary  $\Omega^{(t+1)} \leftarrow \Omega^{(t)}$ , based on equations (14), (15) and (16).
  - 3) If the stopping criterion is satisfied,  $\Omega^* = \Omega^{(t+1)}$ , quit the iteration. Otherwise, increase the iteration counter  $t = t + 1$  and go back to step 1).
-

The purpose of the analysis sparse coding stage is to get the sparse representations  $\mathbf{X}$  of the training signals in  $\mathbf{A}$  based on a given dictionary  $\mathbf{\Omega}$ . The exact representations  $\mathbf{X}$  can be calculated directly by simply multiplying the signals in  $\mathbf{A}$  by the dictionary  $\mathbf{\Omega}$ , that is

$$\mathbf{X} = \mathbf{\Omega}\mathbf{A}. \quad (11)$$

Since the initial dictionary is an arbitrary one, the representations obtained in this way may not satisfy the co-sparsity constraints in (10). A hard thresholding operation is therefore applied to enforce the co-sparsity

$$\hat{\mathbf{X}} = HT_l(\mathbf{X}), \quad (12)$$

where  $HT_l(\mathbf{X})$  is the non-linear operator that sets the smallest  $l$  elements (in magnitude) of each column of  $\mathbf{X}$  to zeros. In doing so, the co-sparsity constraints can be enforced.

In the dictionary update stage,  $\mathbf{\Omega}$  is updated assuming known and fixed  $\mathbf{X}$ . In other words, this stage aims at optimizing the following problem

$$\arg \min_{\mathbf{\Omega}} \|\mathbf{X} - \mathbf{\Omega}\mathbf{A}\|_F^2 \quad \text{s.t.} \quad \|\mathbf{\Omega}_{j,:}\|_2 = 1, \quad \forall j. \quad (13)$$

Since the Stiefel manifold  $\mathcal{S}_{m,1}$  is defined as  $\mathcal{S}_{m,1} = \{\mathbf{s} \in \mathbb{R}^m : \mathbf{s}^T \mathbf{s} = 1\}$  [12], the transpose of each row in  $\mathbf{\Omega}$  can be seen as one element in  $\mathcal{S}_{m,1}$ . Thus, the ‘‘line’’ search methods on manifolds can be utilized to deal with problem (13). Here we use the gradient descent line search method on manifolds.

Given that the negative gradient of the objective function (13) with respect to  $\mathbf{\Omega}$  is

$$\mathbf{H} = -\frac{\partial \|\mathbf{X} - \mathbf{\Omega}\mathbf{A}\|_F^2}{\partial \mathbf{\Omega}} = 2\mathbf{X}\mathbf{A}^T - 2\mathbf{\Omega}\mathbf{A}\mathbf{A}^T, \quad (14)$$

the search direction of the  $j$ th row of  $\mathbf{\Omega}$ , i.e. the projection of each row of  $\mathbf{H}$  onto the tangent space of  $\mathcal{S}_{m,1}$ , is [12, pp. 49]

$$\bar{\mathbf{h}}_j = \mathbf{H}_{j,:}(\mathbf{I} - \mathbf{\Omega}_{j,:}^T \mathbf{\Omega}_{j,:}). \quad (15)$$

The line search path for the  $j$ th row of  $\mathbf{\Omega}$  can be written as

$$\mathbf{\Omega}_{j,:}(\alpha) = \begin{cases} \mathbf{\Omega}_{j,:} & \text{if } \|\bar{\mathbf{h}}_j\|_2 = 0, \\ \mathbf{\Omega}_{j,:} \cos(\alpha \|\bar{\mathbf{h}}_j\|_2) + (\bar{\mathbf{h}}_j / \|\bar{\mathbf{h}}_j\|_2) \sin(\alpha \|\bar{\mathbf{h}}_j\|_2) & \text{otherwise,} \end{cases} \quad (16)$$

where  $\alpha$  is the step size. The golden section search method [13] is applied to find a proper step size  $\alpha$ .

### B. Image Recovery Stage

The aim of the image recovery stage is to remove the speckle noise by addressing the optimization problem (8). This is an  $\ell_1$  regularized problem, which can be tackled with the alternating direction method of multipliers (ADMM) [14]. In ADMM form, (8) can be written as the following equality-constrained convex optimization problem

$$\arg \min_{\mathbf{Y}, \mathbf{T}} \sum_{i=1}^m \sum_{j=1}^n (\mathbf{Y}_{i,j} + e^{\mathbf{Z}_{i,j} - \mathbf{Y}_{i,j}}) + \lambda \|\mathbf{T}\|_1 \quad (17)$$

s.t.  $\mathbf{T} = \mathbf{\Omega}\mathbf{Y}$ ,

where  $\mathbf{T} = \mathbf{\Omega}\mathbf{Y}$ . The introduction of the variables in  $\mathbf{T}$  is to eliminate the optimization variables in  $\mathbf{Y}$  appearing in the  $\ell_1$  regularization term of (8) and thus make the alternating update of variables possible.

The augmented Lagrangian method is applied to convert (17) to an unconstrained problem. In particular, using a dual parameter  $\mathbf{B} \in \mathbb{R}^{p \times n}$ , the augmented Lagrangian function for (17) is developed by adding a penalty term  $\langle \mathbf{B}, \mathbf{\Omega}\mathbf{Y} - \mathbf{T} \rangle$  and an extra quadratic term related to the constraint  $\mathbf{T} = \mathbf{\Omega}\mathbf{Y}$ , leading to the new objective function as follows

$$\begin{aligned} L_\gamma(\mathbf{Y}, \mathbf{T}, \mathbf{B}) &= \sum_{i=1}^m \sum_{j=1}^n (\mathbf{Y}_{i,j} + e^{\mathbf{Z}_{i,j} - \mathbf{Y}_{i,j}}) + \lambda \|\mathbf{T}\|_1 \\ &\quad + \gamma \langle \mathbf{B}, \mathbf{\Omega}\mathbf{Y} - \mathbf{T} \rangle + \frac{\gamma}{2} \|\mathbf{\Omega}\mathbf{Y} - \mathbf{T}\|_F^2 \\ &= \sum_{i=1}^m \sum_{j=1}^n (\mathbf{Y}_{i,j} + e^{\mathbf{Z}_{i,j} - \mathbf{Y}_{i,j}}) + \lambda \|\mathbf{T}\|_1 \\ &\quad + \frac{\gamma}{2} \|\mathbf{B} + \mathbf{\Omega}\mathbf{Y} - \mathbf{T}\|_F^2 - \frac{\gamma}{2} \|\mathbf{B}\|_F^2, \end{aligned} \quad (18)$$

with  $\gamma > 0$  being the penalty coefficient. The ADMM algorithm iteratively updates each of the variables  $\{\mathbf{Y}, \mathbf{T}, \mathbf{B}\}$ , while keeping the rest fixed. In the  $t$ -th iteration, it consists of the following steps

$$\mathbf{Y}^{(t+1)} = \arg \min_{\mathbf{Y}} L_\gamma(\mathbf{Y}, \mathbf{T}^{(t)}, \mathbf{B}^{(t)}) \quad (19)$$

$$\mathbf{T}^{(t+1)} = \arg \min_{\mathbf{T}} L_\gamma(\mathbf{Y}^{(t+1)}, \mathbf{T}, \mathbf{B}^{(t)}) \quad (20)$$

$$\mathbf{B}^{(t+1)} = \mathbf{B}^{(t)} + (\mathbf{\Omega}\mathbf{Y}^{(t+1)} - \mathbf{T}^{(t+1)}). \quad (21)$$

In fact, herein ADMM can be interpreted as reducing the  $\ell_1$  regularized problem to solving a sequence of  $\ell_2$  (squared) regularized problems [14]. For the minimization of (19), the gradient descent method using a fixed step size is applied. For (20), there is the closed-form solution [14]

$$\mathbf{T}^{(t+1)} = ST_{\frac{\lambda}{\gamma}}\{\mathbf{\Omega}\mathbf{Y}^{(t+1)} + \mathbf{B}^{(t)}\}, \quad (22)$$

where  $ST_{\frac{\lambda}{\gamma}}$  is the entry-wise soft-thresholding operator defined by

$$ST_{\frac{\lambda}{\gamma}}(\beta) = \begin{cases} \beta - \frac{\lambda}{\gamma} \cdot \text{sgn}(\beta) & \text{if } |\beta| \geq \frac{\lambda}{\gamma}, \\ 0 & \text{otherwise} \end{cases} \quad (23)$$

where  $\text{sgn}(\beta)$  returns the sign of  $\beta$ .

The ADMM iterations (19), (20) and (21) are performed until the change of  $\mathbf{Y}^{(t+1)}$  is relatively small compared with  $\mathbf{Y}^{(t)}$ . The restored log-image  $\hat{\mathbf{y}}$  can be obtained by reshaping the solution to (17), and thus the denoised image  $\hat{\mathbf{g}}$  is obtained by taking the exponential transform of  $\hat{\mathbf{y}}$ .

## IV. SIMULATION RESULTS

In this section, experiments for synthetic speckled images and real SAR images are presented respectively.

For our proposed RSN-ADL algorithm, the images shown in Fig. 1 were used as the training corpus. Specifically, the training samples employed to learn the analysis dictionary  $\mathbf{\Omega}$

were the logarithmic transforms of 20000 patches that were extracted randomly from these corpus images. The size of the training patches was  $8 \times 8$ . The dictionary was initialized as the finite difference operator [6], [8]. The co-sparsity for dictionary learning was set as  $l = 100$ . The Analysis SimCO algorithm was performed with 2000 iterations.



Fig. 1. Training images used for learning the analysis dictionary.

### A. Experiments with Synthetic Speckled Images

We used 3 test images: “Cameraman”, “Nîmes” and “Fields”, as presented in Fig. 2. These images are commonly used for evaluating the algorithms for removing speckle noise. The size of the Cameraman image is  $256 \times 256$ . The size of Nîmes and Fields is  $512 \times 512$ . The synthetic speckled images were generated by multiplying the pixels of the original images by i.i.d. Gamma random variables (c.f. equations (1) and (2)), with different noise levels  $L \in \{10, 4, 1\}$ .



Fig. 2. Test images: Cameraman, Nîmes, Fields.

Our proposed method is compared with three recent algorithms: DFN [1] (which outperforms AA [4] and SO [5]), MIDAL [2], and the method proposed in [3]<sup>1</sup>. For description convenience, the method proposed in [3] is referred to as multiplicative noise removal via dictionary learning (MNR-DL) due to the dictionary learning technique involved in the method.

The denoising results are assessed using the peak signal to noise ratio (PSNR), as in [1] and [3]. For a clean image  $\mathbf{g} \in \mathbb{R}^N$ , the PSNR of its denoised version  $\hat{\mathbf{g}} \in \mathbb{R}^N$  is defined as

$$\text{PSNR} = 10 \log_{10} \frac{N |\max(\mathbf{g}) - \min(\mathbf{g})|^2}{\|\hat{\mathbf{g}} - \mathbf{g}\|_2^2} \quad (\text{in dB}) \quad (24)$$

where  $\max(\cdot)$  and  $\min(\cdot)$  return the maximum value and the minimum value of their operands respectively.

The denoising results are presented in Table I, with bold fonts highlighting the best result in each case. In this table, the results of DFN are obtained from the original paper [1]. The results of MNR-DL for Cameraman and Nîmes with noise levels  $L = 10$  and  $L = 4$  are also from the original paper [3].

<sup>1</sup>The codes of DFN and MIDAL were downloaded from {<https://fadili.users.greyc.fr/software.html>} and {<http://www.lx.it.pt/~bioucas/publications.html>} respectively. We thank the authors of [3] for sharing their code via email.

For the results of MNR-DL in other cases, different parameters (i.e.  $\lambda$  in the objective function of MNR-DL [3]) were tested and the best results are reported here. Similarly, the Lagrangian multiplier  $\lambda$  in our model was also tuned by searching roughly to get the highest PSNR. The parameters of MNR-DL and our proposed method are summarized in Table II. For the MIDAL algorithm, its parameters were set at their default values as in [2]. Fig. 3 shows the denoised versions of the Nîmes image with the noise level  $L = 1$ .

TABLE I  
THE DENOISING PSNR RESULTS IN DECIBELS.

L	Algorithm	Cameraman	Nîmes	Fields
10	DFN	26.08	27.80	28.04
	MIDAL	25.40	27.93	27.84
	MNR-DL	<b>27.32</b>	<b>28.85</b>	28.48
	RSN-ADL	25.39	28.25	<b>28.83</b>
4	DFN	22.98	25.84	26.32
	MIDAL	23.42	25.74	26.14
	MNR-DL	<b>24.91</b>	<b>26.34</b>	26.92
	RSN-ADL	23.47	26.16	<b>27.15</b>
1	DFN	19.82	22.64	22.89
	MIDAL	<b>20.81</b>	23.03	23.38
	MNR-DL	19.42	22.95	22.20
	RSN-ADL	20.55	<b>23.67</b>	<b>24.05</b>

From Table I, we can see that our proposed method outperforms the baseline algorithms for the Fields image, in all noise level cases. When  $L = 1$ , the performance of our algorithm is also the best for the Nîmes image, while MIDAL achieves the best PSNR for Cameraman. In the  $L = 4$  cases of the images Cameraman and Nîmes, the denoising results of our method are not as good as that of MNR-DL, but better than the results obtained by DFN and MIDAL.

TABLE II  
THE PARAMETERS USED IN THE COMPARISON OF TABLE I.

L	Algorithm	Cameraman	Nîmes	Fields
10	RSN-ADL	0.4	0.3	0.5
	MNR-DL	—	—	3.6
4	RSN-ADL	0.7	0.5	1
	MNR-DL	—	—	0.6
1	RSN-ADL	1.6	1.5	3.5
	MNR-DL	1	3.1	0.01

### B. Experiments with Real SAR Images

For this set of experiments, we test our proposed method with some real SAR images<sup>2</sup> as shown in the left column of Fig. 4. The Lagrangian multiplier  $\lambda$  was set as 0.5 for all the SAR images. The denoised images are presented in the right column of Fig. 4. We can see that our proposed method is able to remove speckle noise from the SAR images while keeping

<sup>2</sup>The test SAR images were downloaded from {<https://github.com/zhangyiwei79/Opticks-SAR/tree/master/SAR%20images>}

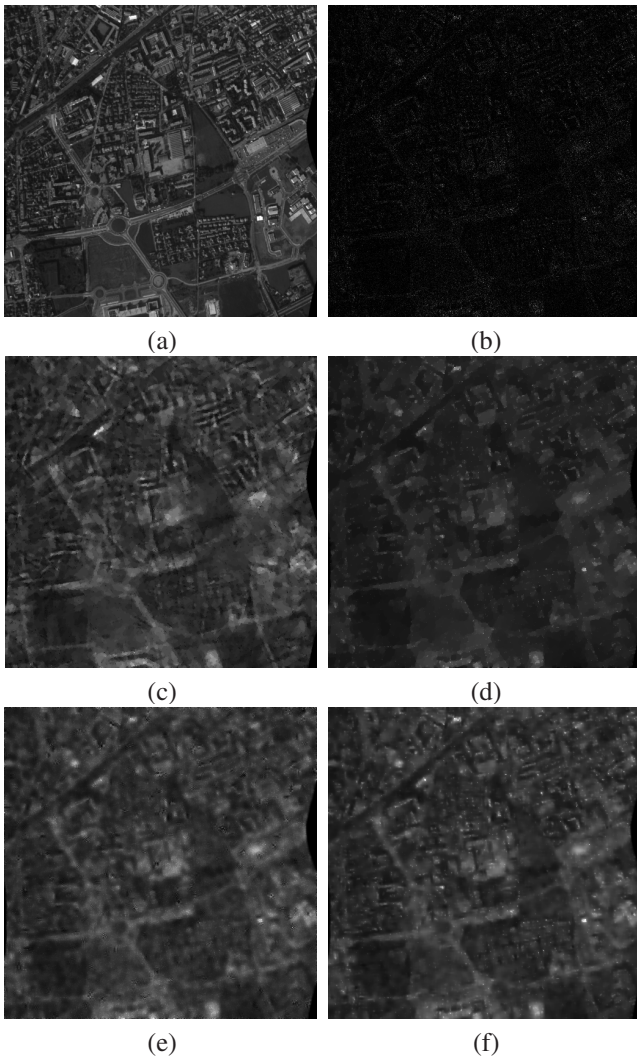


Fig. 3. Results for the Nîmes image (noise level:  $L=1$ ). (a) Original. (b) Noisy. (c) DFN (22.98 dB). (d) MIDAL (23.03 dB). (e) MNR-DL (22.95 dB). (f) RSN-ADL (23.67 dB).

their geometric structures, leading to the denoised images with better visual quality.

## V. CONCLUSION

We have proposed a method for removing speckle noise via analysis dictionary learning. This method addresses the denoising problem in the log-domain, leading to a convex formulation. An analysis dictionary is learned from the logarithmic transforms of some image patches and then this dictionary is employed in a regularization term for restoring the image in the log-domain. The optimization is addressed with ADMM. Simulation results with synthetic images and real SAR images demonstrate the encouraging performance of our proposed method.

## ACKNOWLEDGMENT

This work was supported by the Engineering and Physical Sciences Research Council (EPSRC) Grant number EP/K014307/1 and the MOD University Defence Research Collaboration in Signal Processing.

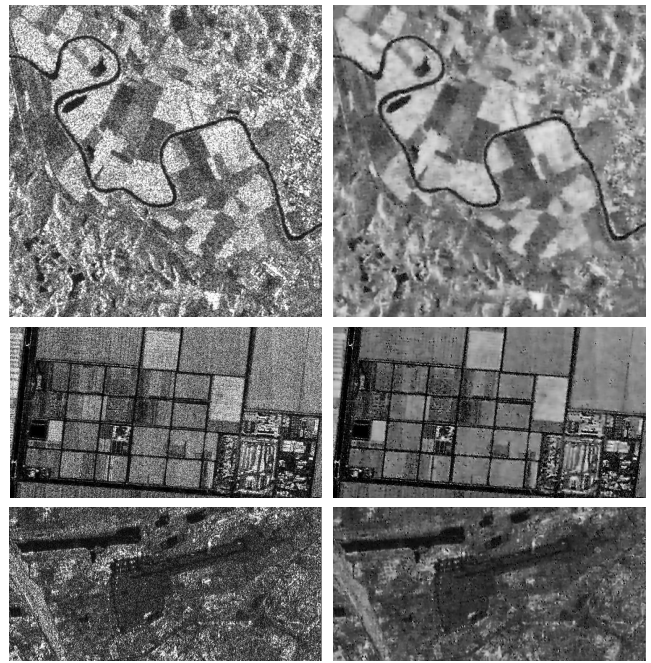


Fig. 4. Original images (left column) and denoised images (right column) obtained by RSN-ADL.

## REFERENCES

- [1] S. Durand, J. Fadili, and M. Nikolova, "Multiplicative noise removal using 11 fidelity on frame coefficients," *J. Math. Imaging Vis.*, vol. 36, no. 3, pp. 201–226, 2010.
- [2] J. M. Bioucas-Dias and M. A. Figueiredo, "Multiplicative noise removal using variable splitting and constrained optimization," *IEEE Trans. Image Process.*, vol. 19, no. 7, pp. 1720–1730, 2010.
- [3] Y.-M. Huang, L. Moisan, M. K. Ng, and T. Zeng, "Multiplicative noise removal via a learned dictionary," *IEEE Trans. Image Process.*, vol. 21, no. 11, pp. 4534–4543, 2012.
- [4] G. Aubert and J.-F. Aujol, "A variational approach to removing multiplicative noise," *SIAM J. Appl. Math.*, vol. 68, no. 4, pp. 925–946, 2008.
- [5] J. Shi and S. Osher, "A nonlinear inverse scale space method for a convex multiplicative noise model," *SIAM J. Imaging Sci.*, vol. 1, no. 3, pp. 294–321, 2008.
- [6] S. Nam, M. E. Davies, M. Elad, and R. Gribonval, "The cosparsity analysis model and algorithms," *Appl. Comput. Harmon. Anal.*, vol. 34, no. 1, pp. 30–56, 2013.
- [7] M. Yaghoobi, S. Nam, R. Gribonval, and M. Davies, "Constrained overcomplete analysis operator learning for cosparsity signal modelling," *IEEE Trans. Signal Process.*, vol. 61, no. 9, pp. 2341–2355, 2013.
- [8] R. Rubinstein, T. Peleg, and M. Elad, "Analysis K-SVD: A dictionary-learning algorithm for the analysis sparse model," *IEEE Trans. Signal Process.*, vol. 61, no. 3, pp. 661–677, 2013.
- [9] S. Hawe, M. Kleinstueber, and K. Diepold, "Analysis operator learning and its application to image reconstruction," *IEEE Trans. Image Process.*, vol. 22, no. 6, pp. 2138–2150, 2013.
- [10] J. Dong, W. Wang, and W. Dai, "Analysis SimCO: A new algorithm for analysis dictionary learning," in *Proc. Int. Conf. Acoust., Speech, and Signal Process.*, 2014, pp. 7193–7197.
- [11] S. Ravishanker and Y. Bresler, "Learning sparsifying transforms," *IEEE Trans. Signal Process.*, vol. 61, no. 5, pp. 1072–1086, 2013.
- [12] P.-A. Absil, R. Mahony, and R. Sepulchre, *Optimization Algorithms on Matrix Manifolds*. Princeton University Press, 2009.
- [13] W. Dai, T. Xu, and W. Wang, "Simultaneous codeword optimization (SimCO) for dictionary update and learning," *IEEE Trans. Signal Process.*, vol. 60, no. 12, pp. 6340–6353, 2012.
- [14] S. Boyd, N. Parikh, E. Chu, B. Peleato, and J. Eckstein, "Distributed optimization and statistical learning via the alternating direction method of multipliers," *Foundations and Trends in Machine Learning*, vol. 3, no. 1, pp. 1–122, 2011.

# Link-by-Link Coded Physical Layer Network Coding on Impulsive Noise Channels

Yuanyi Zhao	Martin Johnston,	Charalampos Tsimenidis	Li Chen
School of Electrical and Electronic Engineering Newcastle University Newcastle-upon-Tyne, UK Email: y.zhao3@ncl.ac.uk	School of Electrical and Electronic Engineering Newcastle University Newcastle-upon-Tyne, UK Email: martin.johnston@newcastle.ac.uk	School of Electrical and Electronic Engineering Newcastle University Newcastle-upon-Tyne, UK Email: charalampos.tsimenidis@newcastle.ac.uk	School of Information Science and Technology Sun Yat-sen University Guangzhou, China Email: chenli55@mail.sysu.edu.cn

**Abstract**—Physical-Layer Network Coding (PNC) employed on a conventional two-way relay channel (TWRC) is an active research area due to the potential doubling of the throughput compared with traditional routing. In this paper, we investigate the effects of impulsive noise added at the relay of a TWRC employing link-by-link coded PNC, where the coding scheme of interest is the turbo code. The Gaussian mixture model is chosen to model the impulsive noise and its effect on the performance of rate  $\frac{1}{2}$  and rate  $\frac{1}{3}$  turbo codes on the TWRC is evaluated through simulation results and extrinsic information transfer (ExIT) charts. An error floor analysis is also presented for different mixtures,  $\alpha$ , of impulsive noise and theoretical bounds are derived that explain the source of the error floors exhibited in the simulation results.

**Index Terms**—PNC, impulsive noise, iterative decoding, ExIT chart.

## I. INTRODUCTION

Physical-layer network coding (PNC) is a technique for wireless two-way relay channels (TWRC) [1], which exploits interference at a relay node to boost the throughput. Traditionally, it would require four time slots for two source nodes to exchange a message on the TWRC, but PNC requires only two times-slots: a multiple access (MAC) phase and a broadcast (BC) phase. In this paper, we consider a type of PNC called *link-by-link coded PNC*, where encoding and decoding takes place at the relay and source nodes in both time slots. It is widely acknowledged that iterative decoding schemes have significant advantages when combined with PNC. In [2], Hausl introduced an extension of the conventional two-way relay communication with a joint network-channel coding method for PNC. The study of Fang *et al.* [3] investigated the performance degradation of hierarchical decode-and-forward (HDF) turbo coded PNC on a conventional two-way relay communications compared to a single user end-to-end turbo coded system. Guan [4] showed an improved PNC method based on turbo codes and  $M$ -ary phase-shift keying (M-PSK), analysing the transmission energy consumption of the proposed scheme and showing how the enhanced PNC method can halve transmission energy consumption at the relay node over conventional PNC. Also Tang [5] shows a turbo network coding based relay model and its decoding method for the

quasi-static fading multi-access up-link channel. The study of Ao *et al.*[6] has investigated the physical-layer network coding in wireless networks, and propose a joint physical network coding with turbo code as channel coding implementation scheme for multiple-access channel, which performance of the proposed scheme is promising to approach information theoretical limits of the traditional network-coding scheme. Zeng *et al.* [7] presents a noncoherent detection of turbo code with iterative differential phase-shift keying (DPSK) demodulation over PNC in TWRC, which show that the iterative processing converges can be faster with Rayleigh fading channel. Furthermore, the study by Ferrett [8] pointed out that, digital network coding could improves the throughput of the two-way relay channel, by allowing multiple sources to transmit simultaneously to the relay. Tao *et al.*[9] addressed the convergence behavior of the iterative receiver of the channel coded PNC at the relay, it has enables the convergence analysis by using the extrinsic information transfer (EXIT) chart, and thus facilitates the design of channel-coded PNC schemes.

It is generally assumed that the noise added at the relay and sink nodes has a Gaussian distribution, but there are some scenarios where the noise could be impulsive, such as jamming, power line communications or machinery interference. Impulsive noise can severely degrade performance of communication systems and it is interesting to investigate how the presence of impulsive noise affects the performance of a TWRC applying PNC at the relay. After a review of the literature it appears that the effect of impulsive noise on a conventional TWRC employing PNC has not been considered. Of particular interest is the effect of impulsive noise on the iterative turbo decoder employed at the relay, which is the focus of this paper.

When evaluating the performance of an iterative decoding scheme, it is important to investigate the convergence behaviour of the iterative decoding algorithm, which can be achieved using extrinsic information transfer (EXIT) charts [10]. To obtain an EXIT chart for the turbo decoder effected by impulsive noise, we need to know the probability density function (pdf) of the noise. To achieve this, the Gaussian mixture model (GMM) has been selected [11][12] with a

probability density function (pdf),  $p_G(x)$ , that is defined by two-terms, i.e.,

$$p_{GMM}(x) = (1 - \alpha)p_G(x) + \alpha p_I(x), \quad (1)$$

where  $0 \leq \alpha \leq 1$ , is the mixture constant, with larger values of  $\alpha$  denoting more impulsiveness. The terms  $p_G(x)$  and  $p_I(x)$  are two Gaussian pdfs, where  $p_I(x)$  has a much larger variance than  $p_G(x)$ , and  $p_{GMM}(x)$  is the resulting heavy-tailed distribution.

The structure of this paper is presented as followings: Section II describes the system model of link-by-link channel-coded PNC on a conventional two-way relay communications. This is followed by an EXIT chart analysis of the turbo decoder at the relay of the conventional two-way relay communications in Section III. In Section IV, simulation results and discussions are presented, followed by an error floor analysis and conclusions are given in Section V.

## II. SYSTEM MODEL

The system model of the conventional two-way relay communications employing turbo codes combined with PNC is shown in Fig.1. During the MAC phase two assumptions are made: The channel has perfect synchronization and power control and the relay receives packets from each node with the same symbol energy  $E$  [13]. Two source nodes,  $A$  and  $B$ , have no direct-link to each other and instead transmit their messages through the relay. Let  $m_A \in \{0, 1\}^k$  and  $m_B \in \{0, 1\}^k$  be the  $k$ -bit binary messages sent from node  $A$  and node  $A$ . The information sequences are encoded resulting in  $c_A \in \{0, 1\}^n$  and  $c_B \in \{0, 1\}^n$ , where  $n$  is the length of the codes and two turbo codewords are mapped to signal in modulator. It is also assumed that the sources and relay employ the same interleavers. Therefore, the received information sequence at the relay can be expressed as[14]

$$y = x_A + x_B + \eta, \quad (2)$$

where  $x_A$  and  $x_B$  are the electromagnetic signals transmitted from nodes  $A$  and  $B$  respectively,  $\eta$  is the noise added at the relay and  $(x_A, x_B) \in \{1 + j, 1 - j, -1 - j, -1 + j\}$ . The sum of the two transmitted signals  $x_R$  can have nine possible complex values. The relay must then determine the log-likelihood ratio (LLR) of  $y$  given that  $x_R = x_A + x_B$  was transmitted,  $L(y|x_A + x_B)$ . This is decoded at the relay to give the message  $m_R = m_A \oplus m_B$ , where  $\oplus$  is the XOR operation. The decoded message is then re-encoded to give  $c_R = c_A \oplus c_B$ , which is mapped to constellation points and broadcast back to nodes  $A$  and  $B$ . At nodes  $A$  and  $B$ , the received signal is decoded to obtain  $m_R$ , where node  $A$  can obtain  $m_B$  by performing the XOR of  $m_R$  with its known binary message  $m_A$ , as shown in (3). A similar operation is performed at node  $B$  to obtain  $m_A$ .

$$m_B = m_A \oplus (m_A \oplus m_B) \quad (3)$$

The turbo decoder comprises two soft-input-soft-output (SISO) component decoders, which exchange the extrinsic and the *a priori* information with each other in an iterative

manner. Essentially, the turbo decoder will be decoding a vector of LLR values that give a measure of the reliability of the combination of both source nodes codewords. Since turbo codes are linear this means the sum of any two codewords is another valid codeword, which can also be decoded. From the resulting nine-point constellation diagram at the relay, each received symbol  $y$  is demapped to a pair of LLR values,  $L(y|m_R^{(1)})$  and  $L(y|m_R^{(2)})$ , which are a measure of the reliability of the two XORed transmitted bits,  $m_R^{(1)}$  and  $m_R^{(2)}$ , where the superscript denotes the first or second bit and  $m_R^{(1)} = m_A^{(1)} \oplus m_B^{(1)}$  and  $m_R^{(2)} = m_A^{(2)} \oplus m_B^{(2)}$ .

## III. EXIT CHART ANALYSIS OF LINK-BY-LINK CODED PNC AT THE RELAY

In order to analyse the behaviour of the turbo decoding algorithm at the relay, the EXIT chart is introduced, which tells us the number of iterations required for a decoder to converge at a particular SNR, or conversely that the system will not converge at a particular SNR. To generate the EXIT chart characteristics, it is necessary to introduce the concepts of the turbo decoder first. Let  $I(X; A)$  denote the mutual information between the *a priori* LLR  $A$  and the transmitted symbol  $X$  and let  $I(X, E)$  denote the mutual information between the extrinsic LLR  $E$  and  $X$  [15]. In the iterative decoding process,  $A$  is obtained from the other decoder. The extrinsic LLR  $E$  is produced by the turbo decoders based on the received sequence and  $A$ . According to Bayes' rule, the distribution of  $X$  at the relay can be expressed as:

$$p(y) = \sum_{\tilde{x}} p(y|X = \tilde{x})P(X = \tilde{x}), \quad (4)$$

where the value of  $\tilde{x}$  are relate to the modulation scheme, and  $P(X = \tilde{x})$  is the probability. By substituting (4) into (1) we can obtain  $p_G(y)$ .

By using the Kullback-Leibler distance, the mutual information between  $X$  and  $A$  can be computed as[15]:

$$I(X; A) = \int_{-\infty}^{+\infty} \sum_{\tilde{x}} p_G(X, y) \log_2 \left( \frac{p_G(X, y)}{p(X)p_G(y)} \right) dy, \quad (5)$$

where  $p_G(X, y)$  is the joint probability distribution of  $X$  and  $A$  and also  $p(X)$  and  $p_G(y)$  are the marginal distributions. Finally, by applying Bayes' rule we can rewrite (5) as

$$I(X; A) = \int_{-\infty}^{+\infty} \sum_{\tilde{x}} p_G(y|X = \tilde{x})P(X = \tilde{x}) \log_2 \left( \frac{p_G(y|X = \tilde{x})}{p_G(y)} \right) dy. \quad (6)$$

The extrinsic LLR  $E$  from the output of the decoder can be used to determine  $I(X; E)$  by generating a histogram of the extrinsic outputs. Since the distribution of  $E$  is not Gaussian we can compute  $I_{X;E}$  as [3]

$$I(X; E) = 1 - \frac{1}{N} \sum_{n=1}^N \{\log_2(1 + e^{-X L_G(y|X)})\}. \quad (7)$$

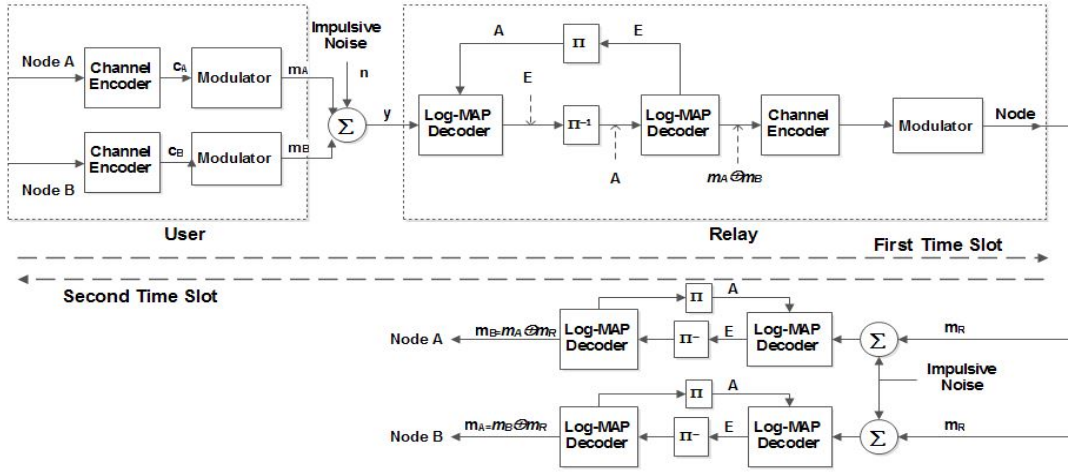


Fig. 1: System model showing turbo codes encoder and iterative decoding processing the PNC system.

When performing the EXIT chart analysis, we chose values of varying  $\alpha$  from 0.01 and 0.1 to analyse the convergence behaviour of the turbo codes at the relay of the conventional two-way relay communications. From Fig.2a it can be seen that the lowest SNR, or pinch-off SNR limit, where the rate  $\frac{1}{2}$  turbo coded PNC system converges is 3.1dB. The trajectory in the EXIT chart indicates that approximately 12 or 13 iterations are required to achieve convergence. Similarly, Fig.2b shows the EXIT charts for the rate  $\frac{1}{3}$  turbo code, and we observe that the pinch-off SNR limit for the turbo code is 2.7dB with approximately 10 iterations required. Fig.2c shows the EXIT charts of the rate  $\frac{1}{2}$  turbo code when  $\alpha = 0.1$ . In this case, the pinch-off SNR limit of the turbo code is 16.5dB and it takes about 4 iterations for the decoder to achieve convergence. Again, we also see this behaviour in the EXIT charts of the rate  $\frac{1}{3}$  turbo codes shown in Fig.2d, where the rate  $\frac{1}{3}$  turbo code has a 1.5dB advantage over the rate  $\frac{1}{2}$  turbo code.

#### IV. RESULTS AND DISCUSSION

##### A. BER performance and pinch-off SNR

In this section, the performance of turbo codes are simulated and are validated by the previous EXIT chart analysis. At the relay, any large positive or negative impulses are clipped so that their energy is no greater than the transmitted symbol energy  $E$ . The performance of coded PNC is seriously affected on additive impulsive noise channels resulting in error floors, as shown in Fig.3. For the turbo codes, a rate  $\frac{1}{2}$   $(37, 21)_8$  recursive systematic convolutional code (RSC) with a constraint length of five is used to obtain a rate  $\frac{1}{3}$  unpunctured turbo code and a rate  $\frac{1}{2}$  punctured turbo code. The rate  $\frac{1}{2}$  punctured turbo code performs slightly worse than the rate  $\frac{1}{3}$  turbo code when  $\alpha = 0.01$  and the waterfall regions for both codes start at around an SNR of 3dB, which is supported by the EXIT charts in Fig. 2a and 2b. When  $\alpha = 0.5$ , the channel is very impulsive and both codes have similar performance. The pinch-off SNR limits of the rate  $\frac{1}{2}$  and  $\frac{1}{3}$  turbo codes for

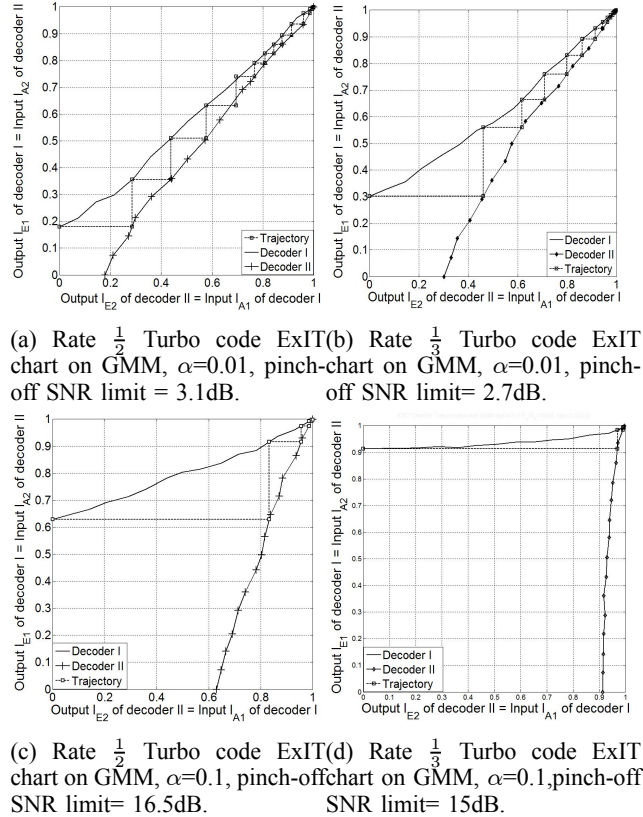


Fig. 2: Comparison of Rate  $\frac{1}{2}$  and Rate  $\frac{1}{3}$  Turbo code EXIT chart on GMM.

values of  $\alpha = 0, 0.01, 0.05, 0.1, 0.2$  and  $0.5$  are summarised in Table I.

##### B. Turbo code error floor analysis

As shown in Fig.3 when  $\alpha = 0.1$ , turbo codes exhibit an error floor at a BER of  $10^{-2}$  at 14dB. This error floor is caused by the impulsive noise during transmission but in order to explain this a lower bound on the BER of the turbo

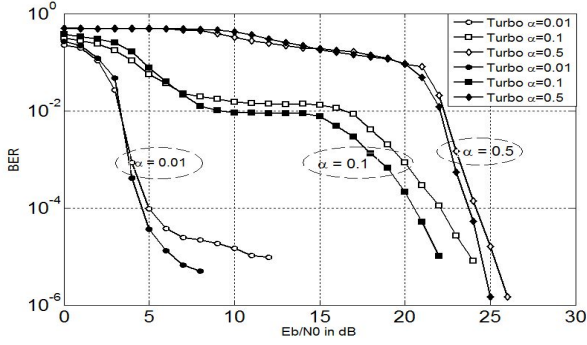


Fig. 3: BER performance of rate  $\frac{1}{2}$   $(37, 21)_8$  Turbo code (white squares) and  $\frac{1}{3}$   $(37, 21, 37)_8$  Turbo code (black squares) with impulsive noise at the relay, Interleaver length = 50,000 bits, 5 iterations

TABLE I: COMPARISON OF PINCH-OFF SNR LIMIT BETWEEN RATE  $\frac{1}{2}$  AND RATE  $\frac{1}{3}$  TURBO CODES WHEN  $0 \leq \alpha \leq 0.5$ .

$\alpha$	Turbo R= $\frac{1}{2}$	Turbo R= $\frac{1}{3}$
0	2.2dB	1.7dB
0.01	3.1dB	2.7dB
0.05	3.8dB	3.2dB
0.1	16.5dB	15dB
0.2	19.5dB	18dB
0.5	21.5dB	21dB

code will be derived. We assume that the all-zero codeword is transmitted and the decoder will choose the  $k$ th codeword  $\mathbf{c}_k$  over the all zero codeword  $\mathbf{c}_0$  with a probability of

$$P(\mathbf{c}_k|\mathbf{c}_0) = Q\left(\sqrt{2R_c d_k \frac{E_b}{N_0}}\right), \quad (8)$$

where  $R_c$  is the code rate and  $d_k$  is the weight of  $k$ th codeword. The BER of turbo code can be expressed as[15]:

$$P_b \lesssim \frac{1}{K} \sum_{w \geq 2} w n_w Q\left(\sqrt{2R_c d_{w,min} \frac{E_b}{N_0}}\right), \quad (9)$$

where  $n_w$  denotes the number of information sequences of weight  $w$  that generate codewords of weight  $d_{w,min}$ , and  $d_{w,min}$  is the minimum codeword weight among all codewords that are generated by information sequences of weight  $w$ . In order to derive the lower BER bound at the relay, (8) needs to be redefined to take into account the summed signals that result in an extended constellation with points that do not all occur with equal likelihood. On the AWGN channel the probability that the turbo decoder will choose  $\mathbf{c}_k$  over  $\mathbf{c}_0$  can be approximated as

$$P(\mathbf{c}_k|\mathbf{c}_0) \approx \frac{3}{2} Q\left(\sqrt{2R_c d_k \frac{E_b}{N_0}}\right). \quad (10)$$

By substituting (10) into (9), the lower BER bound of turbo codes at the relay is:

$$P_b^R \lesssim \frac{3}{2K} \sum_{w \geq 2} w n_w Q\left(\sqrt{2R_c d_{w,min} \frac{E_b}{N_0}}\right), \quad (11)$$

On the GMM impulsive noise channel, the lower BER bound for turbo codes at the relay is

$$P_b^{GMM} \lesssim \frac{3}{2K} \sum_{w \geq 2} w n_w \left( (1-\alpha) \sqrt{2R_c d_{w,min} \frac{E_b}{N_G}} + \alpha \sqrt{2R_c d_{w,min} \frac{E_b}{N_I}} \right), \quad (12)$$

where  $N_G$  and  $N_I$  are the noise power spectral densities for the Gaussian and impulsive terms in the GMM, which are related to the overall noise power spectral density of the GMM noise,  $N_0$ , as  $N_0 = (1-\alpha)N_G + \alpha N_I$ . A comparison of the lower bounds of rate  $\frac{1}{2}$  and  $\frac{1}{3}$  turbo codes are shown in Figs.4 to 7. We observe that as  $\frac{E_b}{N_0}$  increases the simulated BER results converge to the lower bound. However, the simulated results also show an error floor region and we found that this closely matches the bound obtained just from the second term in (12), i.e.

$$P_b^I = \alpha \sqrt{2R_c d_{w,min} \frac{E_b}{N_I}}. \quad (13)$$

This shows that at low SNRs it is only the impulses due to the GMM noise that effect the performance of the turbo code.

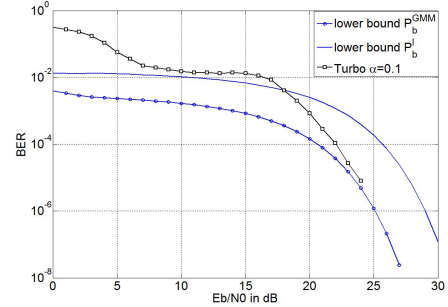


Fig. 4: Comparison of rate half turbo code on PNC at relay,  $\alpha = 0.1$  with lower bound  $P_b^{GMM}$  and the higher impulsive lower bound  $P_b^I$ .

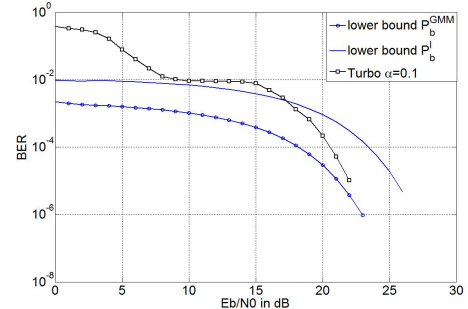


Fig. 5: Comparison of rate  $\frac{1}{3}$  turbo code on PNC at relay,  $\alpha = 0.1$  with lower bound  $P_b^{GMM}$  and the higher impulsive lower bound  $P_b^I$ .

In Fig.4 and Fig.5 the mixture is  $\alpha = 0.1$  and it can be seen that at low SNR the simulated results match closely with the higher impulsive bound  $P_b^I$  (13) and converges with the

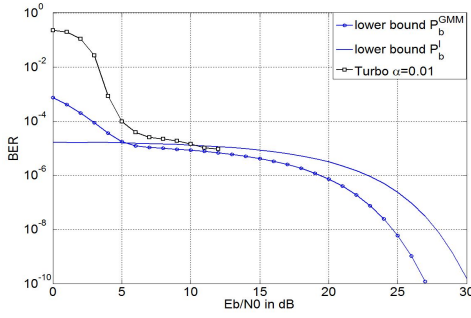


Fig. 6: Comparison of rate half turbo code on PNC at relay,  $\alpha = 0.01$  with lower bound  $P_b^{GMM}$  and the higher impulsive lower bound  $P_b^I$ .

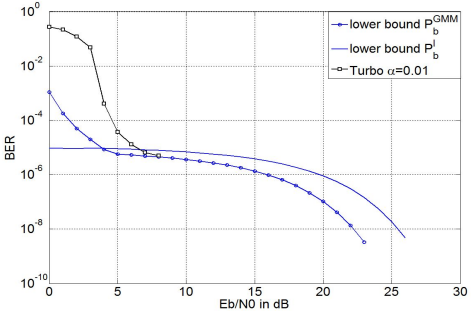


Fig. 7: Comparison of rate  $\frac{1}{3}$  turbo code on PNC at relay,  $\alpha = 0.01$  with lower bound  $P_b^{GMM}$  and the higher impulsive lower bound  $P_b^I$ .

error floor region from approximately  $8dB$  to  $15dB$ . As SNR increases the simulated results then start to converge with the lower bound in (12). Fig.6 and Fig.7 show the lower bounds and simulated results when  $\alpha = 0.01$ . In this case, we observe that the impulsive bound  $P_b^I$  does not have a significant effect on the turbo code performance since the impulsive mixture is much lower and the error floor region is consequently much smaller. As before, the simulated turbo code performance converges with the lower bound in (12) at higher SNRs.

## V. CONCLUSIONS

In this paper, an analysis of turbo codes combined with link-by-link PNC on additive impulsive noise channels has been investigated at the relay of a conventional TWRC. We have shown that the performance of turbo codes is seriously affected on the GMM noise channel when the mixture is high and ExIT charts have been presented showing the convergence behaviour of the turbo decoder for different mixtures of impulsiveness. The pinch-off SNR values for rate  $\frac{1}{2}$  and  $\frac{1}{3}$  turbo codes have also been determined from the ExIT charts and match closely with the simulation results. Finally, the error floors caused by impulsive noise are analysed by determining the lower bound on the performance of turbo codes at the relay. We observed that for higher mixtures the error floor is determined solely by the impulses of the GMM noise channel at low SNRs, but this effect quickly reduces with increasing SNR and the Gaussian noise part of the GMM noise channel has more of an effect on the performance.

## REFERENCES

- [1] S. Zhang, S. C. Liew, and P. L. Lam, "Hot topic: physical layer network coding," in *Proceedings of the 12th annual international conference on Mobile Computing and Networking (MobiCom)*, Aug. 2006, pp. 358–365.
- [2] C. Hausl and J. Hagenauer, "Iterative network and channel decoding for the two-way relay channel," *Communications, 2006. ICC '06. IEEE International Conference on*, pp. 1568 – 1573, June 2006.
- [3] D. Fang and A. Burr, "Performance degradation of turbo coded physical layer network coding on the two-way relay channel," in *IEEE 22nd International Symposium on Personal Indoor and Mobile Radio Communications (PIMRC)*, 2011, pp. 1748 – 1752.
- [4] G. Ke, "Improvement of physical-layer network coding method in relay networks," *Communications and Mobile Computing (CMC), 2010 International Conference*, pp. 457 – 460, 12-14 April 2010.
- [5] C. S. Suhua Tang, Jun Cheng and R. Suzuki, "Turbo network coding for efficient and reliable relay," *Communication Systems, 2008. ICCS 2008. 11th IEEE Singapore International*, pp. 1603 – 1608.
- [6] A. Zhan, "Joint design of channel coding and physical network coding for wireless networks," *Neural Networks and Signal Processing, 2008 International Conference*, pp. 512 – 516, 7-11 June 2008.
- [7] W. Zeng, "Turbo dpsk in bi-directional relaying," *Wireless Communications and Networking Conference Workshops (WCNCW), 2013 IEEE*, pp. 155 – 159, 7-10 April 2013.
- [8] T. Ferrett, "An iterative noncoherent relay receiver for the two-way relay channel," *Communications (ICC), 2013 IEEE International Conference on*, pp. 5903 – 5908, 2013.
- [9] T. Huang, T. Yang, J. Yuan, and I. Land, "Convergence analysis for channel-coded physical layer network coding in gaussian two-way relay channels," in *8th International Symposium on Wireless Communication Systems (ISWCS)*, 2011, pp. 849 – 853.
- [10] S. T. Brink, "Convergence of iterative decoding," *Electronics Letters*, vol. 35, no. 10, pp. 806–808, 1999.
- [11] D. Middleton, "Statistical-physical models of electromagnetic interference," *IEEE Transactions on Electromagnetic Compatibility*, vol. 19, pp. 106–127, 1977.
- [12] D. Middleton, "Procedures for determining the parameters of the first-order canonical models of class a and class b electromagnetic interference," *IEEE Transactions on Electromagnetic Compatibility*, vol. 21, pp. 190–208, 1979.
- [13] R. H. Louie, Y. Li, and B. Vucetic, "Practical physical layer network coding for two-way relay channels: Performance analysis and comparison," *IEEE Trans. Wireless Comm.*, vol. 9, no. 2, pp. 764–777, 2010.
- [14] S. T. Brink, J. Spiedel, and R. H. Yan, "Iterative demapping and decoding for multilevel modulation," in *Global Telecommunications Conference*, 1998, pp. 579–584.
- [15] T. K. Moon, "Error correction coding: Mathematical methods and algorithms," *ISBN=0-471-64800-0*, pp. 619 – 627, June 2005.

# A New Asymmetric Correlation Kernel for GNSS Multipath Mitigation

Steven Miller  
School of ECEE  
SenSIP Center  
Arizona State University  
Email:smiller@aperio-dsp.com

Xue Zhang  
School of ECEE  
SenSIP Center  
Arizona State University  
Email: xzhan154@asu.edu

Andreas Spanias  
School of ECEE  
SenSIP Center  
Arizona State University  
Email: spanias@asu.edu

**Abstract**—Multipath is the dominant error source in precise positioning Global Navigation Satellite Systems (GNSS) such as the United States Global Positioning System (GPS). These systems utilize the satellite signal time of arrival estimates to solve for position. Multipath corrupts the time of arrival estimates by distorting the signal tracking phase discriminator; which results in a slowly time-varying phase bias. This bias ranges from several centimeters to tens of meters. The sub-meter bias is the most problematic for centimeter positioning systems. Moreover, in addition to multipath, the GPS spread spectrum code is unbalanced for certain space vehicles which can lead to a code tracking phase bias. A new correlation kernel is proposed as part of a multipath mitigating delay-locked-loop code phase discriminator that does not suffer a tracking bias due to unbalanced spreading codes. This new algorithm performance is compared to existing techniques with respect to position bias and robustness.

**Index Terms**—multipath, correlation, DSSS, GPS

## I. INTRODUCTION

Global Navigation Satellite Systems (GNSS) provide the enabling technology for real-time, autonomous vehicle navigation and control in such diverse applications as construction, mining, farming, and fishing [1]. Consequently, there is commercial interest to increase measurement accuracy and integrity while simultaneously reducing the system cost. Modern GNSS receivers provide real-time position accuracy of a few centimeters. All GNSS receivers estimate a satellites signal time of arrival to solve for position and time. The quality of these time-of-arrival (TOA) estimates are directly dependent upon accurate tracking of the direct sequence spread spectrum (DSSS) code and carrier phase. Unfortunately, multipath is a dominant error source within these systems since it corrupts the signal phase estimates with a time-varying bias.

GNSS receivers utilize a coherent correlator for signal detection and data modulation. A complex signal model for a DSSS receiver operating on a real signal,  $r(t)$ , is shown in Figure 1. The block consists of a phase discriminator, a loop filter, a Numerically Controlled Oscillator (NCO) and a code kernel generator. Two kernels are generated: (1) A model,  $\hat{x}(t)$ ,

The authors from Arizona State University were supported in part by the SenSIP Center and the NSF FRP 1231024 award. Author S. Miller was supported in part by Hemisphere GPS.

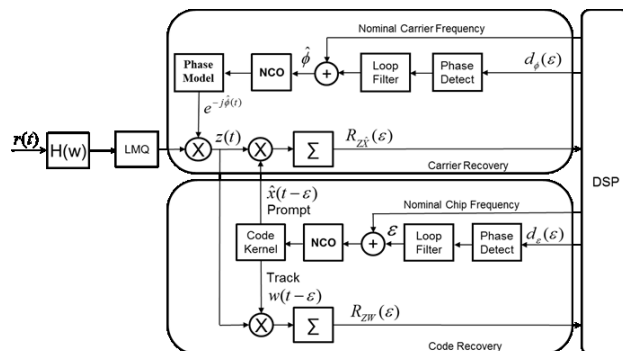


Fig. 1. Receiver Complex Signal Analysis Model.

of the transmitted code sequence  $x(t)$ ; and (2) a code tracking kernel,  $\omega(t)$ . The kernel  $\hat{x}(t)$  is correlated with  $z(t)$  to form the statistic  $R_{Z\hat{X}}(\epsilon)$ . This complex valued statistic is used to form the carrier tracking loop discriminant,  $d_\phi(\epsilon)$  and decode the satellites data bits. The kernel  $\omega(t)$  is also correlated with  $z(t)$  to form the statistic  $R_{ZX}(\epsilon)$ . This kernel can be designed with multipath mitigation properties and used as part of the code phase error discriminator,  $d_\epsilon(\epsilon)$ . The code phase discriminator estimates the phase error between the incoming measured signal and the code model. The filtered phase error is output from the loop filter and provides a delta-phase which is accumulated in the NCO to adjust the model phase and drive the phase error to zero. The control loop will advance or retard the model in time until it aligns with the incoming signal. When no multipath exists, the maximum likelihood estimator is optimal, and it can be found by solving for when the cross correlation of the incoming signal and the derivative of the spreading code reference model is zero. Since the spreading code sequence is known in advance, the Early Minus Late (EML) discriminator describe by [2] and [3] can be used.

In the literature, current multipath mitigating techniques for DSSS signals consist of EML delay locked loops (DLL) or windowed EML DLLs. The EML DLL phase phase discriminator obtains phase alignment by cross-correlating the incoming signal with a composite model equal to a  $\delta$ -chip early model minus a  $\delta$ -chip late model [4]–[6]. The methods so far build the correlation waveform utilizing a linear combination

of EML and are even symmetric [3], [7]–[10]. These solutions have the disadvantage of narrowing the tracking range and lowering the discriminator gain to  $\delta$ . Until [11], [12],  $w(t)$ , has been limited to linear functions of the spreading code which produced an even functioned  $w(t)$ . The multipath distortion can also be reduced by designing the code tracking kernel,  $w(t)$ , to meet specified objects such as a non-ambiguous BOC discriminant [13], [14]. However, the resulting correlation kernel pulses are narrow and the effects of a band limited precorelation filter were not considered.

Although the maximum likelihood (ML) code bit transition estimator when not in the presence of multipath is optimal [1], [15], [16], this only holds for even symmetric correlation kernels or for equal probable transition and non-transitions for asymmetric correlation kernels. A new multipath mitigating algorithm is introduced that utilizes a non-symmetric correlation kernel that considers non-equal transition and non-transition probabilities is proposed in this paper.

The rest of this paper is organized as the follows. In Section II, a novel non-symmetric correlation kernel is proposed. Following this, in Section III, the proposed correlation kernel is compared with the existing techniques and the simulation results are presented. Finally, Section IV contains concluding remarks.

## II. A NOVEL NON-SYMMETRIC CORRELATION KERNEL DESIGN

### A. System Model

Four different correlation kernels exist corresponding to the four transitions states: (1) Low to high transition; (2) high to low transition; (3) no transition but model low; and finally (4) no transition but model high. These kernels do not have to be the same; nor are they constrained to have equal energy (sum of kernel weight squared) since separate accumulators can be maintained for each state and the results scaled based upon the ratio of kernel weights. Recall that the EML correlation signals are even symmetric about the model transition point as. This symmetry is not required and other correlative kernels that are non-symmetric can be used. If not symmetric about the zero phase error point, a balancing mass is required otherwise a phase discriminator bias will result: The phase discriminator will have a non-zero output corresponding to zero phase error. Phase error bias is eliminated for non-symmetric transition kernels by introducing a balancing mass such as a non-transition kernel. Consequently, non-symmetric transition kernels accompanied by non-transition kernels must account for transition and non-transition probabilities otherwise a phase discriminator bias will result. Note that in this case non equal transition and non-transition probabilities will result in a phase discriminator bias whereas in the EML case only the discriminator gain is reduced and no bias occurs.

Each correlation kernel can be formed using the upper bits of the code NCO, which defines the region of support, to address a look-up-table for the kernel weights. A design goal for a correlative discriminator with multipath mitigating

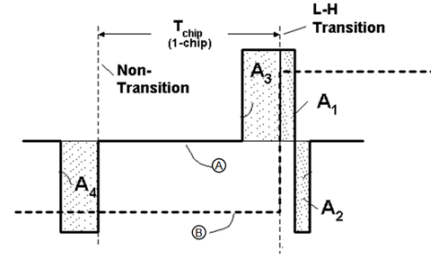


Fig. 2. Low to High Transition with Perfect Track Phase Alignment.

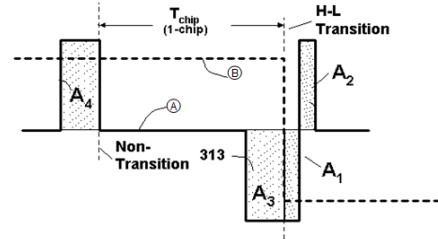


Fig. 3. High to Low Transition with Perfect Track Phase Alignment.

properties is to: (1) Provide an unbiased code-phase error estimate insensitive to multipath; (2) Provide an unambiguous discriminator; and (3) Provide a wide linear-operating region. Note that multipath is inherently time delayed and can cause a positive or negative code phase error bias depending upon if the multi-path phase has the same or opposite sign as the main signal path respectively.

### B. A novel non-symmetric correlation kernel design

Figure 2 and Figure 3 show the code signal, **B**, undergoing a low-to-high (L-H) and high-to-low (H-L) transition respectively. Furthermore, both figures show the applicable correlation kernels. Referring to Figure 2, the track reference signal contains the Non-Transition correlation kernel comprised of pulse  $A_4$ , and L-H transition correlation kernel consisting of pulses  $A_1$ ,  $A_2$  and  $A_3$ . The code takes a L-H transition coincident with regions  $A_1$  and the  $A_3$ . Pulse  $A_4$  is shown aligned to the end of a non-transition code chip (one for which the sign does not change in the next chip). Pulse  $A_2$  follows pulse  $A_1$  and is of opposite sign. When the track signal **A** is aligned in phase to the code signal **B**, the area  $A_1$  is equal to  $A_2$  and the area  $A_3$  is equal to  $A_4$ . This equalization is denoted as a MB.

Referring to Figure 2, the track reference signal contains the Non-Transition correlation kernel comprised of pulse  $A_4$ , and L-H transition correlation kernel consisting of pulses  $A_1$ ,  $A_2$  and  $A_3$ . The code takes a L-H transition coincident with regions  $A_1$  and the  $A_3$ . Pulse  $A_4$  is shown aligned to the end of a non-transition code chip (one for which the sign does not change in the next chip). Pulse  $A_2$  follows pulse  $A_1$  and is of opposite sign. When the track signal **A** is aligned in phase to the code signal **B**, the area  $A_1$  is equal to  $A_2$  and the area  $A_3$

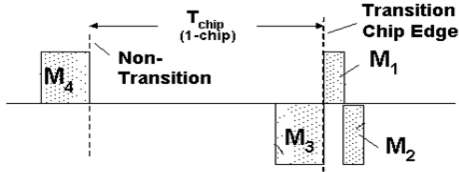


Fig. 4. MB Kernel with Perfect Track Signal Phase Alignment.

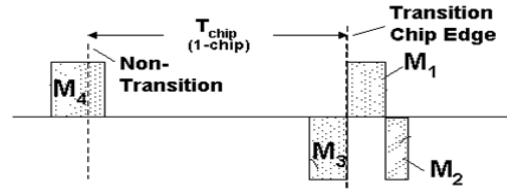


Fig. 5. Late Track Signal.

is equal to  $A_4$ . This equalization is denoted as a MB.

The track reference signal  $A$  acts as a multiplier and enable for the code signal  $B$ . The product is zero wherever the track reference signal  $A$  is zero, and non-zero wherever the correlation kernels exist. The non-zero portion has amplitude that is the product of both the amplitude of the code and the amplitude of the track reference, including sign.

Figure 4 shows the product of the track reference signal and the code signal when both are phase aligned. The product pulses have areas  $M_1$ ,  $M_2$ ,  $M_3$  and  $M_4$  respectively and are referred to masses. The areas of these masses are proportional to the corresponding areas  $A_1$ ,  $A_2$ ,  $A_3$  and  $A_4$  of the track reference signal, but are scaled in amplitude by the height of the code signal. The masses also contain some sign reversals relative to the original pulses due to multiplication by the code signal.

Figure 4 holds for both L-H transitions, and H-L transitions. Regardless of the direction of the code transition (H-L or L-H),  $M_2$  and  $M_3$  are negative while  $M_1$  and  $M_4$  are positive. This is by design. A further property relates to the areas of  $M_1$ ,  $M_2$ ,  $M_3$  and  $M_4$ . When the track reference signal and the code signal are aligned in phase, the areas cancel to zero when summed together. Specifically,

$$(M_2 = -M_1), \text{ and } (M_3 = -M_4). \quad (1)$$

Therefore

$$M_1 + M_2 + M_3 + M_4 = 0. \quad (2)$$

Thus, the track reference signal is mass-balanced about the code signal so as to yield a zero summation.

Figure 5 shows the result of delaying the track reference signal relative to the code (the track reference signal lags the code signal). The masses  $M_1$  through  $M_4$  of the track signal are seen to shift right relative to the codes level transition. The mass gains positive area so that  $M_1$  increases by a positive amount. The mass loses negative area, so that  $M_3$  also effectively increases by a positive amount. Thus, there is a net positive increase in mass (or correlation) relative to Figure 4. Precisely,

$$M_1 + M_2 + M_3 + M_4 = 2\epsilon \quad (3)$$

where  $\epsilon$  is the increase in the area of  $M_1$  and also the increase in area of  $M_3$ .

Figure 6 shows the case when the track reference signal leads the code signal. The masses  $M_1$ , through  $M_4$  are seen to shift left relative to the code sign transition. The mass loses

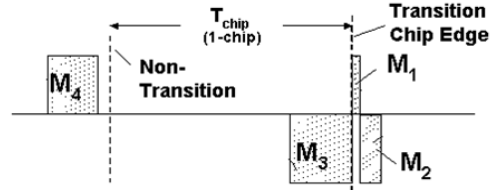


Fig. 6. Early Track Signal.

positive area so that  $M_1$  decreases in value. The mass  $M_3$  gains negative area. Thus, there is a net decrease in mass relative to Figure 4. Precisely,

$$M_1 + M_2 + M_3 + M_4 = -2\epsilon, \quad (4)$$

where  $\epsilon$  is the decrease in area of both  $M_1$  and  $M_3$ .

The mass summations represent the process of computing a correlation between the track-reference signal and the code signal. This acts as a measure of phase error between the track reference signal and the code signal.

Referring to Figure 7, the chip transition acts as the zero-phase reference. Phase error is thus measured by a displacement,  $\epsilon$ , relative to zero. Positive,  $\epsilon$ , is taken so the code signal leads the track reference signal. At zero phase error ( $\epsilon=0$ ), the masses  $M_1$ , through  $M_4$  balance. For some positive constants  $\gamma$  and  $\sigma$ , the relationship is

$$\begin{aligned} M_1 &= \frac{\gamma}{2} \\ M_2 &= -\frac{\gamma}{2} \\ M_3 &= \frac{\sigma}{2} \\ M_4 &= -\frac{\sigma}{2}, \end{aligned} \quad (5)$$

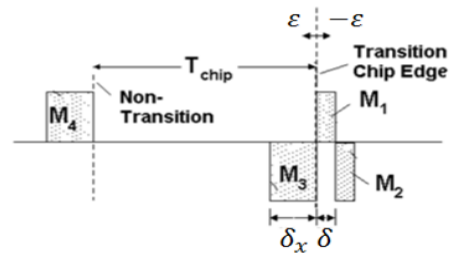


Fig. 7. Non-Transition and Transition Correlation Kernels.

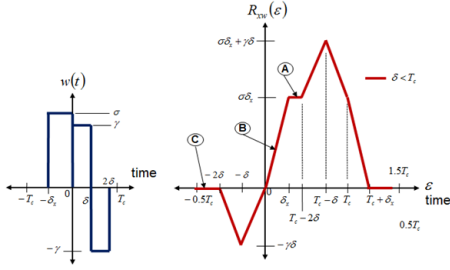


Fig. 8. Code Phase Discriminator Gain,  $R_{XW}(\epsilon)$ .

so that,

$$M_1 + M_2 + M_3 + M_4 = 0. \quad (6)$$

Figure 8 shows a plot of the Mass Balance (MB) discriminator as a function of true phase error. Notice that the point of zero phase error gives a zero MB and hence zero phase discriminator. The phase discriminator curve for small phase errors is of constant slope (linear) and is positive for positive phase error (code phase leading reference phase). This linear region is denoted as segment **B**. It reaches a maximum of  $x$  on the right-hand end of the linear region, at a phase error of  $\epsilon = \sigma x$ . As true phase error continues in the positive direction, the discriminator levels off to a constant value as shown by segment **A**. Similarly, moving left, it reaches a peak negative value of  $-\gamma\sigma$  at a phase error of  $\epsilon = \sigma$  and then slopes back to zero as phase error becomes more negative, reaching zero at  $-2\sigma$ . The discriminator becomes zero over the region **C** outside of a phase error of  $-1$  chip. Due to its asymmetric shape, it is referred to as an asymmetric correlative-phase-discriminator.

The MB discriminant is an unbiased phase error estimator and conventional linear control techniques can be utilized to maintain near zero phase error. During tracking, the phase error will typically reside within the linear portion, and linear control assumptions hold true. Even larger positive phase errors, up to one chip in duration, are zeroed out by a feedback control loop since the phase discriminator remains non-zero and positive when phase error is positive. However, due to the asymmetric nature of the phase discriminator curve, reverse is not true. If phase error exceeds a value of  $-2\sigma$ , the phase discriminator goes to zero where it remains for negative phase errors up to  $-1$  chip. In this region the feedback control will not be able to zero out the phase error. A solution for this problem is provided in [6].

Recall that the phase discriminator is calculated by correlating over many code chips, some with transitions in sign and some without. Appendix A shows that the number of code transitions does not match the number of non-transitions for every GPS L1CA code sequence. For an unbiased discriminator, the MB must take into account this imbalance.

Refer again to Figure 7, recall the mass  $M_3$  at the sign transition must balance the mass  $M_4$  at the non-transition whenever the track reference signal and code signal are aligned. Consider all chips within the code sequence, then the

MB becomes

$$N_T \times M_1 + N_T \times M_2 = 0, \quad (7)$$

and

$$N_T \times M_3 + N_N \times M_4 = 0, \quad (8)$$

where  $N_T$  is the number of code sign transitions and  $N_N$  is the number of non-transitions.

When  $M_2 = -M_1$  and  $M_3 = -M_4$  a zero MB is not achieved unless  $N_N = N_T$ . Therefore, a scale factor  $\alpha$  is introduced for which the final correlation of all non-transitions is multiplied. The scale factor  $\alpha$  is given by,

$$\alpha = \frac{(N_T \times |M_3|)}{(N_N \times |M_4|)}, \quad (9)$$

when  $|M_3| = |M_4|$ , which is the case described so far and also convenient for implementation, then,

$$\alpha = \frac{N_T}{N_N}. \quad (10)$$

The MB then becomes,

$$N_T \times M_1 + N_T \times M_2 = 0, \quad (11)$$

and

$$N_T \times M_3 + N_N \times M_4 = 0, \quad (12)$$

which holds true for any nonzero  $N_N$  and  $N_T$ . Generally, many arrangements of scaling the transition correlation to the non-transition correlation are possible. For example, choose any numbers  $\beta_1$  and  $\beta_2$  such that,

$$\frac{\beta_2}{\beta_1} = \alpha, \quad (13)$$

and then multiply the transition correlation by  $\beta_1$  and the non-transition correlation by  $\beta_2$  to satisfy the MB. This will give a MB,

$$\beta_1 \times (N_T \times M_1 + N_T \times M_2) = 0, \quad (14)$$

and

$$\beta_1 \times N_T \times M_3 + \beta_2 \times N_N \times M_4 = 0, \quad (15)$$

In summary, to produce an unbiased correlative-phase-discriminator with a non-symmetric transition kernel, two correlations must be performed and summed together with appropriate scaling. One correlation operates over code sign transitions and the other operates over non-transitions. An alternative is to move the mass  $M_4$  to lie within a transition chip and perform correlations only on transition chips. Recall the asymmetric nature of the correlation kernels necessitates the counting of code transitions and code non-transitions to achieve an unbiased phase estimate.

### III. SIMULATION RESULTS

In the simulation, we compare the EML DLL and the MB algorithm under different multipath conditions, as shown in Figure 9 and 10 respectively. From these two figures one can see that the MB algorithm exhibits significantly less phase bias for each multipath scenario. Therefore, we can conclude that the proposed MB algorithm outperforms the DLL algorithms.

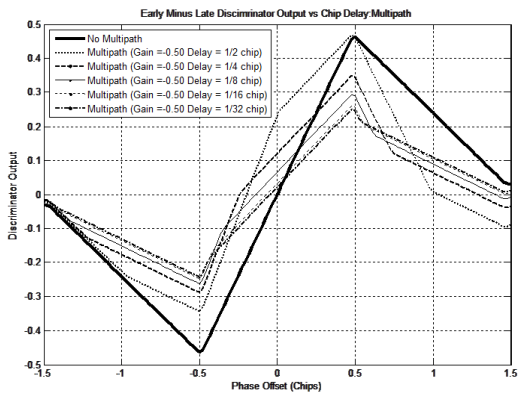


Fig. 9. Early Minus Late Simulation Results.

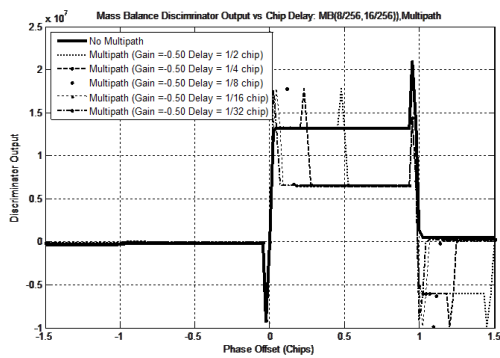


Fig. 10. Mass-Balance Simulation Results.

#### IV. CONCLUSIONS

In this paper, a new multipath mitigating algorithm was introduced that utilizes a non symmetric correlation kernel to reject multipath with a delay spread of at least 3% of the spreading code period. This algorithm is unbiased and requires two correlations arms that must be summed together with appropriate scaling. One correlation operates over code sign transitions (L-H and H-L) and the other operates over nonover non-transitions. The asymmetric nature of the correlation kernels necessitates the counting of code transitions and code non-transitions to achieve an unbiased phase estimate.

#### REFERENCES

- [1] S. Miller, "Multipath mitigating correlation kernels," Ph.D. dissertation, Arizona State University, December 2013.
- [2] E. Kaplan, *Understanding GPS: Principles and Applications*. Artech House Telecommunication Library, 1996.
- [3] B. Townsend and P. Fenton, "A practical approach to the reduction of pseudorange multipath errors in a 11 GPS receiver," in *Proceedings of ION GPS-94*, 1994, pp. 143–148.
- [4] J. Spilker and D. Magill, "The delay-lock discriminator-an optimum tracking device," *Proceedings of IRE*, vol. 49, no. 9, pp. 1403–1416, 1961.
- [5] A. Polydoros and C. Weber, "Analysis and optimization of correlative code-tracking loops in spread-spectrum systems," *IEEE transactions on communications*, vol. 33, no. 9, pp. 30–43, 1985.
- [6] W. Hurd and T. Anderson, "Digital transition tracking symbol synchronizer for low SNR coded systems," *IEEE transactions on communication technology*, vol. 18, no. 2, pp. 30–43, 1970.

- [7] L. Garin and J. Rousseau, "Enhanced strobe correlator multipath rejection for code and carrier," in *Proceedings of ION GPS-97*, 1997, pp. 559–568.
- [8] J. Ray, "Mitigation of GPS code and carrier phase multipath effects using a multi-antenna system," Ph.D. dissertation, University of Calgary, 2000.
- [9] M. Braasch, "Isolation of GPS multipath and receiver tracking errors," *Navigation: Journal of the Institute of Navigation*, vol. 41, no. 4, 1994.
- [10] S. Miller and A. Spanias, "An unbiased multipath mitigating delay locked loop correlation kernel for unbalanced direct sequence spreading codes," Sedona, May 2008.
- [11] W. J. Gill, "A comparison of binary delay-lock loop implementations," *IEEE transactions on Aerospace Electron. Syst*, vol. AES-2, pp. 415–424, 1966.
- [12] A. Polydoros and C. Weber, "Analysis and optimization of correlative code-tracking loops in spread-spectrum systems," *IEEE transactions on communications*, vol. 33, no. 9, pp. 30–43, 1985.
- [13] F. Sousa, F. Nunes, and J. Leitao, "Strobe pulse design for multipath mitigation in boc gnss receivers," in *IEEE Position, Location, And Navigation Symposium*, 2006, pp. 348–355.
- [14] M. Whitehead and S. Miller, "Unbiased code phase discriminator," Patent 4, 2011.
- [15] A. Spanias, *Digital Signal Processing; An Interactive Approach - 2nd Edition*, ISBN: 978-1-4675-9892-7. Lulu Press on-demand Publishers, May 2014.
- [16] J. Foutz, A. Spanias, and M. Banavar, *Narrowband dirrection of arrival estimation for antenna arrays*, *Synthesis lectures on antennas*, ISBN: 978-1598296501. Morgan and Claypool Publishers, August 2008.

# FRACTIONAL COSINE TRANSFORM (FRCT)- TURBO BASED OFDM FOR UNDERWATER ACOUSTIC COMMUNICATION

Yixin Chen

Centre for Excellence in Signal and Image Processing (CeSIP)  
University of Strathclyde  
Glasgow, UK  
yixin.chen@strath.ac.uk

Carmine Clemente

Centre for Excellence in Signal and Image Processing (CeSIP)  
University of Strathclyde  
Glasgow, UK  
carmine.clemente@strath.ac.uk

John. J. Soraghan

Centre for Excellence in Signal and Image Processing (CeSIP)  
University of Strathclyde  
Glasgow, UK  
j.soraghan@strath.ac.uk

Stephan Weiss

Centre for Excellence in Signal and Image Processing (CeSIP)  
University of Strathclyde  
Glasgow, UK  
stephan.weiss@strath.ac.uk

**Abstract**—In this paper, a hybrid Discrete Fractional Cosine Transform (DFrCT) with Tikhonov regularization based Turbo Minimum mean square error (MMSE) equalization (DFrCT-Turbo) is presented to suppress inter-carrier interference (ICI) over underwater acoustic channels (UWA). The scheme is based on Orthogonal Frequency Division Multiplex (OFDM) scenario. In addition, an optimal order selecting method for DFrCT is developed by maximizing carrier to interference ratio (CIR) to UWA channel character. Simulation results show that BER improvement of up to 5dBs over traditional orthogonal based methods with moderate complexity.

**Keywords**—Discrete Fractional Cosine Transform (DFrCT), carrier to interference ratio (CIR), Tikhonov regularization based Turbo Minimum mean square error (MMSE) equalization

## I. INTRODUCTION

There are two main obstacles of communication over underwater acoustic channel (UWA) [1], significant time delays that may reach fractions of seconds and severe Doppler spread attributed to high mobility between transmitter and receiver. An increase in the number of subcarriers in OFDM systems contributes to a decrease of subcarrier spacing bandwidth. Consequently such schemes can suffer from loss of orthogonality of subcarriers, caused by high Doppler spread, contributing to Inter-Carrier-Interference (ICI) [2]. Recent research that has focused on the suppression of ICI with low complexity methods, can be divided into prior FFT and post FFT methods [2]. Post FFT mainly deals with equalization techniques. By exploring the band nature of frequency channel matrix, block band MMSE (BMMSE)

methods are used [3], in which symbols are jointly equalized in a block, and the complexity is linear to block length, lower than that of conventional MMSE which grows cubically with subcarrier numbers.

The performance of the BMMSE could be further improved incorporating interference cancellation, such as maximum-likelihood and decision feedback approaches.

Iterative detection and decoding techniques were introduced in [4]-[6], such as the block turbo equalizer. These are based on the exchange of soft extrinsic information (most often log-likelihood ratios (LLRs)) between MMSE equalization, and maximum a posteriori probability (MAP) decoder. Banded equalization with iterative data detection has been shown to offer superior robustness against errors of channel estimation, which usually occurs in the UWA scenario [7]-[8].

To compete with the doubly selective (both time and frequency selective) nature of UWA channels, in our previous work the conventional FFT demodulation in the OFDM was replaced by the Fractional Fourier Transform (FrFT) [9] which transforms the signal into an intermediate domain between time and frequency. Doubly selective channel response was shown to be concentrated into narrower bands, allowing ICI in adjacent subcarriers to be concentrated around main diagonal of channel frequency matrix. The Fractional Cosine Transform (FrCT), based on the eigen-decomposition of the DCT kernel, has been shown to offer better energy concentration than FrCT and FFT with less complexity [10].

In this paper, a novel block turbo MMSE equalization method for OFDM scenario based on Discrete Fractional Cosine Transform (DFrCT), called DFrCT-Turbo is presented. An optimal order selecting scheme for the DFrCT is provided. At the analysis stage, a doubly selective channel scenario is

simulated and the results show the superior performance of the DFrCT-Turbo approach compared to conventional turbo equalization and DFrFT-OFDM. Moreover, the BER performance is further improved by incorporating convolutional error correction coding.

The remainder of paper is organized as follows. Section 2 presents the proposed DFrCT-Turbo based algorithm, with a DFrCT-OFDM block, a low complexity block turbo equalization based on Tikhonov regularization, and an optimal order selecting scheme. In section 3, simulation results and discussions are reported. Section 4 concludes the paper.

**Notation:** In this paper, transpose, conjugate and conjugate transpose are denoted as  $[\cdot]^T$ ,  $[\cdot]^*$  and  $[\cdot]^H$  respectively.  $diag\{\cdot\}$  denotes a diagonal matrix produced by a vector  $[\cdot]_{i,j}$  extracts the  $i$ th row and  $j$ th column element from a matrix. Finally,  $\langle \cdot \rangle_N$  is the modulo- $N$  calculation.  $\|\cdot\|$  indicates the Frobenius norm

## II. System model

### A. DFrCT-Turbo Transceiver

The proposed DFrCT-Turbo system shown in Figure 1 consists of several blocks. At first, switch 1 is open and switch 2 is closed. The system works in optimal order selection model to search the optimal order  $\alpha_{opt}$  range from -1 to 1. An initial order of -1 is used.

The input signal  $s_n$  is passed through conventional rate  $1/2$  ECC and interleaver modules. The encoded data vector is then transformed into time domain using an inverse DFrCT of order  $\alpha$ . The separate parallel data streams are then converted to a serial data after adding cyclic prefix. The serial received data stream is corrupted by a doubly selective channel with additive white Gaussian noise  $n$ . The output of the channel is fed into the IDFrCT optimal order selection module. The optimal order  $\alpha_{opt}$  is feedback to transmitter.

Then, the switch 1 is closed and switch 2 is open. The input signal  $s_n$  goes through the transmitter and channel again with IDFrCT at optimal order  $\alpha_{opt}$  and the received signal is converted to a parallel data stream, which is processed by the DFrCT at optimal order  $\alpha_{opt}$  after discarding cyclic prefix. Then, the Tikhonov regularization based turbo MMSE equalization is carried out on each block of symbols jointly, and iteratively interchanges extrinsic information with the convolutional decoder.

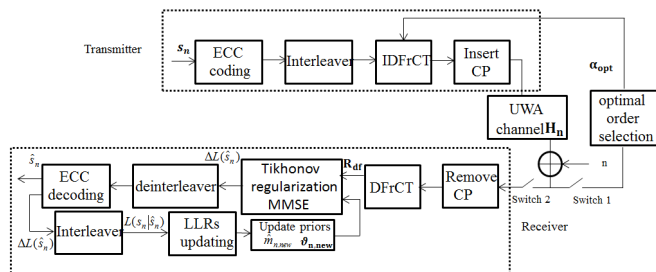


Figure 1: Diagram of DFrCT-Turbo Transceiver

### B. Discrete Fractional Cosine Transform (DFrCT)

The Discrete Fractional Cosine Transform (DFrCT) [11], is a generalization of the cosine transform (DCT), transforms a function into an intermediated domain between time and frequency, according to the rotation of time-frequency distribution via angle or order. In our previous work [10], the DFrCT of order  $\alpha$  was expressed in matrix vector notation as below:

$$\mathbf{y}_\alpha = \mathbf{F}_\alpha \mathbf{x} \quad (1)$$

Where

$$\mathbf{y}_\alpha = [y_\alpha[0], y_\alpha[1] \dots y_\alpha[N-1]]^T, \\ \mathbf{x} = [x[0], x[1] \dots x[N-1]]^T$$

and  $\mathbf{F}_\alpha$  is the  $N$  point Fractional Cosine Transform matrix. Similarly, the inverse DFrCT is written as

$$\mathbf{x} = \mathbf{F}_\alpha^H \mathbf{y}_\alpha = \mathbf{F}_{-\alpha} \mathbf{y}_\alpha \quad (2)$$

It represents one of the main components of the proposed algorithm and is described in the next section.

### C. Discrete Fractional Cosine Transform (DFrCT) OFDM system

The DFrCT based OFDM system, replaces both the Discrete Fourier (DFT) and inverse Discrete Fourier Transform (IDFT) blocks by the DFrCT and IDFrCT respectively. The  $\mathbf{N}_a$ -block binary sequence mapped by BPSK constellation  $\mathbf{s} = [s_1 \dots s_{N_a}]$ ,  $s_n \in \pm 1$ , is allocated into  $N$  subcarriers via a binary matrix, denoted as

$$\mathbf{J} = \left[ \begin{array}{c} \mathbf{0}_{N_a \times (N-N_a)/2} \mathbf{I}_{N_a} \mathbf{0}_{N_a \times (N-N_a)/2} \end{array} \right]^T \quad (3)$$

where  $\mathbf{0}_{L \times M}$  is an  $L \times M$  diagonal zero matrix, and  $\mathbf{I}_L$  is an  $L \times L$  identity matrix.

Then, the signal, modulated by the IDFrCT, is corrupted by a doubly selective (DS) channel. After removing cyclic prefix, the received signal  $\mathbf{R}_n$  is expressed as

$$\mathbf{R}_n = \mathbf{H}_n \mathbf{s}_n + \mathbf{v}_n \\ = \mathbf{H}_n \mathbf{F}_{-\alpha} \mathbf{J} \mathbf{d}_n + \mathbf{F}_\alpha \mathbf{v}_n \quad (4)$$

where  $\mathbf{H}_n$  represents the time domain channel matrix characterized by

$$[\mathbf{H}_n]_{i,j} = \begin{cases} h[n-L+i, i-j] & i \geq j, \\ h[n-L+i, L+i-j-1] & i < j \end{cases}$$

The received signal after DFrFT demodulation can be then expressed as

$$\mathbf{R}_{df} = \mathbf{J}^H \mathbf{F}_\alpha \mathbf{H}_n \mathbf{s}_n + \mathbf{F}_\alpha \mathbf{v}_n \\ = \mathbf{J}^H \mathbf{F}_\alpha \mathbf{H}_n \mathbf{F}_{-\alpha} \mathbf{J} \mathbf{d}_n + \mathbf{F}_\alpha \mathbf{v}_n \\ = \mathbf{J}^H \mathbf{H}_{df} \mathbf{J} \mathbf{d}_n + \mathbf{F}_\alpha \mathbf{v}_n \quad (5)$$

According to the frequency channel matrix  $\mathbf{H}_{df} = \mathbf{F}_{-\alpha} \mathbf{H}_n \mathbf{F}_\alpha$ , if the channel is time invariant,  $\mathbf{H}_n$  is a convolutional matrix and the band structure of  $\mathbf{H}_{df}$ , therefore, will be diagonal. However, the band structure of  $\mathbf{H}_{df}$  over doubly selective channel is not diagonal, and energy spreads into adjacent subcarriers, contributing to ICI. The structure of  $\mathbf{H}_{df}$  becomes banded, with nonzero off-diagonal coefficients, most of which concentrates around the main diagonal. Notice that,

the complexity grows linearly with the length of the OFDM block, thus introducing the requirement of low-complexity equalization. The binary matrix not only mitigates the adjacent channel interference, but also eliminates coupling components at the upper right and bottom left corner of  $\mathbf{H}_{df}$ .

Due to the fact that the majority of components are distributed around the main diagonal, masked channel matrix is applied to reduce the computational complexity of  $\mathbf{H}_{df}$ , defined as

$$\mathbf{B} = \begin{cases} [\mathbf{H}_{fm}]_{i, <i+u>_{N+1}}, & -U \leq u \leq U \\ 0, & \text{otherwise} \end{cases} \quad (6)$$

where  $U$  could be selected to be proportional to the Doppler bandwidth, confining the non-zero elements to be confined to  $U$  off-diagonals above and below the main diagonal of  $\mathbf{H}_{fm}$ .

#### D. Selection of optimal order

As mentioned above, the off-diagonal coefficients representing ICI spread around the main diagonal of  $\mathbf{H}_{df}$ , and the allocation of its power changes according to fractional order  $\alpha$  of DFrCT-OFDM. When the system reaches its optimal order, the coefficients on or along the main diagonal will be the largest, which means non-diagonal elements contributes to the least ICI. Consequently, the sub channel carrier frequencies variation matches the high time-frequency distortion of the channel. In this paper, the search of optimal order  $\alpha_{opt}$  is based on exploiting carrier-to-interference ratio (CIR), defined as

$$CIR = \frac{\sum_{n=1}^N \|\mathbf{B}(n,n)\|^2}{\sum_{k=1, k \neq n}^N \|\mathbf{B}(n,k) - \mathbf{B}(n,n)\|^2} \quad (7)$$

where  $\mathbf{H}_{df}$  is replaced by the masked channel matrix  $\mathbf{B}$ , as mentioned in 2.3. Subsequently, the optimal order can be estimated as a maximum CIR problem, as follows

$$\alpha_{opt} = \arg\{\alpha \in [-1, 1] | [CIR]\} \quad (8)$$

The iterative search approach can be applied within the range of  $\alpha$  from  $-1$  to  $1$ . It is obvious that the selection of optimal order  $\alpha$  depends on the channel properties, including number of subcarriers  $N$ , Doppler shift, number of resolvable paths and channel power delay profile. The optimal order  $\alpha_{opt}$  searched at the receiver is then sent back to the transmitter as illustrated in Fig 1.

#### E. Tikhonov regularization based turbo MMSE equalization

Turbo equalization is a Bayesian iterative method that is obtained by estimating prior information, including the mean  $\mathbf{M} = [\bar{\mathbf{m}}_1 \dots \bar{\mathbf{m}}_N]$  and the auto-variance  $\mathbf{V} = \text{diag}[\vartheta_1 \dots \vartheta_N]$  of the symbols. Initially, there is no prior information, so we assume for all the symbols, the linear MMSE estimate of the  $n^{\text{th}}$  subcarrier is denoted as

$$\hat{\mathbf{s}}_n = \bar{\mathbf{m}}_n + \mathbf{G}_n^H (\mathbf{R}_{df} - \mathbf{B}\mathbf{M}) \quad (9)$$

Where the coefficients of  $n^{\text{th}}$  subcarrier is denoted as [6]

$$\mathbf{g}_n = (\mathbf{B}\mathbf{V}\mathbf{B}^H + \gamma\mathbf{I})^{-1} \mathbf{b}_k \vartheta_n \quad (10)$$

where  $\mathbf{b}_k$  is the  $k^{\text{th}}$  column of  $\mathbf{B}$ , and  $\gamma$  denotes the inverse of

signal to noise ratio ( $\text{SNR}^{-1}$ ).

However, the doubly selective channels could be highly ill-conditioned, which means that the ratio between the largest eigenvalue and the smallest eigen value of the channel matrix may become very large. Therefore, at high SNR, the inverse matrix contained in the MMSE formula is subject to significant numerical errors, contributing to less stable of equalization. In order to address this problem, a Tikhonov regularization based MMSE algorithm is proposed which replaces the inverse of Signal to noise ( $\text{SNR}^{-1}$ ) ratio by inversed modified signal to interference (SINR) ratio [12], which is described as follows

$$SINR = \frac{1 - P_o}{P_o + \gamma} \quad (11)$$

Where  $P_o$  represents the out of band power, defined as

$$P_o = \frac{\|\mathbf{H}_{df} - \mathbf{B}\|^2}{N_a} \quad (12)$$

where  $N_a$  represents the uncompensated ICI that falls in a specific data subcarrier. The total uncompensated ICI must be divided by the number  $N_a$  of data subcarriers. Equation (10) therefore, can be rewritten as

$$\mathbf{G}_n = (\mathbf{B}\mathbf{V}\mathbf{B}^H + SINR * \mathbf{I})^{-1} \mathbf{b}_k \vartheta_n \quad (13)$$

In addition, the matrix inversion of a banded matrix in the MMSE equalizer leads to a significant increase in computational complexity.  $\mathbf{LDL}^H$  factorization equalization [3] is applied to exploit the band structure of  $\mathbf{G}_n$ .

Based on the output of equalizer  $\hat{\mathbf{s}}_n$ , the extrinsic log-likelihood ratio (LLR) in Figure 1 is  $\Delta\mathbf{L}(\hat{\mathbf{s}}_n)$ , which represents the soft information based on the maximum a posteriori (MAP) criterion. Assuming that the estimate  $\hat{\mathbf{s}}_n$  meets the requirement of conditionally Gaussian distribution with probability density function (PDF), then  $\Delta\mathbf{L}(\hat{\mathbf{s}}_n)$  may be written as

$$\Delta\mathbf{L}(\hat{\mathbf{s}}_n) = \mathbf{p}(\hat{\mathbf{s}}_n | \mathbf{s}_n) = \frac{1}{\pi\sigma_n^2} \exp\left(-\frac{|\hat{\mathbf{s}}_n - \mu_n|^2}{\sigma_n^2}\right) \quad (14)$$

where  $\mu_n$  and  $\sigma_n^2$  represent the mean and variance, which could be denoted as

$$\mu_n = E\{\hat{\mathbf{s}}_n | \mathbf{s}_n\} = \bar{\mathbf{m}}_n + \mathbf{G}_n^H \mathbf{b}_k (\mathbf{s}_n - \bar{\mathbf{m}}_n), \quad \text{with } \mathbf{s}_n = \pm 1 \\ \sigma_n^2 = \text{Cov}(\hat{\mathbf{s}}_n, \hat{\mathbf{s}}_n | \mathbf{s}_n) \quad (15)$$

The a posteriori LLR  $\mathbf{L}(\mathbf{s}_n | \hat{\mathbf{s}}_n)$  is obtained by the sum of the extrinsic LLR  $\Delta\mathbf{L}(\hat{\mathbf{s}}_n)$  and the a priori LLR  $\mathbf{L}(\mathbf{s}_n)$  as follows [7]:

$$\frac{P(\mathbf{s}_n = +1 | \hat{\mathbf{s}}_n)}{P(\mathbf{s}_n = -1 | \hat{\mathbf{s}}_n)} = \ln \frac{p(\mathbf{s}_n | \mathbf{s}_n = +1)}{p(\mathbf{s}_n | \mathbf{s}_n = -1)} + \frac{P(\mathbf{s}_n = +1)}{P(\mathbf{s}_n = -1)} \quad (16)$$

From the input data it is noted that the a priori LLR is available before the equalization. The calculation of the updated mean and auto-variance of the estimated symbol is as follows [8]:

$$\bar{\mathbf{m}}_{n, \text{new}} = \tanh(\mathbf{L}(\mathbf{s}_n | \hat{\mathbf{s}}_n) / 2) \\ \vartheta_{n, \text{new}} = 1 - (\bar{\mathbf{m}}_{n, \text{new}})^2 \quad (17)$$

After that, the updated means  $\bar{\mathbf{m}}_{n, \text{new}}$  and variance  $\vartheta_{n, \text{new}}$  of current iteration are feedback to equalization, ready for next iteration as illustrated in Figure 2. The posteriori LLR of current iteration  $\mathbf{L}(\mathbf{s}_n | \hat{\mathbf{s}}_n)$  used an a priori LLR for the next iteration  $\mathbf{L}_{\text{new}}(\mathbf{s}_n)$ . In the system, the extrinsic soft information LLR  $\Delta\mathbf{L}(\hat{\mathbf{s}}_n)$  calculated from equalization is sent to convolutional decoder for further update of LLR information

mean and auto-variance.

### III. Simulation Result and Discussion

The DFrCT-Turbo was simulated, and its performance compared to that from the turbo equalization based on conventional OFDM and DFrCT-OFDM. The channel in this simulation is selected as doubly selective Rayleigh fading channel, with perfect channel state information. In addition, a rate 1/2 convolution coding is incorporated to improve the performance.

#### A. Simulation set up

The number of subcarriers is  $N=128$ , of which 96 are active and the length of cyclic prefix is  $L=8$ . The normalized Doppler frequency is  $sf_d = 0.30\Delta f$ , where  $\Delta f$  is the normalized subcarrier spacing. The UWA channel is modeled as Rayleigh fading channel with exponential multipath intensity profile of  $[-7.2, -4.2, -6.2, -10.5, -12.2, -14.0]$  dB and time delay profile of  $[0, 0.02, 0.05, 0.16, 0.23, 0.5]$  ms. The signal to noise ratio (SNR) ranges from 0 to 80dB. In addition, the low complexity equalizer is set at  $U=6$  and the number of Monte Carlo runs is 10000. [13]

#### B. Simulation performance analysis

Figure 2 compares the BER performance of the DFrCT-Turbo, conventional OFDM scheme with Tikhonov regularization based turbo MMSE equalization and DFrCT-OFDM. The optimal order obtained is 0.95. It can be seen that performance of DFrCT-Turbo is superior to that of conventional OFDM with a BER improvement of 1dB. The reason of positive results is that non-zero band of the channel matrix in the fractional domain is lower than the conventional frequency domain, especially in doubly selective channel. In other words, the allocation of the band of conventional OFDM distributes over more frequencies than that of DFrCT, which means the energy of  $H_{df}$  based on DFrCT concentrates closer to the diagonal, contributing to less ICI and better BER performance.

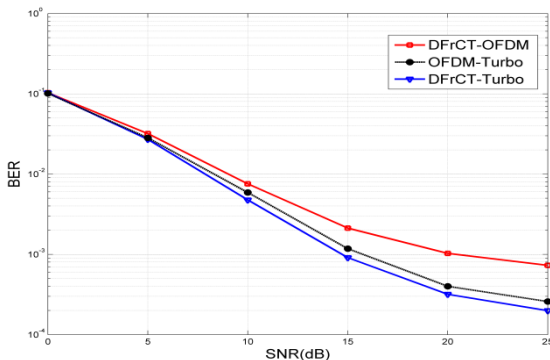


Figure2: BER of DFrCT-Turbo and OFDM-Turbo, and DFrCT-OFDM

Figure 2 shows that the DFrCT-Turbo is superior to DFrCT-OFDM by approximately up to 5dB for SNR values greater than 15dBs, This performance improvement is attributed to the iterative performance of Tikhonov regularization based turbo MMSE equalization.

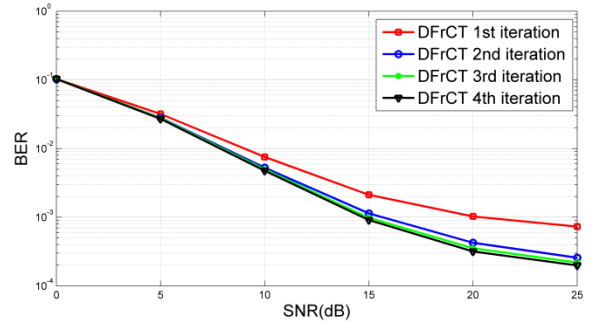


Figure3: BER of DFrCT-Turbo from iteration 1 to 4

Figure 3 shows the performance of the proposed DFrCT-Turbo at different equalization iterations. It can be seen that the BER improves as the number of iteration increases converging to the optimum at the 4<sup>th</sup> iteration.

Figure 4 improves the performance of the proposed turbo equalization of DFrCT-Turbo by implementing error correction coding, which is a rate 1/2 convolutional code with generator matrix  $[1 \ 0 \ 1, 1 \ 1 \ 1]$  and random interleaving. The iteration number is set at 2. It is observed that a performance improvement of up to 30dB for SNR values at 15dBs can be achieved using ECC. The BER of DFrCT with coding decreases to 0 when SNR value is over 15dBs, so it is not displayed in Figure 4.

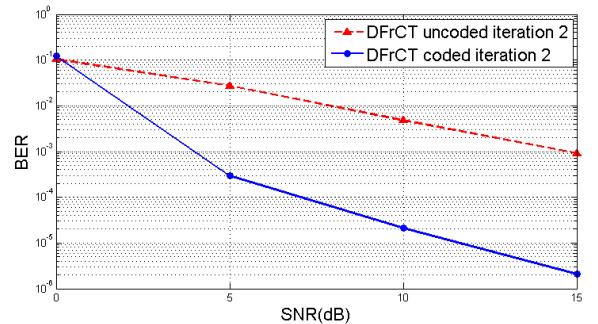


Figure4: Comparison of BER of DFrCT with or without convolutional coding

### IV. Conclusion

A novel DFrCT-Turbo system based on the hybrid use of the Discrete Fractional Cosine Transform (DFrCT), Tikhonov regularization based turbo MMSE equalization and low complexity banded MMSE equalization, and has been presented. The simulation results demonstrate that ICI is significantly mitigated under doubly selective channel compared to the conventional OFDM at moderate complexity providing an improvement in the overall Bit Error Rate.

### ACKNOWLEDGEMENT

This work was supported by the Engineering and Physical Sciences Research Council (EPSRC) Grant number

#### REFERENCE

- [1] M. Stojanovic and J. Preisig, "Underwater acoustic communication channels: Propagation models and statistical characterization," *IEEE Commun. Mag.*, vol. 47, no. 1, pp. 84-89, Jan. 2009.
- [2] Y. M. Aval, and M. Stojanovic, "Differentially Coherent Multichannel Detection of Acoustic OFDM Signals," *IEEE Journal of Oceanic Engineering.*
- [3] L. Rugini, P. Banelli, and G. Leus, "Low-complexity banded equalizers for OFDM systems in Doppler spread channels," *EURASIP Journal on Applied Signal Processing*, vol. pp. 1-13, 2006.
- [4] B. Li, S. Zhou, M. Stojanovic, L. Freitag, and P. Willett, "Multicarrier Communication over underwater acoustic channels with non-uniform Doppler shifts," *IEEE J. Ocean. Eng.*, vol. 33, no. 2, pp. 198-209, Apr. 2008.
- [5] J. Huang, S. Zhou, J. Huang, C.R. Berger, and P. Willett, "Progressive inter-carrier interference equalization for OFDM transmission over time-varying underwater acoustic channels," *IEEE J. Sel. Topics in signal process.*, vol. 5, no. 8, pp. 1524-1536, 2011.
- [6] K. Fang, L. Rugini, and G. Leus, "Low-complexity block turbo equalization for OFDM systems in time-varying channels," *IEEE Trans. Signal Process.*, vol.56, no. 11, pp. 5555-5566, Nov. 2008.
- [7] P. Schniter, "Low-complexity equalization of OFDM in doubly selective channels," *IEEE Transactions on Signal Processing*, vol. 52, no. 4, pp. 1002-1011, April 2004.
- [8] S. Ahmed, M. Sellathurai, S. Lambotharan, and J. A. Chambers, "Low complexity iterative method of equalization for single carrier with cyclic prefix in doubly selective channels," *IEEE Signal Process. Letter.*, Vol. 13, no. 1, pp. 5-8, Jan. 2006.
- [9] A. Solyman, S. Weiss and J.J. Soraghan, "Hybrid DFrFT and FFT based Multimode Transmission OFDM System." *presented at the ICEENG*, 2012 Cairo, Egypt.
- [10] A. Solyman, S. Weiss and J.J. Soraghan, "A Novel Orthogonal Chirp Division Multiplexing (OCDM) Multicarrier Transceiver Based on the Discrete Fractional Cosine Transform." *Presented at the MIC-WCMC*, 2013 Valencia, Spain, 2013
- [11] P. Soo-Chang and D. Jian-Jiun, "Fractional cosine, sine, and Hartley transforms," *Signal Processing, IEEE Transactions on*, vol. 50, pp. 1661-1680, 2002.
- [12] L. Rugini, P. Banelli, and G. Leus, "OFDM communications over time-varying channels", *Chapter7 of Wireless Communications over Rapidly Time-Varying Channels*, eds. F. Hlawatsch and G. Matz, Academic Press, 2011.
- [13] A. Solyman, S. Weiss and J.J. Soraghan, "Low-Complexity LSMR Equalization of FrFT-Based Multicarrier Systems in Doubly Dispersive Channels," *presented at the ISSPIT 2011*, Bilbao Spain, 2011.

# Practical Identification of Specific Emitters used in the Automatic Identification System

Takashi Iwamoto

Advanced Technology R&D Center, Mitsubishi Electric Corporation  
Amagasaki, Hyogo 661-8661, Japan  
Email: Iwamoto.Takashi@bp.MitsubishiElectric.co.jp

**Abstract**—There are increasing demands for radio systems to work in more hostile conditions these days. Communication protocols used already by many users, however, need considerable efforts to be modified to increase resistance against deception. Identification technologies of emitters are expected to offer an additional layer to prevent fraudulent devices from accessing wireless systems. They have been developed to distinguish emitters even of the same product based only on emitted signals as well as to handle a large variety of signals efficiently. In this paper a hierarchical identification method consists of a classification of signals into subclasses and an identification of signals in the same subclass is presented; modulation symbol sequences are utilized to classify Automatic Identification System signals into subclasses efficiently and an identifier of a set of binary support vector machines is trained on one of the hardest subclass of signals emitted by the six similar emitters mounted on the six boats. These are the largest number of boats servicing in the same regular line in Japan. Experimental results of identification show practical mean accuracy of 97.6% under a controlled S/N, which corresponds to that of signals sampled over a distance of 100 km.

## I. INTRODUCTION

There are increasing demands for radio systems to work in more hostile conditions these days. Communication protocols used already by many users, however, need considerable efforts to be modified to increase resistance against deception. For example, the Automatic Identification System (AIS) [1] was originally designed for collision avoidance and has been spread widely to be regarded as a key part for achieving maritime awareness [2], [3]. Nowadays AIS faces possibility of counterfeited information emission [4] since whole codes including the identifier of the emitter, the Maritime Mobile Service Identity, are published.

Identification technologies of emitters, sometime referred to as Specific Emitter Identification, are expected to offer an additional layer to prevent fraudulent devices from accessing wireless systems. They have been developed to distinguish emitters even of the same product based only on emitted signals as well as to handle a large variety of signals efficiently. When an emitter is identified different from an authentic one, it is difficult to be camouflaged. Early ideas of identifications are shown in [5], [6]. Signals of different modulations are classified with Support Vector Machine (SVM) [7] and three cell phones made by different manufactures are classified with Multiple Discriminant Analysis [8]. A pair of AIS emitters of the same product were identified with the optimal linear discriminant function [9].

To accomplish more practical identification of a larger number of emitters, a hierarchical identification method is presented in this paper. Pattern rationals are introduced based on modulation symbol sequences to classify AIS signals into subclasses efficiently. Fine identifier of signals of the same symbol sequence using a set of  $\nu$ -SVM [10] with a linear kernel function is trained on one of the hardest subclass of signals emitted by the six emitters mounted on the six similar boats. This is the largest number of the boats servicing in the same line in Japan. Experimental results of identification show practical accuracy of 97.6% under the controlled S/N, which corresponds to that of signals sampled over a distance of 100 km.

## II. CHARACTERISTICS OF AIS SIGNALS

AIS emitters emit bursts of radio waves modulated with the Gaussian Minimum Shift Keying (GMSK) modulation [11] to broadcast data bits at a rate of 9600 bits per second. The timing of signal is quantized with a bit period  $T = 1/9600 \simeq 104.17 \times 10^{-6}$  second. During the initial  $6T$  periods of a burst, no frequency modulations are specified. Only the transient power of a signal is defined to be larger than  $-50$  dB of a steady state power  $P_{ss}$ . After the  $6T$  periods, 24 bits of Training Sequence (TS) start and 8 bits of Start Flag (SF) follow. The power of the first and the second TS bits must be contained in the range from  $-3$  dB to  $+1.5$  dB of  $P_{ss}$  and thereafter until the end of a burst in the range from  $-1$  dB to  $+1.5$  dB of  $P_{ss}$ . Both TS and SF sequences are common to all emitters. Each bit sequence is encoded into a sequence of two modulation frequency states by the Non Return Zero Inverted (NRZI) encoding; a waveform is specified as giving a change in the frequency corresponding to a data bit value of zero and no change corresponding to a data bit value of one.

From a frequency modulation sequence a physical signal is generated by GMSK. A waveform of an amplitude  $a$  and a center frequency  $f_c$  modulated with GMSK at time  $t$  is expressed by

$$r(t) = a \exp(i(2\pi f_c t + \phi(t, \mathbf{s}))), \quad (1)$$

where

$$\phi(t, \mathbf{s}) = 2\pi h \sum_{k \in K} s_k q(t - kT) \quad (2)$$

is the so called *excess phase* constructed from a modulation index  $h$  and a modulation symbol sequence  $\mathbf{s} = (\dots, s_{k-1}, s_k, s_{k+1}, \dots)$  with  $s_k \in \{-1, 1\}$  for  $k \in K$ . The

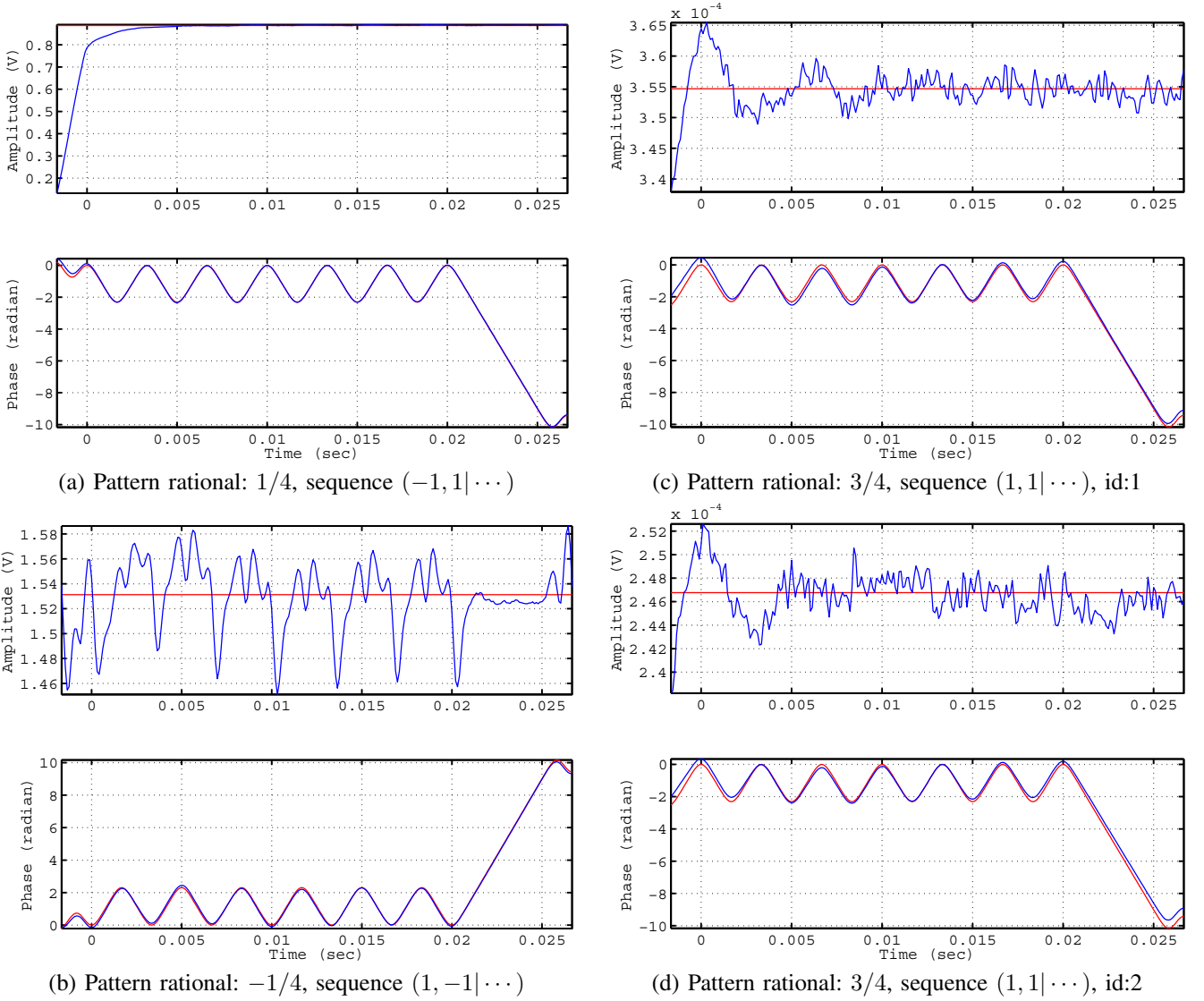


Fig. 1. Waveforms of signals emitted by four AIS emitters. Amplitudes (in upper panels) and phases (in lower panels) are plotted against time whose origin is set to the start of the Training Sequence. Signals (a) and (b) are sampled through line and (c) and (d) are through antenna in field. Averaged amplitudes and analytic phase waveforms are also plotted in red lines.

phase response function  $q(t) = \int_{-\infty}^t g(\tau) d\tau$  is derived from the frequency response function

$$g(t) = \frac{\pi h}{2T} (\operatorname{erfc}(T_-) - \operatorname{erfc}(T_+)), \quad (3)$$

where  $T_{\pm} = A(t \pm T/2) / (\sqrt{2}T)$  (double-sign corresponds) with  $A = 2\pi BT / \sqrt{\ln 2}$ , the constant  $B$  represents the bandwidth of the Gaussian filter at  $-3$  dB of the maximum, and the complementary error function is defined as

$$\operatorname{erfc}(x) = \frac{2}{\pi} \int_x^{\infty} \exp(-\tau^2) d\tau. \quad (4)$$

By carrying this integration, the phase response function is

represented as

$$q(t) = \frac{\pi h}{\sqrt{2}A} \left( \operatorname{erfc}(T_-)T_- - \operatorname{erfc}(T_+)T_+ - \frac{1}{\sqrt{\pi}} \{ \exp(-T_-^2) - \exp(-T_+^2) \} \right) \quad (5)$$

and shows an infinite but exponential-decreasing impulse response time.

Throughout this paper, physical signals are sampled by a 14-bit A/D converter of our Tektronix WCA280A communication analyzer into in-phase and quadrature (I-Q) components at a rate of 320 k samples per second. A signal composed of I-Q components is regarded as a vector of real components. Examples of sampled waveforms emitted by four emitters are shown in Fig. 1; each waveform is displayed by both an amplitude graph and a phase graph against time whose origin is set to the beginning of TS. The plot range of time

corresponds to a duration of two preceding bits, TS, and SF. The numerically averaged amplitudes of measured signals are plotted by a red lines in amplitude graphs. An approximating phase waves forms defined by the equation (1) with phenomenological modulation sequences chosen manually are plotted by red lines in phase graphs.

As seen in Fig. 1, phases graphs before TS are well described by analytic waveforms, though not specified explicitly. It is natural to assume that physical signals preceding to TS are generated with certain modulation symbols to fill the impulse response time of the implemented GMSK filter. We denote a sequence of modulation symbols as  $(\dots, s_{-2}, s_{-1} | s_0, s_1, \dots, s_{31}, \dots)$ , where the subsequence  $(s_0, s_1, \dots, s_{23})$  and  $(s_{24}, s_{25}, \dots, s_{31})$  correspond to TS and SF respectively. A subsequence  $(\dots, s_{-2}, s_{-1})$  corresponds to an phenomenological sequence of pre-modulation symbols. There are two frequency modulation sequences onto which TS and SF can be encoded by NRZI depending on the sign of the previous symbol  $s_{-1}$ , as seen in the sub figures (a) and (b).

The length of a phenomenological sequence before TS varies as a signal to noise ratio changes observable length of a phenomenological sequence. For example, the measured signal shown in the sub figure (a), it is difficult to estimate  $(s_{-6}, s_{-5}, \dots, s_{-3})$  due to its small amplitude. A pattern rational is introduced as

$$P = \sum_{k=1}^6 2^{-k} s_{-k} \quad (6)$$

to represent a phenomenological sequence and to keep values close even when large noises make observation of a phenomenological sequence of modulation symbols in a early position difficult. Up to the present time, we have observed more than three thousand bursts and pattern rationals of  $-31/32, -15/16, -11/32, -5/16, -1/4, 1/4, 3/4, 15/16,$  and  $31/32$ .

As a practical test of identification, AIS signals including ones emitted by the six emitters mounted on the six sister boats in the same service shown by dashed line in Fig. 2 are sampled through antenna located at the two positions indicated by triangles; this is the largest number of the ships in the same regular service in Japan. All signals emitted by the six sister boats have the same pattern rational and look similar; two signals emitted by two emitters are shown sub figures (c) and (d) in Fig. 1 respectively. They are well assumed to be emitted by emitters of the same product judged from the previous observation [9].

As seen in Fig. 1, difference between signals of different pattern rationals have larger vector norm in  $L^2$  sense than that between signals of the same pattern rationals. Thus the pattern rationals work for efficient screening of signals.

### III. IDENTIFICATION WITH SUPPORT VECTOR MACHINE

As shown in sub figures (c) and (d) in Fig. 1, a pair of emitters can emits almost identical radio waves with subtle difference. To achieve fine classification  $\nu$ -SVM [10] in widely used library [12] is adopted.

$\nu$ -SVM is a binary classifier of an input vector  $\mathbf{x}$  to an indicator  $y$  optimized over a training set of sam-

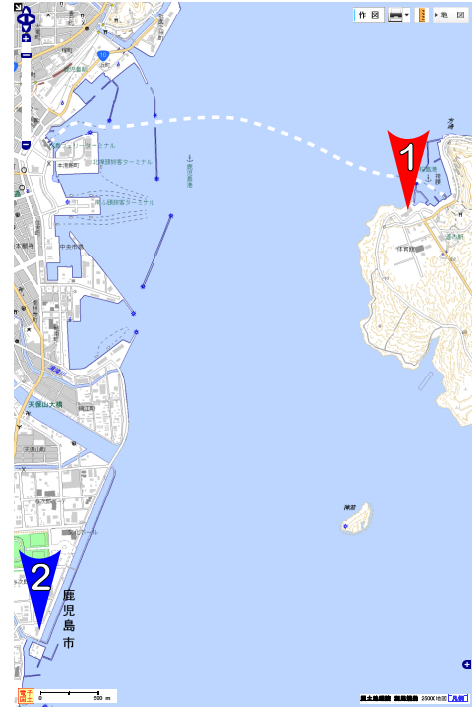


Fig. 2. The regular line in which the six sister boats service is plotted by a white dashed line and two antenna positions are indicated by triangles labeled with 1 and 2 respectively on a map, whose background map data, symbols, and labels are distributed by Denshi-Kokudo, the electronic mapping system by Geospatial Information Authority of Japan.

ples  $\{(\mathbf{x}_j, y_j) \in \mathbb{R}^N \times \{-1, 1\} | j \in J\}$ . The classifier is constructed in a form

$$\text{sgn}(f(\mathbf{x})) = \text{sgn} \left( \sum_{j=1}^J y_j \alpha_j K(\mathbf{x}_j, \mathbf{x}) + b \right) \quad (7)$$

with a kernel function  $K : \mathbb{R}^N \times \mathbb{R}^N \rightarrow \mathbb{R}$  and the solution  $\alpha$  of the optimization problem defined with a parameter  $\nu$  as

$$\begin{aligned} \min_{\alpha} \quad & \frac{1}{2} \alpha^T Q \alpha \\ \text{subject to} \quad & 0 \leq \alpha_j \leq 1/J \\ & \sum_j \alpha_j \geq \nu \\ & \sum_j y_j \alpha_j = 0, \end{aligned} \quad (8)$$

where the  $(i, j)$ -component of the matrix  $Q \in \mathbb{R}^{J \times J}$  is defined by  $Q_{i,j} := y_i y_j K(\mathbf{x}_i, \mathbf{x}_j)$ . It is known that the number of non-zero components  $\{\alpha_j\}$  is limited and a vector  $\mathbf{x}_j$  corresponding to a non-zero component is called a support vector. The parameter  $\nu$  is also known to control the upper bound of the ratio of training errors as well as the lower bound of the ratio of the number of the support vectors to realize a practical classifier.

When applying a SVM to distinguish a pair of almost identical signals,  $\mathbf{x}$  and  $\mathbf{x} + \delta\mathbf{x}$ , values  $f(\mathbf{x})$  and  $f(\mathbf{x} + \delta\mathbf{x})$  are expected to be opposite sign. A linear kernel  $K(\mathbf{x}, \mathbf{x}') = \langle \mathbf{x}, \mathbf{x}' \rangle$  is adopted in this paper due to a useful relation  $f(\mathbf{x} + \delta\mathbf{x}) = f(\mathbf{x}) + f(\delta\mathbf{x})$  to cancel out the first term in

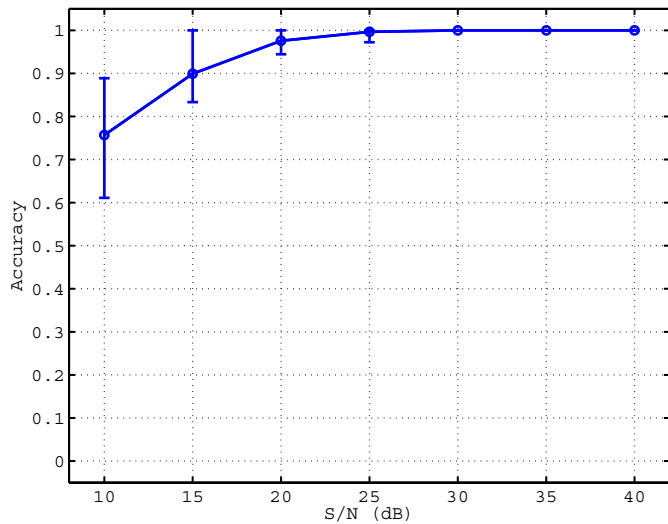


Fig. 3. Mean accuracy of identification of signals over 16 random sequences are plotted with circle marks and minimum and maximum values are indicated by bars against the S/N ratios of signals, respectively.

the right side, which is numerically dominant, by a constant  $b$  and to avoid numerical difficulty for precise evaluation of output signs.

There are several methods to construct a multi-class classifier from a set of binary classifiers. The so-called one-to-one support vector machine is reported to show good performance [13] and is adopted in the simulation as follows.

From a training set of a pair of the  $m$ -th and the  $n$ -th emitters, a classifier  $\text{sgn}(f_{m,n}(\mathbf{x}))$  is optimized as described above. When classify a new input  $\mathbf{x}$ , the result of each binary classifier is regarded as a vote and the indicator that collect the largest number of votes is selected.

To evaluate identification of real signals in field, six signals from each of the six emitters sampled through antenna at position 1 are added with white Gaussian noises to have S/N ratio of 40 dB and constitute a training set. A 6-class classifier is constructed from 15 ( $= \binom{6}{2}$ ) binary classifiers that are optimized on the training set. A evaluation set are generated from six signals from each of the six emitters sampled through antenna at the position 2. S/N ratios of raw signals are more than 50 dB except ones from one ship that turned out to be in different service positioned farther from the antenna than others, of more 44.5 dB. From each signal samples for evaluation are generated with additional white Gaussian noises of 16 different random seeds to control S/N values from 10 dB to 40 dB, respectively.

The classifier trained on the training set is applied on the evaluation set. Accuracy of identification of samples at S/N ratios from 10 dB to 40 dB are measured over 16 random seeds. Mean values are plotted with circle marks in Fig. 3. Both minimum and maximum values among random sees are also indicated by bars. Practical accuracy 0.976 of identification of signals are observed against the 20dB S/N. This ratio is converted by simple geometric calculation to an equivalent distance of more than 100 km between the antenna and the emitters.

## IV. CONCLUSION

In this paper practical identification of emitters is investigated. A hierarchical identification method consists of efficient screening based on the pattern rationals and fine identification using a  $\nu$ -SVM classifier with a linear kernel composed into a multi-class classifier with one-vs-one scheme is presented. Physical signals emitted by emitters mounted on the six sister boats are collected in the two positions to train and to evaluate the classifier. The training set are composed of six signals sampled from each boats near the regular service line. The evaluation set of signals are generated from signals sampled about 5 km away from the regular service line. S/N ratios of raw signals are more than 50 dB (except ones from one ship that turned out to be in different service and was positioned farther than others from the antenna of more than 44.5 dB). From each signal samples for evaluation are generated with additional white Gaussian noises of 16 different random seeds to control S/N values from 10 dB to 40 dB, respectively. Practical mean accuracy 97.6% of identification of signals at a 20dB S/N are observed. This ratio is converted by simple geometric calculation to an equivalent distance of more than 100 km between the antenna and the emitters. More tuning of classifiers is also helpful to increase accuracy.

## REFERENCES

- [1] *Technical characteristics for an automatic identification system using time-division multiple access in the VHF maritime mobile band*, International Telecommunication Union (ITU) Recommendation M.1371-4, 2010.
- [2] J. E. Lake (coordinator), "Border and transportation security: overview of congressional issues," *Congressional Research Service Report for Congress*, Order Code RL32705, 2004.
- [3] F. Jangal, M. A. Giraud, M. Morel, J. P. Mano, A. Napoli, and A. Littaya, "Sense, enrich and classify: the ScanMaris workshop for assessment of vessel's abnormal behavior in the EEZ," in *Proc. of OCEANS'08*, 2008, pp. 15–18.
- [4] M. Balduzzi, A. Pasta, and K. Wilhoit, "A security evaluation of AIS automated identification system," in *Proc. of Annual Computer Security Applications Conference (ACSAC)*, 2014, pp. 436–445.
- [5] P. J. Ferrell, "Method and Apparatus for Characterizing a Radio Transmitter," U. S. Patent 5,005,210, filed in 1987.
- [6] A. L. Roe, "Artificial neural networks for ESM emitter identification-an initial study," in *IEE Colloquium on Neural Networks for Systems*, 1991.
- [7] G. Zhang, W. Jin, and L. Hu, "Radar emitter signal recognition based on support vector machines," in *Proc. of Control, Automation, Robotics and Vision Conference (ICARCV)*, 2004, pp. 826–831.
- [8] D. R. Reising, M. A. Temple, and M. J. Mendenhall, "Improving intra-cellular security using air monitoring with RF fingerprints," *IEEE Wireless Communications and Networking Conference, WCNC 2010*, pp. 1–6.
- [9] T. Iwamoto, "Radiometric Identification of Emitters in the Automatic Identification System," in *Proc. of IEEE Military Communications Conference (MILCOM) 2013*, pp. 447–452.
- [10] B. Schölkopf, A. Smola, R. C. Williamson, and P. L. Bartlett. "New support vector algorithms," *Neural Computation*, vol. 12, pp. 1207–1245, 2000.
- [11] K. Murota and K. Hirade, "GMSK modulation for digital mobile radio telephony," *IEEE Transactions on Communications*, vol. 29, no. 7, pp. 1044–1050, 1981.
- [12] C.-C. Chang and C.-J. Lin, "LIBSVM: a library for support vector machines," in *ACM Transactions on Intelligent Systems and Technology (TIST)*, 2011, vol. 2, no. 3, pp. 27–66.
- [13] C.-W. Hsu and C.-J. Lin, "A comparison of methods for multiclass support vector machines," *IEEE Transactions on Neural Networks*, vol. 13, pp. 415–425, 2002.

## Author Index

- A**
- Ahmed, Sajid ..... 36  
 Ahrens, Andreas ..... 50  
 Alouini, Mohamed-Slim ..... 36  
 Andrecki, Marian ..... 1
- B**
- Bhatia, Vimal ..... 41, 84, 89  
 Bhaumik, Shovan ..... 99, 109  
 Bikdash, Marwan ..... 94  
 Blair, Calum ..... 16  
 Bridle, Helen ..... 118  
 Bucciarelli, Marta ..... 31
- C**
- Cao, Jianlin ..... 21  
 Chambers, Jonathon A. .... 11, 132  
 Chen, Li ..... 137  
 Chen, Yixin ..... 147  
 Cheng, Chi ..... 6  
 Clamante, Carmine ..... 147  
 Clark, Daniel E. .... 1, 26, 118  
 Clemente, Carmine ..... 21, 65  
 Contu, Micaela ..... 31  
 Corr, Jamie ..... 113
- D**
- Davies, Mike ..... 60  
 de Lamar, Rodrigo C. .... 55  
 Delande, Emmanuel D. .... 1  
 Di Bisceglie, Maurizio ..... 65  
 Dong, Xiao ..... 79  
 Dong, Jing ..... 132
- F**
- Feng, Pengming ..... 11
- G**
- Gaglione, Domenico ..... 21  
 Galdi, Carmela ..... 65  
 Guo, Fucheng ..... 128
- H**
- Hopgood, James R. .... 123  
 Houssineau, Jeremie ..... 1, 118
- I**
- Ilioudis, Christos V. .... 21
- J**
- Iwamoto, Takashi ..... 152  
 Izzo, Alessio ..... 65
- K**
- Karagol, Serap ..... 94  
 Karlsen, Brian L. .... 104  
 Ketpan, Watcharapong ..... 74  
 Kumar, Nagendra ..... 89  
 Kumar Singh, Abhinoy ..... 99, 109  
 Kumar Tomar, Nutan ..... 99
- L**
- Leng, Mei ..... 6  
 Liguori, Marco ..... 65  
 Liu, Yang ..... 128  
 Lochmann, Steffen ..... 50  
 Lombardo, Pierfrancesco ..... 31
- M**
- Madia, Francesco ..... 31  
 Marques, Paulo ..... 70  
 Massardo, Marco ..... 31  
 McDougall, Craig ..... 118  
 McGrath, John S. .... 118  
 McKenna, Isabella ..... 118  
 McWhirter, John G. .... 113  
 Miller, Steven ..... 142  
 Mitra, Rangeet ..... 41  
 Mulgrew, Bernard ..... 26
- N**
- Naqvi, Syed Mohsen ..... 11  
 Nielsen, Esben ..... 104
- O**
- Ozgonenel, Okan ..... 94
- P**
- Pailhas, Yan ..... 46  
 Pedersen, Morten T. .... 104  
 Persico, Adriano Rosario ..... 21  
 Petillot, Yvan ..... 46

Phonsri, Seksan.....	74
Proudlar, Ian K. ....	113

**Q**

Qian, Rongrong .....	74
Quitin, Francois .....	6

**R**

Radhakrishnan, Rahul.....	99
Radius, Andrea .....	70
Razul, Sirajudeen Gulam.....	6
Robertson, Neil M. ....	16, 123
Ruan, Hang .....	55

**S**

Samson See, Chong Meng.....	6
Sandmann, Andre .....	50
Schlangen, Isabel.....	118
Sellathurai, Mathini .....	74
Shukla, Sidharth.....	84
Soraghan, John.....	21, 65, 147
Spanias, Andreas .....	142
Stallone, Rossella.....	31
Sthapit, Saurav.....	123

**T**

Tadiparthi, Satish.....	94
Tay, Wee Peng.....	6
Thompson, John.....	16
Thompson, Keith .....	113
Thompson, John.....	123
Tobin, Rachael.....	118
Tonolini, Francesco .....	118
Tsimenidis, Charalampos .....	137

**U**

Uney, Murat.....	26
------------------	----

**W**

Wang, Wenwu .....	11, 132
Weiss, Stephan.....	113, 147
Wu, Di .....	60

**Y**

Yaghoobi, Mehrdad .....	60
Yildiz, Dogan.....	94

**Z**

Zhang, Yunhua .....	79
Zhang, Min .....	128
Zhang, Xue .....	142
Zhao, Yuanyi .....	137

# Sensor Signal Processing for Defence Conference

22 - 23 September  
Royal College of Surgeons  
Edinburgh

SSPD 2016

## Important Dates:

Submission of Papers: 22nd April 2016

Notification of Paper Acceptance: 24th June 2016

Final version of Paper Due: 22nd July 2016

The Sensor Signal Processing for Defence Conference is organised by the University Defence Research Collaboration (UDRC) in Signal Processing. SSPD 2016 aims to bring together researchers from academia, industry and government organisations interested in Signal Processing for Defence.

**Call for papers: [www.sspdconference.org](http://www.sspdconference.org)**

Papers are solicited from the following areas:-

- Array Signal Processing
- Image Processing
- Radar, Sonar and Acoustic
- Multimodal Signal Processing
- Multi-Target Tracking
- Signal Acquisition and Sensor Management
- Multiple-input and multiple-output (MIMO)
- Data Fusion
- Source Separation
- Anomaly Detection
- Distributed Signal Processing
- Low Size Weight & Power Solutions
- Target Detection and Identification
- Electro-Optic Sensing

All submitted papers will be peer reviewed. We are awaiting confirmation of Technical Sponsorship from the IEEE Signal Processing Society and IEEE Aerospace and Electronic Systems Society. Sponsored by Dstl and EPSRC.

Expressions of interest – email [janet.forbes@ed.ac.uk](mailto:janet.forbes@ed.ac.uk)

